The University of Sheffield
Faculty of Science
Department of Physics and Astronomy

Time-resolved photophysics of orange carotenoid protein trapped in trehalose-sucrose glass films

James P. Pidgeon

Supervised by Dr. Jenny Clark

A thesis submitted for the degree of
Doctor of Philosophy

December 2022

Abstract

This thesis presents studies on the photophysics of the orange carotenoid protein (OCP), a natural single-carotenoid-binding protein found in cyanobacteria, here binding canthaxanthin.

We initially studied OCP to test a hypothesis forwarded in studies of light-harvesting complexes (LHCs) from purple photosynthetic bacteria. A protein-induced carotenoid twist in some LHCs putatively sensitises intramolecular singlet fission (SF), thus yielding the relatively long-lived (microsecond) triplet states observed. SF has promise in boosting solar photovoltaic efficiency, among other applications with a presently unmet requirement of microsecond triplet lifetimes. OCP is among the simplest systems for a direct test of the twist-induced intramolecular SF hypothesis.

To prevent artefacts associated with its native photoprotective function involving a light-induced conformational change, we trap OCP in a trehalose-sucrose glass matrix, which we demonstrate yields identical initial photophysics to conventional buffer measurements.

We found that OCP-twisted canthaxanthin does not yield the triplet population promised by the aforementioned studies. Indeed, a follow-up study inspired by this work (included as an appendix here) shows that SF in those LHCs proceeds on adjacent carotenoid and bacteriochlorophyll molecules, and significantly contributes to solar energy harvesting.

We then tested a recent suggestion in the OCP literature that the light-induced photoconversion in OCP is triggered by a long-lived carotenoid singlet-like feature, dubbed S*. By examination of the pump wavelength dependence on the OCP photophysics in films and in buffer, we show that S* does not correlate with the photoconversion yield, ruling out S* as a sole trigger of the process. Dark-adapted OCP was found to have significant ground-state heterogeneity, with S* arising from it.

We follow up with a hypothesis that the trigger is instead through a <1% yield

of intersystem crossing triplets, though we lack a direct measurement, owing to difficulty in measuring the low yield of photoproducts.

Declaration

The work within this thesis was completed by the author, unless explicitly stated in the text where the work involves collaboration. Throughout, the first person plural 'we' is used as in standard scientific convention. This work has never been submitted for a degree at any other institution. Excluding its appendices, this thesis is within the 80 000 word limit.

James P. Pidgeon

First submission
December 2022

Minor corrections
July 2023

Acknowledgements

It has been fantastic working in Sheffield, and among my general thanks, I would like to specifically thank several people.

I first thank my supervisor, Jenny Clark. She is a brilliant supervisor. All the enthusiastic discussions about new results, all the scientific writing advice, all the general support in making Fast Spectroscopy a great group to work in – I couldn't imagine a better supervisor. Thank you.

Second, I thank my long-time collaborator, George A. Sutherland. It was his idea to study the orange carotenoid protein, and he synthesised the vast majority of protein/trehalose samples studied in this thesis. It has been fantastic working with you the past few years, thank you.

Third, I thank Shuangqing (Simon). Thank you for all your help throughout with setup building, on experimental days, and for your input on the direction of the projects.

I thank Daniel P. and Andrew for getting me started in the cleanroom and laser labs, and for introducing me to carotenoids. I extend my thanks to David, who showed me around the transient absorption systems, and inspired my more serious use of Python. I thank Kyriacos, Rahul, and Kirsty for their help in the BODIPY dye microcavity work, among other experiments using your equipment. Sayantan, thank you for your laser expertise; many useful non-linear optics discussions. Thank you to the present Fast Spectroscopy group members; Daniel H., Ravi, Rob, Eman, Samara, and Robbie; it's been great fun to work with and get to know you. Many thanks to others for their input, help, encouragement, and some good laughs over the years: Mack, Jozra, Sandra, Francesco, Harry, Yoichi, Dan F., Pete, Ravi, Tom, ... – thank you. You have all made Sheffield such a terrific place to be in throughout my PhD. Special thanks to Amanda for all your support throughout the past few years; it really has helped me get the most out of it.

Finally, I would like to thank my parents, Yvonne and Bob, and my siblings, Mike, Connie, and George, for all their encouragement and support. I really am

lucky to be a Pidgeon. Thank you.

Funding: James P. Pidgeon thanks the EPSRC for funding support through a Doctoral Training Partnership Scholarship (grant code: EP/R513313/1).

Publications

G. A. Sutherland, D. Polak, D. J. K. Swainsbury, S. Wang, F. C. Spano, D. B. Auman, D. G. Bossanyi, J. P. Pidgeon, A. Hitchcock, A. J. Musser, J. E. Anthony, P. L. Dutton, J. Clark, and C. N. Hunter, 'A Thermostable Protein Matrix for Spectroscopic Analysis of Organic Semiconductors', *Journal of the American Chemical Society* **142**, 13898–13907 (2020).

G. A. Sutherland[†], J. P. Pidgeon[†], H. K. H. Lee, M. S. Proctor, A. Hitchcock, S. Wang, D. Chekulaev, W. C. Tsoi, M. P. Johnson, C. N. Hunter, and J. Clark, 'Twisted Carotenoids Do Not Support Efficient Intramolecular Singlet Fission in the Orange Carotenoid Protein', *The Journal of Physical Chemistry Letters* **14**, 6135–6142 (2023).

S. Wang[†], G. A. Sutherland[†], J. P. Pidgeon, D. J. K. Swainsbury, E. C. Martin, C. Vasilev, D. J. Gillard, R. K. Venkatraman, D. Chekulaev, A. I. Tartakovskii, C. N. Hunter, and J. Clark, 'Singlet fission contributes to solar energy harvesting in photosynthesis', in submission at *Science* (November 2022).

J. P. Pidgeon[†], G. A. Sutherland[†], M. S. Proctor, A. Hitchcock, S. Wang, D. Chekulaev, R. Jayaprakash, R. K. Venkatraman, M. P. Johnson, C. N. Hunter, and J. Clark, 'Transient spectroscopy on orange carotenoid protein trapped in trehalose glasses show that photoswitching is not triggered by dark singlet states', in preparation.

D. Z. Hook, S. Wang, D. T. W. Toolan, R. C. Kilbride, D. J. Gillard, R. K. Venkatraman, J. P. Pidgeon, and J. Clark, 'The origin of high photochemical stability in car paint: rapid nonradiative decay in Pigment Red 254', in preparation.

[†]These authors contributed equally.

Conference presentations

The University of Sheffield, LaserLab 1st Anniversary Symposium, Sheffield, United Kingdom (June 2019) – Poster: 'New BODIPY Dyes Designed for Polaritonics'.

13th International Conference on Optical Probes of Organic and Hybrid Optoelectronic Materials and Applications (OP2019), Vilnius, Lithuania (July 2019) – Poster: 'New BODIPY Dyes Designed for Polaritonics'.

The University of Sheffield, Materials and Biological Physics Group Away day, Sheffield, United Kingdom (January 2020) – Talk: two-minute flash presentation summarising current PhD work. Poster: 'New BODIPY Dyes Designed for Polaritonics'.

IOP Biological Physics Group, Early Career Online One-Day Meeting, online (December 2020) – Talk: 'Femtosecond spectroscopy of trapped orange carotenoid protein / A twist in the chromophore backbone is not the determinant for generation of pairs of long-lived excited states'.

The University of Sheffield, Virtual Science Graduate School Showcase 2020, online (January 2021) – Poster: 'Femtosecond spectroscopy of trapped orange carotenoid protein'.

Royal Society of Chemistry, Faraday Joint Interest Group Conference 2021, online (March 2021) – Poster: 'Trapping Protein Conformations: Ultrafast Spectroscopy of Active/Inactive Orange Carotenoid Protein'.

International Carotenoid Society, The 1st Virtual International Conference on Carotenoids (VICC 2021), online (June 2021) – Talk: 'Time-resolved spectroscopy of trapped orange carotenoid protein – questioning the role of S* as a photocycle

trigger'.

Gordon Research Seminar (GRS), Electronic Processes in Organic Materials, Renaissance Tuscany Il Ciocco, Italy (June 2022) – Poster: 'Orange carotenoid protein photocycle is not triggered by long-lived singlets'.

Gordon Research Conference (GRC), Electronic Processes in Organic Materials, Renaissance Tuscany Il Ciocco, Italy (June/July 2022) – Poster: 'Orange carotenoid protein photocycle is not triggered by long-lived singlets'. **Award: Royal Society of Chemistry, *Sustainable Energy & Fuels* Poster Prize.**

Royal Society of Chemistry, Faraday Joint Interest Group Conference 2023, Sheffield, United Kingdom (April 2023) – Talk: 'Singlet fission occurs through intermolecular heterofission in purple bacterial photosynthetic complexes and contributes to solar energy harvesting'.

Contents

Chapter 1

Introduction

To mitigate the potential crises resulting from anthropogenic climate change, it is imperative we transition to clean methods of energy production.[1] Solar energy harvesting using photovoltaics is likely to play an important role in this,[2] as is clear from its currently untapped potential: estimates place the total average solar radiation power available at Earth's surface around 1000 times the current total worldwide power consumption.[3,4]

Current progress in solar photovoltaic deployment is promising. In 2021, 3.7% of electricity worldwide was generated by solar energy harvesting, a record following an average growth of 33% per year for the last ten years, and continuing this growth up to 2030 is suggested to be key in meeting proposed net-zero carbon dioxide emissions by 2050.[5,6] The vast majority of commercial photovoltaic technology incorporates the semiconductor silicon, which has shown promising reductions in its monetary cost of deployment in recent years.[7]

However, the maximum theoretical power conversion efficiency in single-junction silicon photovoltaics is limited to ∼33%, the 'Shockley-Queisser limit'.[8] The best real single-junction silicon devices made in laboratories show efficiencies of $26.7 \pm 0.5\%$,[9,10] fast approaching the Shockley-Queisser limit, while currently deployed commercial devices show efficiencies of around ∼15–20%.

It is apparent that efficiency improvements for solar photovoltaics are required along the path to net-zero by 2050, but the Shockley-Queisser limit looms as a potential barrier to efficiency improvements and, arguably, continued deployment. Considering that the key loss mechanisms leading to the ∼33% limit are thermalisation of high-energy photons above the silicon band-gap (1.1 eV) and non-absorption of low-energy photons below it, we wonder if these losses can be mitigated in next-generation device designs.[11]

Indeed, downcoversion of high-energy photons into multiple pairs of charge carriers (rather than one pair post-thermalisation) within photovoltaics may be achieved through singlet fission (SF), a spin-allowed excitation multiplication process where a singlet excited state converts into a pair of triplet states.[12–15] Theoretical calculations suggest that SF-based tandem silicon photovoltaics yield maximum power conversion efficiencies around ∼45%, far exceeding the Shockley-Queisser limit of ∼33%.[16,17] Aside from potentially boosting solar photovoltaic efficiency, SF may also see application in non-linear optics,[18–20] OLEDs,[21] and quantum technologies.[22–25] However, despite the promise of SF,[26,27] practical application is currently limited due to the small number of known SF materials, none of which appears ideal.[11,14]

One group of SF material that merits further investigation are the carotenoids.[28] They are ubiquitous in nature, taking key roles within the light-harvesting complexes (LHCs) in plants and bacteria.[29] As the (bacterio)chlorophylls are non-absorbing in the green region, carotenoids take the role of green light absorption, with subsequent energy transfer to the (bacterio)chlorophylls, thus boosting the photosynthetic yield.[30] Carotenoids also take roles in non-photochemical quenching of excess absorbed light energy, singlet oxygen quenching,[31] and for colouration[32] (the latter also within many animals, including lobsters[33] and canaries[34]).

Carotenoids have been demonstrated to undergo rapid intermolecular SF between aggregated molecules. However, as most of the resulting triplets decay on timescales too short (sub-nanosecond)[35–40] for the aforementioned applications, aggregated carotenoids are presently unsuitable as a SF material.[12] However, intramolecular SF (intra-SF) on a single carotenoid yielding ultrafast formation of long-lived (microsecond timescale) triplets has been forwarded in certain LHCs from purple photosynthetic bacteria.[41–45] Reportedly, a carotenoid twist induced by the protein environment stabilises the two geminate triplets at each end of the carotenoid molecule.[41,42] If this is indeed the case, it is an exciting result, as synthetic protein designs could sensitise and tune long-lived triplets for the various aforementioned applications.[40,46] However, the LHCs under study contain multiple carotenoids and bacteriochlorophylls in close contact, with no direct measurement presently for intra-SF propensity in a single twisted carotenoid.

To test for the putative intra-SF within a single twisted carotenoid, we initially turned to maquettes. These are man-made synthetic proteins consisting of a 4-α-helical structure encapsulating a spectroscopic material of interest.[46,47] By modifying the inner amino acid residues, we can tune the properties of the encapsu-

lated active material, in this case a twist of a single carotenoid that hypothetically sensitises intra-SF. Unfortunately, our recent study on maquettes (Ref.[40]) showed that binding of a single conjugated molecule is unlikely, and carotenoid-binding maquettes were demonstrated to form misfolded supramolecular assemblies with ∼10–60 nm diameter.[40]

As the synthetic proteins presently appear difficult for a controlled study testing intra-SF reactivity in twisted carotenoids,[40] we look (again) to nature for the simplest possible caroteno-proteins for assay of intra-SF. It turns out that one is the orange carotenoid protein (OCP),[48–55] which takes a non-photochemical quenching function in cyanobacteria. See Figure 3.2 for structural model and absorbance spectra. Crucially, it binds only one keto-carotenoid. In the inactive 'orange form' of OCP (OCPo) this carotenoid is twisted, while in its active 'red form' (OCPr) the carotenoid is relatively planar,[48,50] presenting a simpler system to test for twist-induced SF propensity than the LHCs. However, a complication arises in the native photoactivity of OCP: an OCPo→OCPr phototransition is mediated by absorption of white-light, while back-conversion from OCPr→OCPo may occur in the dark. This makes isolated OCPo and OCPr challenging to study with spectroscopy without the use of potentially artefact-inducing techniques, such as: the use of low temperature[56] which is non-physiological; the use of OCP homologues[57] or mutants[58–61] which may not demonstrate the same photophysics as native OCP; and spectral deconvolution techniques[51,53,62–65] whose assumptions are not reasonable for carotenoid systems.[66–70]

As an artefact-free means to study OCPo and OCPr binding canthaxanthin (CAN) at room temperature without complete OCPo⇌OCPr transitions, we fix each conformation in trehalose-sucrose glass. Both trehalose and sucrose are natural sugars, with trehalose biosynthesised by plants under stressful conditions (*e.g.* drought) to protect native protein foldings.[71,72] We show in both Chapters 5 and 6 that trehalose-sucrose glass (herein 'trehalose') indeed fixes OCPo and OCPr in their native conformations, preventing the large conformational change associated with their overall transitions.

We demonstrate in Chapter 5 that both OCPo and OCPr in trehalose glass show no signatures of efficient triplet generation. This is despite the CAN twist in OCPo and relative planarity in OCPr, the former suggested to permit localisation of the two geminate intra-SF triplets at each end of the CAN molecule.[41,42] Furthermore, a review of the aforementioned literature on purple bacterial LHCs shows that their results appear to be incompatible with SF from an intramolecular

origin. We conclude that intra-SF does not occur along a single twisted CAN in OCP, and is unlikely to occur in purple bacterial LHCs, contrary to the currently purported view.[41–45]

Since our results on OCP do not support a carotenoid intra-SF scheme in purple bacterial LHCs, we question what mechanism quickly generates long-lived triplets in those systems. Indeed, the study on OCP inspired a study primarily headed by Shuangqing Wang and George A. Sutherland on those LHCs, included as Appendix A (the thesis author contributed to synthesis of the study and some measurements). We found that SF occurs in an intermolecular heterofission scheme, with the triplets localising on adjacent carotenoid and bacteriochlorophyll molecules, and that the SF process boosts the carotenoid-to-bacteriochlorophyll energy transfer by up to 27%, improving the photosynthetic yield at the cost of increased risk of oxidative damage to the bacteria.

Following our initial studies on OCPo/OCPr in trehalose glass, we noted some points raised in the OCP literature meriting further investigation, namely: (1) its OCPo→OCPr photoconversion mechanism;[48–51,53,54,59,60,73] (2) the subsequent non-photochemical quenching (NPQ) process by OCPr upon binding to the phycobilisomes (the light-harvesting antenna in cyanobacteria).[55,74–78] Point (1) is of relevance as understanding the mechanism of photoconversion is interesting from an evolutionary standpoint,[52] but also as the photoswitch in OCP appears to be unique,[79,80] and a better understanding may lead to new synthetic designs for molecular machinery, with potential applications for light adaptation[81] or energy storage.[82] Point (2) is of relevance as understanding NPQ has led to further understanding of the overall photosynthetic process in other systems; for example, tuning of the NPQ process in tobacco has been shown to boost dry mass per plant by 14–20%.[83] Indeed, certain cyanobacterial strains are well-established food crops in the form of 'spirulina',[84–86] and further implicated in the production of chemical feedstock for (*e.g.*) biofuels, while not requiring conventional arable land.[87–90] Meanwhile, the cyanobacteria *Prochlorococcus* and *Synechococcus* alone fix ∼11.4% of the global carbon mass fixed per year,[91,92] while other cyanobacteria contribute to nitrogen fixation,[93,94] and some produce hydrogen gas under certain growth conditions.[94–96] Clearly, any potential photosynthetic yield enhancement in cyanobacteria has wide-ranging benefits in the face of climate change.

Therefore, for point (1), we set out to test a suggestion in the OCP literature proposing that the transition is triggered by a relatively long-lived carotenoid

singlet-like feature, dubbed S*.[53,60,61] In Chapter 6, we verify that our OCPo in trehalose glass gives similar results to OCPo in solution despite the overall transitions being prevented in the former, permitting elucidation of the photoconversion process by studying trehalose films. We then find that the pump (excitation) wavelength dependence on S* (in trehalose) and the OCPo→OCPr photoconversion yield (in buffer) do not match, which suggests that S* cannot be the sole trigger for the photocycle in OCP. In fact, S* arises from significant ground-state heterogeneity in OCPo; we hypothesise that this 'S*-like form' of OCPo that is predominantly excited with light ≤480 nm shares its origin in a feature previously seen in studies on carotenoids in solution.[97,98]

Having rejected the literature hypothesis regarding S*, we follow up on our studies on point (1) by presenting a hypothesis that photoconversion is instead triggered by keto-carotenoid triplet states formed by low yield through intersystem crossing (ISC). In Chapter 7 we explain our synthesis of this hypothesis along with preliminary measurements displaying circumstantial evidence. Ultimately, we lack a direct measurement confirming or rejecting this hypothesis, largely owing to the difficulty in measuring photoproducts with around 0.1–1.0% yield.[53,59,80,99]

Recalling that the mechanism of NPQ by OCPr bound to phycobilisomes is not well-understood (point (2)), we were motivated to study the mechanism by probing the radiative and non-radiative decay properties of OCPo and OCPr in trehalose. Indeed, our preliminary measurements of the emission spectra of OCPo/OCPr in trehalose suggest that OCPo is relatively emissive in comparison to OCPr, see Appendix C. Time-resolving the rapid fluorescence emission (∼100 fs time constant for carotenoids[30,100]) is a necessity to further characterise the (non-)radiative decay, and we therefore set out to build a transient grating photoluminescence spectroscopy (TGPLS) setup,[101] which should yield the time resolution and broadband detection required. Despite key progress made, as described in Section 4.6, the TGPLS setup is not currently operational, in part due to the COVID-19 pandemic.

We note that another motivation for the construction of the TGPLS is the study and characterisation of other samples based on π-conjugated molecules studied by our group with rapid emission, in particular those showing a significant angular dependence to their emission. In Appendix D, we present the results of an initial project involving characterisation of new BODIPY dye structures designed for formation of cavity-polaritons upon incorporation into microcavities. These

indeed show a marked angular dependence to their steady-state reflectivity and emission.

Chapter 2

Background

2.1 Introduction

In this chapter, we outline the current underlying understanding and theory behind both π-conjugated molecules and the sub-class of carotenoids (specifically β-carotene-like carotenoids). Key relevant literature for carotenoids and the orange carotenoid protein is reviewed throughout Chapters 5, 6, and 7, particularly in their introductions. Here, we keep the discussion somewhat broader for applicability to the conjugated molecules of interest in Appendix A (bacteriochlorophylls) and in Appendix D (BODIPY dyes).

The authors note this chapter is a fairly light overview of the current understanding. A fully comprehensive description of all effects is beyond the scope of this thesis. More detail may be found in the references of this chapter. In particular, we suggest Refs.[30,31,100,102] for carotenoids, Refs.[103–106] for π-conjugated molecules more broadly, and Refs.[12–14] for singlet fission specifically.

2.2 Electronic structure

2.2.1 The Born-Oppenheimer approximation

Spectroscopy deals with the interaction of light with matter and the associated changes in energetics, so we would like to describe the energies of our concerned molecules using quantum physics. In principle, any system may be written in quantum terms of a wavefunction Ψ that is generally a function of spatial and temporal coordinates. Then the physical observables may be obtained through operators, which in the case for energy E would be the Hamiltonian operator H.

This gives us our familiar form of the time-independent Schrödinger equation[†]

$$H\,|\Psi\rangle = E\,|\Psi\rangle \tag{2.1}$$

where the energy eigenvalues are termed stationary states.[107] For our molecules, this Hamiltonian may be considered as three contributions: the electronic term $H_{\text{e–e}}$ purely from the electrons (their kinetic energies and electron-electron electrostatic potential energies from Coulombic repulsions); the nuclear term $H_{\text{n–n}}$ similarly from the nuclei (nuclear kinetic energies and nuclear-nuclear electrostatic potential energies from Coulombic repulsions); and a cross electron-nuclear term $H_{\text{e–n}}$ (which is purely electrostatic potential energy from mutual Coulombic attraction between electrons and nuclei). So we write the Hamiltonian as

$$H(\mathbf{r},\mathbf{R}) = H_{\text{e–e}}(\mathbf{r}) + H_{\text{n–n}}(\mathbf{R}) + H_{\text{e–n}}(\mathbf{r},\mathbf{R}) \tag{2.2}$$

where $\mathbf{r} \equiv \{\mathbf{r}\}$ is the set of electronic coordinates and $\mathbf{R} \equiv \{\mathbf{R}\}$ is the set of nuclear coordinates. The electronic term may be written

$$H_{\text{e–e}}(\mathbf{r}) = \underbrace{\sum_i \frac{\mathbf{p}_i^2}{2m}}_{T_{\text{e}}(\mathbf{r})} + \underbrace{\frac{1}{2}\sum_{i,j\neq i}\frac{e^2}{4\pi\varepsilon_0|\mathbf{r}_i-\mathbf{r}_j|}}_{V_{\text{e–e}}(\mathbf{r})} \tag{2.3}$$

where the first term ($T_{\text{e}}(\mathbf{r})$) describes electronic kinetic energy and the second term ($V_{\text{e–e}}(\mathbf{r})$) describes the electronic electrostatic potential.[‡] $\mathbf{p}_i$ is the momentum operator on electron i, m is the mass of one electron, e is the elementary charge, and ε_0 is the vacuum permittivity. Similarly, the nuclear term may be written

$$H_{\text{n–n}}(\mathbf{R}) = \underbrace{\sum_\alpha \frac{\mathbf{P}_\alpha^2}{2M_\alpha}}_{T_{\text{n}}(\mathbf{R})} + \underbrace{\frac{1}{2}\sum_{\alpha,\beta\neq\alpha}\frac{Z_\alpha Z_\beta e^2}{4\pi\varepsilon_0|\mathbf{R}_\alpha-\mathbf{R}_\beta|}}_{V_{\text{n–n}}(\mathbf{R})} \tag{2.4}$$

where the first term ($T_{\text{n}}(\mathbf{R})$) and second term ($V_{\text{n–n}}(\mathbf{R})$) are the nuclear kinetic energy and nuclear electrostatic potential terms respectively. $\mathbf{P}_\alpha$ is the momentum operator on nucleus α, M_α is the mass of nucleus α, and Z_α is the proton number of nucleus α. Finally, the cross electron-nuclear term may be written

$$H_{\text{e–n}}(\mathbf{r},\mathbf{R}) = V_{\text{e–n}}(\mathbf{r},\mathbf{R}) = -\sum_{i,\alpha}\frac{Z_\alpha e^2}{4\pi\varepsilon_0|\mathbf{R}_\alpha-\mathbf{r}_i|} \tag{2.5}$$

[†]In this thesis we omit 'hats' from generic operators, *e.g.* $\hat{H} \equiv H$, to avoid confusion later between operators and unit vectors.

[‡]Note that the factor $1/2$ offsets a double-counting contribution. The factor and summation may be re-written $\frac{1}{2}\sum_\alpha\sum_{\beta\neq\alpha} \leftrightarrow \sum_\alpha\sum_{\beta>\alpha}$.

which is purely an electrostatic potential term $V_{\text{e–n}}(\mathbf{r}, \mathbf{R})$; note that as it arises from Coulombic attraction, it carries a minus sign.

A typical carotenoid molecule (*e.g.* β-carotene) contains around 300 electrons and 100 nuclei. This is impossible to solve with Equation 2.1 *via* analytical or computational techniques. In fact, systems involving only a few bodies such as a toy model of a hydrogen atom in vacuum are analytically solvable, with heavier atoms such as a carbon atom impossible.[104,108] Fortunately, we can make a number of assumptions that give us descriptive and accurate results for the case of carbon, and in turn our conjugated molecules.

A key simplifying assumption concerns the separation of the behaviour of the electrons and the nuclei, called the Born-Oppenheimer approximation.[109] The electrostatic forces on both are mutual, yet the electrons are $\sim 10^4$ times less massive than the nuclei, so the motion of the electrons will be much faster than the 'slow' nuclei. We can therefore decouple the electrons and the nuclei. Initially (without applying the approximation yet) we can factorise the total wavefunction (neglecting spin for now)

$$|\Psi_{k,\nu}(\mathbf{r}, \mathbf{R})\rangle = |\psi_k(\mathbf{r}; \mathbf{R})\rangle \, |\chi_{k,\nu}(\mathbf{R})\rangle \tag{2.6}$$

into an electronic component ψ_k labelled with electronic state k, and a nuclear component $\chi_{k,\nu}$ associated with the electronic state k and also labelled with a nuclear quantum number ν. We define a Born-Oppenheimer Hamiltonian

$$\begin{aligned} H_{\text{BO}}(\mathbf{r}; \mathbf{R}) &= H(\mathbf{r}, \mathbf{R}) - T_{\text{n}}(\mathbf{R}) \\ &= H_{\text{e–e}}(\mathbf{r}) + H_{\text{e–n}}(\mathbf{r}, \mathbf{R}) + V_{\text{n–n}}(\mathbf{R}) \end{aligned} \tag{2.7}$$

which the electronic component $|\psi_k\rangle$ is defined to be an eigenstate of, such that

$$H_{\text{BO}}(\mathbf{r}; \mathbf{R}) \, |\psi_k(\mathbf{r}; \mathbf{R})\rangle = E_k(\mathbf{R}) \, |\psi_k(\mathbf{r}; \mathbf{R})\rangle \tag{2.8}$$

yielding an eigenvalue $E_k(\mathbf{R})$. The eigenvalue is dependent on the nuclear coordinates $\mathbf{R}$ and defines an adiabatic potential energy surface. Both $H_{\text{BO}}(\mathbf{r}; \mathbf{R})$ and $\psi_k(\mathbf{r}; \mathbf{R})$ depend only weakly parametrically on the position of the nuclei. Concerning the total Hamiltonian, we combine Equations 2.1–2.8, and from neglecting the non-adiabatic coupling terms through the aforementioned 'slower nuclei' justification, we obtain

$$H \, |\psi_k(\mathbf{r}; \mathbf{R})\rangle \, |\chi_{k,\nu}(\mathbf{R})\rangle \simeq [T_{\text{n}}(\mathbf{R}) + E_k(\mathbf{R})] \, |\psi_k(\mathbf{r}; \mathbf{R})\rangle \, |\chi_{k,\nu}(\mathbf{R})\rangle \, . \tag{2.9}$$

Inspecting the contents of the square bracket, it is apparent that the 'adiabatic potential energy surface' $E_k(\mathbf{R})$ represents an effective potential in which the

nuclei move with kinetic energy $T_{\mathrm{n}}(\mathbf{R})$. The variation of $E_k(\mathbf{R}_i)$ for a single nuclear coordinate $\mathbf{R}_i$ is shown schematically in Figure 2.1.[104]

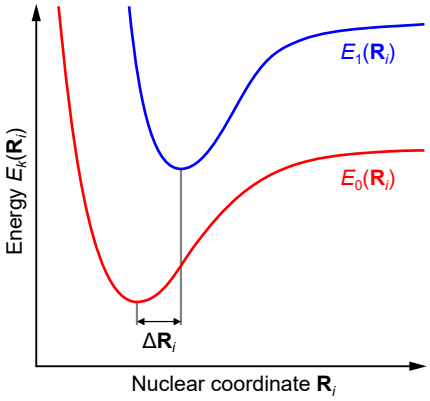

Figure 2.1 – Schematic of adiabatic potential energy surfaces for a π-conjugated molecule. A single nuclear coordinate in a one-dimensional representation is shown for simplicity. Note that the vibrational coordinate for minimum energy is different between $E_0(\mathbf{R}_i)$ and $E_1(\mathbf{R}_i)$, arising from differences in electron density between nuclei for the different electronic states; this results in different electrostatic screenings between the nuclei, and thus different equilibrium distances.[103] This difference in the 'equilibrium geometry' is $\Delta\mathbf{R}_i$.

In addition to the physical 'slower nucleus' basis outlined above, this separation also has an empirical basis. The experimentally measured energy levels associated with the electronic, vibrational, and rotational contributions (latter two associated with the nuclear contribution) has a hierarchy

$$\Delta E_{\mathrm{electronic}} \gg \Delta E_{\mathrm{vibrational}} \gg \Delta E_{\mathrm{rotational}} \tag{2.10}$$

which also enables us to further separate $|\chi_{k,\nu}(\mathbf{R})\rangle$ into a vibrational and rotational component. However, our studies here will not concern the rotational component; in general for conjugated molecules, the measured spectra are broader than the splitting for the rotational energy levels, so they are not resolved.[103] Indeed, all our studied materials have no resolvable signatures due to the rotational component, so herein we omit it and use 'nuclear' and 'vibrational' interchangeably, with ν taken as the vibrational quantum number.

We neglected spin up to this point, but we can also factorise the spin contribution to the total Hamiltonian, assuming that the interactions between the electron spins and orbital angular momenta are negligible. This assumption is important as it leads to the spin selection rules (see Section 2.3.5), and cases

where it breaks down lead to interesting phenomena (*e.g.* intersystem crossing; see Section 2.3.7).[110] So we finally write

$$|\Psi_{k,\nu,\sigma}\rangle = |\psi_k\rangle\,|\chi_{k,\nu}\rangle\,|\varsigma_{k,\sigma}\rangle \tag{2.11}$$

with $\varsigma_{k,\sigma}$ the spin component associated with the electronic state k and additionally labelled with the spin character σ. In short, the separation of the electronic and nuclear behaviour is through the Born-Oppenheimer approximation. A corresponding physical phenomenon is the Franck-Condon principle, which will be discussed further in Section 2.3.3. We note for now that the Born-Oppenheimer approximation has been applied in much of the results of the following discussion.[104,107]

2.2.2 Hybridisation in carbon

As we are studying organic systems, it is useful to review how carbon covalently bonds with itself and hydrogen. A covalent bond may simply be thought of as a pair of electrons that are shared between two atoms. In spectroscopic notation, the orbital configuration of an isolated carbon atom may be written $1s^2\,2s^2\,2p^2$, or in a long form $1s^2\,2s^2\,2p_x{}^1\,2p_y{}^1\,2p_z{}^0$. As other atoms approach our isolated carbon atom, the energetic cost in promoting one of the 2s orbital electrons to the previously-empty $2p_z$ orbital is less than the energy liberated in the formation of bonds. As bonds form, the energies of the 2s and 2p orbitals become comparable, rendering them degenerate; hence hybridisation of the 2s and 2p orbitals occurs, forming new hybrid orbitals of mixed 2s and 2p character.

In the case of sp^3 hybridisation, the 2s and all three 2p orbitals are hybridised, giving 4 electrons each unpaired within four $2sp^3$ orbitals (note the superscript refers to the number of p-orbitals involved in hybridisation) with a configuration that may be written $1s^2\,2s^1\,2sp^3$. We emphasise that this is from the perspective of one carbon within some molecule. Examples where sp^3 hybridisation occurs include the carbons of ethane, $H_3C{-}CH_3$. An electron in a $2sp^3$ orbital of one carbon pairs with the 1s-orbital electron of hydrogen or another $2sp^3$-orbital electron from the other carbon. The resulting molecular (rather than atomic) orbital is termed a σ-orbital, and the associated covalent bond is termed a σ-bond. The bonds formed with sp^3 hybridisation are named single bonds (only one σ-bond), and are orientated at angle ∼109.5° from one another with allowed rotation.[103,104]

The case of sp^2 hybridisation is of particular interest for π-conjugated molecules, and is depicted diagrammatically between a pair of carbons in Fig-

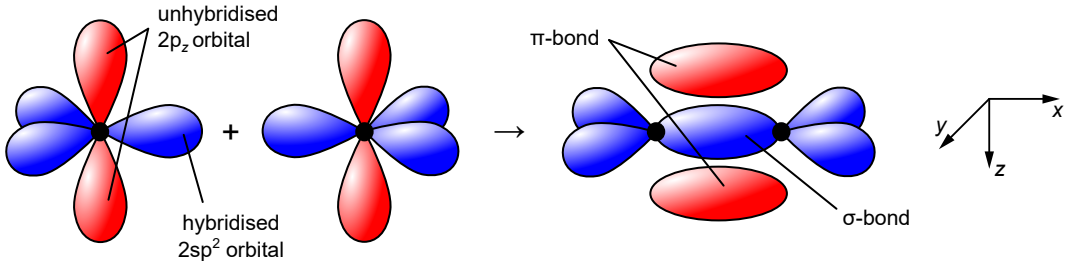

Figure 2.2 – Diagram of 2sp^2 hybridisation between a pair of carbon atoms, leading to a C=C double bond of one σ-bond and one π-bond. The carbon atoms (black circles) lie in a single plane (here the xy plane), and the 2sp^2 orbitals (and concomitant σ-bonds) lie in that plane with angular separation of 120° from each other. The 2p$_z$ orbitals project normally to that plane (here in the z-direction), and the concomitant π-bond forms above and below that plane. The 'three-dimensional' shapes diagrammatically represent regions of high electron density (high probability to find an electron). Note that the left side is not representing two isolated carbon atoms.[103,104]

ure 2.2. The 2s and two of the 2p orbitals (say 2p$_x$ and 2p$_y$) are hybridised, giving 3 electrons each unpaired in three 2sp^2 orbitals with a configuration of 1s^2 2s^1 2sp^2 2p$_z$^{1}. Examples where sp^2 hybridisation occurs include the carbons of ethene, H$_2$C=CH$_2$. Again, an electron in a 2sp^2 orbital of one carbon pairs with the 1s-orbital electron of hydrogen or another 2sp^3-orbital electron from the other carbon. The resulting molecular orbital (bond) is again termed a σ-orbital (σ-bond). Meanwhile, the electron in the 2p$_z$ orbital of one carbon pairs with that of the other, resulting in a molecular orbital (bond) that is termed a π-orbital (π-bond). Hence between the carbons there is one σ-bond and one π-bond, collectively referred to as a double bond. The σ-bonds about each carbon are distributed in a single plane (here the xy plane) orientated at an angle 120° from one another with restricted rotation about the double bond; a rotation would disrupt overlap between 2p$_z$ orbitals and therefore the π-bond lying parallel above and below the plane, which is energetically unfavourable. This restricted rotation leads to stable *cis-trans* isomers in organic molecules.[103,104]

In the case of sp^1 hybridisation, the 2s and one of the 2p orbitals (say 2p$_x$) are hybridised, giving 2 electrons each unpaired in two 2sp^1 orbitals with a configuration of 1s^2 2s^1 2sp^1 2p$_y$^{1} 2p$_z$^{1}. Examples where sp^1 hybridisation occurs include the carbons of ethyne, HC≡CH. The principle is analogous to that of sp^2 hybridisation (see above), although this time one σ-bond and *two* π-bonds are formed between the carbons, collectively referred to as a triple bond. The σ-bonds about

each carbon are distributed along a line (here parallel to x) orientated at an angle 180° from one another with, again, restricted rotation about the triple bond due to the π-orbitals.[103,104]

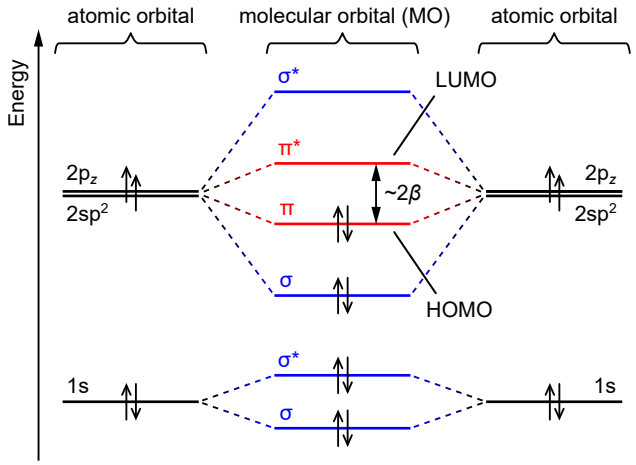

Figure 2.3 – Diagram of molecular orbitals between a pair of 2sp^2-hybridised carbon atoms, demonstrating the LCAO approach. A linear combination of two atomic orbitals gives two molecular orbitals of lower (bonding) and higher (antibonding) energy. The splitting $\sim 2\beta$ between bonding and antibonding orbitals is denoted for the π/π*-orbitals only. Here, the π-orbital is the HOMO, and the π*-orbital is the LUMO. See text for details. Note that the left and right sides are not representing two isolated carbon atoms.[103]

2.2.3 Atomic orbitals, molecular orbitals, and states

In the above discussion, we have implicitly used the linear combination of atomic orbitals (LCAO) approach to build up the molecular orbitals (MO), specifically the 'bonding' orbitals. Through another combination of the atomic orbitals, we can build up 'antibonding' orbitals, denoted with an asterisk/star (*e.g.* π*-orbital) as a shorthand. They are named 'antibonding' as there is an increase in energy upon their formation, unlike bonding orbitals.[108] A diagram of the energy level differences for bonding and antibonding orbitals for a pair of 2sp^2-hybridised carbons is shown in Figure 2.3, but the principle applies for a chain of similarly hybridised carbons also (*i.e.* a conjugated chain, represented with alternating single and double carbon-carbon bonds). The highest-energy MO that is occupied by a pair of electrons is called the highest occupied molecular orbital (HOMO), while the lowest-energy MO with no electrons is called the lowest unoccupied molecular orbital (LUMO). The HOMO and LUMO are collectively referred to as

the frontier orbitals, and are somewhat analogous to the valence and conduction bands of metallic conductors.[103]

The energetic difference between bonding/antibonding orbitals can be thought of as due to constructive/destructive interference between the electron density associated with the atomic orbitals, which screens/allows the electrostatic interaction between the nuclei.[103] The energetic separation (for a pair of identical constituent atoms) is approximately twice the 'exchange/resonance integral' β, labelled for the π- and π*-orbitals in Figure 2.3. The splitting 2β in conjugated molecules for π/π*-orbitals is typically ∼2.5 eV, significantly less than 2β for σ/σ*-orbitals, typically ∼8 eV. This is because the electron density associated with the π/π*-orbitals is not highly localised between the two nuclei, whereas it is highly localised for σ/σ*-orbitals; this is depicted for bonding orbitals in Figure 2.2. These different degrees of localisation affect the extent of the aforementioned screening, leading to the large difference in 2β between π/π*-orbitals and σ/σ*-orbitals. Hence, in conjugated molecules, a π-orbital and π*-orbital being the HOMO and LUMO respectively is typical, and excitations (promotion) of an electron from this HOMO to the LUMO may be possible with visible light (2.5 eV ∼ 500 nm), as long as various 'selection rules' are satisfied (see Section 2.3). Similar optical excitations involving the other molecular orbitals may occur with higher-energy excitation using UV-region light (8 eV ∼ 150 nm), although the photophysics discussed in this thesis will not concern these.[103]

As the energies in π-conjugated molecules are well-separated between the π/π*-orbitals and σ/σ*-orbitals, the σ/core-electrons effectively play the role of screening the electrostatic interactions between the π-electrons and nuclei. We can therefore approximate the σ-electron- and core-electron-associated contributions purely as a modification of the Coulombic potentials ($V_{\text{e–e}}$, $V_{\text{n–n}}$, $V_{\text{e–n}}$) to effective potentials ($V_{\text{e–e}}^{\text{eff.}}$, $V_{\text{n–n}}^{\text{eff.}}$, $V_{\text{e–n}}^{\text{eff.}}$) under which the π-electrons move. Then we can consider only the π-electrons within the equations discussed in Section 2.2.1, and consequently consider the π-electrons only when building up MOs. For example, we can modify the Coulombic electron-electron interaction term of Equation 2.3 into an effective potential

$$V_{\text{e–e}}(\mathbf{r}) = \frac{1}{2}\sum_{i,j\neq i}\frac{e^2}{4\pi\varepsilon_0|\mathbf{r}_i-\mathbf{r}_j|} \mapsto V_{\text{e–e}}^{\text{eff.}}(\mathbf{r}). \tag{2.12}$$

The screening role of the σ/core-electrons can also be treated as a static dielectric constant, which is useful in the exciton picture (see Section 2.2.4).

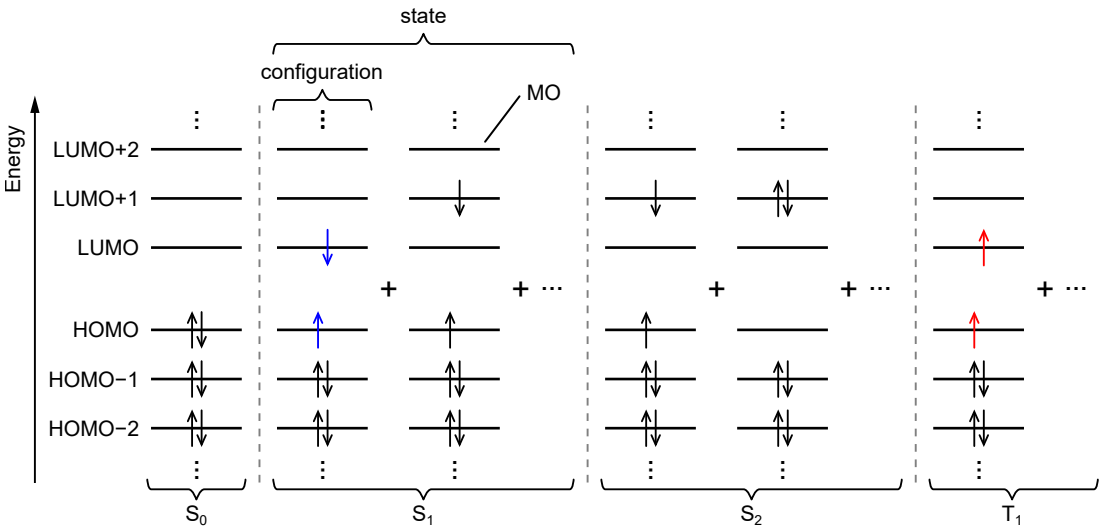

Figure 2.4 – The configuration interaction picture used in building up configurations and states in a molecule from the one-electron MOs. Configurations are only distinguished on MO occupancy, not on the electronic spins; the configuration including blue arrows is equivalent to that including red arrows, but they contribute to singlet and triplet states respectively. See text for further details.[103]

We note that the many-electron 'states' for a molecule do not correspond to the one-electron molecular orbitals, or even 'configurations'. One theoretical picture for building up energetic states for a molecule is the configuration interaction picture, which we illustrate for a fictional molecule in Figure 2.4. Here, the states are built up from a linear combination of configurations, with 'configuration' referring to how electrons are distributed among the MOs. A combination of configurations for a state rather than a singular contribution is necessary due to electron-electron interactions, which are ignored in the initial construction of molecular orbitals (since they are based on one-electron atomic orbitals), but have to be considered in building up states. Further details about the configuration interaction picture may be found in Ref.[105] – here we simply highlight the distinction between MOs, configurations, and states. In particular, if an electron is excited from the HOMO to LUMO, the molecule changes from a configuration giving the ground state to a configuration giving some excited state. But the HOMO itself is not a ground state, and similarly the LUMO itself is not an excited state; they are one-electron molecular orbitals. Furthermore, the HOMO-LUMO energy difference only roughly approximates the ground-excited state energy difference, largely due the former ignoring electrostatic interactions between the new electron in the LUMO and its abscence (electron-hole) in the HOMO (see Section

2.2.4), along with ignoring spin interactions (see Section 2.2.5). We also note that the same configuration(s) may lead to different states; a 'configuration' does not distinguish between cases of the same occupancy but different electron spins, whereas states do, leading to distinct singlet and triplet states in a molecule with different energetics and properties. For example, referring to Figure 2.4, the configuration with the blue arrows pointing antiparallel (so antiparallel electron spins) is formally the same configuration as the one with red arrows pointing parallel (so parallel electron spins), yet the former contributes to a singlet S_1 state while the latter corresponds to a triplet T_1 state.[103] We discuss singlets and triplets in some detail in Section 2.2.5.

2.2.4 Excitons

The promotion of an electron from the HOMO to the LUMO leaves an absence of that electron in the HOMO. This vacancy can be treated as a quasiparticle called an electron-hole (herein 'hole', h^+) with a positive charge of $+e$. We can use this treatment rather than considering the electrons of the LUMO and the MOs below the LUMO, since filled MOs are inert.[108] This hole can interact with the surroundings, and in particular electrostatically attract to the electron (e^-) of charge $-e$ that had been promoted to the LUMO prior. The resulting electron-hole bound pair is termed an 'exciton', and has overall zero charge. Since there is a binding energy associated with the electrostatic attraction, the exciton has less energy than the unbound electron and hole.

In the case of a number of interacting conjugated molecules (in *e.g.* a crystal), the relative static permittivity[†] is typically fairly small ($\varepsilon_r \sim 3.5$), resulting in weak screening of the electrostatic attraction between the electron and the hole.[103] With this strong electrostatic attraction, the excitons are strongly bound (0.1–1 eV binding energy[103,110]) and typically localised on a single molecule/crystal site. These strongly-bound and highly-localised excitons are termed 'Frenkel excitons', and are shown diagrammatically in Figure 2.5a. These excitons can delocalise to several sites at temperatures approaching 0 K, which can yield phenomena such as superradiance.[112–114]

In the case of inorganic semiconductors, ε_r is typically larger ($\varepsilon_r \sim 12$), which leads to the electrostatic attraction between the electron and hole being more

[†]Relative static permittivity (along with absolute static permittivity) are sometimes called 'dielectric constant', but this name is regarded as obsolete by the IUPAC.[111]

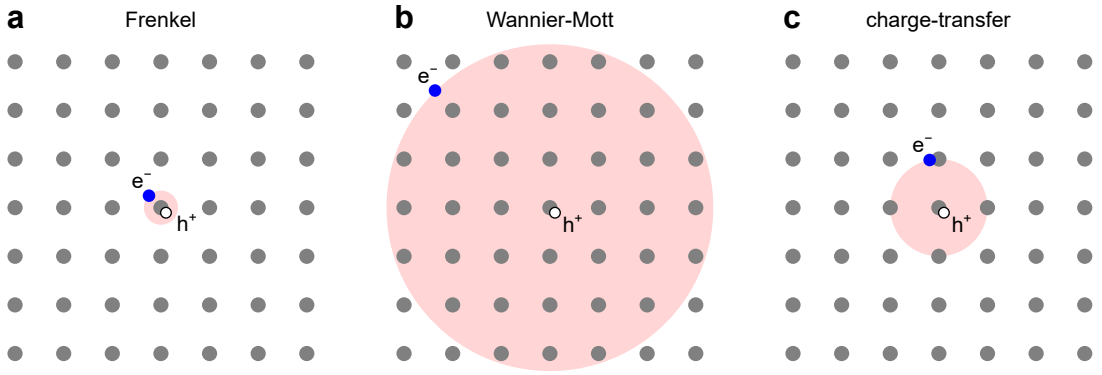

Figure 2.5 – Key types of exciton and their spatial extent. The small grey circles denote molecular sites within a crystal, and the pink circles demonstrate the extent of the exciton wavefunction. (a) Frenkel excitons are highly localised, with 0.1–1 eV electron-hole binding energy, and are typical in organic semiconductors. (b) Wannier-Mott excitons are highly delocalised, have ∼10 meV electron-hole binding energy, and are typical in inorganic semiconductors. (c) Charge-transfer excitons are intermediate between Frenkel and Wannier-Mott excitons.[103,115]

strongly screened. This results in the excitons being very weakly bound (∼10 meV binding energy) and thus highly delocalised. These weakly-bound and delocalised excitons are 'Wannier-Mott excitons', shown diagrammatically in Figure 2.5b.[103]

Finally, the case of an intermediate exciton between the extremes of the Frenkel and Wannier-Mott excitons is termed a 'charge-transfer exciton'. Here, the exciton is moderately localised, with the electron and hole typically lying on adjacent molecules. This is shown diagrammatically in Figure 2.5c.[103,115]

As we are working primarily with conjugated molecules in this thesis, further discussions herein regarding excitons are specifically referring to Frenkel excitons, unless stated otherwise. We note that in this thesis, we study monomeric carotenoids in solution or bound in a protein; the lack of apparent interacting molecular 'sites' (as in our example above of a crystal) can be reconciled by considering the $2sp^2$-hybridised carbon atoms within the π-conjugated region as finer-grained sites. Indeed, carotenoid molecules can host multiple excitons, with the carotenoid S_1 exciton having a predominant character of two tightly-bound triplet excitons (coupled to an overall singlet), denoted ^{1}(TT).[97,116–122]

2.2.5 Singlets and triplets

Considering the overall molecular wavefunction $|\Psi_{k,\nu,\sigma}\rangle = |\psi_k\rangle\,|\chi_{k,\nu}\rangle\,|\varsigma_{k,\sigma}\rangle$, our discussion thus far has concerned the electronic factor $|\psi_k\rangle$. We now discuss the

spin component $|\varsigma_{k,\sigma}\rangle$. The spin of a molecular state is influenced by the spin of all electrons, which are spin-1/2 fermions. The electrons in filled orbitals always form antiparallel pairs (see Figure 2.4) which sum pairwise to zero and overall do not contribute to the total spin. Therefore we can consider only the electrons in unpaired orbitals.

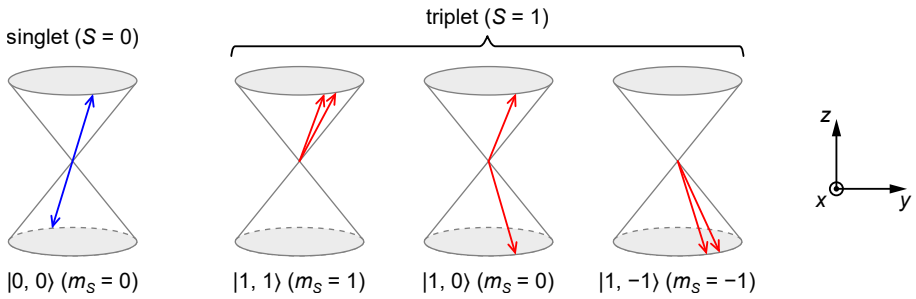

Figure 2.6 – Vector representation of two-electron singlets and triplets. The two electron spins, indicated with arrows, precess about the z-direction. The antiparallel case (blue arrows) is completely out-of-phase and yields a singlet (eigen)state, while the other three cases (red arrows) are in-phase and yield a triplet (eigen)state. The corresponding eigenket $|S, m_S\rangle$ is denoted below each picture.[103]

The condition that electron spins form antiparallel pairs is relaxed when the electrons are in different MOs (*i.e.* different positional sites). We can construct wavefunctions for the pair of electrons with products of the one-electron spins. The two-electron wavefunctions must be eigenstates of the total spin operator squared

$$\mathbf{S}^2 = (\mathbf{S}_1 + \mathbf{S}_2)^2 \tag{2.13}$$

with eigenvalue $S(S+1)$, where S is the spin quantum number. Note the subscripts label electron 1, electron 2. Assuming that we can sensibly define a z-direction in a so-called high-field limit, *e.g.* an external magnetic field $\mathbf{B} = B\hat{\mathbf{z}}$ is being applied, the two-electron wavefunctions must also be eigenstates of the associated operator for the spin's z-component S_z with eigenvalue m_S (magnetic spin quantum number). So using $|\uparrow\rangle$ to denote a one-electron spin wavefunction with $S = 1/2$, $m_S = 1/2$, and using $|\downarrow\rangle$ for $S = 1/2$, $m_S = -1/2$ similarly,[†] we arrive

[†]Note that $|\uparrow\rangle$, $|\downarrow\rangle$ are often written in other works (*e.g.* Ref.[103]) as $|\alpha\rangle$, $|\beta\rangle$ respectively.

at

$$|0,0\rangle = \frac{1}{\sqrt{2}}\left(|\uparrow\rangle_1 |\downarrow\rangle_2 - |\downarrow\rangle_1 |\uparrow\rangle_2\right) \qquad S = 0, m_S = 0 \tag{2.14}$$

$$|1,1\rangle = |\uparrow\rangle_1 |\uparrow\rangle_2 \qquad S = 1, m_S = 1 \tag{2.15}$$

$$|1,0\rangle = \frac{1}{\sqrt{2}}\left(|\uparrow\rangle_1 |\downarrow\rangle_2 + |\downarrow\rangle_1 |\uparrow\rangle_2\right) \qquad S = 1, m_S = 0 \tag{2.16}$$

$$|1,-1\rangle = |\downarrow\rangle_1 |\downarrow\rangle_2 \qquad S = 1, m_S = -1 \tag{2.17}$$

which are the orthonormal spin eigenstates for the two-electron system in the high-field limit.[103] Note that the eigenkets are written $|S, m_S\rangle$ here.

In the case where a pair of electrons align in a antiparallel manner (*i.e.* Equation 2.14, blue arrows in Figures 2.4 and 2.6), the spin eigenvalue is $S = 0$ and the magnetic spin eigenvalue is $m_S = 0$, so the eigenstate is said to be a singlet. Meanwhile, in a 'parallel' alignment case (*i.e.* Equations 2.15–2.17, red arrows in Figures 2.4 and 2.6), there are three distinct alignments which yield the same spin eigenvalue $S = 1$ but with differing magnetic spin eigenvalues $m_S = -1, 0, 1$, with any of these eigenstates termed a triplet.[†103,105]

Experimentally observed states in molecules are all antisymmetric under electron (fermion) exchange. This is a consequence of the *Pauli principle*: 'the total wavefunction must be antisymmetric under the exchange of any pair of identical fermions, and symmetric under the exchange of any pair of identical bosons.' The *Pauli exclusion principle* follows as a consequence: 'no two electrons may occupy the same state.'[105]

Singlets and triplets have an energetic distinction as a result of the Pauli principle. We define a particle exchange operator $P_{1\leftrightarrow 2}$ that has the simple effect of swapping particles around, for example with a generic ket[107]

$$P_{1\leftrightarrow 2}\,|x_1; x_2\rangle = |x_2; x_1\rangle\,. \tag{2.18}$$

If we apply this to the singlet's spin wavefunction (Equation 2.14), we find that an eigenvalue of -1 is yielded:

$$P_{1\leftrightarrow 2}\,|0,0\rangle = \frac{1}{\sqrt{2}}\left(|\uparrow\rangle_2 |\downarrow\rangle_1 - |\downarrow\rangle_2 |\uparrow\rangle_1\right) = -\,|0,0\rangle\,. \tag{2.19}$$

Therefore $|0,0\rangle$ is antisymmetric under electron exchange (herein we drop 'under electron/particle exchange'). This suggests that for the overall wavefunction

[†]Note that 'eigen' is typically dropped in discussing singlet and triplet (eigen)states.

$|\Psi_{k,\nu,\sigma}\rangle$ to be antisymmetric when paired with a singlet spin, the non-spin components $|\psi_k\rangle\,|\chi_{k,\nu}\rangle$ should be symmetric. As the nuclear-associated component $|\chi_{k,\nu}\rangle$ is always a symmetric contribution, the component $|\psi_k\rangle \equiv |\psi_\mathrm{S}\rangle$ describing electronic positions must be symmetric for a singlet. In contrast, applying $P_{1\leftrightarrow 2}$ to any of the triplet spin wavefunctions (Equation 2.15–2.17) yields an eigenvalue of $+1$, so those are symmetric, and therefore the spatial component $|\psi_k\rangle \equiv |\psi_\mathrm{T}\rangle$ must be antisymmetric for a triplet.

We can write the singlet (spin-antisymmetric, spatial-symmetric) spatial wavefunction in terms of electron 1 and 2 (position $\mathbf{r}_1$ and $\mathbf{r}_2$ respectively) in molecular orbitals $|\phi_a\rangle$ and $|\phi_b\rangle$ as

$$|\psi_\mathrm{S}(\mathbf{r}_1,\mathbf{r}_2)\rangle = \frac{1}{\sqrt{2}}\left(|\phi_a(\mathbf{r}_1)\rangle\,|\phi_b(\mathbf{r}_2)\rangle + |\phi_b(\mathbf{r}_1)\rangle\,|\phi_a(\mathbf{r}_2)\rangle\right) \tag{2.20}$$

which is symmetric under $P_{1\leftrightarrow 2}$ as required. Likewise, we can write the triplet spatial wavefunction as

$$|\psi_\mathrm{T}(\mathbf{r}_1,\mathbf{r}_2)\rangle = \frac{1}{\sqrt{2}}\left(|\phi_a(\mathbf{r}_1)\rangle\,|\phi_b(\mathbf{r}_2)\rangle - |\phi_b(\mathbf{r}_1)\rangle\,|\phi_a(\mathbf{r}_2)\rangle\right) \tag{2.21}$$

which is antisymmetric under $P_{1\leftrightarrow 2}$ as required. The operator for the effective electron-electron potential energy ($V_\mathrm{e\text{–}e}^\mathrm{eff.}$ – see Equation 2.12) yields the dominant energetic distinction. If we consider $V = \langle\Psi|\,V_\mathrm{e\text{–}e}^\mathrm{eff.}\,|\Psi\rangle$ for the singlet and triplet spatial wavefunctions, we find that

$$V_\mathrm{S} = \langle\psi_\mathrm{S}(\mathbf{r}_1,\mathbf{r}_2)|V_\mathrm{e\text{–}e}^\mathrm{eff.}(\mathbf{r}_1-\mathbf{r}_2)\,|\psi_\mathrm{S}(\mathbf{r}_1,\mathbf{r}_2)\rangle = C_0 + J_0 \tag{2.22}$$

$$V_\mathrm{T} = \langle\psi_\mathrm{T}(\mathbf{r}_1,\mathbf{r}_2)|V_\mathrm{e\text{–}e}^\mathrm{eff.}(\mathbf{r}_1-\mathbf{r}_2)\,|\psi_\mathrm{T}(\mathbf{r}_1,\mathbf{r}_2)\rangle = C_0 - J_0 \tag{2.23}$$

where the 'Coulomb integral' C_0 is

$$C_0 = \iint \phi_a^*(\mathbf{r}_1)\phi_b^*(\mathbf{r}_2)V_\mathrm{e\text{–}e}^\mathrm{eff.}(\mathbf{r}_1-\mathbf{r}_2)\phi_a(\mathbf{r}_1)\phi_b(\mathbf{r}_2)\,d^3\mathbf{r}_1\,d^3\mathbf{r}_2 \tag{2.24}$$

and the 'exchange/resonance integral' J_0 is

$$J_0 = \iint \phi_a^*(\mathbf{r}_1)\phi_b^*(\mathbf{r}_2)V_\mathrm{e\text{–}e}^\mathrm{eff.}(\mathbf{r}_1-\mathbf{r}_2)\phi_b(\mathbf{r}_1)\phi_a(\mathbf{r}_2)\,d^3\mathbf{r}_1\,d^3\mathbf{r}_2 \tag{2.25}$$

and the key result is that

$$V_\mathrm{S} - V_\mathrm{T} = 2J_0 \equiv E_\mathrm{S\text{-}T} \tag{2.26}$$

where $E_{\text{S-T}}$ is the singlet-triplet exchange energy.[†] As both C_0 and J_0 are typically positive, the end result is that the energy of a triplet state in an organic molecule is typically less than the energy of a comparable singlet state. For most π-conjugated molecules, $E_{\text{S-T}} \sim 1\,\text{eV}$.[12] In summary, because of the Pauli (exclusion) principle, two unpaired electrons in a singlet (antiparallel pairs) may occupy the same positional space (with high wavefunction overlap) which results in increased electrostatic repulsion and a higher overall energy, whereas two unpaired electrons in a triplet (parallel pairs) cannot occupy the same positional space (with low wavefunction overlap) which results in reduced repulsion and a lower overall energy.[103,105]

We complete this discussion by mentioning our assumption in constructing the 'high-field limit' spin eigenstates of the two unpaired-electron system (Equations 2.14–2.17). We assumed we could sensibly define a z-direction, which amounted to S_z being well-defined and so m_S being a good quantum number. In the case where we *cannot* sensibly define a z-direction, S_z is not well-defined and so m_S is not a good quantum number. Fortunately, we still may write one singlet eigenstate and three triplet eigenstates for the total spin operator and arrive to identical conclusions regarding the Coulomb and exchange integrals.[103]

We write our low-field-limit orthonormal spin eigenstates of the two unpaired-electron system as[103,123,124]

$$|\text{S}\rangle = \frac{1}{\sqrt{2}}\left(|\uparrow\rangle_1 |\downarrow\rangle_2 - |\downarrow\rangle_1 |\uparrow\rangle_2\right) \qquad S = 0 \tag{2.27}$$

$$|\text{T}, x\rangle = \frac{1}{\sqrt{2}}\left(|\downarrow\rangle_1 |\downarrow\rangle_2 - |\uparrow\rangle_1 |\uparrow\rangle_2\right) \qquad S = 1 \tag{2.28}$$

$$|\text{T}, y\rangle = \frac{i}{\sqrt{2}}\left(|\downarrow\rangle_1 |\downarrow\rangle_2 + |\uparrow\rangle_1 |\uparrow\rangle_2\right) \qquad S = 1 \tag{2.29}$$

$$|\text{T}, z\rangle = \frac{1}{\sqrt{2}}\left(|\uparrow\rangle_1 |\downarrow\rangle_2 + |\downarrow\rangle_1 |\uparrow\rangle_2\right) \qquad S = 1 \tag{2.30}$$

which are eigenstates to $\mathbf{S}^2$ with eigenvalue $S(S+1)$. Also, we can write

$$S_i |\text{T}, i\rangle = 0 \quad \text{for } i = x, y, \text{ or } z \tag{2.31}$$

meaning (*e.g.* with $i = x$) $|\text{T}, x\rangle$ is an eigenstate with eigenvalue 0 to the operator S_x, the x-component of the total spin operator.[103]

[†]Note the concept of an exchange/resonance integral and associated exchange energy was mentioned earlier in the context of bonding/antibonding orbitals. The exchange integral there was denoted β, and arose from different screenings of the electrostatic interaction *between nuclei* (not between electrons, as is the case here for J_0). For further details, see Section 2.2.3 and Figure 2.3.

2.2.6 Triplet zero-field splitting

We have focused so far on the distinction between singlets and triplets. It turns out that the three triplets are not degenerate in energy, even in the absence of an external magnetic field. The lifting of degeneracy largely arises due to anisotropic dipole-dipole interactions between the magnetic moments of the two unpaired electrons.[103,125] The splitting in energy is referred to as 'zero-field splitting' and is generally parametrised with an additional Hamiltonian contribution

$$H_{\text{zero-field}} = \mathbf{S} \cdot \mathbf{DS} \tag{2.32}$$

where $\mathbf{D}$ is a matrix describing the zero-field splitting interaction.[125] $\mathbf{D}$ is generally diagonalisable and traceless,[125] as in the case where only interspin dipolar interactions are involved. So we can write

$$\mathbf{D} = \begin{pmatrix} D_x & 0 & 0 \\ 0 & D_y & 0 \\ 0 & 0 & D_z \end{pmatrix} \tag{2.33}$$

where by conventional definition[126]

$$|D_z| \geq |D_x| \geq |D_y| \tag{2.34}$$

such that the z-axis corresponds to the maximum dipolar coupling.[125] Since $\mathbf{D}$ is traceless ($\text{Tr}(\mathbf{D}) = D_x + D_y + D_z = 0$), we can use two zero-field splitting parameters rather than three to describe the interaction. These are D and E, defined as

$$D = \frac{3}{2} D_z, \qquad E = \frac{1}{2}(D_x - D_y) \tag{2.35}$$

where, equivalently to the above conventional definition of Equation 2.34,[125,126]

$$-1 \leq 3D/E \leq 0. \tag{2.36}$$

Note that E will always have the opposite sign to D. So we may write Equation 2.32 as

$$H_{\text{zero-field}} = D\left(S_z^2 - \frac{1}{3}\mathbf{S}^2\right) + E\left(S_x^2 - S_y^2\right) \tag{2.37}$$

where S_x, S_y, and S_z are component x, y, and z of the spin operator vector $\mathbf{S}$ respectively.[125]

Within the aforementioned dipolar approximation, the parameter D can be related to the average interspin distance and can be used to estimate the spatial

extent of the triplet exciton, while E can be related to the rhombicity of the **D**-matrix.[12,125] The magnitudes of D and E can be found from electron paramagnetic resonance (EPR) measurements, while confirming their signs typically requires more complex magnetic resonance measurements.[125] Notably, in most π-conjugated molecules, D lies in the range ∼4–10 µeV.[103,127,128]

Using the orthonormal spin-triplet eigenstates $|T, i\rangle$, $(i = x, y, z)$ in the low-field limit (Equations 2.27–2.30), we find that the zero-field splitting yields the following energy perturbations

$$\Delta E_x = -D_x = \frac{1}{3}D - E \tag{2.38}$$

$$\Delta E_y = -D_y = \frac{1}{3}D + E \tag{2.39}$$

$$\Delta E_z = -D_z = -\frac{2}{3}D \tag{2.40}$$

where ΔE_i is the energy difference for the triplet $|T, i\rangle$ upon addition of the zero-field Hamiltonian, and minus signs are included following convention.[†125] The energetic ordering of ΔE_i is dependent on the signs of D and E (again note that they have opposite signs following the conventional definitions of Equations 2.34 and 2.36). An example for positive D (negative E) is shown in Figure 2.11.

The energies of the three triplets can gain an additional difference under the influence of an external magnetic field through the Zeeman effect. The Zeeman Hamiltonian term is

$$H_{\text{Zeeman}} = g_{\text{L}}\mu_{\text{B}}\mathbf{B} \cdot \mathbf{S} \tag{2.41}$$

where g_{L} is the Landé g-factor, μ_{B} is the Bohr magneton, and $\mathbf{B}$ is an externally applied magnetic flux density.

2.3 Light-matter interactions

Having established a basics of the theory of stationary states in conjugated molecules, that is their static energies and physical properties, we next describe how transitions between these states occur. As discussed in Section 2.2.3, the HOMO-LUMO energy gap in π-conjugated molecules is typically small enough for promotion (demotion) of electrons through absorption (emission) of visible photons.[103] This makes the study of these molecules fruitful through spectroscopic techniques involving (mostly) visible-region light.

[†]The reasoning behind the inclusion of the minus signs is not apparent to the thesis author.[125]

2.3.1 Transition dipole moment

Consider a time-dependent electric field that describes light[†]

$$\mathbf{E}(t) = \hat{\mathbf{e}} E_0 \exp(-i\omega t) \tag{2.42}$$

where $\hat{\mathbf{e}}$ is a unit vector in the direction of the electric field,[‡] E_0 is the amplitude, ω is the angular frequency of oscillation, and t is time. This light and its electric field is incident on a π-conjugated molecule, which we can describe using a Hamiltonian

$$H_1(t) = \mathbf{p} \cdot \mathbf{E}(t) = \underbrace{\mathbf{p} \cdot \hat{\mathbf{e}} E_0}_{V} \exp(-i\omega t) \tag{2.43}$$

where $\mathbf{p}$ is the total dipole operator

$$\mathbf{p} = \underbrace{-e \sum_j \mathbf{r}_j}_{\mathbf{p}_\mathrm{e}} + \underbrace{e \sum_k Z_k \mathbf{R}_k}_{\mathbf{p}_\mathrm{n}} \tag{2.44}$$

summing over all electrons labelled j and all nuclei labelled k, where e is the electronic charge and Z_k is the proton number of nucleus k. This Hamiltonian is in addition to the Hamiltonian H introduced in Section 2.2.1 containing electron and nuclear kinetic energies and electrostatic potentials, such that

$$H'(t) = H + H_1(t) \tag{2.45}$$

giving us a new 'total' Hamiltonian $H'(t)$.

Even with application of the various approximations outlined in Section 2.2, working with this new Hamiltonian without further approximation is mathematically impossible. Fortunately, $H_1(t)$ is typically rather small in a 'weak-coupling limit' interaction between light (embodied in $H_1(t)$) and matter (embodied in H), and can be treated as a perturbation.[§] This enables us to use Fermi's golden rule, which relates the transition rate $\Gamma_{i\to f}$ between an initial state $|\Psi_i\rangle$ to a final state $|\Psi_f\rangle$ under the action of the perturbing Hamiltonian.[103,129] Here, the transition rate $\Gamma_{i\to f}$ corresponds to photon absorption, but the treatment for emission is

[†]Throughout this thesis, we invoke an exponential function $\exp(z) \equiv e^z$ where $e \simeq 2.71828$ here is Euler's number. Meanwhile, '$1/e^2$' always invokes Euler's number (see footnote of page 36). Elsewhere, the quantity e should be taken to be the modulus of the electron charge, unless specified otherwise.

[‡]Recall that 'hat' symbols have been omitted for generic operators in order to avoid confusion with hat-donning unit vectors.

[§]Note that we study systems in the 'strong-coupling limit' in Appendix D.

near-identical; we denote the 'radiative rate' of emission as k_r specifically. We write Fermi's golden rule as

$$\Gamma_{i\to f} \simeq \frac{2\pi}{\hbar}|\langle\Psi_f|\, V\, |\Psi_i\rangle|^2 \rho(E_f) \tag{2.46}$$

where $\hbar$ is the reduced Planck constant and $\rho(E_f)$ is the density of final states. An outline of the derivation of Fermi's golden rule is given in Appendix E. Inserting Equation 2.43 into this, noting that $V \equiv \mathbf{p}\cdot\hat{\mathbf{e}}E_0$, we find

$$\Gamma_{i\to f} \simeq \frac{2\pi}{\hbar}E_0^2|\mu_{i\to f}|^2 \rho(E_f) \tag{2.47}$$

where we have defined

$$\mu_{i\to f} \equiv \langle\Psi_f|\, \mathbf{p}\cdot\hat{\mathbf{e}}\, |\Psi_i\rangle \tag{2.48}$$

which is the so-called transition dipole moment. If we apply the Born-Oppenheimer approximation and use the resulting factorised ket of Equation 2.11, we can write Equation 2.48 as

$$\mu_{i\to f} = \langle\varsigma_{f,\sigma'}|\, \langle\chi_{f,\nu'}|\, \langle\psi_f|\, \mathbf{p}\cdot\hat{\mathbf{e}}\, |\psi_i\rangle\, |\chi_{i,\nu}\rangle\, |\varsigma_{i,\sigma}\rangle \tag{2.49}$$

with the initial state (final state) labelled with electronic state i (f), vibrational state ν (ν'), and spin state σ (σ'). We consider the action of each factorised ket on the operator $\mathbf{p}\cdot\hat{\mathbf{e}}$. First, the electronic and nuclear spins are not affected by the electric field of the incident light.[†][103] Second, from the Born-Oppenheimer approximation already applied, the nuclei are too massive and 'slow' to respond significantly to the oscillating electric field; recall that $|\psi_k\rangle \equiv |\psi_k(\mathbf{r};\mathbf{R})\rangle$ has only a weak parametric dependence on the positions of the nuclei. Third, recall that the vibrational/nuclear component is dependent only on the position of the nuclei (*e.g.* $|\chi_{i,\nu}\rangle \equiv |\chi_{i,\nu}(\mathbf{R})\rangle$). Finally, for the term with $\mathbf{p}$'s nuclear component ($\mathbf{p}_\mathrm{n}$), we can use $\langle\psi_f|\psi_i\rangle = 0$, since those electronic states are eigenkets of the Born-Oppenheimer Hamliltonian $H_\mathrm{BO}(\mathbf{r};\mathbf{R})$ by definition (Equation 2.8) and are thus orthogonal.[104] So we can write[103]

$$\mu_{i\to f} \simeq \underbrace{\langle\psi_f|\, \mathbf{p}_\mathrm{e}\cdot\hat{\mathbf{e}}\, |\psi_i\rangle}_{\text{electronic}}\, \underbrace{\langle\chi_{f,\nu'}|\chi_{i,\nu}\rangle}_{\text{Franck-Condon}}\, \underbrace{\langle\varsigma_{f,\sigma'}|\varsigma_{i,\sigma}\rangle}_{\text{spin}} \tag{2.50}$$

which contains $\mathbf{p}$'s electronic component ($\mathbf{p}_\mathrm{e}$) only.

[†]The spins are affected by magnetic fields through the Zeeman effect (Equation 2.41), but the magnitude of that for the incident light (an electromagnetic wave) is very small and can be discarded, as was implicitly done in writing Equation 2.42.

The transition dipole moment is a key parameter affecting the rate of optical transitions, and much of the remaining discussion of this subsection will concern the factors influencing the size of it, namely the three bra-ket factors of Equation 2.50. When any of these three factors is zero, the transition is 'forbidden'. We note that the modulus-square of the transition dipole moment is proportional to the 'oscillator strength'

$$\text{oscillator strength: } f \propto \left|\mu_{i\to f}\right|^2 \tag{2.51}$$

which will be referred to herein as a shorthand for 'the modulus-square of the transition dipole moment'. Furthermore, the transition dipole moment relates to the Einstein A and B coefficients.[103,105,106] Importantly, A and B for atomic transitions (in *e.g.* Ref.[130]) are distinct from those for transitions in polyatomic molecules. Indeed, factors such as the broadness of molecular spectra, their inequivalent absorption and emission spectra, and the refractive index of the medium require consideration.[103] Strickler and Berg[131] presented modified A and B coefficients for molecular transitions, which Ref.[103] summarises.

2.3.2 Orbital selection rules

We first discuss the $\langle\psi_f|\,\mathbf{p}_\mathrm{e}\cdot\hat{\mathbf{e}}\,|\psi_i\rangle$ factor of the transition dipole moment (Equation 2.50), called the electronic factor. First, note that the electronic dipole operator $\mathbf{p}_\mathrm{e}\cdot\hat{\mathbf{e}}$ is of odd symmetry under a spatial inversion operation

$$\mathbf{r}\mapsto-\mathbf{r}. \tag{2.52}$$

Therefore, the initial electronic state $|\psi_i\rangle$ must be of a different symmetry to the final electronic state $|\psi_f\rangle$ for the factor to be non-zero and for the overall transition to be 'dipole-allowed'. Otherwise, the electronic factor evaluates to zero, and the overall transition is said to be 'dipole-forbidden'.[103] Physically, we can treat the $\langle\psi_f|\,\mathbf{p}_\mathrm{e}\cdot\hat{\mathbf{e}}\,|\psi_i\rangle$ factor as a measure of the magnitude of dipolar migration of charge that is concomitant with the transition.[105]

The symmetry of electronic states for a certain molecular geometry can be determined using group theory, and is extensively covered by Ref.[105] for a variety of different molecular symmetries. A general point we highlight is that for systems with an even number of π-electrons, the ground state S_0 can be shown to always have even symmetry (denoted $\mathrm{A_g}$). Hence dipole-allowed absorptive transitions from S_0 have to be to excited states with odd symmetry (denoted $\mathrm{B_u}$). Molecules in the $C_{2\mathrm{h}}$ symmetry group follow that behaviour.[105]

Indeed, most polyenes and carotenoids belong to that C_{2h} symmetry group.[103] The C_{2h} group contains two symmetries: two-fold (180°) rotation symmetry (C_2) and a centre of inversion symmetry (i). The C_{2h} symmetry is overall equivalent to spatial inversion (Equation 2.52). A state that is even under this inversion (positive eigenvalue) is denoted A_g, while a state that is odd under it (negative eigenvalue) is denoted B_u. The letters A and B refer to the C_2 symmetry, while the subscripts g ('gerade'; German for 'even') and u ('ungerade'; German for 'odd') refer to the i symmetry.[103–105]

Furthermore, states extracted from many theoretical treatments of polyenes may also be labelled with particle-hole symmetry.[†119,120] It arises following the assumption of zero-differential overlap, and is not applicable to real polyenes; hence it has been termed an 'artifical symmetry'. If a constructed Hamiltonian has this particle-hole symmetry, then it remains invariant when an electron (particle) is *transformed* into a hole under the particle-hole operation

$$c_{i\sigma}^{\dagger} \mapsto (-1)^i c_{i\bar{\sigma}} \equiv (-1)^i h_{i\sigma}^{\dagger} \tag{2.53}$$

where $c_{i\sigma}^{\dagger}$ ($c_{i\sigma}$) creates (destroys) an electron with spin σ in orbital i, $h_{i\sigma}^{\dagger}$ creates a hole with spin σ in orbital i, and $\bar{\sigma}$ refers to an opposite spin to σ. There are two requirements for particle-hole symmetry to hold: (1) The model lattice must consist of a periodic arrangement of two different 'sites', with nearest-neighbour one-electron hybridisation between the sites. The sites could correspond to different bond lengths in a polyene, with alternating double bonds (a short site) and single bonds (a long site).[‡104] (2) Every site should have an equivalent amount of total potential energy. For a finite linear chain, this would mean that variations in the electron-electron potential energy arising from mutual repulsion (greatest centrally in the chain) should balance out the variations in the electron-nuclear potential energy arising from attraction (again greatest centrally in the chain).[104] States with particle-hole symmetry are denoted with + or −, which refer to the associated eigenvalue. We note that there are two conventions in the literature, distinguished by swapping +/− labels. We follow the convention of (*e.g.*) Ref.[119] and denote so-called ionic states with +, and covalent states with −. Besides, in experimental studies, these labels are dropped, since particle-hole symmetry is not applicable to real systems.

[†]Also known as electron-hole symmetry, charge-conjugation symmetry, and Pariser alternacy symmetry.

[‡]Such arrangements involving bond alteration typically arise through Peierls distortion.[103,104,132,133]

To summarise, the polyene/carotenoid electronic states as found with theoretical models are labelled with $n^{2S+1}\mathrm{X}^{\pm}$, where:

- n is an overall quantum number, and can be thought to denote the energetic ordering of states with the same symmetry/multiplicity,
- S is the spin of the level, and $2S+1$ is its multiplicity,
- X is $\mathrm{A_g}$ or $\mathrm{B_u}$ for even or odd $C_{2\mathrm{h}}$ symmetry respectively,
- $\pm$ is $+$ or $-$, referring to states distinguished in models assuming zero-differential overlap.[120]

Within this picture, the singlet electronic states for a β-carotene-like carotenoid are labelled $1^1\mathrm{A_g^-}$ (ground state; $\mathrm{S_0}$), $2^1\mathrm{A_g^-}$ (first excited singlet state; $\mathrm{S_1}$) and $1^1\mathrm{B_u^+}$ (second excited singlet state; $\mathrm{S_2}$).[119] One-photon transitions are allowed under symmetry provided the $\mathrm{A_g}/\mathrm{B_u}$, and $+/-$ labels both change; for example, the transition $1^1\mathrm{A_g^-}\rightarrow 2^1\mathrm{A_g^-}$ ($\mathrm{S_0}\rightarrow\mathrm{S_1}$) is said to be symmetry-forbidden, while the one-photon $1^1\mathrm{A_g^-}\rightarrow 2^1\mathrm{B_u^+}$ ($\mathrm{S_0}\rightarrow\mathrm{S_2}$) is symmetry-allowed.[30,100]

However, carotenoids not belonging to the $C_{2\mathrm{h}}$ symmetry group have been demonstrated experimentally to have a dipole-forbidden $\mathrm{S_1}$. Indeed, carotenoid *cis*-isomers or those substituted with functional groups have a heavily distorted π-conjugation and do not belong to $C_{2\mathrm{h}}$, but nevertheless have a dipole-forbidden $\mathrm{S_1}$ state.[134–136] This forbiddenness regardless of symmetry is thought to arise from the significant contribution of the singlet triplet-pair state $^1(\mathrm{TT})$ to the $\mathrm{S_1}$ state in polyenes/carotenoids.[97,116–122]

We close this subsection by noting that the magnitude of $\langle\psi_f|\,\mathbf{p}_\mathrm{e}\cdot\hat{\mathbf{e}}\,|\psi_i\rangle$ increases with the extent of orbital overlap between the initial and final electronic states. Hence, in addition to 'testing' if the transition is dipole-allowed, the electronic factor also controls the size of the overall optical transition. For example, even if a transition is dipole-allowed under symmetry with a non-zero electronic factor, and allowed under the other two factors within the transition dipole moment, if the orbital overlap is poor, $\langle\psi_f|\,\mathbf{p}_\mathrm{e}\cdot\hat{\mathbf{e}}\,|\psi_i\rangle$ would be relatively small, resulting in an overall weak transition (low oscillator strength).[103,106]

2.3.3 Franck-Condon principle

We secondly discuss the so-called Franck-Condon factor, which is the $\langle\chi_{f,\nu'}|\chi_{i,\nu}\rangle$ term of the transition dipole moment (Equation 2.50). While the other factors within the transition dipole moment affect the overall transition intensity between electronic states (by selection rules and orbital overlap), this term is the one to

give absorption and emission spectra of π-conjugated molecules their characteristic appearance of a succession of peaks.[103]

Consider the total Hamiltonian $H_k(\mathbf{R})$ for an organic molecule in electronic state k after application of the Born-Oppenheimer approximation,

$$H_k(\mathbf{R}) \simeq \underbrace{\sum_{\alpha} \frac{\mathbf{P}_\alpha^2}{2M_\alpha}}_{T_\mathrm{n}(\mathbf{R})} + E_k(\mathbf{R}) \tag{2.54}$$

(*cf.* Equation 2.9). This is parametrised in terms of $\mathbf{R} \equiv \{\mathbf{R}\}$, the nuclear coordinates. We note the quadratic appearance of the minima of the adiabatic potential energy surfaces $E_k(\mathbf{R})$ (see Figure 2.1 for a one-dimensional schematic). This motivates using a coordinate transformation to describe small displacements about that 'quadratic' minimum, and use the results for a quantum harmonic oscillator. To make this easier mathematically, we transform the coordinates $\mathbf{R}$ into the 'normal coordinates' $\mathbf{Q}_k$, defined about the potential energy minimum. Using these new coordinates and considering quadratic terms only (*i.e.* the nuclear motions are small), we re-cast Equation 2.54 into

$$H_k(\mathbf{Q}_k) \simeq \sum_{\alpha} \left(\frac{\mathbf{P}_\alpha^2}{2M_\alpha} + \frac{1}{2} M_\alpha \omega_{k,\alpha}^2 \mathbf{Q}_{k,\alpha}^2 \right) \tag{2.55}$$

which has the familiar form for a quantum harmonic oscillator Hamiltonian with mass M_α and angular frequency $\omega_{k,\alpha}$ (force constant $K_{k,\alpha} = M_\alpha \omega_{k,\alpha}^2$). For each normal mode α of the molecule associated with nucleus α and electronic state k, all the nuclei oscillate with that same $\omega_{k,\alpha}$. We can write the usual result for quantum harmonic oscillator energies

$$E_{k,\alpha,\nu_\alpha} = \left(\nu_\alpha + \frac{1}{2} \right) \hbar \omega_{k,\alpha} \tag{2.56}$$

which are the vibrational energy levels, with $\nu_\alpha = 0,\ 1,\ 2,\ \ldots$ the vibrational quantum number.[103,110,129,137]

Despite our simplifications, Equation 2.55 is, in analytical terms, very challenging to work with. Fortunately, for most π-conjugated molecules (and certainly for carotenoids), it turns out that only a few high-energy vibrational modes significantly couple to electronic transitions.[138] For example, in carotenoids, the C=C stretching mode of wavenumber $\sim$1520 cm^{-1} (energy $\hbar\omega_0 \sim 0.19$ eV) and the C−C stretching coupled with C−H in-plane bending mode of wavenumber $\sim$1150 cm^{-1} ($\sim$0.14 eV) are the dominantly coupled high-energy vibrational modes.[41,48,139]

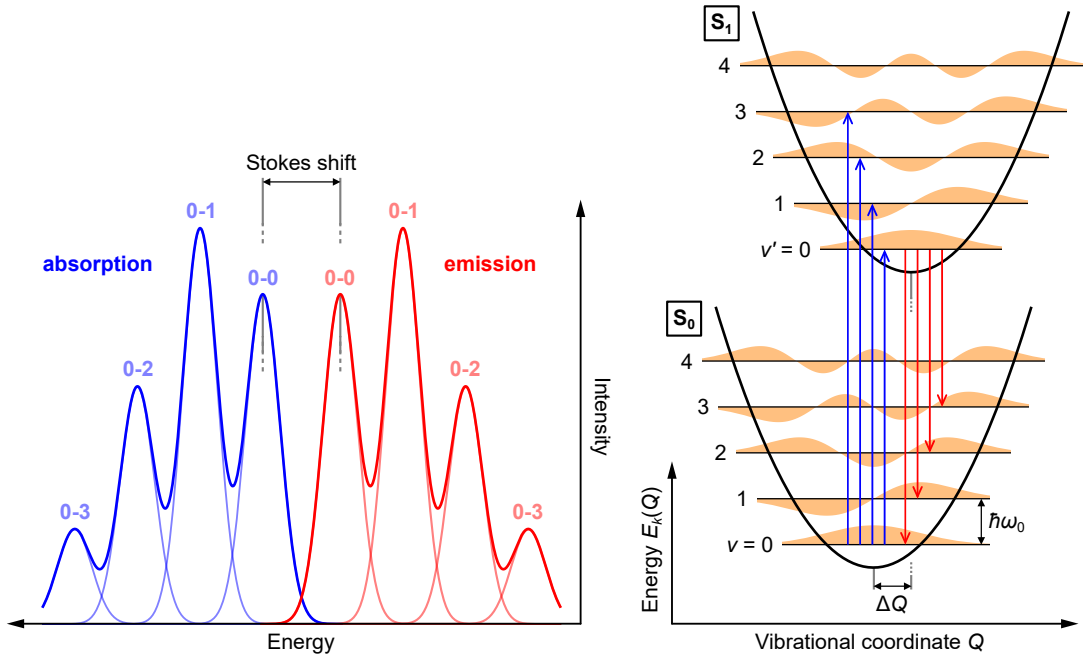

Figure 2.7 – The Franck-Condon principle for a displaced oscillator with one dominant high-energy vibrational mode yielding vibronic peaks through vibrational transitions. An electronic $S_0 \rightarrow S_1$ transition involving photon absorption is concomitant with vibrational transitions (blue up-arrows), yielding vibronic (vibrational and electronic) peaks (light blue curves), which sum to an overall absorption spectrum (blue curve). An emissive electronic $S_1 \rightarrow S_0$ transition is similarly concomitant with vibrational transitions (red down-arrows), yielding vibronic peaks (light red curves), which sum to an overall emission spectrum (red curve). A displaced oscillator yields mirror images for the absorption and emission spectra. The Stokes shift (depicted on the left of the figure) typically arises from coupling to low-energy vibrational modes (not depicted on the right).[140] Note that the arrows are representing vibrational transitions, not electronic/vibronic transitions at specific Q. See text for details.

For simplicity here, we consider one high-energy vibrational mode of energy $\hbar\omega_0$ and mass M (force constant $K = M\omega_0^2$) dominantly coupled to the electronic transition. We work with a typical case where the angular frequency ω_0 stays the same between the electronic states (a so-called displaced oscillator). We also note that $\hbar\omega_0 \sim 0.19\,\text{eV}$ is much greater than typical thermal energies ($\sim$25 meV at room temperature), so the $\nu = 0$ vibrational level is occupied in the initial state. We depict this diagrammatically with the various simplifications in the right side of Figure 2.7.

We first consider an absorption process, so we start in the $\nu = 0$ level in the lower adiabatic potential energy surface associated with the electronic state

S_0. We consider a typical conjugated molecule with an dipole-allowed S_1 (recall that in polyenes/carotenoids, S_1 is dipole-forbidden, and absorption occurs from $S_0 \rightarrow S_2$). In a promotion from $S_0 \rightarrow S_1$, the vibrational coordinate Q does not change on the timescale of electron motion under the Born-Oppenheimer approximation. The transition is said to be 'vertical', and the immediate point reached on electronic state S_1's potential energy surface is the so-called Franck-Condon region. This immediate point may be in *any* of the vibrational levels of S_1 (*i.e.* $\nu' = 0, 1, 2, \ldots$; the vibrational level transition is usually written ν-ν', *e.g.* 0-1) with the probability of occupancy dictated by the modulus-square of the Franck-Condon factor $|\langle \chi_{f,\nu'} | \chi_{i,0} \rangle|^2$. This is what leads to the characteristic succession of peaks seen in the absorption spectrum,[103] depicted as a blue curve on the left of Figure 2.7. At later times, if the molecule was in a vibrational level $\nu' > 0$, transitions occur to lower vibrational levels by transfer of energy to lower-energy vibrational modes of the molecule on subpicosecond timescales.[110] This redistribution process is termed *intra*molecular vibrational redistribution (IVR). Since the lifetime of an excited electronic state (here S_1) is typically about a nanosecond, while IVR is on picosecond timescales, the molecule typically reaches vibrational level $\nu' = 0$ while in the S_1 state. Note that upon reaching $\nu' = 0$, the molecule in excited state S_1 has a different 'equilibrium' vibrational coordinate Q compared to that for ground state S_0; in other words, the minima of the adiabatic potential energy surfaces is offset by ΔQ. This change in 'equilibrium geometry' arises due to differences in electron density between the nuclei for excited and ground electronic states, which results in different electrostatic screenings between the nuclei.[103] This was noted in Figure 2.1 as well.

We now discuss an emission process. Recall from above that, post-absorption, a molecule typically reaches a $\nu' = 0$ vibrational level well before decay *via* emission from electronic state $S_1 \rightarrow S_0$. Therefore, in emission of a photon, we expect an associated vibrational transition from $\nu' = 0$ in S_1 to ν in S_0 (*i.e.* 0-ν). The emission process is physically analogous to the absorption process outlined above, with the molecule eventually reaching the $\nu = 0$ level in S_0 through IVR. Note that with the various simplifications specified above, the Franck-Condon factor associated with (*e.g.*) a 0-2 absorptive transition ($\nu = 0, \nu' = 2$) is equal to the Franck-Condon factor associated with a 0-2 emissive transition ($\nu' = 0, \nu = 2$), *i.e.* $|\langle \chi_{f,\nu'=2} | \chi_{i,\nu=0} \rangle|^2 = |\langle \chi_{f,\nu=2} | \chi_{i,\nu'=0} \rangle|^2$. Since we are working with the typical case of a displaced oscillator, such that the angular frequency ω_0 (hence separation between vibrational levels, $\hbar\omega_0$) is the same for the S_1 and S_0 states, the

resulting emission spectrum is simply a mirror image of the absorption spectrum towards lower energies.[†] This is depicted in Figure 2.7 to the left; absorption is depicted in blue, and emission is depicted in red.

From the above paragraphs, we can write the energies of the vibronic (vibrational and electronic) transitions involved in absorption ($S_0 \rightarrow S_1$) and emission ($S_1 \rightarrow S_0$) processes as

$$E^{\text{abs.}}_{0\text{-}\nu'} = E^{\text{abs.}}_{0\text{-}0} + \nu' \hbar\omega_0 \tag{2.57}$$

$$E^{\text{em.}}_{0\text{-}\nu} = E^{\text{em.}}_{0\text{-}0} - \nu \hbar\omega_0. \tag{2.58}$$

These formulations demonstrate an important point: the 0-0 vibronic transition associated with absorption ($E^{\text{abs.}}_{0\text{-}0}$) is typically offset to a higher energy than the 0-0 vibronic transition associated with emission ($E^{\text{em.}}_{0\text{-}0}$). This is shown in the absorption and emission spectra in Figure 2.7, and the energy difference is termed the Stokes shift[‡][111]

$$\text{Stokes shift} = E^{\text{abs.}}_{0\text{-}0} - E^{\text{em.}}_{0\text{-}0}. \tag{2.59}$$

Stokes shifts can arise from coupling of low-energy vibrational modes to the electronic transition; note this can occur for a single molecule in a vacuum, without breaking the Born-Oppenheimer approximation. More typically, for an organic molecule (solute) in solution (solvent), solvation dynamics can lead to Stokes shifts, and these effects can be treated analogously to vibrational redistribution of low-energy modes coupling to the absorption/emission. For these modes, it is the molecule's solvent environment that changes geometry and relaxes after reaching the Franck-Condon region, rather than the molecule itself.[103] The molecule may dominantly couple to an 'internal' high-energy vibrational mode, *e.g.* the aforementioned C=C stretching mode ($\hbar\omega_0 \sim 0.19\,\text{eV}$), leading to the appearance of one *apparent* vibrational mode coupled to the transition, with the absorption/emission offset by the Stokes shift due to *non-apparent* coupling to low-energy modes of the molecule or solvent.[140] This is essentially what we are

[†]We note that a distorted (or displaced *and* distorted) oscillator has angular frequencies different between the excited and ground states. Therefore, they yield absorption and emission spectra that are not mirror images, as the spacing between vibrational peaks will be different for the two processes. However, with the other simplifying assumptions applied, the Franck-Condon factors between comparable peaks in absorption/emission (say, again, the 0-2 peak for both) are the same.[103]

[‡]Negative Stokes shifts are sometimes called an anti-Stokes shift.[111] We note that Stokes shifts are sometimes taken between the absorption and emission maxima, which may be inaccurate to the Stokes shift from the IUPAC definition[111] of Equation 2.59.

depicting to the left in Figure 2.7, which the right side of the figure would not yield.

We note that such phenomena can give a significant time-dependence in the spectra, particularly relevant for transient spectroscopy of carotenoids. The conjugated molecule absorption/emission schemes above imply that after IVR, the molecule still has vibrational energy, but contained in its low-energy vibrational modes. This remaining vibrational energy is transferred from the molecule to the solvent in a process termed vibrational energy transfer (VET). Finally, solvent-to-solvent VET occurs, sometimes specifically dubbed 'vibrational cooling' (VC) as the solvent in the immediate vicinity of the molecule loses vibrational energy and cools down.[†141–143] In most π-conjugated molecules, VET occurs on a ∼10 ps timescale, thus proceeding IVR but preceding decay of the electronic state in a near-sequential manner. VET leads to narrowing of the spectra over time. Furthermore, the aforementioned solvation dynamics can occur over a large range of times (∼100 fs to 10 ns) through various mechanisms.[141,143] The time-dependence of such phenomena may be observed in time-resolved spectroscopy (such as transient absorption; see Section 4.4). In particular, carotenoids have been demonstrated to have rapid non-radiative decay[‡] of comparable timescale to that for VET, thus depositing energy rapidly into the surroundings and causing local heating and subsequent VC. This yields significant IVR/VET-associated signatures in the transient absorption signatures of carotenoids.[66–70]

Having above discussed the energetic positions of the 0-ν vibronic replica for single ($\alpha = 0$) dominantly-coupled vibrational mode (energy $\hbar\omega_0$, mass M), we seek to evaluate their intensities within an absorption/emission spectrum. We can do this by finding the modulus-square of the Franck-Condon factor $|\langle\chi_{f,\nu}|\chi_{i,0}\rangle|^2$ for the 0-ν transition. We use the solutions for the wavefunctions of a quantum harmonic oscillator (Equation 2.55), which turn out to be the Hermite functions[105,144] (shown as orange filled curves in Figure 2.7)

$$\chi_{k,\nu} = \frac{1}{\sqrt{2^\nu \nu!}} \left(\frac{M\omega_0}{\pi\hbar}\right)^{\frac{1}{4}} \exp\left(-Q^2 \frac{M\omega_0}{2\hbar}\right) H_\nu\left(Q\sqrt{\frac{M\omega_0}{\hbar}}\right) \tag{2.60}$$

[†]We note that some works,[141] particularly those of the carotenoid literature,[66–70,98] refer to molecule-to-solvent VET as VC. In this thesis, we follow the definitions of *e.g.* Refs.[142,143] and define VC as solvent-to-solvent VET.

[‡]Specifically internal conversion; see Section 2.3.6 for details on non-radiative decay and its types.

where H_ν are the physicist's Hermite polynomials[144]

$$H_\nu(z) = (-1)^\nu \exp\left(z^2\right) \frac{\mathrm{d}^\nu}{\mathrm{d}z^\nu} \left[\exp\left(-z^2\right)\right]. \tag{2.61}$$

Using these to evaluate the integral over Q (which, in effect, is evaluating the overlap between relevant orange filled curves in Figure 2.7), we obtain[104]

$$\left|\langle \chi_{f,\nu} | \chi_{i,0} \rangle\right|^2 = \frac{S^\nu e^{-S}}{\nu!} \tag{2.62}$$

which notably is the form of a Poissonian distribution with mean S, which is the 'Huang-Rhys parameter' of form

$$S = \frac{M\omega_0}{2\hbar} |\Delta Q|^2 = \frac{\frac{1}{2}K|\Delta Q|^2}{\hbar\omega_0} \tag{2.63}$$

where ΔQ is the change in equilibrium nuclear coordinate (see Figure 2.7). The Huang-Rhys parameter represents the mean number of vibrational quanta ($\hbar\omega_0$) involved in a vibrational excitation of energy $\frac{1}{2}M\omega_0^2|\Delta Q|^2 = \frac{1}{2}K|\Delta Q|^2$ associated with the overall transition. In other words, we can define a geometric reorganisation (or relaxation) energy[103,104]

$$E_{\text{rel.}} = S\hbar\omega_0. \tag{2.64}$$

We note S can be determined from the ratio between the 0-1 and 0-0 peaks in absorption (or emission):[104]

$$S = \frac{\left|\langle \chi_{f,1} | \chi_{i,0} \rangle\right|^2}{\left|\langle \chi_{f,0} | \chi_{i,0} \rangle\right|^2}. \tag{2.65}$$

We close this section with model expressions for absorption and emission that approximate those measured in experiments. Note that these are for the case of a displaced oscillator with one dominant vibrational mode of energy $\hbar\omega_0$. We combine the vibronic transition energies (Equations 2.57 and 2.58), the Franck-Condon factors (Equation 2.62), and spectral broadening (discussed subsequently in Section 2.3.4) to give a model absorption

$$A(\hbar\omega) \propto (n\hbar\omega) \sum_\nu \frac{S^\nu e^{-S}}{\nu!} \Gamma\left[\hbar\omega - \left(E_{0\text{-}0}^{\text{abs.}} + \nu\hbar\omega_0\right)\right] \tag{2.66}$$

and a model emission

$$I(\hbar\omega) \propto (n\hbar\omega)^3 \sum_\nu \frac{S^\nu e^{-S}}{\nu!} \Gamma\left[\hbar\omega - \left(E_{0\text{-}0}^{\text{em.}} - \nu\hbar\omega_0\right)\right] \tag{2.67}$$

where $\hbar\omega$ is the transition energy (ω is the transition angular frequency), $n \equiv n(\hbar\omega)$ is the refractive index of the sample medium (which may have dependence on transition energy), and Γ is a linewidth function (see Section 2.3.4). The factor $(n\hbar\omega)$ and $(n\hbar\omega)^3$ for absorption and emission (respectively) accounts for the photon density-of-states in the sample medium and its influence on the absorption and emission from the sample.[103,145]

2.3.4 Broadening and disorder

In Equations 2.66 and 2.67 modelling absorption and emission spectra respectively, we used a 'linewidth function' Γ to account for the broadness of the vibronic replica. It highlights a point not presently accounted for within our descriptions above: the spectra of π-conjugated molecules in solution/solids at ambient temperatures are typically broad. The broadening of the 'lines' (implied frequently above to be Dirac delta functions) to the broad 'peaks' arises from a variety of sources associated with an ensemble (distribution) of molecules.

We consider isolated molecules in the condensed state initially, *i.e.* we will discuss dilute solutions/solids and will consider intermolecular interactions later. Cases where all the molecules in a system are equally (homogeneously) subject to some mechanism affecting the transition yields homogeneous broadening. These cases typically give a Lorentzian linewidth[103,146]

$$\text{Lorentzian: } \Gamma_{\mathrm{L}}(\hbar\omega) = \frac{(\gamma/2)^2}{(\hbar\omega)^2 + (\gamma/2)^2} \quad \text{(homogeneous)} \tag{2.68}$$

where γ here is full-width at half-maximum (FWHM) and $\Gamma_{\mathrm{L}}(0) = 1$ here by definition. A key type of homogeneous broadening present in all systems is natural (or lifetime) broadening. It can be viewed as a consequence of the uncertainty principle between energy and time; note the Fourier transform of an exponential decay is a Lorentzian profile.[146]

Cases where all the molecules in a system are randomly subject to some mechanism affecting the transition yields inhomogeneous broadening. The central limit theorem of statistics implies that these cases give a Gaussian linewidth[103,146]

$$\text{Gaussian: } \Gamma_{\mathrm{G}}(\hbar\omega) = \exp\left(-\frac{(\hbar\omega)^2}{2\sigma^2}\right) \quad \text{(inhomogeneous)} \tag{2.69}$$

where σ is the standard deviation (or the 'disorder parameter') of the Gaussian and $\Gamma_{\mathrm{G}}(0) = 1$ here by definition. $2\sigma\sqrt{2\ln 2}$ is the Gaussian FWHM, and 4σ is

the so-called $1/e^2$ full-width.[†] For π-conjugated molecules in solutions or solids, inhomogeneous broadening may arise because of a distribution of interactions between the molecules and their environment (which can also lead to a Stokes shift, as discussed in Section 2.3.3).[103]

The net broadening due to the different processes outlined above may be found through convolution. However, in most solution/solid systems at ambient temperatures, the inhomogeneous broadening mechanisms are dominant.[103] It is also more mathematically straightforward to work with a Gaussian profile than a convolved Lorentzian/Gaussian profile (a Voigt profile). Therefore, most fitting of the spectra of π-conjugated molecules assumes a Gaussian linewidth (Equation 2.69).[103,145]

Even considering these broadening effects, the absorption/emission spectra of π-conjugated molecules at ambient temperatures may not resemble those predicted by Franck-Condon theory. For the aforementioned dilute systems, it may simply be the case that the absorbing transition is not equivalent to the emissive transition.[103] Intermolecular effects between the solute molecules within concentrated solutions and solids can heavily distort the spectra, and add new radiative and non-radiative channels.[103,110] Such effects can lead to 'J-aggregated' molecules with narrow, redshifted features in both absorption and emission, with a theoretical enhancement to the photoluminescence quantum yield (PLQY) of emission.[‡112,113,147,148] Furthermore, absorption/emission spectra can appear broader simply due to the presence of multiple ground-state species, possibly through different conformations of the molecule of study. Indeed, in Chapter 6, we find that is the case for (transient) absorption spectra of dark-adapted orange carotenoid protein.

2.3.5 Spin selection rules

Finally, we discuss the $\langle \varsigma_{f,\sigma'} | \varsigma_{i,\sigma} \rangle$ 'spin factor' in the transition dipole moment (Equation 2.50). The spin factor is simply unity if the spin (S) of the initial $|\varsigma_{i,\sigma}\rangle$-state and final $|\varsigma_{f,\sigma'}\rangle$-state are equal, a case that is 'spin-allowed'. Meanwhile, the spin factor is zero if the spins are different between the initial and final states, a case that is 'spin-forbidden'.[103]

[†]The $1/e^2$ full-width is invoked in charactering laser beams with approximately two-dimensional Gaussian (TEM_{00}) profiles, especially within the context of fluence calculations (see Section 4.5). Note that e here Euler's number, so $1/e^2 \equiv \exp(-2)$; see footnote of page 24.

[‡]We study molecules that readily J-aggregate in Appendix D.

However, it is known that nominally spin-forbidden transitions between states with different spins can weakly occur. For example, the emission of photons from a triplet excited state to the singlet ground state (*i.e.* $T_1 \rightarrow S_0$) is well-known. This triplet-to-singlet photoemission is called 'phosphorescence', distinguished from spin-allowed photoemission events dubbed 'fluorescence'. Intersystem crossing (ISC) is another spin-forbidden transition that nevertheless occurs weakly. The physical mechanism by which these spin-forbidden transitions may occur is spin-orbit coupling, which will be discussed in Section 2.3.7. We note that spin-allowed transitions typically occur on a much faster timescale than the forbidden ones; fluorescence in π-conjugated molecules typically occurs on ∼ns–µs timescales, while phosphorescence occurs on ∼ms–s timescales, several orders of magnitude higher.[103,106]

2.3.6 Non-radiative decay

In addition to the radiative transitions discussed in the previous sections, intramolecular transitions between electronic states can also occur non-radiately, with no 'radiation' (photons) involved. We note and print two famous empirical rules in chemistry:

- Kasha's rule – 'the photoemitting electronic level of a given multiplicity is the lowest excited level of that multiplicity,'[111,149]
- Vavilov's rule – 'The quantum yield of photoemission is independent of the wavelength of exciting radiation.'[111]

These two empirical rules imply that an optically prepared high-energy state of a certain multiplicity rapidly and efficiently relaxes to the lowest-energy excited state of the same multiplicity through non-radiative decay.

Despite the name 'non-radiative decay', it *typically* appears to refer to transitions between electronic states, and is distinguished from features such as IVR (see Section 2.3.3). For IVR, transitions indeed occur without radiation, but since they are between the vibrational levels of a single electronic state, it is typically not termed non-radiative decay.[103] Intersystem crossing (ISC), which involves transitions between electronic states of different multiplicities (*e.g.* singlet to triplet state) may be considered a type of non-radiative decay. ISC will be discussed in Section 2.3.7. Meanwhile, non-radiative transitions between states of the same multiplicity (*e.g.* singlet to singlet) are termed internal conversion, and will be discussed below.[103]

The multiple types of non-radiative decay are typically encapsulated in a total non-radiative decay rate constant k_{nr}, contrasting with the radiative decay rate constant k_{r}. If a certain transition is said to be emissive, it means $k_{\mathrm{r}} > k_{\mathrm{nr}}$. Carotenoids such as β-carotene are typically non-emissive; k_{r} for the one-photon-allowed $S_2 \rightarrow S_0$ transition is much smaller than k_{nr} for $S_2 \rightarrow S_1$ (also recall S_1 is one-photon forbidden, so $S_1 \rightarrow S_0$ has $k_{\mathrm{r}} \ll k_{\mathrm{nr}}$ as well), which limits their photoluminescence quantum yield (PLQY) to ∼0.1%.[30,150]

We will briefly discuss the aforementioned same-multiplicity non-radiative decay, dubbed 'internal conversion', and two special cases through a 'conical intersection' or in the vicinity of an 'avoided crossing'. We first discuss internal conversion in π-conjugated molecules in the typical case.[†] Here, a transition between electronic states with the same spin multiplicity (that is, singlet to singlet, or triplet to triplet) occurs non-radiatively and isoenergetically purely through a change in the nuclear coordinates. This is a breakdown of the Born-Oppenheimer approximation (Section 2.2.1), as a change in the nuclear coordinates is causing a transition between electronic states.

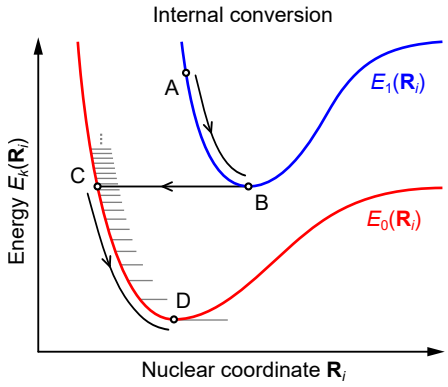

Figure 2.8 – Internal conversion occurring in a scheme of transitions between adiabatic potential energy surfaces. Initially, starting at A on potential energy surface $E_1(\mathbf{R}_i)$, IVR/VET occurs along AB towards the minimum. Internal conversion occurs along BC from $E_1(\mathbf{R}_i)$ to $E_0(\mathbf{R}_i)$; note that this is isoenergetic, with only a change in nuclear coordinates $\mathbf{R}_i$. IVR/VET then occurs along CD to the bottom of $E_0(\mathbf{R}_i)$. Note that the vibrational levels (thin grey lines) become more dense for greater $E_0(\mathbf{R}_i)$.

A scheme involving both internal conversion and IVR/VET is depicted in Fig-

[†]This internal conversion of chemical physics is not to be confused with the internal conversion of nuclear physics. The latter refers to an process where an excited nucleus transfers its energy non-radiatively to an electron, ejecting the electron from the atom.[151]

ure 2.8. IVR/VET to the lowest vibrational levels ($\nu_\alpha = 0$, where α denotes vibrational mode) is typically fast (IVR lifetime ~100 fs, VET lifetime ~10 ps),[106,110] as there are a large number of vibrational energy levels with relatively small spacing, resulting in rapid transitions.[103] Meanwhile, in most π-conjugated molecules, $S_1 \rightarrow S_0$ internal conversion is typically a slower process (>ns in acenes[110]), so it is the rate-limiting step in such a scheme. For β-carotene-like carotenoids however, the time constant for $S_2 \rightarrow S_1$ internal conversion is ~100 fs, and the time constant for $S_1 \rightarrow S_0$ internal conversion is ~5 ps.[30,100] Those rapid timescales yield the emergent phenomena associated with IVR/VET previously mentioned in Section 2.3.3.[66–70]

We outline a model by Siebrand[152,153] yielding a well-known proportional relation for the transition rate of internal conversion k_{IC} called the energy gap law, which was determined empirically from experimental work before Siebrand and other's efforts.[110] We start with a formulation of Fermi's golden rule (Equation 2.46). As the Born-Oppenheimer approximation has broken down, the usual separation of the total wavefunction into electronic, vibrational, and spin components (Equation 2.11) cannot be used (*i.e.* $|\Psi_{k,\nu,\sigma}\rangle \neq |\psi_k\rangle\,|\chi_{k,\nu}\rangle\,|\varsigma_{k,\sigma}\rangle$). Siebrand works outside of the Born-Oppenheimer approximation, and gets[154]

$$k_{IC} \simeq \frac{2\pi}{\hbar}\mathbb{J}^2\mathbb{F}\rho \tag{2.70}$$

where $\mathbb{J}$ is an energy term containing the non-adiabatic coupling between the initial and final electronic states, and $\mathbb{F}$ is a Franck-Condon factor containing the overlap of the initial and final vibrational wavefunctions. $\mathbb{F}$ here may be expressed

$$\mathbb{F} = \sum_P P\left(\prod_\alpha \left|\left\langle \chi_{f,\nu'_\alpha,\alpha} \middle| \chi_{i,\nu_\alpha=0,\alpha}\right\rangle\right|^2\right) \tag{2.71}$$

where $\sum_P P$ is an operator permuting the vibrational quanta among the vibrational modes α (subject to energy conservation), $|\chi_{i,\nu_\alpha=0,\alpha}\rangle$ is the initial vibrational wavefunction with zero vibrational quantum number ($\nu_\alpha = 0$) for mode α, and $\left|\chi_{f,\nu'_\alpha,\alpha}\right\rangle$ is a final vibrational wavefunction with vibrational quantum number ν'_α for mode α. Equations 2.70 and 2.71 are complicated multi-dimensional equations, but we can make some approximations and yield the energy-gap law. We consider only the vibrational mode (denoted with quantum number ν_0, *i.e.* $\alpha = 0$) which has the highest vibrational energy ($\hbar\omega_0$) among modes significantly coupled to the final electronic state, which in most π-conjugated molecules is the C=C stretching mode.[103] Immediately following an internal conversion, the vibrational

energy in the final state is equal to the energy difference between the minimum energies (zero vibrational quanta) of the initial and final state (ΔE), so we can write the vibrational quantum number in the final state as $\nu'_0 = \Delta E/\hbar\omega_0$. We recall that there are many vibrational levels in a molecule with relatively small spacing. At high vibrational levels in a general case (going beyond the 'quadratic potential'/quantum harmonic oscillator scheme of Section 2.3.3), the spacing between vibrational levels decreases (shown in Figure 2.8; thin grey lines denote vibrational levels). This spacing dependence gives an exponential dependence of the Franck-Condon factor $\mathbb{F}$ on ν'_0. Therefore, evaluation of the terms in Equation 2.70 gives us the energy gap law

$$k_{\mathrm{IC}} \propto \exp\left(-\frac{\gamma \Delta E}{\hbar\omega_0}\right) \tag{2.72}$$

where γ is a quantity that is dependent on various molecular parameters.[103,110]

We now discuss the special cases of internal conversion through a conical intersection or around an avoided crossing. For the Born-Oppenheimer approximation to hold, the different adiabatic potential energy surfaces have to be well-separated.[155] In the case of small or no separation, the Born-Oppenheimer approximation breaks down (again), new non-radiative decay processes occur, and the overall internal conversion rate does not follow the energy gap law (Equation 2.72).

In the case of a conical intersection, two potential energy surfaces directly overlap and are truly degenerate. A one-dimensional schematic is shown in Figure 2.9a; note that at least two reaction coordinates are required for a conical intersection to exist.[156] The name 'conical intersection' refers to the double cone-like appearance near the overlap point of the surfaces in a two-dimensional picture.[†] Near a conical intersection point, the non-Born-Oppenheimer coupling between electronic states is strong, as is the coupling to (and between) vibrational modes. Hence internal conversion *via* a conical intersection occurs at timescales dependent on $\hbar\omega_0$, and can be around several femtoseconds, *i.e.* many orders of magnitude faster than that by internal conversion without conical intersection.[157,158]

It has been argued that the β-carotene $S_2 \rightarrow S_1$ non-radiative decay ($\sim$100 fs time constant) is mediated by a conical intersection,[159] although it is generally accepted that non-radiative decay in carotenoids occurs *via* internal conversion without conical intersection.[30,100,150] Some works on π-conjugated molecules argue

[†]Conical intersections have been termed by some as 'diabolical points', as diabolo toys resemble double cones.[157]

that *cis-trans* photoisomerisation about C=C double bonds (a 'non-adiabatic event') occurs *via* a conical intersection.[156]

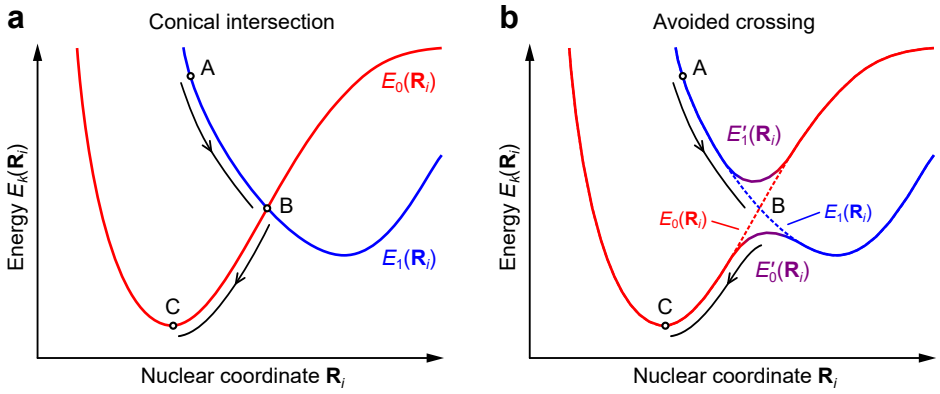

Figure 2.9 – Conical intersection (a) and avoid crossings (b) within schemes of transitions between potential energy surfaces. (a) A scheme with a conical intersection. Initially, starting at A on adiabatic potential energy surface $E_1(\mathbf{R}_i)$, IVR occurs along AB towards the surface intersection point. The conical intersection occurs at B from $E_1(\mathbf{R}_i)$ to $E_0(\mathbf{R}_i)$; note that this involves no change in energy or nuclear coordinates. IVR then occurs along BC to the bottom of $E_0(\mathbf{R}_i)$. Despite this one-dimensional representation, at least *two* reaction coordinates are required for a conical intersection to exist. **(b)** A scheme with an avoided crossing. Initially, starting at A on adiabatic potential energy surface $E'_1(\mathbf{R}_i)$, IVR occurs along AB towards the avoided crossing region. The avoid crossing occurs around B from $E'_1(\mathbf{R}_i)$ to $E'_0(\mathbf{R}_i)$. IVR then occurs along BC to the bottom of $E'_0(\mathbf{R}_i)$. Note that the diabatic potential energy surfaces $E_0(\mathbf{R}_i)$ (red dotted lines) and $E_1(\mathbf{R}_i)$ (blue dotted lines) mix to form the adiabatic potential energy surfaces $E'_0(\mathbf{R}_i)$ and $E'_1(\mathbf{R}_i)$ (purple solid lines) around the conical intersection point B.

Another case of non-radiative decay with non-Born-Oppenheimer behaviour is through an avoided crossing. The phenomenon appears frequently in quantum mechanics[†] and has been dubbed level anticrossing,[160] intended crossing,[111] and 'von Neumann–Wigner theorem' in honour of the namesakes' theoretical work on the subject.[161] The diabatic potential energy surfaces mix around the avoided crossing region, resulting in adiabatic potential energy surfaces that do not intersect. This is depicted schematically in Figure 2.9b. Note that avoided crossings tend to occur in the vicinity of conical intersections.[111]

[†]For example, avoided crossings between pure triplet-pair states are depicted in Figure 2.12c.

2.3.7 Spin-orbit coupling

We discussed the spin selection rules for radiative transitions in Section 2.3.5, which implied that radiative transitions between states of different spins are nominally spin-forbidden. Nevertheless, weak emissive transitions such as $T_1 \rightarrow S_0$ phosphorescence have been observed in conjugated molecules.[†103] Further, although non-radiative transitions between states of different spins are also nominally spin-forbidden (encapsulated in the $\mathbb{J}$ term of Equation 2.70), through so-called intersystem crossing (ISC),[‡] we do see triplet signatures forming *via* non-radiative channels after initial excitation into singlet states.[§] Both phosphorescence and ISC are mediated by 'spin-orbit coupling'. In rough terms, the (total) orbital angular momentum $\mathbf{L}$ of the electrons couples to the (total) spin angular momentum $\mathbf{S}$, so the sum $(\mathbf{L} + \mathbf{S})$ has to be conserved. Therefore, the usual conservation of spins is somewhat relaxed, permitting phosphoresence and ISC to weakly occur. We can characterise the perturbation caused by spin-orbit coupling using H_{SO}, the spin-orbit Hamiltonian.[103,164]

We briefly refer to the toy model of the hydrogen-like atom with nuclear charge Ze and a single electron at distance r from the nucleus to demonstrate key proportionalities arising from H_{SO} (a formulation considering a molecule is unnecessarily complex here). It can be shown that H_{SO} may be approximately written as[¶166]

$$H_{\mathrm{SO}} \simeq \frac{(g_{\mathrm{S}} - 1)}{2m^2c^2} \frac{1}{r} \frac{\partial V(r)}{\partial r} \mathbf{L} \cdot \mathbf{S} \tag{2.73}$$

where $g_{\mathrm{S}} \simeq 2$ is the electron g-factor, m is the electron mass, $V(r)$ is the Coulombic potential energy, $\mathbf{L}$ is the orbital angular momentum of the electron, and $\mathbf{S}$ is its spin angular momentum. Inserting the usual form of $V(r) = -Ze^2/4\pi\varepsilon_0 r$ yields

$$H_{\mathrm{SO}} \simeq \frac{Ze^2(g_{\mathrm{S}} - 1)}{8\pi\varepsilon_0 m^2 c^2} \frac{1}{r^3} \mathbf{L} \cdot \mathbf{S}. \tag{2.74}$$

It is apparent from this that H_{SO} is sensitively dependent on r; as an electron approaches a nucleus, the spin-orbit coupling becomes very large. Furthermore,

[†]Indeed, some studies claim to observe phosphorescence from β-carotene, but it could have been the case that an impurity was emitting and yielding the signatures observed.[162,163]

[‡]Note that some works distinguish intersystem crossing (ISC) from singlets to triplets against reverse intersystem crossing (RISC) from triplets to singlets.[164,165]

[§]Note that ISC is distinct from singlet fission (SF), which is a spin-allowed triplet generation process. See Section 2.4 for details on SF.

[¶]We note that the Thomas precession has been accounted for here, a phenomenon from special relativity which (in short) has the effect $g_{\mathrm{S}} \mapsto (g_{\mathrm{S}} - 1)$.[166]

if we evaluate the expectation value of $1/r^3$ using the analytic wavefunctions for a hydrogen-like atom, it can be shown that

$$\left\langle \frac{1}{r^3} \right\rangle \propto Z^3 \tag{2.75}$$

which allows us to write the important proportionality

$$H_{\mathrm{SO}} \propto Z^4. \tag{2.76}$$

This shows that H_{SO} is also sensitively dependent on Z. In fact, in molecules (rather than the hydrogen-like atom above), it is thought that the Z-dependence is a power from 4 to 5 (rather than exactly 4).[103] Therefore, in the presence of heavy atoms, the spin-orbit coupling in molecules becomes very large.

When heavy atoms are directly incorporated into a molecule, the resulting enhancement in H_{SO} is dubbed the internal heavy atom effect. However, heavy atoms nearby an unsubstituted organic molecule can give changes in H_{SO}, provided there is sufficient orbital overlap; this is dubbed the external heavy atom effect. The latter effect may be achieved by using certain solvents or doping with halogens or high-Z metal ions,[103] and was attempted for ISC enhancement in Section 7.2.3 using iodine ($Z = 53$) and salts of europium ($Z = 63$) and platinum ($Z = 78$).

We note that spin-orbit coupling can be enhanced by the nature of the initial state (Ψ_i) and final state (Ψ_f), which we can see (in a basic sense) by writing[164]

$$\langle H_{\mathrm{SO}} \rangle = \langle \Psi_f | \, H_{\mathrm{SO}} \, | \Psi_i \rangle \tag{2.77}$$

and noting ($\mathbf{L} + \mathbf{S}$) may be conserved overall. If the Ψ_i and Ψ_f states have a different orbital character, $\langle H_{\mathrm{SO}} \rangle$ is enhanced. This is noted qualitatively in El-Sayed's rule,[167,168] where (for example) the $^1(\mathrm{n},\pi^*) \rightarrow ^3(\pi,\pi^*)$ intersystem crossing (ISC) rate is faster than that for $^1(\pi,\pi^*) \rightarrow ^3(\pi,\pi^*)$.[111,164,169] The notation here denotes the spin multiplicity (m) and the HOMO, LUMO character of a state, *i.e.* ^{m}(HOMO,LUMO), and n denotes a non-bonding orbital. Indeed, El-Sayed's rule is possibly the means by which keto-carotenoids (*e.g.* canthaxanthin), which have non-bonded orbitals within the carbonyl oxygen, have an order of magnitude faster ISC than comparable unsubstituted carotenoids (*e.g.* β-carotene).[99] In Chapter 7, we hypothesise that the orange carotenoid protein (OCP) binds keto-carotenoids such as canthaxanthin specifically for the relatively efficient formation of triplet states *via* ISC.

Furthermore, the $\langle H_{\mathrm{SO}} \rangle$ term can be enhanced through 'vibronic spin-orbit coupling' if there are vibrational modes that perturb the spin-orbit Hamiltonian.[164,169–171] In a simple picture, a vibration is quenched (or enhanced) to conserve $(\mathbf{L} + \mathbf{S})$. We can mathematically describe vibronic spin-orbit coupling by expanding Equation 2.77 in terms of the perturbing vibrational coordinates (Q_α) up to first-order:[170]

$$\langle H_{\mathrm{SO}} \rangle = \langle \chi_f | \chi_i \rangle \langle \psi_f | H_{\mathrm{SO}} | \psi_i \rangle + \sum_\alpha \langle \chi_f | Q_\alpha | \chi_i \rangle \frac{\partial \langle \psi_f | H_{\mathrm{SO}} | \psi_i \rangle}{\partial Q_\alpha}. \tag{2.78}$$

The resulting zero-order term is the usual direct spin-orbit coupling term, while the first-order term is the first-order vibronic spin-orbit coupling term. Note that vibronic spin-orbit coupling terms of higher order exist.[164,171]

We can write an expression for the intersystem crossing (ISC) rate between two states of different spin multiplicities by treating H_{SO} as a weak perturbation within Siebrand's model, which we have previously discussed for the case of internal conversion (see Section 2.3.6). We write[154]

$$k_{\mathrm{ISC}} \simeq \frac{2\pi}{\hbar} \mathbb{J}_{\mathrm{SO}}^2 \mathbb{F} \rho \tag{2.79}$$

where the energy term $\mathbb{J}_{\mathrm{SO}}$ contains a dependence on H_{SO},[172] $\mathbb{F}$ is the Franck-Condon factor containing the overlap of the initial and final vibrational wavefunctions (Equation 2.71), and ρ is the density of final states.[154] As is the case for internal conversion (Section 2.3.6), evaluation of the Franck-Condon factor yields a dependence on the vibrationally-relaxed energy gap ΔE between the states (not dissimilar to the energy gap law for internal conversion, Equation 2.72). If two states of different multiplicity have a small energetic difference, k_{ISC} between them may be large, even in the case of small H_{SO}. Indeed, rapid intersystem crossing has been demonstrated for anthracene in solution from $\mathrm{S}_1 \rightarrow \mathrm{T}_2$, owing to both the small energy gap and large Franck-Condon factor $\mathbb{F}$ associated with the transition.[173–175]

We note also that spin-orbit coupling also mediates phosphorescence. Taking the example of phosphorescence from the triplet T_1 to the ground-state singlet S_0, we can write an expansion for a 'perturbed' triplet wavefunction $|\mathrm{T}_1'\rangle$ (in contrast to the unperturbed states without primes) using first-order time-independent perturbation theory[103,129]

$$|\mathrm{T}_1'\rangle = |\mathrm{T}_1\rangle + \sum_k \frac{\langle \mathrm{S}_k | H_{\mathrm{SO}} | \mathrm{T}_1 \rangle}{E(\mathrm{T}_1) - E(\mathrm{S}_k)} |\mathrm{S}_k\rangle \tag{2.80}$$

where E denotes the energy of a state. We can write a similar expansion for a 'perturbed' ground-state singlet $|S_0'\rangle$

$$|S_0'\rangle = |S_0\rangle + \sum_k \frac{\langle T_k| H_{SO} |S_0\rangle}{E(S_0) - E(T_k)} |T_k\rangle \tag{2.81}$$

and use both within a form of Fermi's golden rule (Equation 2.46) to yield an expression for the phosphorescence rate. As the energy gaps between T_1 and S_k are generally smaller than those for S_0 and T_k, the perturbed triplet $|T_1'\rangle$ makes the dominant contribution to the phosphorescence rate. In other words, the singlet admixtures within the nominal triplet state contributes the majority of oscillator strength for phosphorescence, and those admixtures are mediated by H_{SO}'s perturbation.[103]

2.4 Singlet fission (SF)

Singlet fission (SF) is a spin-allowed excitation (or, more strictly, exciton) multiplication process where a singlet excited state leads to two 'geminate' triplet excited states.[12–15] SF was first invoked to explain the temperature-dependent fluorescence signatures of crystalline anthracene by Singh *et al.* in 1965.[176] Notably, the reverse process of triplet-triplet annihilation (TTA), where two possibly non-geminate triplets combine to form a singlet, was observed before SF, also within crystalline anthracene.[177]

In this section, we will discuss singlet fission (SF) in π-conjugated molecules in fairly broad terms to review the current understanding. The past two decades have seen an explosion of interest in SF (see Figure 2.10), and we seek to take this new knowledge and apply it to carotenoids, the molecules of study in this thesis. In particular, Chapter 5 concerns the lack of *intra*molecular singlet fission (intra-SF) observed in a single carotenoid that is twisted within its protein complex, despite a common hypothesis within the literature on light-harvesting complexes suggesting that intra-SF occurs in twisted carotenoids.[41–45] Reviewing the broader SF literature will aid us in resolving this apparent discrepancy.

2.4.1 A brief history of SF

As stated above, the reverse process of singlet fission (SF), called triplet-triplet annihilation (TTA), was observed prior to SF. Two annihilating triplets produced by direct laser excitation within anthracene crystals were proposed to form a singlet,

which then would radiatively decay, resulting in observable 'delayed' fluorescence persisting at times beyond that expected by the 'prompt' fluorescence under the intrinsic radiative lifetime.[177] Johnson, Merrifield, *et al.* later showed that the intensity of the delayed fluorescence is dependent on an externally applied magnetic field.[178,179] Weak magnetic fields ($B \sim 50\,\mathrm{mT}$) would produce marked changes in the delayed fluorescence intensity, despite the Zeeman energies associated with weak fields (roughly $\mu_B B \sim 3\,\mu\mathrm{eV}$) being several orders of magnitude less than the energies of the excited electronic states involved (∼eV). It led the authors to wonder if some kind of spin selection rule is satisfied more (or less) frequently depending on an external magnetic field, considering that two triplet spins may couple to an overall singlet spin. In 1970, the authors published a famous kinetic scheme for TTA, the 'Merrifield model',

$$\mathrm{T}_1 + \mathrm{T}_1 \underset{k_{-1}}{\overset{k_1}{\rightleftharpoons}} (\mathrm{TT}) \xrightarrow{k_2} \mathrm{S}_1 \tag{2.82}$$

where T_1 denotes a free triplet, (TT) denotes a triplet-pair, and S_1 denotes a singlet.[180] We note that in this model, it is assumed that the triplet pairs do not interact through exchange coupling (*i.e.* $J = 0$), so today we could write (TT) as $(\mathrm{T...T})^l$ (see Section 2.4.2 for further details).[181] The (TT)→S_1 step is the one affected by the external magnetic fields through changing the singlet projections of (TT), leading to the observed signatures in the prompt/delayed fluorescence (see Section 2.4.3 for further details).[160,165,181,182]

Meanwhile, around 1970, the reverse process of TTA, singlet fission (SF), was clearly demonstrated in tetracene crystals.[183,184] Groff, Merrifield, *et al.* also studied tetracene, and began incorporating the 'reverse' SF within their 'forward' TTA schemes.[182,185] We may write an adaption of the Merrifield model (Equation 2.82) as

$$\mathrm{T}_1 + \mathrm{T}_1 \underset{k_{-1}}{\overset{k_1}{\rightleftharpoons}} (\mathrm{TT}) \underset{k_{-2}}{\overset{k_2}{\rightleftharpoons}} \mathrm{S}_1 \tag{2.83}$$

which now includes a S_1→(TT) step. The forward process (left to right) represents TTA, while the backward process (right to left) represents SF. We write another formulation of this as Equation 2.93, dubbed the 'modified Merrifield model', which includes a time dependence for the exchange coupling strength $J(t)$ (further details in Section 2.4.2).[180,181]

Following the initial interest in SF and TTA from the early 1960s up to the mid-1970s, the topics entered a slight dormancy, until it was suggested in 2004 by Nozik, Michl, and co-workers that the use of SF/TTA in tandem photovoltaics could improve their overall efficiency.[186–188] This led to an exponential-like growth

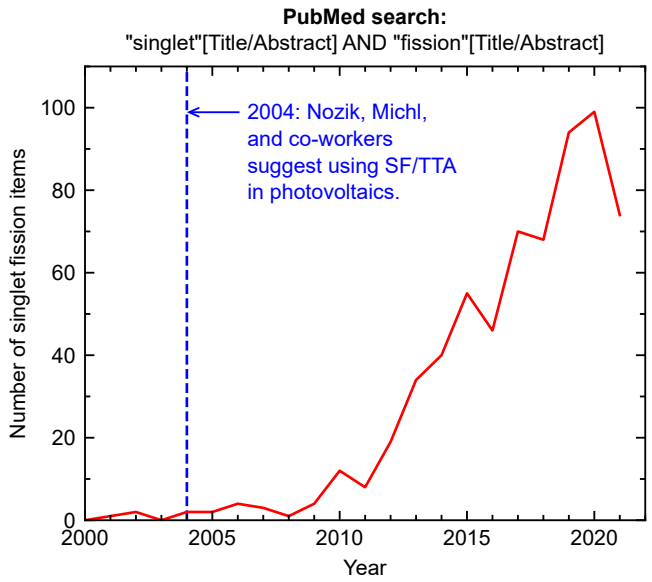

Figure 2.10 – Number of items on PubMed with 'singlet fission' in the title or abstract per year. Search performed on 17 November 2022 on PubMed, with search term: `"singlet"[Title/Abstract] AND "fission"[Title/Abstract]`

from around then up to 2020 in the number of works per year including including 'singlet' and 'fission' within the title or abstract; see Figure 2.10, which shows the results of a PubMed search.

We elaborate on the potential solar photovoltaic efficiency improvements promised by SF and TTA. For a single-junction silicon photovoltaic, the theoretical maximum power conversion efficiency (the total efficiency of conversion from solar irradiation to electricity) is the Shockley-Queisser limit[8] of ∼33%. This limit arises from two key loss mechanisms:

(1) Photons with energy E_γ incident on the photovoltaic with E_γ lower than the silicon band-gap of $E_g = 1.1\,\text{eV}$, *i.e.* $E_\gamma < E_g$, are not absorbed.[11]

(2) For photons with energies $E_\gamma > E_g$ incident on the photovoltaic, one exciton with $E_\gamma - E_g$ worth of extra vibrational/thermal energy is generated, but that extra thermal energy has no bearing on subsequent charge separation and collection. In effect, the extra energy has been lost due to 'thermalisation'.[11]

As the photoconversion efficiency of real single-junction silicon photovoltaics is approaching the Shockley-Queisser limit, there is interest in exciton multiplication/fusion techniques that can boost efficiencies beyond that ∼33% limit. Namely, TTA may partially mitigate loss mechanism (1), and SF may partially mitigate loss mechanism (2). For example, using SF, two excitons of energies

above E_g could be generated using a photon of initial energy $E_\gamma > 2E_g$, hence two sets of charges are eventually collected from a single high-energy photon. Without downconversion through SF in that case, only one exciton would be generated, and an energy $>E_g$ lost to thermalisation.

Theoretical calculations suggest that tandem photovoltiacs incorporating SF give a maximum power conversion efficiency of the solar spectrum of ∼45%, a huge improvement on the Shockley-Queisser limit of ∼33%.[16,17] Theoretical calculations on similar architectures incorporating TTA are suggested to yield similar efficiency increases.[189,190] In addition to the potential improvement to solar photovoltaic efficiency, SF could also be useful for non-linear optics,[18–20] OLEDs,[21] and possibly quantum technologies[22–25] since pairs of spin-entangled triplet-pairs are produced through SF. However, despite promising results,[26,27] practical applications are yet to be realised, partly due to the limited library of SF materials, none of which is yet ideal.[11,14] It could be argued these difficult practicalities are the reason for the end of the exponential-like growth in the number of SF works per year (Figure 2.10).

In their 2013 review paper,[13] Smith and Michl classified the then-studied SF materials into three classes. Those of 'class I' are distinguished by their $S_0 \rightarrow S_1$ one-photon absorption, and are still presently the most well-studied among SF materials.[191–194]. They are mostly based on acene molecules such as tetracene[195–198] and pentacene.[181,199] SF materials of 'class II' are distinguished by a one-photon absorption usually producing S_2, which arises as the $S_0 \rightarrow S_1$ transition corresponds to a linear combination of two promotions, *e.g.* [(HOMO−1→LUMO) − (HOMO→LUMO+1)]. Examples include naphthalene and pyrene.[13] 'Class III' SF materials include the polyenes and carotenoids. They are distinguished from the other classes for their $S_0 \rightarrow S_2$ one-photon absorption, which is thought to arise because the singlet S_1 has a significant contribution from triplet-pair states.[97,116–122]

2.4.2 Triplet-pair states

The initially formed state following SF is a triplet-pair state, which is denoted (TT) in the Merrifield model (Equation 2.83). It consists of four electrons (in unfilled orbitals) with two electrons per triplet. We seek to characterise the nature of the triplet-pair state more thoroughly than our general descriptions above (Section 2.4.1). We start by constructing spin eigenstates to the four-electron

total spin operator squared, $\mathbf{S}^2$ (eigenvalue $S(S+1)$, spin quantum number S), similarly to the two-electron case of isolated singlets/triplets (Section 2.2.5). We can write, for a pair of excitons, the four-electron total spin as[12]

$$\mathbf{S} = \underbrace{\mathbf{S}_1 + \mathbf{S}_2}_{\mathbf{S}_A} + \underbrace{\mathbf{S}_3 + \mathbf{S}_4}_{\mathbf{S}_B} \tag{2.84}$$

where '1' and '2' are the electrons associated with exciton A ($\mathbf{S}_A = \mathbf{S}_1 + \mathbf{S}_2$), and '3' and '4' are the electrons associated with exciton B ($\mathbf{S}_B = \mathbf{S}_3 + \mathbf{S}_4$). It turns out that there are 16 spin eigenstates (2 singlets, 9 triplets, 5 quintets), of which there are 9 consisting of pairs of triplets. These 9 triplet-pairs have the lowest energy (see Figure 2.11) mediated through the singlet-triplet exchange integral J_0 (see Section 2.2.5). There is 1 singlet triplet-pair, and its spin eigenket may be expressed[200]

$$\begin{aligned}\left|{}^1(\mathrm{TT})\right\rangle = \frac{1}{2\sqrt{3}}\big(&\left|\uparrow\right\rangle_1\left|\downarrow\right\rangle_2\left|\uparrow\right\rangle_3\left|\downarrow\right\rangle_4 + \left|\uparrow\right\rangle_1\left|\downarrow\right\rangle_2\left|\downarrow\right\rangle_3\left|\uparrow\right\rangle_4 + \left|\downarrow\right\rangle_1\left|\uparrow\right\rangle_2\left|\uparrow\right\rangle_3\left|\downarrow\right\rangle_4 \\ &+ \left|\downarrow\right\rangle_1\left|\uparrow\right\rangle_2\left|\downarrow\right\rangle_3\left|\uparrow\right\rangle_4 - 2\left|\uparrow\right\rangle_1\left|\uparrow\right\rangle_2\left|\downarrow\right\rangle_3\left|\downarrow\right\rangle_4 - 2\left|\downarrow\right\rangle_1\left|\downarrow\right\rangle_2\left|\uparrow\right\rangle_3\left|\uparrow\right\rangle_4\big)\end{aligned} \tag{2.85}$$

and there are also 3 triplet triplet-pairs (${}^3(\mathrm{TT})$), and 5 quintet triplet-pairs (${}^5(\mathrm{TT})$). Note that the triplet-pairs are denoted ${}^m(\mathrm{TT})$, where m is the triplet-pair multiplicity which denotes the net spin character. The four-electron triplet-pair states may be expressed in terms of the two-electron triplet states in either the high-field basis (Equations 2.15–2.17) or the low-field basis (Equations 2.28–2.30).[12,201] For example, the singlet triplet-pair spin eigenket may be written

$$\begin{aligned}\left|{}^1(\mathrm{TT})\right\rangle &= \frac{1}{\sqrt{3}}\left(\left|1,0\right\rangle_A\left|1,0\right\rangle_B - \left|1,1\right\rangle_A\left|1,-1\right\rangle_B - \left|1,-1\right\rangle_A\left|1,1\right\rangle_B\right) \\ &= \frac{1}{\sqrt{3}}\left(\left|\mathrm{T},x\right\rangle_A\left|\mathrm{T},x\right\rangle_B + \left|\mathrm{T},y\right\rangle_A\left|\mathrm{T},y\right\rangle_B + \left|\mathrm{T},z\right\rangle_A\left|\mathrm{T},z\right\rangle_B\right).\end{aligned} \tag{2.86}$$

It is worth emphasising that the existence of a triplet-pair that is overall-singlet makes SF spin-allowed; hence SF can proceed efficiently with very fast timescales. For example, triplet formation by intermolecular SF with fastest time constant 65 fs has been shown in aggregates of the carotenoid astaxanthin.[35]

We recall that isolated triplets may be distinguished in energy *via* the zero-field splitting Hamiltonian term (Equation 2.32) and the Zeeman Hamiltonian term (Equation 2.41). Similarly, the triplet-pairs can be distinguished through a similar overall Hamiltonian, although there are additional complications due to

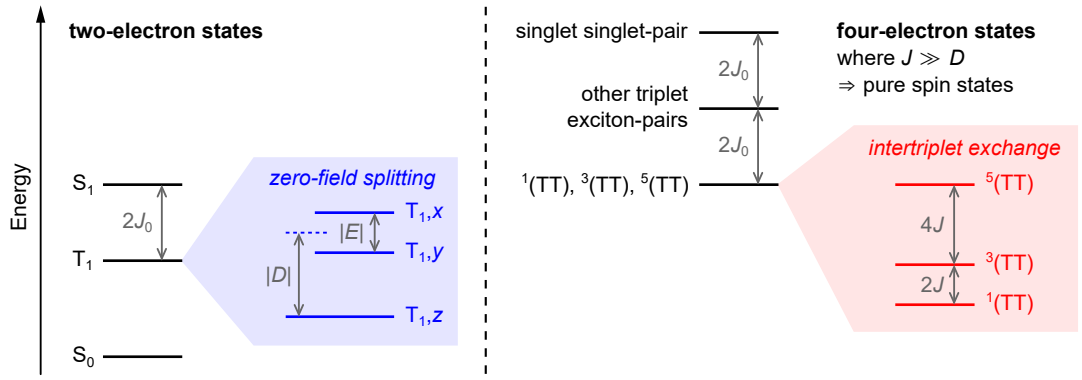

Figure 2.11 – Energies of states in the two-electron model (left) and pure-spin exciton-pairs in the four-electron model (right). Two-electron singlet and triplet excited states are distinguished by twice the singlet-triplet exchange integral $2J_0$ ($2J_0 \sim 1\,\text{eV}$ in most π-conjugated molecules[202]), see Section 2.2.5 for details. The three triplet states are further distinguished by zero-field splitting (intratriplet dipolar) parameters D and E (for most[103,127,128] π-conjugated molecules $D \sim 4$–$10\,\mu\text{eV}$; note we set D positive here, so E is negative), see Section 2.2.6 for details. $J \gg D$ here which leads to four-electron exciton-pair states with well-defined spin (good quantum number). The energies of some combinations are distinguished by $2J_0$, with triplet-pair states having the lowest energies[202] that are further distinguished through J, the intertriplet exchange parameter ($E(^5(\text{TT})) - E(^3(\text{TT})) = 4J$, $E(^3(\text{TT})) - E(^1(\text{TT})) = 2J$ following Ref.[201]). In the case where $J \ll D$, spin is no longer well-defined, and the exciton-pair states have mixed spin character; see text for details.

intertriplet cross terms. We write the overall Hamiltonian containing the triplet-pair distinguishing terms as

$$\begin{aligned} H_{\text{spin}} = &\sum_{i=A,B} \left[H_{\text{zero-field},i} + H_{\text{Zeeman},i} \right] \\ &+ H_{\text{intertriplet dipolar}} + H_{\text{intertriplet exchange}} \end{aligned} \tag{2.87}$$

where the terms in the square brackets are the familiar intratriplet zero-field splitting and Zeeman terms for triplet A and B, while there are two new contributions.

We briefly discuss each contribution in turn. The zero-field term may be written

$$H_{\text{zero-field},i} = D\left(S_{i,z}^2 - \frac{1}{3}\mathbf{S}_i^2\right) + E\left(S_{i,x}^2 - S_{i,y}^2\right) \tag{2.88}$$

where we note that we are assuming a case of identical molecules (such that the D and E parameters are the same per-molecule).[12] We note that the Cartesian coordinate system of molecule B in general does not coincide with that for A, so

a rotation operation must be considered for $H_{\text{zero-field},B}$, as Ref.[124] highlights. Recall that in most π-conjugated molecules[103,127,128] D lies in the range ∼4–10 µeV. Meanwhile, the Zeeman term is simply

$$H_{\text{Zeeman},i} = g_{\text{L}}\mu_{\text{B}}\mathbf{B}\cdot\mathbf{S}_i. \tag{2.89}$$

The intertriplet dipole-dipole term may be expressed

$$H_{\text{intertriplet dipolar}} = \mathbf{S}_A\cdot\mathbf{D}_{\text{inter}}\mathbf{S}_B \tag{2.90}$$

where $\mathbf{D}_{\text{inter}}$ is a matrix describing the intertriplet dipolar interaction. The size of the interaction is typically described with a single scalar X; in general this parameter is very small ($X \sim D/1000$),[203,204] so a precise form for the Hamiltonian term is not important and it is typically written approximately. For example, in Refs.[124,204] it is expressed as

$$H_{\text{intertriplet dipolar}} \simeq X\left[\mathbf{S}_A\cdot\mathbf{S}_B - 3\left(\mathbf{S}_A\cdot\hat{\mathbf{r}}\right)\left(\mathbf{S}_B\cdot\hat{\mathbf{r}}\right)\right]. \tag{2.91}$$

Finally, the intertriplet exchange/resonance term is written[201]

$$H_{\text{intertriplet exchange}} = 2J\mathbf{S}_A\cdot\mathbf{S}_B \tag{2.92}$$

characterised by the scalar J. This parameter describes the intertriplet orbital overlap,[12] and is analogous to the singlet-triplet exchange parameter/integral J_0 (Equation 2.25). We note that some works (*e.g.* Ref.[160]) write J rather than $2J$ here; we follow Ref.[201] and write $2J$.

It turns out that in the case of strong intertriplet exchange coupling, *i.e.* $J \gg D$, the 9 triplet-pair eigenstates to $\mathbf{S}^2$ are also spin eigenstates to the spin Hamiltonian H_{spin} (Equation 2.87).[165] Those spin eigenstates are termed 'pure' spin states. The ^{3}(TT) states and ^{5}(TT) states are separated in energy from the ^{1}(TT) state by $2J$ and $6J$ respectively (see Figure 2.11).[12] We note that the aforementioned alternate expression for $H_{\text{intertriplet exchange}}$ (Equation 2.92) leads to gaps of J and $3J$ respectively (as in *e.g.* Ref.[160]); we follow Ref.[201] and write $2J$ and $6J$ respectively.

Meanwhile, in the case of weak intertriplet exchange coupling, *i.e.* $J \ll D$, spin is no longer a good quantum number and those pure spin states are *not* spin eigenstates to H_{spin}. The 9 new spin eigenstates to H_{spin} may be denoted $(\text{T...T})^l$ (where $l = 1, 2, \ldots, 9$) and are said to be 'mixed' spin states.[†123]

[†]Note that in the specific case of parallel molecules where $J \ll D$, there are 3 pure triplet triplet-pair states, 3 pure quintet triplet-pair states, and 3 triplet-pair states of mixed character.[165]

In many real systems, J is dynamic ($J \equiv J(t)$), with the triplet-pair initially 'correlated' with $J(t) \gg D$, then at later times losing electronic coherence but retaining some spin coherence with $J(t) \ll D$. Eventually the spin coherence is also lost and the triplets become free triplets. Considering this, we can write a 'modified Merrifield' SF scheme as[181]

$$S_1 \rightleftharpoons {}^1(TT) \rightleftharpoons (T...T)^l \rightleftharpoons T_1 + T_1 \tag{2.93}$$

where the modification is the addition of the strongly exchange-coupled ${}^1(TT)$, since the Merrifield model assumed $J = 0$ throughout the SF process, meaning their (TT) state is the $(T...T)^l$ state here.[180,181] Here, the forward process (left to right) represents SF, while the backward process (right to left) represents triplet-triplet annihilation (TTA). Notably, some works denote a single step within this process as the 'singlet fission' step, such as the $S_1 \rightarrow {}^1(TT)$ step, but S_1 and ${}^1(TT)$ are difficult to distinguish in 'class I' materials, and in 'class III' materials (polyenes and carotenoids) S_1 has ${}^1(TT)$ (triplet-pair) character.[12,13,97,116–122] We will refer to the whole process ($S_1 \rightarrow 2 \times T_1$) as SF throughout the remainder of this thesis.

2.4.3 Magnetic field effects

In this subsection, we discuss an important experimental signature for the presence of singlet fission (SF) and, if present, the character of the exchange coupling. Spin has to be conserved in the ${}^1(TT) \rightarrow (T...T)^l$ step, *i.e.* ${}^1(TT) \rightarrow {}^1(T...T)$ is an implicit step in the modified Merrified scheme (Equation 2.93), where ${}^1(T...T)$ is a weakly exchange-coupled singlet triplet-pair state. Hence the the $(T...T)^l$ singlet character, denoted C_S^l, is critically important in SF. C_S^l may be expressed

$$C_S^l = \left\langle {}^1(TT) \middle| (T...T)^l \right\rangle \tag{2.94}$$

with $\left|(T...T)^l\right\rangle$ the spin ket for the weakly exchange-coupled triplet-pair of label l. The rate of the ${}^1(TT) \rightarrow (T...T)^l$ step is proportional to $\left|C_S^l\right|^2$. Importantly, external magnetic fields can modify $\left|C_S^l\right|^2$ *via* the Zeeman term of the spin Hamiltonian.[165,181,182]

Simulations of the magnetic field dependence on the fluorescence and associated parameters in the two limits of $J \ll D$ and $J \gg D$ for a SF material are shown in Figure 2.12. The simulations and the figure were prepared by David G. Bossanyi.[205] We first discuss the case of weakly exchange-coupled triplets

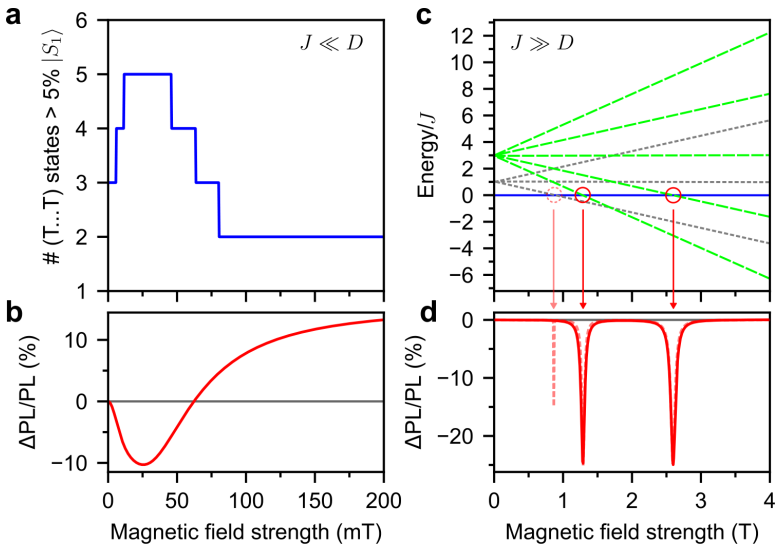

Figure 2.12 – Simulations of the magnetic field dependence in the limits of weak (a,b) and strong (c,d) intertriplet exchange coupling regimes. (a) The number of mixed spin states ($(\mathrm{T...T})^l$) with >5% ^{1}(TT) character, where $J = 0 \ll D$ and molecules are equivalent (parallel). **(b)** The resulting dependence on the fluorescence in a singlet fission material. **(c)** Triplet-pair energies of the pure spin states (^{m}(TT)), where $J = 50\,\mu\mathrm{eV} \gg D$. **(d)** The resulting dependence on the fluorescence for equivalent (parallel) molecules, with dips resulting from mixing between ^{1}(TT) and ^{5}(TT) states at avoided crossings (solid line). For inequivalent molecules, mixing between ^{1}(TT) and ^{3}(TT) states may additionally occur, resulting in an extra dip (dotted line). For the simulations: $D = 5\,\mu\mathrm{eV}$, $E = D/3$, $X = D/10^5$, $g_\mathrm{L} \approx 2$, and angle 45° taken between the magnetic field direction and molecular z-axis. Simulations and figure by David G. Bossanyi.[205]

($J \ll D$) for molecules with parallel alignment (non-parallel alignments are comparable but can yield slightly different results[124,160]). At zero magnetic field, the number of $(\mathrm{T...T})^l$ with >5% ^{1}(TT) character (*i.e.* with $\left|C_\mathrm{S}^l\right|^2 > 0.05$) is only 3. When applying a magnetic field, this rises to 5 for an intermediate flux density ($B \sim D/g_\mathrm{L}\mu_\mathrm{B}$), and then drops to 2 for higher flux densities;[179] this is shown in Figure 2.12a. For this SF material, the increase in the number of singlet-character $(\mathrm{T...T})^l$ results in an increase in the SF yield, which results in a decrease in the number of singlets undergoing fluorescence, and *vice versa*. This results in the characteristic dip-rise dependence of the fluorescence intensity on the applied magnetic field in the case of weak exchange-coupling in a SF material,[160] shown in Figure 2.12b.

Strongly exchange-coupled triplets ($J \gg D$) result in different fluorescence

signatures. In this case, for *most* magnetic flux densities, spin is a good quantum number and we have pure spin eigenstates to the spin Hamiltonian (*e.g.* Equation 2.85 for the singlet triplet-pair). The pure spin eigenstates are magnetic-field independent (but their eigenenergies are not; see Figure 2.12c), and there is no change in the measured fluorescence. The *exceptions* occur when the Zeeman and intertriplet exchange terms become comparable at the avoided crossings, shown in red circles in Figure 2.12c. They are located around flux densities $B \simeq 3J/g_L\mu_B$ and $B \simeq 6J/g_L\mu_B$; there, some of the spin eigenstates to the spin Hamiltonian become singlet-quintet mixtures. An additional avoided crossing can occur in the case of inequivalent molecules (*e.g.* non-parallel alignment in amorphous samples); this occurs around $B \simeq 2J/g_L\mu_B$, with some mixed singlet-triplet eigenstates. At these avoided crossings, the average singlet character of the eigenstates increases, resulting in dips in the fluorescence for a SF,[160] as shown in Figure 2.12d.

2.4.4 Other assays for SF

It is important to note that phenomena unrelated to SF or TTA can lead to magnetic field effects similar to those described above.[206,207] Therefore, other experiments should be used to probe the potential SF/TTA signatures before confirming an assignment. In this subsection, we briefly outline common techniques for this.

Transient electron paramagnetic resonance (EPR) and other magnetic resonance techniques are powerful tools in the assay of triplet and triplet-pair states. Free triplets (T_1) from SF can be distinguished from those formed by intersystem crossing (ISC) through their characteristic EPR profiles, which arise because each process leads to different initial populations of the two-electron triplet states.[12,188,208,209] Furthermore, the strongly exchange-coupled ^{5}(TT) states may also be detected with transient EPR.[12] Meanwhile, EPR is blind to singlet states, including the strongly-coupled ^{1}(TT).

Transient absorption spectroscopy (see Section 4.4 for a brief overview) is a frequent technique used in characterisation of SF materials. Indeed, the strongly-coupled ^{1}(TT) 'excimer' was argued to be present following spectro-kinetic decomposition of transient absorption data of concentrated TIPS-tetracene in solution in a 2015 paper,[210] which motivated its inclusion as an intermediate within subsequent SF schemes.[12] More recently, distinct species-associated difference spectra (SADS) for ^{1}(TT) and a weakly-coupled triplet-pair state have been extracted fol-

lowing global target analysis (a type of spectro-kinetic analysis; see Section 4.4.4 for details) of transient absorption data of TIPS-pentacene in solids[211] and nanoparticles.[212] However, the transient absorption signatures of each state within the SF scheme (Equation 2.93) for many SF materials tend to be broad, overlapping, and similar in appearance.[40] This makes observation of the different states in transient absorption spectra difficult, and caution should be used in assignment of particular states to spectra or components extracted from spectro-kinetic analysis, especially for carotenoids due to their aforementioned IVR/VET signatures.[66–70]

A SF signature that has been taken to be unequivocal[195,213,214] is oscillations superimposed onto the delayed fluorescence. This phenomenon is dubbed 'quantum beating', and it arises from a time dependence in the weakly exchange-coupled singlet triplet-pair state ^{1}(T...T). In contrast with the stationary spin eigenket $|^1(\mathrm{TT})\rangle$ where two-electron ket-products do not evolve with time (see Equation 2.86), those in spin ket $|^1(\mathrm{T...T})\rangle$ do, which in turn gives a time evolution to the product $\langle^1(\mathrm{TT})|^1(\mathrm{T...T})\rangle$. Therefore, the rate of the $^1(\mathrm{T...T})\rightarrow{}^1(\mathrm{TT})$ back-step within a SF scheme carries a time dependence, which leads to the time-dependent beats superimposed onto S_1 delayed fluorescence. The beat frequencies relate to the zero-field splitting D and E parameters; the three measurable beat frequencies are close to combinations such as $\frac{2}{h}(\Delta E_x - \Delta E_y)$, where the ΔE_i are defined in Equations 2.38–2.40 and $h = 2\pi\hbar$ is the Planck constant.[213,214]

Chapter 3

Materials

In this chapter, we briefly introduce the materials of study within the main chapters of this thesis, focusing on their preparation and experimental use. We note that Appendices A and D concern the study of light-harvesting complexes (LHCs) and new dye structures for polaritonic studies respectively; we enclose details of sample preparation specific to those appendices within them.

3.1 Keto-carotenoids

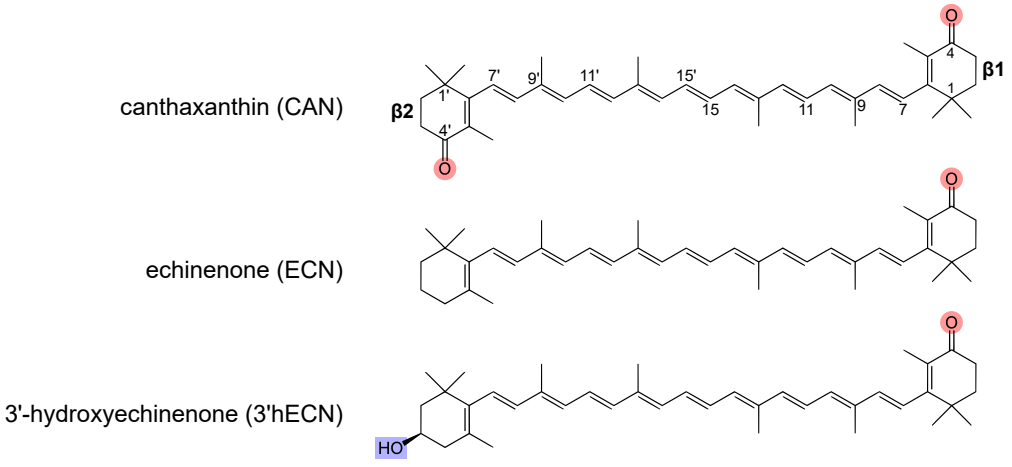

Figure 3.1 – Keto-carotenoids measured in this thesis. Substitutions relative to β-carotene are highlighted, with carbonyl groups in red and hydroxyl in blue. Conventional numeration of carbons and β-rings is indicated for CAN, but apply similarly to the rest of the structures.

The keto-carotenoid canthaxanthin (CAN) forms the main subject of work within this thesis, although largely within the confines of the orange caroten-

oid protein (OCP; see Section 3.2). The structure of CAN is shown in Figure 3.1; substitutions relative to β-carotene are highlighted. The effective conjugation length (defined as the effective number of conjugated double bonds with delocalised π-electrons) of CAN appears to be $N_{\text{eff.}} \approx 9.6$ in solution, similar to β-carotene.[48,102,139] Within Chapter 7, CAN in acetone was used for nanosecond-millisecond transient absorption experiments, including triplet sensitisation experiments using anthracene (see Section 3.4). CAN was also used in transient electron paramagnetic resonance (EPR) measurements by Christopher G. Bailey and Dane R. McCamey at the University of New South Wales.

The CAN used in nanosecond-millisecond transient absorption experiments and transient EPR experiments was purchased from Merck (Sigma-Aldrich, analytical standard, ≥95.0%, 32993-2MG) and used without purification. For the ns–ms transient absorption experiments, the powder was stored in the dark in a freezer at ∼−20 °C, and dissolved in high-purity acetone (Sigma-Aldrich, suitable for HPLC, ≥99.8%, 34850-2.5L-M). Preparations were stored in a fridge (∼2.5 °C) or freezer (∼−20 °C) and used for experiments within a week of preparation.

We note that the CAN and 3′hydroxyechinenone (3′hECN; structure in Figure 3.1) used for certain experiments in the appendices (specifically Figure F.2b and Section G.6) were biosynthesised rather than purchased form Merck, using a similar procedure to echinenone (ECN; structure in Figure 3.1; for synthesis see Section 3.2.2 below). In these cases, biosynthesis and solution preparation was primarily by George A. Sutherland (with contributions from Matthew S. Proctor and Andrew Hitchcock) in Plants, Photosynthesis and Soil, School of Biosciences, University of Sheffield.

3.2 Orange carotenoid protein (OCP)

Orange carotenoid protein (OCP) binding CAN forms the main experimental focus in this thesis. OCP is a small (35 kDa) light-sensitive protein with a dark-adapted globular conformation (orange form of OCP; OCPo) and a light-adapted extended conformation (red form of OCP; OCPr); see Figure 3.2 for previously reported structures from small angle X-ray scattering (SAXS) analysis.[49] It binds a single keto-carotenoid (CAN in all main chapters of this thesis) whose effective conjugation length ($N_{\text{eff.}}$) is relatively extended in OCPr, giving its relative redshift compared to OCPo;[48,56] see Figure 3.2 for CAN-binding OCPo/OCPr absorbance in buffer.

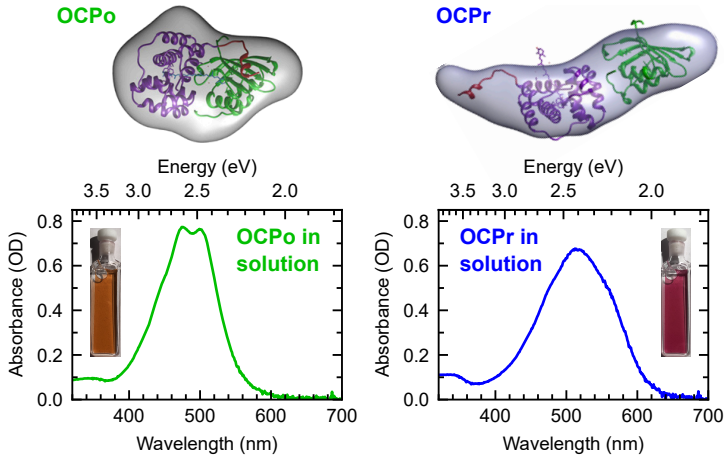

Figure 3.2 – Orange carotenoid protein (OCP) in its OCPo (left) and OCPr (right) forms. A structural model of the photoinduced conformational change from OCPo to OCPr is reproduced from previously reported[49] small angle X-ray scattering (SAXS) analysis. Absorbance spectra of each conformation are displayed below (0 min and 60 min from Figure 6.2a). SAXS data from Ref.[49] (used with permission from PNAS) and absorbance data measured by George A. Sutherland.

In this thesis, the majority of measurements in the main chapters were conducted on CAN-binding OCPo and OCPr samples in solid trehalose-sucrose glass, preventing complete OCPo⇌OCPr transitions; see details in Section 3.3. Otherwise, measurements were conducted on solution samples in buffer B (50 mM HEPES, pH 7.4, 200 mM NaCl). Some supplementary measurements were performed on ECN-binding OCPo and OCPr samples (Figure F.1b and Section G.4) and CAN-binding OCP mutants (Figure F.2 and Section G.5). We discuss the biosynthesis of these samples in the following subsections.

Orange carotenoid protein (OCP) samples were prepared primarily by George A. Sutherland, (with contributions from Matthew S. Proctor and Andrew Hitchcock) in Plants, Photosynthesis and Soil, School of Biosciences, University of Sheffield.

3.2.1 Canthaxanthin-binding OCP

Orange carotenoid protein (OCP) binding near-100% CAN was produced from BL21(DE3) *Escherichia coli* (*E. coli*) using a dual-plasmid system comprised of pAC-CANTHipi[215] and pET28a containing the gene encoding OCP (slr1963) from *Synechocystis* sp. PCC 6803. Briefly, 500 ml cultures were grown at 37 °C (200 rev min^{-1} agitation) in 2 l baffled Erlynmeyer flasks using lysogeny broth me-

dium containing the appropriate concentrations of antibiotics. When the absorbance of the medium at 600 nm had reached $A_{600} = 0.6$ (1 cm path length), protein production was induced by addition of 0.5 mM isopropyl β-D-1-thiogalatopyranoside and the cultures incubated for 16 hours at 18 °C.

Cells were harvested by centrifugation (4,400×g, 30 min, 4 °C) and resuspended in binding buffer (50 mM HEPES, pH 7.4, 500 mM NaCl, 5 mM imidazole). Cells were lysed by sonication and then centrifuged (53,000×g, 30 min, 4 °C). The supernatant was collected and filtered (0.22 µm filter pores) and applied to a Chelating Sepharose Fast Flow column (GE Healthcare) pre-equilibrated with $NiSO_4$. The column was washed with binding buffer, wash buffer (50 mM HEPES, pH 7.4, 500 mM NaCl, 50 mM imidazole), and elution buffer (50 mM HEPES, pH 7.4, 100 mM NaCl, 400 mM imidazole), with the elution pooled for further purification. The protein sample was buffer exchanged into buffer A (50 mM HEPES, pH 7.4) loaded onto a Fast Flow Q-Sepharose column (GE Healthcare) with a linear gradient of 0–1 M NaCl applied. Fractions were analysed by SDS-PAGE and appropriate samples taken forward for size exclusion chromatography on a Superdex 200 Increase column (GE Healthcare) in buffer B (50 mM HEPES, pH 7.4, 200 mM NaCl). Where necessary, OCP samples were concentrated using centrifugal dialysis (VivaSpin, Sartorius).

3.2.2 Echinenone-binding OCP

OCP binding ECN was produced using OCP without a bound carotenoid (apo-OCP) and purified ECN.

To prepare apo-OCP, an identical protocol to CAN-OCP was used (see Section 3.2.1), but with the omission of the pAC-CANTHipi plasmid.

ECN was purified from *E. coli* BL21(DE3) maintaining a dual-plasmid system comprised of pAC-BETA[216] and pCDFduet containing genes for β-carotene hydroxylase (crtR) and β-carotene ketolase (crtO) from *Synechocystis*. Pigments were extracted from whole cells using a 7:2 (v/v) acetonitrile-methanol mixture and phase-partitioned into hexane. Hexane solutions were evaporated under vacuum and the carotenoids resolubilised in chloroform. The carotenoid samples were loaded onto a preparative reverse-phase C18 column (Fortis Universil C18 5 µm, 150×10 mm) and purified using a HPLC protocol similar to that already described.[217] Fractions containing ECN were pooled and evaporated under ultrapure nitrogen. ECN was then solubilised using 10 mg ml^{-1} 1,2-dioleoyl-*sn*-glycero-

3-phosphocholine (DOPC) and mixed with a solution of purified apo-OCP in buffer B (50 mM HEPES, pH 7.4, 200 mM NaCl) for 16 hours.

3.2.3 Mutants of CAN-binding OCP

OCP mutant samples binding near-100% CAN were prepared using an identical method to CAN-OCP (see Section 3.2.1), but with the use of a commercial mutagenesis kit (QuikChange II Site-Directed Mutagenesis Kit, Agilent Technologies) to make the required mutations. For 'W110S', the tryptophan-110 residue has been substituted for a serine-110, resulting in a permanently inactive OCPo-like protein. For 'W288S', the tryptophan-288 residue has been substituted for a serine-288, resulting in a permanently active OCPr-like protein.

3.3 Trehalose-sucrose glass

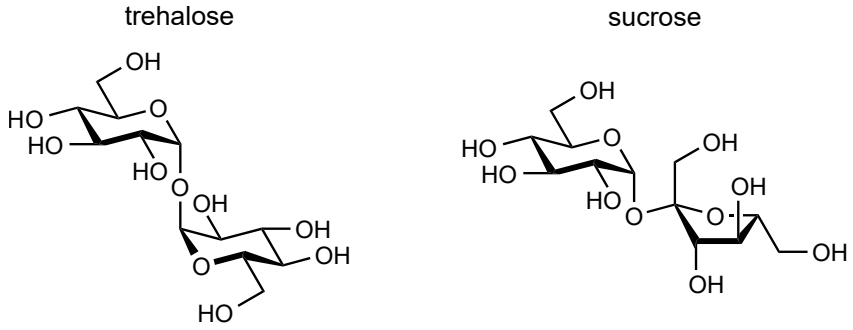

Figure 3.3 – Structures of trehalose (left) and sucrose (right). Note that trehalose is a glucose-glucose disaccharide, while sucrose is a glucose-fructose disaccharide.

The structures of the naturally-occurring sugars trehalose and sucrose are shown in Figure 3.3. Trehalose is synthesised by plants under stressful conditions (extreme temperatures, drought, *etc.*) to fix proteins in their native conformations, thus protecting macromolecular cell architecture.[71,72] Sucrose has also been demonstrated to stabilise protein folding.[218] Trehalose-sucrose (herein 'trehalose') forms a transparent glass following dehydration at temperatures less than 60 °C. We previously used trehalose for solid-state photophysical characterisation of various organic semiconductors.[40] Here we use trehalose to immobilise OCPo and OCPr at room temperature, which prevents the large conformation change associated with the OCPo⇌OCPr transitions. Hence solid-state optical characterisation is enabled without artefacts arising from contaminant OCPo/OCPr or

the use of low temperatures.

Trehalose glass encapsulation of OCPo and OCPr was conducted using a similar method to Sutherland and co-workers.[40] 100 µl of concentrated protein solution (1 cm path length, $A_{\text{max}} \sim 2$) in aqueous buffer (50 mM HEPES, 200 mM NaCl, pH 7.4) was mixed with 100 µl of a trehalose-sucrose mixture (0.5 M trehalose, 0.5 M sucrose). 200 µl of the protein-trehalose mixture was drop-cast in the centre of a quartz-coated glass substrate (S151, Ossila; 15×20×1.1 mm). The substrate was then placed into a vacuum chamber under a vacuum pressure of −70 kPa with anhydrous calcium sulphate desiccant (Drierite) and left at room temperature for a minimum of 48 hours.

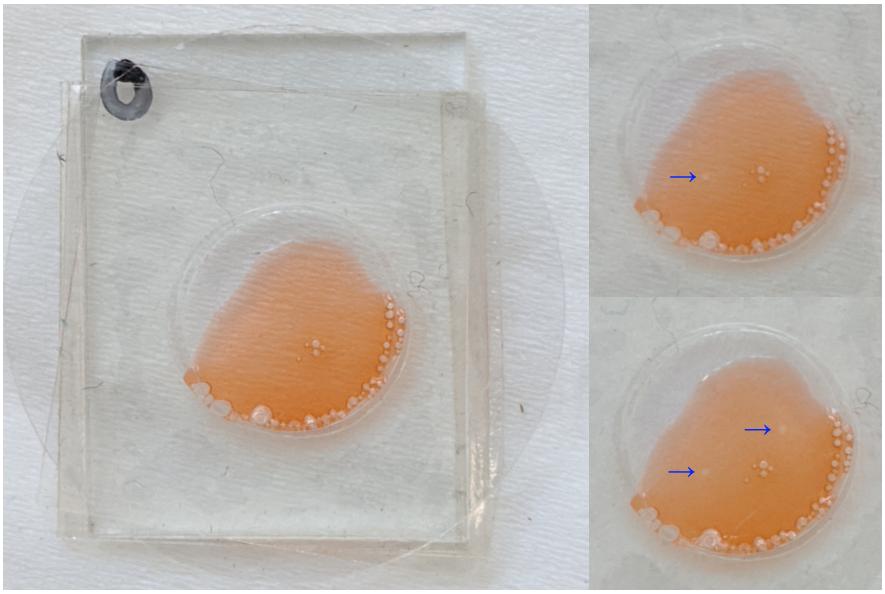

Figure 3.4 – CAN-OCPo sample in trehalose-sucrose glass with cover slip encapsulation. Images to the right are the same sample after a first (top-right) and second (bottom-right) high pump-fluence picosecond transient absorption measurement; note the bleach spots indicated with blue arrows. No transition to OCPr is apparent. In the ∼30 min measurements, the film was pumped with 532 nm, 3.6 mW, 5 kHz pump pulses, with 465 µm and 340 µm the major and minor diameters ($1/e^2$). Therefore the pump fluence was 580 µJ cm^{-2}. The majority of picosecond transient absorption measurements used significantly lower fluences and did not induce significant bleaching.

Some samples were additionally encapsulated with imaging spacers and a cover slip to protect the trehalose against atmospheric rehydration. For these samples, a stack of two imaging spacers (SecureSeal, Grace BioLabs; 9 mm diameter, 0.12 mm thickness) were attached to the quartz-coated glass substrate

(S151, Ossila; 15×20×1.1 mm) and 40 µl of the protein-trehalose mixture drop-cast in the centre of the imaging spacer. The substrate was then placed in vacuum as above; pressure was released under a continuous flow of ultra-pure nitrogen gas, and a glass microscope cover slip (ThermoScientific; 22×22 mm, No.1 thickness) was attached to the upper imaging spacer.

For OCPo samples, all preparation steps and desiccation were conducted in the dark. For OCPr, preparation and desiccation were conducted under bright white light, with samples illuminated for 30 min (1600 µmol photon m^{-2} s^{-1}) prior to the addition of the trehalose-sucrose solution and constant weaker illumination (500 µmol photon m^{-2} s^{-1}) for the duration of the desiccation. After encapsulation, samples were stored at room temperature in the dark.

Trehalose glass encapsulation was performed by George A. Sutherland and Matthew S. Proctor.

3.4 Anthracene

Anthracene is a three-ring acene, structure in Figure 3.5. As noted in the introduction of Section 2.4, anthracene is historically distinguished among π-conjugated molecules as the material in which triplet-triplet annihilation (TTA) was first observed,[177] *and* in which singlet fission (SF) was first proposed.[176] Here, we use it as a CAN triplet sensitiser. Upon excitation of anthracene, it forms triplets *via* fast intersystem crossing,[173–175] which sensitises CAN triplets through excitation energy transfer; see Section 7.2.1.

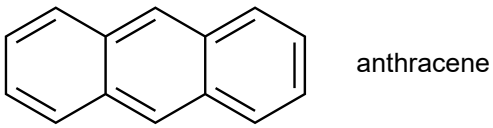

Figure 3.5 – Structure of anthracene.

Anthracene powder (Sigma-Aldrich, sublimed grade, ≥99%, 694959-5G) was stored at room temperature in the dark. Solutions were prepared by dissolving the powder in high-purity acetone (Sigma-Aldrich, suitable for HPLC, ≥99.8%, 34850-2.5L-M). Anthracene in acetone solutions (non-mixed) were subsequently stored in a fridge (∼2.5 °C) or freezer (∼−20 °C). Mixed CAN/anthracene in acetone solutions were prepared by mixing 'stock' solutions with additional dilution to achieve the concentrations required. These mixed solutions were stored in a

fridge or freezer similarly, and used in experiments within a week of preparation. See above (Section 3.1) for further details on CAN.

Chapter 4

Methods

In this chapter, we briefly introduce the principles of experimental methodologies used within the main chapters of this thesis, following with more detail on the experimental setups themselves. In particular, we outline our progress in construction of a transient grating photoluminescence spectroscopy (TGPLS) setup in this chapter; see Section 4.6. Similarly to the materials chapter (Chapter 3), methodologies specific to Appendices A and D are enclosed within those appendices.

4.1 Steady-state absorbance

We start by introducing and discussing some of the theory and terminology regarding the quantity 'absorbance'. This is an experimentally determined quantity that relates to the oscillator strength f.[103,105] Despite its immediate simplicity compared to techniques involving pulsed lasers, steady-state absorbance can yield a massive amount of information on a material of interest.[51,114,139,219–223] However, confusion can arise from how absorbance is measured in double-beam systems and from the myriad of terminology and conventions defining almost the same quantity.[111] For some transparency on these unclear points, we discuss steady-state absorbance with some detail.

4.1.1 Principles

We consider a solid sample consisting of a material of interest with width w on top of a substrate with width w_0 (a solution sample in a cuvette can be considered analogously). For a sample that does not scatter or reflect light, the intensity

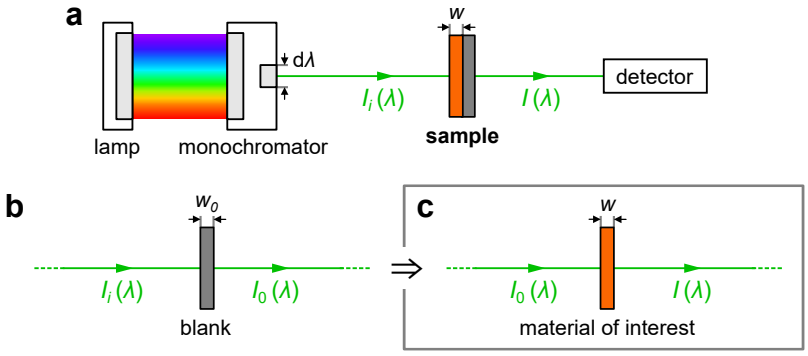

Figure 4.1 – Simplified schematic a of steady-state absorbance measurement. **(a)** The incident excitation from a light source (*e.g.* a lamp) is directed into a monochromator, which scans the centre wavelength λ of the output narrowband light. The initial light intensity $I_i(\lambda)$ is attenuated through absorption by the sample to $I(\lambda)$, with $I(\lambda)$ subsequently measured by a photodetector. (Note that double-beam systems, the reference beam is used to measure $I_i(\lambda)$, so a direct absorbance calculation is possible). **(b)** A comparable measurement using a 'blank' with initial intensity $I_i(\lambda)$ and measured intensity $I_0(\lambda)$ can be used to calculate the absorbance due to the sample itself (blank absorbance removed). **(c)** Schematic of sample absorbance without a blank, comparable to a calculation using the experiments of panels (a,b). See text for details.

reduction by attenuation by an infinitesimal sample width $\mathrm{d}z$ (where z here is a position coordinate directed normally to the sample) may be written

$$\mathrm{d}I = -\alpha(\lambda, z) I(\lambda, z)\, \mathrm{d}z \tag{4.1}$$

where the minus sign denotes the reduction, $\alpha(\lambda, z)$ is the absorption coefficient, and $I(\lambda, z)$ is the intensity at position z. We define an initial intensity at $z = 0$ (prior to the sample) as $I(\lambda, 0) \equiv I_i(\lambda)$ and the transmitted intensity at $z = w + w_0$ (post-sample) as $I(\lambda, w + w_0) \equiv I(\lambda)$. We use the Lambert law,[224,225] which assumes that the material of interest is homogeneous (note that deviations from the Lambert law may occur in systems exhibiting multiphoton processes or large relative populations of photoproducts). Under the Lambert law, the absorption coefficient at all depths within the material of interest is $\alpha(\lambda)$, and similarly for the substrate with absorption coefficient $\alpha_0(\lambda)$. Therefore, performing an integration of Equation 4.1 yields

$$\ln\left(\frac{I(\lambda)}{I_i(\lambda)}\right) = -\alpha(\lambda) w - \alpha_0(\lambda) w_0 \tag{4.2}$$

where ln is the natural logarithm (*i.e.* $\ln \equiv \log_e$ where e is Euler's number, also known as Napier's constant). Note that the intensity ratio may be termed

'transmittance'.[111] There are two apparent complications: typically $I_i(\lambda)$ is an unknown (unless it is being measured using a reference beam, as is the case in double-beam systems), and usually absorption by the substrate is not desirable. Fortunately, we can take care of both by making a comparable measurement on a substrate without the material of interest, usually dubbed a 'blank'. In the case of solution measurements, this blank usually consists of the same cuvette filled with only the solvent the material of interest had been dissolved in; this accounts for absorption by the solvent. Returning to our example using solid samples, if we perform a comparable integration for a measurement of blank substrate of thickness w_0, we get

$$\ln\left(\frac{I_0(\lambda)}{I_i(\lambda)}\right) = -\alpha_0(\lambda)w_0 \tag{4.3}$$

where $I_0(\lambda)$ is the transmitted intensity past the blank. Note that the incident intensity $I_i(\lambda)$ prior to the blank is assumed to be identical to that for the sample here; any deviations in the incident intensity (sometimes called 'lamp drift') can be accounted for by measuring a reference beam intensity, as performed in double-beam systems. Combining Equations 4.2 and 4.3 gives us

$$\tau(\lambda) = -\ln\left(\frac{I(\lambda)}{I_0(\lambda)}\right) \overset{\text{L.}}{=} \alpha(\lambda)w \tag{4.4}$$

where physicists tend to name $\tau(\lambda)$ the 'optical depth' or 'optical thickness' of an active material.[103] Note that $\tau(\lambda)$ may be defined without assumption of the Lambert law (which forms the rightmost part of Equation 4.4).

Typically in the literature for π-conjugated molecules, and in the wider chemistry literature, the absorption of an active material is characterised with a quantity usually called 'absorbance' (in dimensionless units of 'OD', abbreviating 'optical density'), instead of the optical depth $\tau(\lambda)$. The absorbance $A(\lambda)$ is defined

$$A(\lambda) = -\log\left(\frac{I(\lambda)}{I_0(\lambda)}\right) = \frac{\tau(\lambda)}{\ln(10)} \tag{4.5}$$

where log is the base-10 logarithm. Note that absorbance relates to the optical depth with a factor $\ln(10) \simeq 2.30$, and that both terms may be defined without assuming the Lambert law. The IUPAC recommends the term 'napierian absorbance' for $\tau(\lambda)$, and in general recommends distinguishing terms defined with natural logarithms as 'napierian' and terms defined with base-10 logarithms as 'decadic'.[111]

Finally, we make a note of the Beer-Lambert law.[†] This is an extension to the Lambert law, following Beer's empirical observations relating the concentration of dilute solutions to the transmittance.[226] We can write, using the absorbance $A(\lambda)$,

$$A(\lambda) = \epsilon(\lambda)cw \tag{4.6}$$

where $\epsilon(\lambda)$ is the decadic extinction coefficient, c is the concentration of absorbers, and w is the active material/solution width. Despite 'extinction coefficient' remaining a common term,[103] the IUPAC recommends the term 'molar decadic absorption coefficient'.[111] Note that deviations from the Beer-Lambert law occur for solutions or films exhibiting intermolecular effects (such as aggregation) at higher concentrations.[‡111]

4.1.2 The Jacobian correction

Here, we take absorbance as an example to note an important point regarding analysis of spectroscopic measurements in general that is often overlooked, namely the Jacobian correction/conversion.

When a nominal intensity $I(\lambda)$ measurement is made by using *e.g.* a conventional commercial spectrophotometer, the narrowband wavelengths (centre λ) exit the thin slit of a monochromator. Light is eventually directed onto a photodetector, typically a photomultiplier tube.[223] The photodetector counts a certain number of photons within a defined time interval $\mathrm{d}t$. More importantly, the aforementioned thin slit of *finite* width is associated with the wavelength interval $\mathrm{d}\lambda$ (note this is depicted in Figure 4.1). Therefore, the number of photons the photodetector is counting is actually $I(\lambda)\,\mathrm{d}\lambda\,\mathrm{d}t$ rather than the nominal intensity $I(\lambda)$ alone.[§] Any experimental spectrum that plots 'intensity' (perhaps as fluorescence emission) against wavelength is really plotting the quantity $I(\lambda)\,\mathrm{d}\lambda\,\mathrm{d}t$ against wavelength. We drop $\mathrm{d}t$ herein, as it is $\mathrm{d}\lambda$ that generally introduces the mathematical technicalities.[103,227]

A Jacobian correction has to be applied when converting the λ-axis (typically

[†]We note that Lambert discussed his law in 1760,[225] citing and directly quoting a 1729 work by Bouguer, who discovered the law by observing red wine.[224] Hence the Beer-Lambert law is sometimes called the Beer-Lambert-Bouguer law.[111]

[‡]In Appendix D, we study molecules that readily (J-)aggregate at high concentrations.

[§]Some spectroscopy setups detect by dispersing a broadband signal beam onto a photodetector array, such as a CCD. This does not involve use of a monochromator. However, the dependence on $\mathrm{d}\lambda$ is still picked up through the *finite* pixel width.

the bottom x-axis) into, for example, an energy (E) axis. The conversion from the λ-values to E-values using the relation[†]

$$E = \frac{hc}{\lambda} \tag{4.7}$$

is step (1), but it should not be done alone; plotting the unconverted $I(\lambda)\,\mathrm{d}\lambda$ against a converted E is not correct. We must also convert the measured quantity $I(\lambda)\,\mathrm{d}\lambda$ into energy terms, *i.e.* into $I(E)$. We can do this by first writing

$$I(\lambda)\,\mathrm{d}\lambda = I(E)\,\mathrm{d}E \tag{4.8}$$

so conserving the number of photons counted for a wavelength or energy interval, a form of conservation of energy.[227] We then find a relation between the intervals by applying a derivative to Equation 4.7, which yields the 'Jacobian'

$$\frac{\mathrm{d}E}{\mathrm{d}\lambda} = -\frac{hc}{\lambda^2} \tag{4.9}$$

and therefore

$$I(E) = -I(\lambda)\frac{\lambda^2}{hc} \tag{4.10}$$

where the minus sign here can be ignored, as it only reflects the different directions of integration for λ and E. So step (2) in converting between the axes is multiplying $I(\lambda)$ by a factor λ^2/hc for each $(\lambda, I(\lambda))$ coordinate.[‡103,227]

We recall that absorbance, defined in Equation 4.5, involves a ratio of two intensities. It turns out in this case the $\mathrm{d}\lambda$ (and $\mathrm{d}t$) of the two intensities cancel out. Therefore, in converting absorbance against λ to absorbance against E, only step (1) is required, *i.e.* the conversion of the λ-axis into an E-axis using $E = hc/\lambda$. A Jacobian (step (2)) does not need to be applied to the absorbance,[103] or indeed any quantity involving a ratio of intensities, for example the transient absorption quantities ΔA (see Equations 4.14 and 4.15) and $\Delta T/T$ (see Equation 4.13).

In this thesis, plots are sometimes shown with a lower x-axis and an upper x-axis. The lower x-axis is treated as the primary one, so any Jacobian correction necessary is applied with respect to the primary lower x-axis (rather than the secondary upper x-axis). Similarly, plots are sometimes shown with a left y-axis (primary) and a right y-axis (secondary), and Jacobian corrections are made with respect to the primary left y-axis similarly.

[†]Here, h is Planck's constant and c is the speed of light in a vacuum.

[‡]Note that the Jacobian is a general mathematical tool. In evaluation of multiple integrals, the Jacobian is the correction factor to preserve the hypervolumes of infinitesimals following a change of variables. See *e.g.* Ref.[228] for further details.

4.1.3 Absorbance setups

Throughout this thesis, absorbance of samples were measured in a commercial Cary double-beam spectrometer (Cary 60 UV-Vis Spectrophotometer, Agilent Technologies) with both zero and baseline corrections applied with a blank sample inserted (*i.e.* for $I_0(\lambda)$). Occasionally an alternative FluoroMax double-beam spectrometer was used (FluoroMax-4, Horiba, fitted with a Xenon lamp) in a similar manner; cases when the FluoroMax spectrometer was used will be specified.

4.2 Narrowband-pump time-resolved absorbance

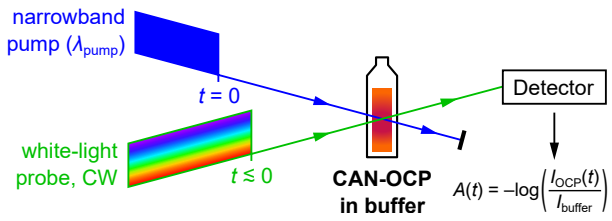

Figure 4.2 – Simplified schematic of the experimental setup for time-resolved absorbance measurements. After time $t = 0$, the sample is constantly photoexcited by narrowband pump light, while its transmission/absorbance spectrum is continuously taken with a weaker broadband white-light probe. The sample here is canthaxanthin-binding orange carotenoid protein (CAN-OCP) in buffer. See text for details.

In this section, we detail our narrowband-pump time-resolved absorbance measurements. We note that this is specific to a sample of orange carotenoid protein (OCP) in buffer; see Section 6.2.4 for context about OCP and this measurement, and Section K.2 for a discussion of experimental oversights that is too detailed to include here. We emphasise that this 'time-resolved absorbance' is distinct to conventional 'transient absorption' spectroscopy (the latter described in Section 4.4).

Time-resolved absorbance spectroscopy on continually-photoconverting OCP in solution under narrowband pump was undertaken using a home-built system, simplified schematic shown in Figure 4.2. OCP in buffer was placed in a 2 mm path length (at normal incidence) quartz cuvette (Hellma 110-2-40). Conversion to OCPr was continuously triggered by narrow-band 'pump' light (78.3 MHz, <10 nm nominal FWHM, ±5 nm nominal centre wavelength accuracy) turned

on at time $t = 0$. This pump light was provided by a supercontinuum laser (SuperK EXTREME EXU-6 PP, NKT Photonics) outfitted with a tuneable filter (SuperK VARIA, NKT Photonics). Pump light was focused by a lens (LA4380, Thorlabs) through the cuvette at ∼40° from the cuvette's normal to minimise transmission and scattering of the pump light into the spectrometer. The power of the pump was controlled such that the number rate of photon absorptions (*i.e.* OCPo excitations) was approximately the same for each pump wavelength, achieved by keeping a constant product

$$P\lambda_{\text{pump}}(1 - 10^{A_{\text{dark}}}) \tag{4.11}$$

where P is the steady-state power of the pump, λ_{pump} is the pump wavelength, and A_{dark} (shown as a green line in Figure 6.9b) is the steady-state absorbance of dark-adapted OCP in buffer determined at normal incidence using a separate spectrometer (FluoroMax-4, Horiba, fitted with a Xenon lamp). The exception to this pump power control was the non-absorbed 675 nm pump, where instead the photon rate was kept the same as that for 550 nm pump (so controlling $P\lambda_{\text{pump}}$ between those two pumps).

We note that pump powers P were not measured close to the sample position to prevent pre-measurement photoconversion and also due to spatial limitations; they were instead measured and controlled at a position such that to reach the sample, reflection by three UV-enhanced aluminium mirrors (PF10-03-F01, Thorlabs) and focusing through the aforementioned lens is required. This results in a slightly wavelength-dependent fraction of power difference between what was measured as P and what was incident on the sample. After measurements were completed, this was checked by positioning the power meter at the sample position and at the far position, and summarised in Table K.2. We note also that A_{dark} was determined at normal incidence, but the pump light was at ∼40° from the cuvette's normal, so that the fraction of pump photons absorbed differs from $(1 - 10^{A_{\text{dark}}})$. We give full details of the pump power control, including an explanation and correction of these noted oversights, in Section K.2; in short, the oversights did not have a substantial effect on our results.

The yield of OCPr was monitored by measuring the absorbance spectrum of OCP using a weak white-light probe from a fibre-coupled halogen-tungsten/deuterium lamp (DH-2000-BAL, Ocean Optics), turned on at $t \lesssim 0$ (just before the pump; turning both on at $t = 0$ was not possible). This white-light was focused onto the sample close to normal incidence using collimating and focus-

ing lenses. The pump and white light were overlapped in the cuvette close to their focuses. The sample-attenuated white light was collimated and focused by subsequent lenses into an optical fibre, in turn coupled to a CCD spectrometer (Andor Shamrock SR-303i-A, Oxford Instruments), measuring white-light transmission through the sample. Absorbance $A(t)$ was calculated using the measured transmission through a cuvette containing solvent (buffer), with the equation

$$A(t) = -\log\left(\frac{I_{\mathrm{OCP}}(t)}{I_{\mathrm{buffer}}}\right) \tag{4.12}$$

where I_{OCP} is the transmission in counts measured by the CCD for OCP in solution, and I_{buffer} is that for buffer only. The pump spot diameter was $\sim$30 µm and the white light spot diameter was $\sim$1 mm at the overlap/sample position; note that these could not be determined precisely using a beam profiler due to the large angle of incidence of the pump beam.

Experimental consistency was verified by repeating the experiment twice on the same OCP in buffer sample. No apparent degradation of the OCP occurred, and back-conversion from OCPr to OCPo in the dark was successful in the $\geq$1 hour between experimental runs. The room temperature was controlled at 18 °C.

Initial set up and use of the system was assisted by Rahul Jayaprakash.

4.3 Resonance Raman

Resonance Raman measurements were performed with a Renishaw inVia Raman system (Renishaw plc., Wotton-Under-Edge, UK) in a backscattering configuration. A 532 nm laser (150–750 µW power) and a 50× objective were used (NA 0.50, spot size $\sim$1 µm). Acquisition times used were in the range 5–30 s.

Harrison Ka Hin Lee performed Resonance Raman measurements under the supervision of Wing C. Tsoi (SPECIFIC, Faculty of Science and Engineering, Swansea University, UK).

4.4 Transient absorption

Transient absorption spectroscopy is a pump-probe(-reference) experimental technique that can yield a wealth of information on the photophysics of π-conjugated molecules. We will not describe the principles in detail here; we direct the reader to other papers[229,230] and theses[205] for a more thorough description.

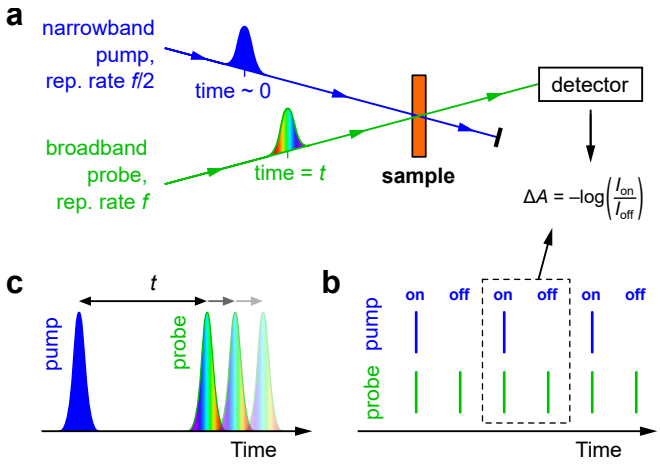

Figure 4.3 – Schematics outlining the principles of pump-probe transient absorption spectroscopy. (a) Broadband probe pulses are incident on a spot on the sample at the repetition rate f, with narrowband pump pulses at repetition rate $f/2$ overlapped at the probe spot. The 'signal' probe is directed to a detector, and its measured intensity is used to calculate the quantity ΔA using the equation shown (same as Equation 4.14). I_{on} is the measured intensity when a pump pulse is present (pump-on), while I_{off} is the measured intensity with no associated pump pulse (pump-off). **(b)** Longer-timescale schematic showing pump and probe pulses simply as lines. This demonstrates the concept of pump-on and pump-off. **(c)** Shorter-timescale schematic showing the temporal delay t between pump and probe pulses in the pump-on case. Information on the time dependence of $\Delta A \equiv \Delta A(t)$ can be found by varying t throughout the experiment. Note that t may be negative, and that $t = 0$ is 'time zero'.

We demonstrate the basics of pump-probe transient absorption in the schematics shown in Figure 4.3 (see caption for details). The quantity ΔA characterising transient absorption is used in this thesis, as it appears to be the convention in studies on caroteno-protein systems. It also relates to the (decadic) absorbance (see footnote in Section 4.4.2). However, some studies (such as those on carotenoids in solution[35]) use the quantity $\Delta T/T$. The two quantities relate *via*

$$\frac{\Delta T}{T} = 10^{-\Delta A} - 1 \tag{4.13}$$

which notably gives a sign change, *e.g.* positive ΔA transforms into negative $\Delta T/T$.

In the proceeding subsections, we discuss the transient absorption systems and data analysis techniques used in this thesis in some detail.

4.4.1 Picosecond transient absorption

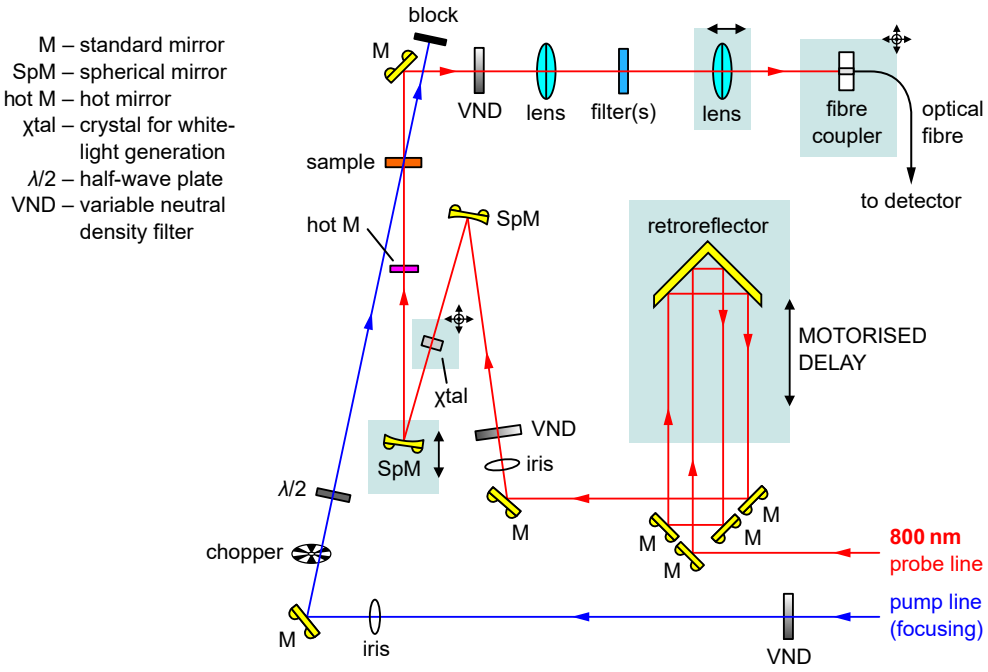

Figure 4.4 – Schematic of the picosecond transient absorption setup. See text for details. Elements in the schematic are not to scale. Optics within kinematic mounts are denoted with semicircular knobs. Adjustable stages are denoted with light green squares with the possible directions of adjustment denoted with arrows.

Picosecond transient absorption spectroscopy was undertaken with a commercial spectrometer (Helios, Ultrafast Systems) outfitted with a Ti:Sapphire seed laser (MaiTai, Spectra Physics) providing 800 nm pulses (84 MHz, 25 fs nominal FWHM) and a Ti:Sapphire chirped-pulse amplifier (Spitfire Ace PA-40, Spectra-Physics) amplifying 800 nm pulses (10 kHz, 12 W average power, 40 fs nominal FWHM). Pump pulses were generated by seeding a part of the 800 nm beam into either a frequency doubler utilising β-barium borate (BBO) crystals (TimePlate, Photop Technologies) for 400 nm excitation by second harmonic generation (SHG), or an optical parametric amplifier (TOPAS Prime, Light Conversion) for 420 nm to 600 nm excitations. An optical chopper was used to modulate the pump frequency to 5 kHz. Pump spectra used for some of the visible/NIR probe experiments are shown in Figure G.1, and pump spectra for the UV-vis probe experiments are shown in Figure J.1. Supercontinuum probes were generated with a part of the 800 nm pulse focused on either a continuously translating CaF_2 crystal for a UV-vis probe (350–750 nm; we note that the use of a hot mirror and

filters typically restricted the range to 370–690 nm, and with low probe in the 370–400 nm sub-range), a sapphire crystal for visible probes (450–800 nm), or a YAG crystal for NIR probes (800–1600 nm). Pump-probe delay was controlled with a motorised delay stage with a random stepping order per-sweep, and the resulting sweeps are averaged. The probe signal was dispersed with a grating and detected with CMOS or InGaAs sensors for UV-vis/visible or NIR, respectively. ΔA is calculated using

$$\Delta A = -\log\left(\frac{I_{\text{on}}}{I_{\text{off}}}\right) \tag{4.14}$$

where I_{on} is the measured probe intensity when pump is on, and I_{off} is the intensity when pump is off. The pump and probe polarisations were set to the magic angle. The room temperature was controlled at 19 °C.

Technical management of the picosecond transient absorption spectrometer was performed by Dimitri Chekulaev. Initial use of the system was assisted by Shuangqing Wang, James D. Shipp, Sayantan Bhattacharya, and David G. Bossanyi.

4.4.2 Nanosecond-millisecond transient absorption

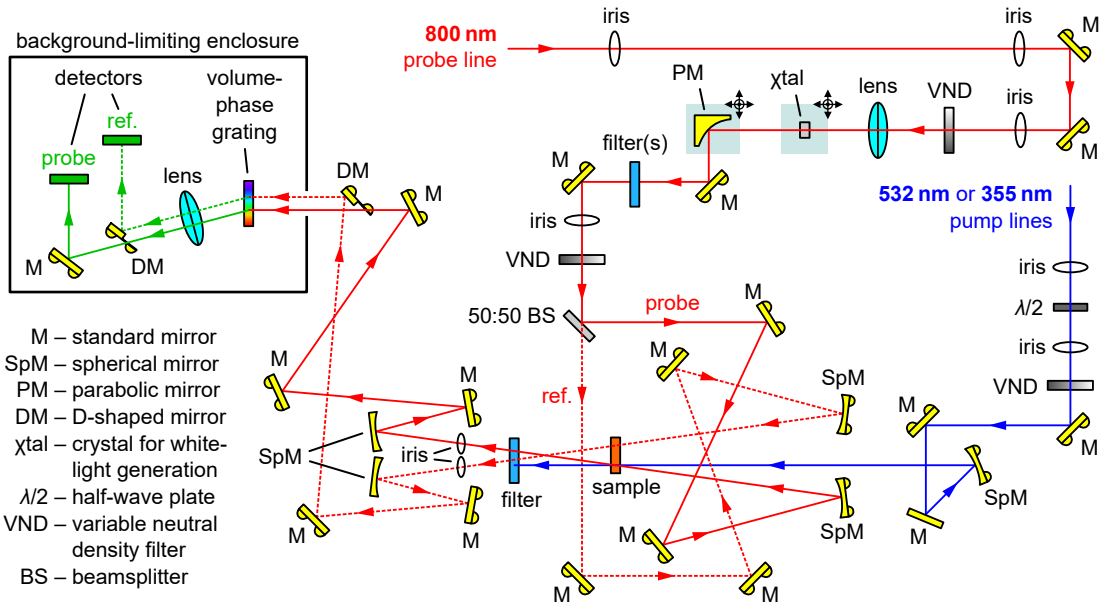

Figure 4.5 – Schematic of the nanosecond transient absorption setup. See text for details. Elements in the schematic are not to scale. Optics within kinematic mounts are denoted with semicircular knobs. Adjustable stages are denoted with light green squares with the possible directions of adjustment denoted with arrows.

Nanosecond to millisecond transient absorption spectroscopy was undertaken with a home-built pump-probe-reference setup. The use of a reference accounted for shot-to-shot fluctuations in the probe pulses (see Equation 4.15), yielding a greater signal-to-noise ratio than if a reference was not used. A Q-switched Nd:YVO_4 laser (Picolo AOT 1, Innolas) outfitted with integrated harmonic modules for frequency-doubling (to 532 nm) or tripling (to 355 nm) provided pump pulses (500 Hz, <800 ps nominal FWHM). A Ti:Sapphire regenerative amplifier (Solstice, Spectra-Physics) provided 800 nm pulses (1 kHz, 4 W nominal power, 90 fs nominal FWHM) for supercontinuum generation. 450–750 nm supercontinuum pulses were generated by focusing part of the 800 nm pulse on a sapphire crystal, and subsequently split into probe and reference beams with a 50:50 beamsplitter. The pump and probe were focused and overlapped on the sample, while the reference was focused on the sample ∼2 mm away from the pump/probe overlap. Pump-probe/reference delay was controlled electronically with a digital delay generator (DG645, Stanford) with a linear stepping order per-sweep, and the resulting sweeps are averaged. To reduce 532 nm pump scatter, typically a 532 nm notch filter (NF533-17, Thorlabs) was placed after the sample, although for some experiments a cuvette containing Rhodamine 6G in acetone placed before the grating was used instead (latter case specified herein). To reduce 355 nm pump scatter, a 395 nm long-pass filter (GG395) is used. The probe and reference were dispersed with a volume phase holographic grating (Wasatch, 360 lines mm^{-1} at 550 nm CW, 30 mm diameter, 3 mm thick, BK7) and directed onto two linear image sensors (S7030, Hamamatsu) driven and read out at the probe/reference repetition rate (1 kHz) by a custom-built board (Entwicklungsbuero Stresing). Transient absorption data was acquired with home-built software. ΔA is calculated using

$$\Delta A = -\log\left(\frac{I_{\text{on}}}{I_{i,\text{on}}}\right) + \log\left(\frac{I_{\text{off}}}{I_{i,\text{off}}}\right) \tag{4.15}$$

where I_{on} ($I_{i,\text{on}}$) are the measured probe (reference) intensities when pump is on, and I_{off} ($I_{i,\text{off}}$) are the measured probe (reference) intensities when pump is off.[†] The pump and probe polarisations were set to the magic angle. The room temperature was controlled at 19 °C.

Construction of the nanosecond-millisecond transient absorption system was

[†]Equation 4.14, which is ΔA for pump-probe transient absorption, is identical to the pump-probe-reference ΔA (Equation 4.15) when $I_{i,\text{on}} = I_{i,\text{off}}$. Note that these equations take the form $\Delta A = A_{\text{on}} - A_{\text{off}}$, where the terms A_{on} and A_{off} are comparable to blank-inclusive decadic absorbance within a double-beam system; see Section 4.1.1.

by Andrew J. Musser, Daniel W. Polak, David G. Bossanyi, and Sayantan Bhattacharya. Initial use of the system was assisted by David G. Bossanyi and Shuangqing Wang.

4.4.3 General analysis of transient absorption data

Surface Xplorer 4.3.0 (Ultrafast Systems) was used in processing the transient absorption datasets. Noisy edges of the spectra were trimmed, and the program's bad spectra replacement procedure was applied. A background correction ('subtract scattered light') was then applied using the spectra before any apparent response from the sample. For ps transient absorption data using the visible and UV-vis probes, chirp correction was applied, choosing points at the first apparent signal for a given dynamic. Chirp was not discernible in the NIR-probe ps transient absorption data nor all ns–ms transient absorption data, so a chirp correction was not applied. Time zero was adjusted to the time of maximum initial signal in ps transient absorption data, while for ns–ms transient absorption data it was adjusted to the time of first signal. Further processing and some analysis was performed with home-built Python code.

4.4.4 Exponential fitting and global lifetime/target analysis

Transient absorption data can have many overlapping features in both spectra (ΔA against wavelength) and dynamics (ΔA against time). Frequently, dynamic fitting with multi-exponential fits and/or spectro-kinetic analysis are employed to disentangle and quantify the contributions. It is worth noting that both of these analysis techniques make some assumptions that are easy to overlook. Multi-exponential fitting implicitly assumes well-defined species within the photophysical system, and that first-order rate equations describing concentration changes between those species may be written (their solutions being a sum of exponentials). Spectro-kinetic analysis assumes bilinearity, meaning that the species spectra are time-independent (*i.e.* well-defined) and that the kinetics (concentration traces) are probe wavelength-independent.[230,231] Recently, Fernandez-Teran *et al.*[232] discussed the assumptions, underlying mathematics, and application of both analysis techniques in a clear manner, using time-resolved absorbance measurements as an example. Monomeric carotenoids have been demonstrated to show strong signatures of intramolecular vibrational redistribution (IVR) and vibra-

tional energy transfer (VET), which break down the assumptions specified above on picosecond timescales; see Refs.[66–70] and Section 6.2.3.

OriginPro 9.6.0.172 (OriginLab) and home-built Python code was used to perform multi-exponential fits.

Glotaran 1.5.1 (https://glotaran.org)[233] (a GUI for TIMP, an R package[234]) was used for global lifetime/target analysis. It is a type of spectro-kinetic analysis. In addition to the bilinearity assumption, global lifetime/target analysis also assumes first-order processes between species, similar to multi-exponential dynamic fitting (see above); the species of global lifetime/target analysis decay multi-exponentially, with optional convolution with a Gaussian time-profile to account for the instrument response function (IRF) of the system. Further, a species with the Gaussian time-profile may be fitted to account for coherent artefacts.[233,234]

4.5 Laser beam power and diameter measurements

Laser beam spot major and minor diameters ($1/e^2$), d_1 and d_2 respectively, were measured at the sample positions with a CCD beam profiler (BC106N-VIS/M, Thorlabs). Unless stated otherwise, laser beam powers were measured slightly before the sample position (off-focus) with a photodiode power sensor (S120VC, Thorlabs) and meter console (PM100A or PM100D, Thorlabs). Both measurements were used in subsequent calculations for the pump fluence using the formula

$$\text{pump fluence} = \frac{P}{f\pi r_1 r_2} = \frac{4P}{f\pi d_1 d_2} \tag{4.16}$$

where P is the measured power, f is the laser repetition rate, and r_1 (r_2) are the major (minor) radii ($1/e^2$) of beam at the sample position.

4.6 Transient grating photoluminescence spectroscopy (TGPLS)

In this section, we describe the need for transient photoluminescence (PL) emission spectroscopy with ∼100 fs time resolution, the principles behind techniques that achieve this, and describe one such technique – namely transient grating photoluminescence spectroscopy (TGPLS). We then summarise our current progress

in construction of our TGPLS setup, then specify in detail the current design. Probing the orange carotenoid protein (OCP) with the completed setup may give insight into its mechanism of non-photochemical quenching (see Appendix C for preliminary steady-state PL emission measurements).

Acknowledgements: Andrew J. Musser initially assisted with TGPLS planning and construction. Shuangqing Wang assisted with TGPLS construction. David G. Bossanyi demonstrated alignment techniques, and wrote the draft TGPLS software. James P. Pidgeon was otherwise principally responsible for TGPLS construction. We thank Sayantan Bhattacharya for the helpful discussions.

4.6.1 Introduction

As discussed throughout the background (Chapter 2), the photodynamics of carotenoids can be extremely rapid, with the vast majority of decay back to the ground state (S_0) occurring within about 30 ps (see *e.g.* Chapter 5), taking the case herein of β-carotene-like ($N_{\text{eff.}} \approx 9.6$) monomeric carotenoids.[30,100,139] Transient absorption spectroscopy with sub-picosecond time resolution has proven useful in investigation of carotenoid photophysics, but as it is not blind to dark states, the resulting spectra can be congested, with assignment of the overlapped features difficult. Furthermore, $S_2 \rightarrow S_N$ excited-state absorption (ESA) features for the one-photon-accessible S_2 (lifetime ∼100 fs) are often marred by the limited time resolution in some systems, pump-associated coherent artefacts (*e.g.* cross-phase modulation[229]), dynamic/spectral overlap with the dark S_1 state (lifetime ∼5 ps), and effects from intramolecular vibrational redistribution (IVR) and vibrational energy transfer (VET).[66–70]

There is a motivation to further probe the radiative and non-radiative dynamics of the carotenoid S_2 state; in the case of orange carotenoid protein (OCP), it may present some insight into the non-photochemical quenching (NPQ) process in its active form (OCPr). An artefact-mitigated avenue to probe one-photon 'bright' states in π-conjugated molecules is photoluminescence (PL) emission spectroscopy, possibly with time resolution. However, for $N_{\text{eff.}} \approx 9.6$ carotenoids, the radiative $S_2 \rightarrow S_0$ transition is typically out-competed by non-radiative decay, including through the non-radiative $S_2 \rightarrow S_1 \rightarrow S_0$ scheme, limiting the PL quantum yield (PLQY) to ∼0.1%.[150] Therefore, fruitful steady-state PL spectroscopy of

these carotenoids requires highly sensitive systems.[†] Meanwhile, for most methods of transient PL spectroscopy, the ∼100 fs lifetime of the S_2 state is typically several orders of magnitude smaller than the time resolution or instrument response function (IRF), making the measured S_2 PL (if any) impossible to time-resolve. For example, a transient PL setup incorporating an intensified CCD (iCCD), such as our iStar DH334T-18U-73 (Andor), can 'gate' PL by turning an intensifier on for a short time. Its shortest gate time possible (∼2 ns) is fundamentally limited by the electronics within the iCCD.[205] Meanwhile, the ∼100 ps time resolution of time-correlated single photon counting (TCSPC) setups is limited by the electronics in streak cameras.

4.6.2 Principle of the TGPLS

As discussed above, there are fundamental time limitations associated with electronic-based gating. We recall that modern commercial pulsed laser systems yield pulses with temporal widths of ∼40–100 fs, so we wonder if we can use these in some way to gate PL. Indeed, that is the principle of laser-gated transient PL setups. Broadly, they induce some type of direct or indirect physical interaction between a 'gate pulse' and the PL from a sample, yielding laser-gated PL. This gated PL is detected, while the non-gated 'background PL' is discarded in some way. By adjusting the time delay between the gate pulse and the PL (or, strictly, the pump/excitation pulse that leads to PL), the temporal dependence of the PL can be built up under a time resolution partially dictated by the gate pulse temporal widths (∼40–100 fs).

We chose to construct a transient grating photoluminescence spectroscopy (TGPLS) setup, first described by Chen *et al.*[101] in their 2014 paper. We show the principle of the setup in a simple schematic, Figure 4.6. Briefly, two gate pulses are overlapped in a gate medium with high third-order susceptibility ($\chi^{(3)}$) relative to other non-linear susceptibility terms ($\chi^{(i)}$, $i \neq 1, 3$). The gate pulses constructively and destructively interfere to yield a grating pattern in light intensity (I). The grating in I modulates a grating in the gate medium's refractive index through the optical Kerr effect, a non-linear optical effect which can be written[235]

$$\Delta n \propto \chi^{(3)} I \tag{4.17}$$

[†]Appendix C presents preliminary measurements of the steady-state $S_2 \rightarrow S_0$ PL spectra of OCPo and OCPr in trehalose. This was enabled by use of a sensitive setup incorporating an intensified CCD (iCCD); see Appendix C text for details.

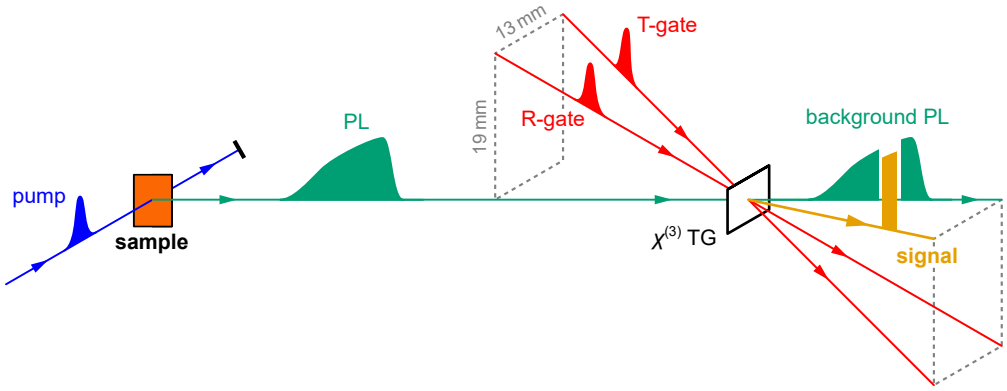

Figure 4.6 – Principle of the TGPLS. A short-lived diffraction grating is achieved through two interfering gate beams (red) modulating the refractive index in a gate medium through the non-linear optical Kerr effect. The signal/gated PL (yellow) of interest is diffracted away from background PL (teal). The time dependence of the PL can be determined by varying the time delay between the pump/excitation pulse (blue) and the gate pulses. See text for details.

where Δn is the change in refractive index. This refractive index grating acts as a diffraction grating existing on the same timescale as the gate pulse temporal widths, and diffracts part of the PL (gated PL) spatially away from the background PL. Typically the first-order diffracted PL is collected, such that geometry of the gate beams, the input/background PL, and first-order gated PL (or 'signal') forms a BOXCARS geometry,[236] satisfying the Bragg and Laue conditions.[101,108]

The TGPLS offers numerous advantages to other laser-gated PL spectroscopy setups, as discussed by Chen and co-workers.[101] In short, it combines large spectral bandwidth (340–1300 nm) and low background, the former difficult in fluorescence upconversion spectroscopy and the latter difficult in Kerr gate spectroscopy. A large spectral bandwidth is a necessity for measurements of $N_{\text{eff.}} \approx 9.6$ carotenoids, as their $S_2 \rightarrow S_0$ PL emission spectra are typically broad.[101] Indeed, our preliminary steady-state S_2 PL spectra of OCPo and OCPr in trehalose are broad; see Figure C.1 in Appendix C. Chen *et al.* achieved a ~200 fs time resolution with their TGPLS, enough to resolve the S_2 PL from β-carotene ($N_{\text{eff.}} \approx 9.6$) in hexane with a decay time constant of ~150 fs; they noted that smaller time resolutions may be achieved by, for example, minimising the number of refractive optics.[101] One interesting feature which (to our knowledge) is yet to be taken advantage of is that the angular dependence of the PL from a static sample is retained within the signal beam. Therefore, both the time and angle dependence of PL may be achievable, ideal for studying polariton PL from microcavity samples (see Appendix D

for an account of polaritonic dyes, including steady-state angular-dependent PL when incorporated into a pair of silver mirrors).

4.6.3 Summary of TGPLS construction progress

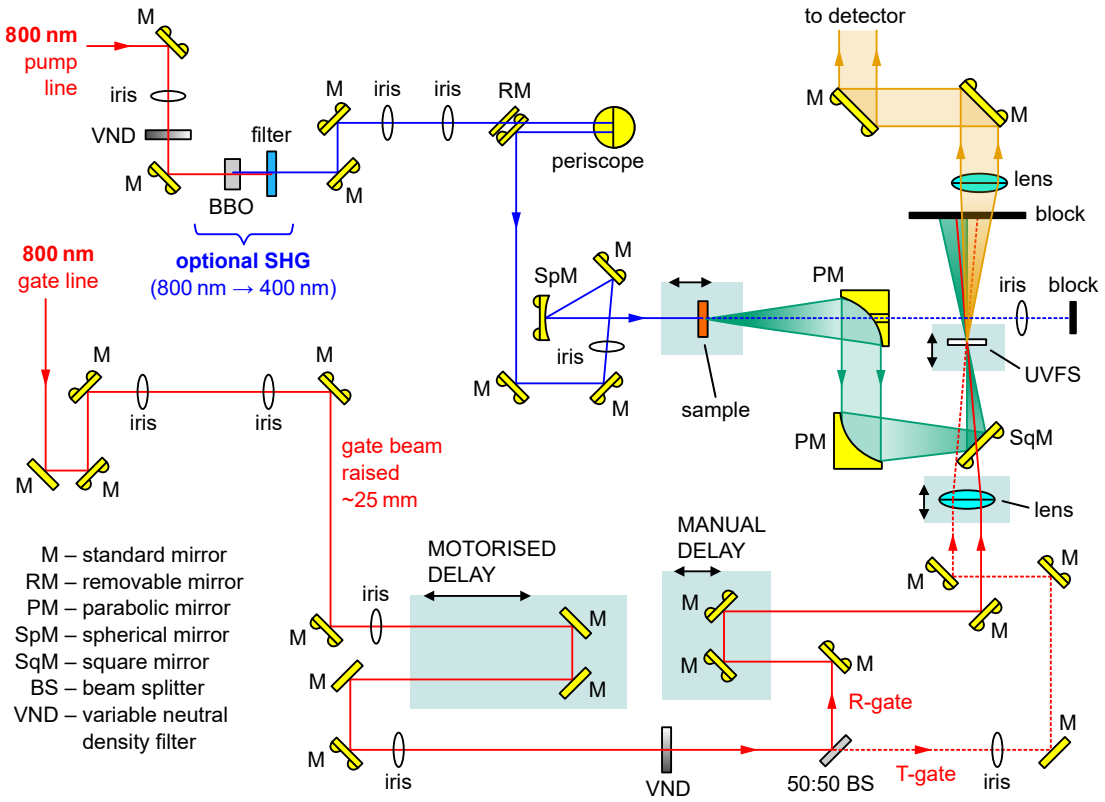

Figure 4.7 – Schematic of the current TGPLS setup. See text for details. Elements in the schematic are not to scale. Optics within kinematic mounts are denoted with semicircular knobs. Adjustable stages are denoted with light green squares with the possible directions of adjustment denoted with arrows.

The current TGPLS setup is depicted in Figure 4.7. As Chen *et al.* used a 800 nm Ti:sapphire system (Spitfire, Spectra-Physics)[101] similar to ours (Solstice, Spectra-Physics), we followed their general design, in particular matching the BOXCARS geometry of the two gate beams and PL beam. Notable deviations from their setup include the use of a focusing parabolic mirror for the PL, rather than a focusing lens for the PL, in order to minimise the refractive optics within the setup. This was to ensure a high time-resolution in our setup.[101] We also do not use a pair of cylindrical lenses to reshape the gate beams, as the natural beam size in our system is comparatively large (~9 mm $1/e^2$ diameter in our system, *cf.* 8 mm width and 2 mm height after reshaping in Chen *et al.*[101]).

In spite of achieving temporal and spatial overlap between all three input beams, verified by imaging the beams with a camera/profiler and by achieving non-collinear SHG using a BBO crystal (see details below, and Figures 4.8 and 4.9), formation of a transient grating within a gate medium has not yet been achieved. This is in spite of trying different high-$\chi^{(3)}$ gate media with different widths, optimising the gate and PL spot sizes at the overlap position, and so forth. We can attribute the non-completion of the setup in part to the COVID-19 pandemic.

4.6.4 Account of the current TGPLS design

We complete this subsection by detailing the current TGPLS setup, and is mainly intended as a reference for future constructors/users of the setup.

The current TGPLS setup is depicted in Figure 4.7. A Ti:Sapphire regenerative amplifier (Solstice, Spectra-Physics) provides 800 nm pulses (1 kHz, 4 W nominal power, 90 fs nominal FWHM, nominal linear horizontal polarisation, ∼9 mm $1/e^2$ diameter), which is used for both gate and pump pulses. Unless specified otherwise, dielectric mirrors (042-0800, EKSMA) are used for ∼45° reflection in the solely-800 nm lines (whole gate line, and pump line prior to the optional SHG), while UV-enhanced aluminium mirrors (PF10-03-F01, Thorlabs) are used for reflection in the pump line past the optional SHG. These mirrors were held in either fixed mounts (LMR1/M, Thorlabs) or kinematic mounts (KM100 or KMS, Thorlabs). Note that kinematic mounts are denoted in Figure 4.7 with semicircular knobs.

Gate alignment is maintained with an initial pair of mirrors in kinematic mounts and an associated pair of irises (IDA15/M, Thorlabs). A subsequent pair of kinematic mirror mounts raises the gate beam by ∼25 mm (compared to the height initially). Relative time delay between the gate and pump pulses (or PL) is controlled with a motorised delay stage (M-511.HD controlled with C-702 Hybrid Controller and PIMikromove software, PI (Physik Instrumente); 102 mm travel range, <0.05 µm nominal accuracy). Fine alignment of the motorised stage was achieved using a CCD beam profiler (BC106N-VIS/M, Thorlabs) imaging the beam; if the beam drifts as the translation stage is scanned, the aforementioned 'height-raising' pair of kinematic mirror mounts is adjusted. The 'short' delay is associated with the first kinematic mirror, while the 'long' delay is associated with the second, analogous to two-mirror two-iris alignment. The gate

pulses are subsequently split with a 50:50 beamsplitter into a 'transmitted' gate pulse (T-gate) and a 'reflected' gate pulse (R-gate). Temporal delay between the T-gate and R-gate is controlled using a manual delay stage (PT1B/M, Thorlabs). The T-gate and R-gate are focused by a Ø50.8 mm plano-convex lens with $f = 150 \pm 2$ mm at 800 nm (110-1511ET+AR800HT, EKSMA; UVFS). The lens position may be controlled using a small-profile manual linear stage. Note that in order to avoid clipping by the lens mount (LMR2/M, Thorlabs) while maintaining the geometry of Chen *et al.*,[101] the gate beams point into the lens ∼19 mm above its axis and slightly downwards from the horizontal (*i.e.* not parallel to its axis). This could potentially be avoided by using a larger-diameter lens. Immediately following the lens, the T-gate and R-gate are separated horizontally between their centres by ∼13 mm and have no vertical separation, which defines part of the BOXCARS geometry (see Figure 4.6). The focusing T-gate and R-gate just pass over a square UV-enhanced aluminium mirror (PFSQ20-03-P01, Thorlabs; 50.8×50.8 mm) in a rectangular (bare-top) kinematic mount (KM200S, Thorlabs) towards the gate medium. The gate medium position may be controlled using a small-profile manual linear stage. The gate medium is intended to eventually be a UVFS plate (WG41010, Thorlabs; Ø25.4 mm uncoated, 1 mm), but to avoid damage to the UVFS plate during initial setup, various float glasses were instead used. Float glass also has a higher $\chi^{(3)}$ (and thus would give a more intense gated signal) at the cost of greater susceptibility terms of higher order (which would give more background/noise in a real measurement). Focusing is just after the gate medium to prevent damage to the gate medium and to make the spatial overlap more robust against drifting in pointing (*e.g.* by thermal effects); the gate beam diameter is ∼110–220 µm at the overlap point within the gate medium. The overlap point is ∼19 mm vertically below the gate beam centre heights immediately following the $f = 150$ mm lens, which defines part of the BOXCARS geometry (see Figure 4.6). Spatial overlap between the T-gate and R-gate was initially verified using a CMOS camera (DCC1645C-HQ, Thorlabs) with ND filters to reduce the beam intensity to prevent damage. Temporal overlap (and spatial overlap verification) was achieved by adjusting the aforementioned R-gate manual delay stage until generation of non-collinear SHG in a $\Theta = 29.2°$ BBO crystal (BBO-601H, EKSMA; 6×6×0.1 mm, $\Phi = 90°$, P/P at 400–800 nm coating) near the gate medium position. Past the gate medium, the residual gate beams are blocked with a beam block.

Pump pulses are optionally doubled from 800 nm to 400 nm using the afore-

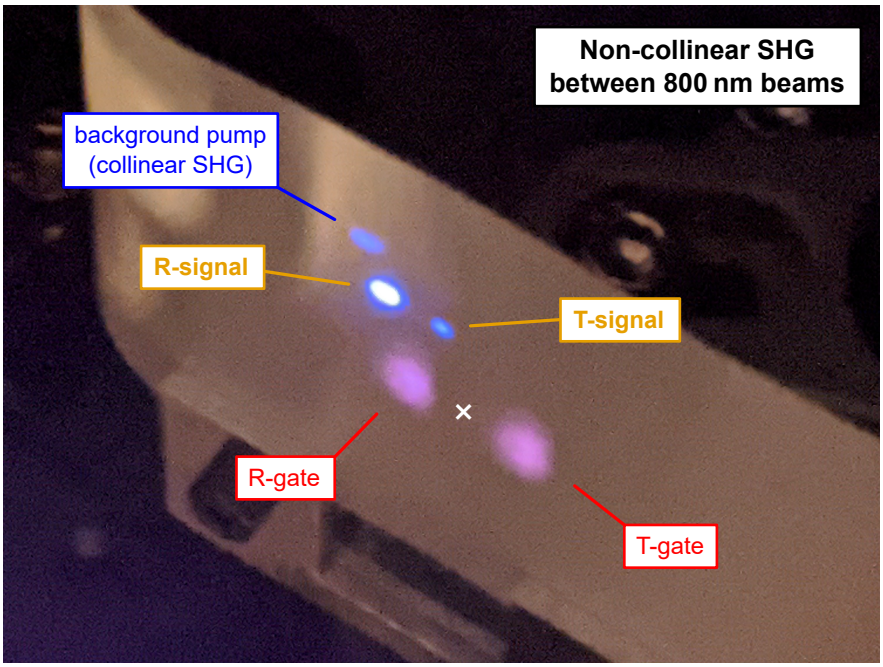

Figure 4.8 – Non-collinear SHG generation between both gate beams and a 800 nm pump. A BBO crystal was placed at the gate medium position, and a beam card placed ∼100 mm past the BBO. Non-collinear SHG between the 800 nm T-gate and 800 nm pump yields a 400 nm beam between them, here dubbed 'R-signal'. Likewise, a 'T-signal' forms between the R-gate and pump. This verifies that the pump, T-gate, and R-gate are spatially and temporally overlapped at time zero. Note that collinear SHG of the 800 nm pump occurs, so here the pump spot contains 400 nm light. Note that non-collinear SHG between the T-gate and R-gate may be attained by tuning the BBO angle, giving a 400 nm beam at the position of the white cross (×).

mentioned $\Theta = 29.2°$ BBO crystal. Residual 800 nm is removed using a bandpass filter (Schott BG39, 1 mm). In the future, tuneable pump pulses may be provided by seeding a commercial optical parametric amplifier (TOPAS Prime, Light Conversion), providing 1000–2600 nm pulses that in turn may be frequency-multiplied by a suitable BBO crystal. Past the optional SHG, pump alignment is maintained with an initial pair of mirrors in kinematic mounts and an associated pair of irises (IDA12/M, Thorlabs). The pump line is initially raised well above the gate lines; it is lowered using a periscope, such that the pump line is lower than the gate lines. The pump and PL lines remain horizontal (about their centres) throughout the rest of the setup, which defines part of the BOXCARS geometry (see Figure 4.6). The pump pulses are focused onto a sample using a spherical mirror. During construction of the TGPLS, Coumarin 153 in acetone in a 1 mm quartz

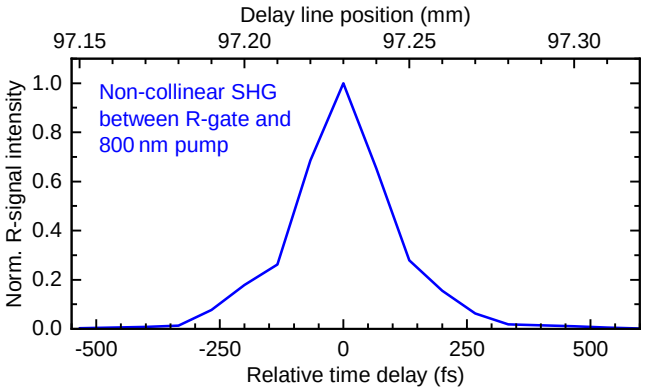

Figure 4.9 – Intensity of non-collinear SHG between one gate beam (R-gate) and a 800 nm pump against relative time delay. The relative time delay (lower x-axis) is calculated from the set distances in the motorised delay stage software (top x-axis). A BBO crystal was placed at the gate medium position. This is effectively an intensity autocorrelation measurement.

cuvette was used as a highly emissive alignment sample. The sample position may be controlled using a manual stage with a micrometer (PT1/M, Thorlabs). Note that removing the sample directs the pump pulses onto the subsequent optics; this was sometimes done in constructing the TGPLS. Furthermore, a diffuser (DBG-2553, UQG Optics) was sometimes used in the sample position to attain a PL-like angular distribution while maintaining the small temporal width associated with the pump. Photoluminescence (PL) emission from the sample is collimated using an Ø50.8 mm off-axis parabolic mirror with reflective focal length $f = 152.4$ mm (MPD269H-P01, Thorlabs; 90°, Ø3 mm hole parallel to focused beam, protected silver). Note that the through-hole removes most of the (residual) pump light. Collimation was verified by attaining a Ø50.8 mm PL spot at distance ∼1.65 m away. While the numerical aperture for PL collection could be enhanced using a shorter reflective focal length parabolic mirror (enhancing the final signal-to-noise ratio, but crucially increasing the maximum angle of emitted PL to the sample normal, important for *e.g.* microcavity samples), the long focal length enables adaptability of the sample space (for *e.g.* a cryostat or magnetic field coils). This collimated PL was subsequently re-focused using a second parabolic mirror (MPD269-G01, Thorlabs; Ø50.8 mm, $f = 152.4$ mm, 90°, protected aluminium). After reflection by the aforementioned square mirror, the PL is focused into the gate medium and overlapped with the T-gate and R-gate. Spatial overlap between the pump/PL and the T-gate/R-gate (along with the focusing of the PL; focus spot diameter ∼30–55 µm) was verified us-

ing a CMOS camera (DCC1645C-HQ, Thorlabs) with ND filters to reduce the beam/PL intensity to prevent damage. Time delay between the pump/PL and gate beams is controlled using the aforementioned motorised delay stage in the gate line. Temporal overlap between the pump/PL and gate lines was initially estimated using string. It was subsequently roughly verified using a photodetector (DET10A/M, Thorlabs; Si-based, 200–1100 nm, 1 ns rise time) and a 200 MHz oscilloscope (TDS2022B, Tektronix). Finally, it was verified by generating non-collinear SHG in the $\Theta = 29.2°$ BBO crystal between the gate pulses and 800 nm pump pulses; see Figures 4.8 and 4.9 (note this also verifies spatial overlap). To measure R-signal intensity in the 'autocorrelation' measurement, a small spectrometer was used (AvaSpec-ULS3648-USB2-UA-25 with AvaSoft 8.3 software, Anvantes). Past the gate medium, residual pump or background PL is blocked using a beam block.

A hypothetical TGPLS signal beam of gated PL is strictly the first-order diffracted PL. This defines the fourth corner within a BOXCARS geometry; see Figure 4.6. This signal beam would be initially collimated using a lens, then refocused into a detector. Our aforementioned iCCD detector (iStar DH334T-18U-73, Andor) connected to a spectrograph (Shamrock 303i, Andor) would have been used for detection; use of the intensifier would increase the signal-to-noise ratio for samples showing weak PL, while electronic gating of it may suppress scattered light and background PL (note the latter is, regardless, spatially separated and blocked).[101]

Chapter 5

Twisted carotenoids do not support efficient intramolecular singlet fission

Singlet fission is the spin-allowed generation of two triplet electronic excited states from a singlet state. Intramolecular singlet fission has been suggested to occur on individual carotenoid molecules within protein complexes, provided the conjugated backbone is twisted out-of-plane (giving a $\nu_4 \sim 980\,\mathrm{cm}^{-1}$ resonance Raman peak). Reportedly, the twist stabilises the two geminate triplets at each end of the carotenoid molecule. However, this hypothesis has only been forwarded in caroteno-protein complexes containing multiple carotenoids and bacteriochlorophylls in close contact. To test the hypothesis on twisted carotenoids in a 'minimal' one-carotenoid system, we study the orange carotenoid protein (OCP). OCP exists in two forms: in its orange form (OCPo), the single bound carotenoid is twisted, whereas in its red form (OCPr), the carotenoid is planar. To enable room-temperature spectroscopy on canthaxanthin-binding OCPo and OCPr in isolation without photoconversion, we trap them in trehalose-sucrose glass. Using transient absorption spectroscopy, we show that there is no evidence of long-lived triplet generation through intramolecular singlet fission, despite the carotenoid twist in OCPo. We discuss these findings together with results from the literature and in the context of recent work on exchange coupled triplets. We conclude that triplet-pairs in single carotenoid molecules, even when twisted, are strongly exchange coupled and are not the origin of singlet fission observed in light-harvesting complexes.

Acknowledgements: George A. Sutherland conceived the study. George

A. Sutherland and Matthew S. Proctor prepared protein samples. Absorbance measurements were performed by George A. Sutherland. Harrison Ka Hin Lee performed Resonance Raman measurements under the supervision of Wing C. Tsoi (SPECIFIC, Faculty of Science and Engineering, Swansea University, UK). Technical management of the picosecond transient absorption spectrometer was performed by Dimitri Chekulaev, while initial use of the system was assisted by Shuangqing Wang, James D. Shipp, Sayantan Bhattacharya, and David G. Bossanyi. James P. Pidgeon performed all transient absorption experiments and analysed all the data presented in this chapter.

5.1 Introduction

Singlet fission (SF) is the conversion of a spin-0 singlet exciton[237] (or excited singlet state) into a pair of triplet (spin-1) excitons.[12–15] This multiexciton generation process has been studied over the past decade primarily because of its promise to improve solar photovoltaic efficiency,[11,16,238–240] as one high-energy photon leads to two low-energy excited states that can subsequently be harvested, reducing energy losses due to thermalisation. SF could also be useful for non-linear optics,[18–20] OLEDs,[21] or even quantum technologies[22–25] by taking advantage of the fact that a single photon creates a pair of spin-entangled quantum states. However, despite promising results,[26,27] practical applications have yet to be realised, in part due to the limited library of materials which undergo SF, none of which is yet ideal.[11,14]

In the search for other SF materials, the polyenes, 'class III' SF materials according to Smith and Michl's categorisation,[13] form an intriguing material class. In these materials, the lowest-lying singlet excited state (S_1, $2A_g$) has dominant triplet-pair character, denoted ^{1}(TT) (see Refs.[12,119,120]) and thus demonstrates negligible one-photon absorption from the ground-state. S_1 is instead accessed by internal conversion following excitation to the strongly absorbing S_2 ($1B_u$) state.

This singlet fission (SF) material class includes conjugated polymers such as polydiacetylene,[241–243] poly(alkyl-thienylenevinylene),[202,244,245] a new generation of donor-acceptor SF polymers,[246–249] quinoidal thiophenes,[250–254] carbene-based diradicaloids,[255] and other antiaromatic core-structured molecules.[256,257] The polyene family also includes the carotenoids, a large class of over 1000 naturally occurring molecules,[28,29] represented here by canthaxanthin (CAN), which forms the subject of this work (structure shown in Figure 5.1a).

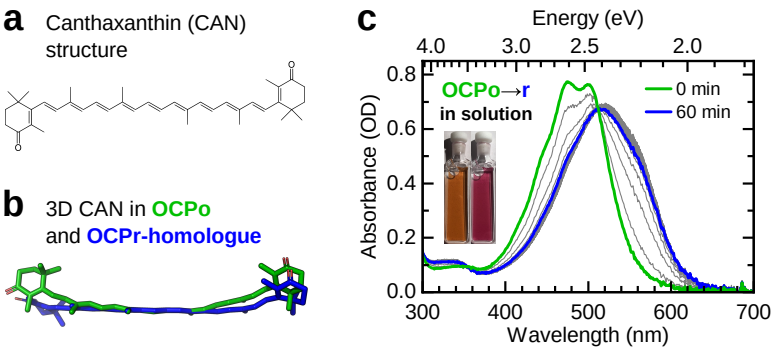

Figure 5.1 – Orange carotenoid protein (OCP) photoswitches from orange (OCPo) to red (OCPr) forms with different carotenoid conformations. The OCP studied here binds a single CAN carotenoid whose skeletal structure is shown in panel (a). The bound CAN conformation depends on the OCP form, as shown in panel (b): when CAN is bound in OCPo (green, data from X-ray diffraction structure PDB 4XB5[50,258]) it has a twisted conformation; when bound in an OCPr N-terminal homologue (blue, data from X-ray diffraction structure of red carotenoid protein, RCP: PDB 4XB4[50,259]) it is planar. (c) In solution, OCPo converts to OCPr under white-light illumination (1600 µmol photon m^{-2} s^{-1}) resulting in a change in colour (see inset) and absorbance spectrum (main panel). The spectra were taken in 1 min intervals under constant white-light illumination. In the dark, OCPr converts back to OCPo (see *e.g.* Figure 6.2). The optical path length for solution measurements was 1 mm. Data in (c) measured by George A. Sutherland.

In comparison with better-studied 'class I' SF materials,[13,191–194] mostly based on molecules such as pentacene[181,199] or tetracene,[195–198] SF in polyenes is less well understood. This is partly due to their complex manifold of low-lying triplet-pair states[116–118] and strong vibronic coupling,[67,69,70] and partly due to the sensitivity of the photophysics to conjugation length and molecular geometry. In polyenes, the lowest-lying ^{1}(TT) state that makes up the dominant contribution[119–122] of S_1 contains tightly bound triplets that are unlikely to easily separate into free triplets[97] without additional energy.[116]

Indeed, while intramolecular singlet fission (intra-SF) has been observed in a variety of long-chain polyenes in solution,[202,241–249] the triplet-pairs in polyenes decay rapidly (ps-ns) to the S_0 ground-state,[12] unlike the recently designed 'class I' intra-SF systems.[192–194,260] Even in carotenoid aggregates, where intermolecular SF occurs,[35–40] the majority of triplet excited states decay to S_0 surprisingly quickly (within a nanosecond).[12,35,40] In isolated carotenoids in solution, the dominant deactivation channel from the photoexcited S_2 state is internal conversion

to S_1. To our knowledge, there is no evidence that monomeric carotenoids in solution demonstrate intramolecular SF (intra-SF).

Nevertheless, in a somewhat similar vein to recent reports that torsion or twisting along a molecular backbone can allow both rapid intra-SF and formation of long-lived triplets in 'class I' SF materials,[193,260] intra-SF along a single *twisted* carotenoid chain to produce long-lived (µs) triplets has been suggested to occur in some photosynthetic light-harvesting complexes (LHCs).[41–45] In these systems, the protein binds the carotenoid so that it is constrained in a twisted geometry. This twist reportedly stabilises a triplet at either end of the molecule.[41,42]

This hypothesis was initially proposed to explain the presence of singlet fission (SF) in the light-harvesting antenna (LH1) from *Rhodospirillum rubrum*, because of the large intermolecular distances between neighbouring carotenoids (>10 Å).[42] More recently, Yu *et al.*[41] observed a correlation between the presence of SF and the so-called ν_4 resonance Raman peak ($\sim$980 cm^{-1}) in LHCs (LH1-RC and LH2) from *Thermochromatium tepidum* and *Rhodobacter sphaeroides* 2.4.1. The intensity of ν_4 is related to carotenoid backbone twisting,[41,48] so this finding allowed them to suggest that backbone twisting of the carotenoid is the 'structural determinant' enabling intra-SF. This would be an exciting result, particularly given recent developments in synthetic biology, where novel protein structures could in future be designed to constrain pigments in fixed geometries.[40,46]

To test the hypothesis that singlet fission (SF) can occur along a single twisted carotenoid chain, here we examine a protein that binds a single carotenoid: the orange carotenoid protein (OCP). In OCP the protein exists in two forms (OCPo and OCPr) with the carotenoid in either a twisted (OCPo) or planar (OCPr) conformation, see Figure 5.1. By studying both forms with the protein fixed in a trehalose-sucrose glass, we demonstrate that a twisted backbone is not sufficient to enable intra-SF in a protein-bound carotenoid. In addition, in light of recent work understanding magnetic field effects (MFEs) in SF systems,[160,165] we also discuss published reports of MFE in LHCs from purple bacteria.[261–266] We find that the reported MFEs are also inconsistent with intramolecular SF (intra-SF). Overall, we conclude that intra-SF is not supported on carotenoids bound within OCP and unlikely to occur in LHCs.

5.2 Results

5.2.1 OCPo/OCPr are trapped in trehalose glass

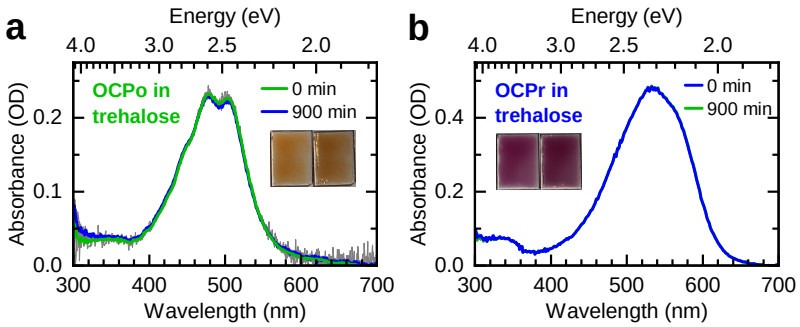

Figure 5.2 – OCPo and OCPr trapped in trehalose glass films. The absorbance spectra of the OCPo film (a) were taken in 1 min intervals under constant white-light illumination (1600 µmol photon m^{-2} s^{-1}) and the spectra of the OCPr film (b) were taken in 1 min intervals at 22 °C in darkness. No changes in spectra were observed in 900 min of respective illumination/darkness. Noise contributions seen in (a) are due to scatter of the white-light illumination from the trehalose glass. Data measured by George A. Sutherland.

Figure 5.1a shows the skeletal structure of canthaxanthin (CAN), which in this study is the only carotenoid bound to the orange carotenoid protein (OCP) with near-100% yield (see Section 3.2.1 for production technique). In solution, upon illumination with white light, the dark-adapted OCPo form undergoes a conformational switch to the OCPr form, with a concomitant red-shift of its absorbance spectrum due to the effective conjugation length extension of the bound carotenoid,[48,56,80,267] see Figure 5.1c. The change is reversible, with back-conversion from OCPr to OCPo occurring in the dark (see *e.g.* Figure 6.2).

Previously published X-ray diffraction structures by Leverenz, Sutter, and co-workers[50] show that the bound carotenoid's conjugated backbone is twisted out of the plane of conjugation in OCPo (PDB 4XB5[258]), while in OCPr N-terminal domain homologues such as red carotenoid protein (RCP) it is relatively planar (PDB 4XB4[259]). The difference between the two conformations of CAN is depicted in Figure 5.1b using data from X-ray diffraction structures.[†50] The different protein conformations containing a twisted (OCPo-bound) and non-twisted

[†]Structures obtained from the RCSB PDB (`https://www.rcsb.org`),[268] a member of the wwPDB (`https://www.wwpdb.org`).[269]

(OCPr-bound) form of CAN provide an uncomplicated model system to study the role of carotenoid geometry on intra-SF.

To avoid the problems associated with using spectroscopy to probe a light-activated conformational switch, we hinder the conformational change by trapping the protein in either its OCPo or OCPr conformations in a trehalose-sucrose glass ('trehalose'; see Section 3.3 for production protocol). This glass matrix prevents OCPo⇌OCPr conversion, as demonstrated in Figure 5.2(a,b), and allows us to probe each conformation in isolation at room temperature, without altering its conformation or photophysics.[40,270]

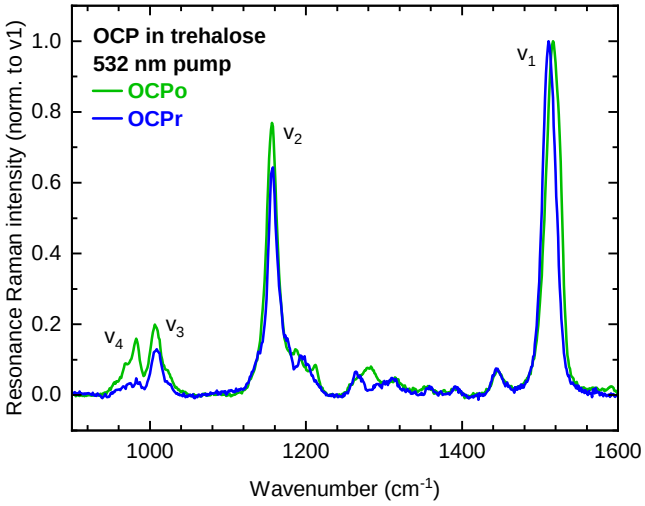

Figure 5.3 – Resonance Raman spectra of OCPo (green) and OCPr (blue) in trehalose films. Vibrational peaks typical of carotenoids are apparent, and labelled following convention.[41,48] The spectra show a significant difference in the intensity of the ν_4 vibrational peak between OCPo and OCPr and a shift of the ν_1 peak. The Raman measurements were performed using a 532 nm laser. Data is averaged from two successive scans, and normalised to the peak ν_1 intensity. Experiment performed by Harrison Ka Hin Lee under the supervision of Wing C. Tsoi (SPECIFIC, Faculty of Science and Engineering, Swansea University, UK), with analysis and figure preparation by James P. Pidgeon.

5.2.2 CAN in OCPo in trehalose is twisted, and planar in OCPr

To confirm the twisted/planar conformations of CAN in OCPo/OCPr[50] when encapsulated in glass films, we turn to resonance Raman spectroscopy. As described

above,[41,48] the presence of a so-called ν_4 peak at $\sim$980 cm^{-1} in the resonance Raman spectrum of carotenoids (due to out-of-plane C−H wagging modes[271]) is generally associated with a backbone twist of the carotenoid.[41,48] Figure 5.2c shows the resonance Raman spectrum of OCPo (blue) and OCPr (green) in trehalose films. Consistent with previous resonance Raman measurements on echinenone-binding OCP,[48] we observe a larger twist-induced ν_4 peak in OCPo than in OCPr. We conclude that CAN in trehalose-encapsulated OCPo forms a twisted geometry, while in OCPr it does not.

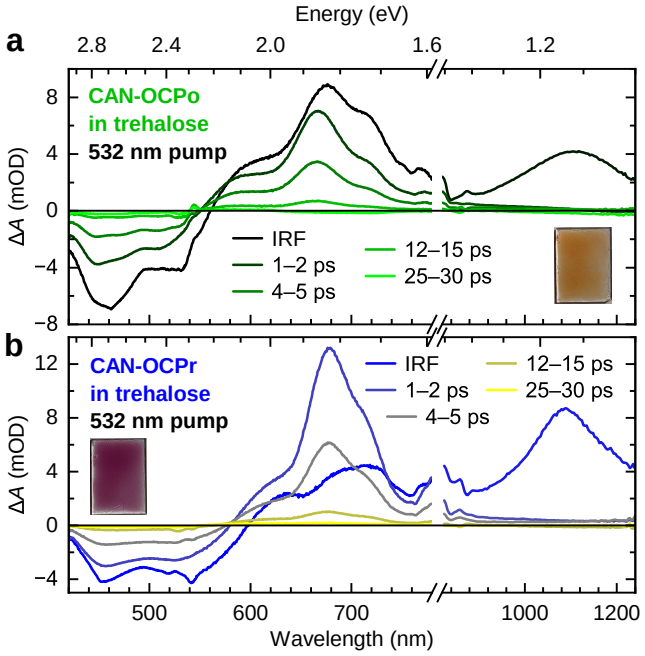

Figure 5.4 – Transient absorption spectra of CAN-binding OCPo (a) and OCPr (b) in trehalose glass. The spectral timeslices have been averaged between the times indicated in the legends and are consistent with an $S_2 \rightarrow S_1 \rightarrow S_0$ decay scheme in both cases, with no discernible long-lived features (see also global lifetime analysis of the data in Section G.3). The films were excited with 532 nm, 5 kHz, $\sim$100 fs, 200 µJ cm^{-2} pump pulses.

5.2.3 No (intra-)SF activity is apparent in OCPo/OCPr

Having established that the canthaxanthin (CAN) backbone is more twisted in OCPo than OCPr, we test the suggestion[41,43,45] that such a twist is the determinant for intramolecular singlet fission (intra-SF) reactivity. Picosecond transient absorption spectroscopy spectra and dynamics are shown in Figures 5.4 and 5.5.

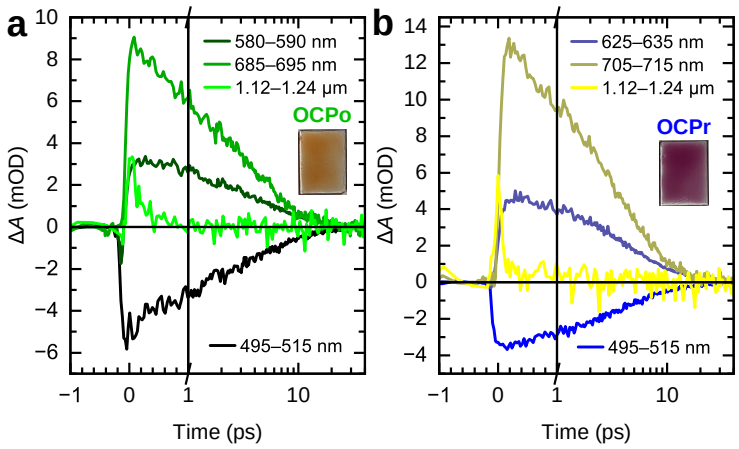

Figure 5.5 – Transient absorption dynamics of CAN-binding OCPo (a) and OCPr (b) in trehalose glass. The dynamics have been averaged between the wavelengths indicated in the legends and demonstrate that no discernible long-lived features are seen. The films were excited with 532 nm, 5 kHz, ∼100 fs, 200 μJ cm^{-2} pulses. Note the plots have a linear time-axis up to 1 ps, and subsequently logarithmic up to 40 ps.

Global lifetime analysis of the data is shown in Section G.3 (Figures G.4 and G.5), but simply from inspection of the raw data in Figure 5.4, we see that all spectral features in both OCPo (green) and OCPr (blue) decay to <1% of the initial population within 30 ps. Importantly, we observe no obvious formation of SF-generated triplets, such as the microsecond-timescale carotenoid triplets reported in light-harvesting complexes in purple bacteria.[41,42] Instead, both OCPo and OCPr broadly demonstrate the expected isolated carotenoid behaviour characterised by rapid internal conversion from S_2 to S_1 (evidenced by the instrument-limited decay of an excited-state absorption (ESA) in the near infrared region), and subsequent decay of S_1-like states to the ground-state.

We conclude that a twist along the carotenoid backbone is not sufficient to enable intra-SF.

5.3 Discussion

The lack of intramolecular singlet fission (intra-SF) in the protein-twisted carotenoid in OCPo appears to question the currently accepted hypothesis that the determinant for intra-SF in carotenoids is a twist along its backbone.[41–45] Indeed, while the carotenoid environment in OCP and photosynthetic complexes are very

different, the carotenoids in OCPo and light-harvesting complexes (LHCs) seem to demonstrate similar backbone twists (see Appendix H and Figure H.1 for further comparison).[41] Therefore, the lack of intra-SF in OCPo suggests it would be worth revisiting the machanism of SF in purple bacterial LHCs, particularly considering recent work on the nature of intermediate triplet-pair states involved in SF, as probed by magnetic-field-dependent measurements.[160,165] We therefore return to the original studies of SF in these LHC systems and discuss them in light of this recent work.[160,165]

5.3.1 Magnetic field dependence of SF in LHCs shows $J \ll D$

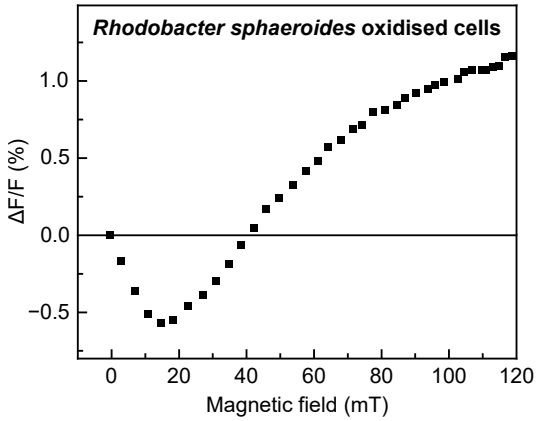

Figure 5.6 – Magnetic field effect (MFE) of *Rhodobacter sphaeroides*. Data reproduced from Ref.[261] and used with permission from Elsevier. The data is plotted as the normalised change in fluorescence $\Delta F/F$ (detected at 890 nm) as a function of the magnetic field strength upon 515 nm excitation in oxidised cells of *Rhodobacter sphaeroides* 2.4.1, with 1 mM $K_3Fe(CN)_6$ added. $A_{850–960} = 0.35$; optical path length 2 mm.

Singlet fission (SF) in light-harvesting complexes (LHCs) was first observed in a series of experiments that probed the magnetic field dependence of their fluorescence.[261–263] Representative data from Ref.[261] for oxidised cells from *Rhodobacter sphaeroides* 2.4.1 are reproduced in Figure 5.6; similar behaviour has been reported for whole cells and isolated LHCs from several strains of purple bacteria.[261–263,266] The shape of the magnetic field effect (MFE) in Figure 5.6, with an initial dip in fluorescence as the field increases from 0 to 40 mT, and then a rise in fluorescence to saturation beyond 100 mT, is a characteristic signature

of SF. This behaviour is very well described by the kinetic model by Johnson and Merrifield,[123,124,179,181,182] published in the 1960s and 70s. An important, but often overlooked, assumption of this model is that the triplet-pairs generated by SF do not interact through exchange coupling, *i.e.* $J = 0$ in the Merrifield model (where J is the intertriplet exchange interaction). With $J = 0$, the SF-generated triplet-pair eigenstates have mixed spin character, often denoted $(\mathrm{T...T})^l$, where $l = 1, 2, \ldots, 9$ labels the nine possible triplet-pair states.[181] Within the Merrifield model, therefore, the rate of SF is controlled by the size of the singlet projections of the $(\mathrm{T...T})^l$ states. For example, in equivalent parallel molecules at zero field, of the nine possible triplet-pair states,[200] only three have >5% singlet projection.[124,165] These three states will contribute appreciably to SF yield.

Application of a magnetic field such as that in Figure 5.6 causes the energies of the ($M_S \neq 0$) triplet and quintet components of the triplet-pair states to change according to the Zeeman term in the spin Hamiltonian.[165] Singlet components (or those with $M_S = 0$) remain at fixed energies and therefore application of a magnetic field alters the singlet projections of the triplet-pair states. At low applied fields (<40 mT) more states have greater singlet projection and therefore the rate of SF increases, reducing the relative fluorescence yield. At higher applied fields, fewer states have appreciable singlet projection, the SF rate decreases, and the relative fluorescence yield increases.

5.3.2 Triplets on a single carotenoid molecule have $J \gg D$

Recent work shows[160,165] that the low-field Merrifield-type MFE behaviour, such as that observed in Figure 5.6, can therefore only be observed when the intertriplet exchange interaction J is negligible, or more precisely when $J \ll D$,[272] where D is the intra-triplet dipolar zero-field splitting parameter. In carotenoids (and most organic molecules), D is relatively small (∼4–10 µeV).[127,128] If J increases beyond D, the MFE has a different behaviour, showing dips in fluorescence at much higher field strengths.[160,165,273,274] Therefore, to determine whether SF along a single carotenoid chain is capable of producing the measured MFEs in LHCs, we must estimate the values of J and D.

Before doing so we make several observations about the carotenoids involved in SF in LHCs of purple bacteria: (1) the $S_0 \rightarrow S_2$ absorbance spectra of the carotenoids in light-harvesting antenna are similar to their all-*trans* forms in organic solvent and depend sensitively on carotenoid conjugation length.[44,275] A

full break in conjugation along the chain would lead to a dramatic blue-shift of the carotenoid absorption feature that is not observed; (2) the carotenoid $T_1 \rightarrow T_n$ excited-state absorption feature seen in transient absorption of LHCs[42–45] is very similar to that seen in aggregated carotenoids of comparable conjugation lengths forming triplets by intermolecular SF.[35–37,40] The $T_1 \rightarrow T_n$ feature is also sensitive to carotenoid conjugation length,[44,276,277] and a conjugation break along the chain would similarly lead to a blue-shift that is not observed; (3) the dipolar D and E parameters of the SF-generated triplets in LHCs from transient electron parametric resonance (EPR) spectroscopy[266] are similar to full-chain triplet D and E parameters, rather than to their half-chain alternatives.[266] These observations suggest that the conjugation along the chain is not broken, even in the LHC antenna protein, and therefore that the triplets at either end of the chain maintain orbital overlap and, presumably, non-negligible J.

The exchange interaction, J, between triplets within a pair is equal to one sixth of the energy difference between the pure singlet triplet-pair, denoted ^{1}(TT), and the pure quintet, ^{5}(TT) (following the convention for J in *e.g.* Ref.[201]). In addition, to first approximation, the energy of ^{5}(TT) is equal to twice the free triplet energy.[12,116,200] In carotenoids, as described above, the lowest energy singlet state is predominantly a pure singlet ^{1}(TT) state. Therefore, comparison between twice the energy of a triplet on half a chain against the energy of S_1 on a full chain provides an indication of the exchange interaction.

Recent high-level density matrix renormalisation group (DMRG) calculations of the Pariser-Parr-Pople-Peierls Hamiltonian[116] calculate that $2 \times E(T_1)$ for a half chain is higher in energy than S_1 ($\approx^1$(TT)) for a full chain at all conjugation lengths. This is supported by experimentally determined energies: for diphenylhexatriene with $N = 5$ conjugated double bonds, $2 \times E(T_1) = 3.02 \pm 0.1$ eV,[276,278] while for spheroidene with twice the number of double bonds ($N = 10$), $E(S_1) = 1.77$ eV.[279] This would indicate an exchange interaction of $J = 0.2$ eV, which is orders of magnitude larger than the dipolar parameter $D \sim 4$–10 µeV.[127,128] These energies indicate that the triplets within ^{1}(TT) should be strongly exchange coupled.

The triplets within a single carotenoid chain are therefore strongly exchange coupled ($J \gg D$), even in a protein that twists the carotenoid backbone,[41] as no breaks in conjugation along the carotenoid chain have been observed (*i.e.* no observable shifts in absorption spectra[44] or changes in dipolar D and E parameters[266]). Therefore, MFEs such as those reproduced in Figure 5.6, that were the

initial proof of SF in purple bacteria, cannot be explained with an intramolecular model of SF.

5.4 Conclusions

We conclude that singlet fission (SF) to produce long-lived triplets does not occur along a single twisted carotenoid chain in OCP, and is unlikely to occur on a single carotenoid chain in purple bacterial light-harvesting complexes (LHCs), contrary to the currently purported view.[41–45] We conclude this because (1) immobilised OCPo – an uncomplicated, minimal carotenoprotein – shows similar twisted carotenoid geometry to LHCs, but shows no evidence of SF, (2) the magnetic field effects (MFEs) used to identify SF in purple bacteria are irreconcilable with intramolecular SF without a significant break in conjugation (the latter not observed in LHCs).

These findings therefore call into question the mechanism of SF that is observed in LHCs. A study within our group on the mechanism is currently concluding, with a paper recently submitted to the journal *Science*. This is primarily the work of Shuangqing Wang and George A. Sutherland (joint first authors), with the thesis author the third author. A complete discussion of this study within the main body of this thesis is beyond its scope, but we include the current draft submission as Appendix A and its supplementary materials as Appendix B.

Chapter 6

OCP photocycle is not triggered by long-lived dark singlet 'S*'

The orange carotenoid protein (OCP) is the water-soluble mediator of non-photochemical quenching in cyanobacteria, a crucial photoprotective mechanism in response to excess illumination. OCP converts from a globular, inactive state (OCPo) to an extended, active conformation (OCPr) under high-light conditions, resulting in a concomitant redshift in the absorption of the bound carotenoid. There is a debate on the initial steps in OCP photoconversion, and a better understanding may lead to applications in synthetic biology. As in the previous chapter, OCP was trapped in either the active or inactive state by fixing each protein conformation in trehalose-sucrose glass. Glass-encapsulated OCPo did not convert under intense illumination and OCPr did not convert in darkness, allowing the optical properties of each conformation to be determined at room temperature. We measured pump wavelength-dependent transient absorption of OCPo in glass films and found that initial OCP photoproducts are still formed, despite the glass preventing completion of the photocycle. By comparison to the pump wavelength dependence of the OCPo to OCPr photoconversion yield in buffer, we question recent suggestions that a long-lived carotenoid singlet-like feature (S*) is responsible for triggering OCP photoconversion, and show that the long-lived singlet is associated with ground-state heterogeneity within OCPo.

Acknowledgements: George A. Sutherland conceived the study. George A. Sutherland and Matthew S. Proctor prepared protein samples. George A. Sutherland measured the absorbances in Figures 6.1a and 6.2. Technical management of the picosecond transient absorption system was performed by Dimitri Chekulaev, while initial use of the system was assisted by Shuangqing Wang, James

D. Shipp, Sayantan Bhattacharya, and David G. Bossanyi. Construction of the nanosecond-millisecond transient absorption system was by Andrew J. Musser, Daniel W. Polak, David G. Bossanyi, and Sayantan Bhattacharya, while initial use of the system was assisted by Shuangqing Wang and David G. Bossanyi. Rahul Jayaprakash assisted in initial set up and use of the narrowband-pump time-resolved absorbance setup. Ravi Kumar Venkatraman discussed the literature, particularly in regard to spectroscopic signatures of hydrogen-bond breaking. James P. Pidgeon performed all transient absorption experiments, performed the narrowband-pump time-resolved absorbance experiment, and analysed all the data presented in this chapter.

6.1 Introduction

Oxygenic photosynthetic organisms have evolved mechanisms to protect themselves from excess light conditions and the consequent formation of damaging reactive oxygen species. In cyanobacteria, this photoprotective response occurs over two different timescales. On long and medium timescales (hours/days), photoprotection is achieved by attenuation of protein expression and state transitions.[280,281] On shorter timescales (seconds/minutes) photoprotection relies on a small (35 kDa), water-soluble, single carotenoid-binding protein known as the 'orange carotenoid protein' (OCP), structure in Figure 6.1. This photoprotection process, sometimes referred to as 'non-photochemical quenching' (NPQ), is initiated by the absorption of white light by the OCP. Under these conditions, OCP undergoes a conformational change from a globular, inactive conformation (OCPo) to an extended, active state (OCPr)[49,50,282] allowing it to bind to and dissipate excess energy in the photosynthetic light-harvesting phycobilisome.[283–285] OCP's photoinduced conformational change is accompanied by a redshift of its absorption spectrum, changing colour from orange (OCPo) to red (OCPr) (Figure 6.1a) as the effective conjugation length ($N_{\text{eff.}}$) of the bound carotenoid extends.[48,56,80,267]

While several groups have recently focused on understanding the mechanism of OCPr-induced PBS quenching,[55,62,74–78,284,286–288] here we focus instead on understanding the initial step of the OCP photocycle to help determine how excitation leads to the dramatic conformational change from OCPo to OCPr. The answer to this question is of interest because the photoswitch in OCP appears to be unique,[79,80] and unlike other molecular and pigment-protein photoswitches

such as rhodopsin[289] or phytochrome.[290] This OCP photoswitch is, nevertheless, relevant to an entire class of primary producers in many ecosystems,[52] and understanding the mechanism in greater depth will not only help our understanding of these key organisms, but may also help develop biomimetic optoelectronic or photonic technologies for light adaptation[81] or energy storage.[82]

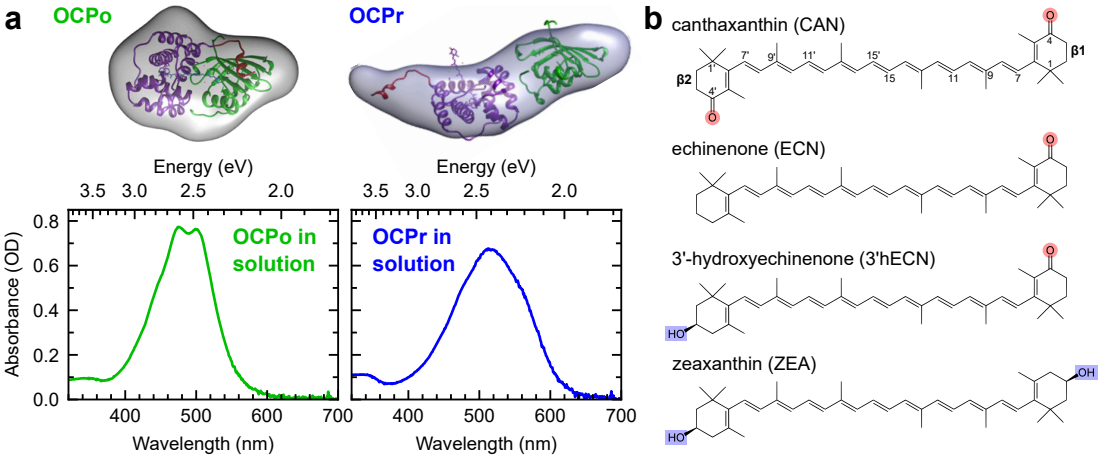

Figure 6.1 – OCP conformational change and carotenoids discussed in this study. (a) Structural model of the conformational change from OCPo (left) to OCPr (right) from previously reported[49] small angle X-ray scattering (SAXS) analysis. Absorbance spectra of each conformation is displayed below (0 min and 60 min from Figure 6.2a). **(b)** Chemical structures of carotenoids discussed in this study; substitutions relative to β-carotene are highlighted, with carbonyl groups in red and hydroxyl in blue. Conventional numeration of carbons and β-rings is indicated for CAN, but apply similarly to the rest of the structures. Absorbance data measured by George A. Sutherland; SAXS data from Gupta and co-workers, used with permission from PNAS.[49]

The significant work reported to date on this protein suggests that in the orange form (OCPo), the carotenoid is bound to the protein in a twisted, strained geometry.[48,79,282] It is held in this strained geometry mainly by hydrogen-bonding between its β1-ring carbonyl group (C=O) and two absolutely conserved amino acid residues in the C-terminal domain of the protein: tryptophan 288 and tyrosine 201.[79,80,282] Upon photoexcitation, at some time both hydrogen-bonds are believed to break,[79] either releasing the strain allowing the carotenoid to planarise and translocate into the N-terminal domain,[53,60,79,267,291–293] or simply as a result of N- and C-terminal domain separation.[73]

While there is consensus that the initial trigger of the OCP photocycle is absorption of blue/green light by the carotenoid, the processes immediately following this photoabsorption and the causes of hydrogen-bond breakage between

the carbonyl group and protein Trp288/Tyr201 are an active topic of debate. An initial hypothesis that light absorption induces rotation of the carotenoid's β1-ring (*i.e.* about the C6-C7 single bond), resulting in breaking the hydrogen-bonds,[58,59] was disproved using dynamic crystallography of OCP.[79] Indeed, a more recent study combining dynamic crystallography and optical spectroscopy suggests that hydrogen-bond breaking occurs because of domain separation.[73] A recent comprehensive study using time-resolved UV-visible and polarised mid-infrared spectroscopy was able to follow the electronic and vibrational degrees of freedom through the OCP photocycle from femtoseconds to 0.5 ms.[53] A key hypothesis of this study is that photoexcitation of a carotenoid excited state, dubbed S*, triggers the photocycle. The presence of a mysterious S* feature in transient absorption spectroscopy studies of carotenoids has plagued the literature for several decades. Therefore, we provide a brief literature review to clarify the current understanding of S* in OCP and in the wider carotenoid literature.

We start our discussion with a description of S* as a generic spectral feature without assigning it to any distinct excited-state or process at this point. S* is a catch-all term for a photoinduced absorption spectral feature located at the red edge of the $S_0 \rightarrow S_2$ ground-state bleach, and distinct from the main singlet S_1 excited state absorption band.[100] The S* feature is typically weak (∼1–5% of the $S_1 \rightarrow S_n$ absorption intensity) with a long lifetime (∼20–100 ps) compared to the S_1 absorption features. The S* feature is sometimes also associated with narrowing of the ground-state bleach and often shows pump (excitation) wavelength-dependent behaviour (it is relatively more intense with higher-energy excitation).[64,97,98] This broad definition of the S* spectral feature and its location at the edge of the ground-state bleach, which can be prone to artefacts (because depositing energy into a system can lead to an increase in local temperature, resulting in changes in the sample's refractive index and absorption spectrum in the probe region), means that S* has been assigned to a variety of different phenomena.[44,70,98,100]

In OCP the authors of Ref.[53] suggest that the S* feature represents a key intermediate electronic excited state that drives the switch from OCPo to OCPr. They hypothesise that S* is a structurally distorted form of the lowest singlet excited state in carotenoids,[53,294,295] and that this distortion enables hydrogen-bond rupture between C=O and Trp288/Tyr201. A more recent study by Yaroshevich *et al.* supports the hypothesis that S* is a distinct excited state,[61] but suggests that it enables accumulation of intramolecular charge transfer (ICT) states which are themselves responsible for hydrogen-bond breaking.[61] In both of these pictures,

hydrogen-bond breaking should occur during the S* lifetime, as has been reported in a study of OCP mutants containing only one tryptophan residue, Trp288 (the one involved in hydrogen-bonding to C=O).[60] However, hydrogen-bond breaking should also be observable through shifts in the transient mid-infrared or UV-vis absorption spectra, as a blue-shifted excited-state absorption of the C=O band,[296] or as a photo-induced absorption to the blue-edge of the ground-state bleach in UV-vis transient absorption spectroscopy.[61] To our knowledge, neither of these features have been observed on the S* timescale (∼20–100 ps), although it is possible that these features are simply outside of the measured spectral ranges[53] or obscured by other spectral features. The aforementioned study using time-resolved crystallography and optical spectroscopy suggests that the hydrogen-bond breakage occurs on 5–10 min timescales merely as a consequence of N- and C-terminal domain separation, as opposed to being more directly photoinduced.[73]

Other research by Balevičius *et al.* supports the hypothesis that observation of an S* feature in visible transient absorption spectroscopy is key to understanding the trigger to photoswitching in OCP.[69] However, Balevičius' study on carotenoids in solvent, together with earlier work,[66–68] suggest that the S* spectral feature is not an excited-state signature, but instead arises due to transient heating of the carotenoid and solvent during and immediately following internal conversion.[69] Internal conversion in carotenoids is incredibly rapid and most of the energy deposited into OCP by light (∼2 eV) is converted into vibrational or kinetic energy within ∼100 fs to 20 ps through intramolecular vibrational redistribution (IVR) and vibrational energy transfer (VET) to the surroundings. IVR and VET populate both higher-lying vibronic levels ($\nu \geq 1$) in the ground (S_0) and excited (S_1) electronic states[66–68] and cause local heating in the form of population of low-energy molecular, solvent, or protein vibrational/rotational modes. Both of these result in transient spectral features in the ground-state bleach spectral region which could be assigned to S*.[66–70] From these carotenoid-in-solution studies, Balevičius *et al.*[69] suggested that the S* seen in OCP by Konold *et al.*[53] was consistent with a residual 'hot ground state', associated with a non-equilibrium distribution of carotenoid vibronic populations as well as elevated local temperature (rather than a distinct excited state), that may provide enough energy to break the weak hydrogen-bonds[69] (estimated to have a bond energy of ∼8 kcal mol^{-1} or 0.35 eV per molecule[61]).

Still others claim that the S* feature in transient absorption spectroscopy is not due to an intermediate excited state, or due to heating, but is instead

due to inhomogeneity of the sample. The inhomogeneity is observed as a pump wavelength-dependent change in resonance Raman[48] and transient absorption spectra[51,54,57,64,297] and is usually attributed to carotenoid conformational inhomogeneity as the carotenoid adopts more than one conformation in the ground-state,[48,51,54,222] possibly due to spontaneous hydrogen-bond disruption.[60] This spectral heterogeneity has been observed in OCPo binding 3′-hydroxyechinenone (3′hECN),[297] echinenone (ECN),[48,51,64,222] canthaxanthin (CAN),[51] and zeaxanthin (ZEA),[51] in N-terminal domain helical carotenoid proteins (HCP) HCP2 and HCP3 containing CAN,[57] and in the non-canonical OCP2 clade.[†54]

The hypothesis that the pump wavelength dependence of OCP spectral features is due to conformational heterogeneity of the carotenoid has basis in studies of isolated carotenoid in solution.[97,98,299–301] For example, an important study by Ostroumov *et al.*[98] demonstrated that the pump wavelength dependence could be removed by purifying β-carotene immediately prior to measurement. The resulting transient absorption spectra of all-*trans* β-carotene showed no sign of the putative S* spectral feature. While the aforementioned transient heating due to rapid internal conversion is also predicted to show some pump wavelength dependence,[68] the effect is small and short-lived, and cannot on its own explain the sometimes dramatic changes in transient absorption spectra in relation to pump wavelength.[97]

As described above, the literature places great emphasis on the S* feature because it is widely believed to be directly correlated with the first steps of the photoswitching mechanism of OCP.[53,60,61] We find that the evidence for this key assumption is largely circumstantial and requires further scrutiny. Therefore, here we aim to test the hypothesis that the S* spectral feature is directly correlated with photoswitching. To do this, we measure the relative yield of both S* and the OCPo→OCPr photoconversion process as a function of pump wavelength. Measuring the relative yield of S* is challenging, because of the inherent problem of using light to probe a light-activated protein. As we shine light on OCPo, it changes from OCPo to OCPr making it difficult to untangle the different spectral contributions from either form. To mitigate this problem, many groups rely on measurements in solution using a flow cell or similar and some form of global data

[†]Note that the canonical clade of OCP (studied in this thesis) is sometimes dubbed OCP1 in order to distinguish it from other clades. Then the orange form of OCP1 may be written OCP1o, and its red form as OCP1r, and likewise for OCP2o and OCP2r. 'OCP' in this thesis should be taken as OCP1, unless specified otherwise.[54,298]

analysis,[51,53,62–65] on samples immobilised at cryogenic temperatures to avoid the photoconversion,[56] or on OCP mutants.[58–61] The first technique requires large volumes of OCP and the data analysis may be complicated by the presence and dynamic changes of contaminating photoconverted product. The second introduces temperature effects that no longer reflect the natural environment and the third may alter protein folding or perturb the native interaction with the carotenoid.[†]

To solve these problems, we trapped wild-type OCP from *Synechocystis* sp. PCC 6803 in either its OCPo or OCPr form at room temperature using a trehalose-sucrose glass. Trehalose is a naturally-occurring sugar used by plants to protect macromolecular cell architecture under drought conditions by fixing proteins in their natively folded states.[72] Trehalose-sucrose (herein referred to simply as 'trehalose') forms an optically-clear glass following dehydration at temperatures less than 60 °C, enabling the optical characterisation of encapsulated materials[40] and allowing the independent effects of temperature and protein immobilisation to be resolved.[71,270] In addition, as we have found that the same sample can be measured without degradation in several different measurements, it offers a more efficient use of material. We use the trehalose glass system to probe the excited state dynamics of wild-type OCP containing near-100% canthaxanthin (CAN) at room temperature using pump wavelength-dependent transient absorption spectroscopy.

We show that fixing the OCP in trehalose enables measurements to be conducted in both its orange and red state without contamination of alternative optical forms and that the transient spectroscopy of OCPo is identical to that measured in buffer using a flow cell (up to at least 0.7 ms). We find that the S* feature (defined here as a relatively blueshifted singlet feature with ∼65 ps time constant) in OCPo has a clear pump wavelength dependence. The photoswitching yields (in buffer) do not show the same pump wavelength dependence as the S* feature. Therefore we conclude that the S* spectral feature cannot be directly correlated with the photoswitching yield and the dominant S* contribution merely arises from ground-state OCPo heterogeneity.

[†]Our own experiments on OCP mutants have shown some odd results; see Section G.5 for visible- and NIR-probe picosecond transient absorption.

6.2 Results

6.2.1 OCP binding ∼100% CAN avoids carotenoid heterogeneity

To work out what is happening in OCP, we would like to simplify the system as much as possible. When extracted from *Synechocystis*, OCP proteins contain one of several carotenoids that proportionally vary depending on the method used for production, leading to heterogeneous samples that make understanding the photophysics difficult. For example, when expressed from the wild type locus, OCP contains 95% 3′-hydroxyechinenone (3′hECN) and 5% echinenone (ECN), but when overexpressed under the control of the psbAII promoter the composition is 70% ECN, 16% 3′hECN, and 14% zeaxanthin (ZEA).[302] As relatively large amounts of material were required for the experiments described herein and as unity carotenoid composition was desirable to avoid heterogeneity, alternative production approaches were necessary. When maintained in *E. coli*, the pAC-CANTHipi plasmid generates almost 100% canthaxanthin content.[215] Here we employed a dual plasmid system, comprised of pAC-CANTHipi to generate carotenoid (∼100% CAN)[215] and pET28a::OCP to produce OCP. Maintenance of both plasmids in BL21(DE3) *E. coli* allows incorporation of the carotenoid *in vivo* producing OCP binding near-100% CAN. See Section 3.2.1 for further details. Unless stated otherwise, all experimentation was conducted with OCP containing near-100% CAN.

6.2.2 Trapping in trehalose does not alter initial photophysics

To study the early-time photophysics of OCP without problems associated with full photoconversion of the sample during measurement, we trapped the protein in a trehalose-sucrose glass matrix[40] (herein referred to simply as 'trehalose'); see Section 3.3 for production protocol. The lack of complete photoconversion in trehalose is demonstrated in Figure 6.2. Here we monitored the absorbance spectra of OCPo/OCPr in buffer (a,c) and in trehalose (b,d) as a function of time either under illumination with intense white-light (1600 µmol photon m^{-2} s^{-1}; Figure 6.2a,b) or in the dark (Figure 6.2c,d) at room temperature. Full photo-conversion of OCPo in solution occurred within 6 min of illumination and the reverse conversion complete within 60 min in darkness. No conversion was observed in either

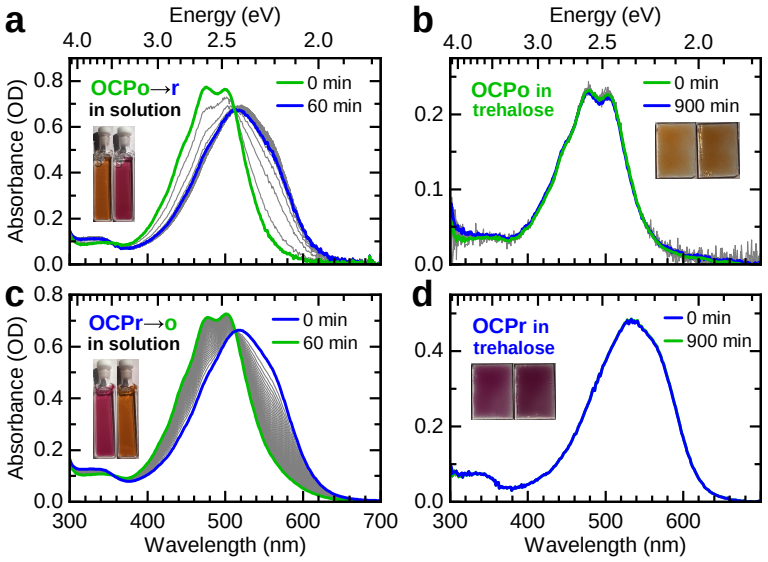

Figure 6.2 – Conversion of OCP in solution (a,c) and in trehalose glass (b,d). Absorbance spectra of OCPo (a,b), taken in 1 min intervals under constant white-light illumination (1600 µmol photon m^{-2} s^{-1}), or OCPr (c,d) taken in 1 min intervals at 22 °C in darkness. Noise contributions seen somewhat in (a) (strongly in (b)) are due to scatter of the white-light illumination from the cuvette (from the trehalose glass). The optical path length for solution measurements was 1 mm. Data measured by George A. Sutherland.

sample encapsulated in trehalose during the 15 hours measured, with absorbances the same at all times (Figure 6.2e).

Transient absorption spectra of OCP in trehalose are shown in Figure 6.3a–c. To confirm that the early-time photophysics of OCP is not impacted by being trapped in the trehalose, or by the presence of only one carotenoid type (near-100% CAN), we compare these spectra to solution measurements (Figure 6.3d) and those reported in the literature (*e.g.* Ref.[51,53,57]). We find that the spectra of OCP measured on these timescales in trehalose show no obvious differences to those measured in flowed solution over the same timescales. For example, the picosecond spectra and dynamics (Figure 6.3a,b) are similar to those observed in CAN-binding OCP,[51] RCP,[51] and N-terminal domain helical carotenoid proteins (HCP) HCP2 and HCP3 in solution.[57] This includes the presence of significant excited-state absorption (ESA) in the 700 nm to 900 nm spectral range that is due to intramolecular charge transfer (ICT) state absorption.[51,57] The longer-time behaviour (Figure 6.3c) is also near-identical to results for solution measurements in buffer (Figure 6.3d; see Appendix I for further comparison, including dynamic

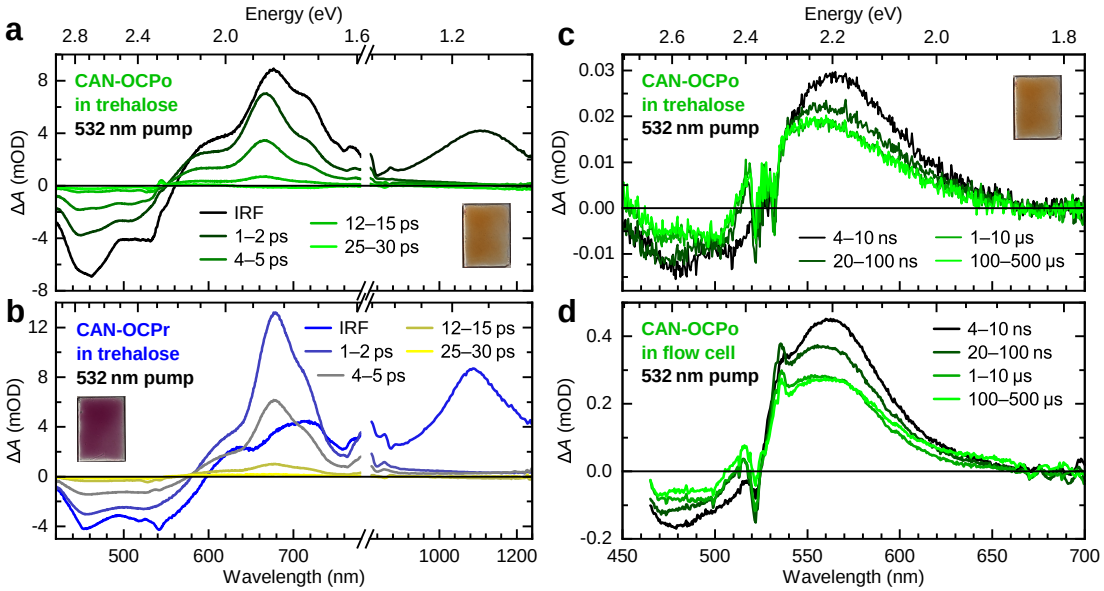

Figure 6.3 – Transient absorption spectra on picosecond (a,b) and ns–ms (c,d) timescales of CAN-binding OCP in trehalose glass (a–c) and in buffer (d) with pump wavelength 532 nm. When OCP is encapsulated in trehalose, singlet decay occurs over ∼5 ps (a,b) and long-lived and static features are seen on the long-time (c), consistent our ns–ms measurement of OCPo in buffer (constantly refreshed by use of a flow cell) and with the literature on OCPo and OCPr in buffer.[51,53,57] Spectra have been averaged between the times indicated. Pump fluence was set to 200 µJ cm^{-2} for (a–c), and to 1600 µJ cm^{-2} for (d). For panels (a,b), the instrument response function (IRF) spectrum was taken at a nominal delay of 0 fs, and is heavily impacted by a coherent artefact.

traces and the results of global lifetime analysis) and on 3′hECN-binding OCP reported recently.[53] Overall, therefore, our results demonstrate that the early-time photophysics of CAN-OCPo is not affected by the trehalose environment.

Importantly, we also observe no photoconversion during the transient measurements on trehalose films: inspection of the films after all experiments with pulsed lasers show no detectable colour change (apart from bleaching in measurements using high pump fluences; see Figure 3.4), and the transient absorption spectra of individual sweeps from panel (c) did not change over the course of the experiment (over 18 hours).

To summarise, trapping the OCPo and OCPr protein conformations in trehalose glass prevents the full OCPo→OCPr photoconversion. However, the initial photophysics (up to 0.7 ms) remains unchanged in the trehalose compared with buffer and OCP remains in its native form within the trehalose. Trehalose-OCP

films therefore provide us with stable solid state samples that can help elucidate the mechanism of OCPo→OCPr photoconversion. To test the recent hypothesis that a long-lived singlet (often dubbed S*) is an initial trigger for the photoconversion mechanism,[53,60,61] we first turn to pump wavelength-dependent transient absorption measurements on OCPo in trehalose.

6.2.3 Multiple ground-state conformations of OCPo are apparent

Transient absorption spectra of OCPo in trehalose using pump wavelengths in the range $\lambda_{\text{pump}} = 400\,\text{nm}$ to 600 nm are shown in Figure 6.4. Here, to ensure a constant excitation density at each pump wavelength, we tuned the pump powers to target an initial ∼3 mOD peak GSB response at 1 ps. For most pump wavelengths, this resulted in a relatively low pump power (see Figure J.1 for pump profiles and powers used). We chose to use a probe spanning 370 nm to 690 nm to better resolve the GSB region.

We start by describing spectra with 495 nm pump, close to the peak absorption of OCPo and similar to pump wavelengths used in previous reports.[48,51,53,57] As expected, the spectra show signatures of S_1 decay (∼5 ps visible ESA decay) and associated effects due to intramolecular vibrational redistribution (IVR) and vibrational energy transfer (VET) (*e.g.* narrowing, shifting, changes in vibronic lineshapes; see Refs.[68,69] for details). We note that carotenoids, particularly ketocarotenoids such as CAN, demonstrate a wealth of different diabatic states and that any S_1-like features we observe likely originate from S_1/ICT (and other) admixtures, with confounding effects due to IVR/VET. In this work to simplify the discussion we describe the states as S_1, S_2, *etc.* with the implicit assumption of them being mixed states.

We now discuss the impact of redder pump wavelengths (from 495 nm to 600 nm) on the OCPo photophysics. For all times >1 ps, as λ_{pump} increases from 495 nm to 600 nm, we observe a continuous spectral evolution, consisting of two main factors: (1) a decrease in the S_1-S_n ESA vibronic replica around 585 nm, together with an apparent narrowing of the entire ESA feature, and (2) a continuous change in the GSB vibronic structure, with the peak around 507 nm increasing relative to the ∼481 nm peak. While (1) could be partially explained in terms of effects associated with IVR and VET, as modelled by Balevičius *et al.*,[68] the effect we observe is significantly more pronounced and long-lived, and therefore

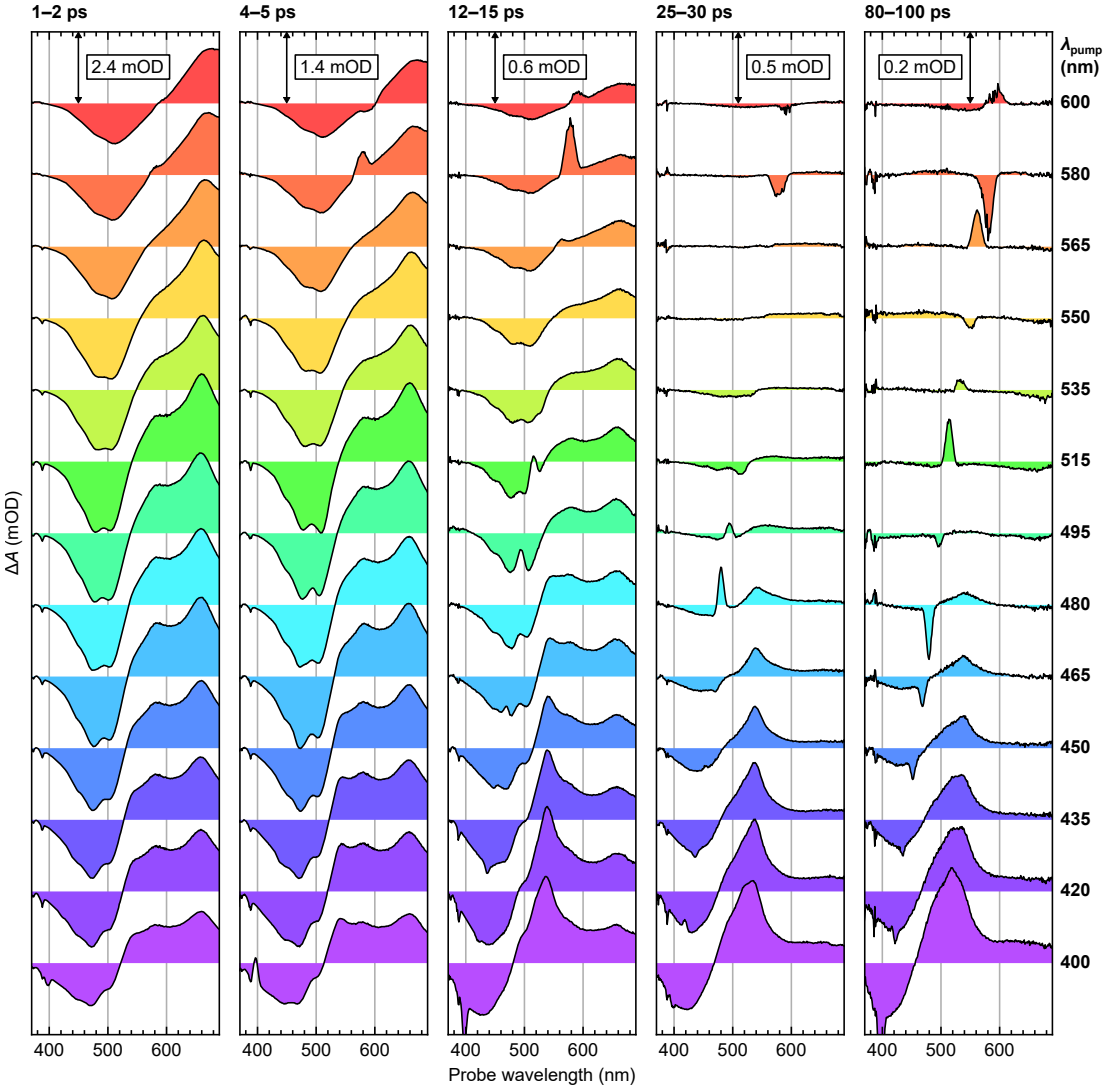

Figure 6.4 – Transient absorption spectra of CAN-binding OCPo in trehalose glass with pump wavelengths in the range 400 nm to 600 nm (specified on the right). Spectra have been averaged between the times specified on the top, with arrows denoting the size of the y-axis scale (ΔA in mOD) for that column of spectra. Pump powers were tuned to give an initial $\sim$3 mOD peak GSB response at 1 ps. We observe that higher-energy (lower wavelength) pump wavelengths (400-480 nm: blue/purple) give rise to long-lived features previously assigned to S*-like features.[53] As the pump wavelength is tuned to lower energies (longer wavelengths), the spectra continuously shift spectrally, demonstrating ground-state heterogeneity. Note that sharp positive and negative peaks are due to noise in the pump scatter region.

cannot be solely due to IVR and VET. In addition, considerations of IVR and VET do not explain (2). We therefore assign the λ_{pump}-dependence of the spectra as the result of heterogeneity in CAN-OCPo with a presence of multiple ground-

state species, as others have done for OCP.[48,51,54,57,64,297] As discussed below, we hypothesise that CAN-OCPo forms either a predominantly 'blueshifted form' favorably excited with bluer pump wavelengths and a 'redshifted form' (distinct from OCPr) favourably excited with redder pump wavelengths. Both forms have similar lifetimes associated with their respective S_2 ($\sim$100 fs time constant; see global target analysis in Section J.5), S_1 ($\sim$5 ps), IVR, and VET.

Pumping with wavelengths $\lambda_{\text{pump}} = 480$ nm and bluer results in the formation of additional and distinct S_1-like excited-state features with significantly longer decay time constants than the expected $\sim$5 ps. For $\lambda_{\text{pump}} = 480$ nm to 400 nm, features appear in the 25–30 ps and 80–100 ps spectra, and are stronger with decreasing pump wavelength. These have a comparatively unstructured GSB, and an ESA consisting of broad peak(s) around 520 nm to 540 nm and a long, unstructured red tail. These features are consistent with additional ground-state species of OCPo that are only excited at $\sim$480 nm and below, very similar to the contribution reported as S* and assigned to ground-state non-all-*trans* conformations in studies of carotenoids in solution.[97,98] To be consistent with the OCP literature, we will refer to this as an S*-like feature. Its spectrum is similar to that described as S* by Konold *et al.*[53] for 3′hECN-OCP and thought to be the precursor of OCP switching.[53,60,61] It is also similar to the S~ state reported by Niziński *et al.* in ECN-OCP, who assign it to a non-photoactive carotenoid 'impurity' (*e.g.* β-carotene) in their OCP.[64] We note that while largely obscured by this new S*-like feature, the aforementioned spectral evolution behaviour described above by (1) and (2) are still present with $\lambda_{\text{pump}} = 400$ nm to 480 nm.

We observe a similar λ_{pump}-dependence in OCPr, but have only used $\lambda_{\text{pump}} =$ 532 nm and 485 nm; we have not performed a full study. See Section G.2 for details and figures.

To summarise, from inspection of the spectra of pump wavelength-dependent transient absorption on OCPo in trehalose (Figure 6.4), we have identified ground-state heterogeneity within OCPo, including a form with a long-lived ($\sim$65 ps) decay time constant that we term S*-like.[†]

[†]A different sample spot was pumped and probed per λ_{pump}. The sample spots chosen were practically random. The transient absorption spectra and dynamics for different sample spots probed with near-identical pumps (the same nominal λ_{pump} between different 'bands') are shown in Figures J.2 and J.3. The spectra and dynamics appear near-identical under these near-identical pumps with different sample spots. Given this, and the directed (as opposed to random) trends that we see, we rule out heterogeneity across the sample volume as the source of the phenomena. See Appendix J for details.

A usual next step in the analysis of OCP transient absorption data is to disentangle and quantify these contributions using analysis such as dynamic fitting with multi-exponential fits, or spectro-kinetic analysis such as global lifetime/target analysis.[51,53,62–65] However, due to the IVR and VET apparent within the S_1 lifetimes, these analyses are not completely suited for this system. In particular, the aforementioned multi-exponential dynamic fitting implicitly assumes well-defined species, and that first-order rate equations describing concentration changes between species may be written (their solutions being a sum of exponentials). Meanwhile, global lifetime/target analysis assumes that the spectra of the species are time-independent (*i.e.* well-defined) and that the dynamic (concentration) profiles are probe wavelength-independent,[230–232] a condition called bilinearity. These assumptions do not hold due to the effect of IVR and VET.[66–70]

Regardless, we perform some of this analysis here, namely a global triexponential fit of normalised dynamics in the >500 fs time-region to determine the long-lived S*-like yield (Figure 6.5), and global target analysis applied to all times to compare with literature (Figure 6.6).

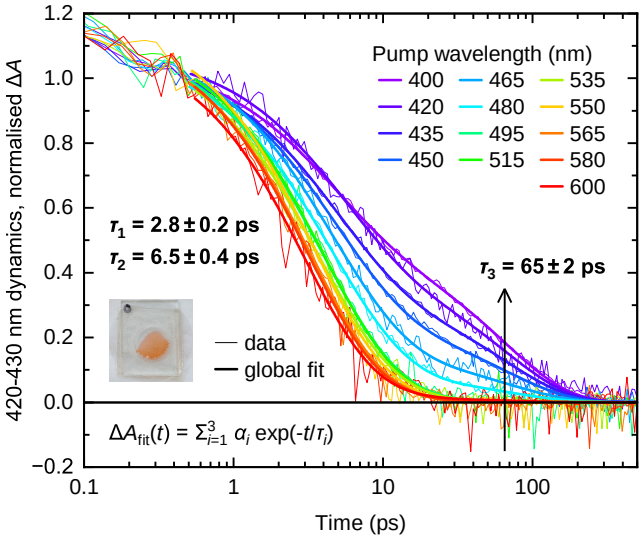

Figure 6.5 – Normalised dynamics and a triexponential global fit (equation inset bottom-left) in the long-lived GSB region for transient absorption experiments using different pump wavelengths on CAN-binding OCPo. The S*-like amplitude clearly increases as pump wavelength is reduced from 480 nm to 400 nm. Dynamics are taken as the 420–430 nm probe range average, and subsequently normalised to average one in the 0.35 ps to 0.65 ps range. Errors denote fit parameter standard errors.

For the global triexponential fit of normalised dynamics (Figure 6.5), we take

the average ΔA in the 420 nm to 430 nm probe range (close to the peak GSB of the long-lived singlet features – see Figure 6.4), normalise ΔA such that its average is 1 in the 0.35 ps to 0.65 ps range (the averaging accounts for noise), plot against time, and fit for times >500 fs (beyond any features associated with the coherent artefact and decay of S_2 states) with a global triexponential fit with the following equation:

$$\Delta A_{\text{fit}}(t) = \alpha_1 \exp(-t/\tau_1) + \alpha_2 \exp(-t/\tau_2) + \alpha_3 \exp(-t/\tau_3). \tag{6.1}$$

Here t is delay time in the transient absorption, α_i are fitted amplitudes with the applied lower-bound condition $\alpha_i \geq 0$, and τ_i are fitted time constants that are shared between the different pump wavelengths in the global fit. The dynamics and fit are shown in Figure 6.5, the fit parameters are printed in Table J.1, and we plot α_i against pump wavelength in Figure 6.9a. We see that the fitted α_3 (amplitude associated with $\tau_3 = 65 \pm 2$ ps: error denotes fit parameter standard error) is significantly greater than zero only with $\lambda_{\text{pump}} \leq 480$ nm, and that α_3 increases with bluer pump wavelengths. Meanwhile, the fitted α_1 and α_2 (associated with $\tau_1 = 2.8 \pm 0.2$ ps and $\tau_2 = 6.5 \pm 0.4$ ps respectively) are non-zero for all pump wavelengths, although α_1 is generally decreasing with decreasing pump wavelength. As there is conflation between the S_1 decay of different ground-state forms along with the non-exponential decay associated with IVR and VET on these timescales, the physical correspondence of these short-lived components cannot be assigned.

We depict a sample of our global target analysis models in Figure 6.6a, and a selection of the results in Figure 6.6b–d, with further details in Section J.5. Here we apply models involving 3 or 4 components depending on the pump wavelength, hence resulting in 3 or 4 species-associated difference spectra (SADS). The 3-component model (Figure 6.6a, excluding blue box) sufficiently fits transient absorption data with pumps from 495 nm to 580 nm, while a fourth component (Figure 6.6a, SADS4-inclusive) is required to fit the data with pumps from 400 nm to 480 nm, once again consistent with the presence of long-lived forms of OCPo and associated S*-like features for $\lambda_{\text{pump}} \leq 480$ nm. We note that the profile of all SADS and their fitted time constant t_i vary with pump wavelength, suggesting that the model is not valid with this dataset. We discuss further, give plots of all SADS, and show additional models in Section J.5.

In short, using pump wavelength-dependent transient absorption measurements on OCPo in trehalose, we have found evidence of heterogeneity in OCPo

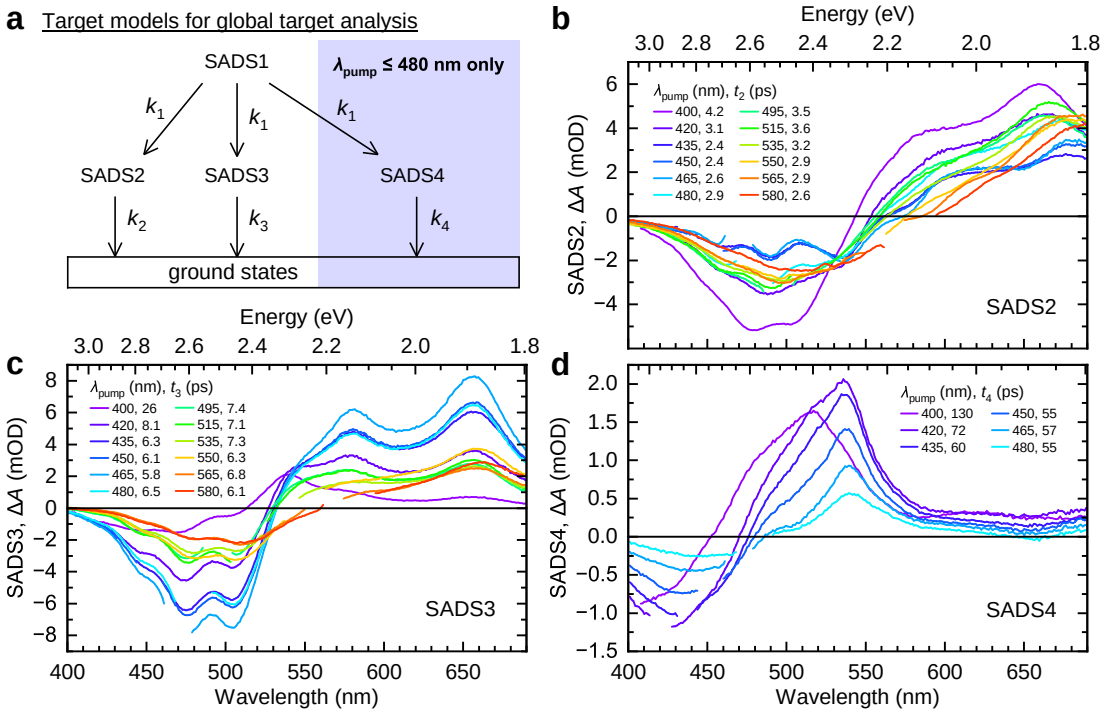

Figure 6.6 – Sample of the results of global target analysis performed on the transient absorption data. (a) Target models used in the global target analysis, with resulting species-associated difference spectra (SADS) shown in the other panels: **(b)** SADS2, **(c)** SADS3, **(d)** SADS4; note that SADS4 is fitted only with pump wavelengths ≤480 nm. Full details and additional global target analysis is shown in Section J.5.

with populations of distinct OCPo 'forms', including an S*-like form (denoted S*-like here in reference to the literature, *e.g.* Ref.[53]). We have quantified the proportion of this S*-like feature as a function of λ_{pump}. If, as reported recently,[53,60,61] this S*-like feature is a trigger for the OCPo to OCPr photocycle, the OCPr yield should show a similar excitation wavelength dependence. Therefore, in the next section, we turn to quantifying the excitation wavelength-dependence of the solution OCPo→OCPr phototransition yield.

6.2.4 λ_{pump} dependence of photoconversion is not the same as S*

We quantify the yield of OCPo→OCPr photoconversion as a function of pump wavelength using absorbance measurements of dark-adapted OCPo in buffer as a function of time, Figure 6.7b. A simplified diagram of the experiment is shown in Figure 6.7a. The pump power was tuned to give approximately the same rate

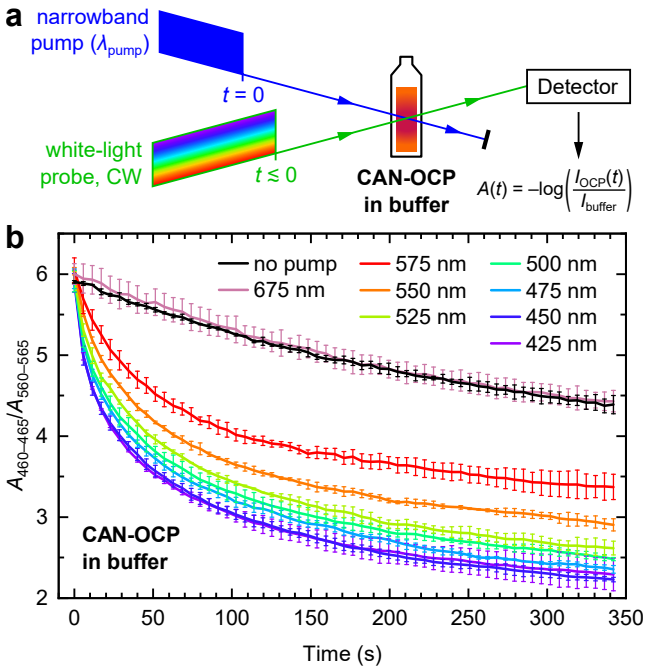

Figure 6.7 – Experimental setup for absorbance measurements of CAN-binding OCP in buffer that is continually photoconverted by narrowband pump light (a), and average absorbance ratios against time (b). The pump power was tuned to give approximately the same OCPo excitation rate per-pump wavelength (except for 675 nm). All absorbed pump wavelengths give a conversion yield greater than the white-light probe alone, with the yield increasing as pump wavelength is reduced from 575 nm to 425 nm. Absorbance ratios are averaged from three experimental replicates, and the error bars show the standard deviation. The cuvette width was 2 mm.

of OCPo excitations for each pump wavelength (except for 675 nm) based on the dark-adapted absorbance; see Section 4.2 for further experimental details. The conversion from OCPo to OCPr can be tracked by monitoring the ratio of absorbance due to OCPo at 460–465 nm and that of OCPr at 560–565 nm ($A_{460-465}/A_{560-565}$). The dynamics in Figure 6.7b are the average of three experimental replicates.

Figure 6.7b shows that the OCP photocycle is triggered by excitation into the OCPo absorption band, right down to the band-edge. Indeed, we observe photoconversion with pump wavelengths that do not generate S*-like features in transient absorption spectroscopy measurements (>480 nm, see Figure 6.4). This suggests that the S*-like feature is not required for photoswitching.

However, rather surprisingly, we do find that the photoconversion dynamics

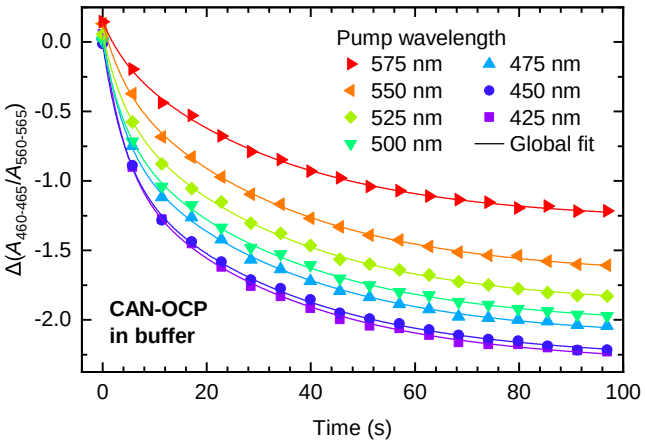

Figure 6.8 – Difference average absorbance ratios against time for CAN-binding OCP in buffer under excitation with narrowband laser light, fitted with a global biexponential fit. Points are data and lines are the global biexponential fit. Only the data points shown (<100 s) are fitted. See Table K.1 for the fitting parameters.

(Figure 6.7b) have a pump wavelength dependence. Before describing this pump wavelength-dependent behaviour in detail, we first note that the control no-pump experiment (white light alone) and the non-absorbed pump (675 nm) both trigger similar OCPo→OCPr photoconversion. In subsequent analysis, we account for this 'background' white light-induced photoconversion by subtracting the average absorbance-ratio dynamic obtained without the pump (probe light only) from the ratio at each pump wavelength to obtain

$$\Delta\left(\frac{A_{460-465}}{A_{560-565}}\right) = \left(\frac{A_{460-465}}{A_{560-565}}\right) - \left(\frac{A_{460-465}}{A_{560-565}}\right)_{\text{no pump}}. \tag{6.2}$$

The resulting difference dynamics are plotted as points in Figure 6.8 and are fitted using a global biexponential fit

$$\Delta\left(\frac{A_{460-465}}{A_{560-565}}\right)_{\text{fit}} = \beta_0 - \beta_1\left[1-\exp\left(-\frac{t}{T_1}\right)\right] - \beta_2\left[1-\exp\left(-\frac{t}{T_2}\right)\right] \tag{6.3}$$

to quantify the pump wavelength dependence of the photoconversion temporal behaviour. Here t is the time after the pump is turned on, β_0 is a fitted offset term, β_1, β_2 are fitted amplitudes, and T_1, T_2 are fitted time constants that are shared between the different pump wavelengths in the global fit. The fit is shown as lines in Figure 6.8, the fitted β_1 ($T_1 = 4.12 \pm 0.18$ s; error denotes fit parameter standard error) and β_2 ($T_2 = 32.9 \pm 0.7$ s) are plotted as points in Figure 6.9b, and other fitted parameters are shown in Table K.1. A key finding is that although the

amplitude term of the slower component (β_2) is roughly the same for each pump wavelength, the amplitude for the faster component (β_1) significantly increases with decreasing pump wavelength.

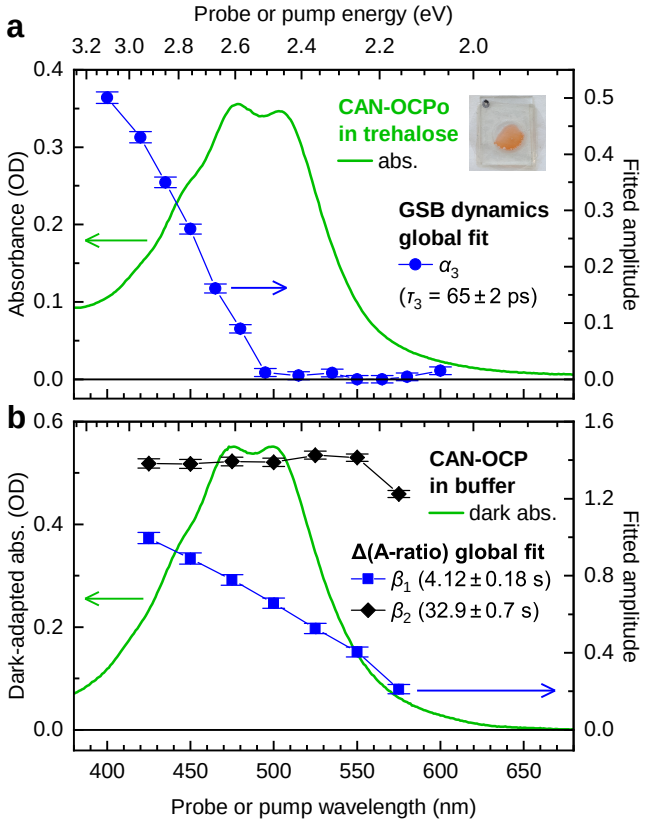

Figure 6.9 – Fitted amplitudes from the global fits of dynamics for different OCP experiments, with dark-adapted absorbance of OCPo samples studied. **(a)** Absorbance of OCPo in trehalose (line, left axis), with fitted amplitude α_3 from a global triexponential fit of picosecond transient absorption dynamics (points, right axis). **(b)** Absorbance of dark-adapted (initially) OCPo in buffer (line, left axis), with fitted amplitudes β_1, β_2 against pump wavelength from a global biexponential fit of photoconverting solution dynamics (points, right axis). The apparently large absorbance at low wavelengths for OCPo in trehalose compared to that in buffer is due to increased scatter in the trehalose sample. Error bars denote fit parameter standard errors. Fits are shown and described in Figure 6.5 and Table J.1 for transient absorption, and Figure 6.8 and Table K.1 for photoconverting solution.

Using the amplitudes as a proxy for relative yield of photoswitching (Figure 6.7) or S*-like features (Figures 6.4 and 6.5), we compare the relative yield of OCPr in buffer to the yield of the S*-like features in trehalose. Figure 6.9a shows the amplitude (α_3 due to the S*-like features) from the triexponential global

fit of transient absorption dynamics (Figure 6.5) overlayed with the OCPo in trehalose absorbance spectrum, and Figure 6.9b similarly shows the amplitudes from the photoconversion experiment (Figure 6.7) in buffer overlayed with the dark-adapted OCPo in buffer absorbance. We find that photoconversion and the S*-like features do not follow the same pump wavelength dependence. Indeed, α_3 has a distinct threshold pump wavelength (480 nm), while β_1 and β_2 have amplitude at all pump wavelengths measured. The reason for the pump wavelength dependence of β_1 and β_2, and thus the photoconversion behaviour, is unclear.

To summarise, time-resolved absorbance measurements of continually-photoconverting OCP in buffer have shown that: (1) all wavelengths absorbed by OCPo cause the transition to OCPr, (2) photoconversion yield increases with decreasing pump wavelength, with the significant increase in the amplitude of a 'fast' (∼4 s) component, and (3) the pump wavelength dependence of the S*-like feature in transient absorption spectroscopy cannot explain the pump wavelength-dependent photoconversion yield. This leads us to reject the recent hypotheses[53,60,61] that long-lived singlets are the trigger for the photocycle.

6.3 Discussion

6.3.1 OCPo in trehalose forms pre-OCPr photoproducts

We have trapped OCPo binding ∼100% canthaxanthin (CAN) in trehalose glass, preventing the overall transition to OCPr according to absorbance spectra under intense white-light (Figure 6.2), yet the transient absorption spectroscopy (Figure 6.3a,c) shows very similar features to that observed in-buffer by us (Figure 6.3d) and in the literature.[51,53] The spectroscopic changes observed in trehalose persist up to 0.7 ms, far longer than the longest-lived features observed for β-carotene-like carotenoids (including CAN) when in solution, and inspection of the films and individual transient absorption sweeps show that no permanent change is induced by laser excitation (aside from bleaching in high pump-fluence measurements; see Figure 3.4). Therefore the trehalose prevents the overall transition to OCPr, yet the trehalose does not prevent the initial (pre-OCPr) photoproducts from forming.

We do not assign identities (protein conformation, interactions such as hydrogen-bonds, *etc.*) of the initially formed photoproducts seen in our spectroscopic measurements. These identities are under active debate in the literature, with experimental work[50,53,293] and theoretical studies[267,291,292] generally suggesting a

process involving rupture of the hydrogen-bonds between the β1-ring carbonyl group and Typ201/Tyr288, subsequent translocation of the carotenoid into the NTD, and final separation of the CTD and NTD, giving OCPr. Some studies question if the translocation occurs,[79] and a recent study suggested that carotenoid photoisomerisation and subsequent structural rearrangements are the first events that occur, with hydrogen-bond breakage merely a secondary effect accompanying domain separation.[73] Regardless, these suggestions are consistent with (1) the initial formation of spectrally redshifted 'compact' intermediates, which appears to occur for both our CAN-OCPo in trehalose (Figure 6.3c) and in buffer in a flow cell (Figure 6.3d), and (2) the eventual formation of OCPr with its extended conformation, prevented when in trehalose and allowed when in buffer (Figure 6.2).

6.3.2 Trehalose permits solid-state OCPo/OCPr measurements

We highlight the ease and efficient use of material of in-trehalose OCP measurements. The UV-vis-probe picosecond transient absorption measurements partially depicted in Figure 6.4 involved ∼15 distinct measurements on a single CAN-OCPo in trehalose sample (pump-probing a different sample spot per-measurement), which could be stored at room-temperature (in the dark as a standard precaution) without degradation or photoconversion in the weeks between sets of measurements. It contrasts with our own CAN-OCPo in a flow cell transient absorption (Figure 6.3d), requiring a large quantity (10 ml with maximum decadic absorption coefficient ∼0.5 mm^{-1}) of solution and thorough equipment preparation (cleaning of the flow system, control against conversion in ambient light), resulting a a single measurement with significant noise in the dynamics (see Figure I.1) and with the possibility of contaminant CAN-OCPr. Outside of use of a flow cell or similar,[51,53,62–64] studies involving samples at conversion-preventing cryogenic temperatures[56] or OCP mutants[58–61] have their own experimental limitations or difficulties, and can introduce associated artefacts. With our verification that the transient absorption signatures for CAN-OCPo in trehalose and in buffer are similar, it presents the trehalose glass system as a relatively straightforward, material-efficient, and artefact-mitigated method for spectroscopic studies of OCPo and OCPr.

6.3.3 OCPo shows ground-state heterogeneity and IVR/VET

From careful inspection of our pump wavelength-dependent transient absorption spectra (Figure 6.4), we have shown that multiple ground-state species of OCPo are present. There is an 'S*-like form' that is only apparent with pump wavelengths ≤480 nm, is clearly proportionally excited the most at the bluest pump wavelength (400 nm; see Figure 6.5), clearly has the bluest GSB (highest S_2 energy) of the forms, and has a relatively long decay time constant (∼65 ps). A pump wavelength of 495 nm appears to predominantly excite a 'blueshifted form', with a relatively short decay time constant (≤10 ps, noting the conflation caused by IVR/VET effects). The reddest pump wavelength of 600 nm appears to predominantly excite a 'redshifted form', with the reddest identified GSB contribution (lowest S_2 energy) and a time constant similar to the blueshifted form.

Assignments of ground-state heterogeneities in OCPo and OCPr have frequently been made in the OCP literature.[48,51,54,57,60,64,222,291,297,303] The first hints of multiple forms of OCP come from a 2005 paper from Polívka *et al.*, where it was suggested that 3′-hydroxyechinenone (3′hECN) is able to bind to OCP with a form with strong hydrogen-bonds and another form with weak hydrogen-bonds, giving a pump wavelength-dependent heterogeneity in transient absorption spectroscopy using 495 nm and 530 nm pumps.[303] Later work by this group assigned that heterogeneity as due to contaminant OCPr within dark-adapted OCPo samples,[297] with fits of the steady-state absorbance requiring a broad red-end OCPr-associated Gaussian required in addition to a typical carotenoid-in-solution-like progression (plus a low-absorbance, broad, blue-end Gaussian). However, that contaminant assignment was rejected by Kish *et al.*[48] as resonance Raman spectroscopy on ECN-binding OCP led them to exclude an OCPr contaminant assignment as the ν_1 peak associated with OCPr does not appear within dark-adapted OCPo samples. In fact, they showed that the ν_1 peak in ECN-OCPo has a blue shoulder, which becomes enhanced using a relatively blue pump.[48] They concluded that at least two ECN configurations must exist in ECN-OCPo, one with shorter effective conjugation length being responsible for the blue-end shoulder[48]. Furthermore, Slouf *et al.*[51] were able to reasonably fit the steady-state absorbance spectrum of OCP binding ZEA, which does not undergo photoconversion and is permanently in the OCPo form,[217] with two offset ZEA-like spectra (plus a low-absorbance, broad, blue-end Gaussian). Along with transient absorption spectroscopy using

540 nm and 470 nm pumps on CAN-OCPo, ECN-OCPo, and ZEA-OCPo showing similar spectral heterogeneity to that seen in this paper (*e.g.* Figure 6.4), Slouf *et al.* concluded that the heterogeneity is not due to contaminant OCPr in OCPo samples, but due to the OCPo accommodating carotenoid molecules with different configurations, supporting Kish *et al.*'s interpretation.[51]

We discuss how such features seen in the OCP literature may have their origin partially in the S*-like feature seen in this work. In the aforementioned study by Kish *et al.*, a ν_1 shoulder is seen in ECN-OCPo at a higher wavenumber (energy) of 1527 cm^{-1} than the main ν_1 peak at 1518 cm^{-1}. The shoulder becomes enhanced using a pump wavelength of 488.0 nm compared to the redder pumps used (514.5 nm and up) where the resulting ν_1 profile looks similar per-pump wavelength. It is known for carotenoids/polyenes that there is a dependence on the effective conjugation length ($N_{\text{eff.}}$) with a number of the photophysical properties. As the $N_{\text{eff.}}$ increases, the S_1 lifetime and energy decreases, the $S_0 \rightarrow S_2$ transition energy decreases, and the ν_1-peak energy decreases.[102,294,304] Indeed, Kish *et al.* noted the blue 1527 cm^{-1} shoulder corresponds to $N_{\text{eff.}} = 9$, equivalent to a hypothetical ECN molecule whose β1 and β2 rings do not contribute to the $N_{\text{eff.}}$.[48] However, complete non-participation of β1 and β2 rings to $N_{\text{eff.}}$ has not been observed (to our knowledge), and out-of-plane distortions of the terminal rings are unlikely to change $N_{\text{eff.}}$ enough to give the S*-like lifetime around 65 ps seen here.[51,304]

We turn to studies of carotenoids in solution, where signatures extremely similar to our S*-like features have been identified in samples that are nominally all-*trans*, but unpurified. A transient absorption study of β-carotene in solution by Ostroumov *et al.* showed that a long-lived contribution with lifetime 20–100 ps disappears if the samples are purified to all-*trans*-β-carotene prior to a measurement. A 3-level carotenoid model with consideration of VET in the S_1 state is then sufficient to explain the photophysics in these purified samples.[98] It was suggested that the 'impurities' removed through purification might be due to chromophore products from β-carotene, such as shorter conjugation-length carotenoids. Work by Polak *et al.* undertaking pump wavelength-dependent transient absorption measurements on β-carotene and astaxanthin (a keto-carotenoid) in toluene confirmed the pump wavelength dependence of the long-lived contribution and showed the dependence in turn matches Ostroumov *et al.*'s impurity absorbance.[97] The wavelength dependence of Ostroumov *et al.*'s impurity absorbance and Polak *et al.*'s long-lived signal amplitude both follow a similar profile to our own

pump wavelength dependence on the long-lived S*-like state in OCPo (*e.g.* the dependence on α_3 on pump wavelength; Figure 6.9a). From the observations and assignments made regarding the ECN-OCPo resonance Raman spectra by Kish *et al.*[48] and the similarity to an 'impurity' contribution identified for carotenoid-in-solution studies,[97,98] we hypothesise that the S*-like feature in OCPo is due to ground-state contributions of CAN-associated chromophores. The precise identity of these chromophores are to be determined. We note that a very similar assignment for a 60–100 ps feature was made in a paper undertaking transient absorption on ECN-OCPo, although they suggested that their 'impurity'-OCP fraction does not photoconvert.[64] This contrasts with our finding where the in-buffer OCPo→OCPr yield increases with decreasing pump wavelength down to 425 nm, where the S*-like form would be predominantly excited (*e.g.* Figure 6.9). The aforementioned in-solution work by Polak *et al.* suggested a *cis*-isomer origin to their 'impurity',[97] but *cis*-isomers would be expected to absorb at wavelengths ≥495 nm,[300] which does not match our λ_{pump} dependence on the S*-like feature's amplitude (Figure 6.9), and to our knowledge a *cis*-isomer of the studied carotenoids has not been shown to have a ∼65 ps S_1-associated lifetime.

The identities of the ground-state forms found using $\lambda_{\text{pump}} \geq 495$ nm, such as the redshifted form and blueshifted forms of OCPo, are difficult to elucidate. We are confident that these exist due to significant changes in the ESA vibronic replica intensities and the GSB vibrational structure in transient absorption experiments scanning pump wavelengths from 495 nm to 600 nm (Figure 6.4). Notably, we observe IVR and VET signatures at all pump wavelengths, but the pump wavelength dependence of these cannot explain the extent of the changes in the transient absorption spectra.[66–70] As explained in Section 6.2.3, the effects of IVR and VET make application of multi-exponential dynamic fitting and global lifetime/target analysis not completely suited for this system, particularly with the redshifted form and blueshifted form appearing to decay with similar lifetimes. We recall our global triexponential fit of the normalised dynamics in the 420–430 nm GSB region (Figure 6.5); while $\tau_3 = 65$ ps can safely be associated with the S*-like state of the S*-like form of OCPo due to its 1-order time difference between that and the earlier-time dynamics, the extracted $\tau_1 = 2.8$ ps and $\tau_2 = 6.5$ ps have a mixed and unknown physical correspondence, likely mixed S_1/IVR/VET for multiple ground-state OCPo forms. Meanwhile, the SADS2 and SADS3 (Figure 6.6b,c) extracted from global target analysis also have an unknown correspondence, and vary significantly with pump wavelength. Applying a model accounting

for IVR and VET such as those designed by Balevičius *et al.*[66–69] is beyond the scope of the current study, considering the ground-state heterogeneity within the OCPo system.

We hypothesise that OCPo forms such as our redshifted and blueshifted forms arise from relatively minor ground-state distortions in the bound carotenoid. A small change to the CAN conformation will not significantly change its effective conjugation length ($N_{\text{eff.}}$), but the CAN will be in a different environment (with different interactions with the protein residues) between the forms.[102,139] The similar S_1 profiles (*i.e.* similar probe-wavelength positions of the $S_1 \rightarrow S_n$ vibronic replica) and decay times of our redshifted and blueshifted forms of OCPo can be attributed to the relative insensitivity of the S_1 lifetime and energy to the environment (namely its polarity);[305] S_1 is more sensitive to $N_{\text{eff.}}$.[275,304] Meanwhile, the changes to the GSB from transient absorption experiments between the two forms (*i.e.* the changes in GSB scanning pumps between 495–600 nm) and the redshifted form appearing to be at lower energy in the OCPo absorbance spectra[51,222,297] can be attributed to the relative sensitivity of the $S_0 \rightarrow S_2$ transition energy on the environment.[102] However, we recall the resonance Raman spectroscopy by Kish *et al.* on ECN-OCPo,[48] identifying two ν_1 peaks at 1527 cm^{-1} and 1518 cm^{-1}; we previously assigned the 1527 cm^{-1} 'shoulder' as due to the S*-like form in CAN-OCPo, so both the redshifted and blueshifted forms would have a ν_1 wavenumber of 1518 cm^{-1}, within experimental tolerances. We note that ν_1 wavenumber for carotenoids has some dependence on the environment, although not to the same extent as the $S_0 \rightarrow S_2$ transition energy.[48,102,139] In the literature, similar heterogeneities have occasionally been assigned as due to differences in keto-carotenoid hydrogen-bonding to Tyr201 and Trp288,[60,303] but as ZEA-OCP has no carbonyl group at carbon 4 yet still shows similar heterogeneity,[51] a pure hydrogen-bond-heterogeneity origin to the redshifted form and blueshifted form appears unlikely.[54] We highlight a theoretical study by Pigni *et al.* modelling the CAN-OCP phototransition; the results of well-tempered metadynamics indicated a redshifted form of the initial CAN-OCPo, compared to the main form identified. In their redshifted form, the CAN β1-ring still forms hydrogen-bonds to Tyr201 and Typ288, but the protein environment is reorganised, giving a relatively planar CAN configuration with a different position for the β2-ring within the NTD.[291]

In short, we have *identified* multiple ground-state forms within CAN-OCPo, three of the forms here dubbed 'redshifted form', 'blueshifted form', and 'S*-like form'. By comparison to the OCP and carotenoid literature, we *hypothesise* that

forms such as the redshifted and blueshifted form arise due to minor distortions of the CAN leading to different interactions between the CAN and the protein. Meanwhile, we *hypothesise* that the S*-like form shares an origin in a feature identified in studies of carotenoids in solution.[97,98] The confounding effects of IVR and VET within CAN-OCPo makes evaluation of these hypotheses through analysis of the transient absorption data alone difficult, particularly for the redshifted and blueshifted forms. Key experiments to test these hypotheses may include further pump-probe measurements (such as mid-IR transient absorption) with comparable tuning of the pump wavelength, as well as resonance Raman spectroscopy with tuning of the pump wavelength and with time-resolution to study the dynamics of each form.

6.3.4 No singlet states are associated with photoswitching

Long-lived singlet excited states have recently been suggested to play a pivotal role in the initial steps in the OCPo to OCPr photoconversion process.[53,60,61] This argument suggests that the so-called S* state in 3′hECN-OCPo is a structurally distorted form of S_1 formed upon S_2 relaxation that results in structural strain on the conjugated backbone, leading to the breaking of the hydrogen-bonds from the protein to the β1-ring. Through sequential-model global lifetime analysis on transient absorption data with UV-vis and mid-IR probes, this 'S* state' was assigned a 24 ps lifetime.[53]

We have shown that the photoconversion yield does not correlate with the long-lived S*-like feature in CAN-OCPo. With reference to Figure 6.9, there is no apparent correlation between the pump wavelength dependence of the photoconversion yield of CAN-OCPo in buffer and the pump wavelength dependence of the yield of a long-lived (∼65 ps time constant) S*-like feature seen in transient absorption of CAN-OCPo in trehalose. We note our rejection of the hypothesis is independent of the physical identity of the long-lived S*-like feature; we show that it is associated with a ground-state heterogeneity, and hypothesise it arises from CAN-associated chromophores, but neither of these are required for our argument here.

In fact, while photoconversion yield increases with decreasing pump wavelength, all absorbed wavelengths in OCPo appear to trigger the photoconversion. Figure 6.7b clearly shows that the non-absorbed 675 nm pump and a white-light probe is not able to produce an OCPr yield greater than a white-light probe alone,

while all absorbed wavelengths tested cause conversion, with the bluest pump (425 nm) giving the greatest yield and the reddest absorbed pump (575 nm) the least.

We note that the dependence on the yield appears to manifest primarily in the dependence on a fitted amplitude β_1 of a faster component ($T_1 = 4.12\,\mathrm{s}$) in difference dynamics of the data (see Figure 6.8), whereas the amplitude β_2 of a slower component ($T_2 = 32.9\,\mathrm{s}$) has less apparent dependence on the pump wavelength (Figure 6.9b). The physical identity of the fast and slow components are obscure. Verification of experimental oversights (see Section K.2) do not explain the trends in β_1 or β_2.

We note that continuous illumination with a pulsed pump laser and a white-light lamp was performed during this experiment; a single powerful pump pulse and an probe assay of the OCPr yield may be more comparable to other pump-probe techniques (such as our own transient absorption), but as the OCPo→OCPr yield is thought to be ∼0.1–1.0%,[53,59,80] the signal-to-noise ratio of such an experiment would be expected to be very low. Regardless, this type of experiment involving careful control of OCPo excitation in terms of pump wavelength and power with a probe of the OCPr conversion yield has proven useful to test the hypothesis that the long-lived singlet 'S*' triggers the photocycle, and future experiments with a similar design will prove useful in characterising the photoconversion yield of, for example, OCP from different organisms or clades[54,298] and their dependence on pump wavelength and pump power. Indeed, recent similar experiments by Niziński *et al.* investigating C-tagged and N-tagged ECN-OCP have shown a marked dependence between the quantum yield of OCPr formation against 452 nm pump power.[306] They therefore question the literature's implicit assumption that absorption of a single photon initiates a complete photoconversion, and suggest that consecutive absorption of photons throughout the conversion occurs, which would explain their pump power dependence.[306]

6.3.5 Hypothesis: OCPo forms have different photocycle yields

The mechanism of conversion from OCPo to OCPr remains open. What could underlie the pump wavelength dependence on the phototransition yield? We recall our assignments of multiple different ground-state OCPo forms, with a long-lived S*-like form apparent for $\lambda_{\mathrm{pump}} \leq 480\,\mathrm{nm}$, a predominantly excited blueshifted

form apparent at $\lambda_{\text{pump}} = 495\,\text{nm}$, and a predominantly excited redshifted form apparent at $\lambda_{\text{pump}} = 600\,\text{nm}$. It is possible that the S*-like form, upon excitation, has the greatest propensity to form the initial photoproduct, while the redshifted form has the least propensity to do so. This would underlie the apparent excitation dependence on OCPr yield. The physical basis of the apparent propensity is to be elucidated, but could have basis in differences in chromophore binding within the protein, or in the lifetimes and energetics associated with the S_1 state. Indeed, in Chapter 7, we hypothesise that the photocycle is initiated by a carotenoid triplet formed *via* intersystem crossing, and detail our preliminary work in testing this hypothesis. Even if the intersystem crossing rates are identical between the different OCPo forms, the triplet yield (and subsequent OCPr yield in buffer) will be the highest for the form with the longest S_1 lifetime. Here, that would be the S*-like form. Direct measurements are required to elucidate both hypotheses, *i.e.* that ground-state OCPo forms have different photocycle yields, and that the OCPo→OCPr phototransition is triggered by intersystem crossing triplets (see Chapter 7).

We recall the similar 'heterogeneity' assignment for a 60–100 ps feature in a paper undertaking transient absorption on ECN-OCPo, very similar to our assignment of our S*-like feature.[64] It was suggested on the basis of relative amplitudes from dynamic fits of transient absorption data that excitation of their 'impurity'-OCP does not lead to OCPr.[64] This contrasts with our finding where the in-buffer OCPo→OCPr yield increases with decreasing pump wavelength down to 425 nm, where the S*-like form would be predominantly excited (*e.g.* Figure 6.9).

6.4 Conclusions

We fabricated samples of canthaxanthin-binding inactive (OCPo) and active (OCPr) forms of orange carotenoid protein (OCP) in trehalose glass. We found that the completion of the transitions are prevented, enabling static and time-resolved photophysical characterisation of the two forms, giving us insight into the photoconversion process between them. Pump wavelength-dependent transient absorption spectroscopy on the OCPo samples showed significant heterogeneity, and can give the long-lived S*-like features hypothesised to be the trigger for the OCPo→OCPr photoinduced cycle. The pump wavelength dependence of the amplitude of the S*-like features in these transient absorption experiments and the yield of OCPr in solution do not match, and therefore the 'S*' features

cannot be the sole trigger for the OCPo→OCPr photoconversion.

OCPo in trehalose shows the same initial photophysics as OCPo in solution, but without completion of the photocycle to OCPr. With the solid samples being comparatively straightforward to measure, material-efficient, and artefact-free, the trehalose-sucrose glass matrix encapsulation has been demonstrated to be a valid and useful system here.

Future pump-probe experiments (such as mid-IR transient absorption) must consider the impact of pump wavelength on the OCP photophysics. An assay of the pump wavelength dependence on the photoproducts in such experiments may help elucidate: (1) the identities of the initial photoproducts, (2) the identities of the ground-state heterogeneities and their correspondence (if any) to the initial photoproducts, and (3) the mechanism of conversion. This has to be done with careful consideration of the confounding IVR/VET effects.

Chapter 7

Hypothesis: OCP photocycle is triggered by intersystem crossing triplets

In the previous chapter, we rejected the recent suggestions that a long-lived carotenoid singlet-like feature (S*) is the orange carotenoid protein (OCP) photoconversion trigger. In this chapter, we present a hypothesis that the OCPo→OCPr phototransition is initiated by a carotenoid triplet state formed by intersystem crossing, and that a *keto*-carotenoid is required both for binding to the protein and for sufficient triplet yield *via* intersystem crossing (ISC). We present preliminary transient absorption measurements showing that the initial photoproduct in canthaxanthin-binding OCPo resembles the triplet formed by intersystem crossing in monomeric canthaxanthin in solution, both in spectra and lifetime. However, we note issues with these and subsequent measurements, largely arising from the low yield of triplets formed by ISC (0.1–1.0%). Ultimately, causation is not verified, so we neither accept nor reject our hypothesis.

Acknowledgements: George A. Sutherland and Jenny Clark conceived the study. George A. Sutherland and Matthew S. Proctor prepared protein samples. Construction of the nanosecond-millisecond transient absorption system was by Andrew J. Musser, Daniel W. Polak, David G. Bossanyi, and Sayantan Bhattacharya, while initial use of the system was assisted by Shuangqing Wang and David G. Bossanyi. James P. Pidgeon performed all experiments and analysed all the data presented in this chapter.

7.1 Introduction

In Chapter 6, we rejected the suggestions that photoconversion in orange carotenoid protein (OCP) from its orange form to its red form (*i.e.* OCPo→OCPr) is initiated by 'S*', a long-lived carotenoid singlet-like feature.[53,54,61] Elucidating the phototransition trigger is of high interest, as previously discussed in Section 6.1; in particular, it could potentially lead to the development of biomimetic optoelectronic or photonic technologies for light adaptation[81] or energy storage.[82]

We hypothesise that the OCPo to OCPr photoconversion is triggered by photoisomerisation of the keto-carotenoid occurring on the triplet potential energy surface, and that those triplets are formed through intersystem crossing (ISC). We initially make this hypothesis by noting that: (1) the overall photoconversion efficiency for the OCPo to OCPr photoconversion is about 0.2%,[53,59,80] comparable to the 0.1–1.0% triplet yield *via* intersystem crossing in keto-carotenoids including the canthaxanthin (CAN) bound in our OCP samples.[99] (2) Isomerisation of β-carotene, which has a similar (effective) conjugation length to the keto-carotenoids bound by OCP, can occur on the triplet potential energy surface.[307–311] (3) There are known biological processes involving a carotenoid photoisomerisation trigger and subsequent protein conformational changes, namely the photoreceptor units ('opsins' binding the $N = 5$ C=C bonds carotenoid retinal) in animal vision. Upon absorption of light, the initial 11-*cis*-retinal undergoes isomerisation to the all-*trans* form, affecting binding interactions with the protein and causing a conformational change,[312] leading to the phototransduction cascade.[313] Notably, it is thought that retinal photoisomerisation occurs primarily through the triplet state following efficient intersystem crossing, although it can also occur in the singlet state.[314–319]

7.2 Results

7.2.1 Triplets form by ISC in isolated CAN molecules

First, we extract the canthaxanthin (CAN) triplet signature through the excitation energy transfer method, similarly to that reported in carotenoids previously.[309,320,321] Nanosecond-millisecond transient absorption spectra of anthracene-sensitised CAN in acetone are shown in Figure 7.1. The solution is a 100:1 molar ratio of anthracene (5 mM) and CAN (50 µM) in acetone (see Figure F.3a for the steady-state absorbance spectrum). A 355 nm pump is used, resulting in

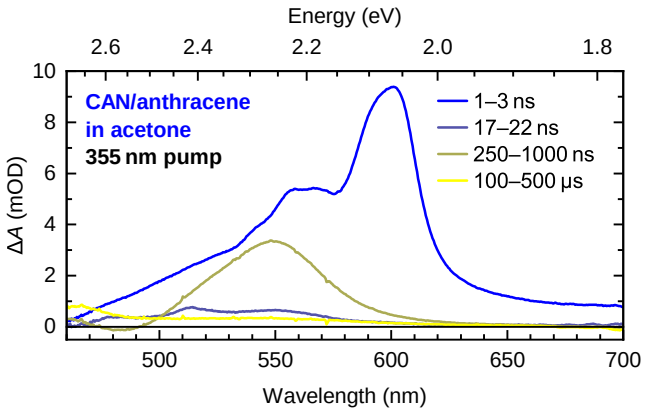

Figure 7.1 – Nanosecond-millisecond transient absorption spectra of anthracene-sensitised CAN in acetone with pump wavelength 355 nm with a visible probe. The solution was a mixture of anthracene (5 mM) and CAN (50 µM) in acetone. The CAN GSB triplet and ESA can be seen in the 250–1000 ns spectrum. Note that the sample was not degassed, resulting in a static feature at long times (see 100–500 µs spectrum), which partially obscures the CAN GSB. Spectra have been averaged between the times indicated. Pump fluence was set to 400 µJ cm^{-2}.

excitation of the anthracene singlet

$$\mathrm{S}_0^{\mathrm{anthracene}} + \hbar\omega_{355\,\mathrm{nm}} \rightarrow \mathrm{S}_1^{\mathrm{anthracene}} \tag{7.1}$$

visible as an ESA in the 1–3 ns spectrum. The anthracene singlet undergoes fast intersystem crossing to predominantly the $\mathrm{T}_2^{\mathrm{anthracene}}$ triplet, with fast internal conversion from that to the $\mathrm{T}_1^{\mathrm{anthracene}}$ triplet.[173–175] We denote these anthracene triplets collectively as $\mathrm{T}_{1,2}^{\mathrm{anthracene}}$, and write

$$\mathrm{S}_1^{\mathrm{anthracene}} \rightarrow \mathrm{T}_{1,2}^{\mathrm{anthracene}} \tag{7.2}$$

with the process resulting in the loss of the singlet ESA feature and the appearance of weak triplet ESA features around 475 nm and 515 nm in the 17–22 ns spectrum. The anthracene triplet undergoes excitation energy transfer to form a CAN triplet

$$\mathrm{T}_{1,2}^{\mathrm{anthracene}} \rightarrow \mathrm{T}_1^{\mathrm{CAN}} \tag{7.3}$$

with associated GSB and ESA visible in the 250–1000 ns spectrum. The CAN triplets then undergo decay back to the CAN ground state

$$\mathrm{T}_1^{\mathrm{CAN}} \rightarrow \mathrm{S}_0^{\mathrm{CAN}}\ (+\hbar\omega_{\mathrm{phosphorescence}}) \tag{7.4}$$

via non-radiative decay or possibly phosphorescence.[†] However, a static (non-decaying) positive-ΔA feature remains, clearly visible in the 100–500 µs spectrum. These are likely due to photoproducts associated with the excitation of anthracene in an oxygen-containing solution. The CAN triplet ESA is shown in Figure 7.2 (blue line); this is extracted from the 250–1000 ns spectrum by first subtracting the 100–500 µs spectrum to remove the static anthracene-associated product, then removing the GSB signal by subtraction of the steady-state absorbance signal (the latter scaled and matched by eye).

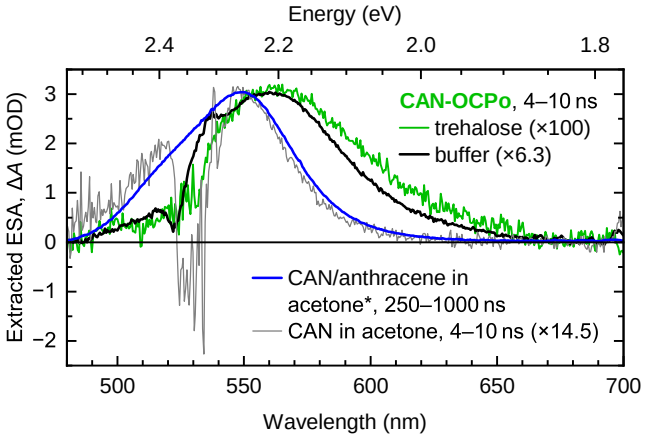

Figure 7.2 – Comparison between ESAs extracted from ns–ms transient absorption experiments on sensitised CAN in acetone (blue), non-sensitised CAN in acetone (grey), CAN-binding OCPo in trehalose (green), and CAN-binding OCPo in flowing buffer (black). The associated spectra were corrected to remove the GSB signal by subtraction of the steady-state absorbance signal (this is rough due to *e.g.* OCPo heterogeneity; see text), along with a correction for the static product in the anthracene-sensitised experiment. For the non-sensitised CAN in acetone, Rhodamine 6G in acetone was used as a 532 nm-pump filter. Note that the extracted ESAs are scaled (see scale factors in legend). See text for details.

To confirm that triplets in isolated (monomeric) CAN may be formed through intersystem crossing, we compare the ns–ms transient absorption spectra between sensitised CAN and non-sensitised CAN. The non-sensitised measurement is shown in Figure 7.3, and was conducted on 50 µM CAN in acetone (see Figure F.3b for the steady-state absorbance spectrum) directly excited by a 532 nm pump with fluence 400 µJ cm^{-2}. Note that the solution was, again, oxygen-containing

[†]Stimulated emission signatures of phosphorescence, if any, would likely not be detected here. The triplet energies of carotenoids with similar (effective) conjugation lengths to CAN are around 1350 nm, well outside the 450–750 nm probe range.[162,322]

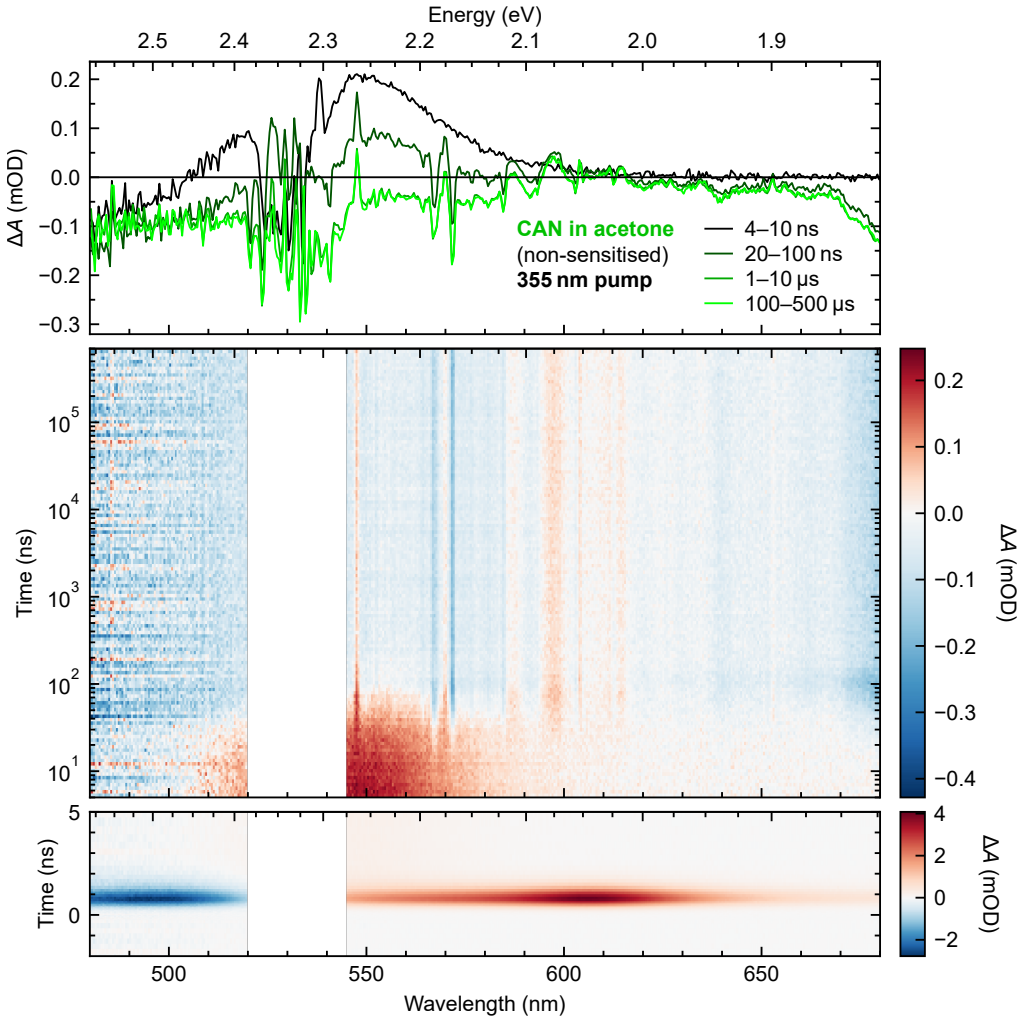

Figure 7.3 – Nanosecond-millisecond transient absorption spectra (top) and surface (middle, bottom) of non-sensitised CAN in acetone with pump wavelength 532 nm with a visible probe. As discussed in the text, the data is heavily affected by strong pump scatter and an extraneous signal appearing at ∼50 ns. Spectra (top) have been averaged between the times indicated. Surfaces (middle, bottom) omit the pump scatter region (520–545 nm) to better map the colour scale to the remaining surface. Note the logarithmic time-scale in the middle panel, and the linear time-scale and different ΔA scale in the bottom panel. Pump fluence was set to 1600 µJ cm^{-2}.

(not degassed). On the experimental day for this measurement, all obtained transient absorption datasets were poor quality; the pump scatter appeared much stronger than normal, and an extraneous signal throughout the data appeared at ∼50 ns time delay and remained static for the greater time delays. The origin of these additional artefacts remains unknown, but it may be the case that since

the expected ISC triplet yield is low (0.1–1.0%),[99] the expected signal is weak relative to noise and artefacts. We were unable to retry the measurement on a subsequent experimental day due to time constraints. We note here that a cuvette containing a laser dye solution (Rhodamine 6G in acetone) was used as a 532 nm pump scatter filter, rather than using a 532 nm notch filter (used in all other 532 nm pump ns–ms transient absorption experiments in this thesis), as it appeared to mitigate the strength of both the pump scatter and ∼50 ns artefact.

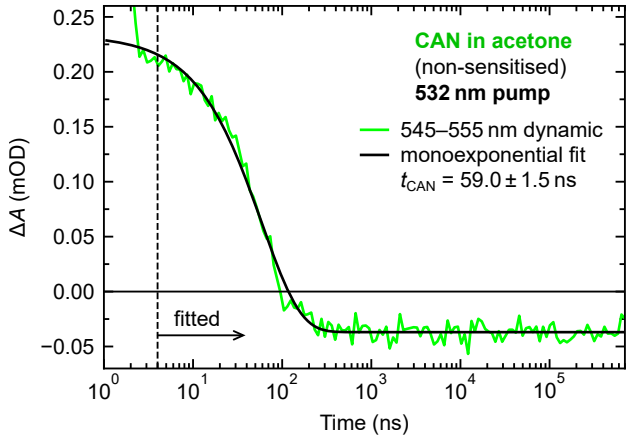

Figure 7.4 – Nanosecond-millisecond transient absorption dynamic and fit in the triplet region for non-sensitised CAN in acetone with pump wavelength 532 nm. An average dynamic in the 545–555 nm region (green) and its monoexponential fit (black) are plotted. The monoexponential fit equation used was $\Delta A_{\text{fit}}(t) = \gamma_0 + \gamma_1 \exp(-t/t_{\text{CAN}})$; γ_0 accounts for the extraneous signal (see text). The fitted time constant is $t_{\text{CAN}} = 59.0 \pm 1.5$ ns (error denotes fit parameter standard error). The fit was performed omitting the initial decaying singlet signal (*i.e.* taken from 4 ns to 0.7 ms). Pump fluence was set to 1600 µJ cm^{-2}.

For ns–ms transient absorption on non-sensitised monomeric CAN in acetone, after instrument-limited decay of the singlet features, a relatively weak decaying signal is present at least up until the ∼50 ns artefact. The profile of this decaying signal is evident in the 4–10 ns spectrum. The ESA contribution for the 4–10 ns spectrum is extracted by subtracting the (scaled and matched by eye) steady-state CAN absorbance from the spectrum to eliminate the GSB contribution. This is shown in Figure 7.2 (grey line) and is extremely similar to the CAN triplet ESA extracted from the sensitised measurement (blue line). This demonstrates that triplets are indeed formed through intersystem crossing in isolated (monomeric) CAN molecules.

We obtain a decay time constant for the triplet signal by fitting a monoex-

ponential function to a dynamic characterising that triplet decay. We take the 545–555 nm (averaged between those wavelengths) dynamic located at the peak positive ΔA of the triplet signal (of Figure 7.3, *i.e.* on data without GSB subtraction). We fit times >4 ns (*i.e.* past the instrument-limited singlet decay) with a monoexponential function with equation

$$\Delta A_{\text{fit}}(t) = \gamma_0 + \gamma_1 \exp(-t/t_{\text{CAN}}) \tag{7.5}$$

where the parameter γ_0 accounts for the extraneous signal that appears at ∼50 ns and becomes static at long times. Figure 7.4 shows the 545–555 nm dynamic and its monoexponential fit. The fitted $\gamma_0 = -0.0369 \pm 0.0008$ mOD and $\gamma_1 = 0.270 \pm 0.003$ mOD, with errors denoting the fit parameter standard errors. The fitted parameter $t_{\text{CAN}} = 59.0$ ns characterises the CAN triplet decay (in an oxic environment), although it is probable that the ∼50 ns artefact distorts the value.

7.2.2 Nanosecond features in OCPo resemble CAN triplets

We then reviewed our similar transient absorption measurements on OCPo binding near-100% canthaxanthin (CAN), shown in previous chapters (Section 6.2.2), to assess if similar triplet-like signals are present. Nanosecond-millisecond transient absorption spectra using 532 nm pump wavelength of OCPo in trehalose glass are shown (again) in Figure 7.5a, and those for OCPo in buffer in a flow cell are shown (again) in Figure 7.5b. After instrument-limited decay of the singlet features (not shown), there is a resolved decay towards a non-zero signal that then remains (no significant further decay) up to the maximum time-delay of 0.7 ms. It is worth noting we are working in oxic conditions here, and that comparable measurements on blank trehalose glass showed no obvious signal. We question if the resolved decay in OCPo is due to the decay of a CAN triplet state.[†]

Taking the 4–10 ns transient absorption spectra for OCPo in trehalose (Figure 7.5a) and in a flow cell (Figure 7.5b) as the spectra that characterise the ns-timescale delay, we take those spectra and extract the ESA signal. This is done by removing the GSB contribution by subtracting the dark-adapted absorbance

[†]We conducted similar ns–ms transient absorption on OCP mutants, but the results were prone to artefacts, similar to those seen for non-sensitised CAN in acetone (Figure 7.3). Given that visible/NIR-probe picosecond transient absorption on the mutants gave some comparatively odd results (Section G.5), we do not show the ns–ms mutant transient absorption in this thesis.

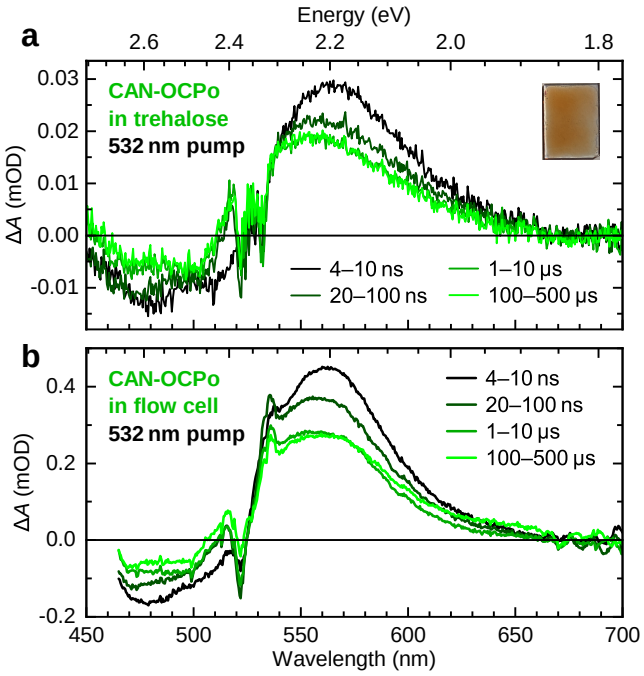

Figure 7.5 – Nanosecond-millisecond transient absorption spectra of CAN-binding OCPo in trehalose glass (a) and in buffer (b) with pump wavelength 532 nm with a visible probe. After instrument-limited decay of the singlet features (not shown), there is decay towards a feature that remains static up to the maximum delay of 0.7 ms. For the measurement in-buffer in panel (b), solution was constantly refreshed using a flow loop. Spectra have been averaged between the times indicated. Pump fluence was set to 200 µJ cm^{-2} for (a), and to 1600 µJ cm^{-2} for (b).

spectra of the samples (scaled and matched by eye). This is notably quite rough, as Chapter 6 has shown that there is significant ground-state heterogeneity and vibrational effects in the photophysics of OCPo (see *e.g.* Section 6.2.3). The 'true' GSBs in the transient absorption spectra at the 532 nm pump wavelength are likely to be a subset of broader 'total' ground-state absorbance spectra.

The resulting extracted ESAs are shown in Figure 7.2. ESAs for both OCPo in trehalose (green) and flowing buffer (black) are fairly similar in profile and broadness to the CAN triplet ESAs for sensitised (blue) and non-sensitised (grey) CAN in solution. However, the OCPo ESAs appear to be relatively redshifted. This could be attributable to different environments for the CAN (a protein environment in CAN-OCP, in contrast to the polar environment for CAN in acetone), and/or due to the aforementioned subtraction of relatively broad steady-state absorbance spectra rather than a 'true' GSB contribution at the lased pump wavelengths.

We now compare the time constants characterising nanosecond decay in monomeric canthaxanthin and OCPo. Section I.2 details and shows the results of global lifetime analysis of the transient absorption data of OCPo shown in Figure 7.5. The fitted time constants for the evolution-associated difference spectra (EADS) depend slightly on whether trehalose or a flow cell is used, along with the number of components used in the sequential model (four or five components), but a SADS with ∼30–45 ns time constant is fitted in all cases, with the previous SADS having time constants within the instrument response (time constants <1 ns) and the subsequent EADS having time constant at least ∼7 µs. These ∼30–45 ns time constants are comparable to the $t_{\mathrm{CAN}} = 59.0\,\mathrm{ns}$ time constant characterising CAN triplet decay (see Figure 7.4). Konold *et al.*'s study demonstrates similar EADS decay time constants; in a sequential model applied to ps–ms transient absorption data of OCPo binding 3′-hydroxyechineone (3′hECN) in buffer, similar EADS were fitted, one with a time constant of 50 ns (or 33 ns in a control measurement with lower pump power).[53] See Section I.2 for further discussion of our and Konold *et al.*'s global lifetime analysis. In short, it appears that in oxic conditions the characteristic lifetime of CAN triplet decay is similar to the lifetime for decay of the first photoproduct in OCPo.

We have shown that the initial photoproduct in OCPo resembles the CAN triplet formed *via* ISC for isolated monomers, both in spectra and lifetime. This supports our hypothesis that the OCP phototransition is initiated by carotenoid triplet states formed by ISC. However, to confirm or reject our hypothesis, a more direct measurement is required.

7.2.3 Attempts at direct measurements were inconclusive

Our initial attempt in a more direct test of our hypothesis involved similar spectroscopic measurements on OCPo samples doped with various 'heavy' (high atomic number Z) species. If triplets are indeed being formed in OCPo *via* intersystem crossing (ISC) and triggering the photocycle as per our hypothesis, then doping with high-Z species would enhance the ISC rate and triplet yield through enhancement of spin-orbit coupling by the external heavy-atom effect.[164,169,172] Therefore the yield of the first photoproduct would be greater in these doped OCPo samples than in the non-doped OCPo samples. If there is no change in yield, it does not rule out our hypothesis, as it may be the case that increase in ISC/triplet yield is negligible under the sensitivity of our equipment.

OCPo in trehalose films doped with either a europium ($Z = 63$) or platinum ($Z = 78$) salt had a lower attainable optical density and showed much stronger scattering than non-doped films, making spectroscopic measurements difficult. Only visible-region picosecond transient absorption on europium-doped OCPo in trehalose yielded sufficient signal, but showed no significant difference to similar measurements on non-doped OCPo in trehalose. Following this, spectroscopy on OCPo in buffer doped with iodine ($Z = 53$) was attempted, but this showed a steady-state absorbance resembling free CAN in solution, and there was no apparent photoconversion under strong white light. These were likely due to the iodine covalently reacting with key tyrosine residues in the protein, affecting the CAN binding.

Following the inconclusive results of OCPo samples doped with high-Z species, we undertook a collaboration with Christopher G. Bailey and Dane R. McCamey at the University of New South Wales, involving transient electron paramagnetic resonance (EPR) measurements. If triplets are being formed *via* ISC for CAN in solvent or OCPo in trehalose, the EPR signal will have a unique resonance profile specific to ISC triplets.[†][12,188,208,209] It is also possible that information such as the time dependence of the carotenoid's D and E parameters could be determined from the transient EPR measurements, which would give some information about the time dependence of the triplet-induced structural alterations (*e.g.* photoisomerisation) of the CAN and/or the OCP protein environment. We note that EPR is blind to singlet states.[125]

Both the CAN in solvent and OCPo in trehalose did not show any discernible EPR signal in all attempted experiments, even at high laser intensities. While this could indicate that no triplets are being formed *via* ISC for both CAN in solvent and OCPo in trehalose, we have demonstrated here that ISC triplets are formed for CAN in acetone by comparison to the sensitised triplet signal (Section 7.2.1). Therefore, it is more likely that the triplet signal is too weak to detect under the system's signal-to-noise ratio.[125] Indeed, the ISC triplet yield is around 0.1–1.0% in keto-carotenoids (including CAN) in toluene,[99] while that yield for samples fruitfully studied with EPR, such as porphyrin oligomers,[125] are in the range 30–100%.[323] Our own nanosecond-millisecond transient absorption measurements on non-sensitised samples were performed over a very long time (or with high fluence) in a setup incorporating a reference beam in order to attain sufficient signal at

[†]Triplets from singlet fission (SF) will also have a unique resonance profile, but recall that Chapter 5 ruled out efficient intramolecular SF in OCP (and light-harvesting complexes).

times >4 ns. For example, the OCPo in trehalose measurement (Figure 7.5a) ran for over 18 hours.

7.3 Discussion

7.3.1 Carotenoid triplets *via* ISC enable structural distortions

We recall that we hypothesised that keto-carotenoid triplets formed by intersystem crossing (ISC) trigger the OCP phototransition partially by comparison to the mechanism seen in opsins binding retinal, another carotenoid (point (3) in Section 7.1).[312,313] Retinal photoisomerisation from the 11-*cis* isomer to the all-*trans* isomer is thought to occur primarily through the triplet state following relatively efficient ISC, but photoisomerisation can also occur in the singlet excited states.[314–319] We note that retinal has a conjugation length (number of C=C bonds) of $N = 5$, while the keto-carotenoids bound by OCP have $N = 11$. Given the large conjugation length dependence on the overall carotenoid photophysics,[102,117,119,120,139,275] the comparison of retinal to $N = 11$ carotenoids is questionable. Hence, rather than make extensive comparisons to retinal ($N = 5$), we discuss the literature regarding ISC triplets carotenoids of comparable conjugation length to CAN ($N = 11$) in the context of our results on OCP. Recall that also motivated our hypothesis (point (2) in Section 7.1).

It is known that photoisomerisation in carotenoids with similar conjugation lengths to those bound in OCP ($N = 11$) can occur on the triplet potential energy surface. Transient resonance Raman and transient absorption studies on β-carotene in solution have shown that photoisomerisation can occur in the triplet T_1 state; this occurs both with direct photoexcitation[310,311] as well as in sensitisation measurements.[308,309,311] In these studies, central-*cis*-β-carotenes show the most dramatic photoisomerisation with relatively efficient conversion to the *trans* forms upon relaxation of the triplet; however, the *trans*-β-carotenes have been shown to take twisting(s) in the conjugated region (but still remain all-*trans*) in the triplet state, as shown in transient resonance Raman studies,[308,324] along with the usual bond-length alternation inversion in the centre of the conjugated region in the triplet state.[310,325] Furthermore, a transient resonance Raman study on naphthalene-sensitised canthaxanthin (CAN) in benzene suggested that in addition to the isomerisations/twists efficiently seen in the centre of the conjug-

ated region, the C6-C7 and C6′-C7′ single bonds have a propensity to isomerise from *cis* to *trans* (or *vice versa*) in the CAN triplet state.[324] Meanwhile, studies comparing the photoisomerisation yields between cases of direct photoexcitation (and subsequent intersystem crossing) and sensitisation measurements suggest that photoisomerisation does not occur significantly in the S_1 state.[310,311] This contrasts somewhat with the consensus on 11-*cis*-retinal, where photoisomerisation is thought to occur partially in its S_1 state,[314–319] but as stated earlier the comparison of $N = 11$ carotenoids to retinal with $N = 5$ is questionable. We note that isomerisation is known to occur in the ground state of carotenoids (S_0), particularly at high temperatures.[311]

The experiments of Konold *et al.*[53] along with recent theoretical studies[291] have also suggested that the bound keto-carotenoid in OCP undergoes some conformational change before, or during, translocation into the NTD, becoming more planar. This may be consistent with our hypothesis that photoisomerisation *via* the triplet state is responsible for the initial steps in the photoconversion. In particular, Konold *et al.* associate a 50 ns evolution-associated difference spectrum (EADS) extracted from transient absorption spectra of ECN-binding OCP in buffer with a photoproduct they dub P1 where the bound ECN becomes more planar, similar to the planarity seen in OCPr.[48] This matches the extracted time constants from global lifetime analysis using sequential models fitted to our (non-degassed) transient absorption experiments on OCPo (∼30–45 ns, depending on if in trehalose or a flow cell, and the number of model components), and the monoexponential decay time constant for isolated CAN (59.0 ns, see Figure 7.4). However, the aforementioned studies on carotenoid photoisomerisation in solution suggest that a slight twist occurs in the triplet state in all-*trans*-β-carotene,[308,324] rather than increased planarity, as suggested by the studies on OCP (binding a analogous keto-carotenoid). It is possible that interactions between the bound keto-carotenoid and the protein during the translocation process could induce additional twisting/planarity,[291] but this inconsistency requires further investigation, perhaps through transient Raman studies on keto-carotenoids in solution and in OCP, where changes in twisting in the triplet state and associated photoisomerisation and photoconversion products are monitored.

We note that there is some debate in the literature whether isomerisation (partially or completely) of the OCP-bound keto-carotenoid's C6-C7 (C6′-C7′) single bond from a *cis* conformation to a *trans* conformation occurs[48,58,222,267,291] or not[53,79] at some point during the photocycle. While it is established by multiple

studies on photoisomerisation of β-carotene in solution that the energetic barrier of isomerisation between a peripheral *cis* isomer and a *trans* isomer is relatively high, making it relatively inefficient, the aforementioned transient resonance Raman study on naphthalene-sensitised canthaxanthin (CAN) in benzene suggested that isomerisation of the C6-C7 (C6′-C7′) bond can occur in the triplet state.[324]

7.3.2 Hypothesis: Keto-carotenoids for both binding and ISC

The OCP requires a bound keto-carotenoid (CAN, ECN, 3′hECN) in order to photoswitch. Zeaxanthin (ZEA) is structurally similar to the bound keto-carotenoids, but with 3- and 3′-hydroxyl groups rather than 4- and 4′- carbonyl groups. ZEA can bind to the OCP, but with reduced stability, and ZEA is not able to mediate the OCPo→OCPr photoconversion process.[51,217] Interestingly, studies of isolated carotenoids in solution show that ZEA triplets are formed with about an order of magnitude lower yield than CAN ,[99] which within our hypothesis would cause lower-yield photoconversion in ZEA-binding OCP. The lack of ZEA-OCP photoconversion could be due to ZEA being unable to make the key interactions in the photoconversion process to give a final active OCPr product, despite a stable ZEA-OCPo form and the low-yield ZEA triplets. Indeed, it is likely that interactions between the OCP protein and the keto-carotenoid are critical as the carotenoid shuttles into the NTD in the photoconversion process.[267] We therefore hypothesise that the keto-carotenoid carbonyl groups have *two* roles in OCP: (1) to enable sufficient yields of triplets *via* intersystem crossing to trigger the photoconversion, and (2) to permit correct binding with the OCP protein, stabilising the active and inactive forms, and for making the required interactions during conversion.

We recall in Chapter 6 that we demonstrated significant ground-state heterogeneity in CAN-OCPo. An ‘S*-like form’ of OCPo with a comparatively longer S_1 lifetime was identified. It might be the case that such a population has a greater propensity to form triplets (and thus OCPr) simply by virtue of this longer S_1 lifetime (even if the ISC rate is identical between different OCPo forms). Indeed, the yield of OCPr (in buffer) is the greatest when the S*-like form is predominately excited (in trehalose). We emphasise that this also remains a hypothesis; direct measurements are also required to confirm whether the ground-state OCPo forms have different photocycle yields. See Section 6.3.5 for further detail (within

the context of Chapter 6).

7.4 Conclusions

Comparison of CAN-OCPo transient absorption with similar sensitised and non-sensitised measurements on CAN in acetone supports our hypothesis that photoisomerisation on the keto-carotenoid triplet potential energy surface is a trigger for photoconversion process. We also hypothesise that OCP binds specifically *keto*-carotenoids to enable a relatively high intersystem crossing yield, in addition for proper interaction between the keto-carotenoid's carbonyl group and the OCP protein in OCPo, OCPr, and the photoconversion intermediates. While the spectra and lifetime of the CAN triplet formed *via* intersystem crossing for monomers in acetone resembles the initial CAN-OCPo photoproduct, we lack a direct measurement supporting or rejecting this triplet hypothesis.

Highly sensitive transient electron paramagnetic resonance measurements and resonance Raman measurements will be critical in testing if intersystem crossing triplets are indeed involved in the phototransition mechanism. The low intersystem crossing triplet yield (0.1–1.0%) of the keto-carotenoids bound within OCP necessitates a higher signal-to-noise ratio than those achieved in current setup designs. Novel samples sensitising triplet formation in OCPo presents an avenue for tests in the meantime, but this appears difficult to achieve, and comparisons to native/wild-type OCP may be questionable. If triplets are confirmed to be involved, it presents a direction in tuning the overall phototransition efficiency in OCP mutants and OCP-inspired artificial proteins, namely by simply tuning the triplet yield through various techniques (triplet sensitisation, changing the bound chromophore, *etc.*), which would be useful in designing biomimetic machinery with the required sensitivity to light.

Chapter 8

Conclusions

We conclude this thesis with a summary of its substantiated findings, comparing them briefly with those presented in the surrounding literature. We also highlight various points meriting further investigation.

8.1 Summary

This thesis principally concerned the photophysics of the orange carotenoid protein (OCP) binding canthaxanthin (CAN). To prevent artefacts associated with its OCPo⇌OCPr conversion, we fixed both forms in trehalose-sucrose glass films (herein 'trehalose'),[40] which we demonstrated throughout Chapters 5 and 6 to give comparable photophysics to OCPo/OCPr in solution, despite prevention of the overall transition. These solid films required relatively small amounts of material for preparation, were comparatively straightforward to measure, and were able to be measured multiple times, which contrasts with our own in-solution measurements. Further, the solution measurements in the literature often rely on spectro-kinetic analysis techniques to isolate the OCPo and OCPr contributions,[51,53,62–64] and includes samples studied with conversion-preventing cryogenic temperatures[56] or OCP mutants,[58–61] all of which may introduce associated artefacts. Therefore, trehalose fixing of OCPo/OCPr is presented as a material-efficient, artefact-limited, and relatively straightforward means to probe the photophysics of OCP, and indeed any natural[326,327] (or artificial[328]) protein undergoing large conformational changes (or not, as we have demonstrated in Ref.[40] and Appendix A).

Chapter 5 concerns our original intent in studying OCP: testing a literature hypothesis regarding singlet fission (SF) in purple photosynthetic bacterial light-

harvesting complexes (LHCs). It was forwarded that a protein-induced twist in a carotenoid backbone sensitises one-molecule intramolecular SF (intra-SF) on that carotenoid.[41–45] The LHCs contain a number of carotenoids and bacteriochlorophylls in close contact, contrasting with OCP which binds a single ketocarotenoid molecule, presenting OCP as a simpler system to test that hypothesis. As we confirmed that the bound CAN in our OCPo in trehalose is twisted while it is relatively planar in OCPr, we conducted measurements on both OCPo and OCPr, and found no evidence of efficient generation of triplets *via* SF in either conformation. Indeed, by review of the literature on purple bacterial LHCs in light of recent work on SF,[160,165] we showed that intra-SF on a twisted carotenoid is unlikely, counter to the purported view.[41–45]

As the actual mechanism of microsecond triplet generation in purple photosynthetic bacterial LHCs remained unanswered by the initial study on OCP, a study on one of those systems proceeded, namely on *Rhodobacter sphaeroides* reaction-centre light-harvesting 1 (RC-LH1) complexes. This study is included as Appendix A, representing the paper recently submitted to the journal *Science*. Again, this was primarily by Shuangqing Wang and George A. Sutherland, with the thesis author contributing to the synthesis of the study and some measurements. We found that an intermolecular heterofission scheme of SF is the mechanism of microsecond triplet generation in *Rhodobacter sphaeroides* RC-LH1; the triplets localise on adjacent carotenoid and bacteriochlorophyll molecules. We found that the SF *via* intermolecular heterofission boosted the carotenoid-to-bacteriochlorophyll energy transfer in *Rhodobacter sphaeroides* RC-LH1 by up to 27% (13% in wild-type RC-LH1 binding spheroidenone), improving the photosynthetic yield. This is in spite of an increased risk of oxidative damage to the organism. The production of microsecond triplets through a protein-enabled intermolecular heterofission scheme presents a new route for design of synthetic SF materials.[40]

With our trehalose glass encapsulation, we took the opportunity to further characterise OCP in Chapters 6 and 7, focusing on the mechanism of conversion from OCPo→OCPr. In Chapter 6, we tested a literature hypothesis that the photoconversion is initiated by the carotenoid long-lived singlet S* state.[53,60,61] We found that all absorbing pump wavelengths trigger the photoconversion in solution, as opposed to only the wavelengths yielding S*, which led us to reject the notion that the S* feature is the sole OCP photocycle trigger. Furthermore, a significant pump wavelength dependence on the OCPo photophysics was shown, and

identified as largely due to ground-state heterogeneity, with minor dependency *via* intramolecular vibrational redistribution (IVR) and vibrational energy transfer (VET) to the surroundings.[66–70] Future experimental work on OCP (and likely other carotenoid systems[97,98]) must take account of both the ground-state heterogeneity and IVR/VET effects, and the associated pump wavelength dependence on the resulting photophysics.

Having rejected the literature hypothesis that S* triggers OCP photoconversion, we followed up by presenting a hypothesis that the photocycle is instead triggered by keto-carotenoid triplet states formed by low yield through intersystem crossing (ISC). In Chapter 7, we explained our synthesis of that hypothesis, and further hypothesised that OCP binds carotenoids with carbonyl groups specifically for enhanced triplet yield *via* ISC[99] as well as for the required protein interactions during photoconversion.[51,217] However, we presented only indirect evidence supporting the first hypothesis; direct tests are a topic for further study (see below).

8.2 Future work

8.2.1 Potential SF propensity in other light-harvesting systems

To date, SF in photosynthetic complexes has only been observed in those of purple bacteria of an evolutionary relation. Future work in line of that of Appendix A may concern whether SF occurs in other photosynthetic systems, whether it occurs in the intermolecular heterofission scheme identified in the RC-LH1 of *Rhodobacter sphaeroides* (and likely present in *Rhodospirillum rubrum*[329]), and whether the process contributes to light harvesting as in *Rhodobacter sphaeroides*. The aerobic anoxygenic phototrophs that live in shallow oxic waters and bind a high ratio of carotenoid to bacteriochlorophyll molecules are good candidates for such studies.[330–333]

8.2.2 Ground-state forms of OCPo require elucidation

While in Chapter 6 we identified multiple ground-state forms within OCPo and dubbed three of the forms as ‘S*-like form’, ‘blueshifted form’, and ‘redshifted form’, the identities of these forms remains unclear. By comparison to the

OCP[48,102,291] and carotenoid[97,98] literature, we hypothesised that the S*-like form arises from binding CAN-associated chromophores, while the redshifted and blueshifted form arise from minor CAN distortions. Both these hypotheses require some scrutiny. Meanwhile, the physical identities of the 'fast' and 'slow' biexponential components characterising the OCPo→OCPr photoconversion yield in a continuous-pump experiment are obscure. Possible experiments for elucidation here include mid-IR transient absorption and transient resonance Raman spectroscopy, along with further continuous-pump experiments characterising the photoconversion yield. Tuning of the pump wavelength in such experiments is crucial for the determination of the dynamics of each form, while the comparability of pulsed and continuous-wave pumping of OCPo merits some consideration, as recently highlighted elsewhere.[306]

8.2.3 Direct test required for the Chapter 7.2.1 hypothesis

In Chapter 7, we presented a hypothesis that the OCPo→OCPr photoconversion is initiated by a keto-carotenoid triplet state formed by intersystem crossing (ISC). However, we currently lack a measurement showing direct causation of photoconversion *via* a triplet; the evidence from our study and from the literature is circumstantial. As the yield of triplets formed by ISC in keto-carotenoids is low (0.1–1.0%),[99] experimental setups with a higher sensitivity than that presently achievable is required for a direct hypothesis test. While novel samples sensitising triplet formation in OCPo may be an avenue for tests in the meantime, there is a risk the native behaviour of the protein is incomparably affected, such that conclusions extrapolated to wild-type OCP are not valid.

8.2.4 OCP emission studies may elucidate the NPQ mechanism

An important side to OCP we intended to study is the mechanism of non-photochemical quenching (NPQ) by OCPr bound to phycobilisomes (the light-harvesting antenna in cyanobacteria).[55,74–78] It is not presently well-understood, so we were motivated to elucidate the mechanism through study of the radiative and non-radiative decay properties of OCPo and OCPr in trehalose. We were only able to obtain preliminary measurements in the form of steady-state emission measurements, shown in Appendix C. However, they indicate that OCPo is relatively emissive in comparison to OCPr, and (oddly) the spectra are broader

than those previously reported in the literature.[334] Again, we emphasise these are preliminary measurements, and require highly controlled repeats.

The preliminary measurements of OCPo and OCPr emission motivated the construction of a time-resolved emission setup with ∼100 fs resolution, with the intention to further characterise the (non-)radiative decay of OCPo/OCPr. We specifically chose to build a transient grating photoluminescence spectroscopy (TGPLS) setup,[101] details in Section 4.6. Despite maintaining spectral and temporal overlap of the three input beams, the formation of a pulsed-laser-induced transient grating has not been achieved, and thus TGPLS setup is not currently operational. In the meantime, transient emission of OCPo/OCPr may be measured with techniques such as fluorescence upconversion spectroscopy with the required time resolution (though perhaps not with the broadband spectral range required).[101]

8.3 Note

It is worth noting that the study of OCP alone has led to numerous substantiated results and points for further investigation across different disciplines. SF is more within the physical chemistry field, and was the initial motivation of study of OCP. Meanwhile, the OCP photoconversion and quenching mechanism is within the interests of molecular biologists. The thesis author hopes that this motivates some interest in studying natural systems in an interdisciplinary manner.

Appendix A

Singlet fission contributes to solar energy harvesting in photosynthesis

In this appendix, we reproduce our currently submitted draft to the journal *Science* regarding the mechanism of singlet fission (SF) in the light-harvesting complexes (LHCs) of purple photosynthetic bacteria. Note that the currently submitted supplementary materials are reproduced as Appendix B. As previously noted, it is included as an appendix as it does not represent a primary project of the thesis author; Shuangqing Wang and George A. Sutherland are joint first authors. The thesis author contributed to synthesis of the study and some transient absorption measurements (and associated analysis), and is third author.

For incorporation of this appendix and its supplementary materials (Appendix B) into this thesis, minor formatting changes to both have been made, principally the citation style and the (sub)section titles. No modifications to the figures, tables, or ideas presented have been made. Note that some abbreviations and physical quantities are defined differently to the other thesis chapters (for example, N here refers to the *effective* conjugation length, whereas the rest of the thesis uses $N_{\text{eff.}}$).

Acknowledgements: Jenny Clark conceived the study. Shuangqing Wang, George A. Sutherland and Jenny Clark designed the experiments. George A. Sutherland, Elizabeth C. Martin and David J. K. Swainsbury grew all the cells and prepared all the protein samples under the supervision of C. Neil Hunter. Shuangqing Wang performed the static and time-resolved spectroscopic measurements. Shuangqing Wang, Jenny Clark, James P. Pidgeon, George A. Sutherland

and Elizabeth C. Martin analyzed the data. David J. K. Swainsbury assisted with the fluorescence excitation measurements. Cvetelin Vasilev performed the TCSPC measurements. Daniel J. Gillard and Alexander I. Tartakovskii performed and supervised the resonance Raman measurements, respectively. Dimitri Chekulaev and James P. Pidgeon assisted with the transient absorption setup. Ravi Kumar Venkatraman built NOPA. Shuangqing Wang, Jenny Clark and George A. Sutherland wrote the manuscript and prepared the figures with input from all authors. We thank Elliot J. Taffet, Doran I. G. Bennett and William Barford for insightful discussion. We also thank Thomas J. Hayward for help with the electromagnet.

A.1 Paper abstract

The process of photosynthesis, which underpins most life on earth, starts when sunlight is captured by a network of light-absorbing molecules. These molecules are arranged so that the captured energy, now in the form of electronic excitation, transfers from molecule to molecule towards the reaction centers. We show that singlet fission — a process studied to improve photovoltaic device efficiency — is responsible for augmenting the efficiency of energy transfer between carotenoid and bacteriochlorophyll molecules in photosynthetic complexes by up to 27%, improving their light-harvesting capacity. This process relies on the formation of long-lived intermediate triplet excitations on both carotenoid and bacteriochlorophyll molecules (heterofission), risking oxidative damage to the organism to increase light capture. Understanding singlet fission in photosynthetic complexes suggests new strategies for singlet-fission-based technological applications.

A.2 Introduction

Singlet exciton fission (SF) is the conversion of one spin-0 singlet exciton[237] into a pair of spin-1 triplet excitons.[12–15] This multiexciton generation process has several potential applications, such as improving solar cell or display efficiency[16,21,26,27,238–240] by exploiting two-for-one exciton conversion, or developing new technologies for non-linear optics[18–20] or quantum information science.[22–25,335] For most of these applications, the triplet exciton lifetime must be a microsecond or longer.

A remaining puzzle in the SF literature is its role in biology. Ultrafast sub-100 fs SF is known to occur in systems containing natural carotenoid (Crt) pigments.[32,35,38,39,41–45,261,262,329,336–340] These pigments form one of the most ubiquitous groups of organic molecules and are present in most organisms. Given their ubiquity and known association with SF it seems plausible that Crt-based SF may be occurring throughout the natural world. However, to date only a few papers[32,41–45,261,262,329,336–340] have discussed SF in natural systems or explored its function (if any).

To explore the reason for such long-lived triplets, we examine *Rhodobacter* (*Rba.*) *sphaeroides* reaction-center light-harvesting 1 (RC–LH1) complexes containing a range of Crts, Fig. A.1. To build a consistent picture we isolated RC–LH1 complexes, as described previously,[343] from wild-type cells grown under semi-aerobic heterotrophic conditions (94% spheroidenone; Spn) and from engineered strains that produce complexes containing predominantly neurosporene (Neu), spheroidene (Sph), lycopene (Lyc) or diketospirilloxanthin (dikSpx).[344] We also purified complexes from a 15-*cis*-phytoene synthase mutant (ΔCrtB), yielding carotenoidless (Crtless) RC–LH1 complexes. Fig. A.1D shows the structure of the predominant pigments and Fig. A.1E shows the absorption spectra of the complexes in aqueous solutions.

To protect Crtless–RC–LH1 and other complexes from photobleaching under laser illumination, samples were encapsulated in trehalose/sucrose glass, as described previously,[40] for all spectroscopic techniques unless stated otherwise. Trehalose maintains native protein structure on conditions of dehydration, giving equivalent spectroscopic observations compared with aqueous solutions (fig. B.1).[71,270]

We start by studying the Neu-containing complex which is known to produce long-lived carotenoid triplets *via* SF[44] and is reported to demonstrate negligible direct energy transfer from the absorbing state of the Crt, S_2 (Fig. A.1, C and E) to the closest bacteriochlorophyll (BChl) *a* singlet state called Q_x (Fig. A.1, C and E).[44,345] This, together with the recent publication of the detailed *Rba. sphaeroides* RC–LH1 complex structure[341] (Fig. A.1, A and B), make it an ideal model system to study. We assume that the arrangement of pigments in Fig. A.1A does not change significantly as a function of Crt composition, supported by the fact that the RC–LH1 BChl *a* absorption spectra in the 750–900 nm range in Fig. A.1E, and the Crt resonance Raman $\nu_3 : \nu_4$ peak ratio in fig. B.2 (a ratio that is sensitive to protein structure[41,48]), do not depend on the type of Crt bound.

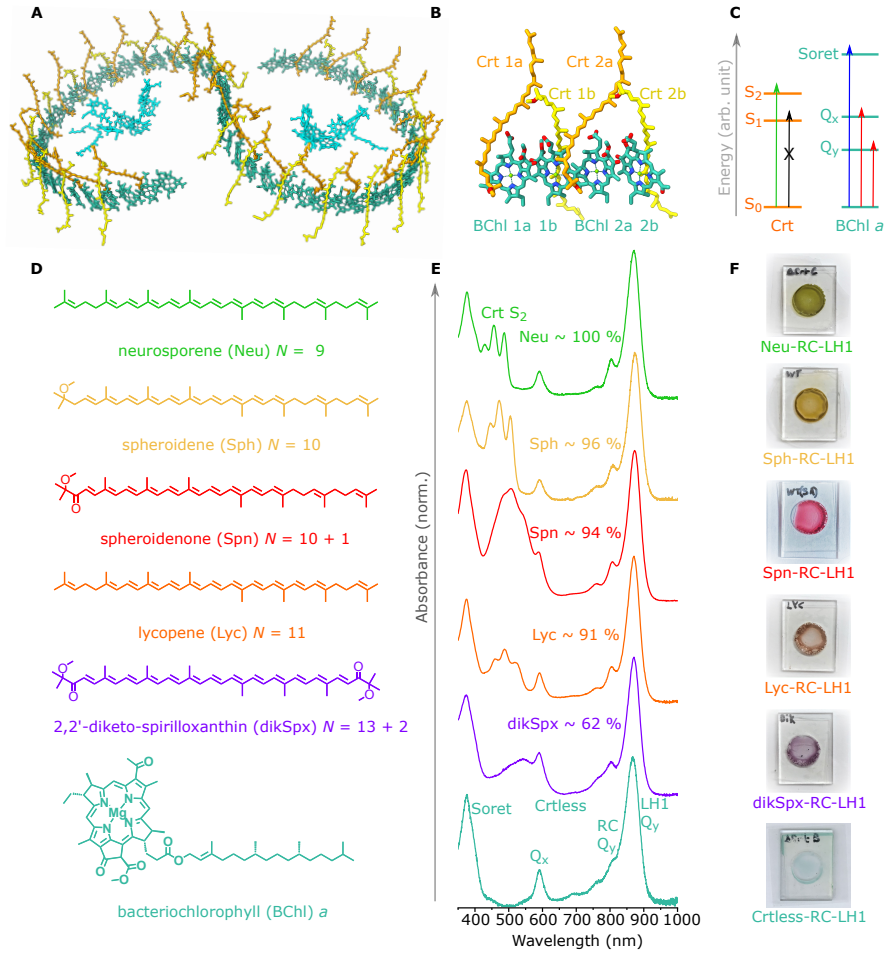

Fig. A.1 – Reaction-Center Light-Harvesting 1 (RC–LH1) complexes from *Rba. sphaeroides*. (**A**) Atomic-resolution structure of the wild-type RC–LH1 complex from *Rba. sphaeroides* with protein residues and BChl *a* phytol tail removed for clarity (PDBID: 7PQD[341]), including BChl *a* (blue-green), Crts (yellow and orange), and RC pigments (cyan). (**B**) Arrangement of Crt and BChl *a* pigments in an adjacent pair of $\alpha\beta$ subunits. Image rendering: ChimeraX.[342] (**C**) Schematic showing relative energies of lowest singlet states of Crt (orange) and BChl *a* (blue-green). Arrows denote absorption transitions measured in panel (E); cross denotes forbidden transition. (**D**) Chemical structures and names (acronyms) of pigments studied here. N denotes the effective Crt conjugation length, '$+i$' indicates the number of conjugated C=O bonds. (**E**) Absorption spectra of RC–LH1 complexes, measured in buffer (optical path length 10 mm, OD $\approx$ 0.08 at 872 nm, Q_y peak). The spectra show BChl *a* Soret, Q_x and Q_y bands as well as the Crt $S_0 \rightarrow S_2$ band. Percentages indicate content of Crt in the RC–LH1 complex. (**F**) Images of RC–LH1 complexes in trehalose/sucrose glass.

A.3 Results

A.3.1 Magnetic field effects and intramolecular SF

SF was first reported in *Rba. sphaeroides* RC–LH1 complexes in the 1980s in a series of experiments probing the relative photoluminescence (PL) yield of BChl *a* as a function of an externally applied weak magnetic field ($< 300\,\mathrm{mT}$).[261,262] This is a key method to detect the presence of SF and we reproduce the data in Fig. A.2A (similar measurements on other Crt-containing RC–LH1 complexes are shown in fig. B.3). Here, similar to extensive work on molecular solids,[123,181,182,346] as the magnetic field increases, the relative emission yield first dips below zero before rising at higher fields.

These effects are very well described by Merrifield and Johnson's kinetic model of SF, developed in the 1960s and 70s[123,124,181,182,347] and provide unambiguous evidence of the presence of SF. Importantly, these effects also provide evidence that the triplet-pairs involved in SF are weakly bound, denoted (T··T),[348] i.e., they demonstrate inter-triplet exchange interactions (J) that are much smaller than the intra-triplet dipolar zero-field splitting parameter (D, $\sim 10\,\mu\mathrm{eV}$).[12,165,266,272] As J depends on orbital overlap, the presence of this low-field magnetic field effect (MFE) demonstrates that the triplets within the pair have *negligible orbital overlap*.[165,273]

Two triplets on the same molecule are unlikely to have negligible orbital overlap unless the molecule also demonstrates clear signatures of broken conjugation along the chain, such as a dramatic blue-shift in absorption (which is not the case for the Crt in RC–LH1, Fig. A.1) or triplet D and E parameters from electron paramagnetic resonance (EPR) spectroscopy equivalent to half-, rather than full-chain, values (which is also not the case, see Ref.[266]). As discussed recently,[349] therefore, the presence of this low-field MFE indicates that SF does not occur on a single Crt, counter to the currently accepted wisdom.[41–45]

A.3.2 Crt–BChl *a* heterofission

If SF does not occur along a single carotenoid, what is the mechanism of SF in the RC–LH1 complex? To answer this question, we turn to transient absorption (TA) spectroscopy, Fig. A.2 (B–D). Upon excitation of the Neu S_2 state at 500 nm, the transient absorption spectra from 1–30 ps in Fig. A.2B are dominated by Neu signatures. The Crt signatures include a vibronically structured ground

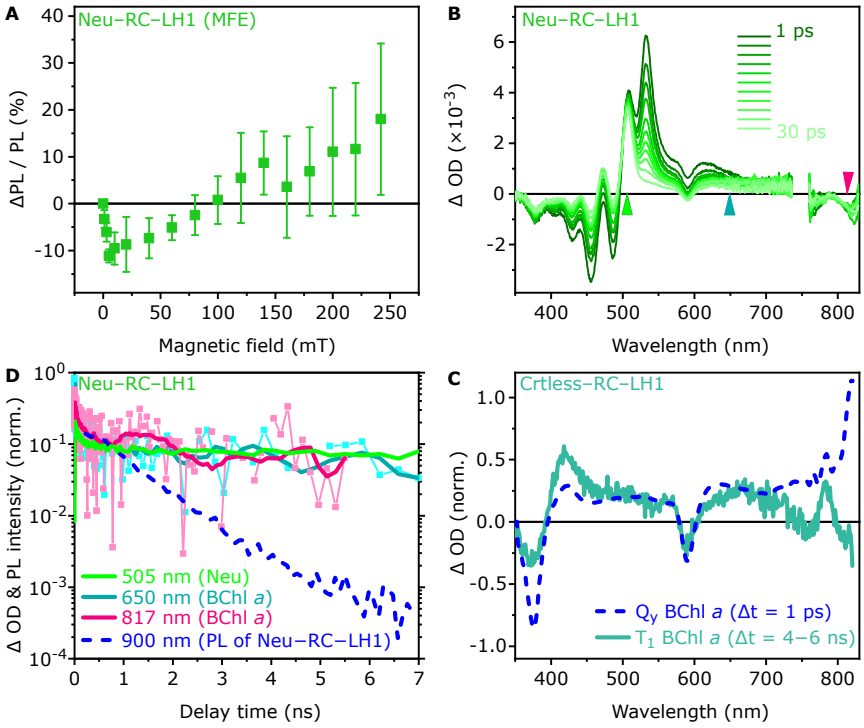

Fig. A.2 – Spectroscopy of Neu-containing RC–LH1 complex (Neu–RC–LH1) trehalose film. (**A**) Magnetic field effect (MFE), measured as the relative change in PL intensity, normalized to zero-field. Detection at 880 nm, 20–40 ns delay, excitation with $\lambda_{ex} = 520$ nm. The curve demonstrates classic Merrifield behavior, indicating presence of SF. Error bars are given by 2σ (standard deviation) from subsequent field up and down scans. MFE of other Crt-containing complexes in fig. B.3. (**B**) Transient absorption spectra of Neu–RC–LH1 complexes at delay times between $\Delta t = 1$–30 ps, $\lambda_{ex} = 500$ nm. Arrows show positions of transients in panel (D). (**C**) RC–LH1 BChl *a* reference spectra of Crtless–RC–LH1 complexes, see Fig. A.1. These normalized spectra were obtained following BChl *a* Q_x excitation (590 nm) and subsequent IC and ISC. Further details and analysis are provided in fig. B.6 and associated Supplementary Text. (**D**) Absorption transients from Neu–RC–LH1 ($\lambda_{ex} = 500$ nm) at wavelengths marked in legend, normalized at 0.7 ns. Data taken at 817 and 650 nm (thin lines with markers) have been smoothed (thick dark lines). The BChl *a* Q_y PL decay (dashed), detected at 900 nm using time-correlated single photon counting (TCSPC) on Neu–RC–LH1 is shown for comparison.

state bleach (420–500 nm) and two excited state absorption (ESA) bands: $S_1 \rightarrow S_n$ (532 nm) and $T_1 \rightarrow T_n$ (507 nm). Overlapping these features are weaker BChl *a* signatures: Soret (375 nm), Q_x (590 nm) and Q_y ($\sim$ 820 nm) ground state bleach and some excited-state absorption features across the visible and near infrared (NIR) spectral ranges. These features appear weak due to the relatively small excited-state absorption coefficients of BChl *a* compared with Crts (fig. B.4).

To assign the weak BChl *a* features in Fig. A.2B to excited-state species, we compare our spectra to BChl *a* reference spectra in Fig. A.2C. These were measured by exciting a Crtless–RC–LH1 from *Rba. sphaeroides* into the BChl *a* Q_x band, and following internal conversion (IC) to Q_y and intersystem crossing (ISC) to T_1 with transient absorption spectroscopy (technical details in figs. B.6, B.7, and B.8). In the visible spectral range (Fig. A.2C) both the Q_y and T_1 excited-state spectra are strikingly similar. Such spectral similarity is well known for porphyrins and chlorins,[350] is not due to two-photon or sequential excitation (fig. B.9), and likely stems from the orbital degeneracy described by Gouterman[351] and others.[352] The similarity makes it difficult to determine, from visible transient absorption spectroscopy alone, whether the early-time BChl *a* signatures we observe in Fig. A.2B originate from excited singlet or triplet states. However, comparison with the reference spectra shows that they diverge in the near infrared spectral range, between 700–820 nm, where Q_y shows an absorption (positive) while the T_1 spectrum shows a bleach (negative).

Returning to the transient absorption spectra with Neu S_2 excitation in Fig. A.2B, we observe that the BChl *a* signatures between 750–800 nm are negative from the earliest measurement times ($\sim$100 fs, fig. B.10A). Comparison with the reference spectra therefore suggests that BChl *a* triplets are formed within our $\sim$100 fs instrument response time in the RC–LH1 complex upon Neu excitation.

To determine the dynamics of these BChl *a* triplets, in Fig. A.2D we plot transients measured at wavelengths marked by the arrows in Fig. A.2B. We plot these single wavelength kinetics as a proxy for triplet dynamics as we were unfortunately unable to perform robust global analysis on this data set due to its complexity, similarity of species spectra and large differences in extinction coefficients (technical details in fig. B.11 and associated Supplementary Text). The BChl *a* bleach (817 nm) and absorption (650 nm) features were chosen as they demonstrate maximum BChl *a* ΔOD (change in optical density) signal where Neu shows negligible absorption after S_1 has decayed.[44] As the BChl *a* signatures are

weak, we have smoothed the raw data to ease analysis (thick lines show smoothing, narrow lines with markers show raw data). These dynamics show that after an initial rapid decay within the first nanosecond, that is due to a combination of S_1 decay ($\tau_{S_1} = 4.6$ ps, Fig. A.3E), energy transfer from S_1 to Q_y (presenting as an apparent bleach decay due to the overlapping rise of Q_y absorption at 817 nm) and Q_y decay (compare to dashed line), the BChl *a* signatures barely decay over 1–7 ns. This slow decay matches the Neu triplet dynamics (505 nm).

The presence of BChl *a* triplet features from the earliest measurement times, and spectral dynamics that match the Neu triplets, suggest that SF in the RC–LH1 complex occurs between Neu and BChl *a*, producing a shared triplet-pair state that we denote (T··T) that is delocalized over both molecules. In other words, Crt excitation produces a pair of triplets, with one triplet residing on the carotenoid and the other on the neighboring BChl *a*. The triplets decay with the same lifetime at least to 6 ns, most likely due to geminate triplet-triplet annihilation (TTA). These results suggest that SF in the RC–LH1 complex occurs *via* 'heterofission', involving two different molecules.

A.3.3 Conjugation length dependence of heterofission and energy transfer

Having demonstrated heterofission in the RC–LH1 complex containing Neu, we extend our study to a range of RC–LH1 complexes containing Crts of different conjugation lengths (Fig. A.1 D–E for absorption spectra and structures). This enables us to determine relative yields of SF and to compare our results with similar studies on the related purple bacterium *Rsp. rubrum* from the literature.[329]

Fig. A.3 shows transient absorption spectra (left) and dynamics (right) for RC–LH1 complexes containing Crts of increasing conjugation length, *N*. Similar to the Neu case described above (Fig. A.2B) and reproduced in Fig. A.3 (A and E), the spectra are dominated by Crt signals. After the Crt S_1 state has fully decayed (right hand panels), the long-lived signatures, represented at 100 ps in the figure, can be assigned to the weakly absorbing BChl *a* Q_y and T_1 states, and dominant Crt triplet absorption denoted by the shaded region in the left panels (strong correlation with triplet reference spectra is shown in fig. B.12[353,354]). Inspection of the data shows two trends as the Crt conjugation length increases: (1) the BChl *a* NIR feature flips from negative (Neu) to positive (Sph, Lyc), suggesting a relative decrease in BChl *a* triplets with increasing conjugation length; and (2)

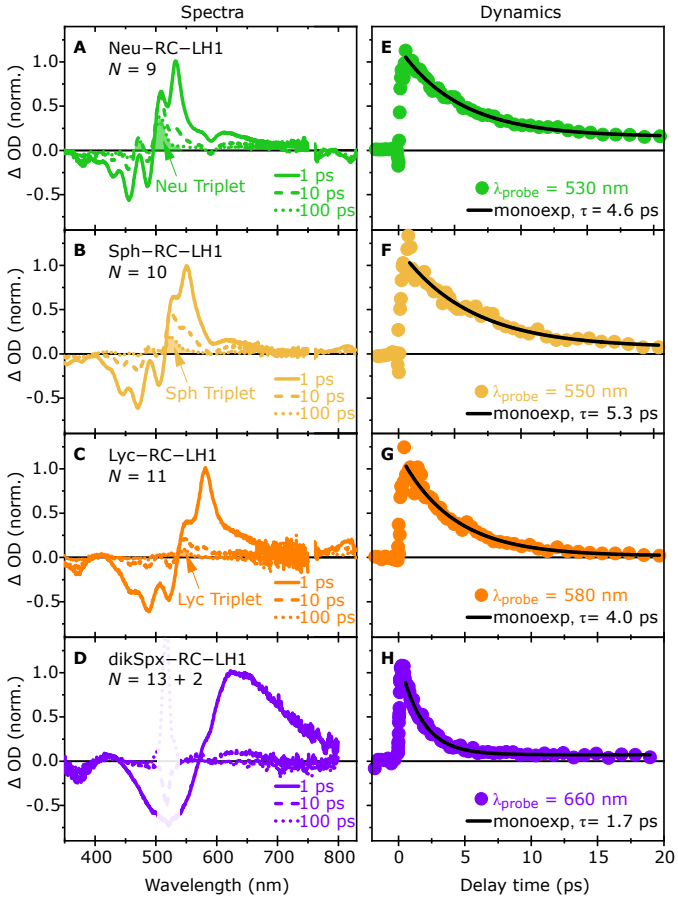

Fig. A.3 – Transient absorption spectroscopy of RC–LH1 complexes containing a series of carotenoids. (**A**–**D**) Transient absorption spectra measured at time delays $\Delta t = 1, 10, 100$ ps for RC–LH1 complexes containing Crts with increasing conjugation length: (**A**) Neu, $N = 9$, (**B**) Sph, $N = 10$, (**C**) Lyc, $N = 11$ and (**D**) dikSpx, $N = 13 + 2$ C=O. The Crt triplet absorption feature ($T_1 \rightarrow T_n$), where present, is shaded, showing a relative decrease in triplet population as N increases. This is accompanied by a flip in the BChl *a* NIR feature from negative (**A**) to positive (**B, C**). The spectra at 1 ps were normalized to the peak of the $S_1 \rightarrow S_n$ absorption band, and the corresponding spectra at 10 ps and 100 ps were normalized by applying the same scaling factors as that for 1 ps. (**E**–**H**) Transient absorption dynamics at the peak of the $S_1 \rightarrow S_n$ absorption (markers). Solid lines are mono-exponential fits to the S_1 decay, with lifetimes marked in the figures. Excitation was at $\lambda_{ex} = 500$ nm for Neu–RC–LH1 (**A**, **E**), and $\lambda_{ex} = 520$ nm for all others. All complexes were measured following encapsulation in trehalose glass.

the relative amplitude of the Crt triplet signal decreases as the conjugation length increases.

We plot the Crt and BChl *a* triplet yield (Φ_T) as a function of conjugation length in Fig. A.4A, using the data from the transient absorption spectra in Fig. A.3 and similar data extracted from Ref.[329]. Details of the yield calculation are available in Supplementary Text and Table B.2. To reduce errors, we have used Crt extinction coefficients published in the same work[355] and used the same method to determine the yield in each case. Therefore, although the absolute yield of Crt or BChl *a* triplets may not be comparable with other reports (our Crt triplet yields are generally lower[41,42,261–263]), the trend with increasing conjugation length is robust.

Fig. A.4A shows that as the conjugation length increases, the yield of both Crt and BChl *a* triplets decreases. The close correlation between Crt and BChl *a* triplet yields further confirms heterofission as the SF mechanism. The trend with increasing conjugation length is present in both *Rba. sphaeroides* (squares) and *Rsp. rubrum* (triangles), despite the fact that *Rba. sphaeroides* contains double the number of Crts, see Fig. A.4C.[356,360] This suggests that heterofission, and the trend we observe, is a general phenomenon among purple photosynthetic bacteria that demonstrate SF, and that it occurs between neighboring Crt (Crt a in Fig. A.1B) and BChl *a*, as Crt b (Fig. A.1B) is missing from the RC–LH1 complex in *Rsp. rubrum*, Fig. A.4C.

Crt-to-BChl *a* exciton energy transfer (EET) also occurs in both these complexes and we plot the EET efficiency (Φ_{EET}) in Fig. A.4B. The data for *Rsp. rubrum* were taken directly from Ref.[329]. The data for *Rba. sphaeroides* were calculated by comparing 1–transmittance and fluorescence excitation spectra (fig. B.14), as described previously.[44,329,343,344,361]

There is a spread in the measured values of Φ_{EET} both in the literature[44,361] and here. For example EET from Neu to BChl *a* in the RC–LH1 complex from *Rba. sphaeroides* range from Φ_{EET} = 67–81% (here, fig. B.14) to 72%[361] and 55%.[44] We have found that aged samples show lower Φ_{EET}, fig. B.14, and therefore the values in Fig. A.4B are from fresh samples (measured within hours of purification). The trend we observe is consistent with literature:[329,344] shorter conjugation length Crts in light-harvesting complexes demonstrate increased EET efficiency. We find that both *Rba. sphaeroides* (circles) and *Rsp. rubrum* (triangles) show a similar decrease in Φ_{EET} as the conjugation length of the incorporated Crt increases: the sample with the highest SF yield (Neu, $N = 9$) also demonstrates the

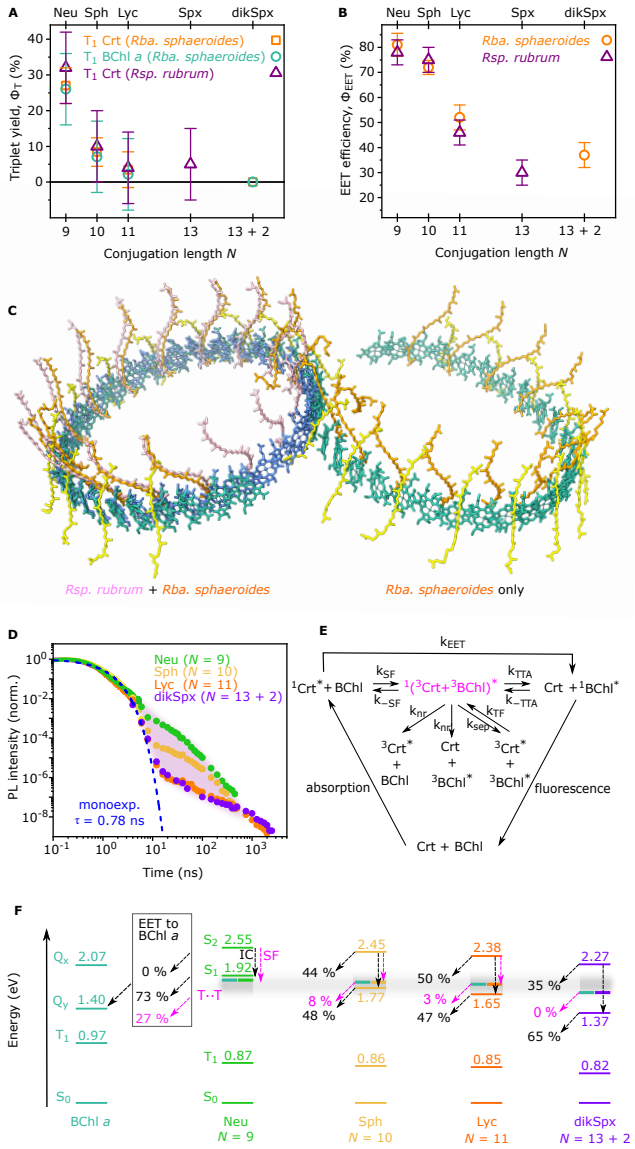

Fig. A.4 – Conjugation length dependence of SF and Crt-to-BChl *a* EET in RC–LH1. (**A**) Triplet yield, Φ_T (Table B.2), as a function of Crt conjugation length, *N*, following Crt excitation using data from Fig. A.3 (*Rba. sphaeroides*) and Ref.[329] (*Rsp. rubrum*). (**B**) Crt-to-BChl *a* EET yield, Φ_{EET} vs. *N*. Values from fig. B.14 (*Rba. sphaeroides*) and Ref.[329] (*Rsp. rubrum*). (**C**) Projection views of RC–LH1 from *Rba. sphaeroides*[341] and *Rsp. rubrum*.[356] (**D**) PL dynamics of RC–LH1 (*Rba. sphaeroides*) in buffer with Crt excitation (Neu: 500 nm, others: 520 nm), detection at 900 nm (Q_y). Solid lines denote TCPSC measurements (normalized at 100 ps), markers denote gated intensified CCD measurements (normalized to TCSPC data), dashed line is a monoexponential function for comparison. The shaded region highlights increased delayed emission due to (T··T)→Q_y EET in Neu–RC–LH1. (**E**) Simplified kinetic scheme following Crt excitation, rates (k_i) are defined by this scheme. (**F**) Simplified schematic showing BChl *a* and Crts excited state energies, gray shading denotes shared triplet-pair (T··T) (energies from Refs.[279,357–359]). Arrows denote selected processes (SF, IC, EET) and best-guess Crt-to-BChl *a* EET yields from different Crt/shared states (% values in Table B.3).

highest EET efficiency in both organisms.

A.3.4 SF-mediated Crt-to-BChl energy transfer

It is surprising, at first glance, that RC–LH1 complexes with high triplet yield (e.g., Neu $\Phi_T = 27 \pm 5\%$) also demonstrate efficient Crt-to-BChl *a* energy transfer ($\Phi_{EET} = 81 \pm 4.6\%$), Fig. A.4, because triplets are usually assumed to be a loss pathway. However, when pairs of triplets are formed geminately from the same photon (fig. B.13 and associated Supplementary Text), they can participate in energy transfer to a singlet exciton as a pair, cooperatively, without energy loss.[362] In organic semiconductors such as rubrene, SF and subsequent so-called geminate triplet-triplet annihilation (TTA) are responsible for 66–90% of the measured emission.[363,364] In these systems, the triplet-pair population generated by SF acts as a reservoir of 'dark' excitons that decay cooperatively through the singlet manifold. Q_y emission *via* TTA has been proposed in light-harvesting complexes,[357] but the triplets were assumed to be generated by intersystem crossing on BChls *a*, rather than by SF on Crts.

Here, to determine whether SF-generated triplet pairs participate in Crt-to-BChl *a* EET, we monitored the Q_y delayed emission of the four RC–LH1 complexes, Fig. A.4D. In all four complexes, the prompt (<10 ns) BChl *a* Q_y emission decays identically, following a monoexponential function (blue dashed line). However, an extra delayed emission component is observed beyond 10 ns and is dependent on the conjugation length of the bound Crt. Delayed emission from radical pair recombination in the RC[365,366] should be present in all four complexes, but this involves BChl and bacteriopheophytin radical pairs and should be independent of Crt conjugation length.[365] We therefore attribute the identical delayed emission in the Lyc- and dikSpx-containing samples to radical pair recombination in the RC, as these complexes also show identical MFE (fig. B.3) associated with radical pair recombination[261,262] and negligible SF. On the other hand, the RC–LH1 complexes that do demonstrate significant SF (Neu and Sph) both also demonstrate an additional delayed emission component, shaded pink in Fig. A.4D.

This additional delayed emission component in RC–LH1 complexes that demonstrate SF occurs on timescales of 10–500 ns, when Crt and BChl *a* triplets are the dominant excited-state species (fig. B.13), and its relative intensity scales with triplet yield. Therefore, we assign it to geminate TTA of SF-generated

triplets to form Q_y. In other words, the shared (T··T) state provides an additional EET pathway to Q_y, denoted by the pink arrow in Fig. A.4F. This additional EET pathway explains how Neu-containing RC–LH1 complexes can demonstrate both high Φ_T and Φ_{EET} at the same time.

We can estimate the contribution of SF to the total Φ_{EET} by estimating the EET efficiency from other Crt states, S_1 and S_2, and comparing it to the total measured value of Φ_{EET} in Fig. A.4B. Niedzwiedzki *et al.*[44] recently hypothesized that $S_2 \rightarrow Q_x$ energy transfer is effectively zero in Neu-containing RC–LH1 from *Rba. sphaeroides*[44] due to small spectral overlap.[345] We estimate the $S_1 \rightarrow Q_y$ efficiency by comparing the change in S_1 lifetime when going from solution[345] to LH1 (Fig. A.3E) using $\Phi_{EET}^{S_1 \rightarrow Q_y} = \left(1 - \frac{\tau_{S_1}^{LH1}}{\tau_{S_1}^{Sol}}\right) \times 100$.[345] This gives an efficiency of 79% (similar to previous reports[44]). Taken together with our triplet yield of $\Phi_T = 27\%$, and our total Neu-to-BChl *a* Φ_{EET} of 81%, we therefore determine an upper limit of the proportion of Crt-to-BChl *a* EET *via* SF to be 27% (figs. B.14 and B.15 and Table B.3).

The errors in these calculations are unfortunately rather large. Nevertheless, in Fig. A.4F we have included best-guess estimates of the proportion of Crt-to-BChl *a* EET that originates from S_2-, S_1- and (T··T), using a combination of our measurements and values from the literature (Table B.3). The trend indicates that shorter conjugation length Crts demonstrate EET from three different pathways: $S_2 \rightarrow Q_x$, $S_1 \rightarrow Q_y$ and $(T\cdot\cdot T) \rightarrow Q_y$ yielding high total Φ_{EET} values, while longer conjugation length Crts show EET only from one (S_2) or two (S_2 and S_1) pathways.

We end this section by noting that the delayed emission in Fig. A.4D decays significantly faster than the triplet reservoir population (determined from transient absorption spectroscopy, fig. B.13). This is likely to be because of spin dephasing. The initially generated triplet-pair state, $^1(T\cdot\cdot T)$ must have overall singlet character to conserve spin, as it originates from S_2. While it is a pure singlet, $^1(T\cdot\cdot T)$ can transfer to Q_y, which is also a singlet state. However, the pure singlet version of (T··T) is not an eigenstate of the system[12] and spin dephasing reduces the singlet character of this state. Following spin dephasing (T··T) has a lower probability of transferring to Q_y. Similar behavior has been observed in organic semiconductor films.[364,367] Therefore, we propose that the delayed emission time-scale is dominated by triplet-pair spin dephasing (10s of nanoseconds), while the transient absorption triplet signature is dominated by population decay (microseconds).

A.3.5 SF occurs in *Rba. sphaeroides* in anoxic and oxic conditions

With heterofission as the mechanism of SF in purple bacteria, the significant yields of carotenoid triplets reported here, and elsewhere in the literature,[41,42,45,263] must be associated with similarly high yields of BChl *a* triplets, a conclusion supported by our data in Fig. A.4A. This is surprising as BChl *a* triplets usually drive singlet oxygen generation and photodegradation,[338,368–370] and accordingly should be avoided.[371,372] Indeed, one of the main roles of Crts is to rapidly quench (B)Chl triplets *via* triplet energy transfer.[372] In heterofission this is not possible: the neighboring Crt (Crt a in Fig. A.1B) is already excited to the triplet state and cannot quench the BChl *a* triplet. One might therefore assume that lack of oxygen in the environment is desirable for safely conducting the SF-mediated EET mechanism and that adaptations must be made to abolish heterofission once oxygen is present.

In response to moderate oxygen tension, *Rba. sphaeroides* uses the enzyme spheroidene monooxygenase (CrtA) to convert spheroidene to spheroidenone (structures in Fig. A.1D); a reaction that consumes molecular oxygen,[373] and results in a Crt that reduces the ratio of dimeric to monomeric RC–LH1[344] and hence minimizes internal chromatophore biogenesis.[374] To determine whether RC–LH1 complexes with Spn still use heterofission, wild-type *Rba. sphaeroides* cells were cultured by heterotrophic, semi-aerobic growth in darkness, giving a RC–LH1 Crt content of 94% Spn.[344]

Fig. A.5 shows the transient absorption spectra (panel A) and dynamics (panel B) of these Spn-containing RC–LH1 complexes excited into the Spn absorption band (520 nm). The data are similar to previous reports[336] and more complex than those in Fig. A.3 as the asymmetric structure of Spn supports an intramolecular charge-transfer (ICT) state.[336] The ICT state absorbs in the NIR, overlapping the BChl *a* Q_y bleach, and is longer-lived than the pure S_1 feature. After the ICT state has decayed (e.g., by 4–6 ns, dark dashed line), we assign the remaining dominant feature to Spn triplet $T_1 \rightarrow T_n$ absorption (shaded). As the MFE (panel C) demonstrates the classic SF behavior described above and the delayed emission in panel D is almost identical to that of Sph-containing RC–LH1 (Fig. A.4D), we conclude that these long-lived Spn triplets are generated *via* SF and that they contribute to Crt-to-BChl *a* EET through geminate TTA. We observe this EET directly from the BChl *a* fluorescence dynamics in Fig. A.4D, where long-

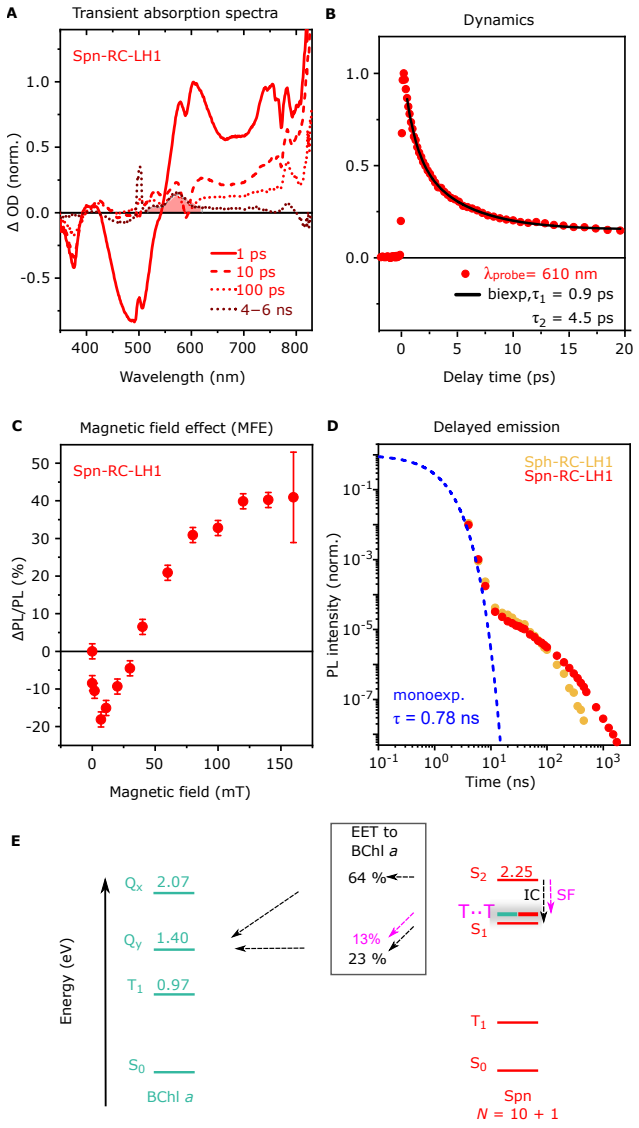

Fig. A.5 – Spectroscopy of Spn-containing RC–LH1 complex (Spn–RC–LH1). Transient absorption spectra (**A**) and dynamics (**B**) of Spn–RC–LH1 complexes measured in a trehalose film with $\lambda_{ex} = 520\,nm$. Spectra are plotted at delay times marked in the figure, the shaded region denotes Spn $T_1 \rightarrow T_n$ absorption. The dynamics at the peak of the S_1/ICT absorption band is fitted bi-exponentially (solid line) with time constants marked in the figure. (**C**) MFE of the relative PL yield, excited at 520 nm, measured on a trehalose film. (**D**) Delayed emission from Spn–RC–LH1 measured in buffer with $\lambda_{ex} = 520\,nm$. Sph–RC–LH1 data from Fig. A.4D shown for comparison. (**E**) Simplified schematic showing BChl *a* and Spn excited state energies, gray shading denotes shared triplet-pair (T··T) (energies from Fig. A.1E and Ref.[359]). Arrows denote selected processes (SF, IC, EET) and best-guess Spn-to-BCh EET yields from different Crt/shared states (% values in Table B.3).

lived triplets recombine (through geminate TTA) to produce delayed BChl *a* fluorescence.

These results suggest that heterofission, and consequent generation of BChl *a* triplets, must occur even in complexes formed in the presence of oxygen. Indeed, in Spn–RC–LH1 both the triplet yield ($\Phi_T = 13.6 \pm 4\%$, Table B.2), and the Crt-to-BChl *a* EET efficiency ($\Phi_T = 87 \pm 3\%$, fig. B.14) are relatively high. Fig. A.5E includes estimates of the relative Crt-to-BChl *a* EET pathways, calculated as in Fig. A.4F: up to 13% of the Crt-to-BChl *a* EET is due to SF in these complexes. We conclude that the overall SF behavior of Spn-containing RC–LH1 is similar to that of Sph-containing complexes, which is surprising, in energetic terms, given the low reported Spn S_1 energy, $E_{S_1} = 1.61\,eV$,[345,375] see Supplementary Text. Nevertheless, we have found that SF occurs efficiently under partially-oxic conditions in *Rba. sphaeroides*. *Rba. sphaeroides* therefore seems to risk singlet oxygen generation (from BChl *a* triplets) to increase EET from Crts to BChls *a*. This is possibly a well-calculated risk, given the particularly strong ability of Spn to quench reactive oxygen species,[376] and the fact that *Rba. sphaeroides* RC–LH1 contains two Crts per $\alpha\beta$ subunit, Fig. A.1B, in contrast to *Rsp. rubrum*,[356,377] Fig. A.4C.

A.4 Discussion

We found above that SF in RC–LH1 complexes from *Rba. sphaeroides* occurs within 100 fs to form triplets on neighboring Crt and BChl molecules, a process termed heterofission. Such fast SF suggests it occurs directly from S_2, as in Crt aggregates,[35,38,40] and as predicted.[116,121] SF should therefore compete with Crt $S_2 \rightarrow S_1$ internal conversion (IC), which also occurs on these timescales.[378] As the IC rate depends on Crt conjugation length (N),[378] increasing by almost an order of magnitude when going from for $N = 9$ to $N = 15$,[378] the competition between IC and SF explains our finding that the SF yield drops with increasing N, Fig. A.4A. For the longest N we measure (dikSpx), for example, IC effectively outcompetes SF. SF yield thus primarily depends on the Crt $S_2 \rightarrow S_1$ IC rate.

As well as ultrafast IC between S_2 and S_1, Crts are excellent at dissipating the electronic energy stored in S_1 to heat ('thermalization'). Due to their strong vibronic coupling, Crts have two orders of magnitude higher non-radiative decay rates from S_1 to the ground-state than most fluorescent or acene-based dyes[12,275] (for a given S_1 energy), resulting in picosecond S_1 lifetimes. This makes

Crts excellent at dissipating excess electronic energy, providing photoprotection in light-harvesting complexes. However, the rapid energy dissipation also limits Crt-to-(B)Chl excitation energy transfer, which must compete with it. SF-mediated energy transfer is a way to side-step this rapid energy dissipation, through the formation of the intermediate triplet states. These states are long-lived because of spin selection rules which protect them from rapid thermalization. SF therefore provides an avenue for increasing the overall Crt-to-BChl energy transfer efficiency by using long-lived protected triplet states that have time (>100 ns) to transfer to BChl Q_y before decaying.

To be useful for energy transfer, SF must be ultrafast (sub-100 fs) and must produce long-lived triplets (>100 ns). These requirements are similar to those for technological applications such as SF-sensitized solar cells or quantum information science. Ultrafast SF generally occurs in systems with strong coupling between locally-excited (S_2), charge-transfer (CT) and triplet-pair (TT) states, and is often synonymous with strong exchange coupling[118,200], and consequently rapid triplet-pair decay.[12] In RC–LH1 complexes, however, we have demonstrated that the triplet pairs are weakly exchange coupled (T··T) and long-lived. The combination of ultrafast SF and weakly-coupled triplets that we observe is unusual. It suggests that either the nature of the coupling changes with time or that even weakly-coupled triplets are directly generated within 100 fs. We observe no evidence of bimolecular TTA in the antenna, see fig. B.13, which is consistent with transient electron paramagnetic resonance studies[379] showing that Crts in LHCs are immobile.[379] We conclude that triplet migration is not the cause of the time-dependent exchange coupling. Instead we hypothesize that, similar to recent work in the field of molecular crystals,[201,380–382] dynamic exchange interactions during SF play a role. A similar concept has been explored in the context of CT states in light-harvesting complexes.[383,384] We speculate that dynamic fluctuations in the relative position of the BChl *a* and Crt pigments enable both rapid SF and formation of weakly-coupled triplets. On longer timescales spin decoherence will also prevent recombination, as described above.

A.5 Conclusions

Purple photosynthetic bacteria typically live in light-limited anoxic conditions and use carotenoids (Crts) to absorb photons in the spectral gap between the bacteriochlorophyll (BChl) *a* absorption bands, and to protect against photoox-

idative damage. Here, we demonstrate that Crts play an additional role in light-harvesting complexes by enabling singlet fission (SF), a process that augments Crt-to-BChl *a* energy transfer by up to 27% (13% in wild-type Spn–RC–LH1).

We have found that, rather surprisingly, SF-mediated energy transfer occurs even in the presence of oxygen in *Rba. sphaeroides*. However, to date SF has only been observed in evolutionarily-similar photosynthetic complexes of purple bacteria. It will be interesting to see whether similar processes occur elsewhere in the natural world, for example in aerobic anoxygenic phototrophs that live in shallow oxic waters and have a characteristic overabundance of Crts,[330–333] or in other photosynthetic systems.

Our findings also open new avenues for exploiting singlet fission for quantum information science,[335] a technology that requires ultrafast formation of long-lived, immobile triplets in scalable systems. We have shown that this can achieved by combining heterofission with a dynamic pigment scaffold; features that could be replicated in more conventional synthetic systems.[40,385,386]

Appendix B

Supplementary materials for Appendix A

B.1 Materials and Methods

B.1.1 RC–LH1 complexes containing a series of carotenoids

Rba. sphaeroides was grown and RC–LH1 complexes were purified according to our method previously described at length.[343] Briefly, for wild-type and mutant stains, a single colony from an M22 agar plate was used to inoculate a 10 mL universal medical specimen tube, containing M22 liquid medium. This was incubated in the dark at 34 °C with agitation (150 rpm) until visibly turbid. This culture was then scaled up to 80 mL, also in liquid M22 medium, in 125 mL Erlenmeyer flasks. Cells were then either cultured by semi-aerobic heterotrophic growth or anaerobic phototrophic growth, as described below.

For semi-aerobic heterotrophic growth, the 80 mL culture was added to 1.6 L M22 liquid medium in a 2 L Erlenmeyer flask and incubated at 34 °C with agitation (150 rpm). For anaerobic phototrophic growth, 1 L M22 medium in a 1.2 L medical flat was sparged with filtered ultrapure N_2 under aseptic conditions. The 80 mL culture was added and the flask filled with additional sparged M22 medium. Flasks were then sealed gently with a rubber stopper and parafilm, agitated with a magnetic stirrer and illuminated with white light (50–500 μmol photons m^{-2} s^{-1}) at room temperature.

Cells were harvested by centrifugation (4,400× g, 30 min, 4 °C), resuspended in resuspension buffer (20 mM HEPES pH8.0, 5 mM EDTA), and lysed by

twice passing through a French pressure cell (18,000 psi, pre-cooled to 4 °C). This solution was centrifuged (27,000× g, 15 min, 4 °C) and the supernatant collected. Membranes were obtained by loading the supernatant onto 15/40% (w/v) sucrose step gradients, prepared in the appropriate tubes for a Beckman Ti45 fixed angle rotor, and centrifuged at 85,000× g, 4 °C for 10–16 h. Chromatophore membranes were harvested from the interface between the two sucrose solutions, diluted six-fold in resuspension buffer, and centrifuged at 185,000× g for 2 h. All supernatant was removed and membrane pellets were resuspended and homogenized in 5 mL resuspension buffer. N-dodecyl-β-D-maltoside (β-DDM) was added to a final concentration of 2% (w/v) and membranes were solubilized at 4 °C for 1 h.

Solutions of resuspension buffer containing 20%, 21.25%, 22.5%, 23.75%, 25%, 50% (w/w) sucrose were prepared in tubes appropriate for a Beckman SW41 Ti rotor. Solubilized membranes were loaded on top of the gradient and centrifuged at 125,000× g at 4 °C for 40 h. The appropriate band for RC–LH1 dimers (or monomers where appropriate) was collected with a fixed needle.

Protein samples were further purified by anion exchange chromatography using a 5 mL Q-sepharose HP column (Cytiva) and a linear gradient of buffer A (50 mM HEPES pH8.0, 1 M NaCl, 0.03% (w/v) β-DDM) to buffer B (50 mM HEPES pH8.0, 1 M NaCl, 0.03% (w/v) β-DDM) over 60 column volumes. Appropriate fractions were pooled, concentrated by centrifugal dialysis, and loaded onto a Superdex 200 Increase 10/300 GL size exclusion chromatography column (Cytiva), pre-equilibrated in 50 mM HEPES pH8.0, 100 mM NaCl, 0.03% (w/v) β-DDM. Apart from the carotenoid-free RC–LH1 sample, fractions with an A875/A280 ratio > 1.4 were pooled for analysis.

For deposition in trehalose/sucrose films, the RC–LH1 samples were concentrated to give A875 values of 10–20 (apart from carotenoid-free RC–LH1, which was approximately 0.5). 40 μL of sample was then mixed with 40 μL of trehalose/sucrose mix (both 0.5 M) and 5 mM sodium ascorbate. Two imaging spacers (Secure Seal diameter 9 mm, thickness 0.12 mm; Grace Bio-Labs) were then stacked on a quartz-coated glass substrate (Ossila) and the RC–LH1 trehalose solution deposited in the center of the spacer. The substrate was placed in a vacuum chamber (-70 kPa) with a large excess of calcium sulfate desiccant (Drierite) and dried for a minimum of 3 days. Following drying, a No. 1 coverslip was applied to the imaging spacer to protect the glass from atmospheric rehydration.

B.1.2 Static spectroscopy

Static absorption spectra were carried out using a Agilent Cary 60 spectrometer. Static fluorescence excitation spectra were acquired with a Jobin–Yvon Fluorolog–3 spectrofluorometer equipped with a Hamamatsu FL-1030 cooled photomultiplier. The spectra were recorded at 898 nm with excitation and emission slits set to 3 and 10 nm, respectively. To minimize reabsorption, the optical density at 872 nm for each sample in buffer solution was adjusted to < 0.1. The fluorescence excitation spectra were collected with a short exposure time and multiple accumulations (~ 7 h in total).

The resonance Raman spectra were measured with film samples at room temperature using a free-space optical set-up. Briefly, the spectra were recorded *via* a SP750 spectrograph (Princeton Instruments) equipped with a holographic 1800 g/mm grating and a back-illuminated liquid nitrogen cooled charge-coupled device (Princeton Instruments, PyLon). Excitation at 532 nm was provided by a single mode diode-pumped solid state laser (Cobolt, 04-01) with power of 1 mW focussed in a spot of 2 μm diameter on the sample and spectral linewidth of < 1 MHz. The spectral resolution of the system was $\sim 0.4\,\mathrm{cm}^{-1}$.

B.1.3 Time-resolved absorption (TA) spectroscopy

The picosecond transient absorption spectra were recorded utilizing a Ti:Sapphire laser system (Spitfire ACE PA-40, Spectra-Physics) delivering pulses with pulse lengths of 40 fs (FWHM) at 800 nm and a repetition rate of 10 kHz. Pump pulses at 500 nm (and 520 nm) were generated in an optical parametric amplifier (TOPAS Prime, Light Conversion). Probe pulses were obtained by supercontinuum generation (SCG) in CaF_2 using the 800 nm Ti:Sapphire fundamental and the fundamental alone. The pump–probe time delay was set using a computer-controlled multi-pass motorized linear delay stage. The polarization of the pump was set to the magic angle (54.7°) with respect to the polarization of the probe. After the sample film, the probe pulses were detected by using a commercial instrument (Helios, Ultrafast Systems) equipped with CMOS detector for the $340 - 830$ nm spectral region.

The nanosecond broadband absorption setup was based on a 90 fs, 1 kHz Ti:Sapphire amplifier (Solstice, Spectra-Physics). Broadband supercontinuum probe pulses between $450 - 700$ nm were generated in a sapphire plate. Pump pulses were provided by an Nd:YVO4 Q-switched laser (Innolas Picolo-AOT)

tuned for second-harmonic (532 nm) output. The pump-probe delay was controlled electronically using a digital delay generator (DG645, Stanford). The polarization of the pump was set to the magic angle (54.7°) with respect to the polarization of the probe. Signal and reference probe pulses created by a beam-splitter were detected spectrally resolved pulse-by-pulse by two CCD cameras (S7030, Hamamatsu) driven and read out at the full laser repetition rate by a custom-built board from Entwicklungsbüro Stresing.

B.1.4 Time-resolved photoluminescence (PL) spectroscopy

The BChl *a* Q_y fluorescence lifetime of the RC–LH1 complex was measured on a home-built time-resolved fluorescence microscope. The microscope was equipped with a 485 nm picosecond diode laser (PicoQuant, PDL 828) as an excitation source. The excitation light was focused by a 100 × objective (PlaneFluorite, NA = 1.4, oil immersion, Olympus). The emitted light was filtered using a 495 nm dichroic beam-splitter (Semrock) and 900/32 nm bandpass filter (Semrock) to remove the background excitation light. The microscope was fitted with a spectrometer (150 lines/mm grating, Acton SP2558, Princeton Instruments) and an electron-multiplying charge-coupled device (EMCCD) camera (ProEM 512, Princeton Instruments) for emission spectrum acquisition. A hybrid detector (HPM-100-50, Becker & Hickl) was used for single photon counting. The modulation of the excitation laser was synchronized with a time-correlated single-photon counting (TCSPC) module (SPC-150, Becker & Hickl) for the lifetime decay measurement. The repetition rate of the laser was set at 1 MHz. The excitation laser power was adjusted to produce a fluence of approximately 2×10^{14} photons pulse^{-1} cm^{-2} The instrument response function (IRF) of the set up was approximately 130 ps.

The nanosecond-millisecond time-resolved photoluminescence spectra were recorded *via* a time-gated intensified charge-coupled device (iCCD; iStar DH334T-18U-73, Andor), coupled to a Shamrock 303i spectrograph. Excitation pulses at 490 and 520 nm were generated from a home-built noncollinear optical parametric amplifier (NOPA) pumped by a 1 kHz regeneratively amplified 800 nm Ti:Sapphire laser (Solstice, Spectra-Physics).

B.1.5 Magnetic field-applied photoluminescence spectroscopy

The magnetic field effects on photoluminescence of the RC–LH1 complex were measured by recording the photoluminescence intensity changes at a series of magnetic field strengths ($0 - 300\,\mathrm{mT}$). The film samples were placed between the poles of a magnet (Newport Instrument, Serial no. 8248/II). Excitation pulses at 490 and 520 nm were created from a home-built NOPA. The photoluminescence was detected at the wavelength $\sim 880\,\mathrm{nm}$ and the delay time $20 - 40\,\mathrm{ns}$ by a spectrograph (Shamrock 303i, Andor) and a time-gated iCCD (iStar DH334T-18U-73, Andor). A 830 nm longpass filter (FEL830, Thorlabs) was placed before the detector to cut out scattered pump light. The magnetic field effects on the RC–LH1 complex were evaluated as $\frac{\Delta PL}{PL} = \frac{PL_B - PL_0}{PL_0}$.

B.2 Trehalose sugar films stabilize the protein structures but have no impact on their photophysical properties

As mentioned in the main text, trehalose forms an optically-clear glass film and is used to protect cellular structures under dehydration conditions by maintaining protein tertiary conformation in the absence of water.[270] The static spectra of the Sph–RC–LH1 complex either encapsulated in trehalose films or dissolved in buffer solutions are similar, indicating that the solid trehalose film does not affect the photophysical properties of RC–LH1 complexes. Note that light scatter is often observed in the 350–600 nm range as precisely controlling the glass thickness, and hence path length, is not possible using the above method.

We note that that we measure the Q_y absorption band of RC–LH1 complexes from *Rba. sph-aeroides* to be at 872 nm, instead of usually reported 875 nm. To confirm the reproducibility of this static spectral feature we prepared these mutant complexes by two different methods: photosynthetically and semi-aerobically, and both batches show the same 872 nm Q_y band. We note that despite the shift, the ratio between the 872 nm and 275 nm bands is the same as previous work: ~ 1.6.

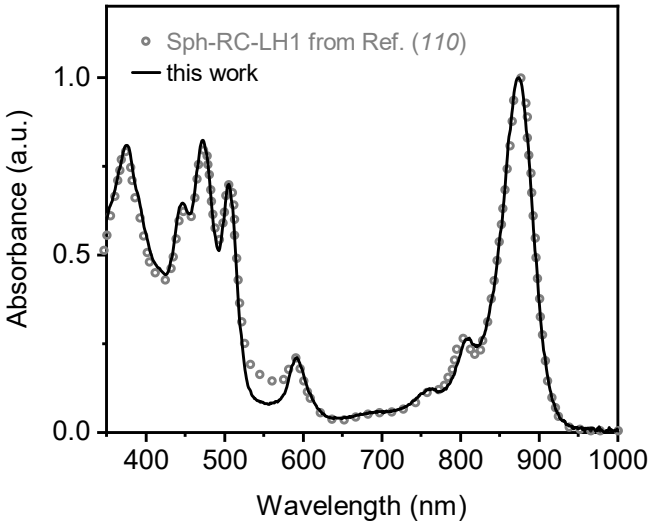

Fig. B.1 – Static absorption spectra of the RC–LH1 complex containing spheroidene in a trehalose film (line) and in buffer solution (circles).[41,387]

B.3 Resonance Raman spectra of RC–LH1 complexes indicates identical structural features for all carotenoids

The $\nu_3 : \nu_4$ peak ratio, see fig. B.2, in the resonance Raman (RR) spectra of Crts indicates the degree of backbone twisting along the chain.[41] To determine whether the Crts within the genetically-modified RC–LH1 complexes adopt similarly twisted conformations, we measured RR spectra of the genetically-modified RC–LH1 complexes from the main text doped into trehalose films at room temperature after excitation at 532 nm (details in section B.1). See fig. B.2.

In the RR spectra, the bands of ν_2 (1150 cm $^{-1}$) and ν_3 (1000 cm $^{-1}$) represent the C−C stretching and C−CH_3 vibrations, respectively. The ν_4 region at $\sim$ 970 cm^{-1} is characteristic of the out-of-plane wag of C−H, which only becomes symmetry-allowed upon nonplanar distortions of the polyene backbone. All four Crts in the RC–LH1 complex from *Rba. sphaeroides* show similar $\nu_3 : \nu_4$ peak ratios suggesting that they are maintained in a similar configuration within the RC–LH1 complex.

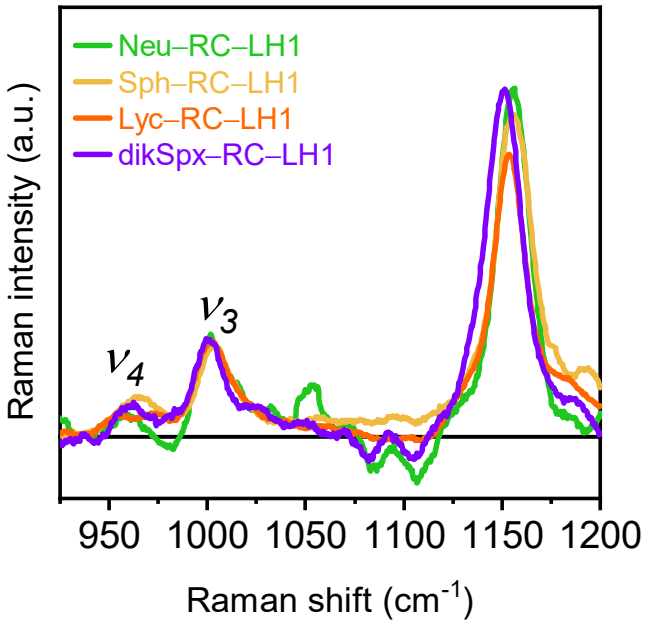

Fig. B.2 – RR spectra of RC–LH1 complexes containing neurosporene (Neu), spheroidene (Spe), lycopene (Lyc), and 2,2'-diketo-spirilloxanthin (dikSpx) upon excitation at $\lambda_{exc} = 532$ nm. The data have been background-subtracted, smoothed using an Adjacent Averaging filter (30 points) and normalized to the ν_3 peak at ∼1000 cm^{-1}. The intensity ratio between this ν_3 peak and the ν_4 peak at ∼970 nm provides an indication of the carotenoid conformation, see Ref.[41] for details. The similarity in this peak ratio suggest that the Crts adopt similar conformations in the RC–LH1 complex. Note that owing to the scatter from the sugar films, the background subtraction is not perfect, particularly for Neu–RC–LH1.

B.4 Magnetic field-dependent measurements

The impact of a weak (<300 mT) magnetic field on photoluminescence (PL) indicates the presence of weakly-bound spin pairs. In photosynthetic pigment-protein complexes such effects can be due to radical pair recombination as the radical electron-hole pairs in the reaction centre recombine, or due to singlet fission. Radical pair recombination typically manifests as a sharp increase in ΔPL/PL at fields below 10 mT (with no negative dip) and saturation above 100 mT.[206,388–390] The typical singlet fission behavior, on the other hand, shows a negative dip (a decrease) followed by an increase with respect to the magnetic field.[123,181,201,347,391] The characteristic singlet fission-induced MFEs in light-harvesting proteins were first reported by Rademaker *et al.* by using a 50 Hz field for purple bacteria at moderate redox potential.[389]

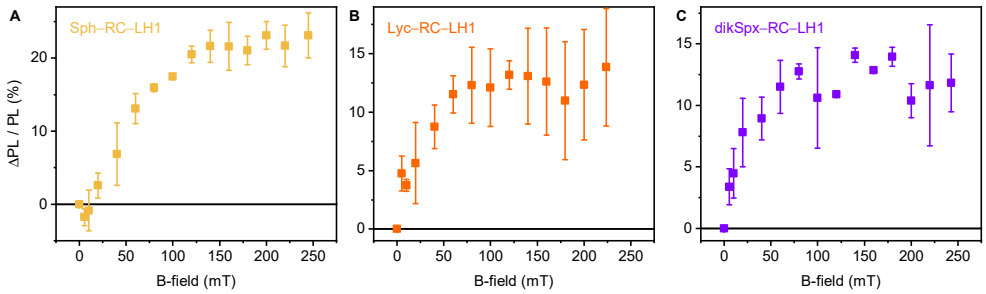

Fig. B.3 – Photoluminescence intensity changes (ΔPL) normalized to the zero-field PL (PL) at detection wavelength 880 nm and delay time 20–40 ns as a function of the magnetic field strengths upon excitation at 520 nm of different carotenoids: (**A**) spheroidene (Sph, $N = 10$), (**B**) lycopene (Lyc, $N = 11$), and (**C**) 2,2'-diketo-spirilloxanthin (dikSpx, $N = 13 + 2$ C=O) in the RC–LH1 complex. Error bars represent the difference between scanning up and down in magnetic field.

The characteristic singlet fission-induced MFEs of a dip below zero (reduction in fluorescence yield) at low field is observable for RC–LH1 complexes containing neurosporene (main text Fig. 2A) and spheroidene (fig. B.3A).

The RC–LH1 complex containing lycopene (fig. B.3C) or 2,2'-diketo-spirilloxanthin (fig. B.3D) shows no dip below zero at low fields, but an almost identical increase in relative fluorescence yield, even at < 10 mT fields. This relative PL changes increases monotonously with magnetic field is characteristic of recombination of radical pairs within the reaction centre to generate BChl *a* fluorescence,[206,388] which is known as the MFEs *via* radical pair mechanism.[389,390] For our RC–LH1 complexes, so-called open RCs were initially formed because

samples were prepared by adding no reducing agent (under non-reducing conditions). Upon excitation, an electron transfer sequence is initiated forming a charge-transfer (CT) state (P^+I^- and P^+Q^-, where P is the reaction center bacteriochlorophyll dimer, Q is the terminal reaction center quinone electron acceptor, and I is the intermediate electron acceptor). For an excitation rate that is higher than the rate constant of the RC back reaction from P^+ to the excited-state P*, for instance 1 kHz in our case, it is known that the RC is in a closed state after a few excitation cycles. In this closed RC the lifetime of radical pair is long enough to allow the CT state to undergo spin mixing and contribute to the delayed fluorescence.[392]

B.5 Transient absorption study of BChl *a* excited singlet and triplet state

B.5.1 Difficulties observing the spectral signatures of BChl *a* excited triplet state in light harvesting complex

We found that the Crt signatures dominate the transient absorption spectra of RC–LH1 complexes (see main-text Figs. 2, 3, 5), despite the presence of significant BChl *a* population. This is well-known.[41,42] Empirically, the reason for this is that Crt molecules have relatively large excited-state extinction coefficients compared with those of BChl *a*. For example, the Crt $T_1 \rightarrow T_n$ excited triplet state peak absorption extinction coefficient is estimated to be roughly ten times larger ($\sim 2 \times 10^5\,M^{-1}\,cm^{-1}$)[355] than the BChl *a* peak triplet absorption coefficient ($\sim 0.2 \times 10^5\,M^{-1}\,cm^{-1}$),[393] see fig. B.4. The transient absorption signals of RC–LH1 in the visible spectral region are therefore dominated by Crt excited-state features and the signatures of BChl *a* are obscured, making assignment difficult.

B.5.2 Spectral similarity of BChl *a* excited singlet and triplet states

It is well-known that porphyrin and chlorin molecules show similar singlet $S_1 \rightarrow S_n$ (in this case $Q_1 \rightarrow S_n$) and triplet $T_1 \rightarrow T_n$ excited-state spectral features.[350] This similarity is unusual for π-conjugated molecules and makes assignment of the

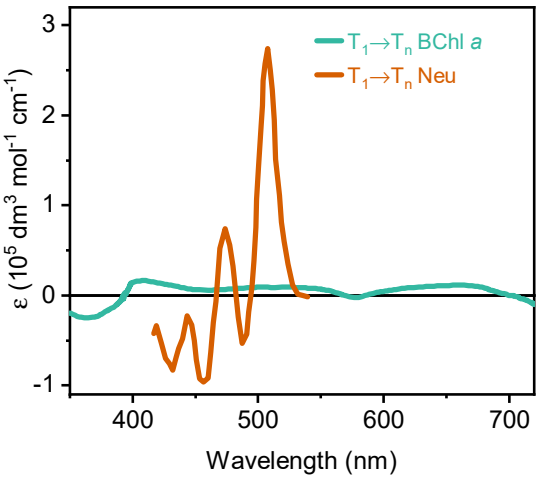

Fig. B.4 – Extinction spectra of BChl *a* $T_1 \rightarrow T_n$ excited state absorption reproduced from Ref.[393], and Neu $T_1 \rightarrow T_n$ excited state absorption reproduced from Ref.[355].

spectral features in the congested RC–LH1 transient absorption spectra difficult. Therefore, here we measured RC–LH1 complexes from a Crtless mutant to obtain reference spectra for $Q_1 \rightarrow S_n$ and $T_1 \rightarrow T_n$.

Fig. B.5 shows two-dimensional maps of the transient absorption spectra for a carotenoidless RC–LH1 complex from *Rba. sphaeroides* after Q_x (590 nm) and Q_y (860 nm) excitation. Interestingly, we observe that the BChl *a* ground state bleach signals at 375 nm and 590 nm last within the entire time window (7 ns). This long-lived BChl *a* excitation is assumed to be due to its triplet state generated *via* intersystem crossing.

During the entire time window in fig. B.6B, the spectral features change very little in shape. However, further inspection demonstrates differences in the region between $700 - 830$ nm as a function of time. In this spectral region we observe positive excited state absorption (ESA) at early time and negative ground state bleach (GSB) at late times, see main text Fig. 2C for normalized spectra. The dynamics at probe wavelengths 760 nm and 806 nm are plotted in fig. B.6C showing the ΔOD sign change beyond 1 ns and the presence of a long-lived (non-decaying) bleach feature at these wavelengths. Importantly, the early-time decay (< 1 ns, ESA signal) matches with the BChl *a* Q_y fluorescence lifetime (blue line, fig. B.6C). This match shows that the positive excited-state absorption (ESA) band between $700 - 830$ nm must be associated with Q_y population. fig. B.6D shows that this ESA band does not depend on pump excitation wavelength (when measured at 1 ps, following internal conversion from Q_x with 590 nm excitation),

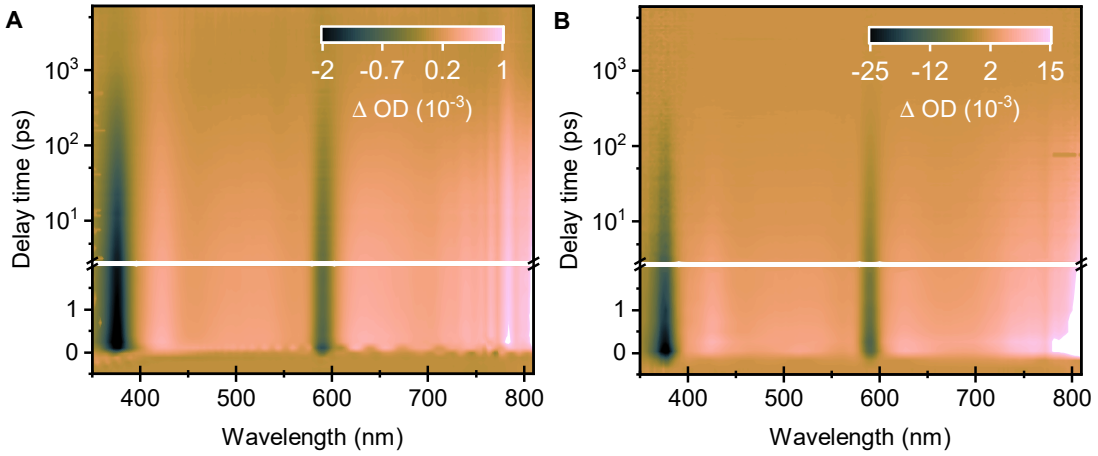

Fig. B.5 – Two-dimensional transient absorption maps showing the change in optical density (ΔOD) of the carotenoidless RC–LH1 complex after excitation at (**A**) 590 nm and (**B**) 870 nm. The results are displayed using a linear time scale from −0.5 to 3 ps and a logarithmic time scale from 3 − 7000 ps.

and is similar to the reported Q_y spectrum from Ref.[394] measured in LH2 complexes from *Rba. sphaeroides*.

We therefore confidently assign the ESA band between 700–830 nm to $Q_y \rightarrow S_n$ absorption. In RC–LH1 Q_y decays with a $\sim$ 1 ns time-constant. The nature of this decay is discussed further below.

MCR–ALS For a more quantitative understanding of the BChl *a* excited-state spectral behavior, we performed global analysis using multivariate curve resolution-alternating least squares (MCR–ALS), see Refs.[395,396] for more details. This MCR–ALS analysis was run on the dataset of the Crtless–RC–LH1 complex after excitation into the BChl *a* Q_x band. We extracted two components with corresponding spectra and dynamics shown in fig. B.7. We assign the pink component in fig. B.7A to Q_y as it closely matches the spectra reported in fig. B.6 and because its population decay is similar to the measured Q_y fluorescence (blue curve in panel B).

As the black spectral component in fig. B.7 rises as the Q_y feature decays, barely decays over 1–7 ns and has spectral features of BChl *a*, we assign it to the triplet T_1 excited-state spectrum.

Comparison with reported BChl *a* T_1 spectra are shown in fig. B.8. Although we cannot compare the entire spectral range due to the shift of the bleach from solution (green dashed) to RC–LH1 (our measurement), we find that reported

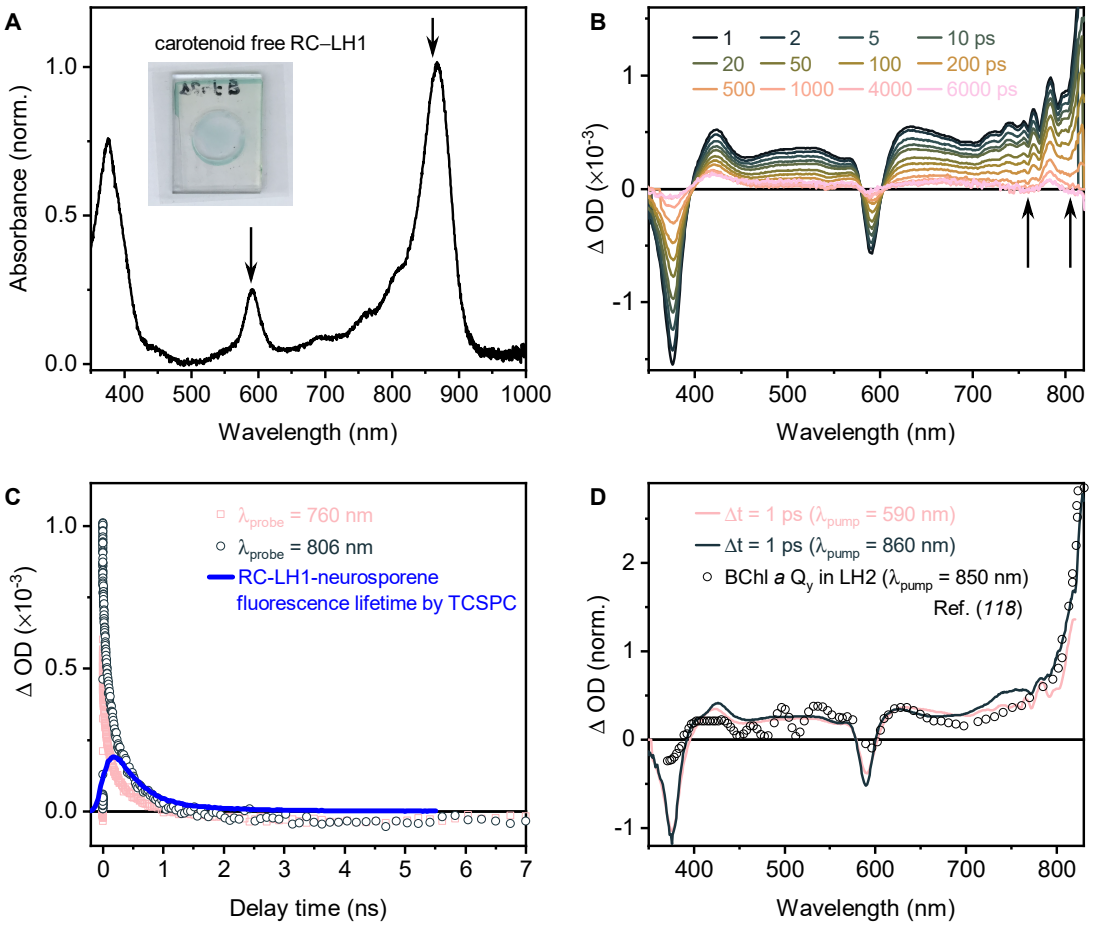

Fig. B.6 – (**A**) Static absorption spectrum of the carotenoidless RC–LH1 complex. Excitation wavelengths (590 and 860 nm) are indicated by vertical arrows. Inset: picture of the sugar film. (**B**) Transient absorption spectra of the carotenoidless RC–LH1 complex after BChl *a* Q_x excitation at 590 nm for delay times between $1-6000$ ps. Vertical arrows indicate the selected probe wavelengths (760 and 806 nm) for plotting the corresponding dynamics in panel (**C**). (**C**) Dynamics at selected wavelengths of 760 and 806 nm decaying to negative after 1 ns. Also plotted is the fluorescence decay (900 nm) measured with TCSPC, normalized to 0.7 ns. Note that TCSPC has a lower temporal resolution which obscures the early-time (sub-200 ps) decay. (**D**) BChl *a* Q_y spectrum obtained at early time ($\Delta t = 1$ ps) after both Q_x (590 nm) and Q_y (860 nm) excitation and the reported BChl *a* Q_y excited-state spectrum measured in LH2 complex from *Rba. sphaeroides*, from Ref.[394].

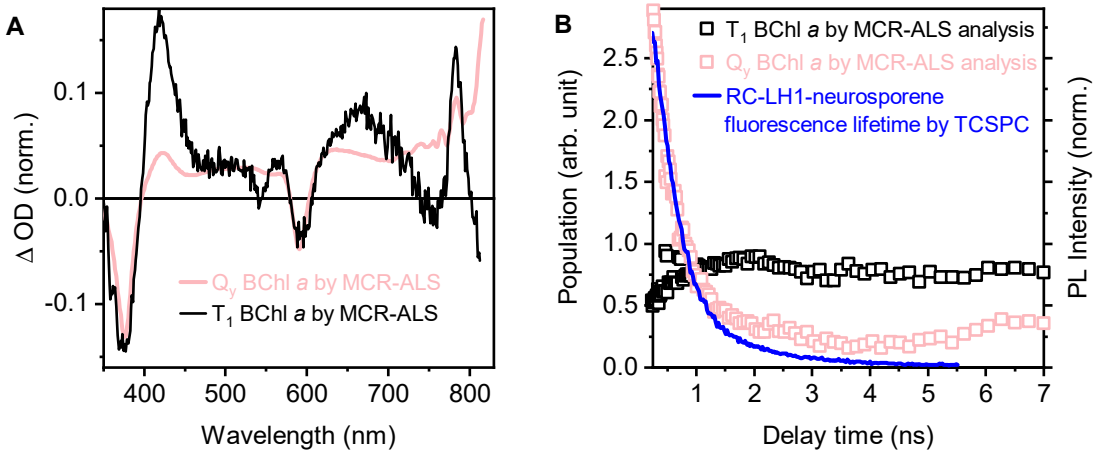

Fig. B.7 – Extraction of Q_y and T_1 components from transient absorption data in fig. B.6 using MCR–ALS (see text): extracted spectra (**A**) and extracted dynamics (**B**).

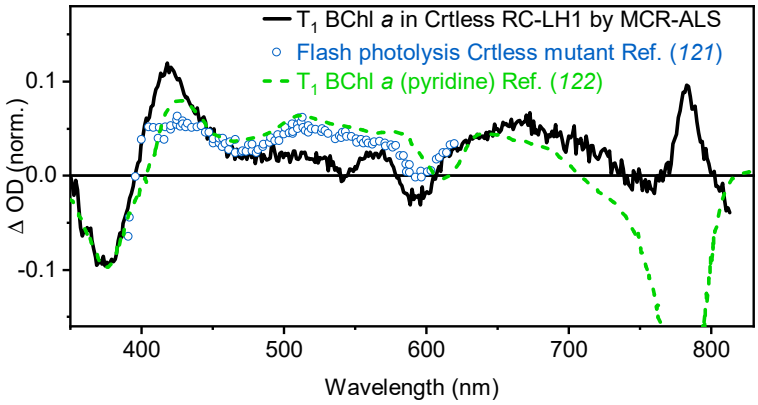

Fig. B.8 – Comparison of MCR–ALS-extracted BChl *a* T_1 spectrum (black) with flash photolysis (μs) excited-state spectrum of a Crtless mutant *Rba. sphaeroides* chromatophore[397] (blue circles) and the T_1 spectrum of BChl *a* in pyridine, measured with flash photolysis.[398] We note that the NIR ground-state bleach region at wavelengths longer than 700 nm is highly dependent on the environment of the chromophore. In RC–LH1, this Q_y feature is red-shifted compared with solution.

spectra nevertheless broadly reproduce the visible spectral components. In addition, absorption-detected microwave resonance (ADMR) spectra of triplets in reaction centre from *Rba. sphaeroides* show similar (though shifted) oscillating absorption/bleach in the NIR spectral range.[399]

In sum, we conclude that the spectra represented in Fig. 2C of the main text (which are almost identical to the MCR–ALS-extracted spectra in fig. B.7) can be assigned to Q_y and T_1 excited-state spectra. Q_y shows a strong absorption between $700 - 830\,\text{nm}$ while the T_1 spectrum is dominated by weak ground-state bleach in this region.

B.5.3 Non-linear fluence dependence of BChl *a* transient absorption spectroscopy

It has been reported that porphyrins have a propensity to demonstrate efficient step-wise two-photon absorption through the S_1 state (the Q state).[352] This has been reported to occur even with relatively low power densities,[352] and may need to be controlled for.

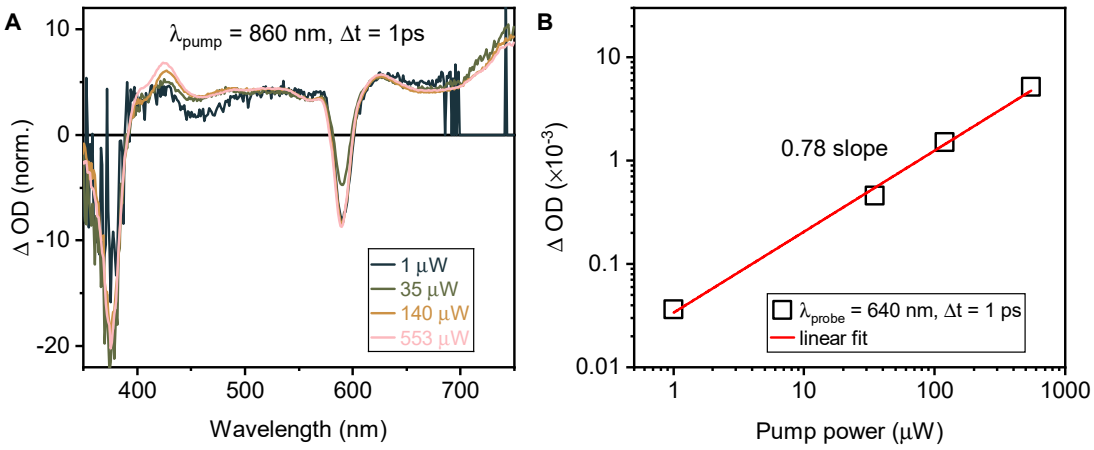

Fig. B.9 – (**A**) Normalized transient absorption spectra of the Crtless–RC–LH1 complex from *Rba. sphaeroides* for delay time of 1 ps after BChl *a* Q_y excitation at 860 nm with pump power from 1–553 μW (200 μm diameter pump spot, 5 kHz rep. rate). (**B**) Dependence of the ESA signal at 640 nm on the pump pulse power. The red line in the log-log plot is the best fit of the experimental data (squares) and has slope 0.78.

Fig. B.9A shows the normalized transient absorption spectra of the Crtless–RC–LH1 complex recorded at delay time of $\Delta t = 1\,\text{ps}$ after Q_y excitation at 860 nm at the power from $1 - 553\,\mu\text{W}$. The excitation power dependence of the

excited-state signal of Q_y state at wavelength of 640 nm and delay time of 1 ps is shown in fig. B.9B.

The figure shows that BChl *a* in RC–LH1 demonstrates weak non-linear behavior at fluences typical of our measurements. We observe both a sub-linear increase in ESA intensity with laser fluence (panel B) and a change in the normalized spectrum (panel A). Determining the reason for the spectral shape change at increased fluence is beyond the scope of this work. However, the relative increase in absorption at 425 nm coupled with the relative decrease in NIR absorption beyond 700 nm is reminiscent of the triplet spectrum in fig. B.8. We therefore hypothesize that sequential excitation in BChl *a* in RC–LH1 enables rapid (sub-picosecond) intersystem crossing through a high-lying state, generating a population of BChl *a* triplets. This non-linear formation of triplets (two photons generate a single triplet) means that triplet yield measurements[41] which use pulsed lasers should ensure that non-linear effects such as this are controlled for.

B.6 Transient absorption spectroscopy for the RC–LH1 complex after Crt excitation

B.6.1 Transient absorption measurements

The time-resolved transient absorption spectra for the RC–LH1 complex containing neurosporene after S_2 excitation at 500 nm are displayed in fig. B.10. The data were acquired up to delay times of 7 ns. Two probe spectra cover the range from 340–735 nm and 750–830 nm. The signals build-up from 0.055 ps to 0.5 ps indicates that both Crt and BChl triplets are formed within our instrumental response function.

B.6.2 Global analysis

The molecular dynamics of the RC–LH1 complex containing neurosporene were quantitatively evaluated by a Glotaran global analysis.[233] An adequate fitting with six components was performed to compare with the previous results on Neu–RC–LH1 from Niedzwiedzki *et al.*[44]. The global analysis results of evolution-associated absorption difference spectra (EADS) with associated time constants are shown in fig. B.11A. The spectra and time constants are in very good agree-

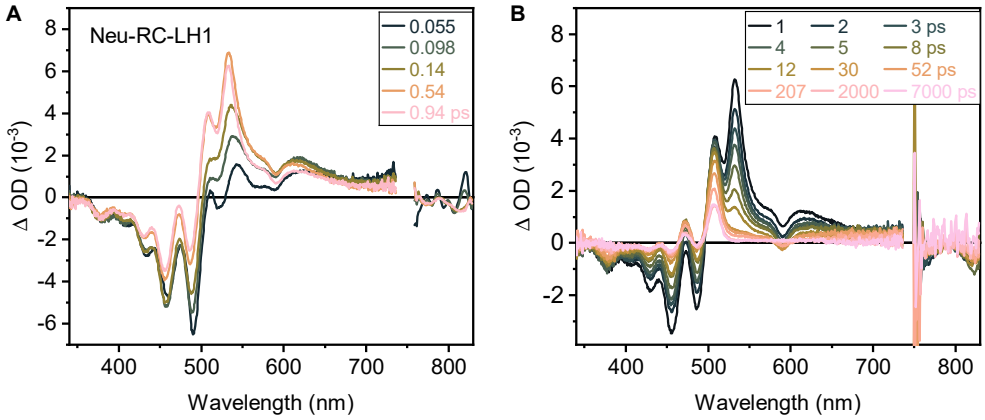

Fig. B.10 – Transient absorption spectra of the RC–LH1 complex containing neurosporene after S_2 excitation at 500 nm for probe wavelengths from 340–830 nm and pump–probe delay times between 0.055–1 ps (**A**); between 1–7000 ps (**B**).

ment with that in Ref.[44]. The target analysis with the kinetic model in Fig. 4E unfortunately failed to present the species spectra that we clearly observed in the raw data. For example, the species with a time constant of $\sim$ 5 ps is assigned to Neu S_1 but the target-analysis spectrum also contains the contributions from Neu T_1 and BChl states.

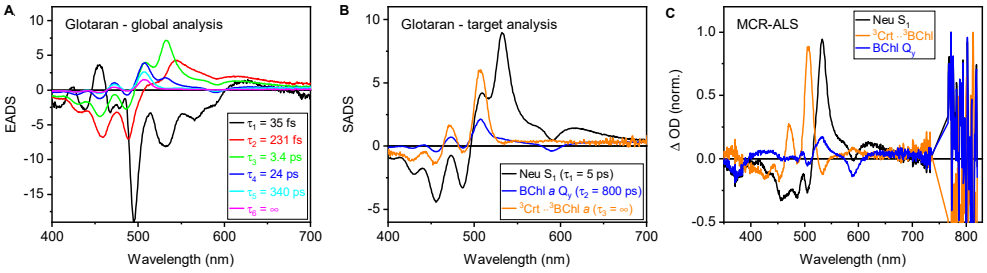

Fig. B.11 – (**A**) Evolution-associated absorption difference spectra (EADS) of photo-excited Neu–RC–LH1 obtained *via* singular value decomposition-based Glotaran global analysis.[233] The dataset of 400–700 nm, -0.5–7000 ps was used for comparison with literature.[44] (**B**) Species associated absorption difference spectra (SADS) obtained by Glotaran target analysis using a kinetic model in Main Text Fig. 4E. The dataset of 1–7000 ps was used.(**C**) Species spectra extracted by MCR–ALS global analysis. The dataset of 350–820 nm, 1–7000 ps was used to simplify the photophysics of excluding of Neu S_2 and BChl Q_x states.

In addition to using Glotaran, which relies on first-order rate target models, we implemented model-free MCR–ALS analysis. We truncated the dataset to 1–7000 ps to exclude the initial S_2 and Q_x states to concentrate on the states

we are more concerned with here: S_1, Q_y, and (T··T). The MCR–ALS-extracted spectra are displayed in fig. B.11B. Unfortunately, we observe clear correlations between spectra. Although the algorithm produced a Neu S_1 spectrum that is similar to reference spectra and uncorrelated with the other spectra, correlations were always found to be present at 520 nm and 780 nm in the other two spectra (orange and blue). The algorithm cannot therefore successfully separate states beyond S_1, perhaps because the spectra are too similar or their signals are too weak (compared to the Neu transient signals). We ran the algorithm with different starting conditions, different numbers of states and on different data sets, but could find no combination that generated uncorrelated spectra.

B.6.3 Carotenoid excited triplet state absorption spectra

To identify that the carotenoid triplet state is generated, we did the transient absorption experiments on RC–LH1 complexes containing neurosporene, spheroidene, lycopene, and 2,2'-diketo-spirilloxanthin and compared the transient spectra with that in the literature of sensitisation experiments on the corresponding carotenoid in organic solvent.

The sensitization experiments were carried out in *n*-hexane. Carotenoids in light harvesting protein which is a highly polarizable environment are in close contact with BChl *a* molecules. The spectra of carotenoids in RC–LH1 complexes differ by a general wavenumber shift due to the higher polarizability of protein environment. The effect of the solvent polarizability on the carotenoid $S_1 - S_2$ electronic transitions[139] explains the shift in carotenoid transient spectra upon binding to the light harvesting complex.

The carotenoid $T_1 \rightarrow T_n$ excited state absorption bands were obtained by nanosecond pump-probe setup after excitation at 532 nm at delay time of 1 μs (figB.12), which are in line with the spectra after triplet-sensitized excitation. The peak (0-0 vibration) of carotenoid excited triplet state absorption locates at 507 nm for neurosporene, 526 nm for spheroidene, 546 nm for lycopene, and $\sim$ 625 nm for 2,2'-diketo-spirilloxanthin. The excited triplet state decays are slow within the displayed time window, while the signal of the S_1 band disappears within < 20 ps as seen in main text (Fig. 3). It should be noted that the apparent initial decay of the carotenoid triplet band is caused by the 0-1 vibronic band of the carotenoid S_1 state.

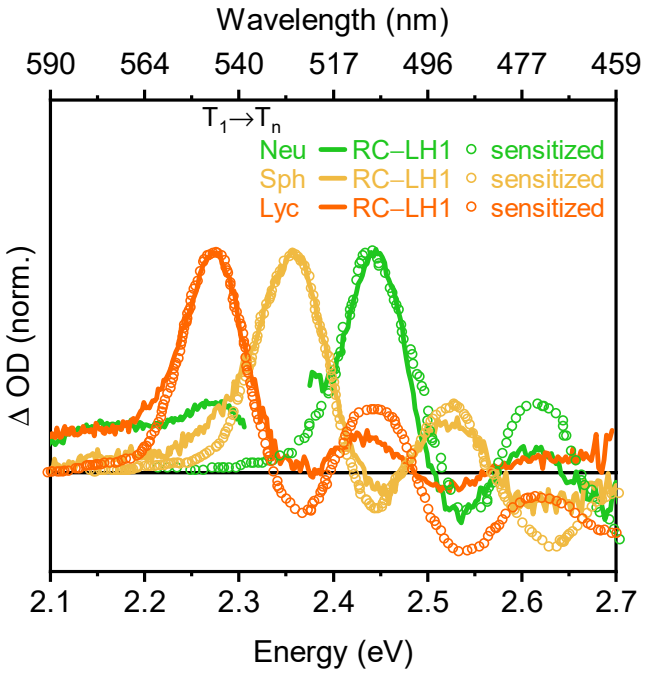

Fig. B.12 – (**A**) Transient absorption spectra of the RC–LH1 complex containing neurosporene, spheroidene, lycopene (solid, $\Delta t = 5\,\mu s$) were measured by nanosecond transient absorption spectroscopy. Carotenoid excited triplet state spectra were obtained at $1.8\,\mu s$ after triplet-sensitized excitation (circles). (**B**) The kinetic traces of carotenoid $S_1 \rightarrow S_n$ excited state absorption at probe wavelength of 540 nm for neurosporene, 560 nm for spheroidene, 575 nm for lycopene, and ~655 nm for 2,2'-diketo-spirilloxanthin. Probe wavelengths are selected to minimize overlap with carotenoid excited triplet state absorption and BChl *a* Q_x ground state bleach signals.

B.6.4 Long-lived carotenoid triplet state

The two-dimensional transient absorption maps for RC–LH1 complexes containing neurosporene, spheroidene, lycopene, and 2,2'-diketo-spirilloxanthin after excitation at 532 nm are shown in fig. B.13 (left panels). The probe spectrum covered the range from 470 to 700 nm by using supercontinuum generation (SCG) in a sapphire plate. The data were acquired up to $\Delta t = 50\,\mu s$, using a linear time scale up to 11 ns and a logarithmic time scale from 11 to 50000 ns. Each map features a prominent long-lived ($\sim \mu s$) excited-state absorption band.

The time profiles of carotenoid $T_1 \rightarrow T_n$ ESA bands at probe wavelength of 508 nm (neurosporene), 490 nm (spheroidene), 545 nm (lycopene), and 630 nm (2,2'-diketo-spirilloxanthin) show independence on the excitation density (right panels in fig. B.13). Triplets of neurosporene and spheroidene are formed within IRF directly followed by a slow decay and independently on the excitation intensity, indicating a geminate triplet pair state generated by singlet fission.

In the case of the RC–LH1 complex containing lycopene or 2,2'-diketo-spirilloxanthin, singlet fission is inefficient (main text). A delayed rise of the carotenoid triplets may results from the triplet energy transfer ($\sim$ 100 ns) from BChl *a* triplet state. BChl *a* triplets are produced *via* intersystem crossing from BChl *a* singlet states that are populated through carotenoid EET or upon direct BChl *a* excitation at 532 nm.

B.7 Discussion of Spn S_1 energy

Crt S_1 energies have been reported using different experimental methods. The generally accepted Spn S_1 energy is 1.61 eV extracted from transient absorption spectroscopy,[345,375] but this energy seems inconsistent with our findings in the main text (Fig. 5). We therefore re-examine the estimated Spn S_1 energy.

The generally accepted neurosporene and spheroidene S_1 energies were determined by using fluorescence spectroscopy[279]. When we use the reported linear regression of S_1 energies with respect to the conjugation lengths ($E(S_1) = 220946 \times \frac{1}{2N+1} + 3681$) we estimate the Spn S_1 energy to be 1.70 eV ($N = 10.5$). The S_1 energies of Crt molecules with longer conjugation lengths were also predicted by using S_1 lifetimes and the energy gap-law.[275,400] Using this energy gap-law we estimate the Spn S_1 energy to be 1.70 eV ($\tau = 6$ ps[345]).

As described above, the Crt S_1 energies were also estimated using transient

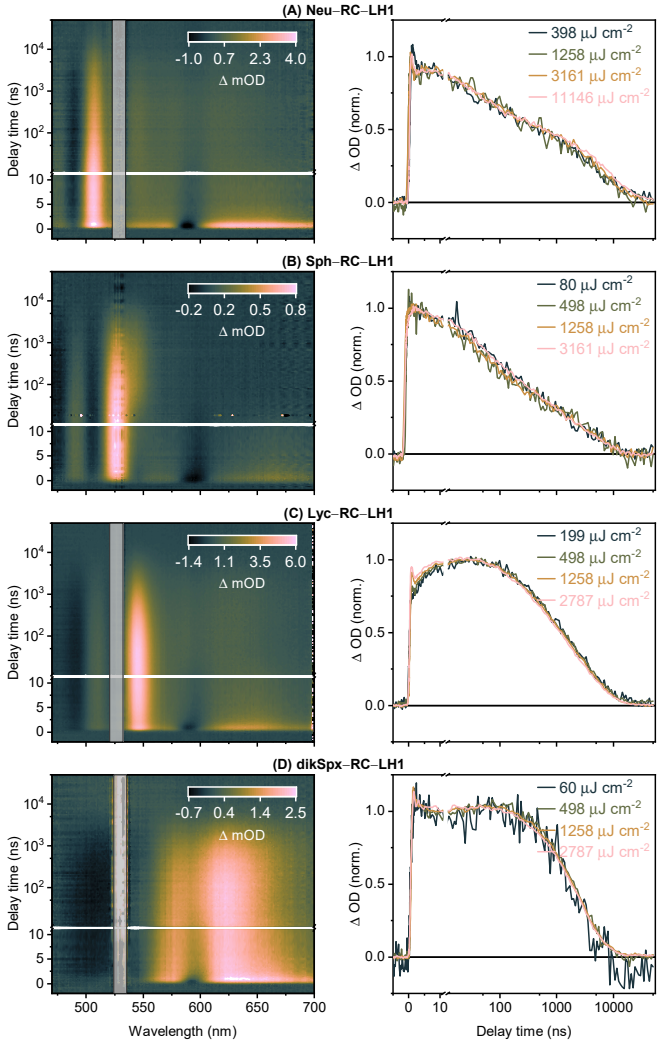

Fig. B.13 – Transient absorption results for RC–LH1 complexes from containing (**A**) neurosporene, (**B**) spheroidene, (**C**) lycopene, and (**D**) 2,2'-diketo-spirilloxanthin upon excitation at 532 nm. The left panels show two-dimensional maps and right panels representative kinetic profiles. The kinetics of carotenoid excited triplet state exhibit no excitation density dependence.

absorption spectroscopy,[345] resulting in a Spn S_1 energy of 1.63 eV. Zigmantas *et al.* used the same technique and reported the energy to be about 1.61 eV.[375]

Table B.1 – Crt S_1 energies estimated using different reported methods.

method	TA spectroscopy[345,375]	fluorescence spectroscopy,[279] energy gap law with S_1 lifetimes[275,400]
Crt	S_1 energy (cm^{-1})	
Neu	14170	15300
Sph	13160	14202
Spn	12800	13724
Lyc	–	13394
rhodopin glucoside	12400	–
Spx	–	11926

With the comparison of the two datasets (Table B.1), it is noted that the transient absorption (TA) results always show a blue shift compared with the fluorescence or energetic gap-law values. Indeed, we find that the TA-obtained value matches the fluorescence 0-1 peak instead of the 0-0 peak. This inconsistency is interesting but we leave further discussion of it to later work and note only that the Spn S_1 energy follows the conjugation length trend of other Crts, despite the presence of an ICT state.

B.8 Triplet yield determination

The concentrations of the triplet state of Crts (neurosporene, spheroidene, spheroidenone, and lycopene) and BChl *a* were directly calculated from TA spectroscopy at pump-probe delay time at $\Delta t = 100\,ps$ and $\Delta t = 2\,ns$, respectively, by using the Lambert-Beer law. The concentration of the carotenoid S_2 state in each case was estimated by the size of the initial ground state bleach amplitude based on the molar extinction coefficients. The extinction coefficients of carotenoid T_1 and S_2 and BChl *a* T_1 are listed in Table B.2.

The triplet state quantum yields of carotenoids and BChl *a* in RC–LH1 complexes after carotenoid S_2 excitation were calculated by comparing the concentration of the triplet state with that of the carotenoid S_2 state. The resulted singlet fission generated triplet yields are collected in Table B.2.

Table B.2 – Extinction coefficients (ϵ) of Crt T_1 and S_2 and BChl *a* T_1, transient signal intensities of excited state absorption (ESA) of Crt T_1 ($\Delta t = 100\,ps$) and BChl *a* T_1 ($\Delta t = 2\,ns$) and initial ground state bleach (GSB) of Crt S_2 for RC–LH1 complexes after Crt S_2 excitation by TA spectroscopy, estimated triplet quantum yields (Φ_T) of Crt and BChl *a* generated *via* singlet fission.

RC–LH1 complex	ϵ^a Crt T_1 (M^{-1} cm^{-1})	ϵ^b Crt S_2 (M^{-1} cm^{-1})	ϵ^c BChl *a* T_1 ($M^{-1}cm^{-1}$)	ESA‡ Crt T_1 (ΔOD)	GSB§ Crt S_2 (ΔOD)	ESA‡ BChl *a* T_1 (ΔOD)	Φ Crt T_1 (%)	Φ BChl *a* T_1 (%)
Neu	2.74E5	1.594E5	1.036E4	2.36E-3	-5.10E-3	8.60E-5	27.0	26.0
Sph	3.09E5	1.736E5	1.036E4	5.68E-4	-3.80E-3	1.60E-5	8.4	7.1
Spn	6.06E4	1.220E5	1.036E4	2.37E-4	-3.50E-3	8.00E-5	13.6	26.9
Lyc	4.95E5	1.815E5	1.036E4	7.67E-5	-8.12E-4	1.00E-6	3.5	2.2

[a] from Ref.[355], [b] from Ref.[401], [c] from Ref.[393], ‡ ESA is for excited state absorption, § GSB is for ground state bleach.

B.9 Estimates of Crt-to-BChl *a* EET

B.9.1 Overall Crt-to-BChl *a* EET by static spectroscopy

Details of static spectroscopy measurements are provided in section B.1. Overall Crt-to-BChl *a* singlet energy transfer efficiency was obtained from comparison of absorptance (1−T, where T is transmittance) and fluorescence excitation spectra. These spectra are plotted in fig. B.14. We determined ratio of the peak intensities at the 0–0 carotenoid $S_0 \rightarrow S_2$ transition where the contribution from BChl *a* is minimal to that in the absorptance spectrum. The fluorescence excitation spectra in fig. B.14 were corrected for the excitation lamp spectrum and response spectrum of the detector and then normalized at the BChl *a* Q_y band.

The overall Crt EET efficiency listed in Table B.3 is the mean value, obtained by averaging 10 nm around the Crt 0–0 vibronic peak. The error is given by 2σ (standard deviation).

Table B.3 – S_1 time constants in solvent and in LH1 complex used to estimate EET efficiency from $S_1 \rightarrow Q_y$, experimentally determined overall EET efficiency with 2σ given as error in parentheses, EET from all different paths.

	S_1 lifetime (ps)			EET efficiency (%)			
	LH1	solution	reference	overall	$S_2 \rightarrow Q_x$	$S_1 \rightarrow Q_y$	$(T\cdot\cdot T) \rightarrow Q_y$
Neu	5	24	Ref.[345]	81 (4.6)	0	73	27
Sph	4.7	9.3	Ref.[402]	72 (2.8)	44	48	8
Spn	2.2	6	Ref.[345]	87 (3)	64	23	13
Lyc	4.5	4.7	Ref.[402]	51 (5)	50	47	3
dikSpx	1.7	1.5	Ref.[403]	35 (5)	35	65	0

B.9.2 Estimated Crt-to-BChl EET from all paths: S_2, S_1 and $(T\cdot\cdot T)$

The $S_2 \rightarrow Q_x$ EET efficiency is the most difficult to estimate, due to the widely different, often model-dependent,[404] values reported in the literature for the same complex. We therefore used best-guess estimates by scaling spectral overlap factors[345] with a broadly accepted experimental value for rhodopin glucoside ($N = 11$),[405] see fig. B.15. These estimates avoid problems associated with

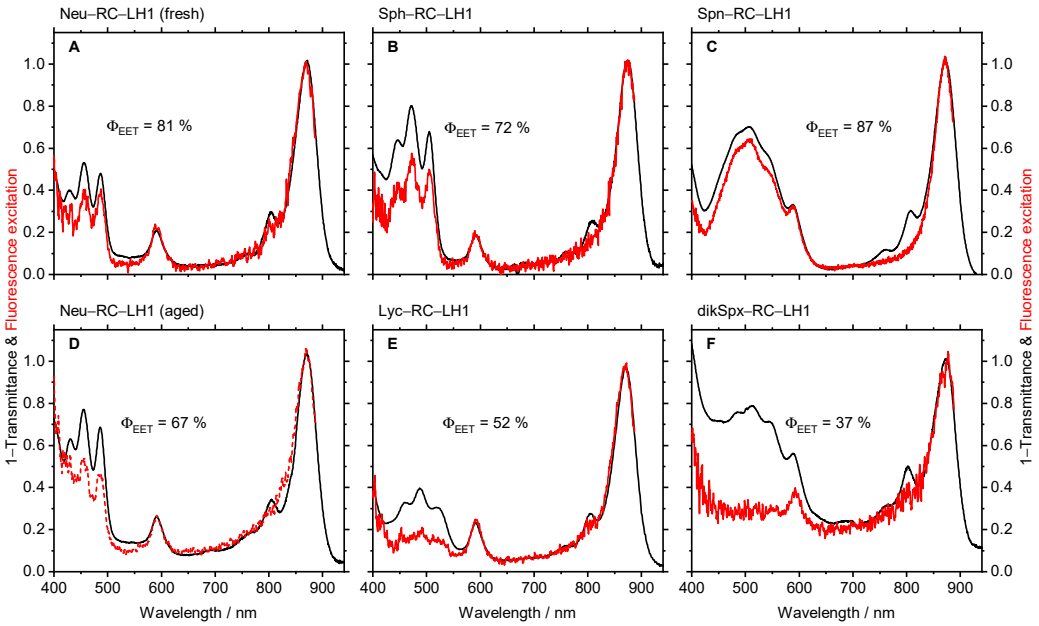

Fig. B.14 – 1–transmittance (black line) and fluorescence excitation (red line) spectra of RC–LH1 complexes containing Neu (**A**), Sph (**B**), Spn (**C**), Lyc (**E**), and dikSpx (**F**). The overall exciton energy transfer efficiency (Φ_{EET}) is displayed in each panel. We note that these spectra were measured within hours of purification and found that Φ_{EET} values obtained on older Neu–RC–LH1 samples had dropped to 67% (**D**).

model-dependent values,[404] but they should nevertheless be treated with caution.

The relative population of S_1 depends on the $S_2 \rightarrow Q_x$ EET efficiency and Φ_T from Fig. 4A and Table B.2 and we thus calculate it as ($100 - \Phi_{EET}^{S_2 \rightarrow Q_y} - \Phi_T$). Then, the $S_1 \rightarrow Q_y$ EET efficiency was estimated by comparing the measured S_1 lifetime from Fig. 3 with those reported in solution[345,402] using $\Phi_{EET} = \left(1 - \frac{\tau_{S_1}^{LH1}}{\tau_{S_1}^{Sol}}\right) \times 100$ (Neu: 79%, Sph: 49%, Spn: 63%, Lyc: 4%, dikSpx: 0%).[345]

Finally, the $(T \cdot\cdot T) \rightarrow Q_y$ energy transfer efficiency was estimated by making up the difference to total Φ_{EET} from Fig. 4B and fig. B.14.

Note that the value for Neu reported in the main text is different from the estimates here, as in the main-text we have used the $S_2 \rightarrow Q_x$ efficiency value (0%) reported by Niedzwiedzki *et al.*[44].

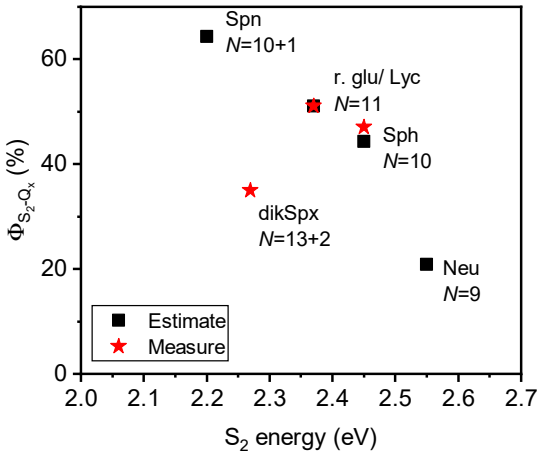

Fig. B.15 – Best-guess estimates of $S_2 \rightarrow Q_x$ energy transfer efficiencies (black squares) obtained by scaling spectral overlap factors reported in Ref.[345] by the broadly accepted experimental value for rhodopin glucoside ($N = 11$).[345] Red stars are measured values for comparison, rhodopin glucoside from Ref.[405], dikSpx from this work and Sph from Ref.[406].

Appendix C

Preliminary: OCPo is relatively emissive compared to OCPr

We briefly outline our preliminary experiments showing that CAN-OCPo in trehalose appears to be relatively emissive compared to CAN-OCPr in trehalose.

CAN-binding OCPo and OCPr in trehalose was prepared as per the methodologies of Sections 3.2.1 and 3.3, notably without glass cover slip encapsulation. The OCPo/OCPr emission spectra were obtained using a home-built setup incorporating an intensified detector. Briefly, a quasi-CW 532 nm pump was generated by a Q-switched Nd:YVO_4 laser (Picolo AOT 1, Innolas; 4 kHz, <800 ps nominal FWHM) outfitted with integrated harmonic modules for frequency-doubling and synchronised with the detector. Laser power was ∼100 µW near the sample position. To prevent damage to the detector from scattered 532 nm pump, a combination of a 532 nm notch filter (NF533-17, Thorlabs) and a 550 nm longpass filter (OG550, Schott) were placed before detection. The emission was measured using an intensified CCD (iStar DH334T-18U-73, Andor) coupled to a spectrograph (Shamrock 303i, Andor). The iCCD was cooled to −30 °C by a Peltier element during measurements. The grating used in the spectrograph has 150 lines mm^{-1} and is blazed at 500 nm. Initial use of the setup was assisted by David G. Bossanyi.

While both the OCPo and OCPr forms show weak fluorescence emission in-line with β-carotene-like ($N_{\text{eff.}} \approx 9.6$) carotenoids,[150] OCPo appears to be relatively emissive compared to OCPr in trehalose. Emission spectra of OCPo and OCPr are shown as green and blue lines (respectively) in Figure C.1, normalised to the red-end tails (∼650 nm) for comparison. It is apparent that the emission of OCPr follows the profile of that of OCPo, with divergence within the absorbance region of OCPr (see thick black line for OCPr absorbance normalised to the maximum).

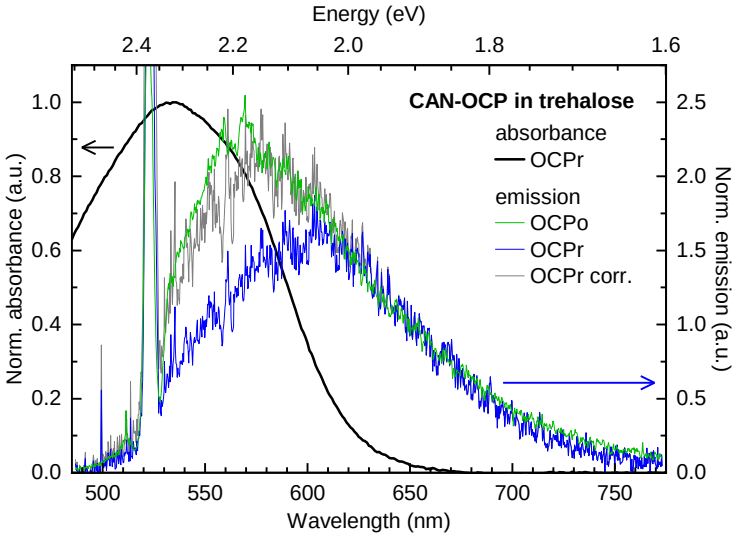

Figure C.1 – Normalised emission spectra of CAN-binding OCPo (green) and OCPr (blue) in trehalose, with absorbance of OCPr (black) used to obtain corrected OCPr emission (grey) accounting for self-absorption. Emission spectra are normalised to average one in the 647–653 nm range (before self-absorption correction). To obtain emission spectra, the films were excited with a 532 nm, ∼100 µW pump. The OCPr absorbance is normalised to its maximum of $A_{\max} \approx 0.5$. We emphasise that these are preliminary measurements.

We apply a self-absorption correction using the methodology of Ref.[223] to yield a corrected OCPr emission spectrum (grey line), which indeed further follows the profile of the OCPo emission.

We note that the emission spectra for CAN-OCPo and (corrected) CAN-OCPr in trehalose does not resemble those previously obtained in the literature for CAN-OCPo or 3′hECN-OCPo in buffer.[334] In particular, ours are significantly broader.

When these preliminary experiments were conducted, we studied trehalose samples without cover slip encapsulation, prone to atmospheric rehydration if stored improperly and permitting a small number of complete OCPo⇌OCPr transitions. It was probable that a small population of OCPo was present in the nominal OCPr sample, which yielded the OCPo-like emission spectrum (filtered by the main population of OCPr). It may be necessary to retry this preliminary measurement with our new sample designs incorporating cover slips, which protect the trehalose against atmospheric rehydration. We should note that no comparable measurement on blank trehalose glass was conducted in the preliminary measurements; emission from trehalose, sucrose, the imaging spacers, *etc.* of

comparable strength to OCPo/OCPr cannot be ruled out, despite the apparent optical transparency of the trehalose system demonstrated in other experiments throughout this thesis. Furthermore, the detector appeared to be miscalibrated by ∼10 nm during these preliminary measurements; note that the (partially filtered) 532 nm pump peak is present around 522 nm. This was left uncorrected in this rough analysis.

These preliminary measurements served as an inspiration for the construction of a transient grating photoluminescence spectroscopy (TGPLS) setup, outlined in Section 4.6. Indeed, time-resolving the emission from both OCPo and OCPr would yield information on their radiative and non-radiative decays, potentially giving insight into the mechanism of NPQ by OCPr bound to phycobilisomes.

Appendix D

New BODIPY dyes designed for polaritonics

BODIPY dyes have previously been dispersed in microcavities to make combined light-matter quasiparticles, cavity-polaritons. To date, these polariton studies have relied on dispersing the BODIPY molecules in a polymer matrix with doping loadings below 10% (by mass) to limit intermolecular interactions and thus prevent fluorescence quenching. However, the low loading leads to films with low optical density, limiting the potential of BODIPY dyes in polaritonic studies due to the low achievable Rabi splitting (coupling strength). Here we characterise the photophysical behaviour of six new BODIPY dyes designed to control intermolecular interactions, either by (1) enhancing theoretically emissive J-aggregate formation or (2) hindering quenching intermolecular interactions. We find that the BODIPYs designed to enhance aggregate formation produce thin films at high loading which are dominated ($66 \pm 3\%$ band area) by a strong, narrow (53 meV FWHM) J-aggregate absorbance band, with a Stokes shift of only 9 meV (quantities for a pure film with no polymer). On the other hand, the BODIPYs designed to avoid aggregate formation demonstrate monomer-like absorbance and fluorescence behaviour, even in thin films with pure loadings.

Acknowledgements: Andrew J. Musser conceived the project. The BODIPY dyes were synthesised and their energetics calculated by Marco Cavazzini, Istituto di Scienze e Tecnologie Molecolari (ISTM), Consiglio Nazionale delle Ricerche (CNR). Daniel W. Polak initially assisted with solution and film sample preparation. Kyriacos Georgiou demonstrated the thermal evaporation system and assisted with the goniometer and PLQY measurements. Rahul Jayaprakash wrote the microcavity simulation program. Kirsty E. McGhee demonstrated the sur-

face profilometer. Claire Greenland initially assisted with temperature-dependent measurements and maintained the experimental setup. James P. Pidgeon prepared all solutions and films, performed all experiments, and analysed all the data presented in this appendix.

D.1 Introduction

BODIPY dyes are a class of highly fluorescent organic dyes incorporating the BODIPY (4,4-difluoro-4-bora-3a,4a-diaza-s-indacene; boron-dipyrromethene) core molecule. They are relatively chemically stable, have high absorptions in the visible region, have high photoluminescence quantum yields (PLQYs), and have relatively small emission linewidths.[407] They have been extensively tested as biological labelling reagents[408–410] and chemosensors,[411–414] and within liquid dye lasers,[415,416] OLEDs,[417] and in dye-sensitised photovoltaic devices.[418]

BODIPY dyes have recently been explored as a polaritonic material by incorporation into microcavities, with strong coupling consistently demonstrated.[418–425] However, fluorescence quenching *via* intermolecular interactions at higher doping concentrations limits the BODIPY dye loadings to around 10%. This in turn limits the optical density and achievable Rabi splitting (coupling strength between exciton and photon modes), and overall limits current BODIPY structures as polaritonic dyes.

We are motived to design and characterise new BODIPY dye structures designed to control intermolecular interactions so that films of high loadings (high optical densities) with minimal fluorescence quenching can be fabricated. We can do this by either: (1) enhancing putatively emissive J-aggregate formation, or (2) hindering quenching intermolecular interactions.

D.2 Materials and methods

For solution measurements, the BODIPY dyes were dissolved in toluene (Sigma-Aldrich, CHROMASOLV Plus for HPLC, ≥99%, 650579-1L) to make up $5\,\mathrm{g\,l^{-1}}$ 'stock' solutions. This was further diluted to around $50\,\mathrm{mg\,l^{-1}}$ and pipetted into a 1 mm path length quartz cuvette. Daniel W. Polak initially assisted with solution preparation.

Solid samples were produced using quartz-coated glass substrates (Ossila, S151). These were cleaned beforehand by sonicating for 10 min in Hellmanex III

(Hellma, 9-307-011-4-507) in just-boiled water, then dipping in successive solvents (hot water, room temperature water, isopropanol), and blow-dried with a nitrogen gun. Once cleaned, some substrates were left under isopropanol and rinsed and dried when needed, although some were stored in air in a polystyrene box. Daniel W. Polak demonstrated the cleaning procedure.

To produce dye-dispersed polymer matrices, polystyrene (Aldrich, average $M_W \sim 192000$, 430102-1KG) was left to dissolve at room temperature in toluene over about a week, making a $25\,\mathrm{g\,l^{-1}}$ 'stock' solution. Different quantities of solid and solution BODIPY dyes and the stock polystyrene solution were used to make the required mass loadings of BODIPY dye and polystyrene in toluene. These solutions were used to make films by spin-coating; the solutions were usually dynamically pipetted onto the spinning substrates and left spinning for about 40 s. Daniel W. Polak initially assisted with solution and film sample preparation.

To produce Ag-Ag microcavities, a bottom silver (Ag) mirror of thickness 200 nm is deposited onto a cleaned substrate using a thermal evaporator (Angstrom Engineering). An active layer of BODIPY dye in a polystyrene matrix is then spun onto the mirror as above, with its thickness tuned by changing the spin-coater spin speed. Finally, a top Ag mirror of thickness 35 nm is deposited on top using the thermal evaporator. Initial instruction of the thermal evaporator system was by Kyriacos Georgiou.

Absorbance and emission spectra of the BODIPY dye solutions and films were taken at room temperature ($T \sim 19\,^\circ\mathrm{C}$) using a Horiba FluoroMax-4 fitted with a Xenon lamp. Emission is collected at right angle (90°) to the incident lamp light. For solutions, normal incidence of the lamp light on the cuvette was used for both absorbance and emission measurements. For films, normal incidence was used for absorbance measurements, while for emission measurements an off-normal angle tuned away from the emission collection (about $-15°$) was used in attempt to maximise signal-to-noise ratio. No self-absorption correction has been applied to the emission data taken with this system shown in this appendix.

Surface profilometry was undertaken using a Bruker DektakXT and the Vision64 software. Solid film thicknesses were found by scratching the films with tweezers and scanning over the scratches with the stylus. The depth of the scratches was found using the software, and a mean depth (from around 5 to 10 depths) was taken as the film thickness. Root mean square surface roughness was found by scanning over an unscratched region and using the software's Pq function. The equipment and software was demonstrated by Kirsty E. McGhee.

Angular white-light reflectivity and emission measurements were undertaken with a goniometer setup consisting of two arms mounted on two concentric motorised arms. For angular white-light reflectivity measurements, the first arm controls the external angle of the incident light onto the microcavity, while the second arm adjusts to collect reflected light from the microcavity. White light from a fibre-coupled Ocean Optics DH-2000 Halogen-Deuterium lamp is focused onto the surface of the microcavity using collimating and focusing lenses on the first arm. The reflected light is collected by two lenses and focused into a fibre optic mounted on the second arm, in turn coupled to an Andor Shamrock CCD spectrometer. Both arms scan an angle θ (external angle of incidence of light onto the microcavity) from 10°–70° with an angular resolution of 1° in reflectivity measurements. For angular emission measurements, the microcavities are excited with a 405 nm laser diode, angled slightly down against the normal to avoid direct reflection into the CCD camera. Emission is collected by second arm, similarly to the reflected light in the reflectivity measurements. The first arm remains fixed, while the second arm scans from 0°–70° with an angular resolution of 1° in emission measurements. Note that the spot studied on the microcavity changed between reflectivity and emission measurements. Spectra taken with both the transverse electric (TE; electric field is orthogonal to the microcavity plane of incidence) and transverse magnetic (TM; magnetic field is orthogonal to the plane of incidence) polarisations were taken, in addition to spectra of the TE polarisation only, achieved using a polariser placed just before the spectrometer. Assistance with the goniometer measurements made in this chapter was provided by Kyriacos Georgiou.

Photoluminescence quantum yield (PLQY) measurements were performed with an integrating sphere setup. The films were mounted inside the sphere and excited using a 532 nm laser diode at an angle of incidence around 30°. The emission is collected into an optical fibre and directed to an Andor Shamrock CCD spectrometer. The data was analysed following that of Refs.[426,427] – in short, a self-absorption correction was made based on a separate emission measurement of the same sample without the integrating sphere. Estimations of the errors in the PLQY were based on measured fluctuations in both the laser light and the sample emission seen in at least 5 experimental replicates. Assistance with the PLQY measurements was provided by Kyriacos Georgiou.

For temperature-dependent steady-state emission measurements, a 405 nm laser (Thorlabs CPS405) is used to excite the sample, and emission is collec-

ted in a reflectivity-like geometry into an optical fibre connected to an Ocean Optics HR2000+ES spectrometer. The sample is held within an Oxford Instruments OptistatDry BLV cryostat used with liquid helium. Samples were initially cooled down to 5 K, and emission measurements were taken at different set temperatures, back up to room temperature. No self-absorption correction has been applied to the emission data taken with this system shown in this appendix. Maintenance of the setup and initial assistance in measurements was by Claire Greenland.

D.3 Results

D.3.1 BODIPY dye structures

All six BODIPY dyes were synthesised by Marco Cavazzini, Istituto di Scienze e Tecnologie Molecolari (ISTM), Consiglio Nazionale delle Ricerche (CNR). Their structures are shown in Figure D.1. J1 and J2 are designed to enhance the formation of J-aggregates. M1 and M2 are designed to have minimal intermolecular interactions, due to the bulky substituents on the 2,6 positions. Note that M1 is a 50:50 mixture of atropisomers. R1 and R2 are smaller (with a smaller π-conjugated region). Calculations by Marco Cavazzini suggest favourable energetics for singlet fission in R1 and R2; an experimental investigation of R1 and R2's singlet fission reactivity is currently underway by Daniel Z. Hook.

D.3.2 Steady-state spectra

Normalised room-temperature spectra for J1, J2, M1, M2, R1, and R2 are shown in Figures D.2, D.3, D.4, D.5, D.6, and D.7 respectively. In all spectra, we see 'monomer' peaks towards the blue end in both absorbance and emission. Vibronic progressions are visible in the absorbance spectra, and, going from solution to films with increasing loading, the ratio of heights between the 0-0 peak and other peaks decreases. In emission, the same effect on the peaks is true for going from solution into a low-loading film, but the ratio of heights between the 0-0 peak and other peaks instead increases as the film loading increases. The shifts in the peak positions towards the red end from solution to films with increasing loading (most clearly seen in M1's spectra in Figure D.4) can be partially attributed to the changing dielectric constant.

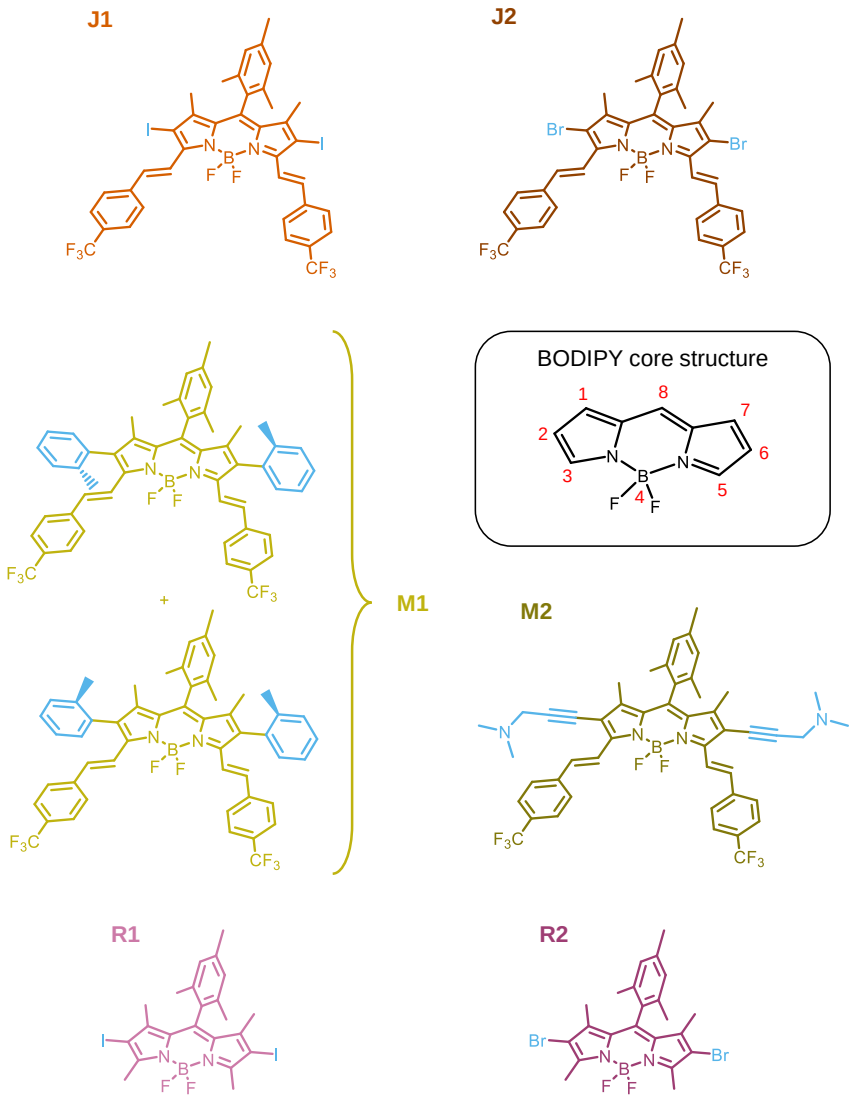

Figure D.1 – Skeletal structures of the BODIPY dyes. The BODIPY core is shown in within the box, and the six new structures are shown outside the box. J1 and J2 have been designed to enhance J-aggregate formation, while M1 and M2 have been designed to hinder intermolecular interactions. The distinct functional groups on the 2,6 positions are coloured blue. Synthesis by Marco Cavazzini.

For J1 and J2 in Figures D.2 and D.3, going from solution to films with increasing loading, new peaks appear and become more intense in both the absorbance and emission. These have relatively small FWHMs (33 meV for J2 at 60%, 53 meV for J2 at 98%), have small Stokes shifts (9 meV for J2 at 98%), and are relatively redshifted compared to the monomer peaks. These properties are typical of J-aggregates. They dominate the spectra at high film loadings, partic-

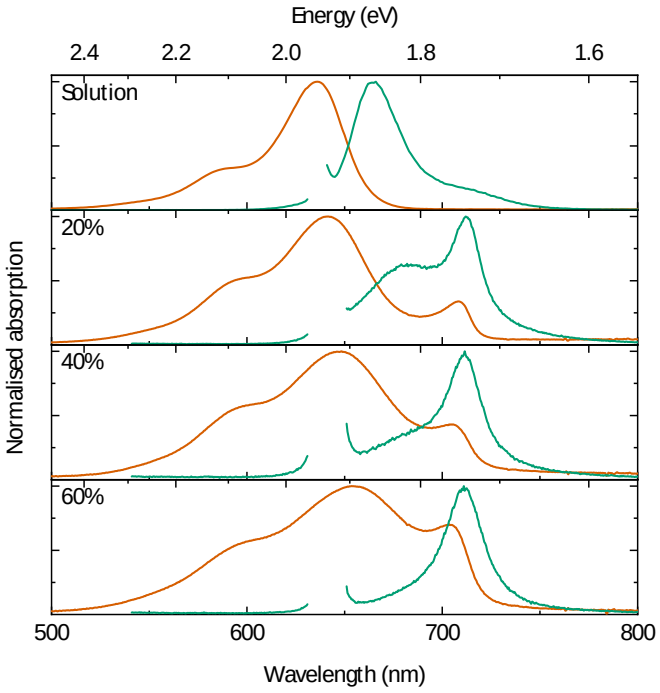

Figure D.2 – Normalised absorbance and emission spectra for J1, in solution and at various film loadings. Spectra are normalised to their maxima. For the emission spectra, the samples were excited at 641.0 nm, and no self-absorption correction has been applied.

ularly in J2; at 98% loading in a J2 film, this new peak has $66 \pm 3\%$ of the area of the absorbance spectrum (the bounds here reflecting different methods of fitting Gaussians and taking areas). Also note that for both J1 and J2 films there are long, low-intensity red tails of emission that increase in intensity with increasing loading.

For M1 in Figure D.4, there are no new spectral features between the solution and film, up to a 98% loading. It appears that M1 has no intermolecular interactions up to high loadings, and always behaves like a monomer. M2 in Figure D.5 (bottom) is similar to M1 in gaining no new features in its absorbance spectra, but its emission in the films gains a broad red tail and is overall weaker.

R1 and R2 in Figure D.6 and D.7 have their absorbance and emission monomer peaks more towards the blue end compared to the other BODIPY dyes, reflecting their reduced π-conjugated region size. R1 is similar to M1 and M2 – it shows no new peaks going from solution to films with increasing loading. However, R2 shows a moderately sharp (86.3 meV FWHM at 60% loading) emission feature towards the red end, which increases in intensity with increasing loading. This could be

due to emission of excited dimers (excimers) in the films, but those usually give broader emission features. Sharp emission features are more typically due to J-aggregates, although no absorbance due to J-aggregates is apparent in the film spectra, suggesting that (if present) they are at low concentration.

We note that for film measurements here, normal incidence was used for the absorbance measurements, while an off-normal angle tuned away from the emission collection was used for emission measurements in attempt to maximise signal-to-noise ratio (see Section D.2 for experimental methods). A possible angular dependence on the emission of the non-microcavity films was not considered here. The potential dependence on angle is currently being investigated by Daniel Z. Hook within the context of R1 and R2's possible singlet fission reactivity.

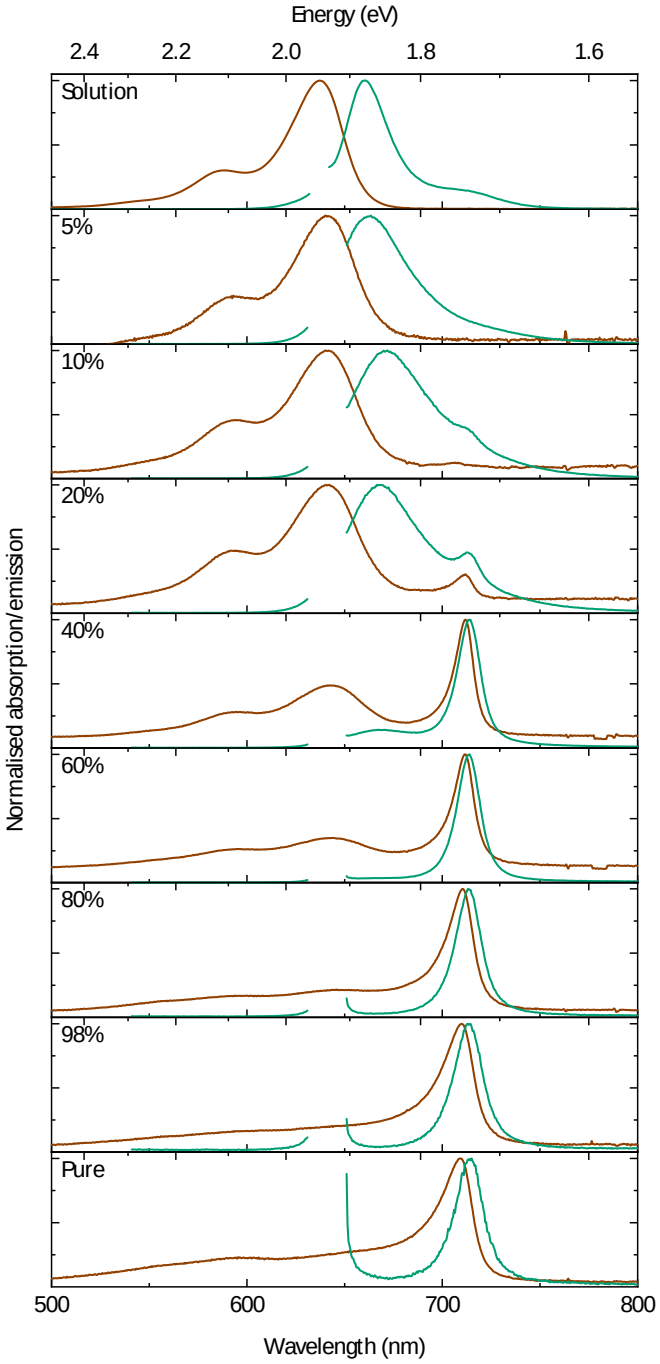

Figure D.3 – Normalised absorbance and emission spectra for J2, in solution and at various film loadings. Spectra are normalised to their maxima. For the emission spectra, the samples were excited at 641.0 nm, and no self-absorption correction has been applied.

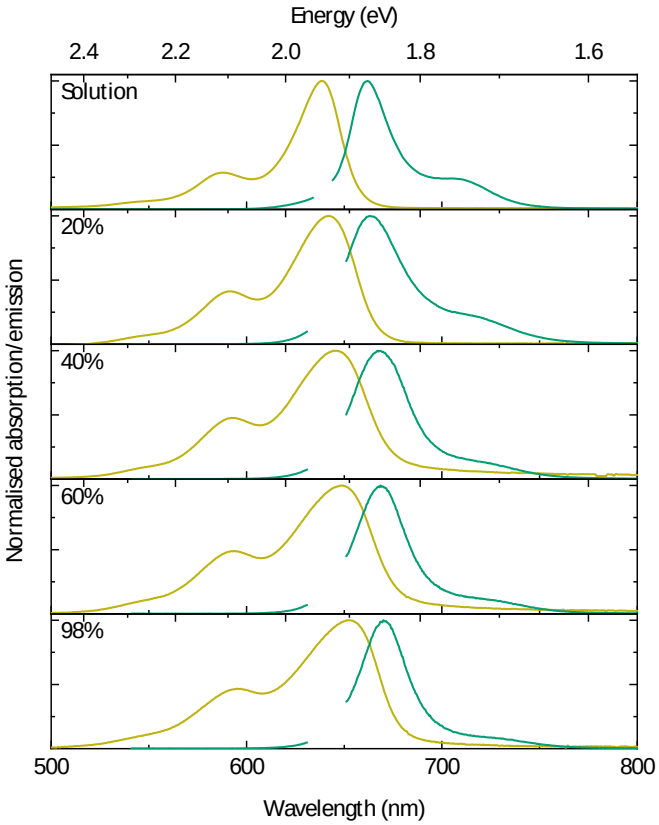

Figure D.4 – Normalised absorbance and emission spectra for M1, in solution and at various film loadings. Spectra are normalised to their maxima. For the emission spectra, the samples were excited at 641.0 nm, and no self-absorption correction has been applied.

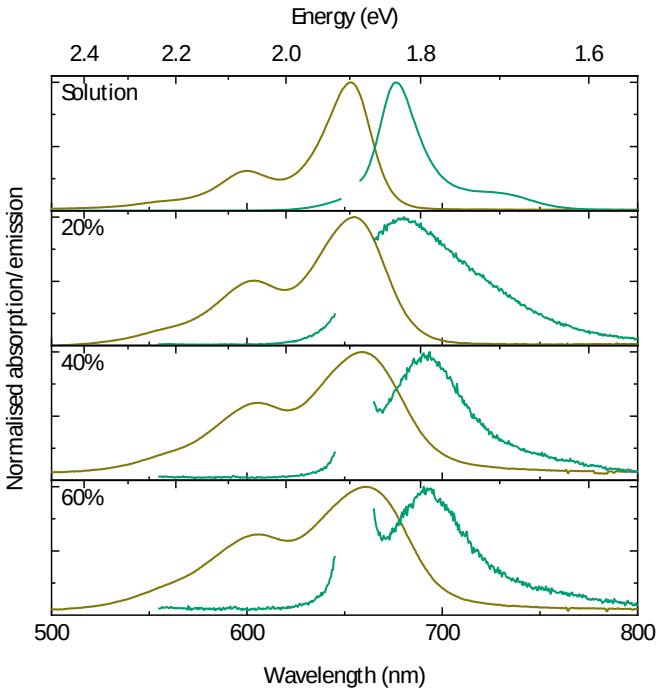

Figure D.5 – Normalised absorbance and emission spectra for M2, in solution and at various film loadings. Spectra are normalised to their maxima. For the emission spectra, the samples were excited at 641.5 nm, and no self-absorption correction has been applied.

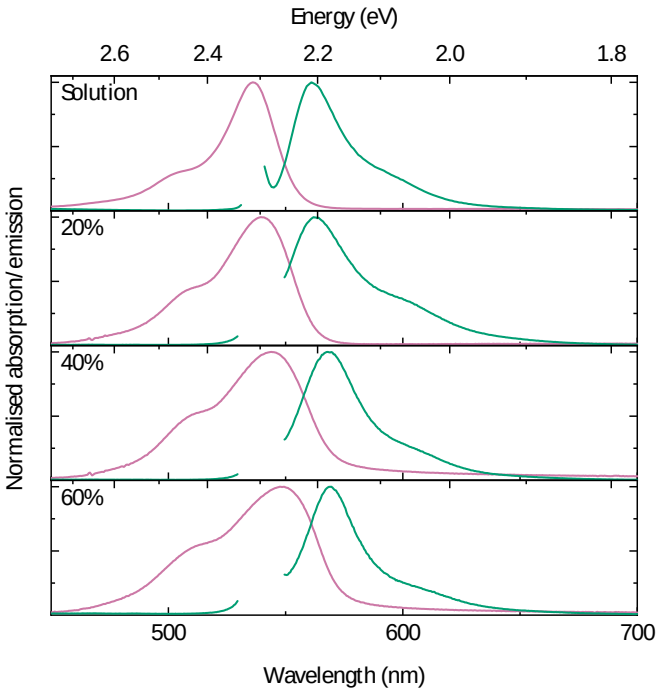

Figure D.6 – Normalised absorbance and emission spectra for R1, in solution and at various film loadings. Spectra are normalised to their maxima. For the emission spectra, the samples were excited at 539.5 nm, and no self-absorption correction has been applied.

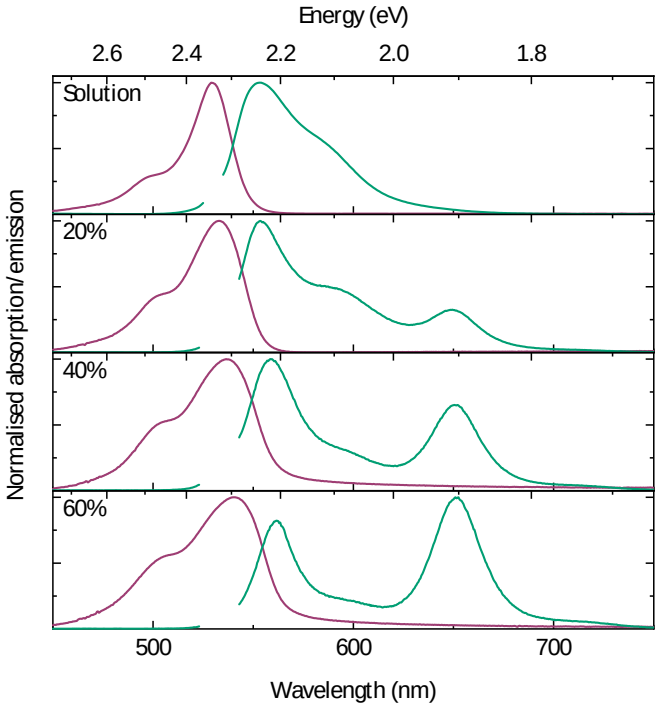

Figure D.7 – Normalised absorbance and emission spectra for R2, in solution and at various film loadings. Spectra are normalised to their maxima. For the emission spectra, the samples were excited at 533.0 nm, and no self-absorption correction has been applied.

D.3.3 Surface profilometry

Loading (%)	5	10	20	80	98
Thickness (nm)	172.2	170.7	66.0	9.4	8.0

Table D.1 – Thicknesses of J2 films at different loadings. All films here were spun-cast at 2000 rev min^{-1}.

The thicknesses of J2 films with loadings from 5% to 98% are shown in Figure D.1. Films with 5% and 10% loadings had sufficient thickness (∼170 nm) and smoothness (root mean square roughness typically <1 nm across a 100 µm length) for incorporation into microcavities. For 'films' with loadings ≥20%, the film thickness and quality degrades, with large crystalline structures (typically about 10 µm diameter and height) seen. Depths were measured along smooth regions of the samples, ignoring the isolated large crystalline structures. Root mean square roughness of the samples were typically <1 nm across a 100 µm length; this was also measured ignoring the large crystalline structures.

The thin and non-smooth 'film' morphologies at high loadings make incorporation of such films within microcavities impossible. Attempts at forming smooth films at high loadings while retaining the high-loading behaviour through use of different initial solvents and annealing techniques post-fabrication were not successful (see Section D.5.1).

D.3.4 Microcavities

Microcavity simulations incorporating a transfer-matrix method model indicated strong coupling in J2 microcavities using low dye loading. The simulation program was written by Rahul Jayaprakash.

Ag-Ag microcavities were fabricated incorporating 5% J2 in polystyrene as the active layer. The bottom silver (Ag) mirror has thickness 200 nm, the thickness of the J2 in polystyrene is tuned between 155-185 nm, and the semitransparent top Ag mirror has thickness 35 nm. Polarised (TE polarisation) white-light reflectivity and emission surfaces for these microcavities are shown in Figure D.8. Similar unpolarised (TE and TM polarisations) surfaces are shown in Figure D.14. Here we see clear splitting forming an upper polariton branch (UPB) and lower polariton branch (LPB). The anticrossing of the exciton and photon modes forms these branches, and is characteristic of strong-coupling.

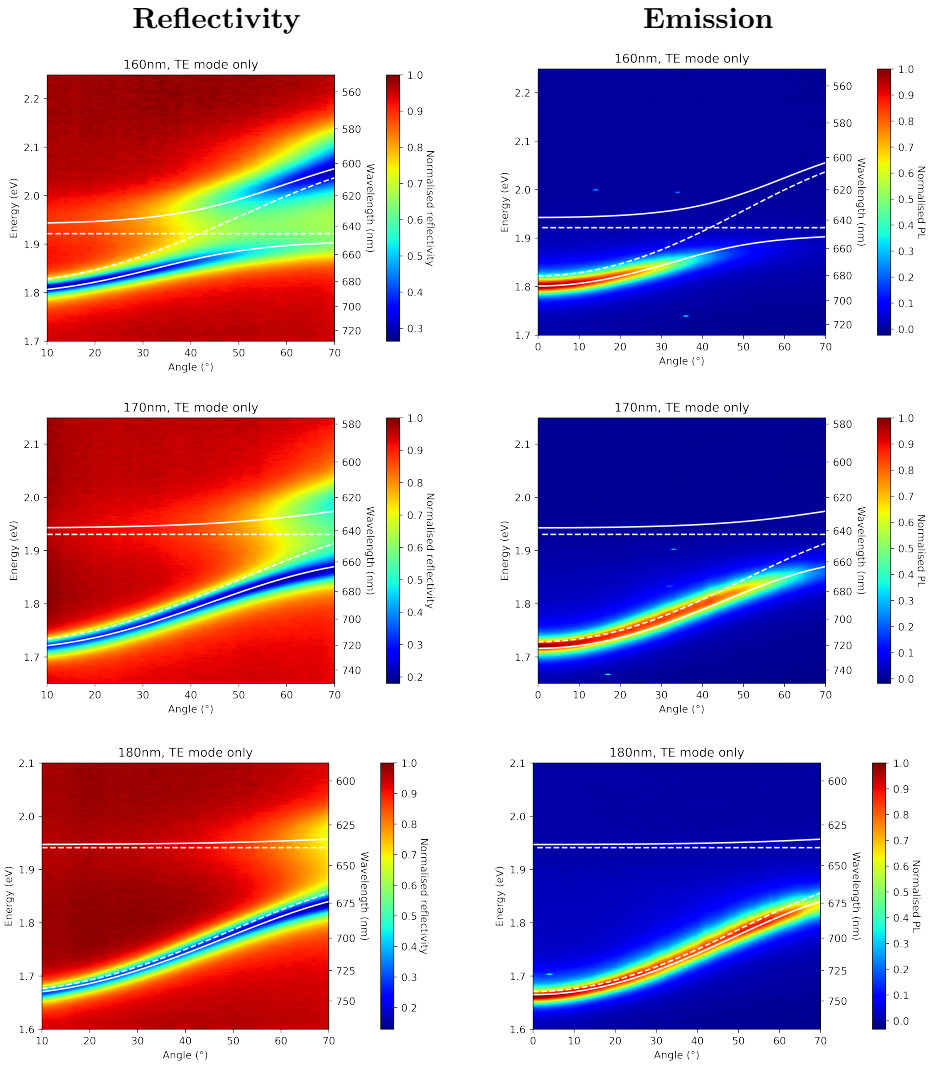

Figure D.8 – Polarised (TE polarisation) white-light reflectivity and emission surfaces of Ag-Ag microcavites with different active layer thicknesses incorporating 5% J2 in polystyrene. The LBP and UBP in the reflectivity surfaces are fitted (solid white lines) from a two-level coupled oscillator model, and the exciton and photon energies from the fit are indicated (dashed white lines). The fitted parameters are shown in Table D.2. The reflectivity fit is shown on the emission surfaces for comparison. Emission surfaces have been Jacobian-corrected. A polariser is used here, so only the TE polarisation is measured.

Active layer thickness (nm)	**UPB fitted (°)**	E_x **(eV)**	E_0 **(eV)**	δ **(meV)**	n	E_R **(meV)**
160	20–70	1.921	1.822	−99.41	2.104	100.4
170	25–70	1.930	1.728	−201.9	2.192	102.6
180	25–70	1.941	1.671	−270.4	2.160	119.9

Table D.2 – Fitted parameters from a two-level coupled oscillator model applied to the polarised white-light reflectivity surfaces of the Ag-Ag microcavities incorporating 5% J2 in polystyrene. The white-light reflectivity data is shown in Figure D.8. The region of the UPB fitted is noted. Note that $\delta = E_0 - E_x$ is a derived parameter.

We fit the polarised white-light reflectivity surfaces with equations derived from a classical two-level coupled oscillator. The full details on the fitting and the equations used are discussed in the Section D.5.2. The fit parameters are shown in Table D.2; E_0 is the minimum ($\theta = 0°$) photon mode energy, E_x is the exciton energy, n is the refractive index within the microcavity, and E_R is the Rabi energy characterising the coupling strength. Note that not all of the UPB data is included in the fit due to low signal-to-noise at low θ. Note the detuning $\delta = E_0 - E_x$ is a derived parameter. The fits are indicated on the surfaces in Figure D.8, where solid white lines show the UPB and LPB and the dashed white lines indicate the exciton energy (E_x) and photon energy (minimum value E_0). The reflectivity fit is replotted on the emission surfaces only for comparison; the emission surface data is not used in the fits. The deviations between the LPB data in the emission surfaces and the LPB fit from the reflectivity surfaces are attributable to the different spots studied on the microcavity surface between reflectivity and emission measurements; there are small variations across a microcavity, mostly in the thickness of the active layer.

With all fits, we derive a Rabi energy of >100 meV, in-line with previous studies on other BODIPY dye-incorporating microcavity structures.[419–425]

D.3.5 PLQYs

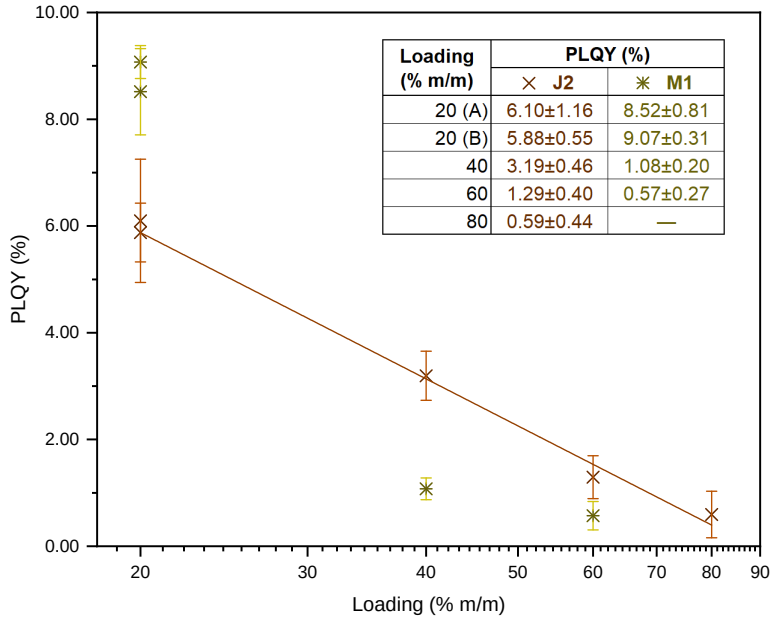

Figure D.9 – PLQYs of J2 and M1 films at 20–100% loadings. The J2 points are fitted with an exponential decay. The inset table shows the PLQY values and their errors. Note that two films at 20% loading were tested (A and B); these films were made identically from the same solution, one after the other. Line shows an exponential fit to J2 PLQYs.

The photoluminescence quantum yields (PLQYs) of some J2 and M1 films are shown in Figure D.9. The PLQYs are similar to that of previously reported BODIPYs.[419,420,428] As film loading increases, the PLQY decreases for both J2 (with an exponential relationship, see fit line) and M1. This is unexpected, as at high loadings, J2 forms nominally emissive J-aggregates that should maintain the PLQY,[112–114] while M1 has monomeric absorption and emission features, so both J2 and M1 would be expected to have appreciable PLQY at high loadings. It is possible that the PLQY is quenched for both due to the greater chromophore density leading to increased excitonic coupling to film impurities and subsequent nonradiative decay processes.[429]

D.3.6 Low-temperature steady-state emission

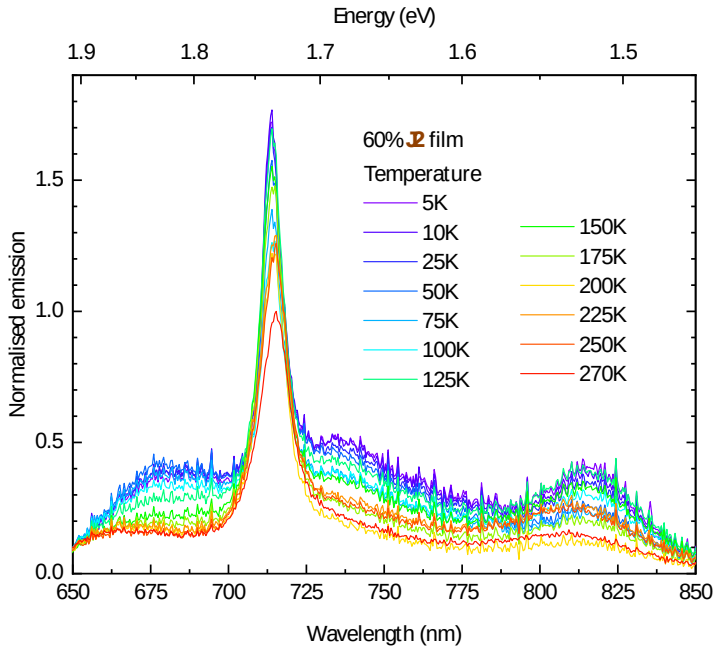

Figure D.10 – Emission spectra for a J2 film with 60% loading at temperatures from 270 K to 5 K. Each spectrum is normalised to the peak intensity of the 270 K spectrum. The sample was excited at 405 nm. No self-absorption correction has been applied.

Temperature-dependent steady-state emission of a 60%-loading J2 film is shown in Figure D.10. Note that each spectrum is normalised to the peak intensity of the 270 K spectrum. As temperature decreases, the whole emission spectrum is enhanced by roughly the same proportion.

Temperature-dependent steady-state emission of a 60%-loading M1 film is shown in Figure D.11. Note that each spectrum is normalised to the peak intensity of the 300 K spectrum. As temperature decreases, we see enhancement of a broad peak towards the red side of the main (monomer-like) room-temperature emission peak. This is likely due to enhanced excimer emission with decreasing temperature.

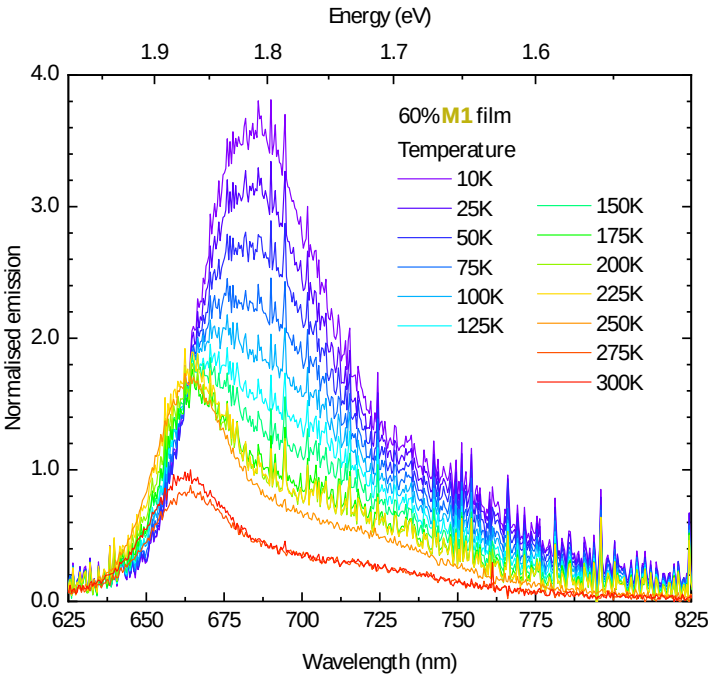

Figure D.11 – Emission spectra for a M1 film with 60% loading at temperatures from 300 K to 10 K. Each spectrum is normalised to the peak intensity of the 300 K spectrum. The sample was excited at 405 nm. No self-absorption correction has been applied.

D.4 Conclusions

We have characterised the photophysics of six new BODIPY dye structures that have been designed to control intermolecular interactions. Solutions and polystyrene films with different dye loadings were prepared and characterised with room-temperature absorbance and emission measurements. The BODIPY dye J2 shows strong J-aggregation at high loading, with a characteristic redshifted and sharp J-aggregate absorbance and emission peak; a pure film of J2 has a J-aggregate peak with $66 \pm 3\%$ band area, 53 meV FWHM, and a Stokes shift of 9 meV. The BODIPY dye M2 retains solution-like (monomeric) spectra, even at loadings approaching pure dye. Microcavities incorporating dilute J2 were fabricated and were shown to undergo strong-coupling, in-line with previous studies on microcavities incorporating BODIPY dyes.

J2 and M1 were further characterised. It was found that the PLQY was quenched at high loading, despite the formation of putatively emissive J-aggregates in J2 and the monomeric behaviour in M1. The emission quenching and the difficulty in producing smooth films at high loading make incorporation of these loadings into microcavities challenging. Future work on dyes for incorporation in microcavities should carefully consider the role of bulk morphology, and tune it through design of the dyes in addition to subsequent fabrication.

D.5 Supplementary information

D.5.1 Solution processing and annealing tests

In attempt to make smooth films of pure J2, solution processing with different combinations of solvent, heating, and filtration before spin-coating was investigated.

Films of pure J2 were spun from a chloroform solution (Aldrich, 288306-100ML; contains 0.5–1% ethanol as a stabiliser) at the spin-coater speeds 2000 rev min^{-1} and 5000 rev min^{-1}. Apart from the different solvent used, the methodology is identical to that of the films spun from a toluene solution.

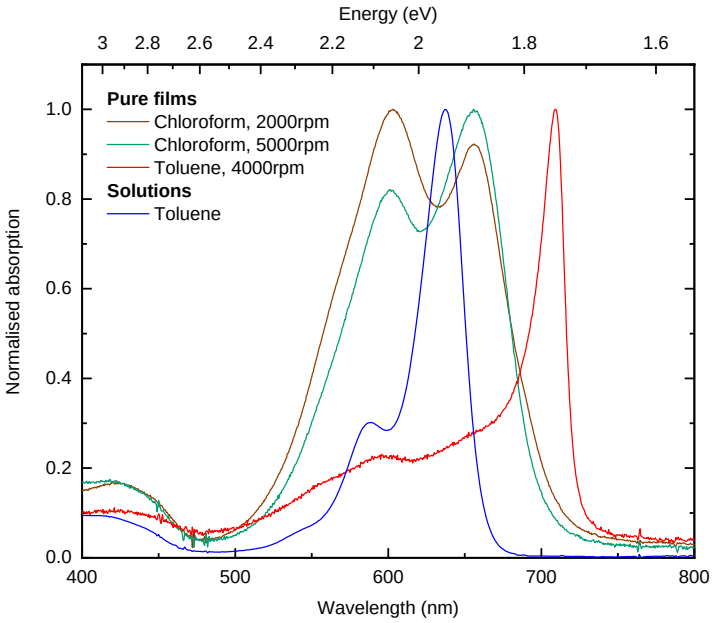

Figure D.12 – Normalised absorbance spectra of pure J2 films spun from chloroform at different spin-coater speeds. Normalised absorbance spectra of a pure J2 film spun from toluene and of J2 in toluene solution is shown for comparison. Each spectrum is normalised to their maximum.

Normalised room-temperature absorbance spectra of pure J2 films spun from chloroform are shown in Figure D.12. Compared to films spun from toluene, the films spun from chloroform have two relatively broad peaks. These peaks are likely due to weakly coupled aggregates. No signatures of J-aggregates like those in high-loading J2 films spun from toluene are seen.

In attempt to get J-aggregates within smooth J2 films, annealing of low-loading 5% J2 films was investigated. Initially we hypothesised that in annealing conditions, the J2 molecules suspended in the polystyrene would migrate to each

other, therefore forming J-aggregates within a smooth film. Both thermal and solvent annealing were attempted. In thermal annealing, 5% J2 films were placed on a hotplate for 10 minutes at various temperatures (60 °C, 80 °C, 100 °C). In solvent annealing, 5% J2 films were placed in a closed environment with toluene or acetone vapour for 4–5 hours, then left in an open environment for 30 minutes to dry completely.

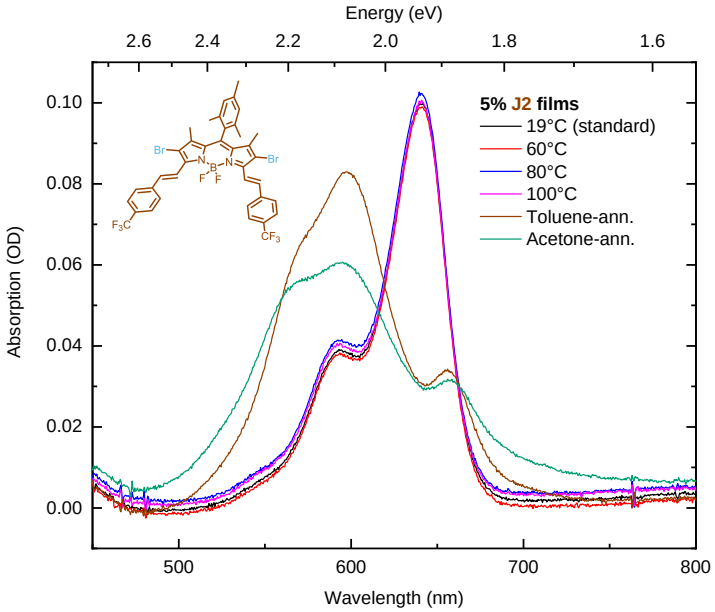

Figure D.13 – Absorbance spectra of a 5% J2 film spun from toluene after preparation and after heating it to various temperatures. Normalised absorbance spectra of a pure J2 film spun from toluene and of J2 in toluene solution is shown for comparison.

Room-temperature absorbance spectra of 5% J2 films spun from toluene and annealed with heat or solvent are shown in Figure D.13. Thermal annealing has no effect on the absorbance spectra, with small variations in the absorbance for all wavelengths attributable to lamp drift in the UV-vis spectrometer. Solvent annealing resulted in relatively broad peaks. These peaks are likely due to weakly coupled aggregates. No signatures of J-aggregates like those in high-loading J2 films spun from toluene are seen.

D.5.2 Microcavities: fitting equations

Polariton energies are given here by the eigenvalues of a matrix for a classical two-level coupled oscillator **A**

$$\mathbf{A} = \begin{pmatrix} E_c & \frac{1}{2}E_R \\ \frac{1}{2}E_R & E_x \end{pmatrix} \tag{D.1}$$

where E_x is the exciton energy, E_R is the Rabi energy (characterising the strength of the coupling between the exciton and photon modes), and E_c is the cavity-photon energy, which has an angular dependence

$$E_c = E_0 \left(1 - \frac{\sin^2\theta}{n^2}\right)^{-1/2} \tag{D.2}$$

where θ is the external angle of incidence of light onto the microcavity, $E_0 = E_c(\theta = 0)$, and n is the refractive index within the microcavity. Note that n here is assumed to be independent of the angle of incidence. Solving for the energy eigenvalues E of **A**, that is, solving

$$0 = \det(\mathbf{A} - E\mathbf{I}) \tag{D.3}$$

where **I** is the identity matrix, gives

$$E = \frac{1}{2}E_c + \frac{1}{2}E_x \pm \frac{1}{2}\left\{[E_c - E_x]^2 + E_R^2\right\}^{1/2} \tag{D.4}$$

where when $\pm$ is taken as $+$, the energies for the UPB are given, and when $\pm$ is taken as $-$, the energies for the LPB are given. Recall that E_c has a dependence on θ (Equation D.2), so Equation D.4 can be rewritten

$$\begin{aligned} E = \frac{1}{2}E_0 \left(1 - \frac{\sin^2\theta}{n^2}\right)^{-1/2} + \frac{1}{2}E_x \\ \pm \frac{1}{2}\left\{\left[E_0 \left(1 - \frac{\sin^2\theta}{n^2}\right)^{-1/2} - E_x\right]^2 + E_R^2\right\}^{1/2}. \end{aligned} \tag{D.5}$$

Equation D.5 is used to fit the polarised (TE polarisation only) white-light reflectivity spectra shown in Figure D.8. First, UPB and LPB peak positions are determined for each angle by fitting two Lorentzians and taking their peak positions. The UPB and LPB positions (E) against θ are fitted in turn with Equation D.5, with E_0, E_x, n, and E_R as fitting parameters. Note that the signal-to-noise ratio in some regions of the UPB was poor, and so not included in the fit (see

Table D.2 for UPB fit regions), whereas the signal-to-noise of the LPB was always sufficient. The results of the fits for microcavities with different active layer thicknesses are shown in Table D.2. Note that the detuning $\delta = E_0 - E_x$ is a derived parameter.

D.5.3 Microcavities: unpolarised surfaces

Unpolarised (TE and TM polarisations) white-light reflectivity and emission surfaces for Ag-Ag microcavities incorporating a layer of 5% J2 in polystyrene are shown in Figure D.14. We again see clear splitting forming an upper polariton branch (UPB) and lower polariton branch (LPB), with further splitting (most apparent at high angles) due to the different polarisations.

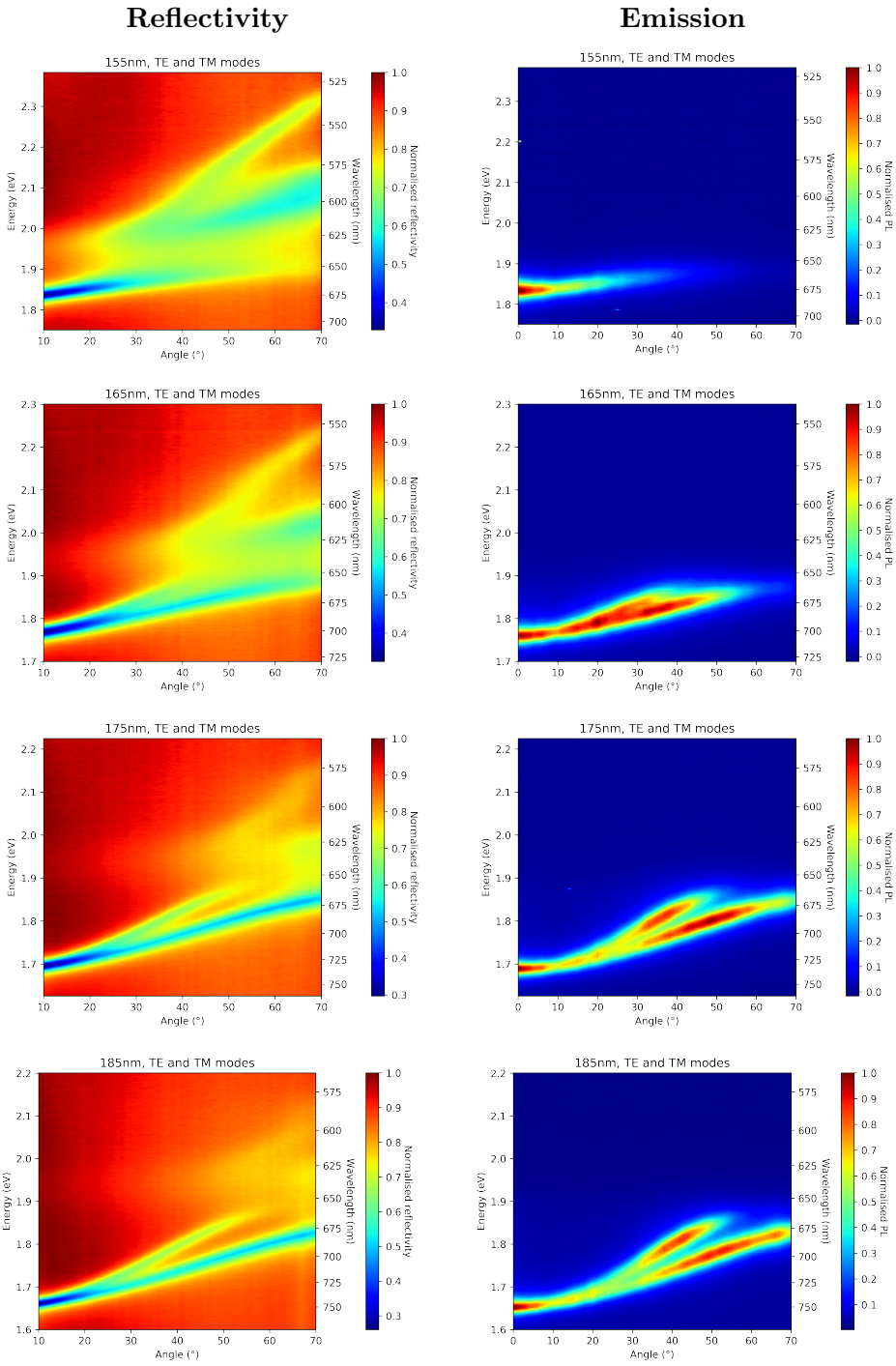

Figure D.14 – Unpolarised white-light reflectivity and emission surfaces of Ag-Ag microcavites with different active layer thicknesses incorporating 5% J2 in polystyrene. Emission surfaces have been Jacobian-corrected. A polariser is not used, so both the TE and TM polarisations are measured.

Appendix E

Derivation of Fermi's golden rule

Following the derivation shown in Binney and Skinner,[129] we outline how our equation for Fermi's golden rule (Equation 2.46) can be obtained through time-dependent perturbation theory.

Consider a system at a time $t = 0$ with Hamiltonian H. We can write the time-independent Schrödinger equation as

$$H\left|n(0)\right\rangle = E_n\left|n(0)\right\rangle \tag{E.1}$$

with time-independent eigenkets $|n(0)\rangle$ and eigenenergies E_n. The time-dependent Schrödinger equation for the system in the stationary state may be written

$$H\left|n(t)\right\rangle = i\hbar\frac{\partial\left|n(t)\right\rangle}{\partial t} \tag{E.2}$$

which, combining with the time-independent Schrödinger equation (Equation E.1) and integrating, leads to

$$\left|n(t)\right\rangle = e^{-iE_nt/\hbar}\left|n(0)\right\rangle. \tag{E.3}$$

Now, consider a perturbed Hamiltonian H'

$$H' = H + H_1(t) \tag{E.4}$$

with a small, time-dependent perturbation $H_1(t)$. We seek approximate solutions to the time-dependent Schrödinger equation

$$i\hbar\frac{\partial\left|\psi(t)\right\rangle}{\partial t} = H'\left|\psi(t)\right\rangle \tag{E.5}$$

for this system. We can write $|\psi(t)\rangle$ in the energy representation

$$\left|\psi(t)\right\rangle = \sum_n a_n(t)\left|n(t)\right\rangle \tag{E.6}$$

where $|\psi(t)\rangle$ is unrestricted, because $a_n(t)$ are arbitrary coefficients and the set of $|n(t)\rangle$ is complete. By inserting Equation E.3 we get

$$|\psi(t)\rangle = \sum_n a_n(t) e^{-iE_n t/\hbar} |n(0)\rangle \tag{E.7}$$

where e here is Euler's number.[†] If we insert this equation into the time-dependent Schrödinger equation (Equation E.5), use the product rule, use Equation E.4, then use Equation E.1, and cancel some terms, we find that

$$i\hbar \sum_n \frac{\partial a_n(t)}{\partial t} e^{-iE_n t/\hbar} |n(0)\rangle = \sum_n a_n(t) e^{-iE_n t/\hbar} H_1(t) |n(0)\rangle \tag{E.8}$$

By pre-multiplying by $\langle f|$ representing a final state (which is an eigenstate of the time-independent Schrödinger equation with unperturbed Hamiltonian H) and using the orthonormality of the eigenstates

$$\langle f|n(0)\rangle = \delta_{fn} \tag{E.9}$$

where δ_{fn} is the Kronecker delta, we get

$$\frac{\partial a_f(t)}{\partial t} = \frac{1}{i\hbar} \sum_n a_n(t) e^{i(E_f - E_n)t/\hbar} \langle f| H_1(t) |n(0)\rangle . \tag{E.10}$$

Say that at time $t = 0$ our system is initially in a stationary state $|n(0)\rangle = |i\rangle$. We can write

$$a_n(0) = \begin{cases} 1, & \text{for } n = i \\ 0, & \text{for } n \neq i \end{cases} \tag{E.11}$$

which we use as boundary conditions. As $H_1(t)$ is a small perturbation, we can make an *first-order approximation* that the primary contribution on the right side of Equation E.10 is due to the term with $n = i$. Therefore, we can write

$$\frac{\partial a_f(t)}{\partial t} \simeq \frac{1}{i\hbar} e^{i(E_f - E_i)t/\hbar} \langle f| H_1(t) |i\rangle \tag{E.12}$$

which upon integration gives

$$a_f(t) \simeq \frac{1}{i\hbar} \int_{t'=0}^{t'=t} e^{i(E_f - E_i)t'/\hbar} \langle f| H_1(t) |i\rangle \, \mathrm{d}t' \tag{E.13}$$

as $a_f(0) = 0$.

[†]Elsewhere in this thesis, the quantity e is the modulus of the electron charge, unless specified otherwise. See footnote of page 24.

Now we assume a form of the perturbing Hamiltonian[†]

$$H_1(t) = Ve^{-i\omega t} \tag{E.14}$$

which notably resembles the form of the perturbing time-dependent electric field of Equation 2.42 and resulting Hamiltonian of Equation 2.43. Inserting Equation E.14 into Equation E.13 gives us

$$a_f(t) \simeq \frac{\langle f|\, V\, |i\rangle}{i\hbar} \int_{t'=0}^{t'=t} e^{i(E_f - E_i - \hbar\omega)t'/\hbar}\, \mathrm{d}t' \tag{E.15}$$

and completing the integration yields

$$a_f(t) \simeq \frac{\langle f|\, V\, |i\rangle}{E_i - E_f - \hbar\omega} \left[e^{i(E_f - E_i - \hbar\omega)t/\hbar} - 1\right]. \tag{E.16}$$

We can write the probability that after time t the system has transferred from state $|i\rangle$ to state $|f\rangle$ as

$$P_f(t) = a_f(t)a_f^*(t) \simeq 4|\langle f|\, V\, |i\rangle|^2 \frac{\sin^2\left[(E_f - E_i - \hbar\omega)t/2\hbar\right]}{(E_f - E_i - \hbar\omega)^2} \tag{E.17}$$

where we have made use of some trigonometric identities and relations to complex exponentials.

Up to this point, we have implicitly assumed that the final state $|f\rangle$ has *exact* energy E_f, implying an *exact* matching of the initial energy E_i through the energy associated with the perturbation $\hbar\omega$. This is an unlikely situation in most systems. It is more usual that there are a significant number of final states $|f\rangle$ with *non-exact* energies E_f lying within $\sim\hbar/t$ of the *exact* $(E_i + \hbar\omega)$. To determine the overall transition probability from an initial state $|i\rangle$ to any one of these $|f\rangle$-states, we perform a sum of the P_f of Equation E.17. Say that there are $\rho(E_f)\,\mathrm{d}E_f$ of these $|f\rangle$-states in the interval $[E_f, E_f + dE_f]$, where $\rho(E_f)$ is the density of final states. We can then write

$$\sum_f P_f(t) \simeq 4 \int |\langle f|\, V\, |i\rangle|^2 \frac{\sin^2\left[(E_f - E_i - \hbar\omega)t/2\hbar\right]}{(E_f - E_i - \hbar\omega)^2} \rho(E_f)\, \mathrm{d}E_f. \tag{E.18}$$

We can make a substitution $x \equiv (E_f - E_i - \hbar\omega)/2\hbar$ (note that $\mathrm{d}E_f = 2\hbar\,\mathrm{d}x$) to re-write Equation E.18 in the form

$$\sum_f P_f(t) \simeq \frac{2}{\hbar} \int |\langle f|\, V\, |i\rangle|^2 \frac{\sin^2\left[xt\right]}{x^2} \rho(E_f)\, \mathrm{d}x \tag{E.19}$$

[†]Since Fourier analysis enables us to approximate any function as a linear combination of trigonometric or exponential functions, this assumption does not lead to a significant loss in generality.

which points to the usage of an expression for the Dirac delta function $\delta(x)$ in the limit $t \to \infty$

$$\lim_{t\to\infty} \frac{\sin^2[xt]}{x^2} = \pi t \delta(x). \tag{E.20}$$

We highlight that $\delta(x)$ takes the form $\delta(x) = \delta(E_f - E_i - \hbar\omega)$; the physical correspondence underlying this will be discussed later. We apply the limit $t \to \infty$ and evaluate the integral of Equation E.19 to give

$$\sum_f P_f(t) \simeq \frac{2\pi t}{\hbar} |\langle f| V |i\rangle|^2 \rho(E_f). \tag{E.21}$$

The total rate of the transitions from the initial state $|i\rangle$ to the final $|f\rangle$-states is

$$\Gamma_{i\to f} = \frac{\partial \left[\sum_f P_f(t)\right]}{\partial t} \tag{E.22}$$

which leads to

$$\Gamma_{i\to f} \simeq \frac{2\pi}{\hbar} |\langle f| V |i\rangle|^2 \rho(E_f) \tag{E.23}$$

which is our familiar equation for Fermi's golden rule, written as Equation 2.46 in Section 2.3.1.

Finally, we conclude this appendix by commenting on the form of the Dirac delta function. We noted it took the form $\delta(x) = \delta(E_f - E_i - \hbar\omega)$ earlier. This actually corresponds to conservation of energy; in reaching a state with energy $E_f = E_i + \hbar\omega$ from an initial state *via* the perturbation, the system has had to absorb an energy $\hbar\omega$. This could correspond to the absorption of a photon with angular frequency ω. If we had used another form of the perturbing Hamiltonian

$$H_1(t) = V e^{+i\omega t} \tag{E.24}$$

where the only distinction from the previous form (Equation E.14) is a positive sign in the phase (rather than negative), the form of the Dirac delta would have taken $\delta(x) = \delta(E_f - E_i + \hbar\omega)$. Again, this embodies conservation of energy; in reaching $E_f = E_i - \hbar\omega$, the system has had to lose an energy $\hbar\omega$. This could correspond to the stimulated emission of a photon with angular frequency ω.

Appendix F

Steady-state absorbance of samples studied with transient absorption

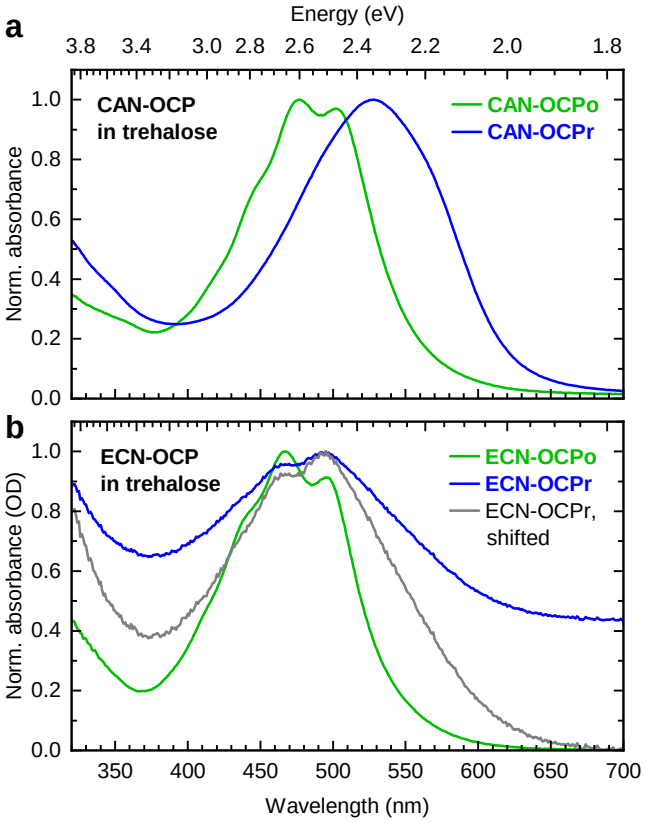

Figure F.1 – Normalised steady-state absorbance spectra of CAN-binding (a) and ECN-binding (b) OCPo (green) and OCPr (blue, grey) in trehalose. Spectra have been normalised to their absorbance maximum, and in the case of 'shifted' ECN-OCPr (panel (b), grey line) additionally normalised to zero absorbance around 700 nm. These absorbances were taken prior to visible/NIR ps transient absorption measurements (*e.g.* Appendix G).

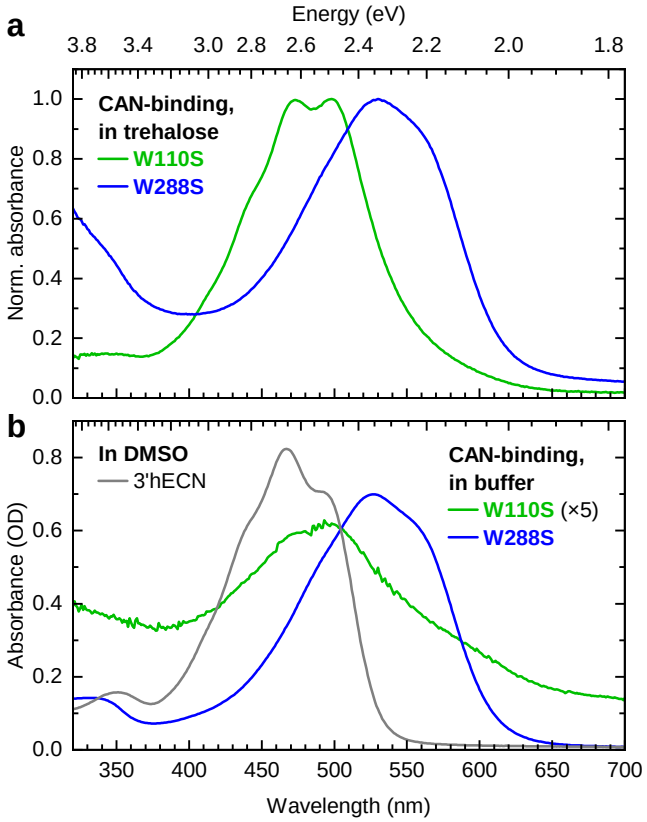

Figure F.2 – Steady-state absorbance spectra of CAN-binding OCP mutants and 3′hECN. (a) Normalised absorbance of CAN-binding W110S (green) and W288S (blue) in trehalose. Here, spectra have been normalised to their absorbance maximum. **(b)** Non-normalised absorbance of CAN-binding W110S (green) and W288S (blue) in buffer, and 3′hECN in DMSO (grey). The W110S in buffer absorbance has been scaled by factor 5. The optical path length was 2 mm. All absorbances were taken prior to visible/NIR ps transient absorption measurements (*e.g.* Appendix G).

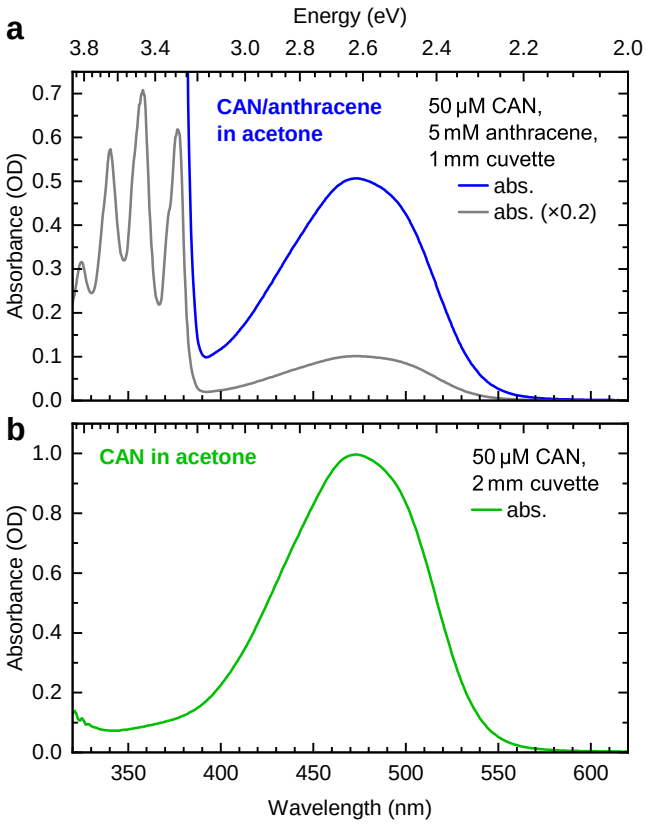

Figure F.3 – Steady-state absorbance spectra of mixed CAN/anthracene (a) or CAN only (b) in acetone. All absorbances were taken prior to visible/NIR ns transient absorption measurements (Section 7.2.1). **(a)** Absorbance of 50 µM CAN, 5 mM anthracene in acetone in a 1 mm cuvette. The blue line is unscaled, and the grey line is scaled (×0.2) to show the anthracene absorbance. **(b)** Absorbance of 50 µM CAN in acetone in a 2 mm cuvette.

Appendix G

Supplementary visible/NIR ps transient absorption materials

In this section, we highlight the results of ps transient absorption with visible- and NIR-region probes under two different pump (excitation) wavelengths on various OCP, OCP mutant, and carotenoid samples in trehalose glass and in solution, in context of the results of the ps transient absorption measurements using a UV-vis probe. We note that the visible/NIR-region measurements are admittedly worse quality than the UV-vis-probe transient absorption (*e.g.* Section 6.2.3), largely due to the significant sample degradation and the strong coherent artefact (from *e.g.* cross-phase modulation[229]) present due to the high pump fluence densities ($200\,\mu J\,cm^{-2}$) used. Furthermore, the set maximum time delay in the measurements was $\sim$40 ps, leading to difficulty in resolving states with lifetimes beyond that. We therefore refrain from assigning a photophysical model to OCPr and the mutants; doing this would require further ps transient absorption measurements with a lower fluence and further excitation wavelengths.

G.1 Pump spectra

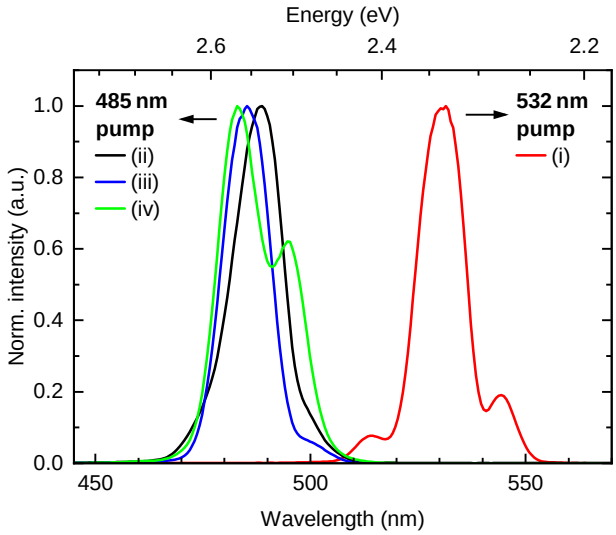

Figure G.1 – Intensity spectra of the pumps used in the visible/NIR ps transient absorption experiments, normalised to the maximum intensity. Small variations in the tuneable pump generation resulted in slightly different pump profiles on each experimental day. 532 nm pump (i) was used in taking the visible-probe data shown in Figures G.2a and G.3a. 485 nm pump (ii) was used in taking the visible-probe data shown in Figures G.2b and G.3b. 485 nm pump (iii) was used in taking the NIR-probe data shown in Figures G.2b and G.3b. 485 nm pump (iv) was used in taking the NIR-probe data shown in Figures G.10 and G.11. The 532 nm pump used in taking the NIR-probe data of Figures G.2a and G.3a was not recorded, and may have had a slightly different spectrum to (i).

G.2 Transient absorption on OCPo and OCPr

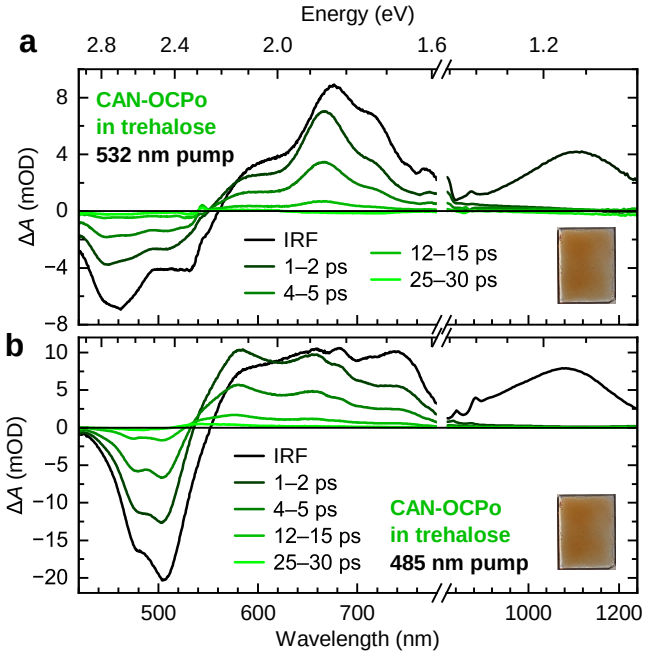

Figure G.2 – Picosecond transient absorption spectra of CAN-binding OCPo in trehalose glass with pump wavelength 532 nm (a) or 485 nm (b) with visible (left) and NIR (right) probes. Note that panel (a) has been depicted previously (Figures 5.4a and 6.3a). Spectra have been averaged between the times indicated. Pump fluence was set to 200 µJ cm^{-2}.

The behaviour of OCPr seemingly matches that of OCPo, including its pump wavelength dependence, although with an overall redshift. The photophysics with 532 nm pump (Figure G.3a) is similar to that of OCPo, although with an overall redshift, consistent with the redshift seen in the steady-state absorbance (*e.g.* Figure 6.2). We see signatures of a longer-lived S*-like feature around 600 nm probe when using 485 nm pump (Figure G.3b), easily seen with the loss of the near-isosbestic point, suggesting that OCPr also has an S*-like feature. However, the OCPr GSB at probe wavelength ∼480 nm appears relatively diminished using 485 nm pump compared to 532 nm pump. This is the opposite to the relation seen in OCPo, most easily seen in the UV-vis-probe transient absorption spectra (Figure 6.4). We note that the signal is noisy in the ∼480 nm region due to the 485 nm pump.

We note that no apparent conversion between forms of CAN-OCP occurred during the experiments, and that the only apparent change in steady-state ab-

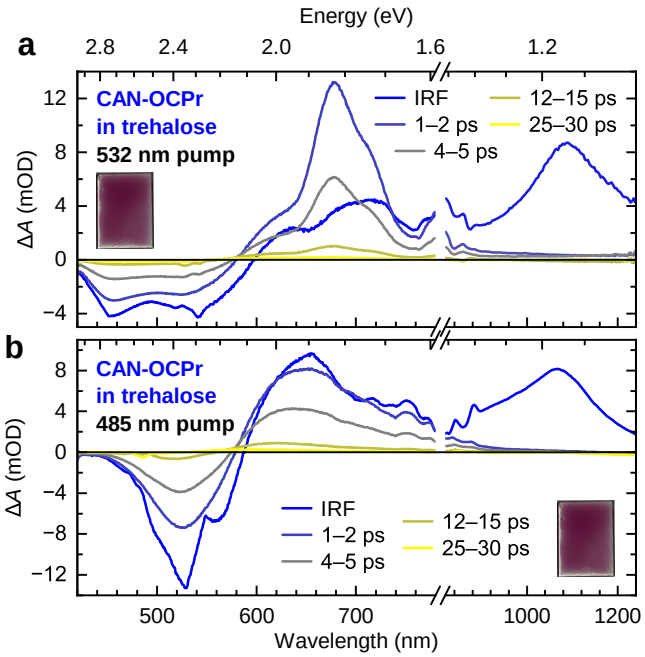

Figure G.3 – Picosecond transient absorption spectra of CAN-binding OCPr in trehalose glass with pump wavelength 532 nm (a) or 485 nm (b) with visible (left) and NIR (right) probes. A pump wavelength dependence on the spectra is apparent. Note that panel (a) has been depicted previously (Figures 5.4b and 6.3b). Spectra have been averaged between the times indicated. Pump fluence was set to 200 µJ cm^{-2}.

sorbance at the probed spot (or in the probed solution) was due to sample degradation.

G.3 Global lifetime analysis

As a comparison of the visible-probe ps transient absorption data of OCPo (Figure G.2) to that using a UV-vis probe (Figure 6.4), in addition to seeing if an S*-associated component is fit in the case for OCPr (Figure G.3), global lifetime analysis on the data was performed. This was done using the Glotaran 1.5.1 software package (`https://glotaran.org`),[233] a GUI for the R package TIMP.[234] Data used had already been processed with the steps outlined in Section 4.4.4; in particular, a chirp correction had already been applied, so that a term to account for chirp did not need to be included in the fitting. Noisy regions in the data due to pump scatter were excluded for all times to ensure a good fit of the rest of the data. Noisy red and blue ends in the data associated with tails of the probe were also excluded, so that the fitted wavelengths were 430 nm to 780 nm. The fitting was weighted favourably at later delay times to ensure good fits; Table G.1 shows the weighting applied. Due to the strong coherent artefact feature in the first 0.5 ps, only data beyond that time was fitted. Thus, in the model, terms to account for the coherent artefact and S_2 states were not included. This left a relatively simple fitted model of a number of decay-associated difference spectra (DADS) decaying exponentially in parallel.

Time range (ps)	Weighting
0.5 – 10	1
10 – 20	2
20 – 30	3
30 – 35	4
>35	5

Table G.1 – Weightings applied to time-ranges of the visible ps transient absorption data for the global lifetime analysis. Note that only data >0.5 ps was fitted, and that the maximum time delay in these experiments was ∼40 ps.

2-component global lifetime analysis of the 532 nm pump data (spectra shown in Figures G.2a and G.3a) are shown in Figures G.4 and G.5. Fitting a 2-component parallel decay model in an artefact-free region of the visible-probe data beyond the initial coherent artefact and S_2-associated response gives two decay-associated difference spectra (DADS) for both the OCPo data and OCPr data, with the longer time-constant DADS relatively weaker and blueshifted in

both cases. A single component is not sufficient to adequately fit the region of the data, and a fitting a third component gives results with spurious DADS profiles. The results for OCPo are consistent (in the sense of the number of components required for a reasonable fit) with a 3-component global target analysis model applied to the UV-vis-probe transient absorption data for pump wavelengths from 495 nm to 580 nm (and for the 2-component global lifetime analysis on the 600 nm pump).

Global lifetime analysis of the 485 nm pump data (spectra shown in Figure G.2b and G.3b) are shown in Figures G.6–G.9. These clearly show the appearance of the S*-like feature, with two components under-fitting (Figures G.6 and G.8); a third component is required to adequately fit the data (Figures G.7 and G.9). The results for OCPo are consistent (in the sense of the number of components required for a reasonable fit) with the 4-component (or 5-component) global target analysis model applied to the UV-vis-probe transient absorption data for 400 nm to 495 nm pump wavelengths.

We note that sample degradation (caused by the higher pump fluences in comparison with the UV-vis transient absorption data) likely affects the fitted time constants and DADS profiles. No further states with longer lifetimes were identified from these analyses of visible-probe transient absorption data, largely due to the limited delay time range chosen in the experiments (up to 40 ps).

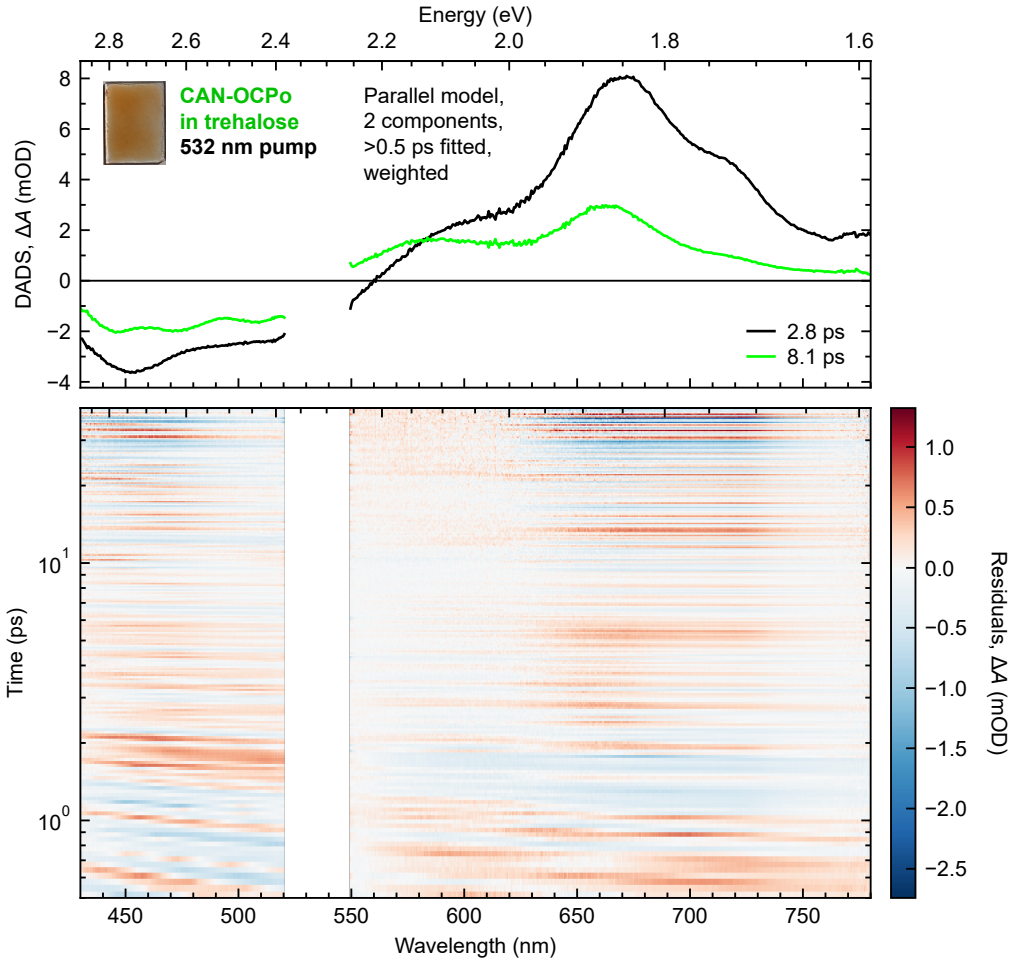

Figure G.4 – Results of global lifetime analysis with a 2-component parallel model on transient absorption data of CAN-binding OCPo in trehalose with pump wavelength 532 nm and a visible probe: DADS (top) and residuals (bottom). Only the wavelength range 430–780 nm and times >0.5 ps were fitted, and noisy data from 520.5–549.5 nm due to significant pump scatter was excluded from the fit. DADS time constants are specified in the legend. Residuals = Data − Fit. See text for further details.

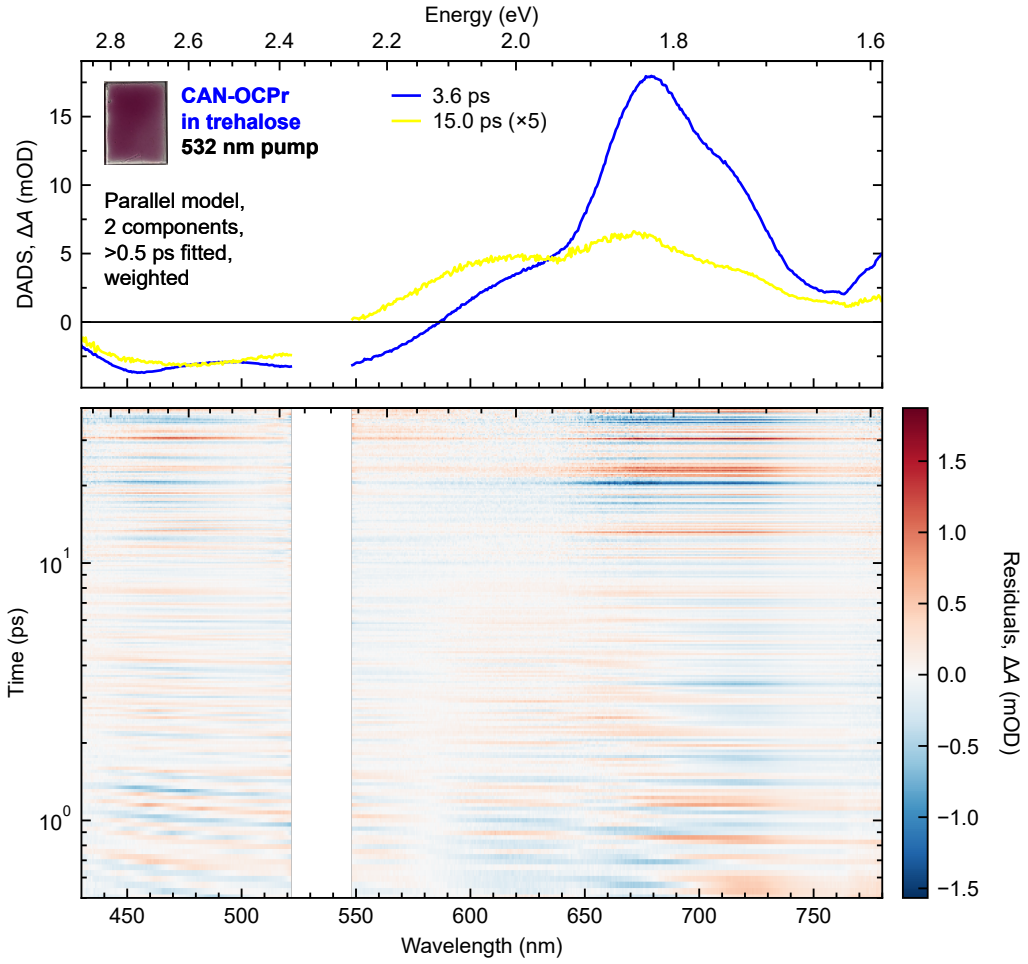

Figure G.5 – Results of global lifetime analysis with a 2-component parallel model on transient absorption data of CAN-binding OCPr in trehalose with pump wavelength 532 nm and a visible probe: DADS (top) and residuals (bottom). Only the wavelength range 430–780 nm and times >0.5 ps were fitted, and noisy data from 522–548 nm due to significant pump scatter was excluded from the fit. DADS time constants are specified in the legend; multiplications refer to scalings applied to the DADS. Residuals = Data − Fit. See text for further details.

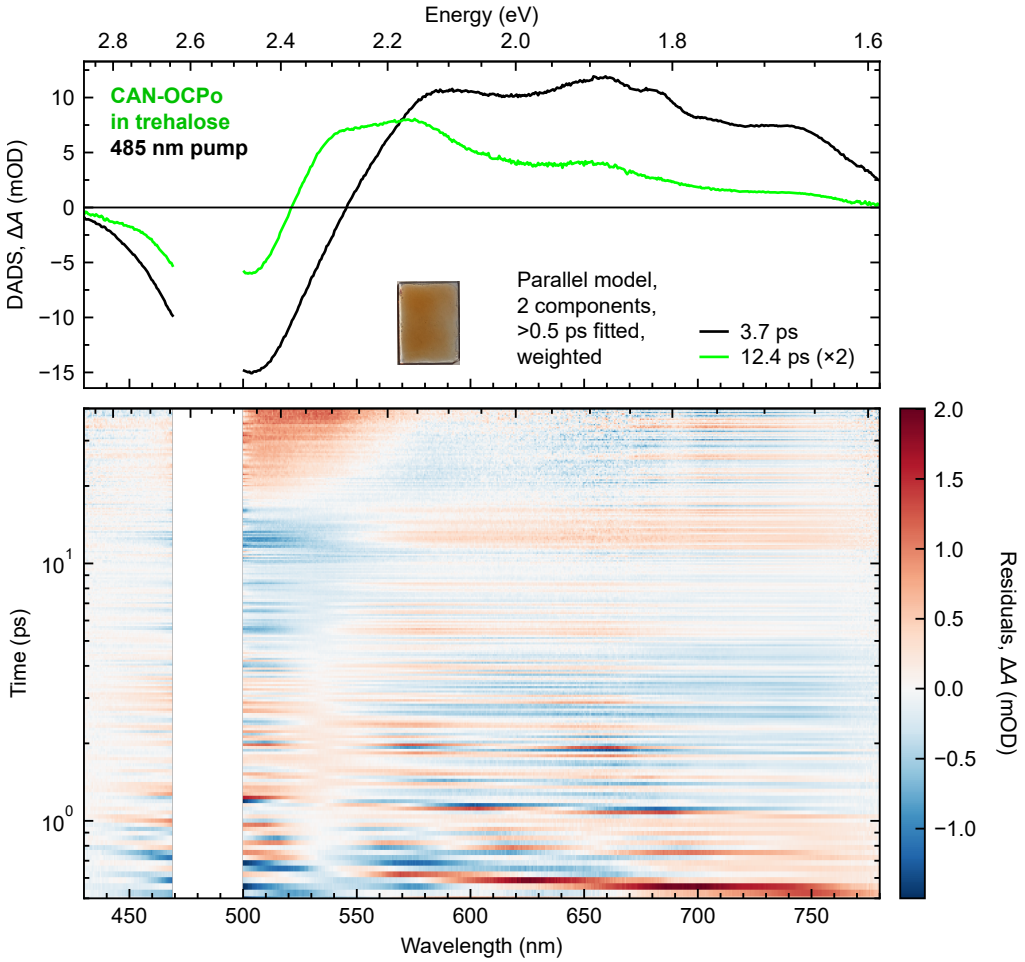

Figure G.6 – Results of global lifetime analysis with a 2-component parallel model on transient absorption data of CAN-binding OCPo in trehalose with pump wavelength 485 nm and a visible probe: DADS (top) and residuals (bottom). From the structure of the residuals, it is apparent that 2 components is not sufficient to fit this data. Only the wavelength range 430–780 nm and times >0.5 ps were fitted, and noisy data from 469.5–500 nm due to significant pump scatter was excluded from the fit. DADS time constants are specified in the legend; multiplications refer to scalings applied to the DADS. Residuals = Data − Fit. See text for further details.

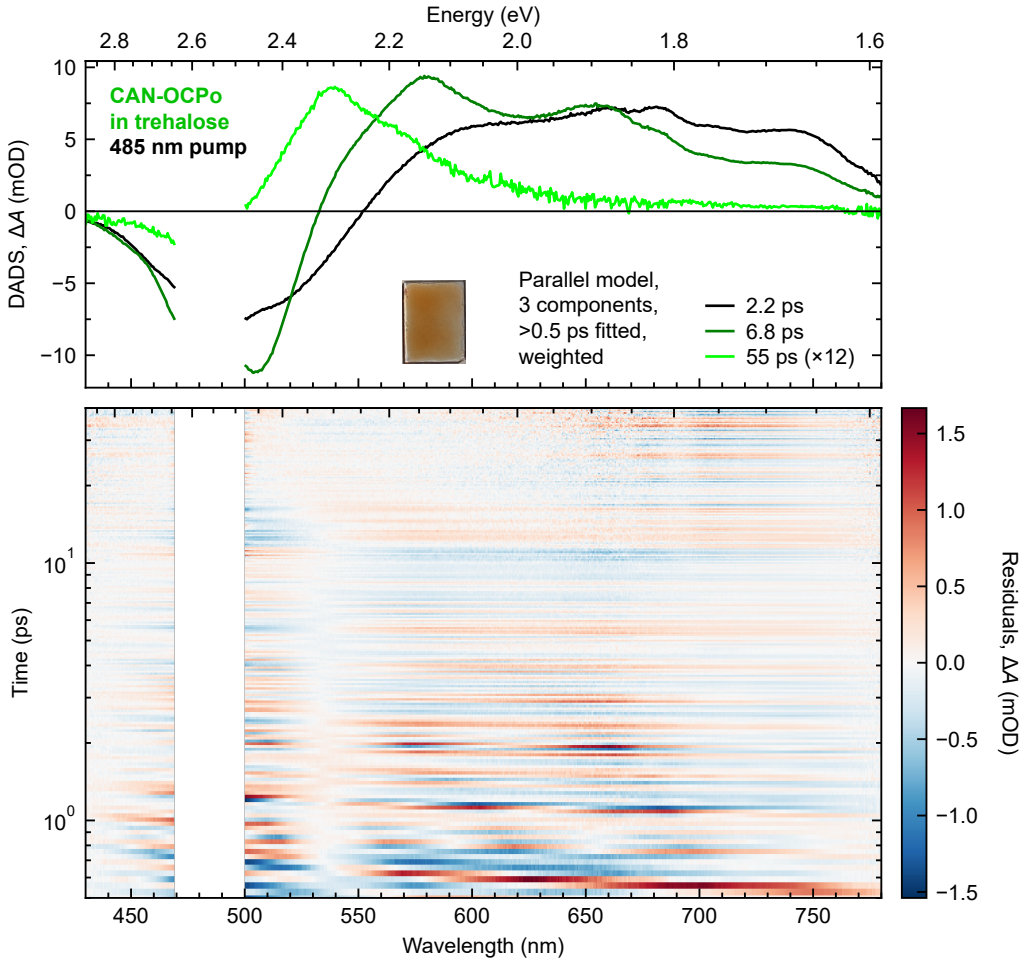

Figure G.7 – Results of global lifetime analysis with a 3-component parallel model on transient absorption data of CAN-binding OCPo in trehalose with pump wavelength 485 nm and a visible probe: DADS (top) and residuals (bottom). Only the wavelength range 430–780 nm and times >0.5 ps were fitted, and noisy data from 469.5–500 nm due to significant pump scatter was excluded from the fit. DADS time constants are specified in the legend; multiplications refer to scalings applied to the DADS. Residuals = Data − Fit. See text for further details.

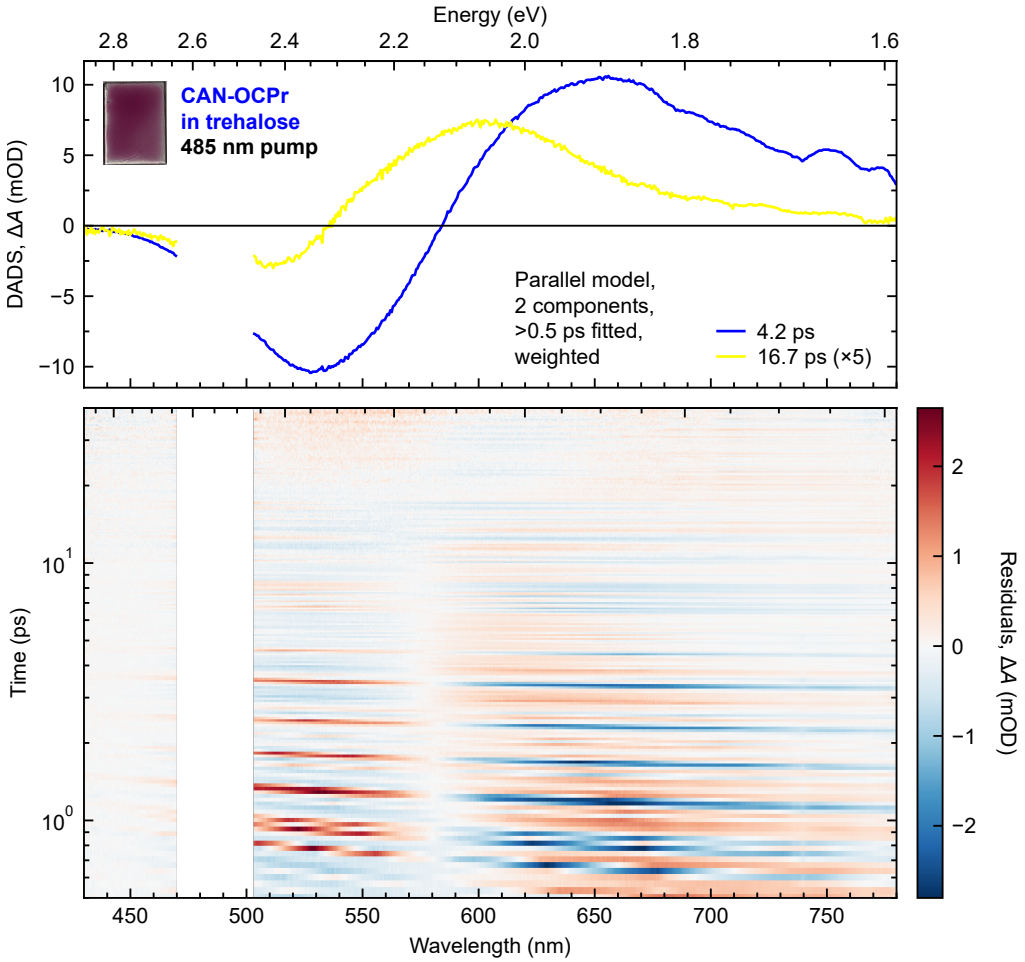

Figure G.8 – Results of global lifetime analysis with a 2-component parallel model on transient absorption data of CAN-binding OCPr in trehalose with pump wavelength 485 nm and a visible probe: DADS (top) and residuals (bottom). Only the wavelength range 430–780 nm and times >0.5 ps were fitted, and noisy data from 470–503 nm due to significant pump scatter was excluded from the fit. DADS time constants are specified in the legend; multiplications refer to scalings applied to the DADS. Residuals = Data − Fit. See text for further details.

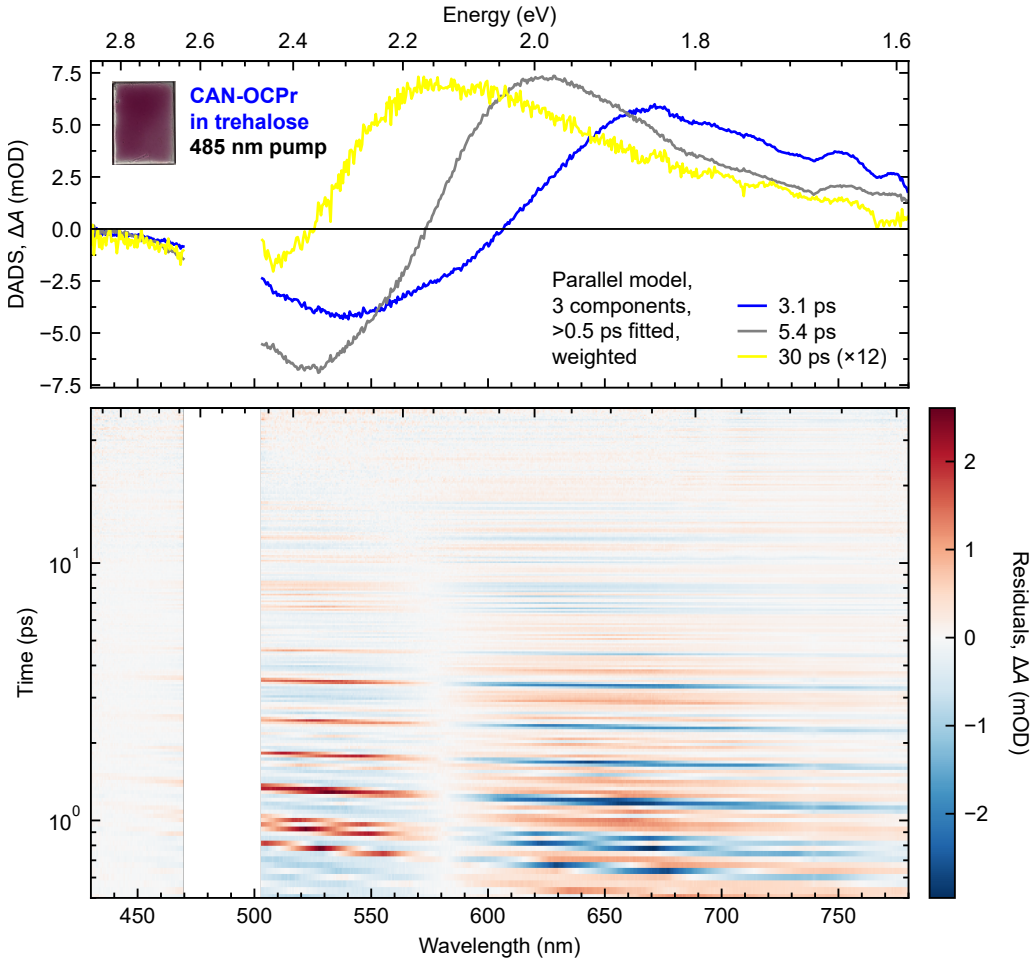

Figure G.9 – Results of global lifetime analysis with a 3-component parallel model on transient absorption data of CAN-binding OCPr in trehalose with pump wavelength 485 nm and a visible probe: DADS (top) and residuals (bottom). Only the wavelength range 430–780 nm and times >0.5 ps were fitted, and noisy data from 470–503 nm due to significant pump scatter was excluded from the fit. DADS time constants are specified in the legend; multiplications refer to scalings applied to the DADS. Residuals = Data − Fit. See text for further details.

G.4 Transient absorption on ECN-binding OCPo/OCPr

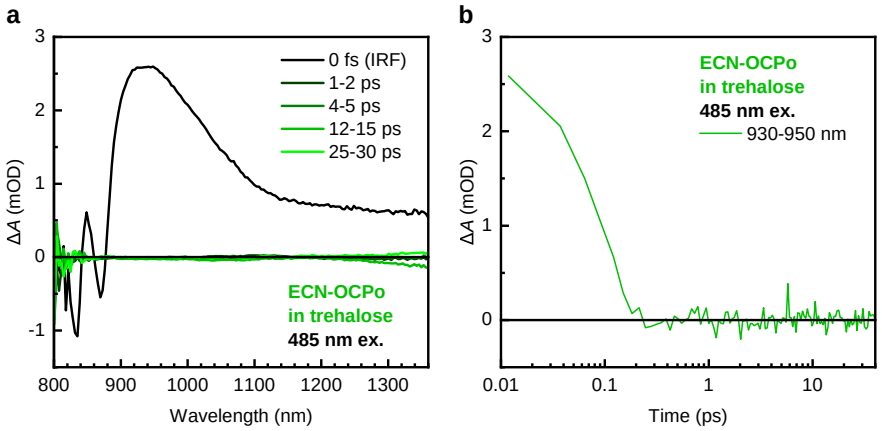

Figure G.10 – Picosecond transient absorption spectra (a) and dynamics (b) of ECN-binding OCPo in trehalose glass with pump wavelength 485 nm with an NIR probe. Similarly to CAN-binding OCPo in trehalose (Figure G.2), no ICT stimulated emission is seen in the NIR region. Spectra and dynamics have been averaged between the times and wavelengths (respectively) indicated. Pump fluence was set to 200 µJ cm^{-2}.

Picosecond transient absorption spectra of ECN-binding OCPo and OCPr in trehalose using a NIR probe and 485 nm pump are shown in Figure G.10 (ECN-OCPo) and Figure G.11 (ECN-OCPr). Similar spectra and dynamics to all the CAN-binding proteins and the monomeric carotenoids in solution are seen.

We note that no stimulated emission (negative ΔA contribution) is seen in the NIR region for *any* of the carotenoid-related samples studied in this thesis, normally indicative of a strong intramolecular charge transfer (ICT) state. This stimulated emission has been observed in OCP binding 3′hECN[56,297] instead of CAN. However, we see that ECN-binding OCPo and OCPr in trehalose shows no apparent stimulated emission (see Figures G.10 and G.11), possibly due to the absence of water (a polar solvent) in the environment and from conducting measurements at 19 °C.[134,430,431] However, as the amplitude of the $S_1 \rightarrow S_n$ ESA in the 700–900 nm probe range for all samples is more comparable to CAN in polar solvents (in contrast to CAN in non-polar solvents),[51,57] we assign a weak ICT character to the S_1-like states.

We note that no apparent conversion between forms of ECN-OCP occurred during the experiments, and that the only apparent change in steady-state ab-

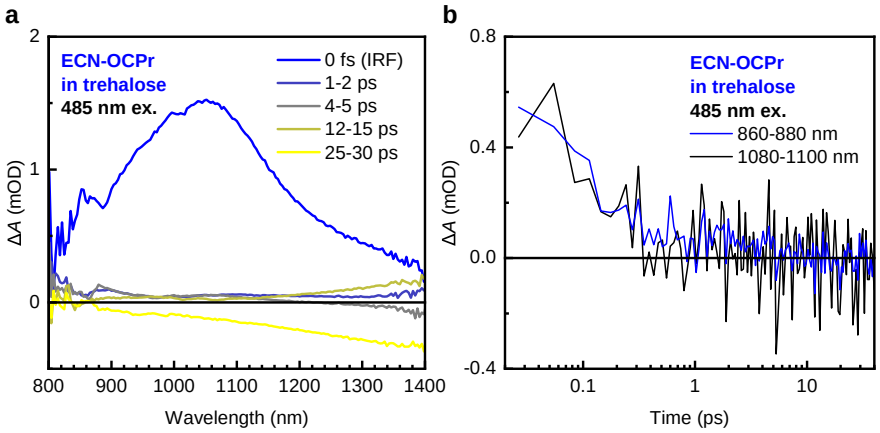

Figure G.11 – Picosecond transient absorption spectra (a) and dynamics (b) of ECN-binding OCPr in trehalose glass with pump wavelength 485 nm with an NIR probe. Similarly to CAN-binding OCPr in trehalose (Figure G.3) and ECN-binding OCPo in trehalose (Figure G.10), no ICT stimulated emission is seen in the NIR region. Spectra and dynamics have been averaged between the times and wavelengths (respectively) indicated. Pump fluence was set to 200 µJ cm^{-2}.

sorbance at the probed spot (or in the probed solution) was due to sample degradation.

G.5 Transient absorption on OCP mutants

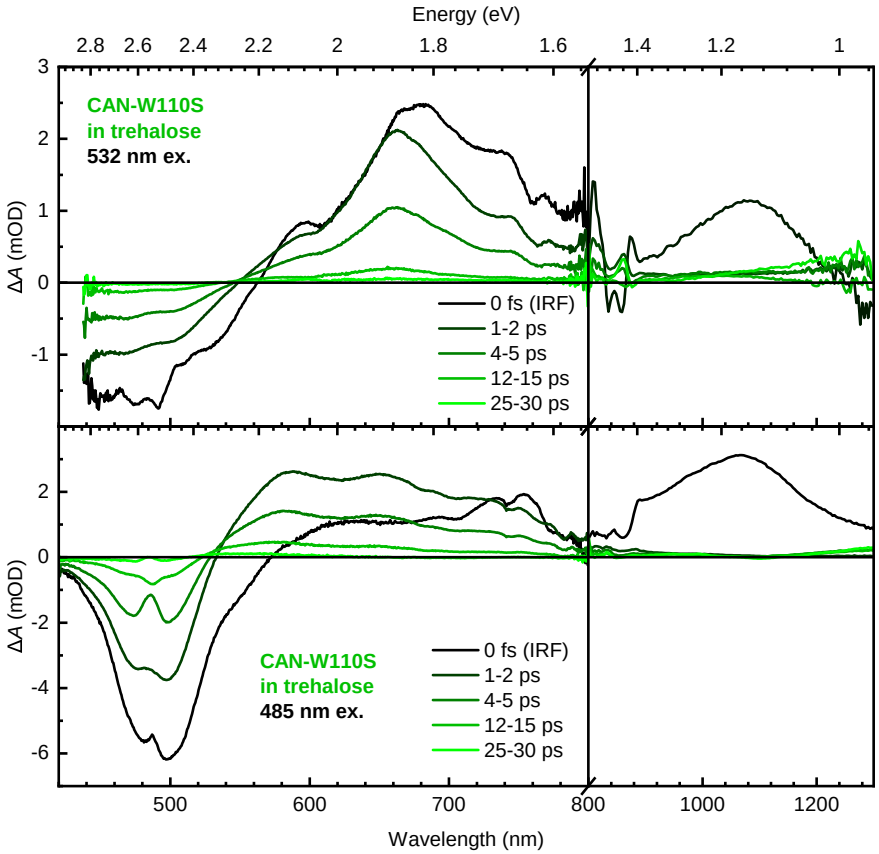

Figure G.12 – Picosecond transient absorption spectra of CAN-binding W110S in trehalose glass with pump wavelength 532 nm (top) or 485 nm (bottom) with visible (left) and NIR (right) probes. As in OCPo in trehalose (*e.g.* Figure G.2), blue-end excitation has signatures of longer-lived states while red-end excitation does not, and no ICT stimulated emission is seen in the NIR region. Spectra have been averaged between the times indicated. Pump fluence was set to 200 µJ cm^{-2}.

The studied mutants are all CAN-binding. The OCPo-like mutant studied is W110S, where the tryptophan-110 residue has been substituted for a serine-110, resulting in a permanently inactive protein. Steady-state spectra of W110S in trehalose glass and in buffer are shown in Figure F.2 (green lines), and ps transient absorption spectra with visible and NIR-region probes are shown in Figure G.12 (trehalose; 532 nm and 485 nm pump) and Figure G.13 (buffer; 532 nm pump only). For W110S in trehalose, no significant difference between the transient absorption features are seen in comparison with OCPo in trehalose, although due to the aforementioned issues with the measurements, this is difficult to confirm. For

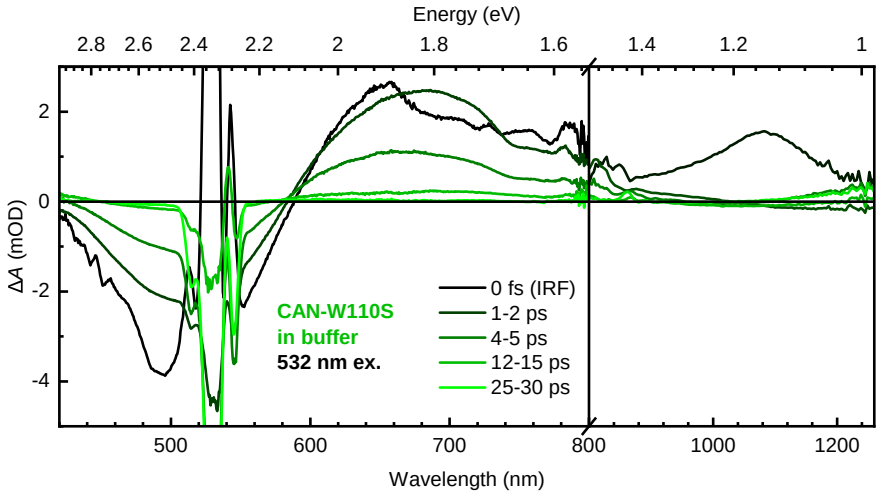

Figure G.13 – Picosecond transient absorption spectra of CAN-binding W110S in buffer with pump wavelength 532 nm with visible (left) and NIR (right) probes. We note that the spectra are different to those seen in W110S in trehalose with 532nm pump (Figure G.12, top); in particular, the isosbestic point is located at a redder wavelength when in buffer. This is likely due to an unknown precipitate forming within the solution. Spectra have been averaged between the times indicated. Pump fluence was set to 200 µJ cm^{-2}.

W110S in buffer, we note that the spectra appear significantly different to those for W110S in trehalose using 532 nm pump (Figure G.12, top), and the pump scatter is significant. These are likely due to an unknown precipitate forming within the solution over time; by the experimental day using 485 nm pump, the solution to be used (an unmeasured proportion) had too much precipitate for a useful measurement. We note that the W110S in trehalose samples did not appear to form precipitate over time, likely because of the trehalose glass preventing the conformational changes associated with precipitation.

The OCPr-like mutant is W288S, where the tryptophan-288 residue has been substituted for a serine-288, resulting in a permanently active protein. Steady-state spectra of W288S in trehalose glass and in buffer are shown in Figure F.2 (blue/grey lines), and ps transient absorption spectra with visible and NIR-region probes using 532 nm and 485 nm pumps are shown in Figure G.14 (trehalose; both pumps) and Figure G.15 (buffer; 532 nm pump only). No significant difference between the transient absorption features are seen in comparison with OCPr in trehalose, although due to the aforementioned issues with the measurements, this is difficult to confirm. For W288S in buffer with 532 nm pump (Figure G.15, top),

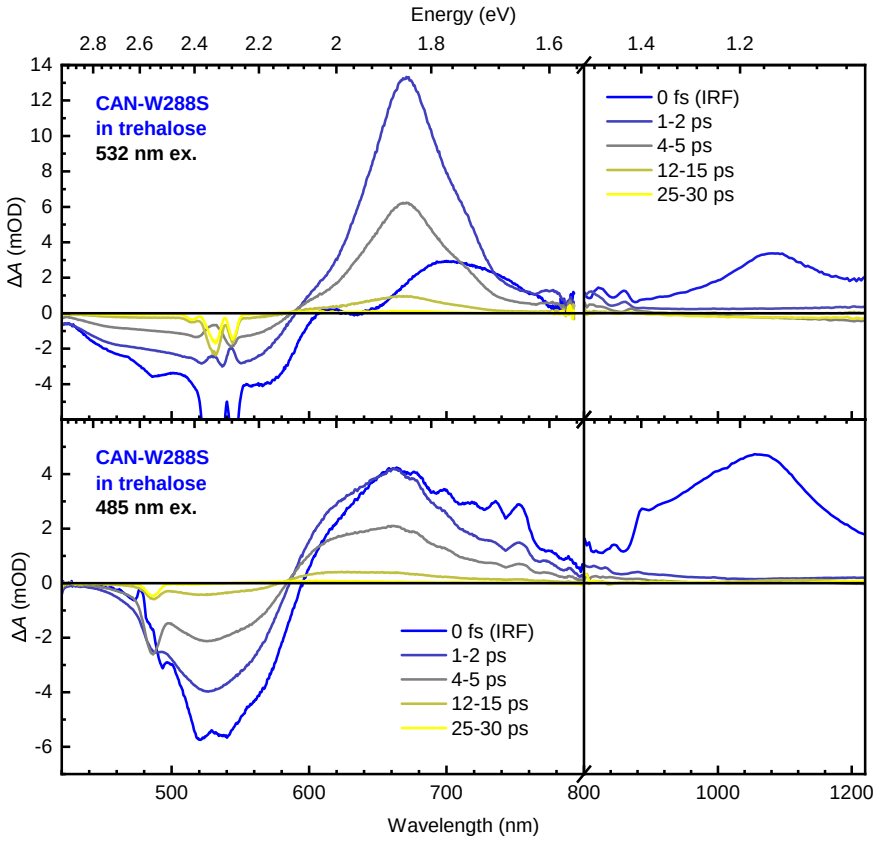

Figure G.14 – Picosecond transient absorption spectra of CAN-binding W288S in trehalose glass with pump wavelength 532 nm (top) or 485 nm (bottom) with visible (left) and NIR (right) probes. As in OCPr in trehalose (*e.g.* Figure G.3), blue-end excitation has signatures of longer-lived states while red-end excitation does not, and no ICT stimulated emission is seen in the NIR region. Spectra have been averaged between the times indicated. Pump fluence was set to 200 µJ cm^{-2}.

we note that ESA peak around 690 nm probe wavelength (associated with absorption from a vibronic replica of the S_1-like states to S_n-like states) is significantly diminished compared to that for OCPr in trehalose (Figure G.3, top) and W288S in trehalose (Figure G.14, top). The corresponding transient absorption results using 485 nm pump (bottom panels) are similar. We do not know why this is the case.

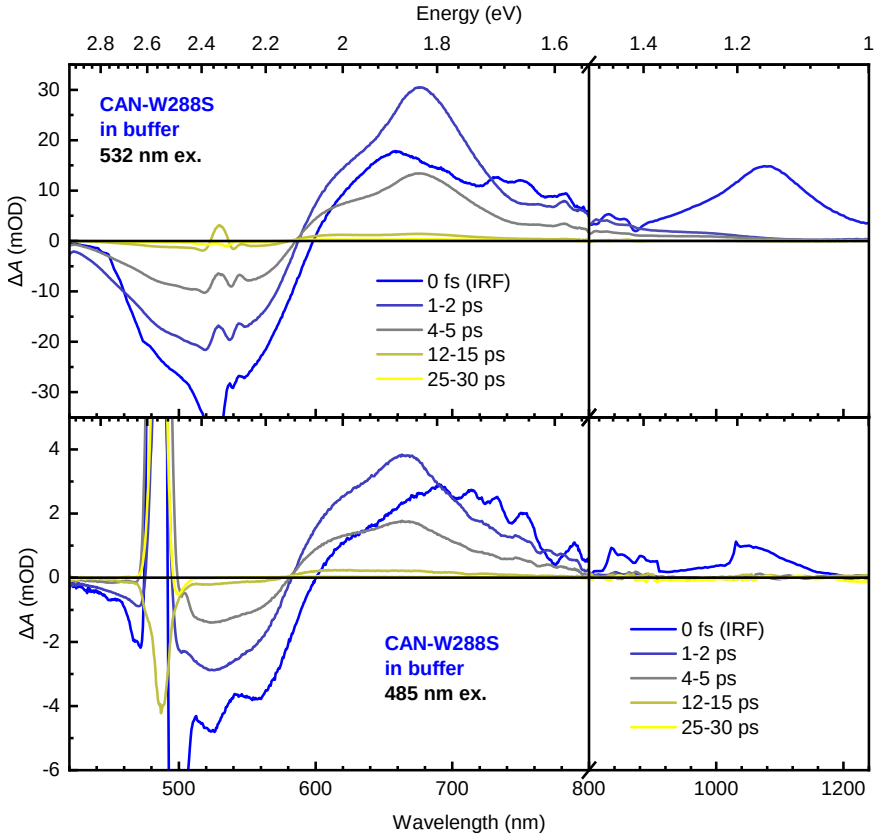

Figure G.15 – Picosecond transient absorption spectra of CAN-binding W288S in buffer with pump wavelength 532 nm (top) or 485 nm (bottom) with visible (left) and NIR (right) probes. As in OCPr in trehalose (Figure G.3 and W288S in trehalose (Figure G.14), blue-end excitation has signatures of longer-lived states while red-end excitation does not, and no ICT stimulated emission is seen in the NIR region. Spectra have been averaged between the times indicated. Pump fluence was set to 200 µJ cm^{-2}.

G.6 Transient absorption on keto-carotenoids in solution

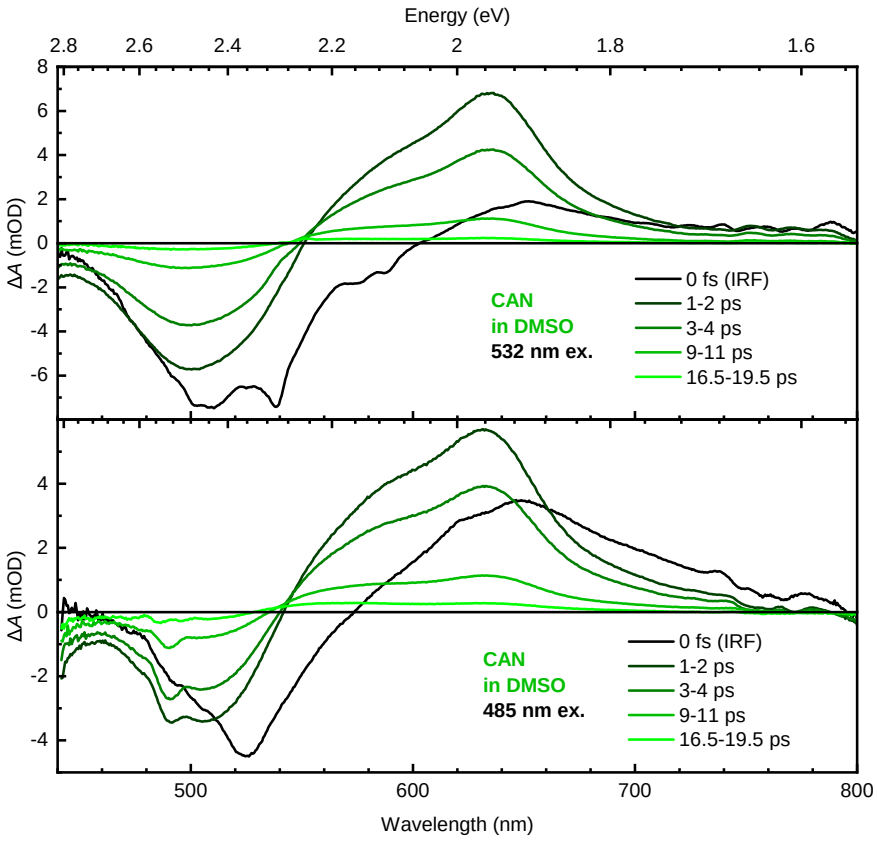

Figure G.16 – Picosecond transient absorption spectra of CAN in DMSO with pump wavelength 532 nm (top) or 485 nm (bottom) with a visible probe. Blue-end excitation has signatures of longer-lived states while red-end excitation does not, and no ICT stimulated emission is seen in the NIR region. Spectra have been averaged between the times indicated. Pump power was set to 0.5 mW, with an estimated (due to no measurement of the pump spot size) fluence in the range 10–100 µJ cm^{-2}.

Picosecond transient absorption spectra of monomeric CAN in DMSO using a visible probe and using 532 nm and 485 nm pumps are shown in Figure G.16. In contrast with the rest of the visible- and NIR-probe ps transient absorption data shown here, the maximum time delay used here was 20 ps, and the pump power used was 0.5 mW. The pump spot size was not measured, so we cannot determine the pump fluence accurately, but based on the range of pump spot sizes previously measured in our ps transient absorption system, we estimate

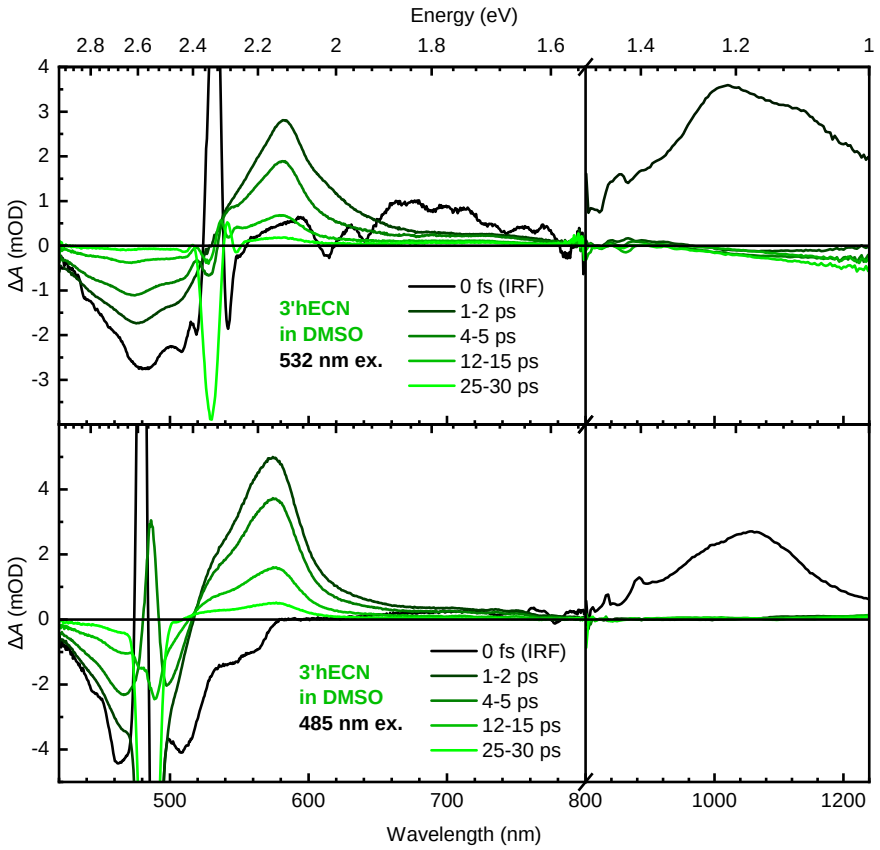

Figure G.17 – Picosecond transient absorption spectra of 3′hECN in DMSO with pump wavelength 532 nm (top) or 485 nm (bottom) with visible (left) and NIR (right) probes. Blue-end excitation has signatures of longer-lived states while red-end excitation does not, and no ICT stimulated emission is seen in the NIR region. Spectra have been averaged between the times indicated. Pump fluence was set to 200 µJ cm^{-2}.

a pump fluence in the range 10–100 µJ cm^{-2}. This relatively low pump fluence led to relatively high-quality measurements, with significantly less degradation and a weaker coherent artefact. The observed photophysics are consistent with a standard carotenoid model, with effects associated with IVR and VET, namely the apparent slower decay of the vibronic replica around 580 nm probe wavelength (compared to the vibronic replica around 615 nm) and its enhancement when using 485 nm pump.[66–70]

Picosecond transient absorption spectra of monomeric 3′hECN in DMSO using visible and NIR probes and using 532 nm and 485 nm pumps are shown in Figure G.17. The observed photophysics are similar to CAN in DMSO, consistent with a standard carotenoid model, with effects associated with IVR and VET, namely

the apparent slower decay of the vibronic replica around 540 nm probe wavelength (compared to the vibronic replica around 580 nm) and its enhancement when using 485 nm pump.[66–70] Pump fluence was set to 200 µJ cm^{-2}, leading to stronger degradation than that for CAN in DMSO.

Appendix H

Comparative resonance Raman spectra of light-harvesting complexes and trehalose

A comparison of the resonance Raman spectra of OCPo/OCPr in trehalose films of this work against the spectra of purple bacterial light-harvesting complexes (LHCs) from Yu *et al.*[41] is shown in Figure H.1. The carotenoid ν_3 peak arises from CH_3 rocking in the plane of carotenoid conjugation, while the ν_4 peak arises from C−H wagging modes out of the plane of conjugation.[41,48,271] Therefore, the ν_4:ν_3 ratio is indicative of the degree of carotenoid backbone twisting.[41] For OCP binding canthaxanthin (CAN) in trehalose in panel (a), we see that OCPo has a greater ν_4:ν_3 ratio, indicating that the CAN in OCPo is twisted while the CAN in OCPr is relatively planar. We do not see any evidence of efficient intramolecular singlet fission (intra-SF) in either OCPo or OCPr; see Chapter 5 for details. For purple bacterial LHCs in panel (b), the LH2 from *Rhodobacter sphaeroides* 2.4.1 (LH2-*Rba*) binding >90% spheroidene[41] has no discernible ν_4 peak, so its ν_4:ν_3 ratio is near-zero and the carotenoids bound within LH2-*Rba* are said to be planar.[41] As LH2-*Rba* was the only LHC studied by Yu *et al.* showing no singlet fission (SF) contribution to its triplet population, the authors hypothesised that the carotenoid twist is the determinant for SF through an intramolecular scheme (*i.e.* through intra-SF).[41] This is counter to the lack of intra-SF in OCPo; see Chapter 5 for details.

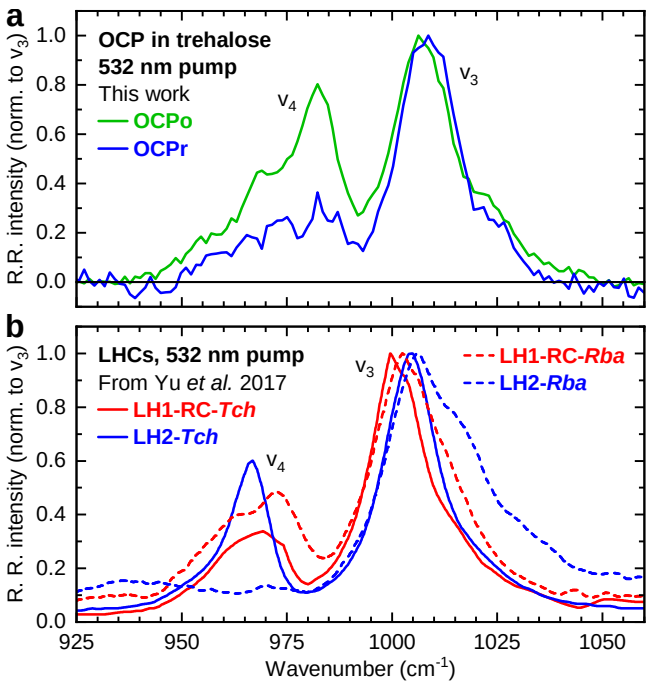

Figure H.1 – Resonance Raman spectra of OCP in trehalose glass films and of purple bacterial LHCs. A 532 nm pump was used in all experiments here, with normalisation to the peak ν_3 intensity. **(a)** The spectra of OCPo (green) and OCPr (blue) are reproduced from Figure 5.2c, zoomed to the ν_3 and ν_4 peaks. Data is averaged from two successive scans. **(b)** The spectra of LHCs from *Thermochromatium tepidum* (LH1-RC-*Tch*, LH2-*Tch*) and *Rhodobacter sphaeroides* 2.4.1 (LH1-RC-*Rba*, LH2-*Rba*) are adapted with permission from Yu *et al.*[41] (copyright 2017 American Chemical Society). Note that LH2-*Rba* has no discernible ν_4 peak.

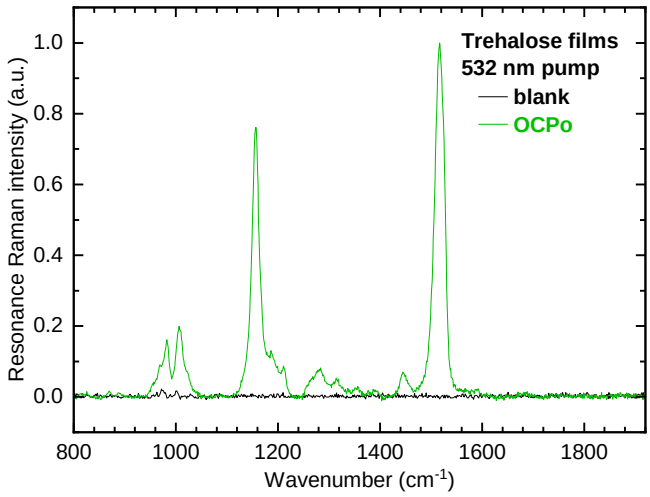

Figure H.2 – Resonance Raman spectra of blank trehalose glass and OCPo in trehalose. The blank trehalose spectrum (black) is almost entirely noise, confirming that the trehalose-sucrose glass is not contributing significant Raman signal in any of the samples incorporating trehalose glass. OCPo in trehalose (green) is shown as a comparison, normalised to to the peak ν_1 intensity. The blank spectrum has been scaled to give a similar noise magnitude at the high-wavenumber end. Both spectra are single scans (not averaged). Measurements were undertaken at room temperature. A 532 nm pump was used. Experiment performed by Harrison Ka Hin Lee under the supervision of Wing C. Tsoi (SPECIFIC, Faculty of Science and Engineering, Swansea University, UK), with analysis and figure preparation by James P. Pidgeon.

Appendix I

Supplementary visible ns–ms transient absorption materials

I.1 Transient absorption dynamics

Nanosecond-millisecond transient absorption dynamics of CAN-OCPo in trehalose at probe wavelengths 500 nm and 555 nm are shown in Figure I.1a as thin lines. This is from the same dataset as that for the spectra of Figures 6.3c and 7.5a. Similar transient absorption dynamics of CAN-OCPo in buffer, refreshed with a flow cell, are shown in Figure I.1b as thin lines. This is from the same dataset as that for the spectra of Figures 6.3d and 7.5b. As discussed in Section 6.2.2, this transient absorption data in buffer shows no obvious differences to CAN-OCPo measured in trehalose or to 3′hECN-OCP reported elsewhere recently.[53]

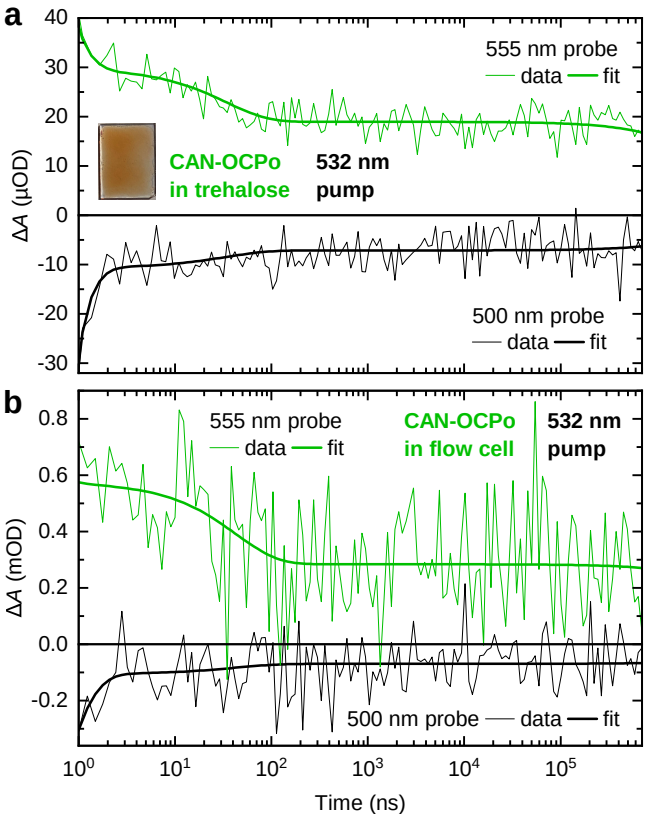

Figure I.1 – Visible-probe ns–ms transient absorption dynamics of CAN-binding OCPo in trehalose (a) and in buffer (b) with pump wavelength 532 nm. Data (thin lines) are a single probe wavelength (*i.e.* not averaged); see Figure 6.3 for spectra (panel (c) for trehalose, panel (d) for buffer). Fit (thick lines) are a single wavelength from the 4-component parallel global lifetime analysis on the data, see Figures I.3 (trehalose) and I.5 (buffer). Note the different y-axis scales between each panel.

I.2 Global lifetime analysis

5-component sequential model	**4-component sequential model**
$t_1 = 100\,\text{ps}$ $t_2 = 1\,\text{ns}$	$t_1 = 100\,\text{ps}$ $t_2 = 1\,\text{ns}$
$t_3 = 50\,\text{ns}$ $t_4 = 10\,\mu\text{s}$ $t_5 = \infty$	$t_3 = 50\,\text{ns}$ — $t_4 = \infty$
IRF centre = 1 ns (trehalose) or 0.65 ns (buffer) IRF FWHM = 0.35 ns	IRF centre = 1 ns (trehalose) or 0.65 ns (buffer) IRF FWHM = 0.35 ns

Table I.1 – Summary of initial parametrisations used in the global lifetime analysis of the visible ns–ms transient absorption data. The time constants t_3, t_4, and t_5 (light green) were chosen to match the ≥50 ns EADS time constants determined by Konold *et al.* when using a higher pump power.[53] The 4-component sequential model omits the 10 µs component. Note that a different initial IRF centre is used for the trehalose and buffer data. As sequential models are being used, the decay rate constants k_i are the inverse of the corresponding time constants t_i ($k_i = t_i^{-1}$).

Global lifetime analysis was also performed on a selection of the ns–ms transient absorption data using similar sequential models Konold *et al.*[53] used for their transient absorption data on 3′hECN-OCP with a 475 nm pump. This was to check if similar >1 ns photoproducts described in their work are being formed in our samples, even when OCPo is within trehalose. This was also done using the Glotaran 1.5.1 software package (`https://glotaran.org`),[233] a GUI for the R package TIMP.[234] Data had already been processed with the steps outlined in Section 4.4.4. Noisy regions in the data due to pump scatter were set to zero ΔA for all times to ensure a good fit of the rest of the data. Noisy red and blue ends in the data associated with tails of the probe were also excluded. A number of models with different numbers of components were applied to the data, with the resulting evolution-associated difference spectra (EADS) corresponding to different photoproducts that exponentially decay into one another in sequence. A summary of the initial choices for time constants (*i.e.* decay rate constants)

and the instrument response function (IRF) centre and FWHM in the applied models is shown in Table I.1.

A 5-component sequential fit to the CAN-OCPo in trehalose transient absorption data gives latter components very similar to those found by Konold *et al.*, both in spectral profile and associated time constant. Figure I.2 shows the fit, with EADS in the top panel and time constants specified in the legend. The first two EADS do not resemble those seen in Konold *et al.*, in terms of spectral profile and especially in associated time constants.[53] This is likely due to the instrument response function in our ns–ms transient absorption setup being ∼1 ns, which is greater than the first three EADS time constants from a 6-component sequential fit in Konold *et al.* (1.4 ps, 4.5 ps, 24 ps), and greater than our own fitted EADS time constants (30.32 ps, 423.5 ps) and Gaussian IRF (FWHM = 350.2 ps). Our own attempts of a 6-component sequential fit result in degenerate EADS. However, the subsequent EADS (29.8 ns, 7.6 µs, 11 ms) closely match those of Konold *et al.* (50 ns, 50 µs, infinite when using a higher pump power, and 50 ns, 25 µs, infinite when using a lower pump power), further demonstrating that we are seeing the same photoproducts as 3′hECN-OCP in solution, despite our CAN-OCPo being trapped in trehalose. We note that the profile of the two EADS associated with 7.6 µs and 11 ms match very closely, with a smaller amplitude decrease in the excited-state absorption (ESA) and especially in the ground-state bleach (GSB) compared to Konold *et al.*'s comparable EADS. We therefore print the results of a 4-component sequential fit on the same data in Figure I.3; it is apparent from the structure of the residuals that omitting a ∼10 µs component does not discernibly affect the fit quality. The 4-component global fit is displayed as dynamics in Figure I.1a as bold lines (data are thin lines).

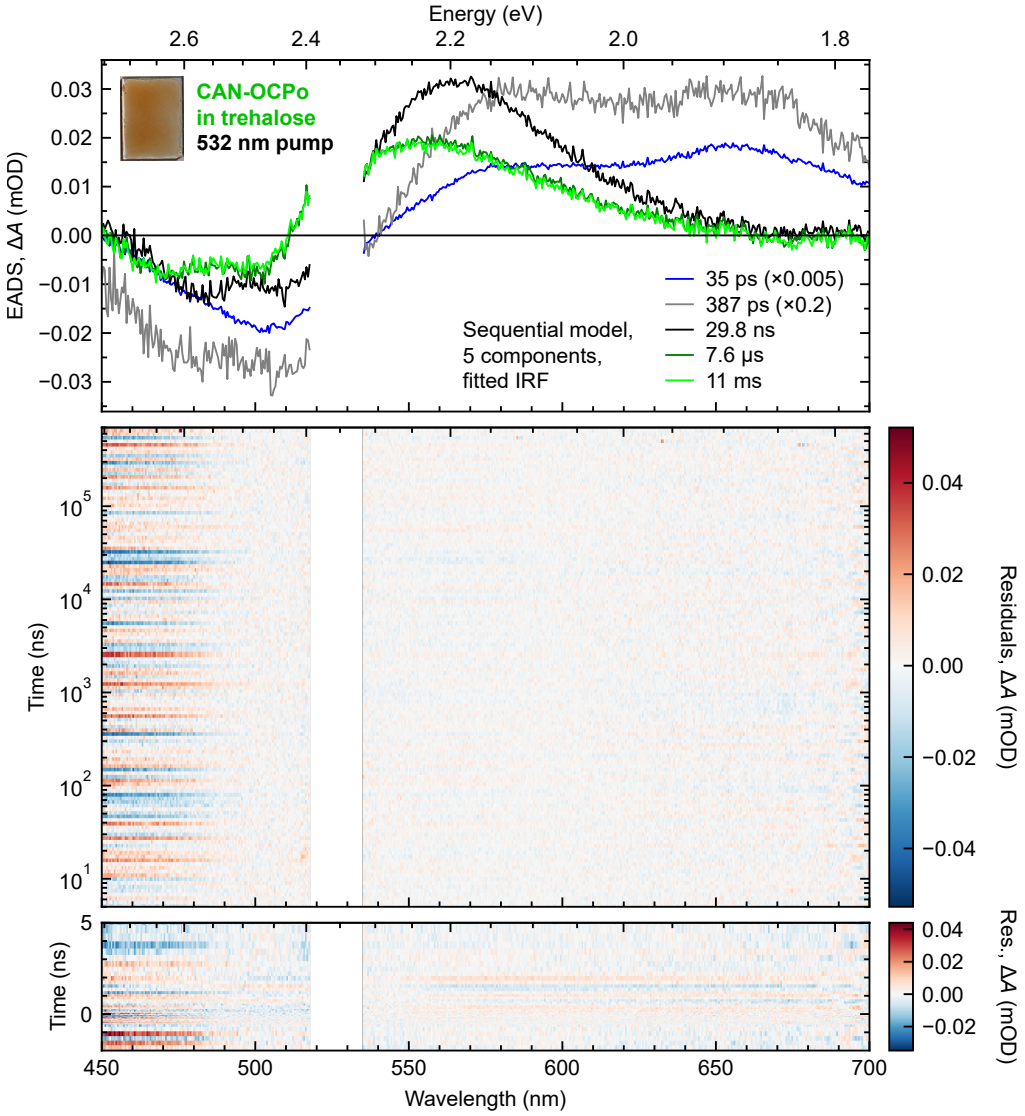

Figure I.2 – Results of global lifetime analysis with a 5-component sequential model on transient absorption data of CAN-binding OCPo in trehalose with pump wavelength 532 nm and a visible probe: EADS (top) and residuals (middle, bottom). Only the wavelength range 450–700 nm was fitted, and noisy data from 518–535 nm due to significant pump scatter was excluded from the fit. EADS time constants are specified in the legend; multiplications refer to scalings applied to the EADS. The fitted IRF has centre 1.09 ns and FWHM 0.36 ns. Residuals = Data − Fit; note the logarithmic time-scale in the middle panel, and the linear time-scale and different residuals scale in the bottom panel. See text for further details.

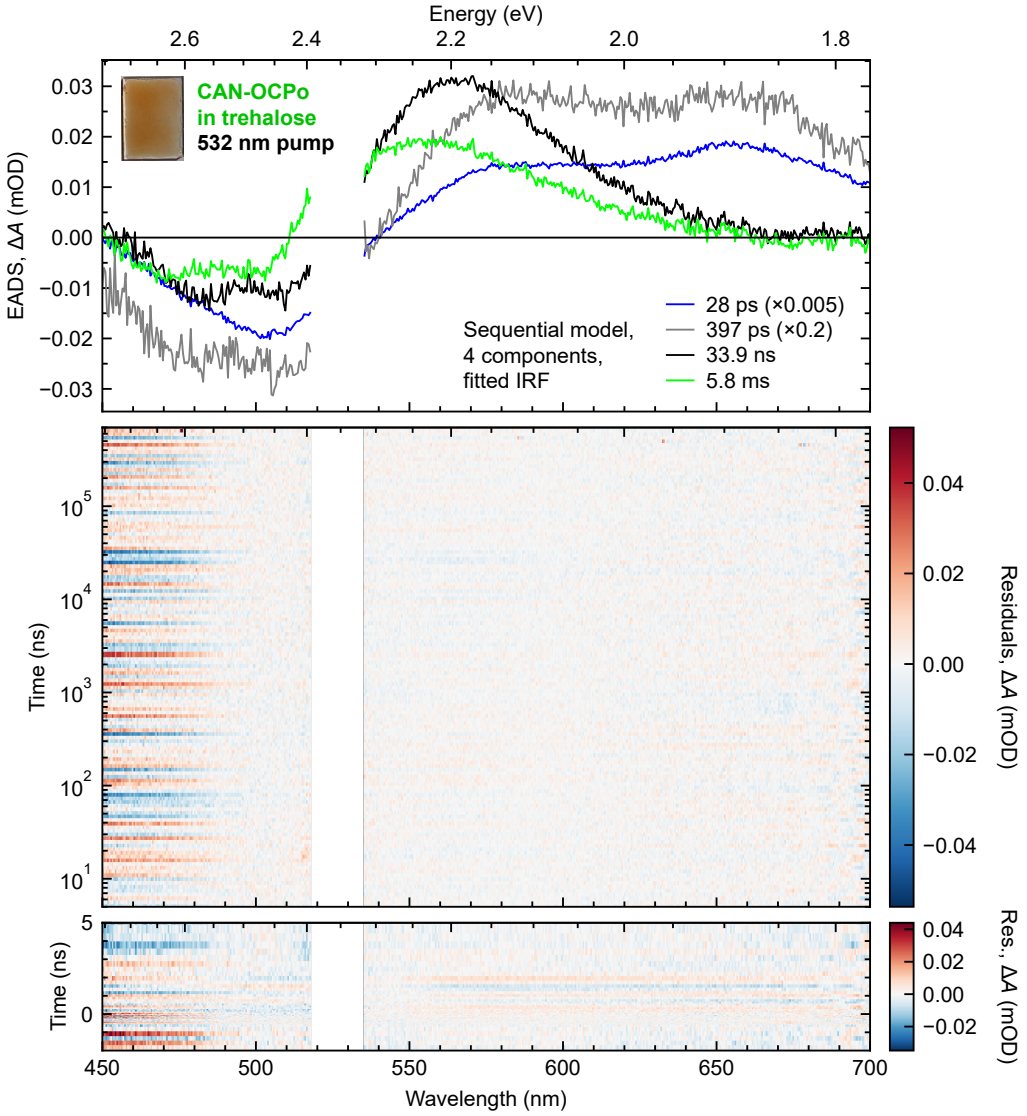

Figure I.3 – Results of global lifetime analysis with a 4-component sequential model on transient absorption data of CAN-binding OCPo in trehalose with pump wavelength 532 nm and a visible probe: EADS (top) and residuals (middle, bottom). Only the wavelength range 450–700 nm was fitted, and noisy data from 518–535 nm due to significant pump scatter was excluded from the fit. EADS time constants are specified in the legend; multiplications refer to scalings applied to the EADS. The fitted IRF has centre 1.09 ns and FWHM 0.36 ns. Residuals = Data − Fit; note the logarithmic time-scale in the middle panel, and the linear time-scale and different residuals scale in the bottom panel. See text for further details.

As a final check, we undertake the same 5-component and 4-component sequential global lifetime analysis on our transient absorption data of CAN-OCPo in buffer in a flow cell, and the results are indeed consistent with both Konold *et al.*'s and our own in trehalose. The 5-component model results are shown in Figure I.4. Here, the EADS associated with 1.6 ms appears to shift to more positive ΔA for all wavelengths, compared to the EADS for 12.4 µs. This is inconsistent with both our in-trehalose results and Konold *et al.*'s results.[53] The 4-component model (dynamics in Figure I.1b and EADS in Figure I.5) where the ∼10 µs EADS is essentially omitted appears to fit the data as well as the 5-component model.

We emphasise that in these global lifetime analyses of the ns–ms transient absorption data, our first two EADS (time constants <1 ns) have little physical significance. We also note that the maximum time delay in these experiments was 0.7 ms, and that the final EADS all have a fitted time constant exceeding that.

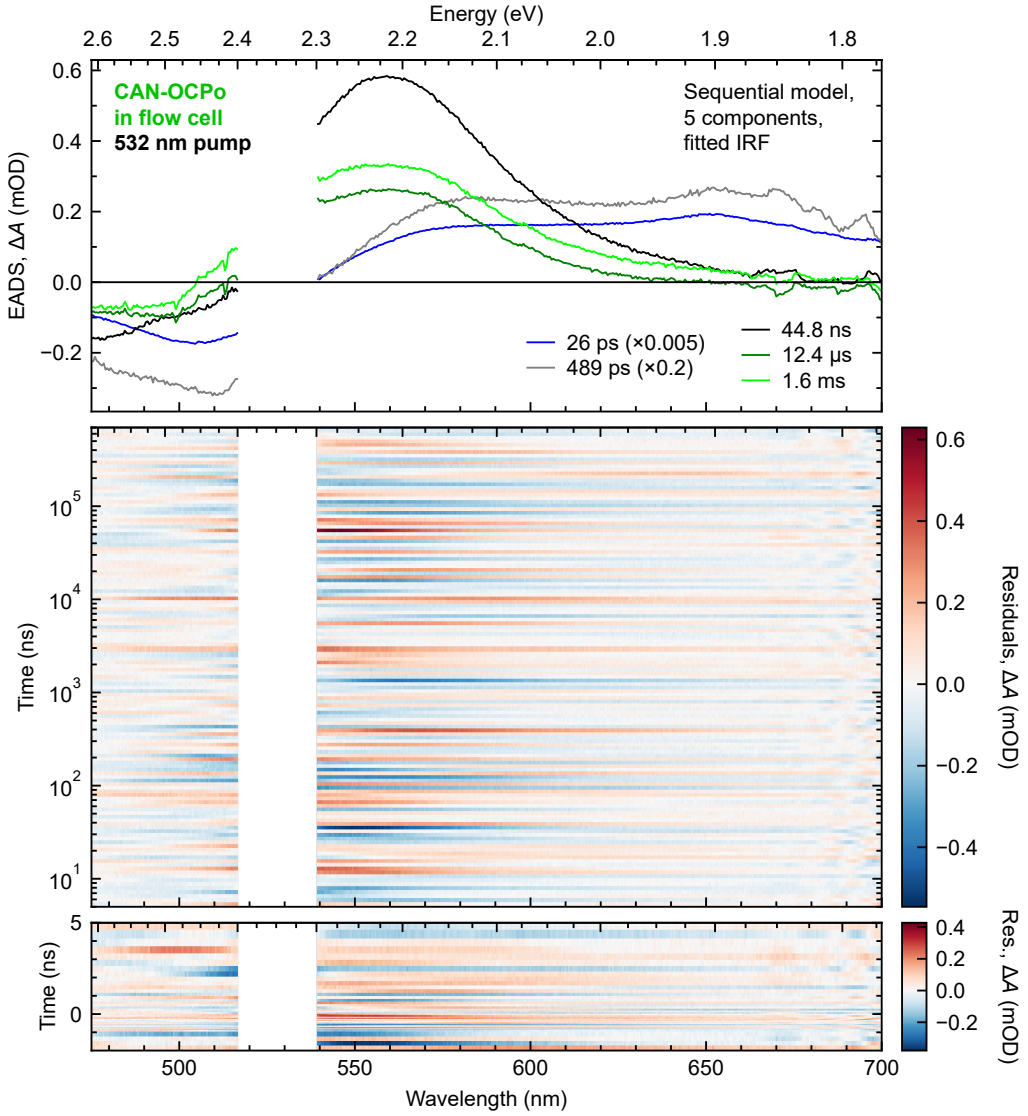

Figure I.4 – Results of global lifetime analysis with a 5-component sequential model on transient absorption data of CAN-binding OCPo in buffer with pump wavelength 532 nm and a visible probe: EADS (top) and residuals (middle, bottom). Only the wavelength range 475–700 nm was fitted, and noisy data from 517–539 nm due to significant pump scatter was excluded from the fit. EADS time constants are specified in the legend; multiplications refer to scalings applied to the EADS. The fitted IRF has centre 0.67 ns and FWHM 0.28 ns. Residuals = Data − Fit; note the logarithmic time-scale in the middle panel, and the linear time-scale and different residuals scale in the bottom panel. See text for further details.

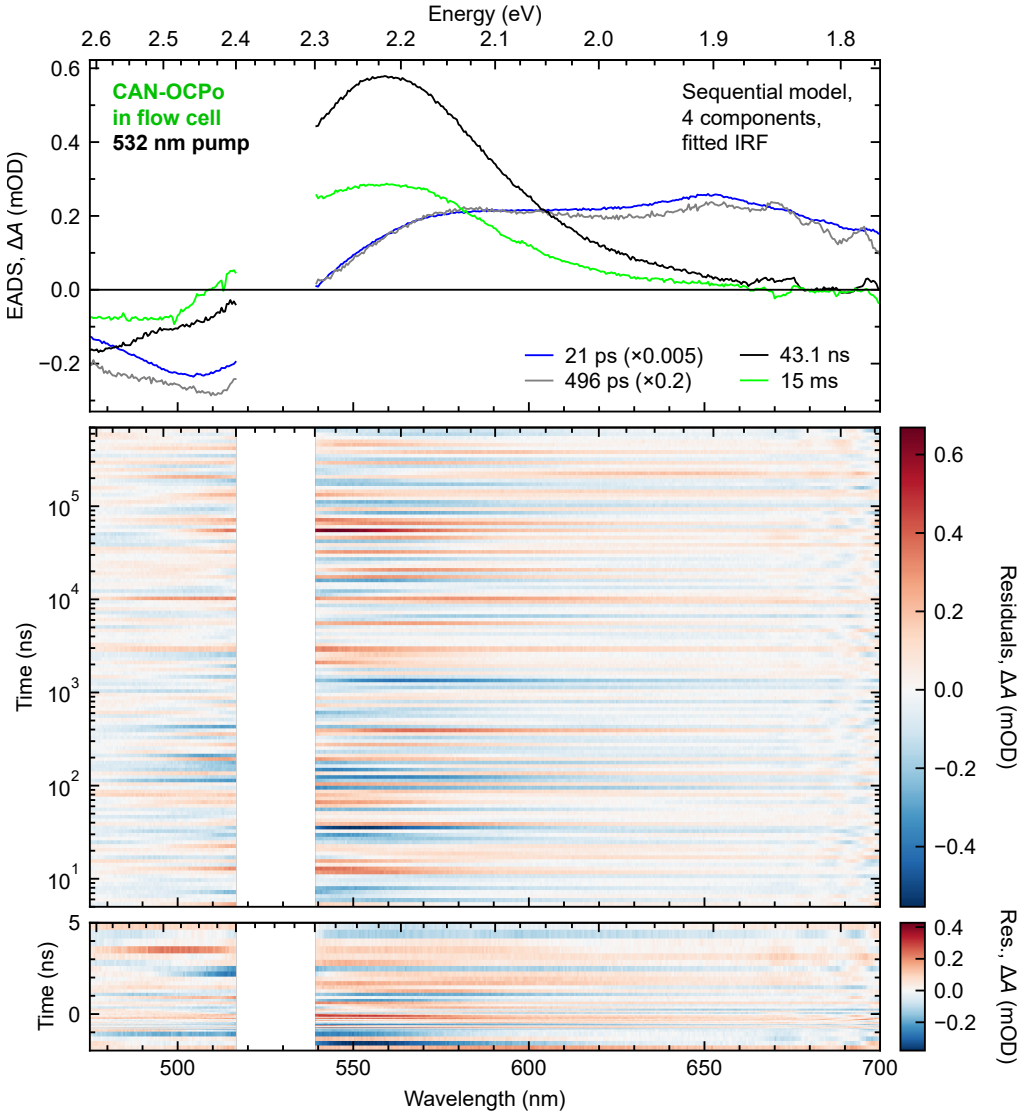

Figure I.5 – Results of global lifetime analysis with a 4-component sequential model on transient absorption data of CAN-binding OCPo in buffer with pump wavelength 532 nm and a visible probe: EADS (top) and residuals (middle, bottom). Only the wavelength range 475–700 nm was fitted, and noisy data from 517–539 nm due to significant pump scatter was excluded from the fit. EADS time constants are specified in the legend; multiplications refer to scalings applied to the EADS. The fitted IRF has centre 0.69 ns and FWHM 0.29 ns. Residuals = Data − Fit; note the logarithmic time-scale in the middle panel, and the linear time-scale and different residuals scale in the bottom panel. See text for further details.

Appendix J

Supplementary UV-vis ps transient absorption materials

J.1 Pump spectra and comments on 'bands'

For our pump wavelength-dependent ps transient absorption measurements on CAN-OCPo in trehalose, we obtain 420 nm to 600 nm pump pulses with an optical parametric amplifier (TOPAS Prime, Light Conversion). Certain pump wavelength 'bands' require a different configuration of the TOPAS Prime. For 420 nm to 480 nm pump pulses, a configuration we dub band (A) is used; for 480–535 nm, band (B) is used; for 535–600 nm, band (C) is used. Measurements using each band were completed on separate experimental days (*i.e.* one day for band (B), one later day for band (A), and so on). We note that for 400 nm pump pulses, a frequency doubler utilising β-barium borate crystals is used instead, and is denoted (TP) (see Section 4.4.1 for further experimental details).

Figure J.1a shows the pump wavelengths used for UV-vis transient absorption measurements depicted in Section 6.2.3 (Figures 6.4, 6.5, and 6.6) and their normalised intensity profiles against wavelength. The legend shows the nominal pump wavelength (as set in WinTopas4), the band used in generating that wavelength, and the measured pump powers (of the 5 kHz pulses measured per-second). Note that band (A) generates the $\lambda_{\text{pump}} = 480$ nm used for experiments in Section 6.2.3, and that band (B) generates the $\lambda_{\text{pump}} = 535$ nm used there also.

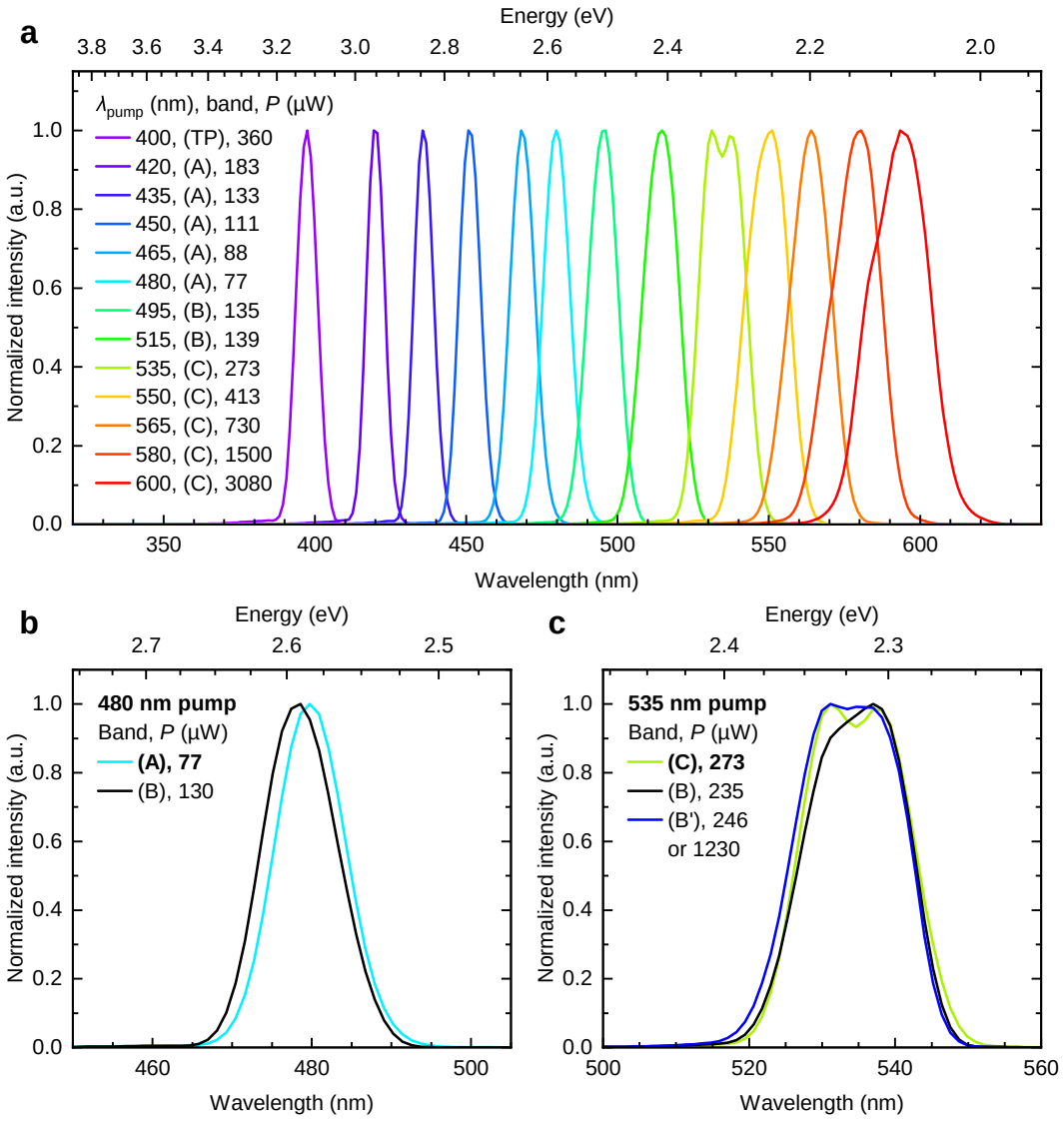

Figure J.1 – Normalised intensity spectra of the pumps used in the UV-vis-probe ps transient absorption experiments, normalised to the maximum intensity. Pump wavelengths (as set in WinTopas4), the TimePlate usage (here dubbed (TP)) or TOPAS Prime configuration for a band (here dubbed (A), (B), (C)), and the measured powers (of 5 kHz pulses measured per-second) are specified in the legend. **(a)** Intensity spectra of the pumps used in the experiments shown in Section 6.2.3 (Figures 6.4, 6.5, and 6.6). **(b)** Intensity spectra of 480 nm pumps in band (A) (Section 6.2.3 data) and band (B) (appendix data; see Figure J.2). **(c)** Intensity spectra of 535 nm pumps in band (C) (Section 6.2.3 data), band (B) (appendix data; see Figure J.3), and band (B′) (appendix data; see Figure J.4). The pump spot sizes at the sample position were generally not measured to save time, but are known to vary per-day and per-pump wavelength, with previous diameter ($1/e^2$) measurements typically in the range 400–800 µm.

J.2 Replicates at same pump wavelengths in different bands

The use of different TOPAS Prime configurations does not have any effect on the transient absorption of CAN-OCPo in trehalose. We undertook control measurements using nominally (as set in WinTopas4) 480 nm and 535 nm pump wavelengths generated using band (B). For $\lambda_{\text{pump}} = 480\,\text{nm}$, a comparison of the normalised intensity spectra between band (A) (Section 6.2.3 experiment) and band (B) (control experiment) is shown in Figure J.1b, and a comparison of transient absorption spectra and dynamics is shown in Figure J.2. The results are near-identical. For $\lambda_{\text{pump}} = 535\,\text{nm}$, a comparison of the normalised intensity spectra between band (C) (Section 6.2.3) and band (B) (control) is shown in Figure J.1c, and a comparison of transient absorption spectra and dynamics is shown in Figure J.3. Again, the results are near-identical. We note that a different CAN-OCPo film spot was used for each measurement, and (as stated above) measurements using each band were done on separate experimental days.

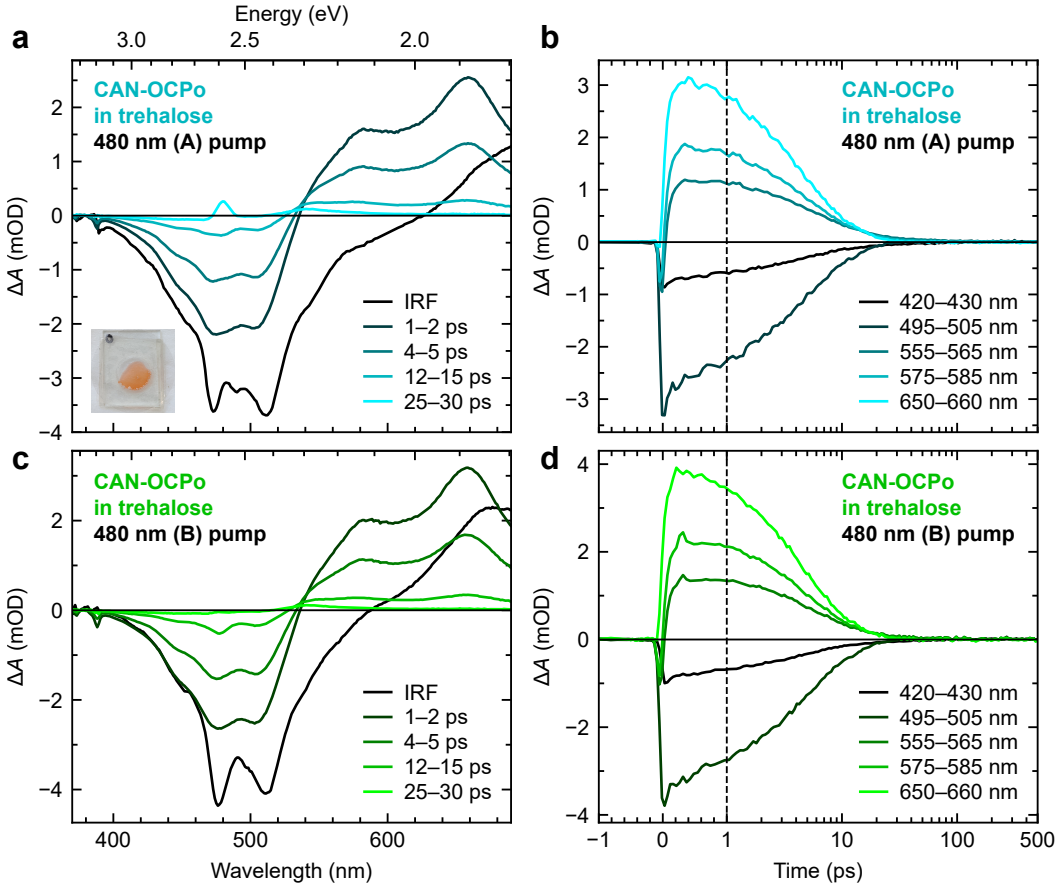

Figure J.2 – Transient absorption spectra (a,c) and dynamics (b,d) on CAN-binding OCPo in trehalose using 480 nm pump wavelength in band (A) (a,b) and band (B) (c,d). Both pumps give near-identical features, with differences attributable to small variations between the pump spectra (see Figure J.1b). We note that a different film spot was used between band (A) and band (B), and each band's measurements were done on separate experimental days. The dynamic plots (b,d) have a linear time-axis up to 1 ps, and subsequently logarithmic up to 500 ps.

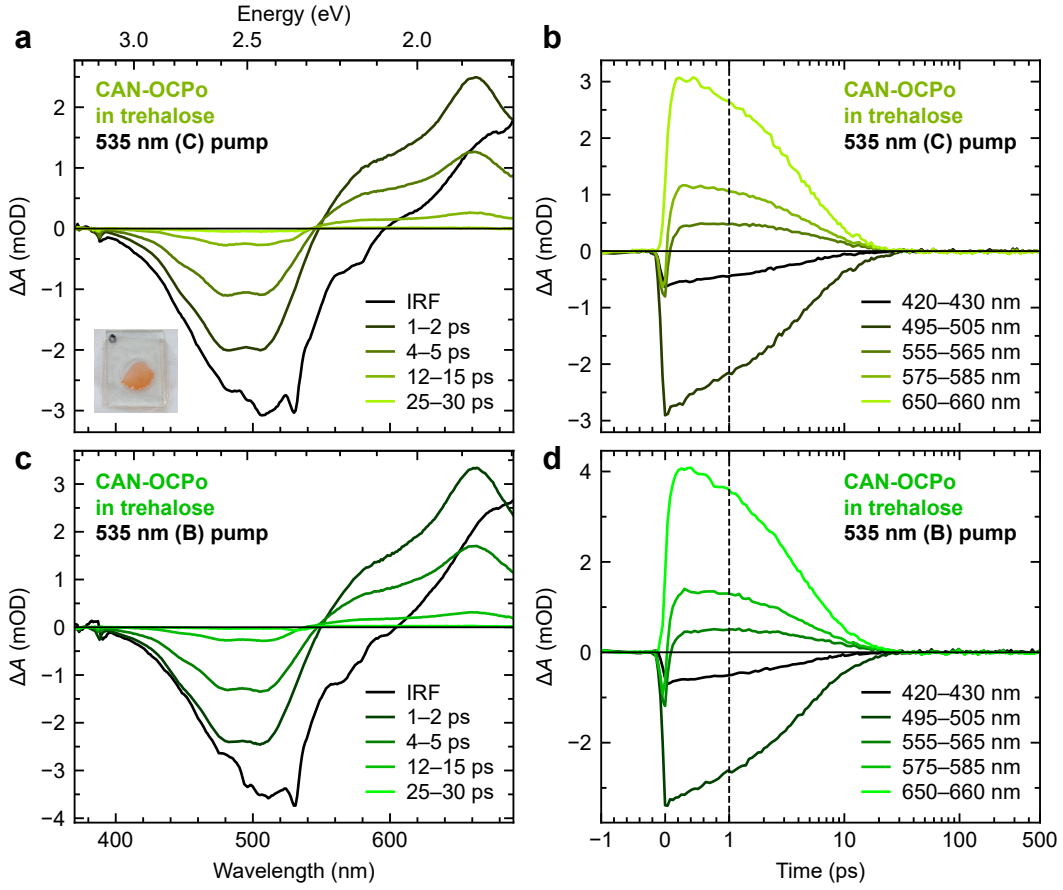

Figure J.3 – Transient absorption spectra (a,c) and dynamics (b,d) on CAN-binding OCPo in trehalose using 535 nm pump wavelength in band (C) (a,b) and band (B) (c,d). Both pumps give near-identical features, with differences attributable to small variations between the pump spectra (see Figure J.1c). We note that a different film spot was used between band (C) and band (B), and each band's measurements were done on separate experimental days. The dynamic plots (b,d) have a linear time-axis up to 1 ps, and subsequently logarithmic up to 500 ps.

J.3 Pump fluence dependence

A brief check of pump fluence dependence shows that the fluence has no effect on the CAN-OCPo in trehalose transient absorption beyond increased degradation, although only a few pump fluences were checked at $\lambda_{\text{pump}} = 535\,\text{nm}$ only. Figure J.4 shows the transient absorption spectra (panels a,c) and dynamics (b,d) using a $10\,\mu\text{J}\,\text{cm}^{-2}$ pump fluence (a,b) and then a $50\,\mu\text{J}\,\text{cm}^{-2}$ pump fluence (c,d) at the same spot on the film. Pump powers for those fluences were tuned following a measurement of the pump diameters ($1/e^2$), which were found to be 934.1 µm (major axis) and 671.1 µm (minor axis). Therefore, 273 µW (a,b) and 1230 µW (c,d) pump powers gave the respective pump fluences. See Section 4.5 for further details on the pump measurements and fluence calculation (*e.g.* Equation 4.16). A subsequent measurement using $200\,\mu\text{J}\,\text{cm}^{-2}$ pump fluence (4920 µW pump power) led to near-complete sample degradation (not shown). We note that band (B′) was the same TOPAS Prime configuration as band (B), but the former was a different experimental day, with additional post-sample probe filters compared to the other UV-vis-probe measurements, along with slightly differing pump intensity spectra (see Figure J.1c).

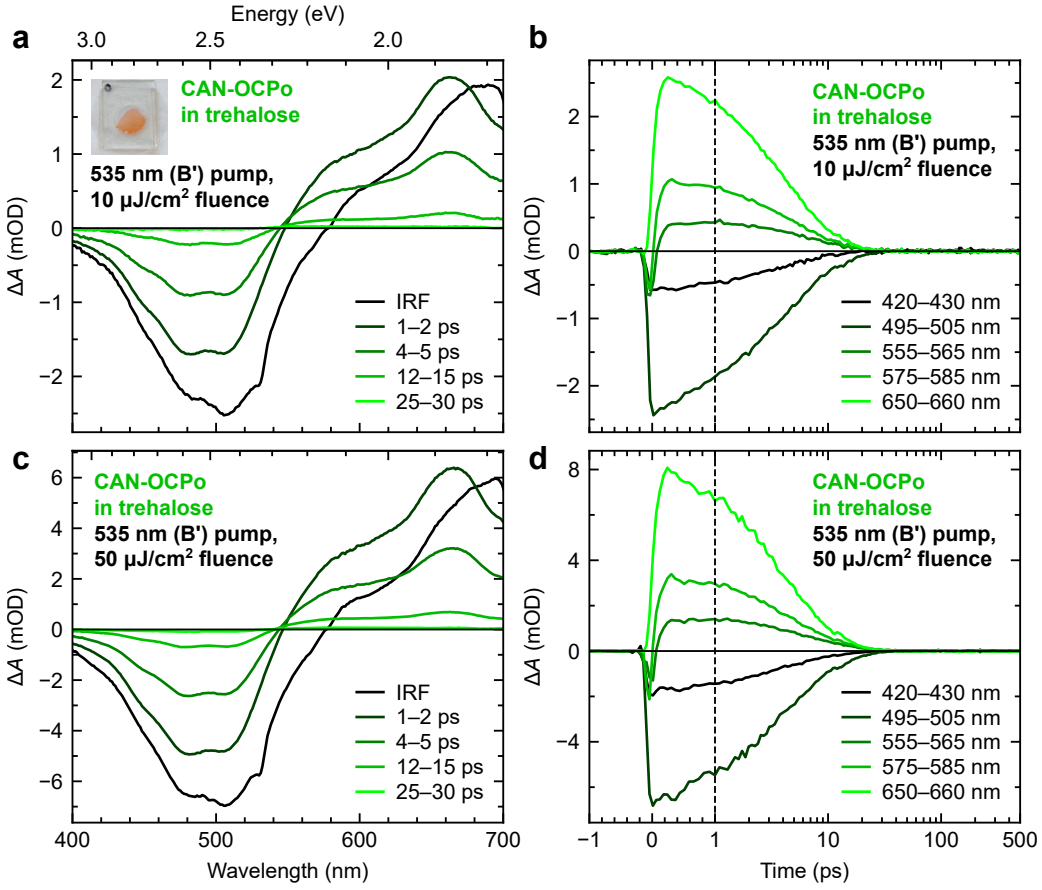

Figure J.4 – Pump fluence dependence on the transient absorption spectra (a,c) and dynamics (b,d) of the same spot on CAN-binding OCPo in trehalose using 535 nm pump wavelength in band (B′). Both the $10\,\mu J\,cm^{-2}$ pump fluence (a,b) and the subsequent $50\,\mu J\,cm^{-2}$ fluence (c,d) gave near-identical spectra (a,c) and dynamics (b,d) on the same film spot, with differences attributable to sample degradation. The dynamic plots (b,d) have a linear time-axis up to 1 ps, and subsequently logarithmic up to 500 ps.

J.4 Global fit of dynamics parameters

λ_{pump} (nm)	α_1	α_2	α_3
400	0.243 ± 0.047	0.315 ± 0.043	0.500 ± 0.010
420	0.167 ± 0.054	0.485 ± 0.047	0.430 ± 0.010
435	0.238 ± 0.055	0.475 ± 0.050	0.350 ± 0.009
450	0.271 ± 0.061	0.540 ± 0.055	0.267 ± 0.009
465	0.333 ± 0.070	0.615 ± 0.063	0.161 ± 0.008
480	0.355 ± 0.072	0.637 ± 0.066	0.090 ± 0.008
495	0.512 ± 0.076	0.598 ± 0.073	0.012 ± 0.007
515	0.533 ± 0.077	0.602 ± 0.074	0.006 ± 0.007
535	0.591 ± 0.073	0.509 ± 0.071	0.011 ± 0.007
550	0.735 ± 0.074	0.452 ± 0.076	0 ± 0.007
565	0.783 ± 0.070	0.361 ± 0.073	0 ± 0.007
580	0.850 ± 0.068	0.297 ± 0.073	0.004 ± 0.007
600	0.909 ± 0.064	0.194 ± 0.070	0.015 ± 0.007

Table J.1 – Fitting parameters found using a global triexponential fit to the data in Figure 6.5. The triexponential equation used is $\Delta A_{\text{fit}}(t) = \alpha_1 \exp(-t/\tau_1) + \alpha_2 \exp(-t/\tau_2) + \alpha_3 \exp(-t/\tau_3)$ with a lower bound $\alpha_i \geq 0$ applied. The fitted time constants are $\tau_1 = 2.8 \pm 0.2\,\text{ps}$, $\tau_2 = 6.5 \pm 0.4\,\text{ps}$, and $\tau_3 = 65 \pm 2\,\text{ps}$; note that as a global fit, these are the same for all pump wavelengths. Errors specified here are fit parameter standard errors.

J.5 Global target analysis

Global target analysis was performed on most of the UV-vis-probe ps transient absorption datasets, as briefly summarized in the Section 6.2.3 (Figure 6.6). This was done using the Glotaran 1.5.1 software package (`https://glotaran.org`),[233] a GUI for the R package TIMP.[234] Since a target model is applied, we term the extracted ΔA-profiles species-associated difference spectra (SADS). Data used had already been processed with the steps outlined in Section 4.4.4; in particular, a chirp correction had already been applied, so that a term to account for chirp

did not need to be included in the fitting. Noisy regions in the data due to pump scatter were excluded for all times to ensure a good fit of the rest of the data. Noisy red and blue ends in the data associated with tails of the probe were also excluded, so that the fitted wavelengths were typically 400 nm to 690 nm. Terms to account for the instrument response function (IRF) and the coherent artefact were included. For the IRF, a Gaussian is convoluted with the exponential decays and parametrised within the model, with its centre and full-width half-maximum (FWHM) fitted. For the coherent artefact, an additional component with the time profile of the IRF is fitted; we do not show this component in our figures.

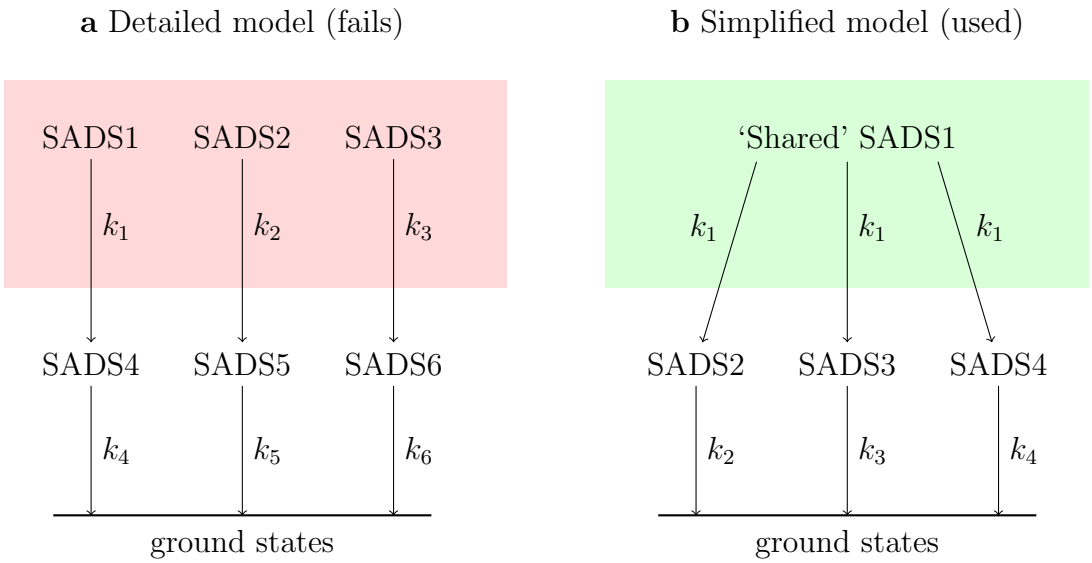

Figure J.5 – Diagrams of representative global target analysis models applied to the UV-vis ps transient absorption data. (a) The model considering distinct S_2 states from ground-state heterogeneities that fails to converge or give reasonable results. **(b)** The simplified model that was used instead, with a shared S_2 state and shared decay rate k_1 to the distinct SADS. The instrument response function and coherent artefact are accounted for in the model. Note that in some applications of the model, the number of SADS is adjusted (*e.g.* SADS4 may be removed, or a SADS5 added). See text for full details.

We generally use a model depicted in Figure J.5b where we fit a SADS corresponding to a single initially populated S_2 state that subsequently decays with an equal (shared) time constant into each of the fitted SADS, with those subsequently decaying with different time constants into the ground state. In Chapter 6, we eventually assign different ground-state heterogeneities within OCPo; a target model possibly more accurate to this is depicted in Figure J.5a. It includes

multiple SADS corresponding to multiple S_2 states that decay individually with different time constants into a paired SADS, subsequently decaying with different time constants into a ground state. However, the ∼100 fs time resolution, the relatively small temporal sampling around time zero, and the coherent artefact obscure distinct states within the first ∼200 fs, so attempts applying the more detailed model failed to converge or give reasonable results. We consequently use the aforementioned model with a single, shared, fast-decaying SADS. Regardless, we believe that this does not remove support for a multiple ground-state assignment.

We find that the 4-SADS model is needed to fit transient absorption datasets with pump wavelengths from 400 nm to 480 nm, but the 3-SADS model is sufficient to fit those with pump wavelengths from 495 nm to 600 nm. The associated fitted decay time constants vary but are somewhat consistent with those extracted from the global triexponential fit of the normalised dynamics (Figure 6.5 and Table J.1). The requirement that a fourth SADS is needed to fit transient absorption datasets for $\lambda_{\text{pump}} \leq 480$ nm is once again consistent with the presence of long-lived forms of OCPo and associated S*-like features for those pump wavelengths.

We note that the four-SADS model somewhat underfits the transient absorption data for the pump wavelength 400 nm (Figure J.6) and possibly 420 nm (Figure J.7) with an observable structure in the residuals. The result of respective five-SADS models are shown in Figures J.18 and J.19. The requirement of SADS5 for a better fit is indicative of further ground-state heterogeneity.

An exception to the 'target' fitting procedure specified above is the analysis of the 600 nm pump wavelength transient absorption data (Figure J.20). As a relatively high pump power is used (see legend in Figure J.1), the coherent artefact is relatively strong, so the early-time dynamics cannot be easily fitted with the target model. We therefore fitted times beyond 0.5 ps with a 2-component parallel global lifetime analysis model with no IRF or coherent artefact terms, very similar to the model applied to the visible-probe transient absorption data (Section G.3), although with no weighting of the data here due to greater maximum delay used (∼500 ps). This corresponds to two decay-associated difference spectra (DADS) decaying in parallel after initial population from the unmodelled (cropped out) S_2 states. DADS1 and DADS2 are comparable to SADS2 and SADS3 respectively.

The variations in the SADS profiles and associated decay time constants per-pump wavelength (particularly for SADS2 and SADS3) are indicative that global

target (and lifetime) analysis is not valid with this dataset. This is because of the effects of intramolecular vibrational redistribution (IVR) and vibrational energy transfer (VET). The assumption of bilinearity (separable spectral and kinetic contributions) in using global lifetime/target analysis[230–232] does not hold, with the IVR/VET essentially giving the spectra some time-dependence.[66–70] Indeed, SADS2 and SADS3 have a mixed and unknown physical correspondence, likely mixed S_1/ICT decay, IVR, and VET between the different ground-state forms of CAN-OCPo. Likewise, SADS1 may correspond to S_2/IVR/VET for multiple CAN-OCPo forms (as discussed above; see Figure J.5), in addition to a potential coherent artefact contribution (the additional IRF-time profile component may not always account for it fully). Meanwhile, SADS4 (and SADS5) can more safely be associated with the S*-like form of OCPo due to the 1-order difference between their associated decay time constants compared to those for SADS1, SADS2, and SADS3.

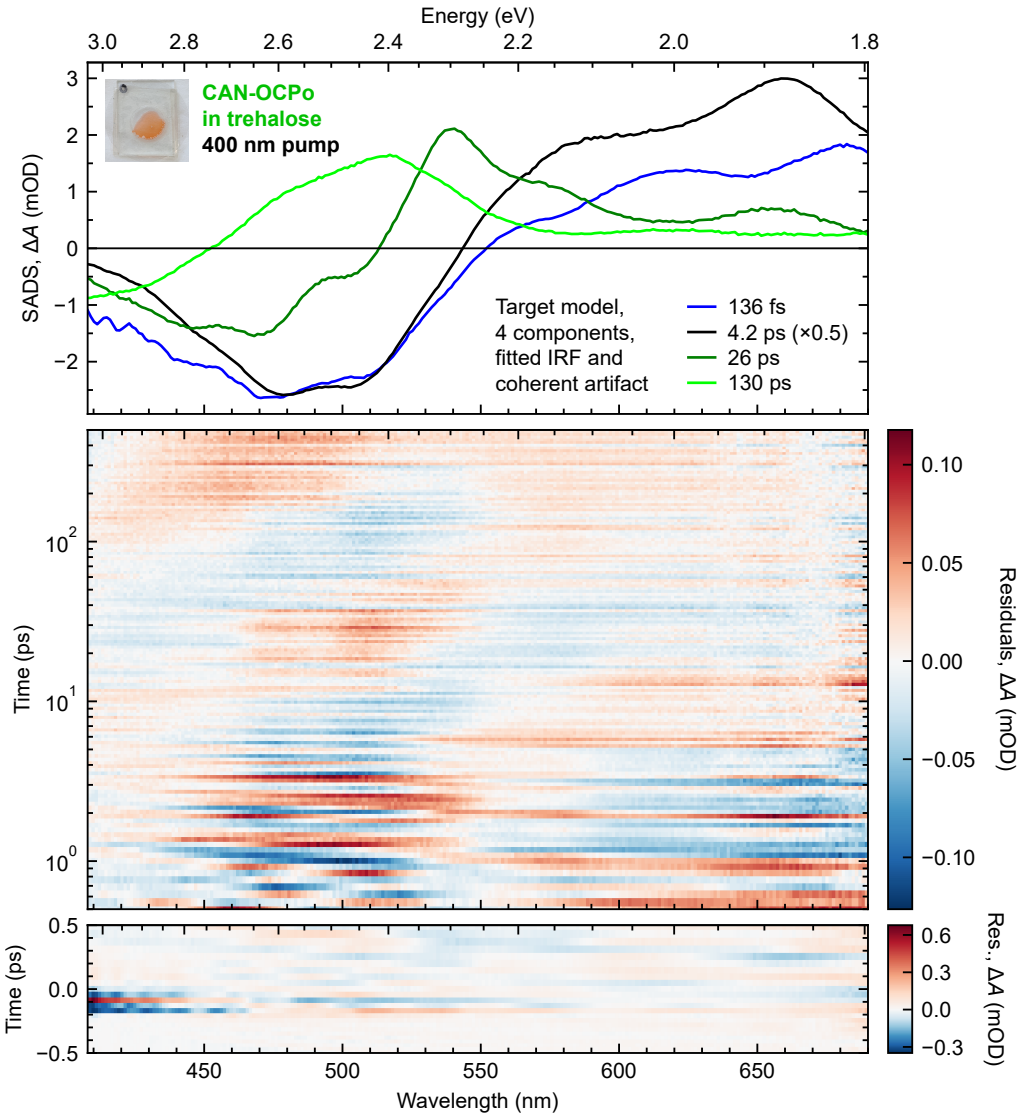

Figure J.6 – Results of global target analysis with a 4-component target model on transient absorption data of CAN-binding OCPo in trehalose with pump wavelength 400 nm and a UV-vis probe: SADS (top) and residuals (middle, bottom). Only the wavelength range 407–690 nm was fitted to exclude noisy data due to low probe light and significant pump scatter. SADS time constants are specified in the legend; multiplications refer to scalings applied to the SADS. The fitted IRF has centre −78 fs and FWHM 64 fs. A coherent artefact with the concentration profile of the IRF was fitted but not shown here. Residuals = Data − Fit; note the logarithmic time-scale in the middle panel, and the linear time-scale and different residuals scale in the bottom panel. See text for further details.

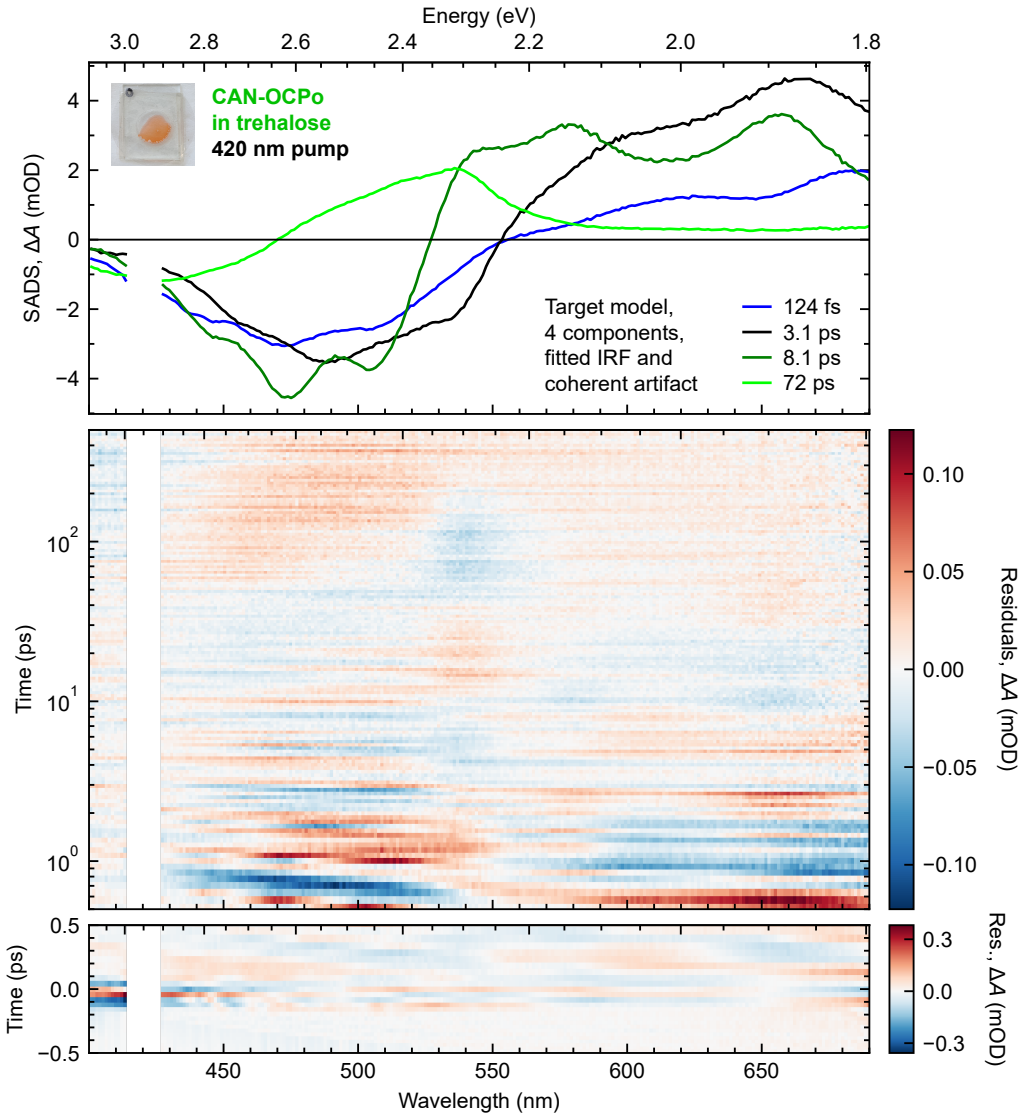

Figure J.7 – Results of global target analysis with a 4-component target model on transient absorption data of CAN-binding OCPo in trehalose with pump wavelength 420 nm and a UV-vis probe: SADS (top) and residuals (middle, bottom). Only the wavelength range 400–690 nm was fitted, and noisy data from 414–427 nm due to significant pump scatter was excluded from the fit. SADS time constants are specified in the legend. The fitted IRF has centre −50 fs and FWHM 47 fs. A coherent artefact with the concentration profile of the IRF was fitted but not shown here. Residuals = Data − Fit; note the logarithmic time-scale in the middle panel, and the linear time-scale and different residuals scale in the bottom panel. See text for further details.

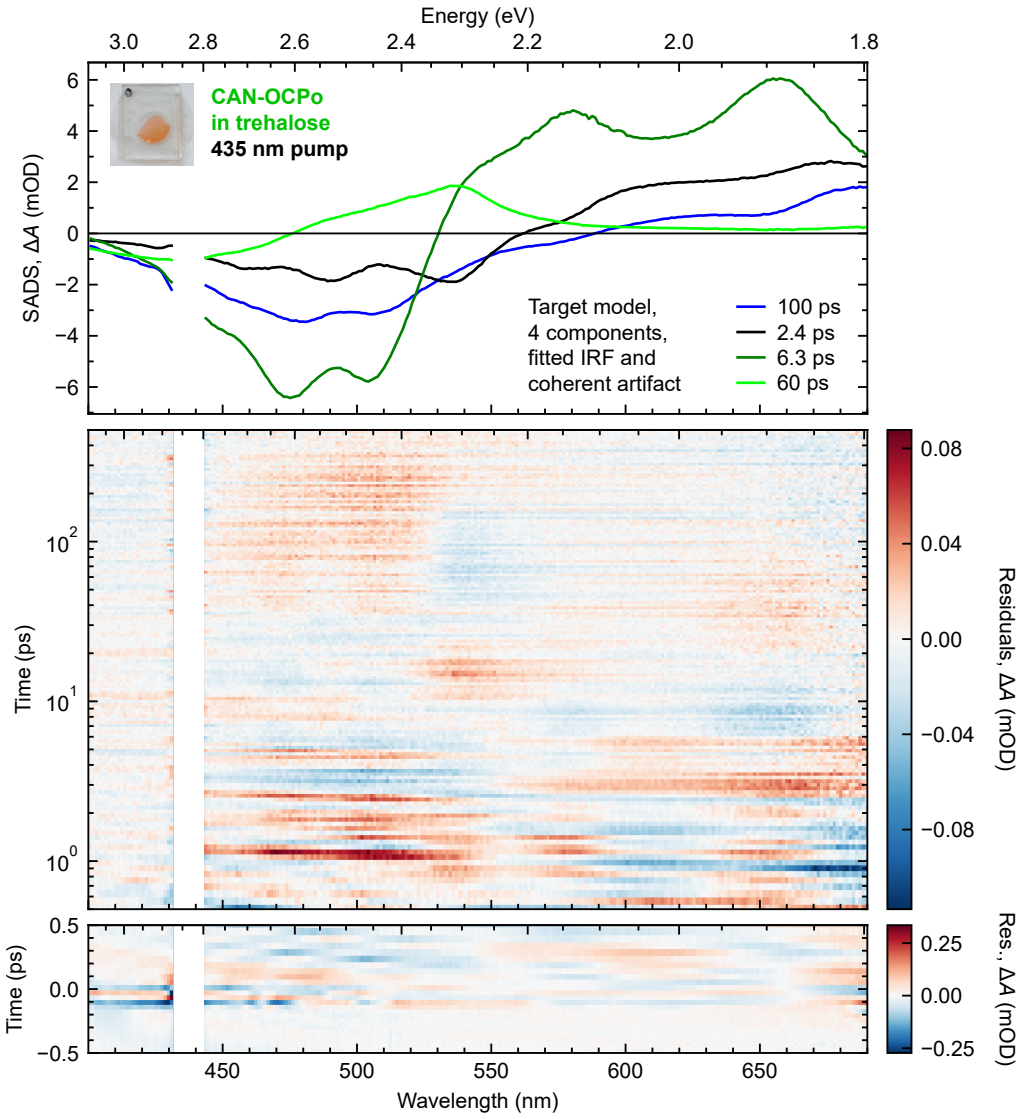

Figure J.8 – Results of global target analysis with a 4-component target model on transient absorption data of CAN-binding OCPo in trehalose with pump wavelength 435 nm and a UV-vis probe: SADS (top) and residuals (middle, bottom). Only the wavelength range 400–690 nm was fitted, and noisy data from 432–443 nm due to significant pump scatter was excluded from the fit. SADS time constants are specified in the legend. The fitted IRF has centre −55 fs and FWHM 36 fs. A coherent artefact with the concentration profile of the IRF was fitted but not shown here. Residuals = Data − Fit; note the logarithmic time-scale in the middle panel, and the linear time-scale and different residuals scale in the bottom panel. See text for further details.

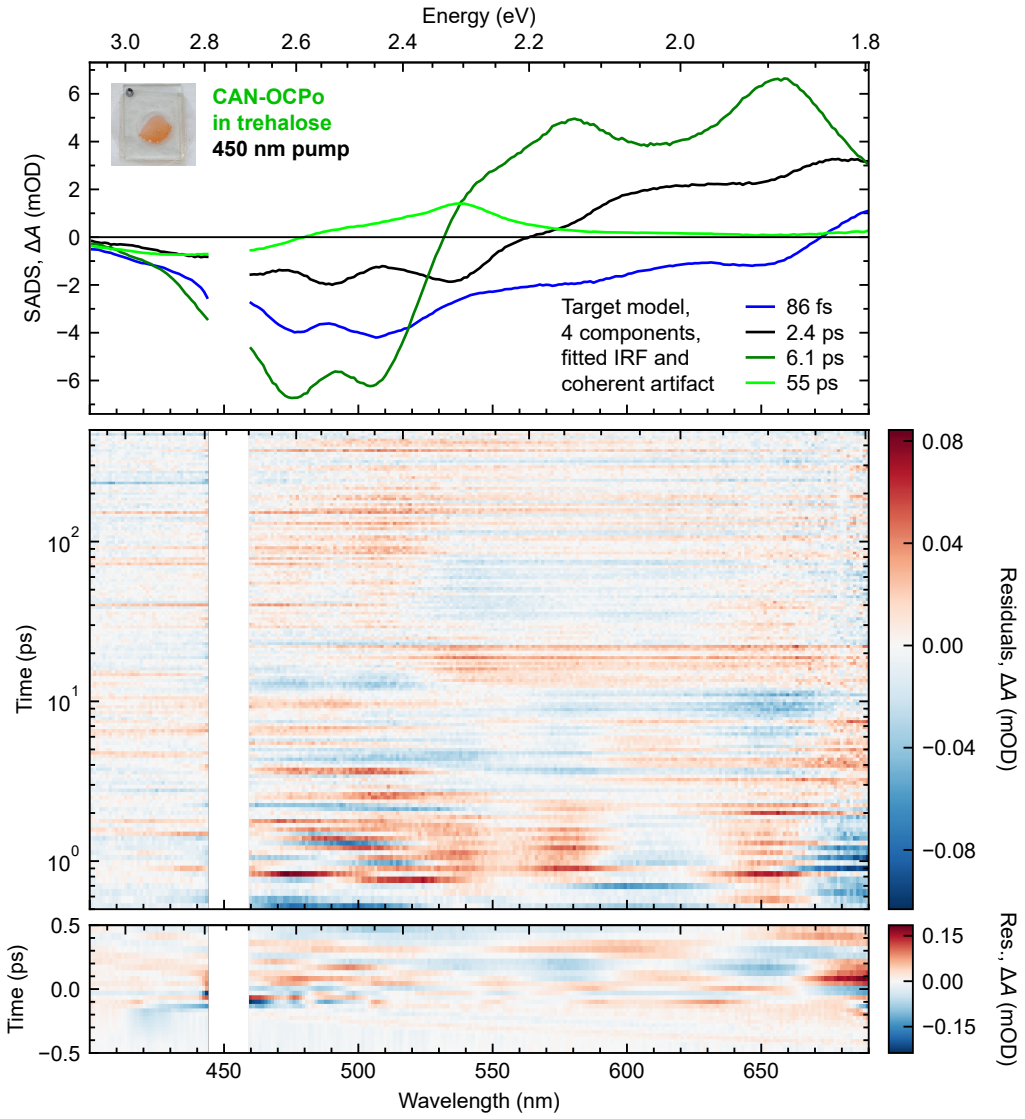

Figure J.9 – Results of global target analysis with a 4-component target model on transient absorption data of CAN-binding OCPo in trehalose with pump wavelength 450 nm and a UV-vis probe: SADS (top) and residuals (middle, bottom). Only the wavelength range 400–690 nm was fitted, and noisy data from 444–459 nm due to significant pump scatter was excluded from the fit. SADS time constants are specified in the legend. The fitted IRF has centre −66 fs and FWHM 30 fs. A coherent artefact with the concentration profile of the IRF was fitted but not shown here. Residuals = Data − Fit; note the logarithmic time-scale in the middle panel, and the linear time-scale and different residuals scale in the bottom panel. See text for further details.

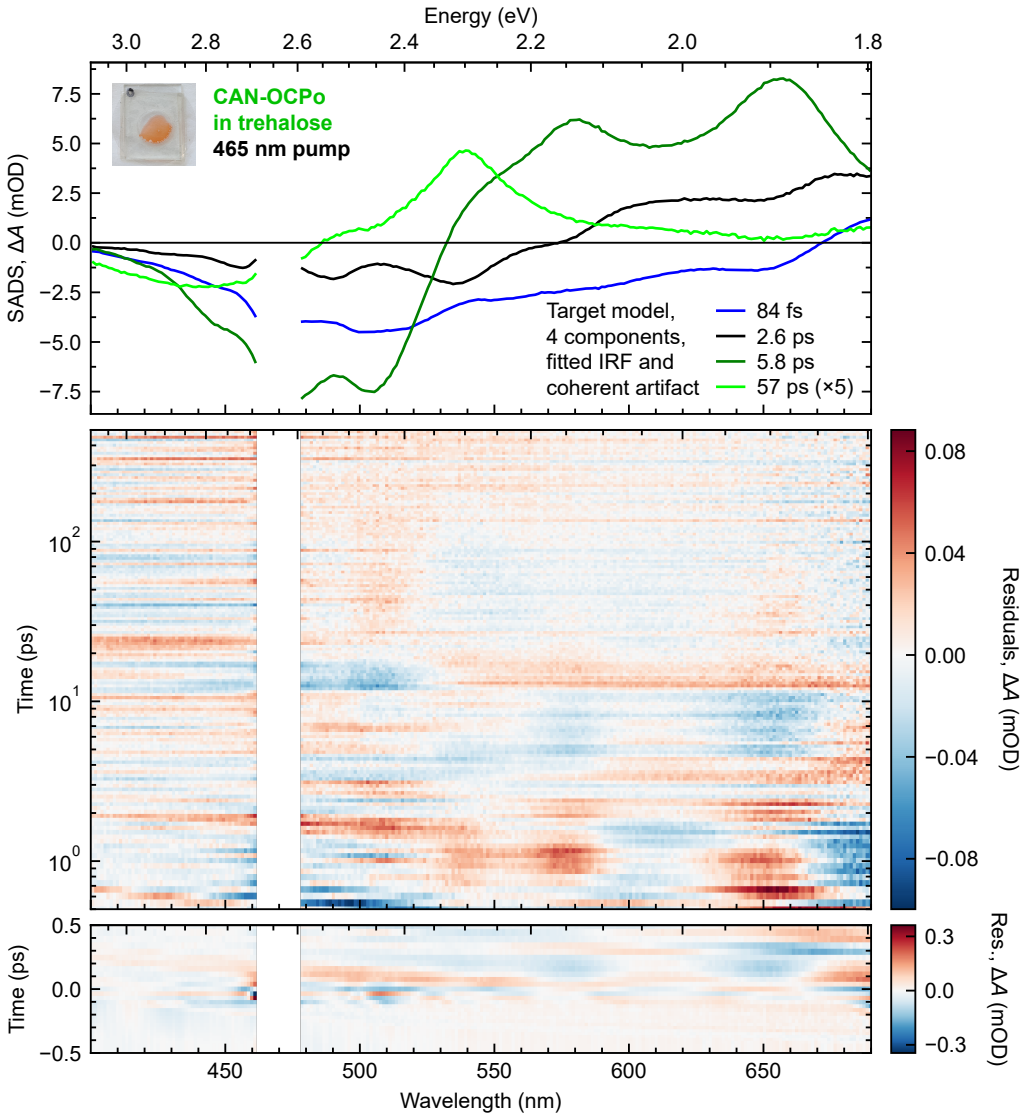

Figure J.10 – Results of global target analysis with a 4-component target model on transient absorption data of CAN-binding OCPo in trehalose with pump wavelength 465 nm and a UV-vis probe: SADS (top) and residuals (middle, bottom). Only the wavelength range 400–690 nm was fitted, and noisy data from 462–478 nm due to significant pump scatter was excluded from the fit. SADS time constants are specified in the legend; multiplications refer to scalings applied to the SADS. The fitted IRF has centre −53 fs and FWHM 26 fs. A coherent artefact with the concentration profile of the IRF was fitted but not shown here. Residuals = Data − Fit; note the logarithmic time-scale in the middle panel, and the linear time-scale and different residuals scale in the bottom panel. See text for further details.

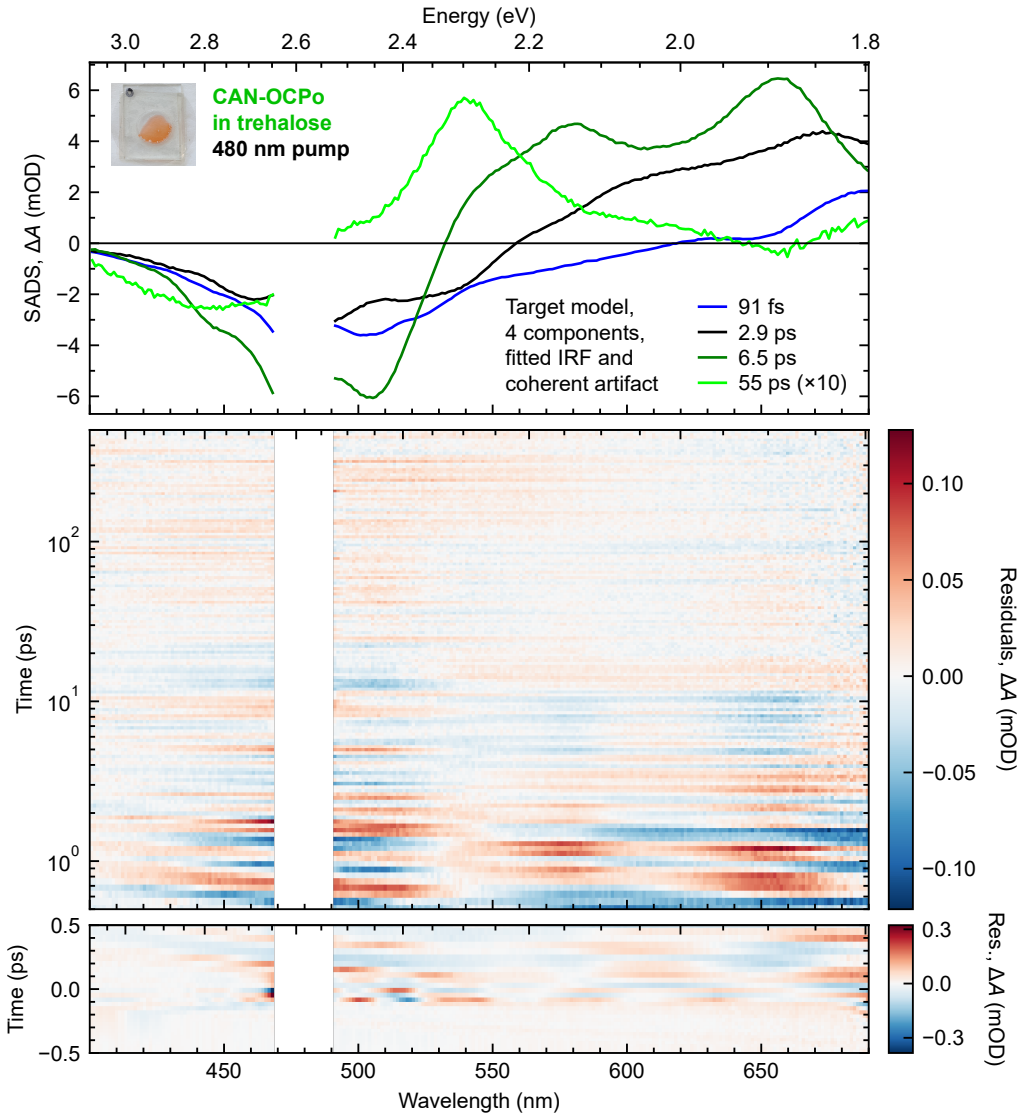

Figure J.11 – Results of global target analysis with a 4-component target model on transient absorption data of CAN-binding OCPo in trehalose with pump wavelength 480 nm and a UV-vis probe: SADS (top) and residuals (middle, bottom). Only the wavelength range 400–690 nm was fitted, and noisy data from 469–491 nm due to significant pump scatter was excluded from the fit. SADS time constants are specified in the legend; multiplications refer to scalings applied to the SADS. The fitted IRF has centre −29 fs and FWHM 31 fs. A coherent artefact with the concentration profile of the IRF was fitted but not shown here. Residuals = Data − Fit; note the logarithmic time-scale in the middle panel, and the linear time-scale and different residuals scale in the bottom panel. See text for further details.

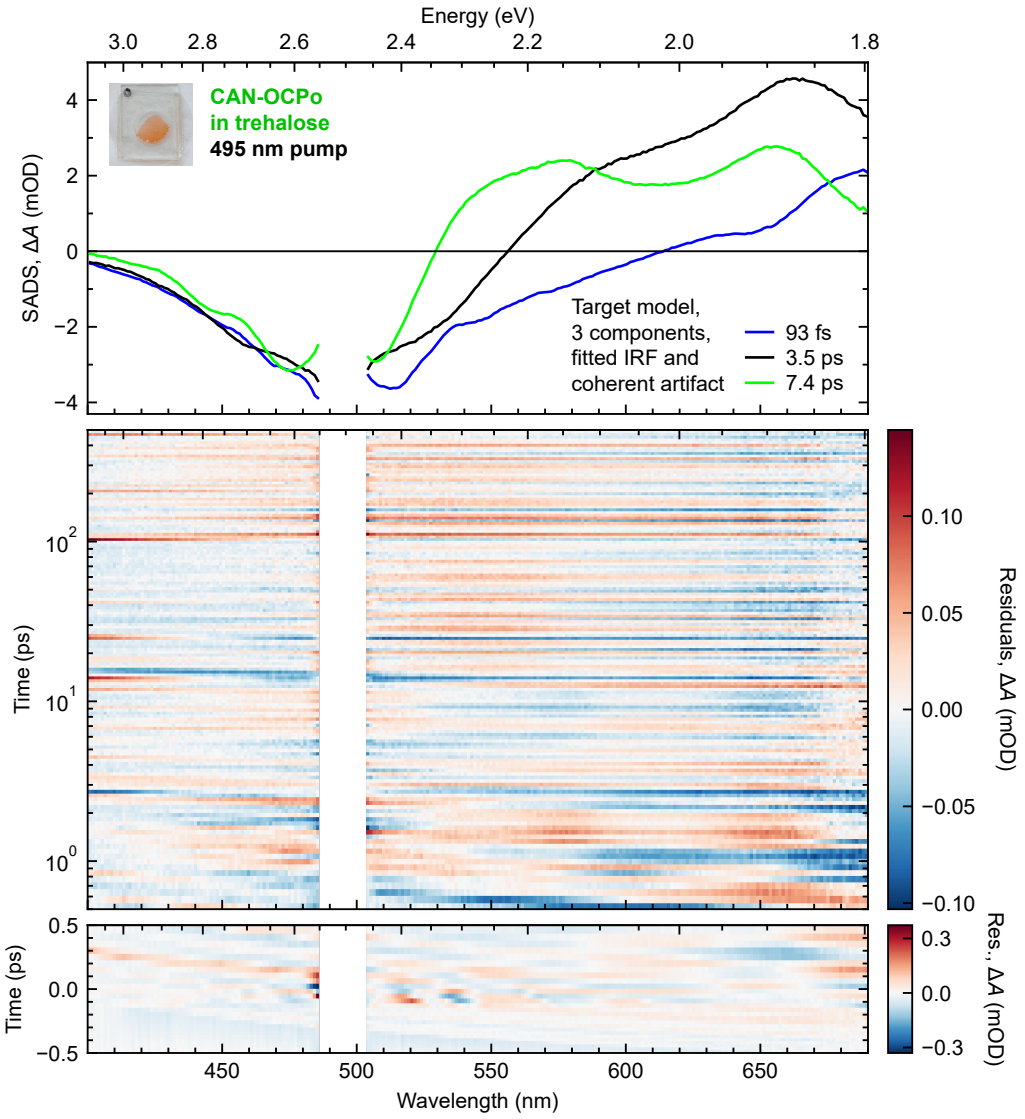

Figure J.12 – Results of global target analysis with a 3-component target model on transient absorption data of CAN-binding OCPo in trehalose with pump wavelength 495 nm and a UV-vis probe: SADS (top) and residuals (middle, bottom). Only the wavelength range 400–690 nm was fitted, and noisy data from 486–504 nm due to significant pump scatter was excluded from the fit. SADS time constants are specified in the legend. The fitted IRF has centre −25 fs and FWHM 38 fs. A coherent artefact with the concentration profile of the IRF was fitted but not shown here. Residuals = Data − Fit; note the logarithmic time-scale in the middle panel, and the linear time-scale and different residuals scale in the bottom panel. See text for further details.

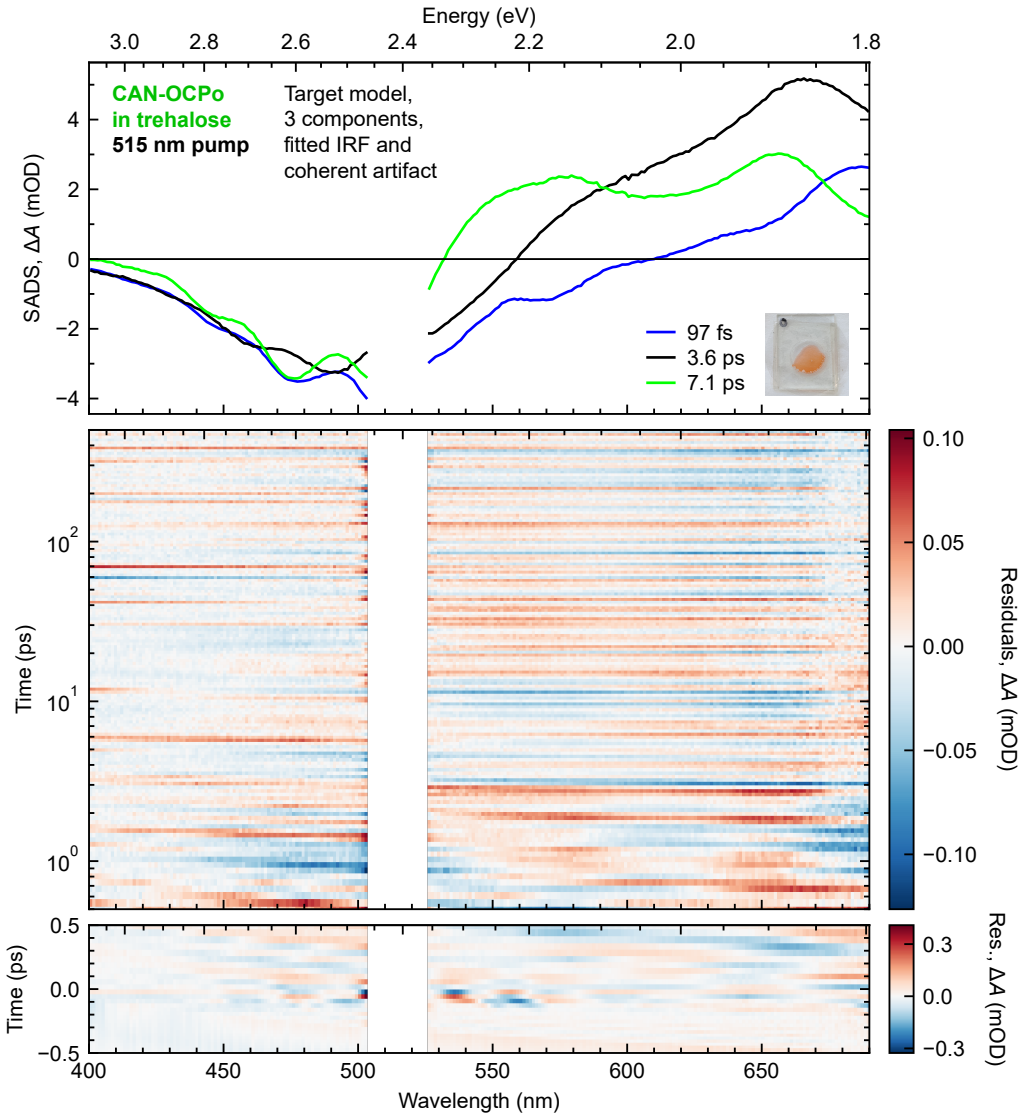

Figure J.13 – Results of global target analysis with a 3-component target model on transient absorption data of CAN-binding OCPo in trehalose with pump wavelength 515 nm and a UV-vis probe: SADS (top) and residuals (middle, bottom). Only the wavelength range 400–690 nm was fitted, and noisy data from 504–526 nm due to significant pump scatter was excluded from the fit. SADS time constants are specified in the legend. The fitted IRF has centre −33 fs and FWHM 33 fs. A coherent artefact with the concentration profile of the IRF was fitted but not shown here. Residuals = Data − Fit; note the logarithmic time-scale in the middle panel, and the linear time-scale and different residuals scale in the bottom panel. See text for further details.

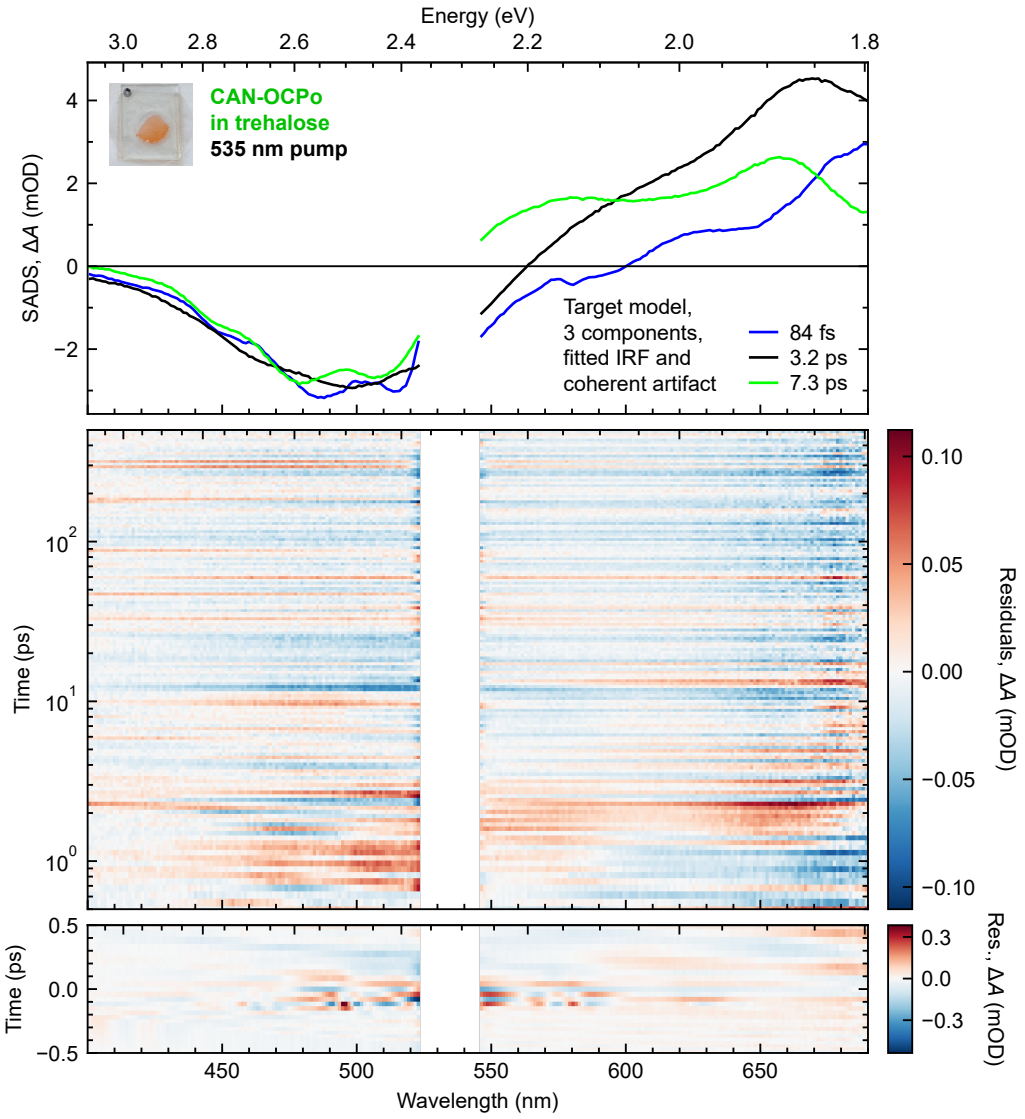

Figure J.14 – Results of global target analysis with a 3-component target model on transient absorption data of CAN-binding OCPo in trehalose with pump wavelength 535 nm and a UV-vis probe: SADS (top) and residuals (middle, bottom). Only the wavelength range 400–690 nm was fitted, and noisy data from 524–546 nm due to significant pump scatter was excluded from the fit. SADS time constants are specified in the legend. The fitted IRF has centre −30 fs and FWHM 53 fs. A coherent artefact with the concentration profile of the IRF was fitted but not shown here. Residuals = Data − Fit; note the logarithmic time-scale in the middle panel, and the linear time-scale and different residuals scale in the bottom panel. See text for further details.

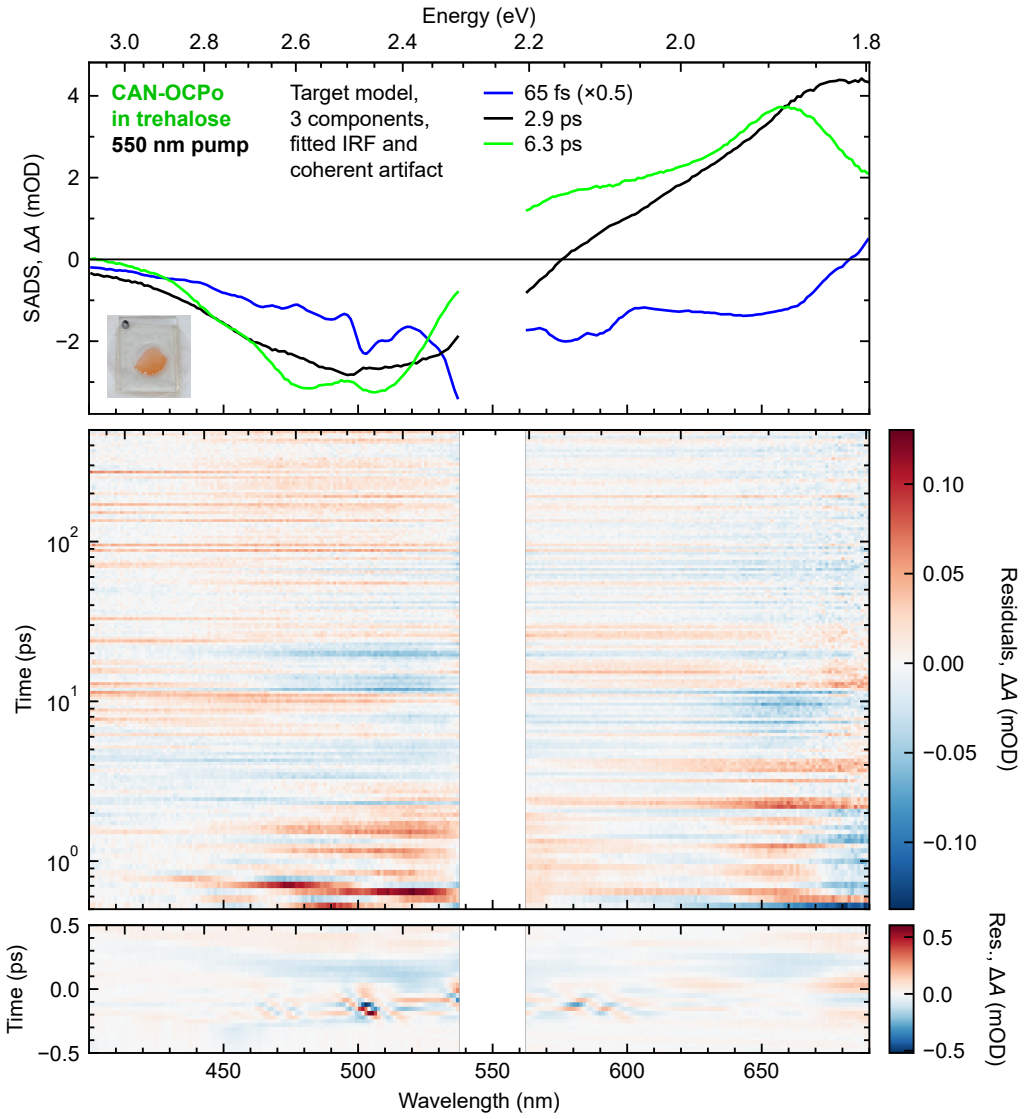

Figure J.15 – Results of global target analysis with a 3-component target model on transient absorption data of CAN-binding OCPo in trehalose with pump wavelength 550 nm and a UV-vis probe: SADS (top) and residuals (middle, bottom). Only the wavelength range 400–690 nm was fitted, and noisy data from 538–562 nm due to significant pump scatter was excluded from the fit. SADS time constants are specified in the legend; multiplications refer to scalings applied to the SADS. The fitted IRF has centre −136 fs and FWHM 51 fs. A coherent artefact with the concentration profile of the IRF was fitted but not shown here. Residuals = Data − Fit; note the logarithmic time-scale in the middle panel, and the linear time-scale and different residuals scale in the bottom panel. See text for further details.

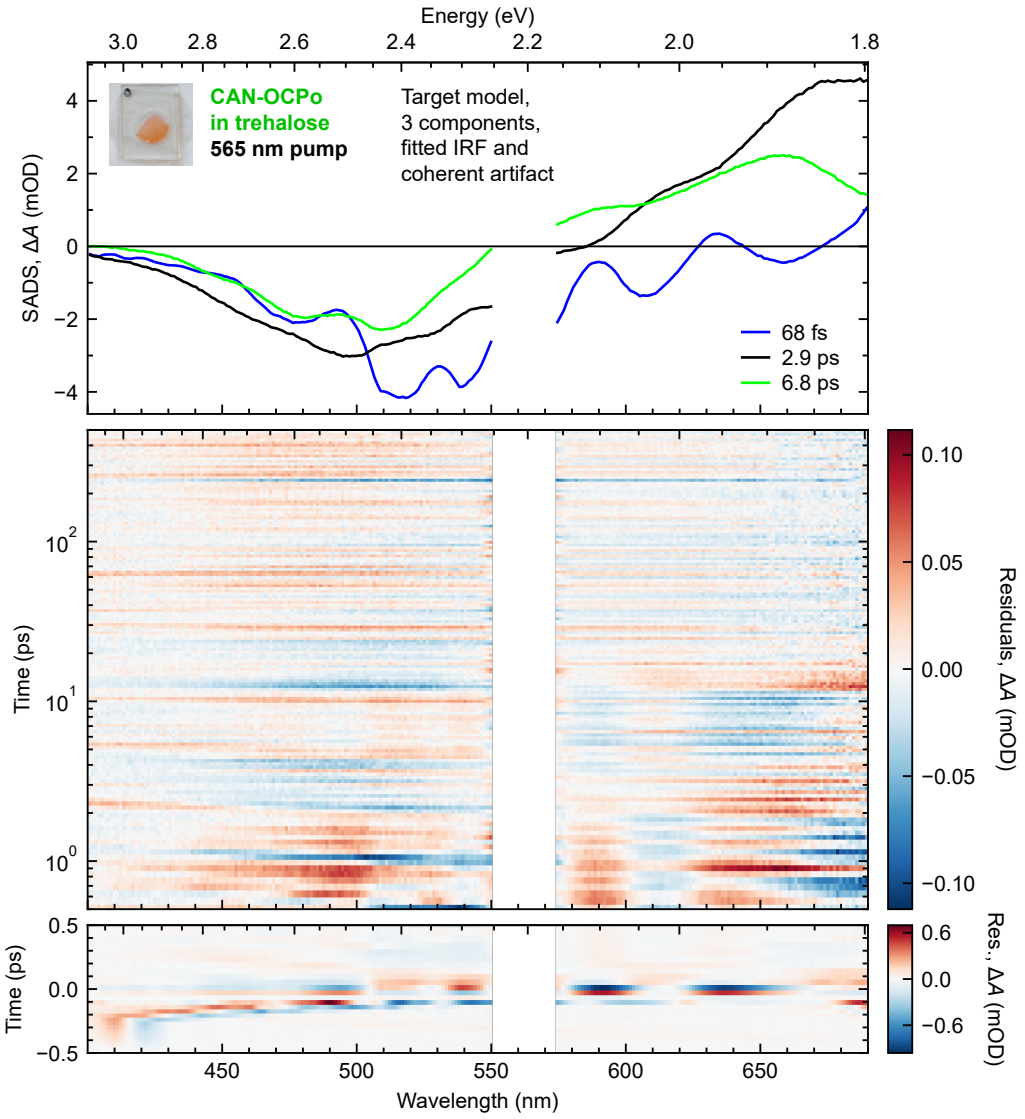

Figure J.16 – Results of global target analysis with a 3-component target model on transient absorption data of CAN-binding OCPo in trehalose with pump wavelength 565 nm and a UV-vis probe: SADS (top) and residuals (middle, bottom). Only the wavelength range 400–690 nm was fitted, and noisy data from 551–574 nm due to significant pump scatter was excluded from the fit. SADS time constants are specified in the legend. The fitted IRF has centre −49 fs and FWHM 5 fs. A coherent artefact with the concentration profile of the IRF was fitted but not shown here. Residuals = Data − Fit; note the logarithmic time-scale in the middle panel, and the linear time-scale and different residuals scale in the bottom panel. See text for further details.

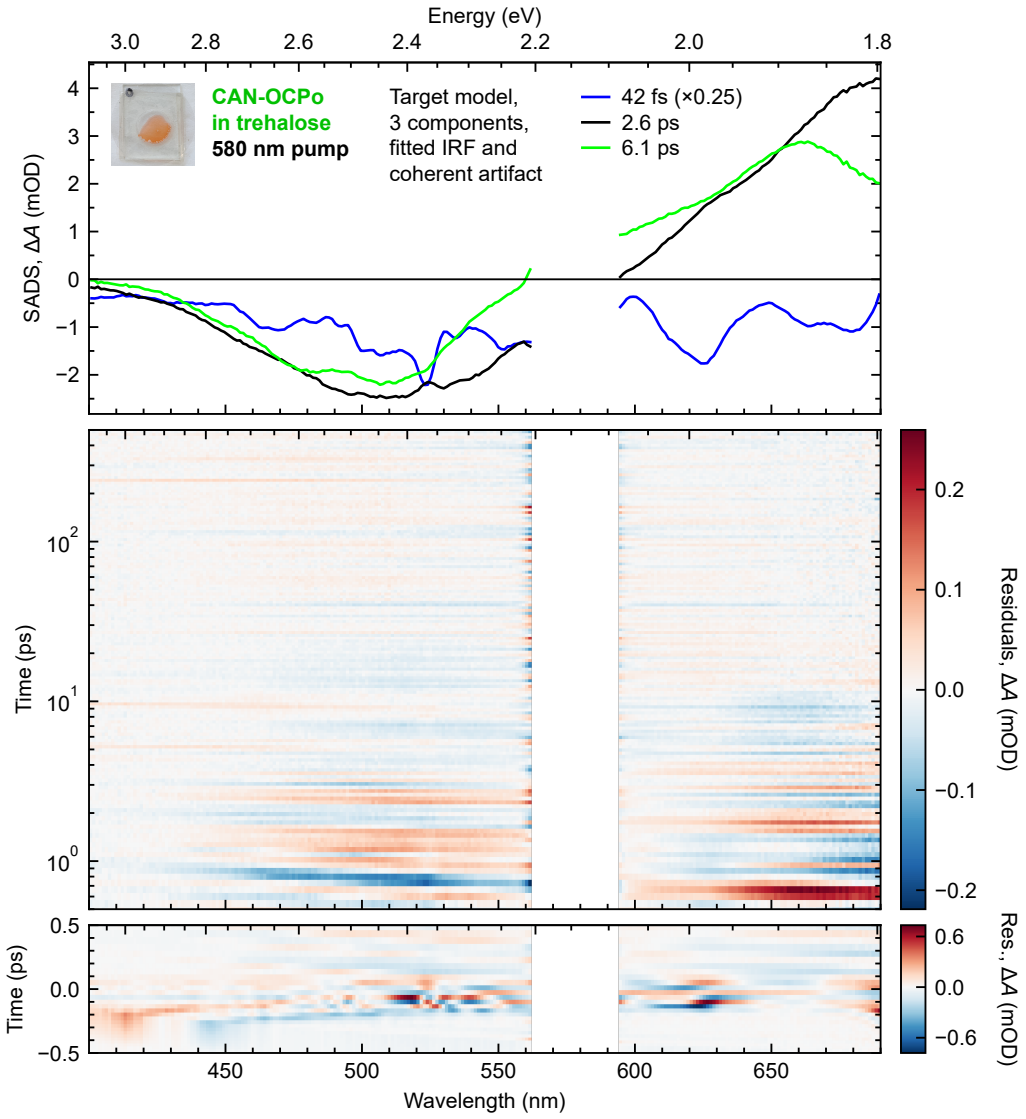

Figure J.17 – Results of global target analysis with a 3-component target model on transient absorption data of CAN-binding OCPo in trehalose with pump wavelength 580 nm and a UV-vis probe: SADS (top) and residuals (middle, bottom). Only the wavelength range 400–690 nm was fitted, and noisy data from 562–594 nm due to significant pump scatter was excluded from the fit. SADS time constants are specified in the legend; multiplications refer to scalings applied to the SADS. The fitted IRF has centre −72 fs and FWHM 43 fs. A coherent artefact with the concentration profile of the IRF was fitted but not shown here. Residuals = Data − Fit; note the logarithmic time-scale in the middle panel, and the linear time-scale and different residuals scale in the bottom panel. See text for further details.

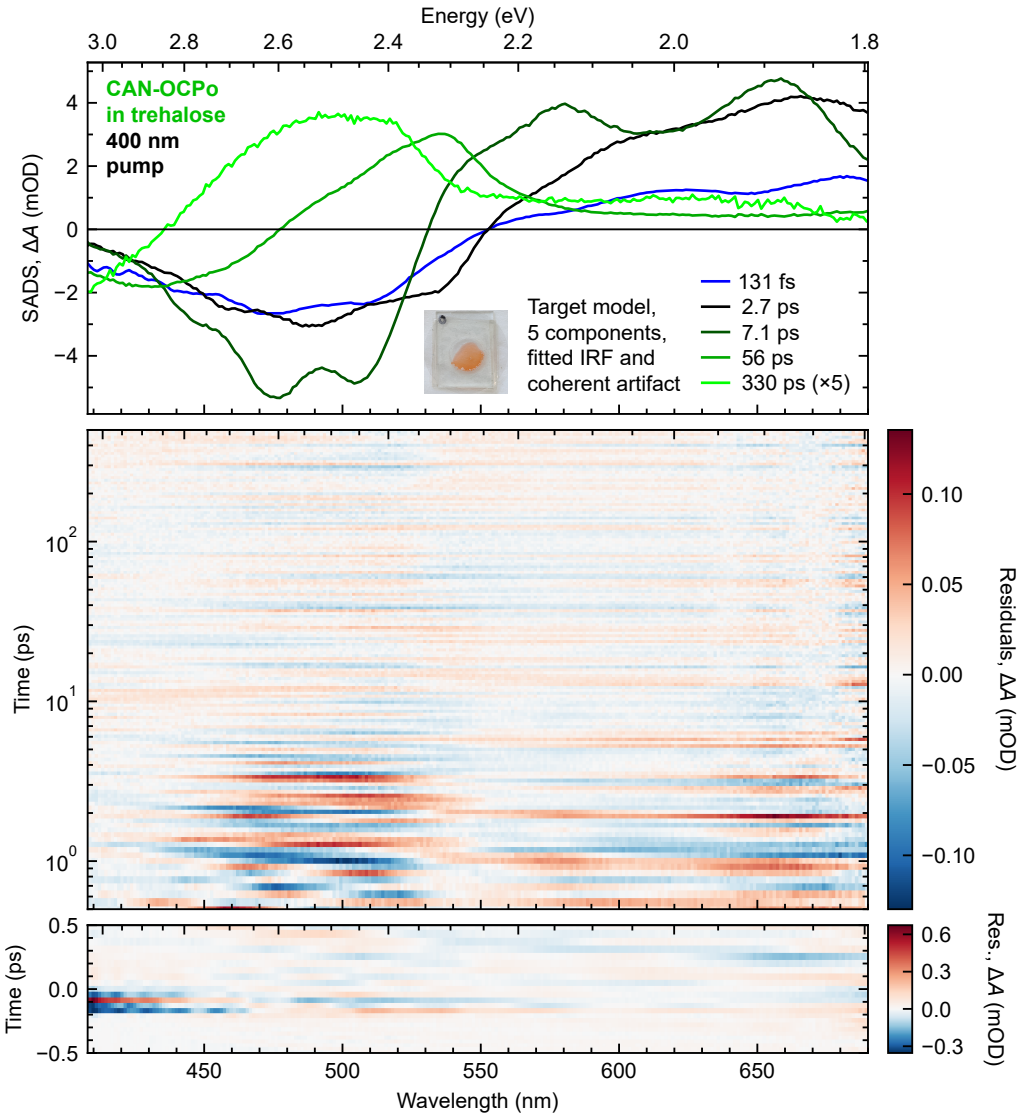

Figure J.18 – Results of global target analysis with a 5-component target model on transient absorption data of CAN-binding OCPo in trehalose with pump wavelength 400 nm and a UV-vis probe: SADS (top) and residuals (middle, bottom). Only the wavelength range 407–690 nm was fitted to exclude noisy data due to low probe light and significant pump scatter. SADS time constants are specified in the legend; multiplications refer to scalings applied to the SADS. The fitted IRF has centre −88 fs and FWHM 59 fs. A coherent artefact with the concentration profile of the IRF was fitted but not shown here. Residuals = Data − Fit; note the logarithmic time-scale in the middle panel, and the linear time-scale and different residuals scale in the bottom panel. See text for further details.

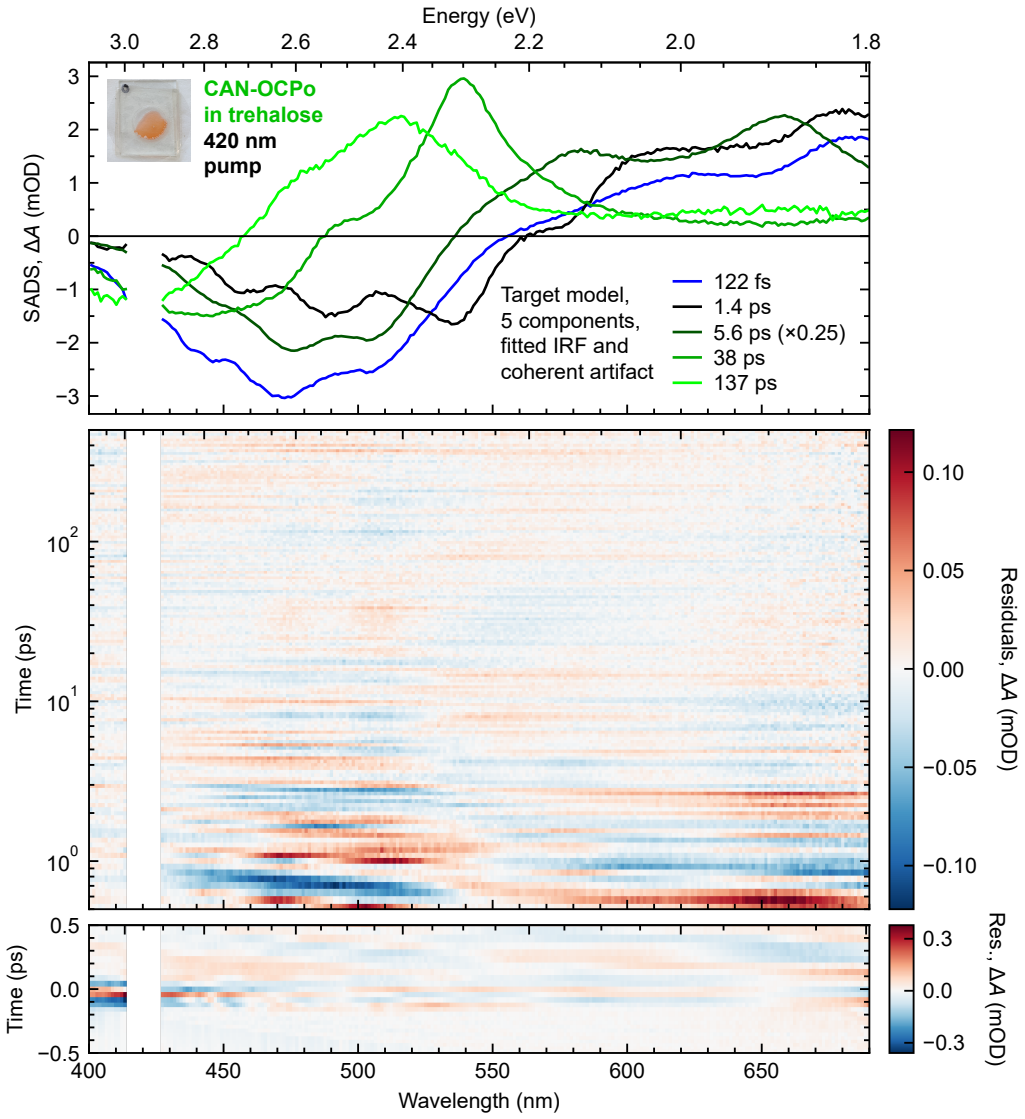

Figure J.19 – Results of global target analysis with a 5-component target model on transient absorption data of CAN-binding OCPo in trehalose with pump wavelength 420 nm and a UV-vis probe: SADS (top) and residuals (middle, bottom). Only the wavelength range 400–690 nm was fitted, and noisy data from 414–427 nm due to significant pump scatter was excluded from the fit. SADS time constants are specified in the legend; multiplications refer to scalings applied to the SADS. The fitted IRF has centre −50 fs and FWHM 46 fs. A coherent artefact with the concentration profile of the IRF was fitted but not shown here. Residuals = Data − Fit; note the logarithmic time-scale in the middle panel, and the linear time-scale and different residuals scale in the bottom panel. See text for further details.

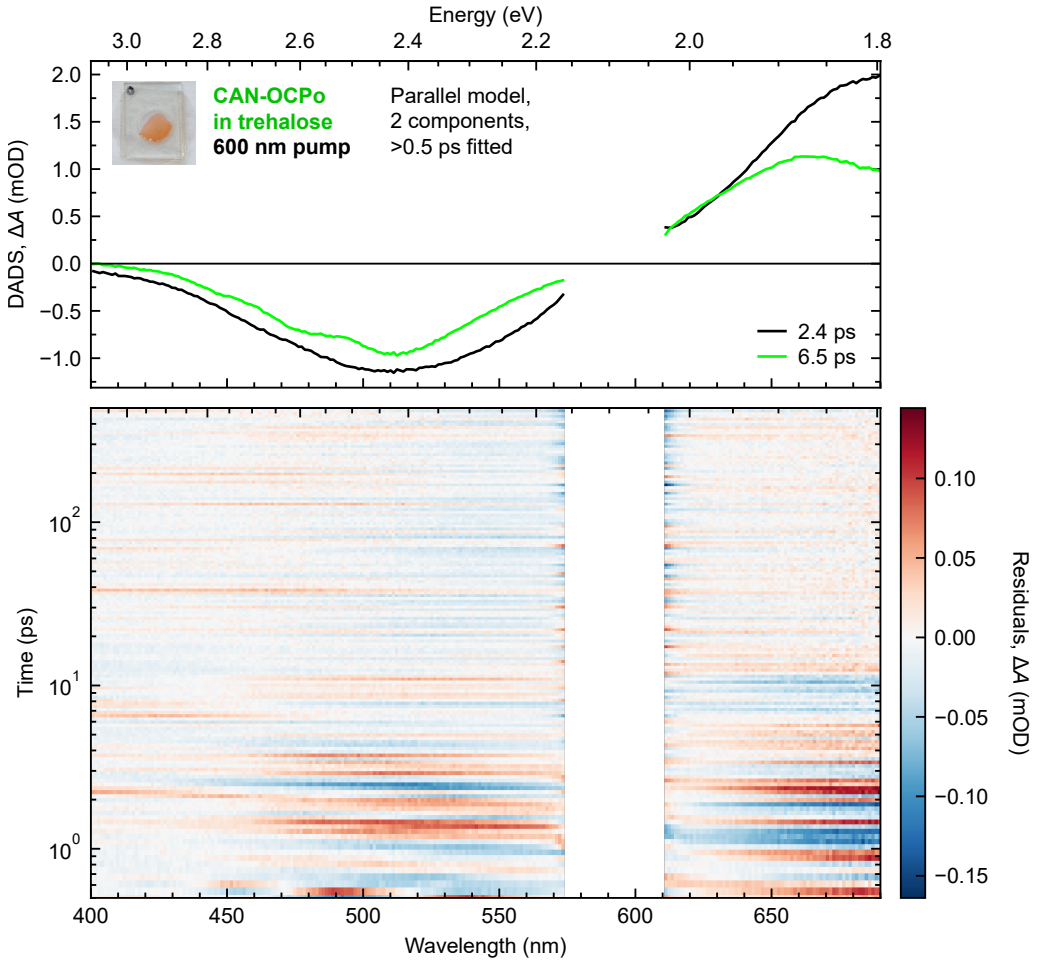

Figure J.20 – Results of global lifetime analysis with a 2-component parallel model on transient absorption data of CAN-binding OCPo in trehalose with pump wavelength 600 nm and a UV-vis: DADS (top) and residuals (bottom). Only the wavelength range 400–690 nm and times >0.5 ps were fitted, and noisy data from 574–611 nm due to significant pump scatter was excluded from the fit. DADS time constants are specified in the legend. Residuals = Data – Fit. See text for further details.

Appendix K

Time-resolved absorbance fit parameters and discussion

K.1 Global fit of difference dynamics parameters

λ_{pump} (nm)	β_0	β_1	β_2
425	0.061 ± 0.014	0.996 ± 0.029	1.383 ± 0.024
450	-0.012 ± 0.014	0.890 ± 0.028	1.381 ± 0.023
475	0.043 ± 0.014	0.779 ± 0.028	1.393 ± 0.022
500	0.006 ± 0.014	0.658 ± 0.027	1.389 ± 0.021
525	0.053 ± 0.014	0.527 ± 0.027	1.426 ± 0.020
550	0.136 ± 0.014	0.405 ± 0.026	1.413 ± 0.019
575	0.147 ± 0.014	0.211 ± 0.024	1.225 ± 0.018

Table K.1 – Fitting parameters found using a global biexponential fit to the data in Figure 6.8. The biexponential equation used is $\Delta\left(A_{460-465}/A_{560-565}\right)_{\mathrm{fit}} = \beta_0 - \beta_1[1 - \exp(-t/T_1)] - \beta_2[1 - \exp(-t/T_2)]$. The fitted time constants are $T_1 = 4.12 \pm 0.18\,\mathrm{s}$ and $T_2 = 32.9 \pm 0.7\,\mathrm{s}$; note that as a global fit, these are the same for all pump wavelengths. Only the times $t < 100\,\mathrm{s}$ are fitted. Errors specified here are fit parameter standard errors.

K.2 Experimental oversights discussion

The number of pump photons incident per second (photon rate) at the power meter position is given by

$$\dot{N}_\gamma = \frac{P}{E_\gamma} = P\frac{\lambda_{\text{pump}}}{hc} \tag{K.1}$$

where P is the steady-state power of the pump, $E_\gamma = hc/\lambda_{\text{pump}}$ is the per-photon energy, λ_{pump} is the pump wavelength, h is Planck's constant, and c is the speed of light in a vacuum. The fraction of pump photons absorbed by the OCP, assuming a zero angle of incidence and negligible scattering from the high-quality cuvette, is

$$F_{\text{dark}} = 1 - 10^{-A_{\text{dark}}} \tag{K.2}$$

where A_{dark} is the steady-state absorbance of the dark-adapted OCP in buffer measured in a separate UV-vis spectrometer at zero angle of incidence. Therefore, overlooking the later-discussed power losses and angle dependence, the number of pump-induced OCPo excitations per second (excitation rate) is given by

$$\dot{N}_{\text{pump}} = \dot{N}_\gamma F_{\text{dark}} = P\frac{\lambda_{\text{pump}}}{hc}\left(1 - 10^{-A_{\text{dark}}}\right) \tag{K.3}$$

which was controlled to a value of $\dot{N}_{\text{pump}} = 2.53 \times 10^{16}\,\text{s}^{-1}$ in the experiment for most pump wavelengths. The exception to this control was for 675 nm pump, where instead the photon rate (Equation K.1) was controlled to $\dot{N}_\gamma = 8.76 \times 10^{16}\,\text{s}^{-1}$, the same as that for $\lambda = 550\,\text{nm}$; this is because OCPo is non-absorbing at 675 nm, and the tuneable filter is unable to reach the higher photon rates (*i.e.* $\dot{N}_\gamma = 1.89 \times 10^{17}\,\text{s}^{-1}$ at $\lambda_{\text{pump}} = 575\,\text{nm}$) when set to 675 nm.

However, as noted in Section 4.2, two of the oversights made require some scrutiny in response to the apparently significant pump wavelength-dependence on the OCPo→OCPr yield. First, the beam path after the pump power measurement position involves reflection by three UV-enhanced Al mirrors and focusing by a lens. This results in a considerable power (photon rate) loss, defined here by a fraction R_P that has some pump-wavelength dependence. R_P was determined once all measurement runs (three experimental replicates) were complete by taking comparative pump power measurements at the usual position as well as the sample position (doing this during the main experiment was impossible due to spatial limitations, and would also cause pre-measurement photocoversion). The resulting correction to the photon rate is

$$\dot{N}_\gamma^{\text{corr.}} = R_P\dot{N}_\gamma = R_P P\frac{\lambda_{\text{pump}}}{hc} \tag{K.4}$$

which we note remains incident on the *cuvette* rather than on the buffer. The second oversight was that the pump light was not close to normal incidence to the cuvette; it was at an angle of incidence $\theta \sim 40°$, resulting in the pump path length within the buffer being extended compared to that at normal incidence by a factor $1/\cos\theta$. Hence, since absorbance is directly proportional to path length in the sample (from the Beer-Lambert law[223]), the corrected absorbance is $A_{\text{dark}}/\cos\theta$, and therefore the correct fraction of pump photons absorbed is

$$F_{\text{dark}}^{\text{corr.}} = 1 - 10^{-A_{\text{dark}}/\cos\theta} \tag{K.5}$$

where we recall that A_{dark} is determined at normal incidence in a separate UV-vis spectrometer. We note we are continuing to assume negligible scattering of the pump off the high-quality cuvette, when for a significantly off-normal angle of incidence this may fail to be the case. Combining these corrections, we obtain

$$\dot{N}_{\text{pump}}^{\text{corr.}} = \dot{N}_{\Upsilon}^{\text{corr.}} F_{\text{dark}}^{\text{corr.}} = R_P P \frac{\lambda_{\text{pump}}}{hc} \left(1 - 10^{-A_{\text{dark}}/\cos\theta}\right) \tag{K.6}$$

which is the corrected pump-induced excitation rate in OCPo.

λ_{pump} (nm)	A_{dark} (OD)	F_{dark}	P (µW)	$\dot{N}_{\Upsilon}$ $\times 10^{-16}$	$\dot{N}_{\text{pump}}$ $\times 10^{-16}$	$F_{\text{dark}}^{\text{corr.}}$	R_P	$\dot{N}_{\Upsilon}^{\text{corr.}}$ $\times 10^{-16}$	$\dot{N}_{\text{pump}}^{\text{corr.}}$ $\times 10^{-16}$
425	0.233	0.415	285	6.10	2.53	0.503	0.55	3.35	1.69
450	0.397	0.599	187	4.23	2.53	0.697	0.54	2.29	1.60
475	0.551	0.719	147	3.52	2.53	0.809	0.54	1.89	1.53
500	0.552	0.719	140	3.52	2.53	0.809	0.52	1.83	1.48
525	0.345	0.548	175	4.62	2.53	0.646	0.51	2.38	1.53
550	0.148	0.289	316	8.76	2.53	0.359	0.49	4.26	1.53
575	0.062	0.134	654	18.9	2.53	0.171	0.48	9.06	1.55
675	0	0	256	8.76	0	0	0.43	3.72	0

Table K.2 – Pump wavelengths and powers used in experiments with photoconverting OCP in buffer, with derived quantities also printed. Corrected quantities were calculated using unrounded values and $\theta = 40°$. See Equations K.1 to K.6 and text for definitions of the quantities.

We print Table K.2 with pump wavelength and the measured or calculated quantities defined in Equations K.1 to K.6, assuming an angle of incidence of $\theta = 40°$. We highlight that the corrected pump-induced excitation rate ($\dot{N}_{\text{pump}}^{\text{corr.}}$) is a minimum for $\lambda_{\text{pump}} = 500\,\text{nm}$, and generally increasing from there in either

λ_{pump}-direction. This does not match the dependence of pump wavelength on the photoswitching dynamics, *e.g.* the wavelength dependence on the amplitudes (β_1, β_2) in the dynamics global fit (Figure 6.9b, Table K.1), so we conclude that the oversights made did not have a substantial effect on the OCPo→OCPr photoswitching.

We note that some significant sources of error here are due to: (1) the pump power fluctuations, (2) the intrinsic error of the Thorlabs S120VC power meter (note that R_P is calculated from two pump power measurements taken per pump wavelength, distinct from the single P pump power measurement taken per pump wavelength per experimental replicate), (3) the visual estimation (rather than a measurement) of the pump angle of incidence θ, and (4) the assumption that there is negligible scattering of the pump off the high-quality cuvette (for the significantly off-normal angle of incidence, this may fail to be the case).

References

[1] IPCC, *Global Warming of 1.5°C: IPCC Special Report on Impacts of Global Warming of 1.5°C above Pre-industrial Levels in Context of Strengthening Response to Climate Change, Sustainable Development, and Efforts to Eradicate Poverty* (Cambridge University Press, Cambridge, New York, 2018).

[2] F. Creutzig, P. Agoston, J. C. Goldschmidt, G. Luderer, G. Nemet, and R. C. Pietzcker, 'The underestimated potential of solar energy to mitigate climate change', *Nature Energy* **2**, 17140 (2017).

[3] J. Goldemberg, *World Energy Assessment: Energy and the Challenge of Sustainability* (United Nations, New York, NY, 2001).

[4] *Total worldwide energy consumption, 2000 and 2021*, U.S. Energy Information Administration (EIA), https://www.eia.gov/international/data/world/total-energy/total-energy-consumption (visited on 08/12/2022).

[5] *Global Electricity Review 2022*, Ember, (2022) https://ember-climate.org/insights/research/global-electricity-review-2022/ (visited on 07/12/2022).

[6] *Net Zero by 2050: A Roadmap for the Global Energy Sector* (International Energy Agency (IEA), Paris, 2021).

[7] *Renewable Power Generation Costs in 2021* (International Renewable Energy Agency (IRENA), Abu Dhabi, 2022).

[8] W. Shockley and H. J. Queisser, 'Detailed Balance Limit of Efficiency of p-n Junction Solar Cells', *Journal of Applied Physics* **32**, 510–519 (1961).

[9] K. Yoshikawa, H. Kawasaki, W. Yoshida, T. Irie, K. Konishi, K. Nakano, T. Uto, D. Adachi, M. Kanematsu, H. Uzu, and K. Yamamoto, 'Silicon heterojunction solar cell with interdigitated back contacts for a photoconversion efficiency over 26%', *Nature Energy* **2**, 17032 (2017).

[10] M. A. Green, E. D. Dunlop, J. Hohl-Ebinger, M. Yoshita, N. Kopidakis, and X. Hao, 'Solar cell efficiency tables (version 59)', *Progress in Photovoltaics: Research and Applications* **30**, 3–12 (2022).

[11] A. Rao and R. H. Friend, 'Harnessing singlet exciton fission to break the Shockley–Queisser limit', *Nature Reviews Materials* **2**, 17063 (2017).

[12] A. J. Musser and J. Clark, 'Triplet-Pair States in Organic Semiconductors', *Annual Review of Physical Chemistry* **70**, 323–351 (2019).

[13] M. B. Smith and J. Michl, 'Recent Advances in Singlet Fission', *Annual Review of Physical Chemistry* **64**, 361–386 (2013).

[14] T. Ullrich, D. Munz, and D. M. Guldi, 'Unconventional singlet fission materials', *Chemical Society Reviews* **50**, 3485–3518 (2021).

[15] H. Kim and P. M. Zimmerman, 'Coupled double triplet state in singlet fission', *Physical Chemistry Chemical Physics* **20**, 30083–30094 (2018).

[16] M. C. Hanna and A. J. Nozik, 'Solar conversion efficiency of photovoltaic and photoelectrolysis cells with carrier multiplication absorbers', *Journal of Applied Physics* **100**, 074510 (2006).

[17] L. M. Pazos-Outón, J. M. Lee, M. H. Futscher, A. Kirch, M. Tabachnyk, R. H. Friend, and B. Ehrler, 'A Silicon–Singlet Fission Tandem Solar Cell Exceeding 100% External Quantum Efficiency with High Spectral Stability', *ACS Energy Letters* **2**, 476–480 (2017).

[18] Y. Liu, C. Zhang, R. Wang, B. Zhang, Z. Tan, X. Wang, and M. Xiao, 'Large Optical Nonlinearity Induced by Singlet Fission in Pentacene Films', *Angewandte Chemie International Edition* **54**, 6222–6226 (2015).

[19] M. Zhao, K. Liu, Y.-D. Zhang, Q. Wang, Z.-G. Li, Y.-L. Song, and H.-L. Zhang, 'Singlet fission induced giant optical limiting responses of pentacene derivatives', *Materials Horizons* **2**, 619–624 (2015).

[20] T. Tonami, T. Nagami, K. Okada, W. Yoshida, and M. Nakano, 'Singlet-Fission-Induced Enhancement of Third-Order Nonlinear Optical Properties of Pentacene Dimers', *ACS Omega* **4**, 16181–16190 (2019).

[21] R. Nagata, H. Nakanotani, W. J. Potscavage, and C. Adachi, 'Exploiting Singlet Fission in Organic Light-Emitting Diodes', *Advanced Materials* **30**, 1801484 (2018).

[22] P. E. Teichen and J. D. Eaves, 'Collective aspects of singlet fission in molecular crystals', *The Journal of Chemical Physics* **143**, 044118 (2015).

[23] C. J. Bardeen, 'Time dependent correlations of entangled states with nondegenerate branches and possible experimental realization using singlet fission', *The Journal of Chemical Physics* **151**, 124503 (2019).

[24] M. Marcus and W. Barford, 'Triplet-triplet decoherence in singlet fission', *Physical Review B* **102**, 035134 (2020).

[25] K. E. Smyser and J. D. Eaves, 'Singlet fission for quantum information and quantum computing: the parallel JDE model', *Scientific Reports* **10**, 18480 (2020).

[26] M. Einzinger, T. Wu, J. F. Kompalla, H. L. Smith, C. F. Perkinson, L. Nienhaus, S. Wieghold, D. N. Congreve, A. Kahn, M. G. Bawendi, and M. A. Baldo, 'Sensitization of silicon by singlet exciton fission in tetracene', *Nature* **571**, 90–94 (2019).

[27] B. Daiber, S. Maiti, S. M. Ferro, J. Bodin, A. F. J. van den Boom, S. L. Luxembourg, S. Kinge, S. P. Pujari, H. Zuilhof, L. D. A. Siebbeles, and B. Ehrler, 'Change in Tetracene Polymorphism Facilitates Triplet Transfer in Singlet Fission-Sensitized Silicon Solar Cells', *The Journal of Physical Chemistry Letters* **11**, 8703–8709 (2020).

[28] J. Yabuzaki, 'Carotenoids Database: structures, chemical fingerprints and distribution among organisms', *Database* **2017**, bax004 (2017).

[29] D. P. Canniffe and A. Hitchcock, 'Photosynthesis. Carotenoids in Photosynthesis – Structure and Biosynthesis', in *Encyclopedia of Biological Chemistry III*, Vol. 2, edited by J. Jez, 3rd (Elsevier, Oxford, 2021), pages 163–185.

[30] T. Polívka and V. Sundström, 'Ultrafast Dynamics of Carotenoid Excited States-From Solution to Natural and Artificial Systems', *Chemical Reviews* **104**, 2021–2072 (2004).

[31] H. Hashimoto, C. Uragami, N. Yukihira, A. T. Gardiner, and R. J. Cogdell, 'Understanding/unravelling carotenoid excited singlet states', *Journal of The Royal Society Interface* **15**, 20180026 (2018).

[32] M. J. Llansola-Portoles, K. Redeckas, S. Streckaité, C. Ilioaia, A. A. Pascal, A. Telfer, M. Vengris, L. Valkunas, and B. Robert, 'Lycopene crystalloids exhibit singlet exciton fission in tomatoes', *Physical Chemistry Chemical Physics* **20**, 8640–8646 (2018).

[33] A. A. C. van Wijk, A. Spaans, N. Uzunbajakava, C. Otto, H. J. M. de Groot, J. Lugtenburg, and F. Buda, 'Spectroscopy and Quantum Chemical Modeling Reveal a Predominant Contribution of Excitonic Interactions to the Bathochromic Shift in α-Crustacyanin, the Blue Carotenoprotein in the Carapace of the Lobster *Homarus gammarus*', *Journal of the American Chemical Society* **127**, 1438–1445 (2005).

[34] R. J. Lopes, J. D. Johnson, M. B. Toomey, M. S. Ferreira, P. M. Araujo, J. Melo-Ferreira, L. Andersson, G. E. Hill, J. C. Corbo, and M. Carneiro, 'Genetic Basis for Red Coloration in Birds', *Current Biology* **26**, 1427–1434 (2016).

[35] A. J. Musser, M. Maiuri, D. Brida, G. Cerullo, R. H. Friend, and J. Clark, 'The Nature of Singlet Exciton Fission in Carotenoid Aggregates', *Journal of the American Chemical Society* **137**, 5130–5139 (2015).

[36] D. Zhang, L. Tan, J. Dong, J. Yi, P. Wang, and J. Zhang, 'Structure and Excitation Dynamics of β-Carotene Aggregates in Cetyltrimethylammonium Bromide Micelle', *Chemical Research in Chinese Universities* **34**, 643–648 (2018).

[37] H.-T. Chang, Y.-Q. Chang, R.-M. Han, P. Wang, J.-P. Zhang, and L. H. Skibsted, 'Singlet Fission Reaction of Light-Exposed β-Carotene Bound to Bovine Serum Albumin. A Novel Mechanism in Protection of Light-Exposed Tissue by Dietary Carotenoids', *Journal of Agricultural and Food Chemistry* **65**, 6058–6062 (2017).

[38] C. Wang and M. J. Tauber, 'High-Yield Singlet Fission in a Zeaxanthin Aggregate Observed by Picosecond Resonance Raman Spectroscopy', *Journal of the American Chemical Society* **132**, 13988–13991 (2010).

[39] C. Wang, D. E. Schlamadinger, V. Desai, and M. J. Tauber, 'Triplet Excitons of Carotenoids Formed by Singlet Fission in a Membrane', *ChemPhysChem* **12**, 2891–2894 (2011).

[40] G. A. Sutherland, D. Polak, D. J. K. Swainsbury, S. Wang, F. C. Spano, D. B. Auman, D. G. Bossanyi, J. P. Pidgeon, A. Hitchcock, A. J. Musser, J. E. Anthony, P. L. Dutton, J. Clark, and C. N. Hunter, 'A Thermostable Protein Matrix for Spectroscopic Analysis of Organic Semiconductors', *Journal of the American Chemical Society* **142**, 13898–13907 (2020).

[41] J. Yu, L.-M. Fu, L.-J. Yu, Y. Shi, P. Wang, Z.-Y. Wang-Otomo, and J.-P. Zhang, 'Carotenoid Singlet Fission Reactions in Bacterial Light Harvesting Complexes As Revealed by Triplet Excitation Profiles', *Journal of the American Chemical Society* **139**, 15984–15993 (2017).

[42] C. C. Gradinaru, J. T. M. Kennis, E. Papagiannakis, I. H. M. van Stokkum, R. J. Cogdell, G. R. Fleming, R. A. Niederman, and R. van Grondelle, 'An unusual pathway of excitation energy deactivation in carotenoids: Singlet-to-triplet conversion on an ultrafast timescale in a photosynthetic antenna', *Proceedings of the National Academy of Sciences* **98**, 2364–2369 (2001).

[43] E. Papagiannakis, J. T. M. Kennis, I. H. M. van Stokkum, R. J. Cogdell, and R. van Grondelle, 'An alternative carotenoid-to-bacteriochlorophyll energy transfer pathway in photosynthetic light harvesting', *Proceedings of the National Academy of Sciences* **99**, 6017–6022 (2002).

[44] D. M. Niedzwiedzki, D. J. K. Swainsbury, E. C. Martin, C. N. Hunter, and R. E. Blankenship, 'Origin of the S* Excited State Feature of Carotenoids in Light-Harvesting Complex 1 from Purple Photosynthetic Bacteria', *The Journal of Physical Chemistry B* **121**, 7571–7585 (2017).

[45] Y. Zhang, C.-H. Qi, N. Yamano, P. Wang, L.-J. Yu, Z.-Y. Wang-Otomo, and J.-P. Zhang, 'Carotenoid Single-Molecular Singlet Fission and the Photoprotection of a Bacteriochlorophyll *b*-Type Core Light-Harvesting Antenna', *The Journal of Physical Chemistry Letters* **13**, 3534–3541 (2022).

[46] G. A. Sutherland, K. J. Grayson, N. B. Adams, D. M. Mermans, A. S. Jones, A. J. Robertson, D. B. Auman, A. A. Brindley, F. Sterpone, P. Tuffery, P. Derreumaux, P. L. Dutton, C. Robinson, A. Hitchcock, and C. N. Hunter, 'Probing the quality control mechanism of the *Escherichia coli* twin-arginine translocase with folding variants of a *de novo*–designed heme protein', *Journal of Biological Chemistry* **293**, 6672–6681 (2018).

[47] T. A. Farid, G. Kodali, L. A. Solomon, B. R. Lichtenstein, M. M. Sheehan, B. A. Fry, C. Bialas, N. M. Ennist, J. A. Siedlecki, Z. Zhao, M. A. Stetz, K. G. Valentine, J. L. R. Anderson, A. J. Wand, B. M. Discher, C. C. Moser, and P. L. Dutton, 'Elementary tetrahelical protein design for diverse oxidoreductase functions', *Nature Chemical Biology* **9**, 826–833 (2013).

[48] E. Kish, M. M. M. Pinto, D. Kirilovsky, R. Spezia, and B. Robert, 'Echinenone vibrational properties: From solvents to the orange carotenoid protein', *Biochimica et Biophysica Acta (BBA) - Bioenergetics* **1847**, 1044–1054 (2015).

[49] S. Gupta, M. Guttman, R. L. Leverenz, K. Zhumadilova, E. G. Pawlowski, C. J. Petzold, K. K. Lee, C. Y. Ralston, and C. A. Kerfeld, 'Local and global structural drivers for the photoactivation of the orange carotenoid protein', *Proceedings of the National Academy of Sciences* **112**, E5567–E5574 (2015).

[50] R. L. Leverenz, M. Sutter, A. Wilson, S. Gupta, A. Thurotte, C. Bourcier de Carbon, C. J. Petzold, C. Ralston, F. Perreau, D. Kirilovsky, and C. A. Kerfeld, 'A 12 Å carotenoid translocation in a photoswitch associated with cyanobacterial photoprotection', *Science* **348**, 1463–1466 (2015).

[51] V. Šlouf, V. Kuznetsova, M. Fuciman, C. B. de Carbon, A. Wilson, D. Kirilovsky, and T. Polívka, 'Ultrafast spectroscopy tracks carotenoid configurations in the orange and red carotenoid proteins from cyanobacteria', *Photosynthesis Research* **131**, 105–117 (2017).

[52] C. A. Kerfeld, M. R. Melnicki, M. Sutter, and M. A. Dominguez-Martin, 'Structure, function and evolution of the cyanobacterial orange carotenoid protein and its homologs', *New Phytologist* **215**, 937–951 (2017).

[53] P. E. Konold, I. H. M. van Stokkum, F. Muzzopappa, A. Wilson, M.-L. Groot, D. Kirilovsky, and J. T. M. Kennis, 'Photoactivation Mechanism, Timing of Protein Secondary Structure Dynamics and Carotenoid Translocation in the Orange Carotenoid Protein', *Journal of the American Chemical Society* **141**, 520–530 (2019).

[54] V. Kuznetsova, M. A. Dominguez-Martin, H. Bao, S. Gupta, M. Sutter, M. Kloz, M. Rebarz, M. Přeček, Y. Chen, C. J. Petzold, C. Y. Ralston, C. A. Kerfeld, and T. Polívka, 'Comparative ultrafast spectroscopy and

structural analysis of OCP1 and OCP2 from Tolypothrix', *Biochimica et Biophysica Acta (BBA) - Bioenergetics* **1861**, 148120 (2020).

[55] A. Wilson, F. Muzzopappa, and D. Kirilovsky, 'Elucidation of the essential amino acids involved in the binding of the cyanobacterial Orange Carotenoid Protein to the phycobilisome', *Biochimica et Biophysica Acta (BBA) - Bioenergetics* **1863**, 148504 (2022).

[56] D. M. Niedzwiedzki, H. Liu, and R. E. Blankenship, 'Excited State Properties of 3′-Hydroxyechinenone in Solvents and in the Orange Carotenoid Protein from *Synechocystis* sp. PCC 6803', *The Journal of Physical Chemistry B* **118**, 6141–6149 (2014).

[57] T. Khan, M. A. Dominguez-Martin, I. Šímová, M. Fuciman, C. A. Kerfeld, and T. Polívka, 'Excited-State Properties of Canthaxanthin in Cyanobacterial Carotenoid-Binding Proteins HCP2 and HCP3', *The Journal of Physical Chemistry B* **124**, 4896–4905 (2020).

[58] E. G. Maksimov, E. A. Shirshin, N. N. Sluchanko, D. V. Zlenko, E. Y. Parshina, G. V. Tsoraev, K. E. Klementiev, G. S. Budylin, F.-J. Schmitt, T. Friedrich, V. V. Fadeev, V. Z. Paschenko, and A. B. Rubin, 'The Signaling State of Orange Carotenoid Protein', *Biophysical Journal* **109**, 595–607 (2015).

[59] E. G. Maksimov, N. N. Sluchanko, Y. B. Slonimskiy, E. A. Slutskaya, A. V. Stepanov, A. M. Argentova-Stevens, E. A. Shirshin, G. V. Tsoraev, K. E. Klementiev, O. V. Slatinskaya, E. P. Lukashev, T. Friedrich, V. Z. Paschenko, and A. B. Rubin, 'The photocycle of orange carotenoid protein conceals distinct intermediates and asynchronous changes in the carotenoid and protein components', *Scientific Reports* **7**, 15548 (2017).

[60] E. G. Maksimov, E. A. Protasova, G. V. Tsoraev, I. A. Yaroshevich, A. I. Maydykovskiy, E. A. Shirshin, T. S. Gostev, A. Jelzow, M. Moldenhauer, Y. B. Slonimskiy, N. N. Sluchanko, and T. Friedrich, 'Probing of carotenoid-tryptophan hydrogen bonding dynamics in the single-tryptophan photoactive Orange Carotenoid Protein', *Scientific Reports* **10**, 11729 (2020).

[61] I. A. Yaroshevich, E. G. Maksimov, N. N. Sluchanko, D. V. Zlenko, A. V. Stepanov, E. A. Slutskaya, Y. B. Slonimskiy, V. S. Botnarevskii, A. Remeeva, I. Gushchin, K. Kovalev, V. I. Gordeliy, I. V. Shelaev, F. E.

Gostev, D. Khakhulin, V. V. Poddubnyy, T. S. Gostev, D. A. Cherepanov, T. Polívka, M. Kloz, T. Friedrich, V. Z. Paschenko, V. A. Nadtochenko, A. B. Rubin, and M. P. Kirpichnikov, 'Role of hydrogen bond alternation and charge transfer states in photoactivation of the Orange Carotenoid Protein', *Communications Biology* **4**, 539 (2021).

[62] R. Berera, I. H. M. van Stokkum, M. Gwizdala, A. Wilson, D. Kirilovsky, and R. van Grondelle, 'The Photophysics of the Orange Carotenoid Protein, a Light-Powered Molecular Switch', *The Journal of Physical Chemistry B* **116**, 2568–2574 (2012).

[63] R. Berera, M. Gwizdala, I. H. M. van Stokkum, D. Kirilovsky, and R. van Grondelle, 'Excited States of the Inactive and Active Forms of the Orange Carotenoid Protein', *The Journal of Physical Chemistry B* **117**, 9121–9128 (2013).

[64] S. Niziński, A. Wilson, L. M. Uriarte, C. Ruckebusch, E. A. Andreeva, I. Schlichting, J.-P. Colletier, D. Kirilovsky, G. Burdzinski, and M. Sliwa, 'Unifying Perspective of the Ultrafast Photodynamics of Orange Carotenoid Proteins from *Synechocystis* : Peril of High-Power Excitation, Existence of Different S* States, and Influence of Tagging', *JACS Au* **2**, 1084–1095 (2022).

[65] T. Khan, V. Kuznetsova, M. A. Dominguez-Martin, C. A. Kerfeld, and T. Polívka, 'UV Excitation of Carotenoid Binding Proteins OCP and HCP: Excited-State Dynamics and Product Formation', *ChemPhotoChem* **6**, e202100194 (2022).

[66] V. Balevičius, A. G. Pour, J. Savolainen, C. N. Lincoln, V. Lukeš, E. Riedle, L. Valkunas, D. Abramavicius, and J. Hauer, 'Vibronic energy relaxation approach highlighting deactivation pathways in carotenoids', *Physical Chemistry Chemical Physics* **17**, 19491–19499 (2015).

[67] V. Balevičius, D. Abramavicius, T. Polívka, A. Galestian Pour, and J. Hauer, 'A Unified Picture of S* in Carotenoids', *The Journal of Physical Chemistry Letters* **7**, 3347–3352 (2016).

[68] V. Balevičius, C. N. Lincoln, D. Viola, G. Cerullo, J. Hauer, and D. Abramavicius, 'Effects of tunable excitation in carotenoids explained by the vibrational energy relaxation approach', *Photosynthesis Research* **135**, 55–64 (2018).

[69] V. Balevičius, T. Wei, D. Di Tommaso, D. Abramavicius, J. Hauer, T. Polívka, and C. D. P. Duffy, 'The full dynamics of energy relaxation in large organic molecules: from photo-excitation to solvent heating', *Chemical Science* **10**, 4792–4804 (2019).

[70] V. Šebelík, C. D. P. Duffy, E. Keil, T. Polívka, and J. Hauer, 'Understanding Carotenoid Dynamics via the Vibronic Energy Relaxation Approach', *The Journal of Physical Chemistry B* **126**, 3985–3994 (2022).

[71] N. K. Jain and I. Roy, 'Effect of trehalose on protein structure', *Protein Science* **18**, 24–36 (2009).

[72] J. G. Sampedro and S. Uribe, 'Trehalose-enzyme interactions result in structure stabilization and activity inhibition. The role of viscosity', *Molecular and Cellular Biochemistry* **256**, 319–327 (2004).

[73] V. U. Chukhutsina, J. M. Baxter, A. Fadini, R. M. Morgan, M. A. Pope, K. Maghlaoui, C. M. Orr, A. Wagner, and J. J. van Thor, 'Light activation of Orange Carotenoid Protein reveals bicycle-pedal single-bond isomerization', *Nature Communications* **13**, 6420 (2022).

[74] D. Harris, O. Tal, D. Jallet, A. Wilson, D. Kirilovsky, and N. Adir, 'Orange carotenoid protein burrows into the phycobilisome to provide photoprotection', *Proceedings of the National Academy of Sciences* **113**, E1655–E1662 (2016).

[75] A. H. Squires, P. D. Dahlberg, H. Liu, N. C. M. Magdaong, R. E. Blankenship, and W. E. Moerner, 'Single-molecule trapping and spectroscopy reveals photophysical heterogeneity of phycobilisomes quenched by Orange Carotenoid Protein', *Nature Communications* **10**, 1172 (2019).

[76] W. Lou, D. M. Niedzwiedzki, R. J. Jiang, R. E. Blankenship, and H. Liu, 'Binding of red form of Orange Carotenoid Protein (OCP) to phycobilisome is not sufficient for quenching', *Biochimica et Biophysica Acta (BBA) - Bioenergetics* **1861**, 148155 (2020).

[77] E. G. Maksimov, W.-J. Li, E. A. Protasova, T. Friedrich, B. Ge, S. Qin, and N. N. Sluchanko, 'Hybrid coupling of R-phycoerythrin and the orange carotenoid protein supports the FRET-based mechanism of cyanobacterial photoprotection', *Biochemical and Biophysical Research Communications* **516**, 699–704 (2019).

[78] P. M. Krasilnikov, D. V. Zlenko, and I. N. Stadnichuk, 'Rates and pathways of energy migration from the phycobilisome to the photosystem II and to the orange carotenoid protein in cyanobacteria', *FEBS Letters* **594**, 1145–1154 (2020).

[79] S. Bandara, Z. Ren, L. Lu, X. Zeng, H. Shin, K.-H. Zhao, and X. Yang, 'Photoactivation mechanism of a carotenoid-based photoreceptor', *Proceedings of the National Academy of Sciences* **114**, 6286–6291 (2017).

[80] A. Wilson, C. Punginelli, A. Gall, C. Bonetti, M. Alexandre, J.-M. Routaboul, C. A. Kerfeld, R. van Grondelle, B. Robert, J. T. M. Kennis, and D. Kirilovsky, 'A photoactive carotenoid protein acting as light intensity sensor', *Proceedings of the National Academy of Sciences* **105**, 12075–12080 (2008).

[81] L. Piccinini, S. Iacopino, S. Cazzaniga, M. Ballottari, B. Giuntoli, and F. Licausi, 'A synthetic switch based on orange carotenoid protein to control blue–green light responses in chloroplasts', *Plant Physiology* **189**, 1153–1168 (2022).

[82] M. A. Dominguez-Martin and C. A. Kerfeld, 'Engineering the orange carotenoid protein for applications in synthetic biology', *Current Opinion in Structural Biology* **57**, 110–117 (2019).

[83] J. Kromdijk, K. Głowacka, L. Leonelli, S. T. Gabilly, M. Iwai, K. K. Niyogi, and S. P. Long, 'Improving photosynthesis and crop productivity by accelerating recovery from photoprotection', *Science* **354**, 857–861 (2016).

[84] R. A. Soni, K. Sudhakar, and R. Rana, 'Spirulina – From growth to nutritional product: A review', *Trends in Food Science & Technology* **69**, 157–171 (2017).

[85] R. R. Siva Kiran, G. M. Madhu, and S. V. Satyanarayana, 'Spirulina in combating Protein Energy Malnutrition (PEM) and Protein Energy Wasting (PEW) - A review', *Journal of Nutrition Research* **3**, 62–79 (2015).

[86] G. Abdulqader, L. Barsanti, and M. R. Tredici, 'Harvest of Arthrospira platensis from Lake Kossorom (Chad) and its household usage among the Kanembu', *Journal of Applied Phycology* **12**, 493–498 (2000).

[87] S. G. Hays and D. C. Ducat, 'Engineering cyanobacteria as photosynthetic feedstock factories', *Photosynthesis Research* **123**, 285–295 (2015).

[88] I. M. Machado and S. Atsumi, 'Cyanobacterial biofuel production', *Journal of Biotechnology* **162**, 50–56 (2012).

[89] P. Savakis and K. J. Hellingwerf, 'Engineering cyanobacteria for direct biofuel production from CO_2', *Current Opinion in Biotechnology* **33**, 8–14 (2015).

[90] P. Farrokh, M. Sheikhpour, A. Kasaeian, H. Asadi, and R. Bavandi, 'Cyanobacteria as an eco-friendly resource for biofuel production: A critical review', *Biotechnology Progress* **35**, e2835 (2019).

[91] P. Flombaum, J. L. Gallegos, R. A. Gordillo, J. Rincón, L. L. Zabala, N. Jiao, D. M. Karl, W. K. W. Li, M. W. Lomas, D. Veneziano, C. S. Vera, J. A. Vrugt, and A. C. Martiny, 'Present and future global distributions of the marine Cyanobacteria *Prochlorococcus* and *Synechococcus*', *Proceedings of the National Academy of Sciences* **110**, 9824–9829 (2013).

[92] C. B. Field, M. J. Behrenfeld, J. T. Randerson, and P. Falkowski, 'Primary Production of the Biosphere: Integrating Terrestrial and Oceanic Components', *Science* **281**, 237–240 (1998).

[93] J. P. Zehr, 'Nitrogen fixation by marine cyanobacteria', *Trends in Microbiology* **19**, 162–173 (2011).

[94] H. Bothe, O. Schmitz, M. G. Yates, and W. E. Newton, 'Nitrogen Fixation and Hydrogen Metabolism in Cyanobacteria', *Microbiology and Molecular Biology Reviews* **74**, 529–551 (2010).

[95] K. Srirangan, M. E. Pyne, and C. Perry Chou, 'Biochemical and genetic engineering strategies to enhance hydrogen production in photosynthetic algae and cyanobacteria', *Bioresource Technology* **102**, 8589–8604 (2011).

[96] D. Dutta, D. De, S. Chaudhuri, and S. K. Bhattacharya, 'Hydrogen production by Cyanobacteria', *Microbial Cell Factories* **4**, 36 (2005).

[97] D. W. Polak, A. J. Musser, G. A. Sutherland, A. Auty, F. Branchi, B. Dzurnak, J. Chidgey, G. Cerullo, C. N. Hunter, and J. Clark, 'Band-edge Excitation of Carotenoids Removes S* Revealing Triplet-pair Contributions to the S_1 Absorption Spectrum', *arXiv preprint*, arXiv:1901.04900 (2019).

[98] E. E. Ostroumov, M. G. M. Reus Michael, and A. R. Holzwarth, 'On the Nature of the "Dark S*" Excited State of β-Carotene', *The Journal of Physical Chemistry A* **115**, 3698–3712 (2011).

[99] B. R. Nielsen, A. Mortensen, K. Jørgensen, and L. H. Skibsted, 'Singlet *versus* Triplet Reactivity in Photodegradation of C_{40} Carotenoids', *Journal of Agricultural and Food Chemistry* **44**, 2106–2113 (1996).

[100] T. Polívka and V. Sundström, 'Dark excited states of carotenoids: Consensus and controversy', *Chemical Physics Letters* **477**, 1–11 (2009).

[101] K. Chen, J. K. Gallaher, A. J. Barker, and J. M. Hodgkiss, 'Transient Grating Photoluminescence Spectroscopy: An Ultrafast Method of Gating Broadband Spectra', *The Journal of Physical Chemistry Letters* **5**, 1732–1737 (2014).

[102] M. J. Llansola-Portoles, A. A. Pascal, and B. Robert, 'Electronic and vibrational properties of carotenoids: from *in vitro* to *in vivo*', *Journal of The Royal Society Interface* **14**, 20170504 (2017).

[103] A. Köhler and H. Bässler, *Electronic Processes in Organic Semiconductors: An Introduction* (Wiley-VCH, Weinheim, 2015).

[104] W. Barford, *Electronic and Optical Properties of Conjugated Polymers*, International Series of Monographs on Physics (Oxford University Press, Oxford, New York, 2008).

[105] P. W. Atkins and R. S. Friedman, *Molecular Quantum Mechanics*, 4th edition (Oxford University Press, Oxford, New York, 2005).

[106] N. J. Turro, V. Ramamurthy, and J. Scaiano, *Modern Molecular Photochemistry For Organic Molecules* (Viva, New Delhi, 2017).

[107] J. M. Brown, *Molecular Spectroscopy*, Oxford Chemistry Primers (Oxford University Press, Oxford, New York, 1998).

[108] S. H. Simon, *The Oxford Solid State Basics* (Oxford University Press, Oxford, New York, 2013).

[109] M. Born and R. Oppenheimer, 'Zur Quantentheorie der Molekeln', *Annalen der Physik* **389**, 457–484 (1927).

[110] M. Pope and C. E. Swenberg, *Electronic Processes in Organic Crystals and Polymers*, 2nd edition, Monographs on the Physics and Chemistry of Materials (Oxford University Press, Oxford, New York, 1999).

[111] S. E. Braslavsky, 'Glossary of terms used in photochemistry, 3rd edition (IUPAC Recommendations 2006)', *Pure and Applied Chemistry*, Pure and Applied Chemistry **79**, 293–465 (2007).

[112] S.-H. Lim, T. G. Bjorklund, F. C. Spano, and C. J. Bardeen, 'Exciton Delocalization and Superradiance in Tetracene Thin Films and Nanoaggregates', *Physical Review Letters* **92**, 107402 (2004).

[113] F. C. Spano, J. R. Kuklinski, and S. Mukamel, 'Temperature-dependent superradiant decay of excitons in small aggregates', *Physical Review Letters* **65**, 211–214 (1990).

[114] F. C. Spano, 'Analysis of the UV/Vis and CD Spectral Line Shapes of Carotenoid Assemblies: Spectral Signatures of Chiral H-Aggregates', *Journal of the American Chemical Society* **131**, 4267–4278 (2009).

[115] J. D. Wright, *Molecular Crystals*, 2nd edition (Cambridge University Press, Cambridge, New York, 1995).

[116] D. J. Valentine, D. Manawadu, and W. Barford, 'Higher-energy triplet-pair states in polyenes and their role in intramolecular singlet fission', *Physical Review B* **102**, 125107 (2020).

[117] D. Manawadu, D. J. Valentine, M. Marcus, and W. Barford, 'Singlet Triplet-Pair Production and Possible Singlet-Fission in Carotenoids', *The Journal of Physical Chemistry Letters* **13**, 1344–1349 (2022).

[118] W. Barford, 'Theory of the dark state of polyenes and carotenoids', *Physical Review B* **106**, 035201 (2022).

[119] P. Tavan and K. Schulten, 'Electronic excitations in finite and infinite polyenes', *Physical Review B* **36**, 4337–4358 (1987).

[120] M. Schmidt and P. Tavan, 'Electronic excitations in long polyenes revisited', *The Journal of Chemical Physics* **136**, 124309 (2012).

[121] E. J. Taffet, F. Fassioli, Z. S. D. Toa, D. Beljonne, and G. D. Scholes, 'Uncovering dark multichromophoric states in Peridinin–Chlorophyll–Protein', *Journal of The Royal Society Interface* **17**, 20190736 (2020).

[122] W. Barford, R. J. Bursill, and M. Y. Lavrentiev, 'Density-matrix renormalization-group calculations of excited states of linear polyenes', *Physical Review B* **63**, 195108 (2001).

[123] G. B. Piland, J. J. Burdett, D. Kurunthu, and C. J. Bardeen, 'Magnetic Field Effects on Singlet Fission and Fluorescence Decay Dynamics in Amorphous Rubrene', *The Journal of Physical Chemistry C* **117**, 1224–1236 (2013).

[124] P. C. Tapping and D. M. Huang, 'Comment on "Magnetic Field Effects on Singlet Fission and Fluorescence Decay Dynamics in Amorphous Rubrene"', *The Journal of Physical Chemistry C* **120**, 25151–25157 (2016).

[125] S. Richert, C. E. Tait, and C. R. Timmel, 'Delocalisation of photoexcited triplet states probed by transient EPR and hyperfine spectroscopy', *Journal of Magnetic Resonance* **280**, 103–116 (2017).

[126] C. P. Poole, H. A. Farach, and W. K. Jackson, 'Standardization of convention for zero field splitting parameters', *The Journal of Chemical Physics* **61**, 2220–2221 (1974).

[127] J. Frick, J. U. V. Schütz, H. C. Wolf, and G. Kothe, 'First Detection of the (Nonphosphorescent) Triplet State in Single Crystals of β-Carotene', *Molecular Crystals and Liquid Crystals Incorporating Nonlinear Optics* **183**, 269–272 (1990).

[128] Y. Teki, J. von Schütz, H. Wachtel, V. Weiss, and H. Wolf, 'Triplet excitons in diphenylbutadiene and diphenylhexatriene single crystals by zero-field delayed fluorescence ODMR', *Chemical Physics Letters* **225**, 124–130 (1994).

[129] J. Binney and D. Skinner, *The Physics of Quantum Mechanics* (Oxford University Press, Oxford, New York, 2013).

[130] M. Fox, *Quantum Optics: An Introduction*, Oxford Master Series in Physics (Oxford University Press, Oxford, New York, 2006).

[131] S. J. Strickler and R. A. Berg, 'Relationship between Absorption Intensity and Fluorescence Lifetime of Molecules', *The Journal of Chemical Physics* **37**, 814–822 (1962).

[132] W. P. Su, J. R. Schrieffer, and A. J. Heeger, 'Solitons in Polyacetylene', *Physical Review Letters* **42**, 1698–1701 (1979).

[133] W. P. Su, J. R. Schrieffer, and A. J. Heeger, 'Soliton excitations in polyacetylene', *Physical Review B* **22**, 2099–2111 (1980).

[134] H. A. Frank, J. A. Bautista, J. Josue, Z. Pendon, R. G. Hiller, F. P. Sharples, D. Gosztola, and M. R. Wasielewski, 'Effect of the Solvent Environment on the Spectroscopic Properties and Dynamics of the Lowest Excited States of Carotenoids', *The Journal of Physical Chemistry B* **104**, 4569–4577 (2000).

[135] L. Fiedor, Heriyanto, J. Fiedor, and M. Pilch, 'Effects of Molecular Symmetry on the Electronic Transitions in Carotenoids', *The Journal of Physical Chemistry Letters* **7**, 1821–1829 (2016).

[136] L. Fiedor, A. Dudkowiak, and M. Pilch, 'The origin of the dark S_1 state in carotenoids: a comprehensive model', *Journal of The Royal Society Interface* **16**, 20190191 (2019).

[137] T. H. Keil, 'Shapes of Impurity Absorption Bands in Solids', *Physical Review* **140**, A601–A617 (1965).

[138] F. C. Spano and L. Silvestri, 'Multiple mode exciton-vibrational coupling in H-aggregates: Synergistic enhancement of the quantum yield', *The Journal of Chemical Physics* **132**, 094704 (2010).

[139] M. M. Mendes-Pinto, E. Sansiaume, H. Hashimoto, A. A. Pascal, A. Gall, and B. Robert, 'Electronic Absorption and Ground State Structure of Carotenoid Molecules', *The Journal of Physical Chemistry B* **117**, 11015–11021 (2013).

[140] S. Karabunarliev, E. R. Bittner, and M. Baumgarten, 'Franck–Condon spectra and electron-libration coupling in para-polyphenyls', *The Journal of Chemical Physics* **114**, 5863–5870 (2001).

[141] A. Rosspeintner, B. Lang, and E. Vauthey, 'Ultrafast Photochemistry in Liquids', *Annual Review of Physical Chemistry* **64**, 247–271 (2013).

[142] A. J. Orr-Ewing, 'Taking the plunge: chemical reaction dynamics in liquids', *Chemical Society Reviews* **46**, 7597–7614 (2017).

[143] R. K. Venkatraman and A. J. Orr-Ewing, 'Solvent Effects on Ultrafast Photochemical Pathways', *Accounts of Chemical Research* **54**, 4383–4394 (2021).

[144] L. D. Landau and E. M. Lifshitz, *Quantum Mechanics: Non-relativistic Theory (Volume 3)*, 3rd, Course of Theoretical Physics (Pergamon Press, Oxford, New York, 1977).

[145] P. K. H. Ho, J.-S. Kim, N. Tessler, and R. H. Friend, 'Photoluminescence of poly(p-phenylenevinylene)–silica nanocomposites: Evidence for dual emission by Franck–Condon analysis', *The Journal of Chemical Physics* **115**, 2709–2720 (2001).

[146] S. Hooker and C. Webb, *Laser Physics*, Oxford Master Series in Physics (Oxford University Press, Oxford, New York, 2010).

[147] M. Kasha, H. R. Rawls, and M. Ashraf El-Bayoumi, 'The exciton model in molecular spectroscopy', *Pure and Applied Chemistry* **11**, 371–392 (1965).

[148] E. G. McRae and M. Kasha, 'Enhancement of Phosphorescence Ability upon Aggregation of Dye Molecules', *The Journal of Chemical Physics* **28**, 721–722 (1958).

[149] C. E. Wayne and R. P. Wayne, *Photochemistry*, Oxford Chemistry Primers (Oxford University Press, Oxford, New York, 1996).

[150] A. N. Macpherson and T. Gillbro, 'Solvent Dependence of the Ultrafast S_2-S_1 Internal Conversion Rate of β-Carotene', *The Journal of Physical Chemistry A* **102**, 5049–5058 (1998).

[151] W. D. Loveland, D. J. Morrissey, and G. T. Seaborg, *Modern Nuclear Chemistry* (John Wiley & Sons, New Jersey, 2006).

[152] W. Siebrand, 'Radiationless Transitions in Polyatomic Molecules. I. Calculation of Franck—Condon Factors', *The Journal of Chemical Physics* **46**, 440–447 (1967).

[153] W. Siebrand, 'Radiationless Transitions in Polyatomic Molecules. II. Triplet-Ground-State Transitions in Aromatic Hydrocarbons', *The Journal of Chemical Physics* **47**, 2411–2422 (1967).

[154] E. W. Schlag, S. Schneider, and S. F. Fischer, 'Lifetimes in Excited States', *Annual Review of Physical Chemistry* **22**, 465–526 (1971).

[155] V. May and O. Kühn, *Charge and Energy Transfer Dynamics in Molecular Systems*, 3rd edition (Wiley-VCH, Weinheim, 2011).

[156] B. G. Levine and T. J. Martínez, 'Isomerization Through Conical Intersections', *Annual Review of Physical Chemistry* **58**, 613–634 (2007).

[157] D. R. Yarkony, 'Conical Intersections: Diabolical and Often Misunderstood', *Accounts of Chemical Research* **31**, 511–518 (1998).

[158] W. Domcke and D. R. Yarkony, 'Role of Conical Intersections in Molecular Spectroscopy and Photoinduced Chemical Dynamics', *Annual Review of Physical Chemistry* **63**, 325–352 (2012).

[159] M. Liebel, C. Schnedermann, and P. Kukura, 'Vibrationally Coherent Crossing and Coupling of Electronic States during Internal Conversion in β-Carotene', *Physical Review Letters* **112**, 198302 (2014).

[160] S. L. Bayliss, L. R. Weiss, A. Rao, R. H. Friend, A. D. Chepelianskii, and N. C. Greenham, 'Spin signatures of exchange-coupled triplet pairs formed by singlet fission', *Physical Review B* **94**, 045204 (2016).

[161] J. Von Neumann and E. Wigner, 'No crossing rule', *Physikalische Zeitschrift* **30**, 467–470 (1929).

[162] G. Marston, T. G. Truscott, and R. P. Wayne, 'Phosphorescence of β-carotene', *Journal of the Chemical Society, Faraday Transactions* **91**, 4059–4061 (1995).

[163] R. J. Cherry, D. Chapman, and J. Langelaar, 'Fluorescence and Phosphorescence of β-Carotene', *Transactions of the Faraday Society* **64**, 2304–2307 (1968).

[164] T. J. Penfold, E. Gindensperger, C. Daniel, and C. M. Marian, 'Spin-Vibronic Mechanism for Intersystem Crossing', *Chemical Reviews* **118**, 6975–7025 (2018).

[165] D. G. Bossanyi, Y. Sasaki, S. Wang, D. Chekulaev, N. Kimizuka, N. Yanai, and J. Clark, 'Spin Statistics for Triplet–Triplet Annihilation Upconversion: Exchange Coupling, Intermolecular Orientation, and Reverse Intersystem Crossing', *JACS Au* **1**, 2188–2201 (2021).

[166] R. M. Eisberg and R. Resnick, *Quantum Physics of Atoms, Molecules, Solids, Nuclei, and Particles*, 2nd edition (John Wiley & Sons, New York, 1985).

[167] M. A. El-Sayed, 'Spin—Orbit Coupling and the Radiationless Processes in Nitrogen Heterocyclics', *The Journal of Chemical Physics* **38**, 2834–2838 (1963).

[168] M. A. El-Sayed, 'Triplet state. Its radiative and nonradiative properties', *Accounts of Chemical Research* **1**, 8–16 (1968).

[169] C. M. Marian, 'Spin–orbit coupling and intersystem crossing in molecules', *WIREs Computational Molecular Science* **2**, 187–203 (2012).

[170] J. Tatchen, N. Gilka, and C. M. Marian, 'Intersystem crossing driven by vibronic spin–orbit coupling: a case study on psoralen', *Physical Chemistry Chemical Physics* **9**, 5209–5221 (2007).

[171] A. C. Albrecht, 'Vibronic—Spin-Orbit Perturbations and the Assignment of the Lowest Triplet State of Benzene', *The Journal of Chemical Physics* **38**, 354–365 (1963).

[172] D. Beljonne, Z. Shuai, G. Pourtois, and J. L. Bredas, 'Spin-Orbit Coupling and Intersystem Crossing in Conjugated Polymers: A Configuration Interaction Description', *The Journal of Physical Chemistry A* **105**, 3899–3907 (2001).

[173] R. E. Kellogg, 'Second Triplet State of Anthracene', *The Journal of Chemical Physics* **44**, 411–412 (1966).

[174] W. T. Stacy and C. E. Swenberg, 'Temperature Dependence of Intersystem Crossing in Crystalline Anthracene', *The Journal of Chemical Physics* **52**, 1962–1965 (1970).

[175] F. Tanaka, M. Okamoto, and S. Hirayama, 'Pressure and temperature dependences of the rate constant for S_1-T_2 intersystem crossing of anthracene compounds in solution', *The Journal of Physical Chemistry* **99**, 525–530 (1995).

[176] S. Singh, W. J. Jones, W. Siebrand, B. P. Stoicheff, and W. G. Schneider, 'Laser Generation of Excitons and Fluorescence in Anthracene Crystals', *The Journal of Chemical Physics* **42**, 330–342 (1965).

[177] R. G. Kepler, J. C. Caris, P. Avakian, and E. Abramson, 'Triplet excitons and Delayed Fluorescence in Anthracene Crystals', *Physical Review Letters* **10**, 400–402 (1963).

[178] R. C. Johnson, R. E. Merrifield, P. Avakian, and R. B. Flippen, 'Effects of Magnetic Fields on the Mutual Annihilation of Triplet Excitons in Molecular Crystals', *Physical Review Letters* **19**, 285–287 (1967).

[179] R. E. Merrifield, 'Diffusion and mutual annihilation of triplet excitons in organic crystals', *Accounts of Chemical Research* **1**, 129–135 (1968).

[180] R. C. Johnson and R. E. Merrifield, 'Effects of Magnetic Fields on the Mutual Annihilation of Triplet Excitons in Anthracene Crystals', *Physical Review B* **1**, 896–902 (1970).

[181] D. G. Bossanyi, M. Matthiesen, S. Wang, J. A. Smith, R. C. Kilbride, J. D. Shipp, D. Chekulaev, E. Holland, J. E. Anthony, J. Zaumseil, A. J. Musser, and J. Clark, 'Emissive spin-0 triplet-pairs are a direct product of triplet–triplet annihilation in pentacene single crystals and anthradithiophene films', *Nature Chemistry* **13**, 163–171 (2021).

[182] R. P. Groff, P. Avakian, and R. E. Merrifield, 'Coexistence of Exciton Fission and Fusion in Tetracene Crystals', *Physical Review B* **1**, 815–817 (1970).

[183] C. Swenberg and W. Stacy, 'Bimolecular radiationless transitions in crystalline tetracene', *Chemical Physics Letters* **2**, 327–328 (1968).

[184] N. Geacintov, M. Pope, and F. Vogel, 'Effect of Magnetic Field on the Fluorescence of Tetracene Crystals: Exciton Fission', *Physical Review Letters* **22**, 593–596 (1969).

[185] R. Groff, P. Avakian, and R. Merrifield, 'Magnetic field dependence of delayed fluorescence from tetracene crystals', *Journal of Luminescence* **1–2**, 218–223 (1970).

[186] A. J. Nozik, R. J. Ellingson, O. I. Micic, J. L. Blackburn, P. Yu, J. E. Murphy, M. C. Beard, and G. Rumbles, 'Unique approaches to solar photon conversion based on semiconductor nanostructures and novel molecular chromophores; dynamics of electron relaxation, interfacial charge transfer, and carrier multiplication', in (–9th June 2004), pages 63–66.

[187] J. Michl, X. Chen, G. Rana, D. B. Popovic, J. Downing, A. J. Nozik, J. C. Johnson, M. A. Ratner, and I. Paci, *Book of Abstracts, DOE Solar Program Review Meetings*, Denver, Colorado, –28th Oct. 2004.

[188] M. B. Smith and J. Michl, 'Singlet Fission', *Chemical Reviews* **110**, 6891–6936 (2010).

[189] M. J. Y. Tayebjee, D. R. McCamey, and T. W. Schmidt, 'Beyond Shockley–Queisser: Molecular Approaches to High-Efficiency Photovoltaics', *The Journal of Physical Chemistry Letters* **6**, 2367–2378 (2015).

[190] J. C. Goldschmidt and S. Fischer, 'Upconversion for Photovoltaics – a Review of Materials, Devices and Concepts for Performance Enhancement', *Advanced Optical Materials* **3**, 510–535 (2015).

[191] C. K. Yong, A. J. Musser, S. L. Bayliss, S. Lukman, H. Tamura, O. Bubnova, R. K. Hallani, A. Meneau, R. Resel, M. Maruyama, S. Hotta, L. M. Herz, D. Beljonne, J. E. Anthony, J. Clark, and H. Sirringhaus, 'The entangled triplet pair state in acene and heteroacene materials', *Nature Communications* **8**, 15953 (2017).

[192] A. B. Pun, A. Asadpoordarvish, E. Kumarasamy, M. J. Y. Tayebjee, D. Niesner, D. R. McCamey, S. N. Sanders, L. M. Campos, and M. Y. Sfeir, 'Ultra-fast intramolecular singlet fission to persistent multiexcitons by molecular design', *Nature Chemistry* **11**, 821–828 (2019).

[193] N. V. Korovina, C. H. Chang, and J. C. Johnson, 'Spatial separation of triplet excitons drives endothermic singlet fission', *Nature Chemistry* **12**, 391–398 (2020).

[194] Z. Wang, H. Liu, X. Xie, C. Zhang, R. Wang, L. Chen, Y. Xu, H. Ma, W. Fang, Y. Yao, H. Sang, X. Wang, X. Li, and M. Xiao, 'Free-triplet generation with improved efficiency in tetracene oligomers through spatially separated triplet pair states', *Nature Chemistry* **13**, 559–567 (2021).

[195] J. J. Burdett, G. B. Piland, and C. J. Bardeen, 'Magnetic field effects and the role of spin states in singlet fission', *Chemical Physics Letters* **585**, 1–10 (2013).

[196] G. B. Piland and C. J. Bardeen, 'How Morphology Affects Singlet Fission in Crystalline Tetracene', *The Journal of Physical Chemistry Letters* **6**, 1841–1846 (2015).

[197] M. J. Y. Tayebjee, R. G. C. R. Clady, and T. W. Schmidt, 'The exciton dynamics in tetracene thin films', *Physical Chemistry Chemical Physics* **15**, 14797–14805 (2013).

[198] M. W. B. Wilson, A. Rao, K. Johnson, S. Gélinas, R. di Pietro, J. Clark, and R. H. Friend, 'Temperature-Independent Singlet Exciton Fission in Tetracene', *Journal of the American Chemical Society* **135**, 16680–16688 (2013).

[199] M. W. B. Wilson, A. Rao, J. Clark, R. S. S. Kumar, D. Brida, G. Cerullo, and R. H. Friend, 'Ultrafast Dynamics of Exciton Fission in Polycrystalline Pentacene', *Journal of the American Chemical Society* **133**, 11830–11833 (2011).

[200] C. Kollmar, 'Electronic structure of diradical and dicarbene intermediates in short-chain polydiacetylene oligomers', *The Journal of Chemical Physics* **98**, 7210–7228 (1993).

[201] T. Yago, K. Ishikawa, R. Katoh, and M. Wakasa, 'Magnetic Field Effects on Triplet Pair Generated by Singlet Fission in an Organic Crystal: Application of Radical Pair Model to Triplet Pair', *The Journal of Physical Chemistry C* **120**, 27858–27870 (2016).

[202] A. J. Musser, M. Al-Hashimi, M. Heeney, and J. Clark, 'Heavy-atom effects on intramolecular singlet fission in a conjugated polymer', *The Journal of Chemical Physics* **151**, 044902 (2019).

[203] S. L. Bayliss, A. D. Chepelianskii, A. Sepe, B. J. Walker, B. Ehrler, M. J. Bruzek, J. E. Anthony, and N. C. Greenham, 'Geminate and Nongeminate Recombination of Triplet Excitons Formed by Singlet Fission', *Physical Review Letters* **112**, 238701 (2014).

[204] R. Wang, C. Zhang, B. Zhang, Y. Liu, X. Wang, and M. Xiao, 'Magnetic dipolar interaction between correlated triplets created by singlet fission in tetracene crystals', *Nature Communications* **6**, 8602 (2015).

[205] D. G. Bossanyi, 'Triplet-Pair States in Exciton Fission and Fusion', PhD thesis (University of Sheffield, 2021).

[206] U. E. Steiner and T. Ulrich, 'Magnetic field effects in chemical kinetics and related phenomena', *Chemical Reviews* **89**, 51–147 (1989).

[207] B. Hu, L. Yan, and M. Shao, 'Magnetic-Field Effects in Organic Semiconducting Materials and Devices', *Advanced Materials* **21**, 1500–1516 (2009).

[208] L. Yarmus, J. Rosenthal, and M. Chopp, 'EPR of triplet excitions in tetracene crystals: spin polarization and the role of singlet exciton fission', *Chemical Physics Letters* **16**, 477–481 (1972).

[209] C. Swenberg, R. van Metter, and M. Ratner, 'Comments on exciton fission and electron spin resonance in tetracene single crystals', *Chemical Physics Letters* **16**, 482–485 (1972).

[210] H. L. Stern, A. J. Musser, S. Gelinas, P. Parkinson, L. M. Herz, M. J. Bruzek, J. Anthony, R. H. Friend, and B. J. Walker, 'Identification of a triplet pair intermediate in singlet exciton fission in solution', *Proceedings of the National Academy of Sciences* **112**, 7656–7661 (2015).

[211] R. D. Pensack, E. E. Ostroumov, A. J. Tilley, S. Mazza, C. Grieco, K. J. Thorley, J. B. Asbury, D. S. Seferos, J. E. Anthony, and G. D. Scholes, 'Observation of Two Triplet-Pair Intermediates in Singlet Exciton Fission', *The Journal of Physical Chemistry Letters* **7**, 2370–2375 (2016).

[212] R. D. Pensack, A. J. Tilley, C. Grieco, G. E. Purdum, E. E. Ostroumov, D. B. Granger, D. G. Oblinsky, J. C. Dean, G. S. Doucette, J. B. Asbury, Y.-L. Loo, D. S. Seferos, J. E. Anthony, and G. D. Scholes, 'Striking the right balance of intermolecular coupling for high-efficiency singlet fission', *Chemical Science* **9**, 6240–6259 (2018).

[213] J. J. Burdett and C. J. Bardeen, 'Quantum Beats in Crystalline Tetracene Delayed Fluorescence Due to Triplet Pair Coherences Produced by Direct Singlet Fission', *Journal of the American Chemical Society* **134**, 8597–8607 (2012).

[214] Z. Wang, C. Zhang, R. Wang, G. Wang, X. Wang, and M. Xiao, 'Weakly coupled triplet pair states probed by quantum beating in delayed fluorescence in tetracene crystals', *The Journal of Chemical Physics* **151**, 134309 (2019).

[215] F. X. Cunningham and E. Gantt, 'A portfolio of plasmids for identification and analysis of carotenoid pathway enzymes: *Adonis aestivalis* as a case study', *Photosynthesis Research* **92**, 245–259 (2007).

[216] F. X. Cunningham Jr, B. Pogson, Z. Sun, K. A. McDonald, D. DellaPenna, and E. Gantt, 'Functional analysis of the beta and epsilon lycopene cyclase enzymes of Arabidopsis reveals a mechanism for control of cyclic carotenoid formation.', *The Plant Cell* **8**, 1613–1626 (1996).

[217] C. Punginelli, A. Wilson, J.-M. Routaboul, and D. Kirilovsky, 'Influence of zeaxanthin and echinenone binding on the activity of the Orange Carotenoid Protein', *Biochimica et Biophysica Acta (BBA) - Bioenergetics* **1787**, 280–288 (2009).

[218] J. Lee and S. Timasheff, 'The stabilization of proteins by sucrose.', *Journal of Biological Chemistry* **256**, 7193–7201 (1981).

[219] F. C. Spano, 'The Spectral Signatures of Frenkel Polarons in H- and J-Aggregates', *Accounts of Chemical Research* **43**, 429–439 (2010).

[220] N. J. Hestand and F. C. Spano, 'Expanded Theory of H- and J-Molecular Aggregates: The Effects of Vibronic Coupling and Intermolecular Charge Transfer', *Chemical Reviews* **118**, 7069–7163 (2018).

[221] J. Clark, C. Silva, R. H. Friend, and F. C. Spano, 'Role of Intermolecular Coupling in the Photophysics of Disordered Organic Semiconductors: Aggregate Emission in Regioregular Polythiophene', *Physical Review Letters* **98**, 206406 (2007).

[222] R. Y. Pishchalnikov, I. A. Yaroshevich, T. A. Slastnikova, A. A. Ashikhmin, A. V. Stepanov, E. A. Slutskaya, T. Friedrich, N. N. Sluchanko, and E. G. Maksimov, 'Structural peculiarities of keto-carotenoids in water-soluble proteins revealed by simulation of linear absorption', *Physical Chemistry Chemical Physics* **21**, 25707–25719 (2019).

[223] J. R. Lakowicz, *Principles of Fluorescence Spectroscopy*, 3rd edition (Springer, New York, 2006).

[224] P. Bouguer, *Essai d'optique, sur la gradation de la lumiere* (Claude Jombert, Paris, France, 1729).

[225] J. H. Lambert, *Photometria sive de mensura et gradibus luminis, colorum et umbrae* (Eberhardt Klett, Augsburg, Germany, 1760).

[226] A. Beer, 'Bestimmung der Absorption des rothen Lichts in farbigen Flüssigkeiten', *Annalen der Physik* **162**, 78–88 (1852).

[227] J. Mooney and P. Kambhampati, 'Get the Basics Right: Jacobian Conversion of Wavelength and Energy Scales for Quantitative Analysis of Emission Spectra', *The Journal of Physical Chemistry Letters* **4**, 3316–3318 (2013).

[228] K. F. Riley, M. P. Hobson, and S. J. Bence, 'Multiple integrals', in *Mathematical Methods for Physics and Engineering*, 3rd edition (Cambridge University Press, Cambridge, 2006), pages 187–211.

[229] R. Berera, R. van Grondelle, and J. T. M. Kennis, 'Ultrafast transient absorption spectroscopy: principles and application to photosynthetic systems', *Photosynthesis Research* **101**, 105–118 (2009).

[230] C. Ruckebusch, M. Sliwa, P. Pernot, A. de Juan, and R. Tauler, 'Comprehensive data analysis of femtosecond transient absorption spectra: A review', *Journal of Photochemistry and Photobiology C: Photochemistry Reviews* **13**, 1–27 (2012).

[231] I. H. van Stokkum, D. S. Larsen, and R. van Grondelle, 'Global and target analysis of time-resolved spectra', *Biochimica et Biophysica Acta (BBA) - Bioenergetics* **1657**, 82–104 (2004).

[232] R. J. Fernández-Terán, E. Sucre-Rosales, L. Echevarria, and F. E. Hernández, 'A Sweet Introduction to the Mathematical Analysis of Time-Resolved Spectra and Complex Kinetic Mechanisms: The Chameleon Reaction Revisited', *Journal of Chemical Education* **99**, 2327–2337 (2022).

[233] J. Snellenburg, S. Laptenok, R. Seger, and K. Mullen, 'Glotaran: A Java-based graphical user interface for the R package TIMP', *Journal of Statistical Software* **49** (2012).

[234] K. M. Mullen and I. H. M. van Stokkum, 'TIMP: An R Package for Modeling Multi-way Spectroscopic Measurements', *Journal of Statistical Software* **18**, 1–46 (2007).

[235] G. New, editor, *Introduction to Nonlinear Optics* (Cambridge University Press, Cambridge, 2011).

[236] A. C. Eckbreth, 'BOXCARS: Crossed-beam phase-matched CARS generation in gases', *Applied Physics Letters* **32**, 421–423 (1978).

[237] C. J. Bardeen, 'The Structure and Dynamics of Molecular Excitons', *Annual Review of Physical Chemistry* **65**, 127–148 (2014).

[238] B. Ehrler, N. Yanai, and L. Nienhaus, 'Up- and down-conversion in molecules and materials', *The Journal of Chemical Physics* **154**, 070401 (2021).

[239] B. Daiber, K. van den Hoven, M. H. Futscher, and B. Ehrler, 'Realistic Efficiency Limits for Singlet-Fission Silicon Solar Cells', *ACS Energy Letters* **6**, 2800–2808 (2021).

[240] B. Ehrler, A. W. Y. Ho-Baillie, E. M. Hutter, J. V. Milić, M. J. Y. Tayebjee, and M. W. B. Wilson, 'Scalable ways to break the efficiency limit of single-junction solar cells', *Applied Physics Letters* **120**, 010402 (2022).

[241] B. Kraabel, D. Hulin, C. Aslangul, C. Lapersonne-Meyer, and M. Schott, 'Triplet exciton generation, transport and relaxation in isolated polydiacetylene chains: Subpicosecond pump-probe experiments', *Chemical Physics* **227**, 83–98 (1998).

[242] R. Pandya, Q. Gu, A. Cheminal, R. Y. Chen, E. P. Booker, R. Soucek, M. Schott, L. Legrand, F. Mathevet, N. C. Greenham, T. Barisien, A. J. Musser, A. W. Chin, and A. Rao, 'Optical Projection and Spatial Separation of Spin-Entangled Triplet Pairs from the S_1 (2^1 A_g^-) State of Pi-Conjugated Systems', *Chem* **6**, 2826–2851 (2020).

[243] G. Lanzani, G. Cerullo, M. Zavelani-Rossi, S. De Silvestri, D. Comoretto, G. Musso, and G. Dellepiane, 'Triplet-Exciton Generation Mechanism in a New Soluble (Red-Phase) Polydiacetylene', *Physical Review Letters* **87**, 187402 (2001).

[244] A. J. Musser, M. Al-Hashimi, M. Maiuri, D. Brida, M. Heeney, G. Cerullo, R. H. Friend, and J. Clark, 'Activated Singlet Exciton Fission in a Semiconducting Polymer', *Journal of the American Chemical Society* **135**, 12747–12754 (2013).

[245] E. Lafalce, X. Jiang, and C. Zhang, 'Generation and Recombination Kinetics of Optical Excitations in Poly(3-dodecylthienylenevinylene) with Controlled Regioregularity', *The Journal of Physical Chemistry B* **115**, 13139–13148 (2011).

[246] E. Busby, J. Xia, Q. Wu, J. Z. Low, R. Song, J. R. Miller, X.-Y. Zhu, L. M. Campos, and M. Y. Sfeir, 'A design strategy for intramolecular singlet fission mediated by charge-transfer states in donor-acceptor organic materials', *Nature Materials* **14**, 426–433 (2015).

[247] Y. Kasai, Y. Tamai, H. Ohkita, H. Benten, and S. Ito, 'Ultrafast Singlet Fission in a Push–Pull Low-Bandgap Polymer Film', *Journal of the American Chemical Society* **137**, 15980–15983 (2015).

[248] K. J. Fallon, P. Budden, E. Salvadori, A. M. Ganose, C. N. Savory, L. Eyre, S. Dowland, Q. Ai, S. Goodlett, C. Risko, D. O. Scanlon, C. W. M. Kay, A. Rao, R. H. Friend, A. J. Musser, and H. Bronstein, 'Exploiting Excited-State Aromaticity To Design Highly Stable Singlet Fission Materials', *Journal of the American Chemical Society* **141**, 13867–13876 (2019).

[249] U. N. V. Huynh, T. P. Basel, E. Ehrenfreund, G. Li, Y. Yang, S. Mazumdar, and Z. V. Vardeny, 'Transient Magnetophotoinduced Absorption Studies of Photoexcitations in π-Conjugated Donor-Acceptor Copolymers', *Physical Review Letters* **119**, 017401 (2017).

[250] J. Casado, R. Ponce Ortiz, and J. T. López Navarrete, 'Quinoidal oligothiophenes: new properties behind an unconventional electronic structure', *Chemical Society Reviews* **41**, 5672–5686 (2012).

[251] O. Varnavski, N. Abeyasinghe, J. Aragó, J. J. Serrano-Pérez, E. Ortí, J. T. López Navarrete, K. Takimiya, D. Casanova, J. Casado, and T. Goodson, 'High Yield Ultrafast Intramolecular Singlet Exciton Fission in a Quinoidal Bithiophene', *The Journal of Physical Chemistry Letters* **6**, 1375–1384 (2015).

[252] A. D. Chien, A. R. Molina, N. Abeyasinghe, O. P. Varnavski, T. Goodson, and P. M. Zimmerman, 'Structure and Dynamics of the ^{1}(TT) State in a Quinoidal Bithiophene: Characterizing a Promising Intramolecular Singlet Fission Candidate', *The Journal of Physical Chemistry C* **119**, 28258–28268 (2015).

[253] H. Kim, B. Keller, R. Ho-Wu, N. Abeyasinghe, R. J. Vázquez, T. Goodson, and P. M. Zimmerman, 'Enacting Two-Electron Transfer from a Double-Triplet State of Intramolecular Singlet Fission', *Journal of the American Chemical Society* **140**, 7760–7763 (2018).

[254] S. Kawata, Y.-J. Pu, A. Saito, Y. Kurashige, T. Beppu, H. Katagiri, M. Hada, and J. Kido, 'Singlet Fission of Non-polycyclic Aromatic Molecules in Organic Photovoltaics', *Advanced Materials* **28**, 1585–1590 (2016).

[255] T. Ullrich, P. Pinter, J. Messelberger, P. Haines, R. Kaur, M. M. Hansmann, D. Munz, and D. M. Guldi, 'Singlet Fission in Carbene-Derived Diradicaloids', *Angewandte Chemie International Edition* **59**, 7906–7914 (2020).

[256] Y. Wu, Y. Wang, J. Chen, G. Zhang, J. Yao, D. Zhang, and H. Fu, 'Intramolecular Singlet Fission in an Antiaromatic Polycyclic Hydrocarbon', *Angewandte Chemie International Edition* **56**, 9400–9404 (2017).

[257] Y. Liu, Y. Wu, L. Wang, L. Wang, J. Yao, and H. Fu, 'Efficient triplet pair separation from intramolecular singlet fission in dibenzopentalene derivatives', *Science China Chemistry* **62**, 1037–1043 (2019).

[258] C. A. Kerfeld, M. Sutter, and R. L. Leverenz, 'Structure of orange carotenoid protein binding canthaxanthin', *PDB*, DOI:10.2210/pdb4XB5/pdb (2014).

[259] C. A. Kerfeld, M. Sutter, and R. L. Leverenz, 'Structure of the N-terminal domain of OCP binding canthaxanthin', *PDB*, DOI:10.2210/pdb4XB4/pdb (2014).

[260] L. M. Yablon, S. N. Sanders, K. Miyazaki, E. Kumarasamy, G. He, B. Choi, N. Ananth, M. Y. Sfeir, and L. M. Campos, 'Singlet fission and triplet pair recombination in bipentacenes with a twist', *Materials Horizons* **9**, 462–470 (2022).

[261] H. Kingma, R. van Grondelle, and L. Duysens, 'Magnetic-field effects in photosynthetic bacteria. I. Magnetic-field-induced bacteriochlorophyll emission changes in the reaction center and the antenna of *Rhodospirillum rubrum*, *Rhodopseudomonas sphaeroides* and *Prosthecochloris aestuarii*', *Biochimica et Biophysica Acta (BBA) - Bioenergetics* **808**, 363–382 (1985).

[262] H. Kingma, R. van Grondelle, and L. Duysens, 'Magnetic-field effects in photosynthetic bacteria. II. Formation of triplet states in the reaction center and the antenna of *Rhodospirillum rubrum* and *Rhodopseudomonas sphaeroides*. Magnetic-field effects', *Biochimica et Biophysica Acta (BBA) - Bioenergetics* **808**, 383–399 (1985).

[263] H. Rademaker, A. J. Hoff, R. Van Grondelle, and L. N. Duysens, 'Carotenoid triplet yields in normal and deuterated *Rhodospirillum rubrum*', *Biochimica et Biophysica Acta (BBA) - Bioenergetics* **592**, 240–257 (1980).

[264] I. B. Klenina, Z. K. Makhneva, A. A. Moskalenko, A. N. Kuzmin, and I. I. Proskuryakov, 'Singlet-triplet excitation fission in light-harvesting complexes of photosynthetic bacteria and in isolated carotenoids', *Biophysics* **58**, 43–50 (2013).

[265] I. B. Klenina, Z. K. Makhneva, A. A. Moskalenko, N. D. Gudkov, M. A. Bolshakov, E. A. Pavlova, and I. I. Proskuryakov, 'Singlet-triplet fission of carotenoid excitation in light-harvesting LH2 complexes of purple phototrophic bacteria', *Biochemistry (Moscow)* **79**, 235–241 (2014).

[266] A. A. Gryaznov, I. B. Klenina, Z. K. Makhneva, A. A. Moskalenko, and I. I. Proskuryakov, 'The Singlet–Triplet Fission of Carotenoid Excitation in Light-Harvesting Complexes from *Thermochromatium tepidum*', *Biophysics* **64**, 847–852 (2019).

[267] M. Bondanza, L. Cupellini, P. Faccioli, and B. Mennucci, 'Molecular Mechanisms of Activation in the Orange Carotenoid Protein Revealed by Molecular Dynamics', *Journal of the American Chemical Society* **142**, 21829–21841 (2020).

[268] H. M. Berman, J. Westbrook, Z. Feng, G. Gilliland, T. N. Bhat, H. Weissig, I. N. Shindyalov, and P. E. Bourne, 'The Protein Data Bank', *Nucleic Acids Research* **28**, 235–242 (2000).

[269] H. Berman, K. Henrick, and H. Nakamura, 'Announcing the worldwide Protein Data Bank', *Nature Structural & Molecular Biology* **10**, 980–980 (2003).

[270] V. Kurashov, M. Gorka, G. E. Milanovsky, T. W. Johnson, D. A. Cherepanov, A. Y. Semenov, and J. H. Golbeck, 'Critical evaluation of electron transfer kinetics in P700–FA/FB, P700–FX, and P700–A1 Photosystem I core complexes in liquid and in trehalose glass', *Biochimica et Biophysica Acta (BBA) - Bioenergetics* **1859**, 1288–1301 (2018).

[271] S. Saito and M. Tasumi, 'Normal-coordinate analysis of retinal isomers and assignments of Raman and infrared bands', *Journal of Raman Spectroscopy* **14**, 236–245 (1983).

[272] H. Benk and H. Sixl, 'Theory of two coupled triplet states', *Molecular Physics* **42**, 779–801 (1981).

[273] S. L. Bayliss, L. R. Weiss, A. Mitioglu, K. Galkowski, Z. Yang, K. Yunusova, A. Surrente, K. J. Thorley, J. Behrends, R. Bittl, J. E. Anthony, A. Rao, R. H. Friend, P. Plochocka, P. C. M. Christianen, N. C. Greenham, and A. D. Chepelianskii, 'Site-selective measurement of coupled spin pairs in an organic semiconductor', *Proceedings of the National Academy of Sciences* **115**, 5077–5082 (2018).

[274] K. Ishikawa, T. Yago, and M. Wakasa, 'Exploring the Structure of an Exchange-Coupled Triplet Pair Generated by Singlet Fission in Crystalline Diphenylhexatriene: Anisotropic Magnetic Field Effects on Fluorescence in High Fields', *The Journal of Physical Chemistry C* **122**, 22264–22272 (2018).

[275] V. Chynwat and H. A. Frank, 'The application of the energy gap law to the S_1 energies and dynamics of carotenoids', *Chemical Physics* **194**, 237–244 (1995).

[276] R. Bensasson, E. J. Land, and B. Maudinas, 'Triplet States of Carotenoids from Photosynthetic Bacteria Studied by Nanosecond Ultraviolet and Electron Pulse Irradiation', *Photochemistry and Photobiology* **23**, 189–193 (1976).

[277] R. Bensasson, E. A. Dawe, D. A. Long, and E. J. Land, 'Singlet → triplet intersystem crossing quantum yields of photosynthetic and related polyenes', *Journal of the Chemical Society, Faraday Transactions 1: Physical Chemistry in Condensed Phases* **73**, 1319–1325 (1977).

[278] S. K. Chattopadhyay, P. K. Das, and G. L. Hug, 'Photoprocesses in diphenylpolyenes. 2. Excited-state interactions with stable free radicals', *Journal of the American Chemical Society* **105**, 6205–6210 (1983).

[279] R. Fujii, K. Onaka, M. Kuki, Y. Koyama, and Y. Watanabe, 'The $2Ag^-$ energies of all-trans-neurosporene and spheroidene as determined by fluorescence spectroscopy', *Chemical Physics Letters* **288**, 847–853 (1998).

[280] J. J. van Thor, C. W. Mullineaux, H. C. P. Matthijs, and K. J. Hellingwerf, 'Light Harvesting and State Transitions in Cyanobacteria', *Botanica Acta* **111**, 430–443 (1998).

[281] C. W. Mullineaux, 'State transitions: an example of acclimation to low-light stress', *Journal of Experimental Botany* **56**, 389–393 (2005).

[282] C. A. Kerfeld, M. R. Sawaya, V. Brahmandam, D. Cascio, K. K. Ho, C. C. Trevithick-Sutton, D. W. Krogmann, and T. O. Yeates, 'The Crystal Structure of a Cyanobacterial Water-Soluble Carotenoid Binding Protein', *Structure* **11**, 55–65 (2003).

[283] D. Kirilovsky, 'Photoprotection in cyanobacteria: the orange carotenoid protein (OCP)-related non-photochemical-quenching mechanism', *Photosynthesis Research* **93**, 7–16 (2007).

[284] L. Tian, M. Gwizdala, I. H. van Stokkum, R. B. Koehorst, D. Kirilovsky, and H. van Amerongen, 'Picosecond Kinetics of Light Harvesting and Photoprotective Quenching in Wild-Type and Mutant Phycobilisomes Isolated from the Cyanobacterium *Synechocystis* PCC 6803', *Biophysical Journal* **102**, 1692–1700 (2012).

[285] D. Kirilovsky and C. A. Kerfeld, 'Cyanobacterial photoprotection by the orange carotenoid protein', *Nature Plants* **2**, 16180 (2016).

[286] L. Tian, I. H. M. van Stokkum, R. B. M. Koehorst, A. Jongerius, D. Kirilovsky, and H. van Amerongen, 'Site, Rate, and Mechanism of Photoprotective Quenching in Cyanobacteria', *Journal of the American Chemical Society* **133**, 18304–18311 (2011).

[287] K. K. Niyogi, O. Bjorkman, and A. R. Grossman, 'The roles of specific xanthophylls in photoprotection', *Proceedings of the National Academy of Sciences* **94**, 14162–14167 (1997).

[288] A. A. Pascal, Z. Liu, K. Broess, B. van Oort, H. van Amerongen, C. Wang, P. Horton, B. Robert, W. Chang, and A. Ruban, 'Molecular basis of photoprotection and control of photosynthetic light-harvesting', *Nature* **436**, 134–137 (2005).

[289] I. Lutz, A. Sieg, A. A. Wegener, M. Engelhard, I. Boche, M. Otsuka, D. Oesterhelt, J. Wachtveitl, and W. Zinth, 'Primary reactions of sensory rhodopsins', *Proceedings of the National Academy of Sciences* **98**, 962–967 (2001).

[290] X. Yang, Z. Ren, J. Kuk, and K. Moffat, 'Temperature-scan cryocrystallography reveals reaction intermediates in bacteriophytochrome', *Nature* **479**, 428–432 (2011).

[291] N. B. Pigni, K. L. Clark, W. F. Beck, and J. A. Gascón, 'Spectral Signatures of Canthaxanthin Translocation in the Orange Carotenoid Protein', *The Journal of Physical Chemistry B* **124**, 11387–11395 (2020).

[292] M. Bondanza, L. Cupellini, F. Lipparini, and B. Mennucci, 'The Multiple Roles of the Protein in the Photoactivation of Orange Carotenoid Protein', *Chem* **6**, 187–203 (2020).

[293] S. Gupta, M. Sutter, S. G. Remesh, M. A. Dominguez-Martin, H. Bao, X. A. Feng, L.-J. G. Chan, C. J. Petzold, C. A. Kerfeld, and C. Y. Ralston, 'X-ray radiolytic labeling reveals the molecular basis of orange carotenoid protein photoprotection and its interactions with fluorescence recovery protein', *Journal of Biological Chemistry* **294**, 8848–8860 (2019).

[294] M. Kloz, J. Weißenborn, T. Polívka, H. A. Frank, and J. T. M. Kennis, 'Spectral watermarking in femtosecond stimulated Raman spectroscopy: resolving the nature of the carotenoid S* state', *Physical Chemistry Chemical Physics* **18**, 14619–14628 (2016).

[295] D. Niedzwiedzki, J. F. Koscielecki, H. Cong, J. O. Sullivan, G. N. Gibson, R. R. Birge, and H. A. Frank, 'Ultrafast Dynamics and Excited State Spectra of Open-Chain Carotenoids at Room and Low Temperatures', *The Journal of Physical Chemistry B* **111**, 5984–5998 (2007).

[296] C. Kolano, J. Helbing, M. Kozinski, W. Sander, and P. Hamm, 'Watching hydrogen-bond dynamics in a β-turn by transient two-dimensional infrared spectroscopy', *Nature* **444**, 469–472 (2006).

[297] T. Polívka, P. Chábera, and C. A. Kerfeld, 'Carotenoid–protein interaction alters the S_1 energy of hydroxyechinenone in the Orange Carotenoid Protein', *Biochimica et Biophysica Acta (BBA) - Bioenergetics* **1827**, 248–254 (2013).

[298] H. Bao, M. R. Melnicki, E. G. Pawlowski, M. Sutter, M. Agostoni, S. Lechno-Yossef, F. Cai, B. L. Montgomery, and C. A. Kerfeld, 'Additional families of orange carotenoid proteins in the photoprotective system of cyanobacteria', *Nature Plants* **3**, 17089 (2017).

[299] A. Polgár and L. Zechmeister, 'Isomerization of β-Carotene. Isolation of a Stereoisomer with Increased Adsorption Affinity', *Journal of the American Chemical Society* **64**, 1856–1861 (1942).

[300] L. Zechmeister, '*Cis-Trans* Isomerization and Stereochemistry of Carotenoids and Diphenylpolyenes', *Chemical Reviews* **34**, 267–344 (1944).

[301] C. A. Pesek and J. J. Warthesen, 'Kinetic model for photoisomerization and concomitant photodegradation of β-carotenes', *Journal of Agricultural and Food Chemistry* **38**, 1313–1315 (1990).

[302] A. Wilson, J. N. Kinney, P. H. Zwart, C. Punginelli, S. D'Haene, F. Perreau, M. G. Klein, D. Kirilovsky, and C. A. Kerfeld, 'Structural Determinants Underlying Photoprotection in the Photoactive Orange Carotenoid Protein of Cyanobacteria', *Journal of Biological Chemistry* **285**, 18364–18375 (2010).

[303] T. Polívka, C. A. Kerfeld, T. Pascher, and V. Sundström, 'Spectroscopic Properties of the Carotenoid 3′-Hydroxyechinenone in the Orange Carotenoid Protein from the Cyanobacterium *Arthrospira maxima*', *Biochemistry* **44**, 3994–4003 (2005).

[304] M. Fuciman, G. Keşan, A. M. LaFountain, H. A. Frank, and T. Polívka, 'Tuning the Spectroscopic Properties of Aryl Carotenoids by Slight Changes in Structure', *The Journal of Physical Chemistry B* **119**, 1457–1467 (2015).

[305] S. Bondarev and V. Knyukshto, 'Fluorescence from the S_1 (2^1Ag) state of all-trans-β-carotene', *Chemical Physics Letters* **225**, 346–350 (1994).

[306] S. Niziński, I. Schlichting, J.-P. Colletier, D. Kirilovsky, G. Burdzinski, and M. Sliwa, 'Is Orange Carotenoid Protein photoactivation a single-photon process?', *Biophysical Reports*, 100072 (2022).

[307] Y. Koyama, Y. Kakitani, and H. Nagae, 'Mechanisms of *Cis-Trans* Isomerization around the Carbon–Carbon Double Bonds via the Triplet State', in cis-trans *Isomerization in Biochemistry*, edited by C. Dugave (Wiley-VCH, Weinheim, 2006), pages 15–51.

[308] H. Hashimoto and Y. Koyama, 'Time-Resolved Resonance Raman Spectroscopy of Triplet β-Carotene Produced from All-Trans, 7-Cis, 9-Cis, 13-Cis, and 15-Cis Isomers and High-Pressure Liquid Chromatography Analyses of Photoisomerization via the Triplet State', *The Journal of Physical Chemistry* **92**, 2101–2108 (1988).

[309] H. Hashimoto, Y. Koyama, K. Ichimura, and T. Kobayashi, 'Time-resolved absorption spectroscopy of the triplet state produced from the all-trans, 7-cis, 9-cis, 13-cis, and 15-cis isomers of β-carotene', *Chemical Physics Letters* **162**, 517–522 (1989).

[310] H. Hashimoto, Y. Koyama, Y. Hirata, and N. Mataga, 'S_1 and T_1 Species of β-Carotene Generated by Direct Photoexcitation from the All-Trans, 9-Cis, 13-Cis, and 15-Cis Isomers As Revealed by Picosecond Transient Absorption and Transient Raman Spectroscopies', *The Journal of Physical Chemistry* **95**, 3072–3078 (1991).

[311] M. Kuki, Y. Koyama, and H. Nagae, 'Triplet-sensitized and thermal isomerization of all-trans, 7-cis, 9-cis, 13-cis and 15-cis isomers of β-carotene: configurational dependence of the quantum yield of isomerization via the T1 state', *The Journal of Physical Chemistry* **95**, 7171–7180 (1991).

[312] H.-W. Choe, Y. J. Kim, J. H. Park, T. Morizumi, E. F. Pai, N. Krauß, K. P. Hofmann, P. Scheerer, and O. P. Ernst, 'Crystal structure of metarhodopsin II', *Nature* **471**, 651–655 (2011).

[313] P. D. Kiser, M. Golczak, and K. Palczewski, 'Chemistry of the Retinoid (Visual) Cycle', *Chemical Reviews* **114**, 194–232 (2014).

[314] H.-o. Hamaguchi, H. Okamoto, and M. Tasumi, 'Transient raman spectra of all-trans-and 9-cis-retinal in the excited triplet state', *Chemistry Letters* **13**, 549–550 (1984).

[315] H.-o. Hamaguchi, H. Okamoto, M. Tasumi, Y. Mukai, and Y. Koyama, 'Transient Raman spectra of the all-trans and 7-, 9-, 11- and 13-mono-cis isomers of retinal and the mechanism of the cis-trans isomerization in the lowest excited triplet state', *Chemical Physics Letters* **107**, 355–359 (1984).

[316] Y. Hirata, N. Mataga, Y. Mukai, and Y. Koyama, 'Picosecond time-resolved absorption study of all-trans- and 9-cis-retinal: configurational relaxation in the triplet state', *Chemical Physics Letters* **134**, 166–170 (1987).

[317] Y. Mukai, Y. Koyama, Y. Hirata, and N. Mataga, 'Configurational changes of retinal in the triplet state: picosecond time-resolved absorption spectroscopy on the 7-cis, 11-cis, and 13-cis isomers and high-performance liquid chromatography analysis of photoisomerization', *The Journal of Physical Chemistry* **92**, 4649–4653 (1988).

[318] N. H. Jensen, R. Wilbrandt, and R. V. Bensasson, 'Sensitized Photoisomerization of *all-trans*- and 11-*cis*-Retinal', *Journal of the American Chemical Society* **111**, 7877–7888 (1989).

[319] M. Merchán and R. González-Luque, '*Ab initio* study on the low-lying excited states of retinal', *The Journal of Chemical Physics* **106**, 1112–1122 (1997).

[320] M. Chessin, R. Livingston, and T. G. Truscott, 'Direct evidence for the sensitized formation of a metastable state of β-carotene', *Transactions of the Faraday Society* **62**, 1519 (1966).

[321] S. Bachilo, 'β-carotene triplet state absorption in the near-IR range', *Journal of Photochemistry and Photobiology A: Chemistry* **91**, 111–115 (1995).

[322] R. Farhoosh, V. Chynwat, R. Gebhard, J. Lugtenburg, and H. A. Frank, 'Triplet Energy Transfer between the Primary Donor and Carotenoids in *Rhodobacter sphaeroides* R-26.1 Reaction Centers Incorporated with Spheroidene Analogs Having Different Extents of π-Electron Conjugation', *Photochemistry and Photobiology* **66**, 97–104 (1997).

[323] M. K. Kuimova, M. Hoffmann, M. U. Winters, M. Eng, M. Balaz, I. P. Clark, H. A. Collins, S. M. Tavender, C. J. Wilson, B. Albinsson, H. L. Anderson, A. W. Parker, and D. Phillips, 'Determination of the triplet state energies of a series of conjugated porphyrin oligomers', *Photochemical & Photobiological Sciences* **6**, 675–682 (2007).

[324] R. Wilbrandt and N.-H. Jensen, 'Time-Resolved Resonance Raman Spectroscopy: Excited Triplet States of Biological Polyenes', *Berichte der Bunsengesellschaft für physikalische Chemie* **85**, 508–511 (1981).

[325] W.-H. Guo, C.-Y. Tu, and C.-H. Hu, 'Cis-Trans Isomerizations of β-Carotene and Lycopene: A Theoretical Study', *The Journal of Physical Chemistry B* **112**, 12158–12167 (2008).

[326] L. Köhler, W. Gärtner, J. Matysik, and C. Song, 'Long-Term Preservation of Short-Lived Photoproducts of Phytochromes at Room Temperature', *ChemPhotoChem* **6**, e202100220 (2022).

[327] S. Sikora, A. S. Little, and T. G. Dewey, 'Room Temperature Trapping of Rhodopsin Photointermediates', *Biochemistry* **33**, 4454–4459 (1994).

[328] G. I. Olgenblum, F. Wien, L. Sapir, and D. Harries, 'β-Hairpin Miniprotein Stabilization in Trehalose Glass Is Facilitated by an Emergent Compact Non-Native State', *The Journal of Physical Chemistry Letters* **12**, 7659–7664 (2021).

[329] J. Akahane, F. S. Rondonuwu, L. Fiedor, Y. Watanabe, and Y. Koyama, 'Dependence of singlet-energy transfer on the conjugation length of carotenoids reconstituted into the LH1 complex from *Rhodospirillum rubrum* G9', *Chemical Physics Letters* **393**, 184–191 (2004).

[330] Z. S. Kolber, C. L. Van Dover, R. A. Niederman, and P. G. Falkowski, 'Bacterial photosynthesis in surface waters of the open ocean', *Nature* **407**, 177–179 (2000).

[331] Z. S. Kolber, F. Gerald, n. Plumley, A. S. Lang, J. T. Beatty, R. E. Blankenship, C. L. VanDover, C. Vetriani, M. Koblizek, C. Rathgeber, and P. G. Falkowski, 'Contribution of Aerobic Photoheterotrophic Bacteria to the Carbon Cycle in the Ocean', *Science* **292**, 2492–2495 (2001).

[332] O. Béjà, M. T. Suzuki, J. F. Heidelberg, W. C. Nelson, C. M. Preston, T. Hamada, J. A. Eisen, C. M. Fraser, and E. F. DeLong, 'Unsuspected diversity among marine aerobic anoxygenic phototrophs', *Nature* **415**, 630–633 (2002).

[333] M. Koblížek, 'Ecology of aerobic anoxygenic phototrophs in aquatic environments', *FEMS Microbiology Reviews* **39**, 854–870 (2015).

[334] J. K. Gurchiek, H. Bao, M. A. Domínguez-Martín, S. E. McGovern, C. E. Marquardt, J. D. Roscioli, S. Ghosh, C. A. Kerfeld, and W. F. Beck, 'Fluorescence and Excited-State Conformational Dynamics of the Orange Carotenoid Protein', *The Journal of Physical Chemistry B* **122**, 1792–1800 (2018).

[335] R. M. Jacobberger, Y. Qiu, M. L. Williams, M. D. Krzyaniak, and M. R. Wasielewski, 'Using Molecular Design to Enhance the Coherence Time of Quintet Multiexcitons Generated by Singlet Fission in Single Crystals', *Journal of the American Chemical Society* **144**, 2276–2283 (2022).

[336] V. Šlouf, P. Chábera, J. D. Olsen, E. C. Martin, P. Qian, C. N. Hunter, and T. Polívka, 'Photoprotection in a purple phototrophic bacterium mediated by oxygen-dependent alteration of carotenoid excited-state properties', *Proceedings of the National Academy of Sciences* **109**, 8570–8575 (2012).

[337] D. M. Niedzwiedzki, C. N. Hunter, and R. E. Blankenship, 'Evaluating the Nature of So-Called S*-State Feature in Transient Absorption of Carotenoids in Light-Harvesting Complex 2 (LH2) from Purple Photosynthetic Bacteria', *The Journal of Physical Chemistry B* **120**, 11123–11131 (2016).

[338] D. M. Niedzwiedzki, D. J. K. Swainsbury, D. P. Canniffe, C. N. Hunter, and A. Hitchcock, 'A photosynthetic antenna complex foregoes unity carotenoid-to-bacteriochlorophyll energy transfer efficiency to ensure photoprotection', *Proceedings of the National Academy of Sciences* **117**, 6502–6508 (2020).

[339] A. Quaranta, A. Krieger-Liszkay, A. A. Pascal, F. Perreau, B. Robert, M. Vengris, and M. J. Llansola-Portoles, 'Singlet fission in naturally-organized carotenoid molecules', *Physical Chemistry Chemical Physics* **23**, 4768–4776 (2021).

[340] E. Papagiannakis, S. K. Das, A. Gall, I. H. M. van Stokkum, B. Robert, R. van Grondelle, H. A. Frank, and J. T. M. Kennis, 'Light Harvesting by Carotenoids Incorporated into the B850 Light-Harvesting Complex from *Rhodobacter sphaeroides* R-26.1: Excited-State Relaxation, Ultrafast Triplet Formation, and Energy Transfer to Bacteriochlorophyll', *The Journal of Physical Chemistry B* **107**, 5642–5649 (2003).

[341] P. Qian, D. J. Swainsbury, T. I. Croll, J. H. Salisbury, E. C. Martin, P. J. Jackson, A. Hitchcock, P. Castro-Hartmann, K. Sader, and C. N. Hunter, 'Cryo-EM structure of the monomeric *Rhodobacter sphaeroides* RC–LH1 core complex at 2.5 Å', *Biochemical Journal* **478**, 3775–3790 (2021).

[342] E. F. Pettersen, T. D. Goddard, C. C. Huang, E. C. Meng, G. S. Couch, T. I. Croll, J. H. Morris, and T. E. Ferrin, 'UCSF ChimeraX: Structure visualization for researchers, educators, and developers', *Protein Science* **30**, 70–82 (2021).

[343] G. A. Sutherland, P. Qian, C. N. Hunter, D. J. Swainsbury, and A. Hitchcock, 'Engineering purple bacterial carotenoid biosynthesis to study the roles of carotenoids in light-harvesting complexes', in *Methods in Enzymology*, Vol. 674 (Elsevier, 2022), pages 137–184.

[344] S. C. Chi, D. J. Mothersole, P. Dilbeck, D. M. Niedzwiedzki, H. Zhang, P. Qian, C. Vasilev, K. J. Grayson, P. J. Jackson, E. C. Martin, Y. Li, D. Holten, and C. Neil Hunter, 'Assembly of functional photosystem complexes in *Rhodobacter sphaeroides* incorporating carotenoids from the spirilloxanthin pathway', *Biochimica et Biophysica Acta (BBA) - Bioenergetics* **1847**, 189–201 (2015).

[345] H. Cong, D. M. Niedzwiedzki, G. N. Gibson, A. M. LaFountain, R. M. Kelsh, A. T. Gardiner, R. J. Cogdell, and H. A. Frank, 'Ultrafast Time-Resolved Carotenoid to-Bacteriochlorophyll Energy Transfer in LH2 Complexes from Photosynthetic Bacteria', *The Journal of Physical Chemistry B* **112**, 10689–10703 (2008).

[346] L. Wang, S. Bai, Y. Wu, Y. Liu, J. Yao, and H. Fu, 'Revealing the Nature of Singlet Fission under the Veil of Internal Conversion', *Angewandte Chemie International Edition* **59**, 2003–2007 (2020).

[347] R. E. Merrifield, 'Magnetic effects on triplet exciton interactions', *Pure and Applied Chemistry* **27**, 481–498 (1971).

[348] G. D. Scholes, 'Correlated Pair States Formed by Singlet Fission and Exciton–Exciton Annihilation', *The Journal of Physical Chemistry A* **119**, 12699–12705 (2015).

[349] G. A. Sutherland, J. P. Pidgeon, H. K. H. Lee, M. S. Proctor, A. Hitchcock, S. Wang, D. Chekulaev, W. C. Tsoi, M. P. Johnson, C. N. Hunter, and J. Clark, 'Twisted Carotenoids Do Not Support Efficient Intramolecular Singlet Fission in the Orange Carotenoid Protein', *The Journal of Physical Chemistry Letters* **14**, 6135–6142 (2023).

[350] D. Kosumi, T. Nishiguchi, Y. Amao, R. Cogdell, and H. Hashimoto, 'Singlet and triplet excited states dynamics of photosynthetic pigment chlorophyll *a* investigated by sub-nanosecond pump-probe spectroscopy', *Journal of Photochemistry and Photobiology A: Chemistry* **358**, 374–378 (2018).

[351] M. Gouterman, 'A Theory for the Triplet-Triplet Absorption Spectra of Porphyrins', *The Journal of Chemical Physics* **33**, 1523–1529 (1960).

[352] S. Tobita, Y. Kaizu, H. Kobayashi, and I. Tanaka, 'Study of higher excited singlet states of zinc (II)-tetraphenylporphin', *The Journal of Chemical Physics* **81**, 2962–2969 (1984).

[353] F. S. Rondonuwu, Y. Watanabe, R. Fujii, and Y. Koyama, 'A first detection of singlet to triplet conversion from the $1^1B_u^-$ to the 1^3A_g state and triplet internal conversion from the 1^3A_g to the 1^3B_u state in carotenoids: Dependence on the conjugation length', *Chemical Physics Letters* **376**, 292–301 (2003).

[354] R. Fujii, K. Furuichi, J.-P. Zhang, H. Nagae, H. Hashimoto, and Y. Koyama, 'Cis-to-trans Isomerization of Spheroidene in the Triplet State as Detected by Time-Resolved Absorption Spectroscopy', *The Journal of Physical Chemistry A* **106**, 2410–2421 (2002).

[355] R. J. Cogdell, E. J. Land, and T. G. Truscott, 'The triplet extinction coefficients of some bacterial carotenoids', *Photochemistry and Photobiology* **38**, 723–725 (1983).

[356] P. Qian, T. I. Croll, D. J. Swainsbury, P. Castro-Hartmann, N. W. Moriarty, K. Sader, and C. N. Hunter, 'Cryo-EM structure of the *Rhodospirillum rubrum* RC–LH1 complex at 2.5 Å', *Biochemical Journal* **478**, 3253–3263 (2021).

[357] F. S. Rondonuwu, T. Taguchi, R. Fujii, K. Yokoyama, Y. Koyama, and Y. Watanabe, 'The energies and kinetics of triplet carotenoids in the LH2 antenna complexes as determined by phosphorescence spectroscopy', *Chemical Physics Letters* **384**, 364–371 (2004).

[358] P. L. Dilbeck, Q. Tang, D. J. Mothersole, E. C. Martin, C. N. Hunter, D. F. Bocian, D. Holten, and D. M. Niedzwiedzki, 'Quenching Capabilities of Long-Chain Carotenoids in Light-Harvesting-2 Complexes from *Rhodobacter sphaeroides* with an Engineered Carotenoid Synthesis Pathway', *The Journal of Physical Chemistry B* **120**, 5429–5443 (2016).

[359] D. A. Hartzler, D. M. Niedzwiedzki, D. A. Bryant, R. E. Blankenship, Y. Pushkar, and S. Savikhin, 'Triplet Excited State Energies and Phosphorescence Spectra of (Bacterio)Chlorophylls', *The Journal of Physical Chemistry B* **118**, 7221–7232 (2014).

[360] K. Tani, R. Kanno, X.-C. Ji, M. Hall, L.-J. Yu, Y. Kimura, M. T. Madigan, A. Mizoguchi, B. M. Humbel, and Z.-Y. Wang-Otomo, 'Cryo-EM Structure of the Photosynthetic LH1-RC Complex from *Rhodospirillum rubrum*', *Biochemistry* **60**, 2483–2491 (2021).

[361] T. Noguchi, H. Hayashi, and M. Tasumi, 'Factors controlling the efficiency of energy transfer from carotenoids to bacteriochlorophyll in purple photosynthetic bacteria', *Biochimica et Biophysica Acta (BBA) - Bioenergetics* **1017**, 280–290 (1990).

[362] Y. Wan, G. P. Wiederrecht, R. D. Schaller, J. C. Johnson, and L. Huang, 'Transport of Spin-Entangled Triplet Excitons Generated by Singlet Fission', *The Journal of Physical Chemistry Letters* **9**, 6731–6738 (2018).

[363] I. Biaggio and P. Irkhin, 'Extremely efficient exciton fission and fusion and its dominant contribution to the photoluminescence yield in rubrene single crystals', *Applied Physics Letters* **103**, 263301 (2013).

[364] D. G. Bossanyi, Y. Sasaki, S. Wang, D. Chekulaev, N. Kimizuka, N. Yanai, and J. Clark, 'In optimized rubrene-based nanoparticle blends for photon upconversion, singlet energy collection outcompetes triplet-pair separation, not singlet fission', *Journal of Materials Chemistry C* **10**, 4684–4696 (2022).

[365] C. C. Schenck, R. E. Blankenship, and W. W. Parson, 'Radical-pair decay kinetics, triplet yields and delayed fluorescence from bacterial reaction centers', *Biochimica et Biophysica Acta (BBA) - Bioenergetics* **680**, 44–59 (1982).

[366] L. Rinyu, E. W. Martin, E. Takahashi, P. Maróti, and C. A. Wraight, 'Modulation of the free energy of the primary quinone acceptor (QA) in reaction centers from *Rhodobacter sphaeroides*: contributions from the protein and protein–lipid(cardiolipin) interactions', *Biochimica et Biophysica Acta (BBA) - Bioenergetics* **1655**, 93–101 (2004).

[367] D. Polak, R. Jayaprakash, T. P. Lyons, L. Á. Martínez-Martínez, A. Leventis, K. J. Fallon, H. Coulthard, D. G. Bossanyi, K. Georgiou, I. I. Petty Anthony J., J. Anthony, H. Bronstein, J. Yuen-Zhou, A. I. Tartakovskii, J. Clark, and A. J. Musser, 'Manipulating molecules with strong coupling: harvesting triplet excitons in organic exciton microcavities', *Chemical Science* **11**, 343–354 (2020).

[368] N. E. Holt, D. Zigmantas, L. Valkunas, X.-P. Li, K. K. Niyogi, and G. R. Fleming, 'Carotenoid Cation Formation and the Regulation of Photosynthetic Light Harvesting', *Science* **307**, 433–436 (2005).

[369] A. Damjanović, T. Ritz, and K. Schulten, 'Energy transfer between carotenoids and bacteriochlorophylls in light-harvesting complex II of purple bacteria', *Physical Review E* **59**, 3293–3311 (1999).

[370] P. Jahns and A. R. Holzwarth, 'The role of the xanthophyll cycle and of lutein in photoprotection of photosystem II', *Biochimica et Biophysica Acta (BBA) - Bioenergetics* **1817**, 182–193 (2012).

[371] H. Kim, H. Li, J. A. Maresca, D. A. Bryant, and S. Savikhin, 'Triplet Exciton Formation as a Novel Photoprotection Mechanism in Chlorosomes of *Chlorobium tepidum*', *Biophysical Journal* **93**, 192–201 (2007).

[372] R. J. Cogdell, T. D. Howard, R. Bittl, E. Schlodder, I. Geisenheimer, and W. Lubitz, 'How carotenoids protect bacterial photosynthesis', *Philosophical Transactions of the Royal Society of London, Series B: Biological Sciences* **355**, 1345–1349 (2000).

[373] P. C. Lee, E. Holtzapple, and C. Schmidt-Dannert, 'Novel Activity of *Rhodobacter sphaeroides* Spheroidene Monooxygenase CrtA Expressed in *Escherichia coli*', *Applied and Environmental Microbiology* **76**, 7328–7331 (2010).

[374] D. E. Chandler, J. Hsin, C. B. Harrison, J. Gumbart, and K. Schulten, 'Intrinsic Curvature Properties of Photosynthetic Proteins in Chromatophores', *Biophysical Journal* **95**, 2822–2836 (2008).

[375] D. Zigmantas, R. G. Hiller, F. P. Sharples, H. A. Frank, V. Sundström, and T. Polívka, 'Effect of a conjugated carbonyl group on the photophysical properties of carotenoids', *Physical Chemistry Chemical Physics* **6**, 3009–3016 (2004).

[376] J. Glaeser and G. Klug, 'Photo-oxidative stress in *Rhodobacter sphaeroides*: protective role of carotenoids and expression of selected genes', *Microbiology* **151**, 1927–1938 (2005).

[377] P. Qian, D. J. K. Swainsbury, T. I. Croll, P. Castro-Hartmann, G. Divitini, K. Sader, and C. N. Hunter, 'Cryo-EM Structure of the *Rhodobacter sphaeroides* Light-Harvesting 2 Complex at 2.1 Å', *Biochemistry* **60**, 3302–3314 (2021).

[378] D. Polli, G. Cerullo, G. Lanzani, S. De Silvestri, K. Yanagi, H. Hashimoto, and R. J. Cogdell, 'Conjugation Length Dependence of Internal Conversion in Carotenoids: Role of the Intermediate State', *Physical Review Letters* **93**, 163002 (2004).

[379] R. Bittl, E. Schlodder, I. Geisenheimer, W. Lubitz, and R. J. Cogdell, 'Transient EPR and Absorption Studies of Carotenoid Triplet Formation in Purple Bacterial Antenna Complexes', *The Journal of Physical Chemistry B* **105**, 5525–5535 (2001).

[380] M. I. Collins, D. R. McCamey, and M. J. Y. Tayebjee, 'Fluctuating exchange interactions enable quintet multiexciton formation in singlet fission', *The Journal of Chemical Physics* **151**, 164104 (2019).

[381] M. J. Y. Tayebjee, S. N. Sanders, E. Kumarasamy, L. M. Campos, M. Y. Sfeir, and D. R. McCamey, 'Quintet multiexciton dynamics in singlet fission', *Nature Physics* **13**, 182–188 (2017).

[382] L. R. Weiss, S. L. Bayliss, F. Kraffert, K. J. Thorley, J. E. Anthony, R. Bittl, R. H. Friend, A. Rao, N. C. Greenham, and J. Behrends, 'Strongly exchange-coupled triplet pairs in an organic semiconductor', *Nature Physics* **13**, 176–181 (2017).

[383] L. Cupellini, S. Caprasecca, C. A. Guido, F. Müh, T. Renger, and B. Mennucci, 'Coupling to Charge Transfer States is the Key to Modulate the Optical Bands for Efficient Light Harvesting in Purple Bacteria', *The Journal of Physical Chemistry Letters* **9**, 6892–6899 (2018).

[384] E. J. Taffet and G. D. Scholes, 'Peridinin Torsional Distortion and Bond-Length Alternation Introduce Intramolecular Charge-Transfer and Correlated Triplet Pair Intermediate Excited States', *The Journal of Physical Chemistry B* **122**, 5835–5844 (2018).

[385] D.-G. Ha, R. Wan, C. A. Kim, T.-A. Lin, L. Yang, T. Van Voorhis, M. A. Baldo, and M. Dincă, 'Exchange controlled triplet fusion in metal–organic frameworks', *Nature Materials* **21**, 1275–1281 (2022).

[386] S. M. Hart, X. Wang, J. Guo, M. Bathe, and G. S. Schlau-Cohen, 'Tuning Optical Absorption and Emission Using Strongly Coupled Dimers in Programmable DNA Scaffolds', *The Journal of Physical Chemistry Letters* **13**, 1863–1871 (2022).

[387] Y. Kakitani, J. Akahane, H. Ishii, H. Sogabe, H. Nagae, and Y. Koyama, 'Conjugation-Length Dependence of the T_1 Lifetimes of Carotenoids Free in Solution and Incorporated into the LH2, LH1, RC, and RC-LH1 Complexes: Possible Mechanisms of Triplet-Energy Dissipation', *Biochemistry* **46**, 2181–2197 (2007).

[388] C. Eichwald and J. Walleczek, 'Model for Magnetic Field Effects on Radical Pair Recombination in Enzyme Kinetics', *Biophysical Journal* **71**, 623–631 (1996).

[389] A. J. Hoff, 'Magnetic field effects on photosynthetic reactions', *Quarterly Reviews of Biophysics* **14**, 599–665 (1981).

[390] H. M. Hoang, V. T. B. Pham, G. Grampp, and D. R. Kattnig, 'Magnetic Field-Sensitive Radical Pair Dynamics in Polymethylene Ether-Bridged Donor–Acceptor Systems', *ACS Omega* **3**, 10296–10305 (2018).

[391] M. Wakasa, M. Kaise, T. Yago, R. Katoh, Y. Wakikawa, and T. Ikoma, 'What Can Be Learned from Magnetic Field Effects on Singlet Fission: Role of Exchange Interaction in Excited Triplet Pairs', *The Journal of Physical Chemistry C* **119**, 25840–25844 (2015).

[392] P. Sebban and I. Moya, 'Fluorescence lifetime spectra of in vivo bacteriochlorophyll at room temperature', *Biochimica et Biophysica Acta (BBA) - Bioenergetics* **722**, 436–442 (1983).

[393] C. F. Borland, D. J. McGarvey, T. G. Truscott, R. J. Codgell, and E. J. Land, 'Photophysical studies of bacteriochlorophyll *a* and bacteriopheophytin *a* — singlet oxygen generation', *J. Photochem. Photobiol. B* **1**, 93–101 (1987).

[394] D. Kosumi, T. Horibe, M. Sugisaki, R. J. Cogdell, and H. Hashimoto, 'Photoprotection Mechanism of Light-Harvesting Antenna Complex from Purple Bacteria', *The Journal of Physical Chemistry B* **120**, 951–956 (2016).

[395] J. Jaumot, R. Gargallo, A. de Juan, and R. Tauler, 'A graphical user-friendly interface for MCR-ALS: a new tool for multivariate curve resolution in MATLAB', *Chemometrics and Intelligent Laboratory Systems* **76**, 101–110 (2005).

[396] J. Jaumot, A. de Juan, and R. Tauler, 'MCR-ALS GUI 2.0: New features and applications', *Chemometrics and Intelligent Laboratory Systems* **140**, 1–12 (2015).

[397] T. G. Monger, R. J. Cogdell, and W. W. Parson, 'Triplet states of bacteriochlorophyll and carotenoids in chromatophores of photosynthetic bacteria', *Biochimica et Biophysica Acta (BBA) - Bioenergetics* **449**, 136–153 (1976).

[398] D. M. Niedzwiedzki and R. E. Blankenship, 'Singlet and triplet excited state properties of natural chlorophylls and bacteriochlorophylls', *Photosynthesis Research* **106**, 227–238 (2010).

[399] G. Hartwich, H. Scheer, V. Aust, and A. Angerhofer, 'Absorption and ADMR studies on bacterial photosynthetic reaction centres with modified pigments', *Biochimica et Biophysica Acta (BBA) - Bioenergetics* **1230**, 97–113 (1995).

[400] H. A. Frank, R. Z. B. Desamero, V. Chynwat, R. Gebhard, I. van der Hoef, F. J. Jansen, J. Lugtenburg, D. Gosztola, and M. R. Wasielewski, 'Spectroscopic Properties of Spheroidene Analogs Having Different Extents of π-Electron Conjugation', *The Journal of Physical Chemistry A* **101**, 149–157 (1997).

[401] T. Sashima, Y. Koyama, T. Yamada, and H. Hashimoto, 'The $1B_u^+$, $1B_u^-$, and $2A_g^-$ Energies of Crystalline Lycopene, β-Carotene, and Mini-9-β-carotene as Determined by Resonance-Raman Excitation Profiles: Dependence of the $1B_u^-$ State Energy on the Conjugation Length', *The Journal of Physical Chemistry B* **104**, 5011–5019 (2000).

[402] J.-P. Zhang, R. Fujii, P. Qian, T. Inaba, T. Mizoguchi, Y. Koyama, K. Onaka, Y. Watanabe, and H. Nagae, 'Mechanism of the Carotenoid-to-Bacteriochlorophyll Energy Transfer via the S_1 State in the LH2 Complexes from Purple Bacteria', *The Journal of Physical Chemistry B* **104**, 3683–3691 (2000).

[403] V. Šlouf, G. Keşan, R. Litvín, D. J. K. Swainsbury, E. C. Martin, C. N. Hunter, and T. Polívka, 'Carotenoid to bacteriochlorophyll energy transfer in the RC–LH1–PufX complex from *Rhodobacter sphaeroides* containing the extended conjugation keto-carotenoid diketospirilloxanthin', *Photosynthesis Research* **135**, 33–43 (2018).

[404] H. A. Frank and T. Polívka, 'Energy Transfer from Carotenoids to Bacteriochlorophylls', in *The Purple Phototrophic Bacteria* (Springer, Dordrecht, 2009), pages 213–230.

[405] A. N. Macpherson, J. B. Arellano, N. J. Fraser, R. J. Cogdell, and T. Gillbro, 'Efficient Energy Transfer from the Carotenoid S_2 State in a Photosynthetic Light-Harvesting Complex', *Biophysical Journal* **80**, 923–930 (2001).

[406] M. Ricci, S. E. Bradforth, R. Jimenez, and G. R. Fleming, 'Internal conversion and energy transfer dynamics of spheroidene in solution and in the LH-1 and LH-2 light-harvesting complexes', *Chemical Physics Letters* **259**, 381–390 (1996).

[407] J. Bañuelos, 'BODIPY Dye, the Most Versatile Fluorophore Ever?', *The Chemical Record* **16**, 335–348 (2016).

[408] J. Karolin, L. B.-A. Johansson, L. Strandberg, and T. Ny, 'Fluorescence and Absorption Spectroscopic Properties of Dipyrrometheneboron Difluoride (BODIPY) Derivatives in Liquids, Lipid Membranes, and Proteins', *Journal of the American Chemical Society* **116**, 7801–7806 (1994).

[409] M.-c. Yee, S. C. Fas, M. M. Stohlmeyer, T. J. Wandless, and K. A. Cimprich, 'A Cell-permeable, Activity-based Probe for Protein and Lipid Kinases', *Journal of Biological Chemistry* **280**, 29053–29059 (2005).

[410] Y. Chen, K. Tsao, S. L. Acton, and J. W. Keillor, 'A Green BODIPY-Based, Super-Fluorogenic, Protein-Specific Labelling Agent', *Angewandte Chemie International Edition* **57**, 12390–12394 (2018).

[411] L. Quan, T. Sun, W. Lin, X. Guan, M. Zheng, Z. Xie, and X. Jing, 'BODIPY Fluorescent Chemosensor for Cu^{2+} Detection and Its Applications in Living Cells: Fast Response and High Sensitivity', *Journal of Fluorescence* **24**, 841–846 (2014).

[412] K. Liu, Y. Zhang, T. Zhou, X. Liu, B. Chen, X. Wang, X. Zhao, J. Huo, Y. Wang, and B. Zhu, 'Sequential recognition of Hg^{2+} and I^- based on a novel BODIPY-salen sensor', *Sensors and Actuators B: Chemical* **253**, 1194–1198 (2017).

[413] S. Xia, J. Shen, J. Wang, H. Wang, M. Fang, H. Zhou, and M. Tanasova, 'Ratiometric fluorescent and colorimetric BODIPY-based sensor for zinc ions in solution and living cells', *Sensors and Actuators B: Chemical* **258**, 1279–1286 (2018).

[414] I. Roy, J.-Y. Shin, D. Shetty, J. K. Khedkar, J. H. Park, and K. Kim, 'E-Bodipy fluorescent chemosensor for Zn2+ ion', *Journal of Photochemistry and Photobiology A: Chemistry* **331**, 233–239 (2016).

[415] C. Ray, C. Schad, F. Moreno, B. L. Maroto, J. Bañuelos, T. Arbeloa, I. García-Moreno, C. Villafuerte, G. Muller, and S. de la Moya, 'BCl_3-Activated Synthesis of COO-BODIPY Laser Dyes: General Scope and High Yields under Mild Conditions', *The Journal of Organic Chemistry* **85**, 4594–4601 (2020).

[416] W. Liu, H. Yu, R. Hu, T. Xu, Y. Lun, J. Gan, S. Xu, Z. Yang, and B. Z. Tang, 'Microlasers from AIE-Active BODIPY Derivative', *Small* **16**, 1907074 (2020).

[417] B. M. Squeo and M. Pasini, 'BODIPY platform: a tunable tool for green to NIR OLEDs', *Supramolecular Chemistry* **32**, 56–70 (2020).

[418] B. M. Squeo, L. Ganzer, T. Virgili, and M. Pasini, 'BODIPY-Based Molecules, a Platform for Photonic and Solar Cells', *Molecules* **26**, 153 (2020).

[419] R. T. Grant, P. Michetti, A. J. Musser, P. Gregoire, T. Virgili, E. Vella, M. Cavazzini, K. Georgiou, F. Galeotti, C. Clark, J. Clark, C. Silva, and D. G. Lidzey, 'Efficient Radiative Pumping of Polaritons in a Strongly Coupled Microcavity by a Fluorescent Molecular Dye', *Advanced Optical Materials* **4**, 1615–1623 (2016).

[420] T. Cookson, K. Georgiou, A. Zasedatelev, R. T. Grant, T. Virgili, M. Cavazzini, F. Galeotti, C. Clark, N. G. Berloff, D. G. Lidzey, and P. G. Lagoudakis, 'A Yellow Polariton Condensate in a Dye Filled Microcavity', *Advanced Optical Materials* **5**, 1700203 (2017).

[421] K. Georgiou, P. Michetti, L. Gai, M. Cavazzini, Z. Shen, and D. G. Lidzey, 'Control over Energy Transfer between Fluorescent BODIPY Dyes in a Strongly Coupled Microcavity', *ACS Photonics* **5**, 258–266 (2018).

[422] K. Georgiou, R. Jayaprakash, A. Askitopoulos, D. M. Coles, P. G. Lagoudakis, and D. G. Lidzey, 'Generation of Anti-Stokes Fluorescence in a Strongly Coupled Organic Semiconductor Microcavity', *ACS Photonics* **5**, 4343–4351 (2018).

[423] A. Putintsev, A. Zasedatelev, K. E. McGhee, T. Cookson, K. Georgiou, D. Sannikov, D. G. Lidzey, and P. G. Lagoudakis, 'Nano-second exciton-polariton lasing in organic microcavities', *Applied Physics Letters* **117**, 123302 (2020).

[424] K. E. McGhee, A. Putintsev, R. Jayaprakash, K. Georgiou, M. E. O'Kane, R. C. Kilbride, E. J. Cassella, M. Cavazzini, D. A. Sannikov, P. G. Lagoudakis, and D. G. Lidzey, 'Polariton condensation in an organic microcavity utilising a hybrid metal-DBR mirror', *Scientific Reports* **11**, 20879 (2021).

[425] R. Pandya, A. Ashoka, K. Georgiou, J. Sung, R. Jayaprakash, S. Renken, L. Gai, Z. Shen, A. Rao, and A. J. Musser, 'Tuning the Coherent Propagation of Organic Exciton-Polaritons through Dark State Delocalization', *Advanced Science* **9**, 2105569 (2022).

[426] Y. Kawamura, H. Sasabe, and C. Adachi, 'Simple Accurate System for Measuring Absolute Photoluminescence Quantum Efficiency in Organic Solid-State Thin Films', *Japanese Journal of Applied Physics* **43**, 7729–7730 (2004).

[427] T.-S. Ahn, R. O. Al-Kaysi, A. M. Müller, K. M. Wentz, and C. J. Bardeen, 'Self-absorption correction for solid-state photoluminescence quantum yields obtained from integrating sphere measurements', *Review of Scientific Instruments* **78**, 086105 (2007).

[428] A. J. Musser, S. K. Rajendran, K. Georgiou, L. Gai, R. T. Grant, Z. Shen, M. Cavazzini, A. Ruseckas, G. A. Turnbull, I. D. W. Samuel, J. Clark, and D. G. Lidzey, 'Intermolecular states in organic dye dispersions: excimers vs. aggregates', *Journal of Materials Chemistry C* **5**, 8380–8389 (2017).

[429] R. Haldar, A. Mazel, M. Krstić, Q. Zhang, M. Jakoby, I. A. Howard, B. S. Richards, N. Jung, D. Jacquemin, S. Diring, W. Wenzel, F. Odobel, and C. Wöll, 'A de novo strategy for predictive crystal engineering to tune excitonic coupling', *Nature Communications* **10**, 2048 (2019).

[430] D. Zigmantas, R. G. Hiller, A. Yartsev, V. Sundström, and T. Polívka, 'Dynamics of Excited States of the Carotenoid Peridinin in Polar Solvents: Dependence on Excitation Wavelength, Viscosity, and Temperature', *The Journal of Physical Chemistry B* **107**, 5339–5348 (2003).

[431] P. Chábera, M. Fuciman, K. Razi Naqvi, and T. Polívka, 'Ultrafast dynamics of hydrophilic carbonyl carotenoids – Relation between structure and excited-state properties in polar solvents', *Chemical Physics* **373**, 56–64 (2010).